10/4/18/90 WB (1)

CONF-891046--Vol.1

DOE/METC-89/6108, Vol. 1
(DE90000424)

Proceedings of the Advanced Research and Technology Development Direct Utilization, Instrumentation and Diagnostics Contractors Review Meeting

Volume I

Editors
D.W. Geiling
P.M. Goldberg

October 1989

Sponsored by
U.S. Department of Energy
Office of Fossil Energy
Morgantown Energy Technology Center
Morgantown, West Virginia
and
Pittsburgh Energy Technology Center
Pittsburgh, Pennsylvania

FOSSIL ENERGY

DO NOT MICROFILM COVER

DISTRIBUTION OF THIS DOCUMENT IS UNLIMITED

DISCLAIMER

This report was prepared as an account of work sponsored by an agency of the United States Government. Neither the United States Government nor any agency thereof, nor any of their employees, makes any warranty, express or implied, or assumes any legal liability or responsibility for the accuracy, completeness, or usefulness of any information, apparatus, product, or process disclosed, or represents that its use would not infringe privately owned rights. Reference herein to any specific commercial product, process, or service by trade name, trademark, manufacturer, or otherwise does not necessarily constitute or imply its endorsement, recommendation, or favoring by the United States Government or any agency thereof. The views and opinions of authors expressed herein do not necessarily state or reflect those of the United States Government or any agency thereof.

DISCLAIMER

Portions of this document may be illegible in electronic image products. Images are produced from the best available original document.

DOE/METC--89/6108-Vol.1

DE90 000424

Proceedings of the Advanced Research and Technology Development Direct Utilization, Instrumentation and Diagnostics Contractors Review Meeting

Volume I

Editors
D.W. Geiling
P.M. Goldberg

Sponsored by
U.S. Department of Energy
Office of Fossil Energy
Morgantown Energy Technology Center
P.O. Box 880
Morgantown, West Virginia 26507-0880
and
Pittsburgh Energy Technology Center
P.O. Box 10940
Pittsburgh, Pennsylvania 15236

Held at
Lakeview Resort and Conference Center
Morgantown, West Virginia

October 3-5, 1989

MASTER

DISTRIBUTION OF THIS DOCUMENT IS UNLIMITED

FOREWORD

The 1989 Advanced Research and Technology Development (AR&TD) Direct Utilization, and Instrumentation and Diagnostics Contractors Review Meeting was held October 3-5, 1989, at the Lakeview Resort and Conference Center in Morgantown, West Virginia. The meeting was sponsored by the U.S. Department of Energy (DOE), Office of Fossil Energy, and the Pittsburgh and Morgantown Energy Technology Centers. Each year the meeting provides a forum for the exchange of information among the DOE AR&TD contractors and interested parties. This year's meeting was hosted by the Morgantown Energy Technology Center and was attended by 230 individuals from industry, academia, national laboratories, and other Governmental agencies. Papers were presented on research related to pyrolysis, combustion phenomena, instrumentation, components, coal beneficiation, ash behavior, heat engines, fluidized bed combustion and gas stream cleanup.

The ten technical sessions were chaired by staff from the Pittsburgh and Morgantown Energy Technology Centers. Because of the large number of ongoing projects, a poster session was included to provide the opportunity for interchange among all researchers supported by AR&TD funds. Papers describing these projects are also included in the proceedings. As part of a continuing effort to evaluate different session formats, the session on Gas Stream Cleanup - Particulates was organized as a panel discussion rather than the traditional format featuring a presentation and a question-and-answer period. The panel discussion stimulated informal discussion and was well received.

The proceedings have been reproduced from camera-ready manuscripts furnished by the authors. Papers have not been refereed or edited.

Donald W. Geiling

Donald W. Geiling
Project Manager
Morgantown Energy Technology Center
1989 Conference Technical Coordinator

TABLE OF CONTENTS

Page

VOLUME I

Program Overview -- C.W. Garrett..... 1

SESSION 1 -- PYROLYSIS AND COMBUSTION -- S.M. Smouse..... 21

Kinetics of Rapid Coal Devolatilization -- T.H. Fletcher and D.R. Hardesty..... 23

Rates and Mechanisms of Combustion of Pulverized Coal Chars -- R.E. Mitchell and D.R. Hardesty..... 33

An Engineering Model for Coal Devolatilization -- S.J. Niksa..... 43

Detailed Model for Practical Pulverized Coal Furnaces and Gasifiers -- P.J. Smith, J.D. Hickerson, and L.D. Smoot..... 55

Combustion Research for Advanced Heat Engines -- L.L. Baxter and D.R. Hardesty..... 65

Advanced Combustion Techniques: Pulse Atomization -- G.A. Richards, D.W. Shaw, G.J. Morris, and M.J. Welter..... 75

SESSION 2 -- INSTRUMENTATION AND DIAGNOSTICS -- C.V. Nakaishi..... 85

Optical Detection of Corrosive Compounds -- R.C. Oldenborg..... 87

On-Line Compositional Detection Techniques -- W.P. Chisholm..... 100

In Situ Real-Time Analysis of Particulates -- D.K. Ottesen and D.R. Hardesty..... 107

SESSION 3 -- SURFACE SCIENCE -- D.H. Finseth..... 117

Fundamental Research on Surface Science in Support of Physical Beneficiation of Coal -- R.J. Good, D.V. Keller, Jr. 119

Analytical Characterization of Coal Surfaces and Interfaces -- E.L. Fuller, R.R. Judkins, and V.J. Tennery..... 144

SESSION 4 -- COMPONENTS -- V.P. Kothari..... 153

Fluid Flow Control Device -- M. Novack..... 155

Valveless Ash Removal From Pressurized Fluid-Bed Combustion Systems -- W.B. Hauserman..... 163

TABLE OF CONTENTS
(continued)

Page

SESSION 5A, 6A, 7A, AND 8A -- MINERAL MATTER BEHAVIOR -- P.M. Goldberg and M.P. Mathur..... 173

Transformation of Inorganic Coal Constituents in Combustion Systems -- A.A. Boni, J.J. Helble, S. Srinivasachar, R.C. Flagan, R.W. Bryers, A.F. Sarofim, J.M. Beer, T.W. Peterson, O.L. Wendt, G.P. Huffman, and F.E. Huggins..... 175

The Fate of Mineral Matter During Pulverized Coal Combustion -- L.L. Baxter and D.R. Hardesty..... 223

Combustion Inorganic Transformations -- S.A. Benson, C.J. Zygarlicke, E.N. Steadman, and D.P. McCollor..... 233

Fluid Mechanics of Ash Deposition -- F.D. Shaffer, E.R. Ramer, J.L.S. Chen, and M.P. Mathur..... 242

Research on Thermophoretic and Inertial Aspects of Ash Particle Deposition on Heat Exchanger Surfaces in Coal-Fired Equipment -- D.E. Rosner..... 252

Radiative Properties of Ash and Slag -- P.R. Solomon..... 256

Optical Properties of Fly Ash -- S.A. Self..... 266

SESSION 5B -- DIESELS -- W.C. Smith..... 279

Wear Reduction Systems: Powder-Lubricated Piston Rings for Coal-Fired Diesel Engines -- H. Heshmat..... 281

Wear Reduction System - Liquid Piston Ring -- R.J. Raymond, T-N. Chen, and L. DiNanno..... 301

Fluidic Coal Feed System -- P.R. Badgley, R. Kamo, A. Holmes, and S. Kumar..... 311

SESSION 6B -- TURBINES -- D.W. Geiling..... 323

Assessment of Fouling, Erosion, and Corrosion of Coal-Fired Gas Turbines -- R.K. Ahluwalia, D.K. Schmalzer, and K.H. Im..... 325

Low-Pressure-Ratio Regenerative Exhaust-Heated Gas Turbine -- D.G. Wilson and W.J. Duggan..... 336

Advanced Turbine Design for Coal-Fueled Engines -- J.H. Wagner and B.V. Johnson..... 348

TABLE OF CONTENTS
(continued)

Page

VOLUME II

SESSION 7B AND 8B -- FLUIDIZED BED COMBUSTION -- P.E. Botros and G.A. Nelkin..... 359

Kinetic Behavior of Solid Particles in Fluidized Beds -- H.O. Kono..... 361

Scale Models of a Fluidized Bed Combustor; Simplification of the Scaling Laws Over All Flow Regimes From Bubbling to Circulating Flow and the Scaling of Heat Transfer -- K.W. Roth and L.R. Glicksman..... 371

Particle Motion at Fluidized Bed Tube Surfaces -- J.F. Drennen and D.H. Howard..... 377

AR&TD Instrumentation Fluidization Research -- G.E. Fasching and N.S. Smith, Jr. 379

Collaborative Research on Fluidization Employing Computer-Aided Particle Tracking -- M.M. Chen..... 399

Studies on Coal Devolatilization and Char Reactivity Under PFBC Conditions -- S.Y. Shiao and J.J. Warchol..... 408

Improved Load Turndown Using a Two-Bed Fluidized Combustor -- R.C. Brown..... 422

SESSION 9 -- GAS CLEANUP - PARTICULATES -- R.C. Bedick..... 433

Thermal/Chemical Degradation of Ceramic Candle Filter Materials -- J. Sawyer, J.J. Brown, and N. Brown..... 435

Cordierite Silicon Nitride Filters -- J. Sawyer and B. Buchan..... 439

A Mechanical Analysis of a Ceramic Cross Flow Filter -- T.E. Lippert, D.M. Bachovchin, E.E. Smeltzer, and R.N. Kleiner..... 446

Thermal/Chemical Degradation of Ceramic Cross-Flow Filter Material -- M.A. Alvin, T.E. Lippert, J.E. Lane, R.E. Tressler, and K. Jakus..... 453

Low Cost Filter Development and Control of Permeability in High Temperature, High Pressure Ceramic Filter Elements -- R.A. Long and J.L. Ferri..... 463

Membrane Filter Technology, RBSN Crossflow Filters -- J. Van Ackeren, M.G. Coombs, and H. Strumpf..... 469

Identification of Materials for Hot-Gas Filter Tubesheets -- R.W. Swindeman and R.R. Judkins..... 479

TABLE OF CONTENTS
(continued)

Page

SESSION 10 -- GAS STREAM CLEANUP - SO_x/NO_x -- N.T. Holcombe..... 485

A Novel Concept for the Ultimate Disposal of Off-Gases From Hot-Gas Desulfurization Processes -- S.K. Gangwal and S.M. Harkins..... 487

N_2O Formation in Combustion Systems -- L.J. Muzio, J.C. Kramlich, and G.S. Samuelsen..... 496

Microbial Removal of SO_2 and NO_x from Flue Gas -- K.L. Sublette and G.D. Suciu..... 512

Super-Equilibrium Sulfur Removal from High Temperature Gases -- J.S. Abichandani, A.U. Chatwani, and D.B. Stickler..... 521

POSTER SESSION..... 529

Knowledge Based System for Fluidization Studies -- S.M. Reddy and R. Bajura..... 531

A Study of Techniques for Reducing Ash Deposition in Coal-Fired Gas Turbines -- R.G. Logan..... 540

Mechanistic Reactor Modeling -- E.J. Boyle..... 554

Advanced Combustion Phenomena -- M.L. Swanson, T.A. Moe, and M.E. Collings..... 555

Contaminant Release and Control - NO_x Studies -- K.H. Casleton and R.J. Balla..... 567

Single Particle Combustion Studies -- D.J. Maloney, E.R. Monazam, and L.O. Lawson..... 573

A Mathematical Model for Tar Release in Rapid Devolatilization of a Softening Bituminous Coal -- G.S. Darivakis, W.A. Peters, J.B. Howard, and A.F. Sarofim..... 582

Fundamental Mechanisms of Hot Gas Cleanup -- J.M. Cook and R.V. Siriwardane..... 590

In-Bed and In-Situ Sulfur Capture -- R.J. Anderson..... 599

High-Temperature Inorganic Membrane Separations -- T. McMahon, L. Gasper-Galvin, and P. Hsu..... 600

The Kinetics of Sulfation of Calcium Oxide -- A.F. Sarofim and J.P. Longwell..... 609

TABLE OF CONTENTS
(continued)

Page

Advanced Research in Instrumentation and Control Technology -- S-H. Sheen and A.C. Raptis..... 618

High Temperature Fluorescence Thermometry -- P.S. Shifflett..... 632

On-Line Particle Characterization in Highly Loaded Streams -- P.C. Yue... 633

Artificial Intelligence in Process Control -- L.O. Lawson, J.P. Hensel, J.D. Thornton, B. Solheim, and D.M. Henry..... 641

Smart Structures for Fossil Energy Applications -- R.O. Claus, S.B. Desu, and K.D. Bennett..... 645

Fossil Energy Instrumentation Research Database -- C.V. Nakaishi..... 654

Innovative Coal-Fueled Diesel Engine Injector -- R. Kakwani and D. Doup.. 655

Waste Characterization -- R.J. Conzemius, R. Markuszewski, and G.A. Junk..... 665

The Effect of Non-Spherical Particles on Optical Sizing Measurements -- S.D. Woodruff..... 669

The Use of Gas Chromatography/Matrix Isolation Infrared Spectroscopy (GC/MI-IR) and Supercritical Fluid Chromatography (SFC) For Waste Characterization -- D.K. Schmalzer, A.S. Boparai, D.W. Green, and M.D. Erickson..... 670

APPENDICES..... 681

Appendix A: Agenda, Advanced Research and Technology Development Direct Utilization, Instrumentation and Diagnostics Contractors Review Meeting..... 683

Appendix B: List of Participants, Advanced Research and Technology Development Direct Utilization, Instrumentation and Diagnostics Contractors Review Meeting..... 694

DIRECT UTILIZATION/INSTRUMENTATION AND DIAGNOSTICS CONTRACTORS REVIEW MEETING

PROGRAM OVERVIEW

Charles W. Garrett

October 3, 1989

Good morning. I'd like to add my welcome to those preceding me today. Once again, here we are at the start of what always is a stimulating few days for me. I always leave this meeting with a renewed enthusiasm for our program and a heightened appreciation of the competence that is brought to bear on its research.

As I've said before, the only purpose of this meeting is to give you all an opportunity to interact with one another and to share your insights with your fellow researchers. The degree to which that interaction occurs is the measure of our conference success. So don't just give a talk and hear a bunch of others -- mix it up among your colleagues, here, in the halls, at the poster session, in the bar, and leave here with a net gain that makes it all worthwhile.

Augie, as usual, you have made your contribution to achieving our objective. Just as in our previous years, the hospitality and arrangements provided by METC are superb -- many thanks to you and your staff for all they have done and will be doing on our behalf over the duration of this meeting.

Before I get to the gist of my comments, many thanks, too, to our in-the-field managers -- John Byam and his METC program managers, and to Jim Hickerson, Phil Goldberg , and our contract representatives at PETC. These are the people who provide the technical direction and management talent without which our program would founder and I would be a complete bust!

But good management alone doesn't mean a thing without good research. Without the competence and diligence of those of you performing our work, we managers would just be spinning our wheels. So my appreciation to all of our investigators for their many contributions -- for they provide the essential ingredients of our program's success.

Recall that last year, on our fifth anniversary, I gave an overview and summary of the five-year period. We have now completed the sixth year and my remarks today will be considerably different. I have a special treat in store for you, as I'll soon reveal.

For five years now, I have harped at you -- I urged use of the method of strong inference, asked for your hypotheses, challenged you regarding the data you were collecting, and pleaded with you about how those data might be analyzed and discussed. I suspect that as you listened, you asked yourself, "What's this guy, a government bureaucrat, know. He criticizes us real scientists, tells us how to do our job, then retreats to his Germantown desk for another year of paper pushing."

Well, since I am in the DOE money give-away business and you are the recipients of that dole, always with the hope of more to come, you've kept those views to yourself (or at least away from me). Rather, you have listened politely. In fact, some of you have even complimented me. (However, I note that those kind words have diminished over time as, I presume, you found they bore no relation to the size of your next contract.)

This morning I have news for you. For the past several years, I too have been at the research bench. It has had to be in complete secrecy since a government bureaucrat is not paid to do science. But today I'm coming out of the closet and reporting my results. And herein lies your treat -- after five years of me criticizing yours, for the first time you will have the opportunity to critique my science. A real opportunity for you!

The Direct Utilization and Instrumentation and Diagnostic Programs are broad, and so has been their research. Think about all the things you've studied. You take coal and wash it, float it, leach it and microwave it. You micronize it, slurry it, agglomerate it, and even explosively comminute it. You atomize it, devolatilize it, pyrolize it, and oxidize it. You stage it, precipitate it, filter it, and sorbentize it. You have studied so many nuances, and delved so deeply into all of the facets of coal combustion science. We've learned a great deal from your work.

So in thinking about what I would examine, it quickly became clear that there was no way I could compete with your skills and track record. When I was to choose my research topic, I knew I had better look at coal combustion from a very different perspective -- one that could not be compared with yours. And thus I formulated my principal problem statement, very simple but one I've not heard before: "Will coal burn?"

There are other differences between my research and yours, as we shall see. But before I tell you about it, I must extend an apology to many of you. The breadth of the Utilization and Instrumentation Programs creates a wide variety of competencies in our audience this morning. Coal combustion, the subject of my study, is only a narrow slice in that spectrum, yet it is both complex and sophisticated. So to those of you on its periphery, I beg forgiveness if some of my comments are beyond understanding. Nevertheless, there are some generic lessons to be learned from my research that apply to all. I'll note them in my concluding remarks.

Now let's turn to the first slide, which presents the standard project information... (Figure 1)

In some respects, my project parallels yours. For example, there is the state completion date for public consumption. However, I am also revealing something not often seen -- the actually intended completion date.

Of course, I'm under the same headquarters pressures you feel and I had to state my hypothesis -- which I chose to be the null hypothesis, to be disproved by counterexample.

Now, my project had to be undertaken in great secrecy, for my superiors at headquarters pay me to write budget myths, not to do research. Under cover, then, I had to acquire some funds and a facility in which to work.

Luckily, one field center had a proven fundraiser and the other a team of facilities experts, all of whom could be highly trusted and who agreed to maintain absolute silence.

Also, as all good scientists do, I have liberally borrowed from the experts in the field. Because of my project secrecy, they were unaware they contributed to my work until this moment. So I gratefully acknowledge them here. Perhaps you'll recognize some of your colleagues. I don't steal rom just anyone; they are the cream of the crop of our coal combustion experts. Actually, I'm proud of this clan -- note that among them are a native american, a president's son, and, of course, the famous "all" brothers...

My pawnbroker was successful in raising some start-up money and, as the next slide shows, my facilities team found a laboratory not far from my Germantown office...(Figure 2)

We have a three-dimensional presentation here, for those of you who would like to take a short walk around the room to see the sides as well as the front.

EXPERIMENTAL SETUP

To maintain credibility, every combustion scientist must have a drop tube furnace, and so my first order of business was to design and build mine and install it in my new laboratory. And here marks another place my research deviated significantly from the norm. You see, my furnace takes into account a force that other drop tube users have ignored -- that of gravity. In just about all drop tubes, the coal falls vertically. But we all know that in most real furnaces, coal is injected horizontally. The gravitational representation in most drop tubes seems to be askew! So my drop tube was carefully designed to have exactly as much up as down, thus neatly negating the effects of gravity on a coal particle traversing its full length. Here is my furnace...(Figure 3)

Other than its unique gravitational aspect, nothing much else is unusual. This device had to be built on a very low budget but it has means for heating the coal, an insulated passage for it, two access ports for diagnostics, and, of course, a means of quenching. Note that by keeping the coal feeder and ash collector equipment identical, simple subtraction enables an easy estimate of the volatile mass.

I learned a few things by trial and error with this furnace. For one thing, I found the coal feeder has to be of sufficient height above the furnace mouth to ensure the dropped coal gets through the entire furnace. As for the quench zone, you with money have all sorts of expensive helium-cooled probes and the like. I couldn't afford that, so I decided to just quench the whole darn outlet. I first tried a water-sprayed vertical outlet in juxtaposition to the vertical inlet. That didn't work -- not enough heat transfer, I guess. I then tried a horizontal outlet immersed in a water bath. It quenched nicely, but no ash came out. Finally, I hit upon the solution you see here -- which works just fine. I did have to add the spray shield to keep my powder dry.

I am going to have to move this upper diagnostic port to a position on the inside of the furnace curve. As it is now, I get an eyeful every time I peer in!

If you'd like to duplicate this novel, low-cost design, here's a bill of materials. You can see they're all available cheaply and locally (Figure 4).

DATA

Now, let's turn to the data I have collected with my furnace. The first thing a combustion scientist does is to collect kinetics data, and the first thing he does with his kinetics data is to make an arrhenius plot to get the activation energy. Doing those things first makes a lot of sense, since both "arrhenius" and "activation" start with the first letter of the alphabet.

But my research was to take a different tack from the usual. And so I focused on the last thing anyone would want to examine -- combustion statics. This being the last thing, it's natural that the zombietic energy, rather than the activation energy, is the value of interest. Of course, to determine the zombietic energy, one has to employ the method of zenopholus, which I did.

The method of zenopholus is not that all different from the method of arrhenius. A semi-log plot is used to determine the relevant constants. The major difference comes from being last rather than first -- everything is skewed around. In fact, the method of zenopholus can be thought of as the complete inverse of that of arrhenius as shown on the next figure, taken from a textbook explanation of the method (Figure 5).

In a manner very similar to arrhenius, the non-burning rate, NBR, is plotted as a function of temperature. A fit through the points yields the slope and intercepts to provide the needed constants.

Unfortunately, when I plotted my data on a rectangular semi-log graph like the textbook example I just showed, I had severe problems, as you can see for yourself (Figure 6).

I was unable to detect any trends, and fitting a straight line plot to the data was impossible. Luckily, I had my field advisors to assist me with this dilemma.

First, my pawnbroker was able to obtain some additional funds, using the contract overrun procedure. That money was coupled with insightful counsel from my facilities team. These resources enabled a lengthy analysis which finally revealed I had used the wrong coordinate system. What I found was that a carefully chosen curvilinear coordinate system was required. Here it is...(Figure 7)

It retains the A semi-log form, of course, but what is unusual are the several circular doodads you can see. By choosing this very special coordinate system, my data plotted very nicely on a straight line, as shown here (figure 8).

Once having this plot, it was an easy matter to obtain the zombietic energy (Figure 9), in which the influence of those circular doodads is clearly

seen. As you might suspect, the curvilinear coordinates I conjured up precluded a determination of the rate constant, "A." This was actually fortunate (in fact you might think it deliberate) for it implied more work was required.

FUTURE WORK

And so, like all good scientists, I need more money and more time. In other words, despite my original aspirations and although my first bundle is expended, I haven't quite been able to finish the test of my postulated hypothesis. But given a follow-on contract, which my pawnbroker is avidly pursuing at the moment, I have great hopes, for clearly the world needs to know the values of "A" and "NBR" (Figure 10).

LESSONS TO BE LEARNED

So much for a report of my project. As I stated at the outset, from my experiences, there are some lessons to be learned -- techniques which you will find applicable to your work regardless of the field of your research. I highlight four (Figure 11).

First, (Figure 12) always have a hypothesis, even if it's meaningless for your work, since headquarters likes them. It's good politics.

Next, (Figure 13) never overlook the mundane. Mine was gravity. It can make your work different from the other guy's, and that's important to source selection teams.

Now, it's highly unethical to alter your data, so never, never do that! But if the data don't fit your expectations, (Figure 14) do what others do -- skip over them quickly in your papers and reports, or play around with your coordinate system. Certainly, you can invent one which will work. Remember, everyone likes straight lines drawn through data points, but the coordinate system can curve all over the place!

Lastly, and most important of all, (Figure 15) never, never, never admit to anyone that you've reached a conclusion regarding your original hypothesis, even though you've spent twice as much money and taken twice as long as your proposal promised. After all, if you actually came to a conclusion, on what would be based your sole-source follow-on contract?

And now you've heard about my research. It's time to hear about yours. I'm looking forward to it.

Thank you very much.

DIRECT UTILIZATION AR&TD

Project Title:	**An Hypothesis Concerning the Burning of Coal**
Principal Investigator:	**C.W. Garrett**
Start Date:	**1 October 1987**
Completion Date (stated):	**1 October 1989**
Completion Date (planned):	**Never (provided grants keep coming)**
Hypothesis:	**Coal will not support combustion**
Pawnbroker:	**I. Buyum**
Facilities:	**U.R.A. Hick & Son**
Contributors:	**Flick Reagan, Dan Baloney, Dans Eerie, Jim Fryabutt, Mike Moans, Smug Boot, Pete Sockaman, Pill Beaters, Jack Howaryah, Don Hardestofall, Leave Sticksa, Veggie Itchall, Saddle Arrow-Fan**

Figure 1

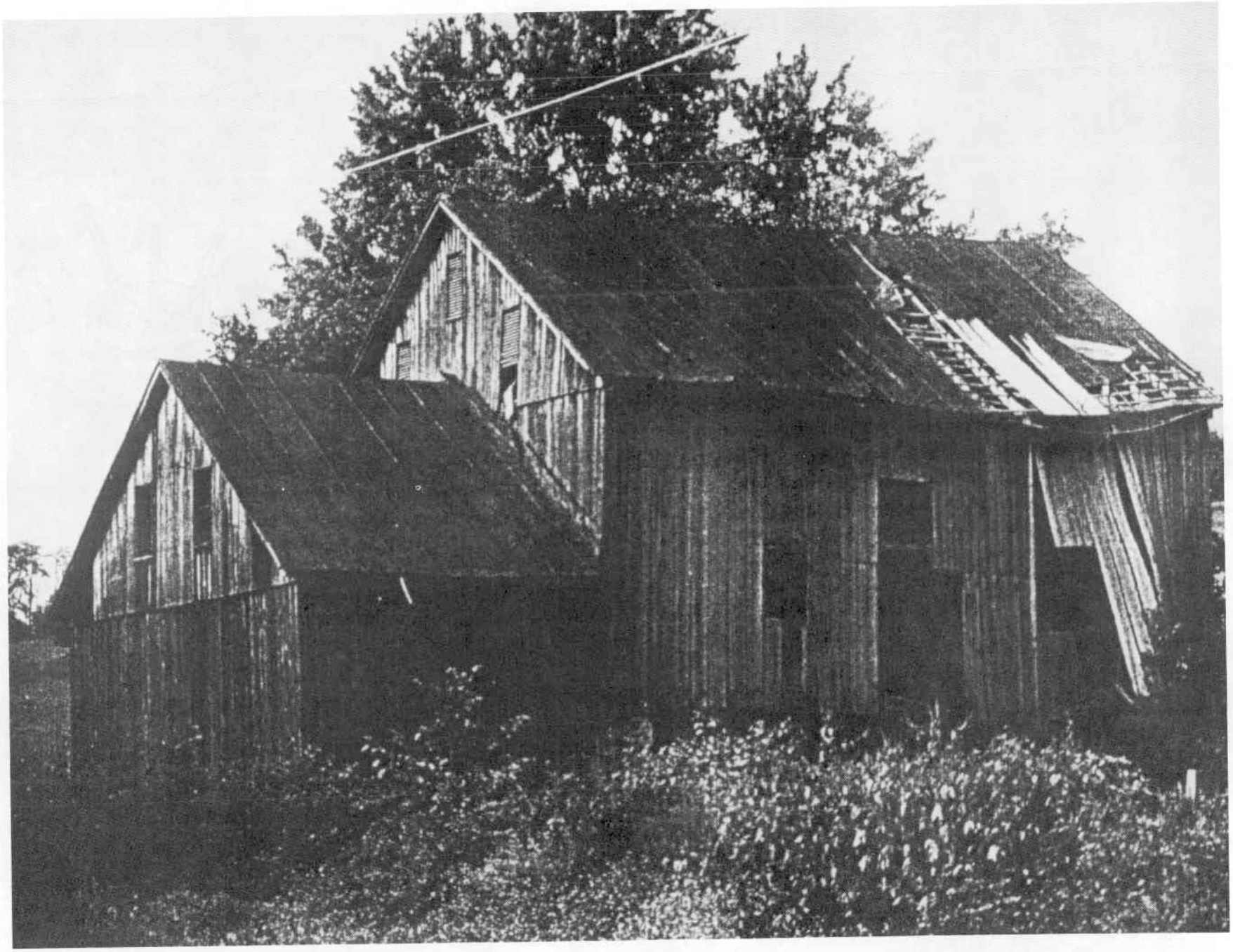
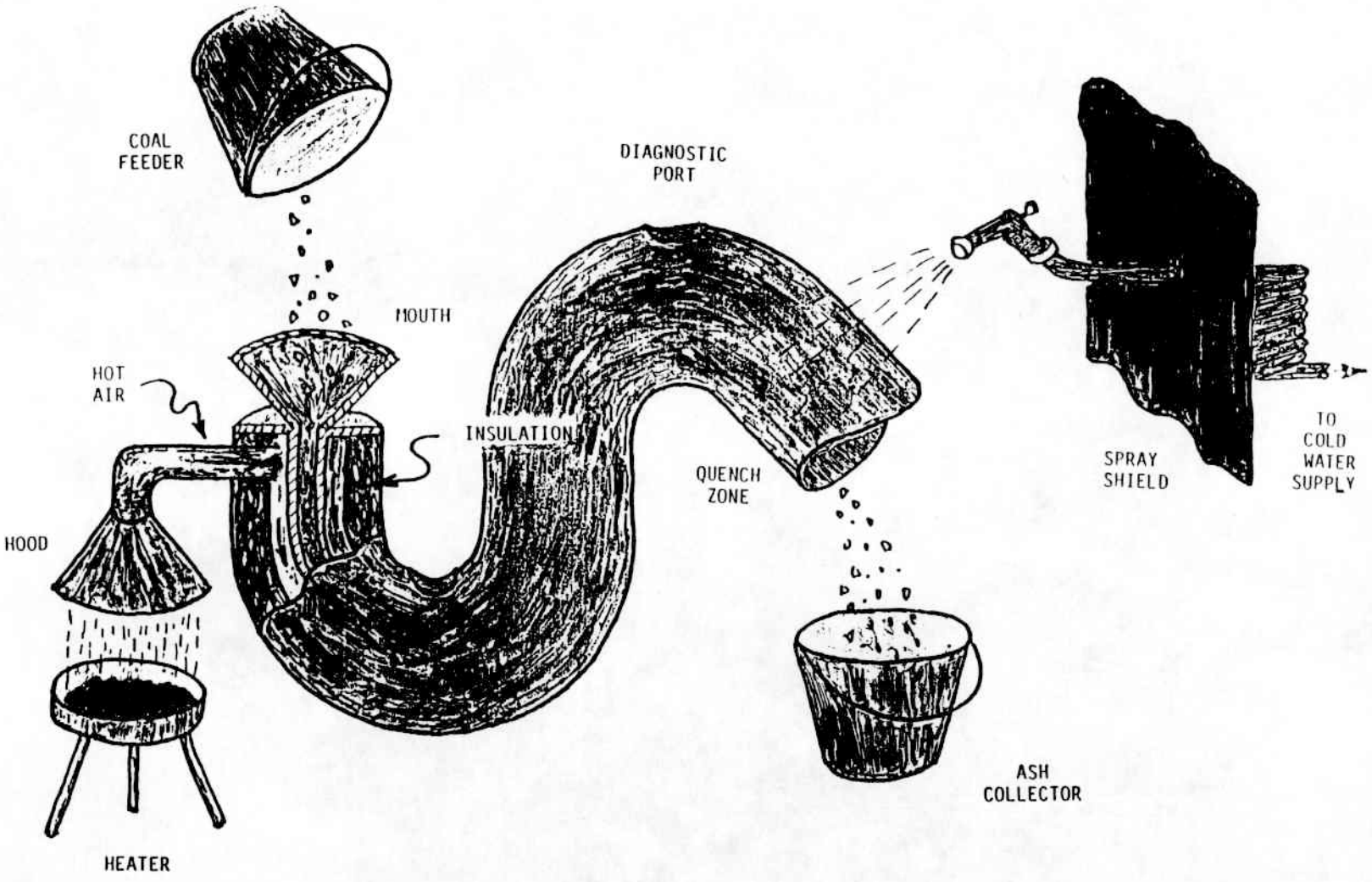


Figure 2



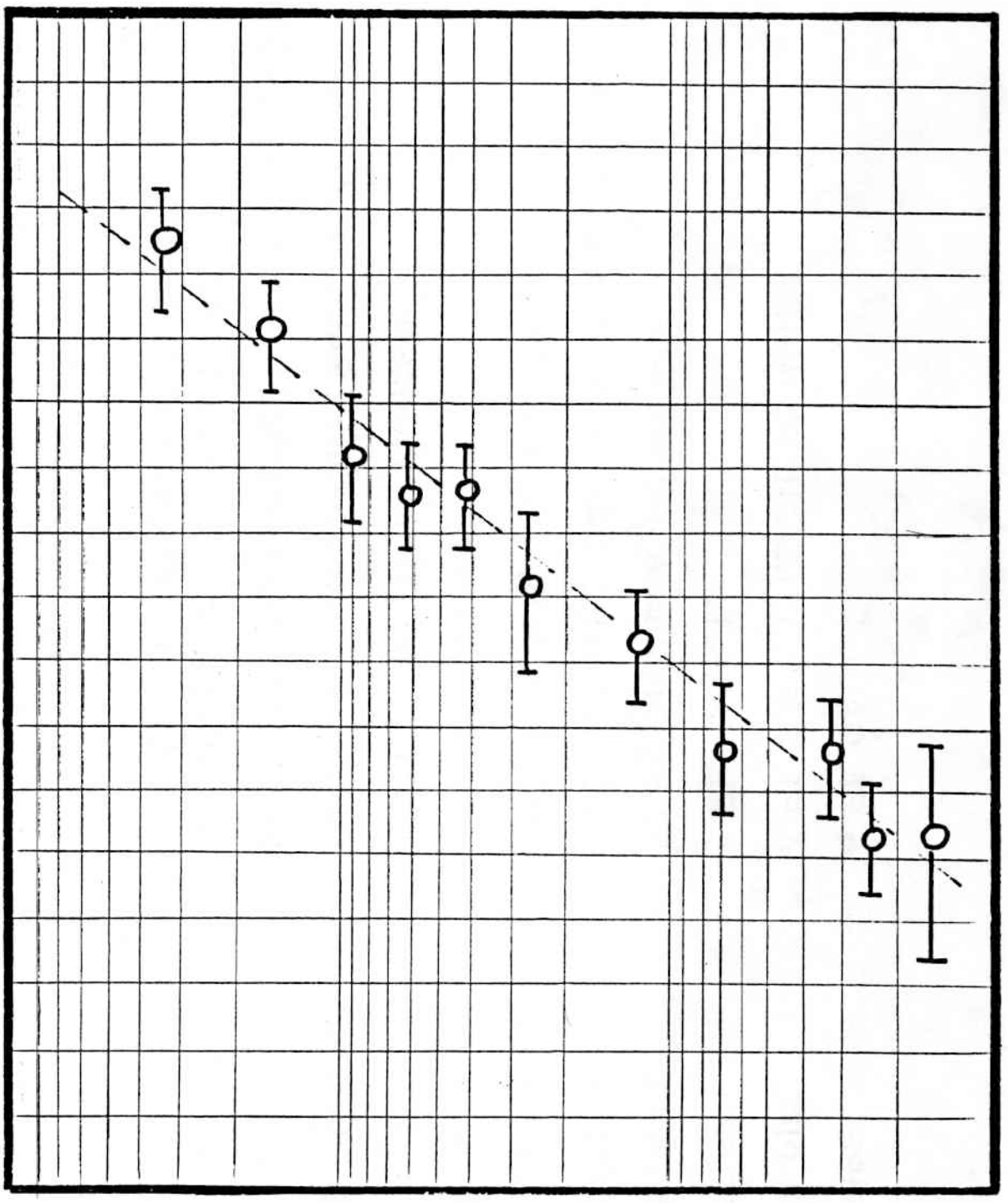
GARRETT DROP TUBE FURNACE

Figure 3

DROP TUBE FURNACE

3/4 IN. PIPE	--	5 FT. GALV.)
4' STOVE PIPE	--	4 FT. GALV.) LOCAL PLUMBER
6" STOVE PIPE	--	4 FT. GALV.)
GARDEN HOSE	--	50 FT. GARDENA MODEL T-50
HOSE NOZZLE	--	LOCKING TYPE; GARDENA MODEL T-51
CHARCOAL GRILL	--	24" DIA.; K-MART MODEL QWM-24
CHARCOAL	--	SAFEWAY "OZARK"
BUCKETS (2)	--	1 GAL. CAP.; LOCAL FARMER
SHOWER CURTAIN	--	SEARS, 5RC600892 (FALL SALE CATALOG)
HEATER HOOD	--	FIREPLACE PART (MODERN); LOCAL NEIGHBOR
INSULATION	--	DOW-CORNING #204 FOAM PEANUTS (AVAILABLE FROM UNITED PARCEL)

Figure 4

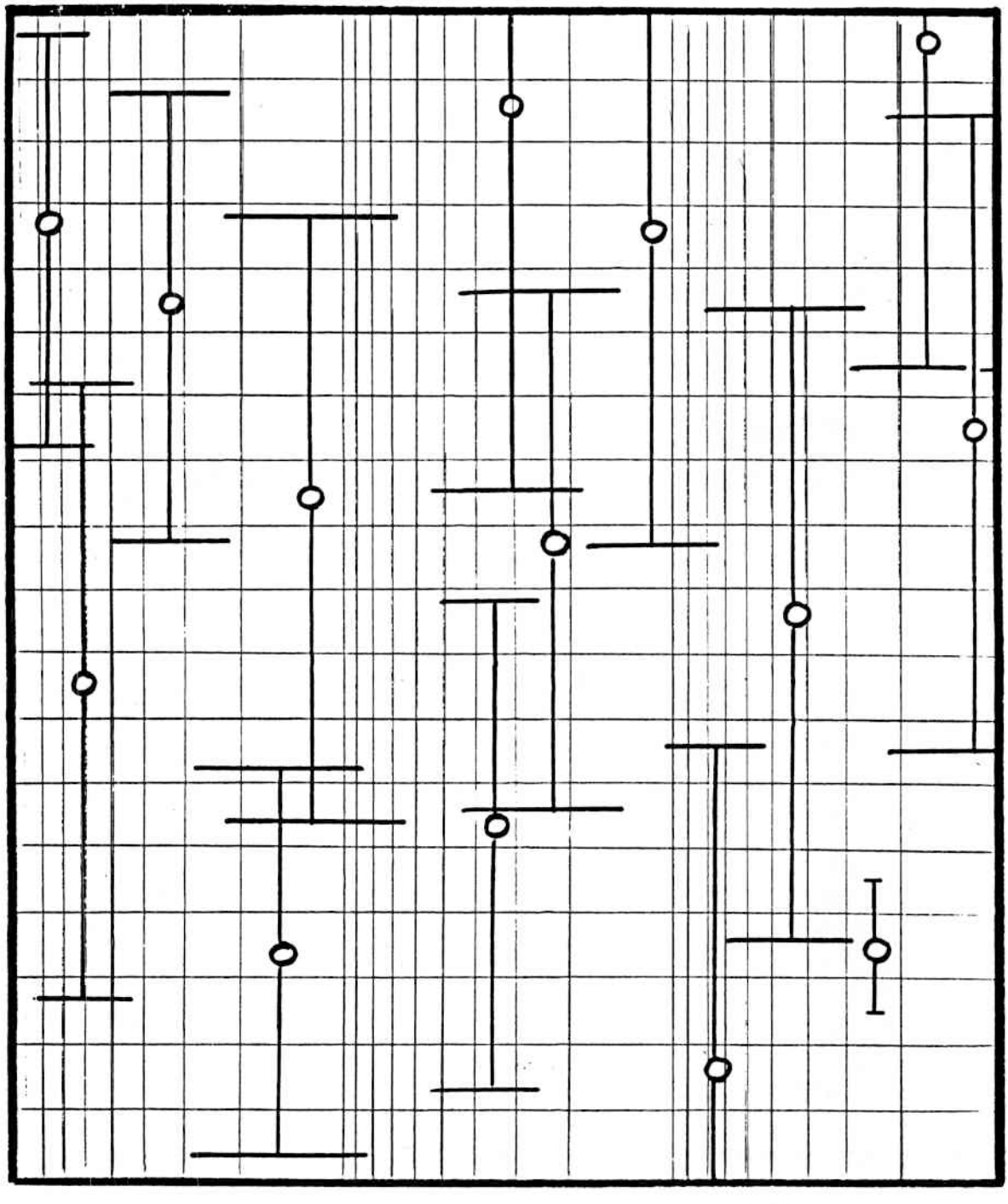


METHOD OF ZENOPHOLUS

NBR=A exp[RT/+Z]

Figure 5

NBR



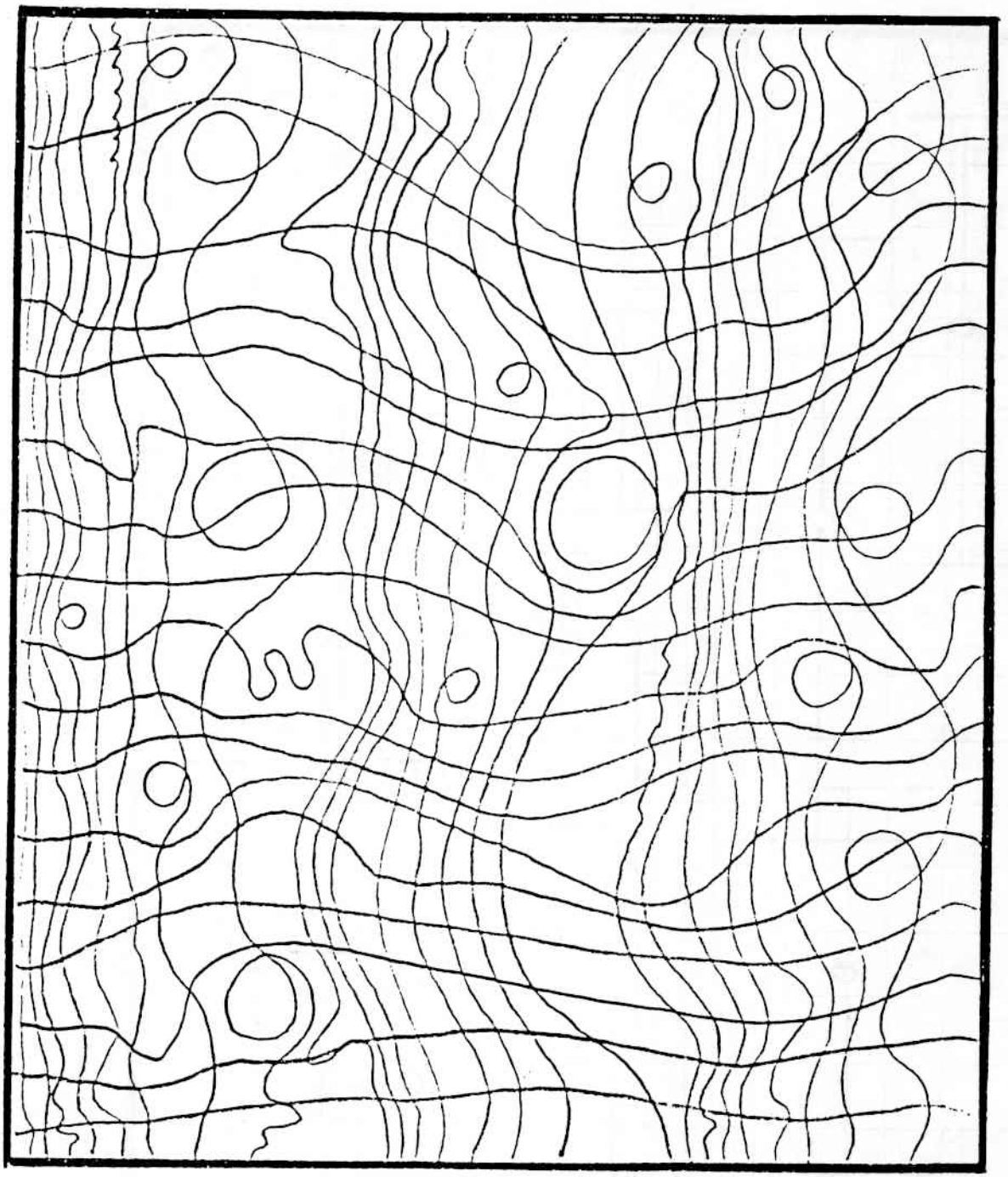
[T/1]

METHOD OF ZENOPHOLUS

NBR=A exp[RT/+Z]

Figure 6

NBR



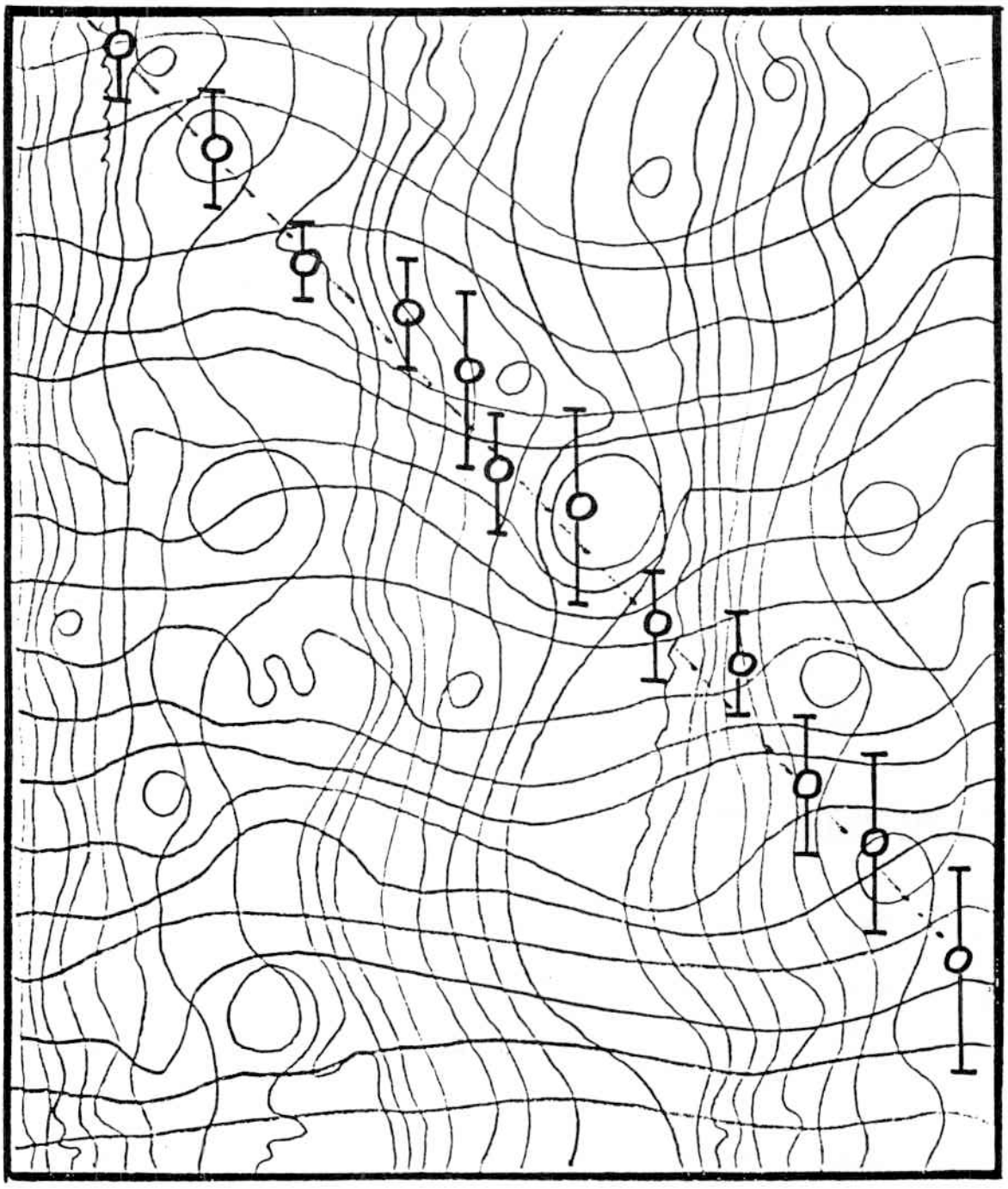
[T/1]

METHOD OF ZENOPHOLUS

NBR=A exp[RT/+Z]

Figure 7

NBR



[T/1]

METHOD OF ZENOPHOLUS

NBR=A exp[RT/+Z]

Figure 8

RESULTS

$$NBR = A \exp[RT/+Z]$$

$$Z = 314159$$

$$A = \text{INDETERMINATE ON CURVILINEAR COORDINATES}$$

Figure 9

FUTURE WORK

- DETERMINE A
- TEST HYPOTHESIS

Figure 10

LESSONS

- HYPOTHESIS
- MUNDANITY
- DATA
- CONCLUSION

Figure 11

LESSONS

- **HYPOTHESIS -- ALWAYS**
- **MUNDANITY**
- **DATA**
- **CONCLUSION**

Figure 12

LESSONS

- HYPOTHESIS -- ALWAYS

- MUNDANITY -- A SAVING GRACE

- DATA

- CONCLUSION

Figure 13

LESSONS

- HYPOTHESIS -- ALWAYS
- MUNDANITY -- A SAVING GRACE
- DATA -- THERE'S GOT TO BE A WAY
- CONCLUSION

Figure 14

LESSONS

- HYPOTHESIS -- ALWAYS
- MUNDANITY -- A SAVING GRACE
- DATA -- THERE'S GOT TO BE A WAY
- CONCLUSION -- NEVER

Figure 15

Session 1
Pyrolysis and Combustion

Chairperson: Scott M. Smouse

The advantages of pulverized coal-firing over other combustion techniques have resulted in its dominance in fossil-fuel power generation, particularly at larger scales. No other process has been as successfully advanced and exploited economically as coal combustion, without a fundamental understanding of the critical process steps. The complex interaction of the many chemical and physical subprocesses in coal combustion, including mass, momentum, and energy transfer, has limited our understanding of the overall process. However, significant progress has been made over the last several years towards understanding not only the detailed chemistry and transport phenomena but also their interactions. This has allowed the development of engineering models of coal devolatilization and char oxidation, which can be applied outside the laboratory to large-scale, practical coal combustion and gasification systems. These comprehensive models are only as good as the submodels of the individual mechanistic steps. As we continue to improve our understanding of coal combustion mechanisms, these models will provide a means to predict, a priori, the effect of coal properties on combustion performance. These advances will be achieved, in part, through research funded by the Department of Energy's Energy Technology Centers in Pittsburgh and Morgantown. This session details the past year's progress in these areas.

KINETICS OF RAPID COAL DEVOLATILIZATION

1. CONTRACT NUMBER: FTPA 0709

CONTRACTOR: Sandia National Laboratories
P. O. Box 969
Livermore, CA 94551-0969

CONTRACT PROJECT MANAGER: Donald R. Hardesty, FTS 234-2321

PRINCIPAL INVESTIGATOR: Thomas H. Fletcher, FTS 234-3687

PETC PROJECT MANAGER: James D. Hickerson

PERIOD OF PERFORMANCE: October 1, 1988 - Continuing

2. OBJECTIVE

The objective of this project is to characterize the physical and chemical processes that constitute the early devolatilization phase of coal combustion as a function of coal type, heating rate, particle size and temperature, and gas-phase temperature and oxygen concentration. Subtasks of this project are listed below:

Subtask 1. Determination of Total Devolatilization Rates.
Subtask 2. Investigation of Physical Structure Changes During Pyrolysis.
Subtask 3. Investigation of Chemical Structure Changes During Pyrolysis.
Subtask 4. Determination of Nitrogen and Sulfur Release Rates.
Subtask 5. Development of Engineering Models of Devolatilization.

Results of this study are intended to apply to pulverized coal combustion systems, and will allow detailed descriptions of the devolatilization behavior for different types of coal based on the local temperature and reaction history. Model descriptions are intended to be simple enough for incorporation into large flame simulation codes, and will be valuable in design or retrofitting of pulverized coal burners.

3. BACKGROUND

The rate of release of coal pyrolysis products is dependent upon particle temperature and reaction histories. During rapid particle heating (10^3 to 10^5 K/s) typical of pulverized combustion applications, published rates of volatiles release for similar coals and similar heating conditions differ by five orders of magnitude at any given temperature. Such differences in reported pyrolysis rates are attributed to insufficient characterization of particle temperature during heatup, since chemical reaction and heat transfer time scales are similar during rapid heating. Strategies for reducing NO_x emissions often require knowledge of near-burner flame structure, which is critically dependent on the rate of pyrolysis and yield of pyrolysis products.

The devolatilization behavior of different types of coal has largely been modeled on an empirical basis, with correlations of potential product yields based on elemental compo-

sition (e.g., Ko, et al., 1988). Solum, et al. (1989) have recently used ^{13}C NMR spectroscopy to quantitatively measure the distribution of carbon in different functional groups in ten different coals from the Argonne Premium Coal Sample Bank. These data show differences in the chemical structure of the solid coal, such as the average aromatic cluster size and the average number of side attachments per aromatic cluster. A primary emphasis of this project is to model the devolatilization behavior of different coals based on detailed knowledge of the chemical structure of the coal, rather than mere elemental composition.

4. PROJECT DESCRIPTION

The primary goal of the past three years of research has been to accurately measure the rates of coal devolatilization at high heating rates. Temperatures, sizes, and velocities of single particles in a laminar flow-reactor are measured using a unique infrared sizing-pyrometer system (Fletcher, 1989a). Thermal emission from individual particles is monitored at wavelengths of 1.3 and 2.2 μm, allowing determination of particle temperatures as low as 850 K. Samples of partially reacted coal particles are collected using a helium-quench probe, including aerodynamic separation of char particles from tars and aerosols. These are the first devolatilization rates that have been determined using temperature measurements of individual particles. Devolatilization rates determined from laboratory experiments for a Pittsburgh #8 hva bituminous coal (PSOC-1451D) are very rapid (Fletcher, 1989b), and are comparable to rates obtained from experiments where average particle cloud temperatures were measured (Solomon, et al., 1986). During the past year, measurements have been performed on a suite of coals selected by PETC in order to examine differences in chemical and physical structures as a function of coal type.

In a collaborative study with the University of Utah, we have initiated measurements of these chemical structures for different coals as a function of the extent of devolatilization under rapid heating conditions. A chemical percolation model for devolatilization was also recently developed as a result of this collaboration (Grant, et al., 1989), which uses some of the ^{13}C NMR data to guide selection of input parameters for different coals. The model uses a single set of coal-independent kinetic parameters, and describes gas and tar yields for different coals as a function temperature history, based on the chemical structure of the parent coal. In the initial development of the model, predictions were performed for three different coals (bituminous, subbituminous, and lignite) for a single heating condition (entrained flow heating at ~10^4 K/s to 1073 K). Extension of model applicability to additional heating conditions was conducted during the last year, and is discussed below.

5. RESULTS

Three major topics will be discussed in this report: (a) Devolatilization behavior of different coals, (b) Chemical structure characteristics of tar and char as a function of temperature and reaction history, and (c) Extension of the chemical percolation devolatilization (CPD) model to a wide range of heating rates and temperatures.

A. Devolatilization Behavior of Different Coals

The devolatilization behavior of five different coals have now been studied in the coal devolatilization laboratory (CDL). Characteristics of these five coals are presented in Table 1. Coals were provided by PETC as part of an effort to use common coals at

several research laboratories, and were sized and aerodynamically classified in a nitrogen environment. In general, the 106-125 μm size fraction was used in these studies to coincide with the Sandia char combustion studies. This size is also compatible with the infrared sizing-pyrometer system. Major mineral elements (Ti, Si, and Al) are used as tracers to determine the fraction of mass released as mineral matter. Total ash is also used as a tracer.

Experiments were conducted in 100 % nitrogen in an entrained flow reactor, with two gas temperature conditions (maximum gas temperatures of 1050 and 1250 K). Typical temperature and mass release histories determined for these coal particles are shown in Figure 1 for the PSOC-1493D Illinois #6 hvb coal (106-125 μm size fraction). Data points are average particle temperatures measured using the sizing-pyrometry system, and residence time is determined from the average particle velocity measurements. Standard deviations of the measured particle temperatures range from 70 K in the rapid heating region to 20 K at the reactor exit. Particle temperature calculations are described by Fletcher (1989a). The local gas temperature in these experiments is also shown. The heating rate is approximately 10^4 K/s, with maximum particle temperatures of approximately 900 and 1150 K for the two cases. The particle temperatures are lower than the gas temperature due to radiative heat loss through the transparent walls of the flow reactor.

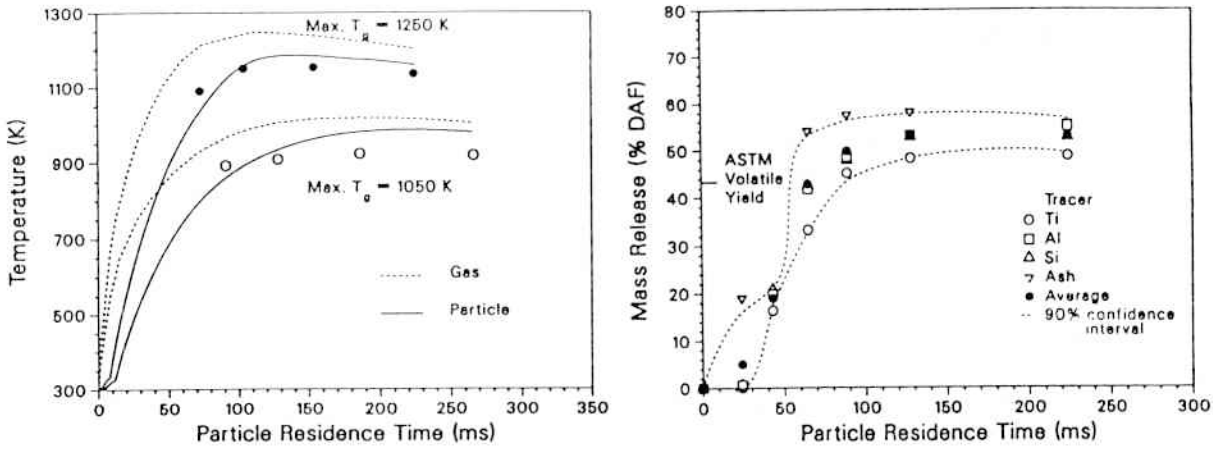


Figure 1. (a) Temperature histories determined for Illinois #6 PSOC-1493D 115 μm diameter particles at the 1250 K and 1050 K gas conditions. Points represent average particle temperature measurements, dashed curves are measured gas temperatures, and solid curves are best fit calculations. (b) Corresponding mass release for 1250 K gas condition.

The total mass release rates determined for the five different coals do not differ significantly at these heating rates and temperatures, and agree with the rapid devolatilization rates reported earlier (Fletcher, 1989b). Total volatile yields are summarized in Table 2. The total volatiles yields from the four highly volatile coals at the 1250 K gas condition are nearly identical, with variations in yield of less than 1% DAF, although the ASTM volatile contents differ by 10% DAF. The inadequacy of the ASTM proximate analysis is well known, but these data provide evidence that the proximate analysis does not even

correctly reflect trends in the amount of volatile matter released as a function of coal rank. The volatile yield data for the low volatile coal were taken from mass balance measurements, since standard ASTM ashing procedures were not found applicable for this coal.

Table 1. Ratio of Volatile Yields Measured in the CDL to the ASTM Volatile Matter Content

Coal Type	%C (DAF)	%H (DAF)	%N (DAF)	%O (DAF)	%S (DAF)	%Ash (DAF)
PSOC-1507D (Zap lignite, 75-106 μm)	66.57	4.26	1.12	25.16	2.89	18.7
PSOC-1445D (New Mexico Blue subbituminous, 106-125 μm)	75.6	5.26	1.32	17.33	0.49	3.48
PSOC-1493D (Illinois #6 hvb bituminous,106-125 μm)	74.12	4.96	1.45	13.18	6.29	11.3
PSOC-1451D (Pittsburgh #8 hva bituminous,106-125 μm)	81.92	6.45	1.65	8.72	1.26	11.2
PSOC-1508D (West Virginia Pocahontas #3 lv bituminous,106-125 μm)	90.80	4.47	1.44	2.68	0.62	16.7

Table 2. Ratio of Volatile Yields Measured in the CDL to the ASTM Volatile Matter Content

Coal Type	V_{ASTM} (% DAF)	V_{1050} (% DAF)	V_{1050}/V_{ASTM} (1050 K)	V_{1250} (% DAF)	V_{1250}/V_{ASTM} (1250 K)
PSOC-1507D	49.6	52.5	1.06	53.7	1.08
PSOC-1445D	46.8	39.6	0.85	53.6	1.15
PSOC-1493D	43.4	43.5	1.00	52.9	1.22
PSOC-1451D	38.7	55.5	1.43	53.1	1.37
PSOC-1508D	17.2	9.6	0.56	13.8	0.80

B. Chemical Structure Characteristics of Tar and Char

Changes in the chemical structure of PSOC-1493D Illinois#6 hvb bituminous coal particles as a function of the extent of devolatilization were studied using ^{13}C NMR spectroscopy. Samples are analyzed at the University of Utah using methods described by Solum, et al. (1989). During this quarter, the unreacted coal and two samples obtained at the 1250 K condition in the CDL have been analyzed, and the data are listed in Table 3. The 43 ms sample corresponds to approximately 850 K and the early stages of pyrolysis

(19% DAF total mass release), while the 89 ms sample corresponds to approximately 1100 K at a location where the majority of tar has been released (43% DAF total mass release).

Table 3. Carbon Structural Parameters Determined from ^{13}C NMR Spectroscopy for PSOC-1493D Illinois #6 Samples

Parameter	0 ms	43 ms	89 ms
Mass Release (% DAF)	0.0	19.0	49.8
Aromatic carbon, $f_a = f_{a'} + f_a^C$	0.71	0.72	0.79
Aromatic carbon, carbonyl subtracted, $f_{a'}$	0.67	0.67	0.74
Protonated aromatic carbon, f_a^H	0.27	0.29	0.34
Non-protonated aromatic carbon, $f_a^N = f_a^P + f_a^S + f_a^B$	0.40	0.38	0.40
Aromatic carbon with oxygen attachment, f_a^P	0.08	0.09	0.07
Aromatic carbon with alkyl attachment, f_a^S	0.17	0.19	0.19
Aromatic bridgehead and inner carbon, f_a^B	0.15	0.10	0.14
Carbonyl, f_a^C	0.04	0.05	0.05
Aliphatic carbon, f_{al}	0.29	0.28	0.21
Aliphatic CH and CH_2, f_{al}^H	0.15	0.18	*
Aliphatic CH_3 and non-protonated carbon, f_{al}^*	0.14	0.10	*
Aliphatics with oxygen attachment, f_{al}^O	0.07	0.07	0.08
Fraction of aromatic carbon that are bridgeheads, $f_a^B/f_{a'}$	0.224	0.149	0.189
Number of carbons per cluster, C	10.8	9.6	9.7
Coordination number, $\sigma+1$	4.0	4.0	3.4

The four most important parameters in this analysis appear to be the fraction of aromatic carbons $f_{a'}$, the aromatic attachments sites per 100 aromatic carbons ($f_a^S + f_a^P$), the fraction of aliphatic carbon f_{al}, and the aromatic carbons per cluster C. The aromaticity of the 89 ms sample has started to increase while the aromatic cluster size remains unchanged. The aliphatic carbon decreases, with little or no change in the number of aromatic attachment sites per 100 aromatic carbon atoms. In other words, the aliphatic groups are released before much change occurs in the aromatic structure of the coal. The cluster size C remains essentially unchanged at about 10 carbons per cluster. The cluster size eventually is expected to reach as high as 20 at longer residence time, as shown by Solum, et al. (1989) for a Pittsburgh #8 hva bituminous coal and a North Dakota Beulah Zap lignite at longer residence times and other temperature histories. There is also little evidence for cross-linking of the coal, since the number of attachment sites remains fairly constant. These data are consistent with the mechanism proposed in the CPD model (Grant, et al., 1989) wherein tar production is accompanied by expulsion of bridge material and stabilization of free radical side chains by either hydrogen transfer reactions or expulsion as light gases. The details of this mechanism are being evaluated, and further NMR studies of Illinois #6 char and tar samples are in progress.

C. Extension of the CPD Model to a Wide Range of Heating Rates and Temperatures

The chemical percolation devolatilization (CPD) model was developed previously (Grant, et al., 1989) as a means to treat devolatilization behavior for different types of coal based on the chemical structure of the parent coal. Coal is treated in the CPD model as a macromolecular array of aromatic ring clusters of various sizes and types which are connected by a variety of chemical bridges of different bond strengths. For simplicity, only two types of bridges are treated: labile bridges L and stable or char bridges c. Percolation statistics applicable to a Bethe lattice (a loopless tree structure) allow a mathematical description of the bridge-breaking process in closed form, providing an efficient alternative to Monte-Carlo techniques. Labile bridges L decompose into a reactive intermediate L^*, which is unstable and reacts quickly in one of two competitive reactions. In one reaction pathway, the reactive intermediate is stabilized (e.g., by hydrogen transfer within the lattice) and forms a side chain rather than recombining to form char. The cleavage of the reactive intermediate L^* constitutes the bridge-breaking step, and is the mechanism that generates tar fragments, as described by percolation statistics. The side chains δ undergo further cracking reactions to form light gas. In a competing reaction pathway, the reactive intermediate may stabilize to form a stable char bridge c with the associated release of additional light gas. The competition for L^* is governed by the ratio of the rate of side chain formation to the rate of char formation, and it is convenient to define a composite rate constant ρ:

$$\rho = \frac{k_\delta}{k_c} = \frac{A_\delta}{A_c} \exp\left[\frac{-(E_\delta - E_c)}{RT}\right] = A_\rho \exp\left[\frac{-E_\rho}{RT}\right] \qquad (1)$$

The dynamic variables of the theory are the bridge population parameters, L and c, and the chain fragment parameter δ. The associated kinetic expressions for the proposed reaction mechanism are presented and discussed by Grant, et al. (1989). In the initial development of the CPD model, E_ρ was set to zero, since the data set of three different coals (Serio, et al., 1987) was obtained over a narrow range of temperatures (~1050 K) and heating rates (~10^4 K/s). In order to extend the applicability of the CPD model to a wide range of temperatures and heating rates, the tar and total volatiles yield data of Gibbins-Matham and Kandiyoti (1988) was used to determine a non-zero value for E_ρ. These investigators used a heated screen to study a Pittsburgh #8 coal at five different heating rates ranging from 1 K/s to 1000 K/s, holding the sample for 30 s at the ultimate temperature of 973 K. Figure 2 shows the comparison of CPD model calculations, with E_ρ = 1.5 kcal/mole and $A_\rho = 2.0\ s^{-1}$, with the data of Gibbins-Matham and Kandiyoti. The procedure for determination of model coefficients is described in more detail by Fletcher, et al. (1989c).

Freihaut (1988) performed experiments on the amount of tar released from a Pittsburgh #8 hva bituminous coal using a heated screen apparatus similar to that used by Gibbins-Matham and Kandiyoti (1988). Tar release data was obtained at slow heating conditions (1 K/s) and at 0 s and 30 s hold times under rapid heating conditions (1000 K/s). The Pittsburgh #8 coal (PSOC-1451D) studied by Freihaut (1988) and by Fletcher (1989b) has different characteristics than the APCSB Pittsburgh #8 coal studied by Gibbins-Matham and Kandiyoti (1988), as mentioned earlier. The coordination number (σ+1) determined for PSOC-1451D is 5.6, rather than 4.8. This difference in σ+1 affects prediction of the tar formation rate. Values for L_0, c_0, and f_∞ for PSOC-1451D are

obtained from least squares fits to Freihaut's heated screen data (tar and total volatiles yields) at 1000 K/s with zero hold time at the maximum temperature. Results of this least squares fit are $L_0 = 0.325$, $c_0 = 0.130$, $f_\infty = 0.293$. The comparison with Freihaut's tar and total volatiles yields at 1000 K/s, 0 s hold time, is shown in Figure 3a. The model predicts both the yield and temperature dependence of the char formation and tar release data. The slight decrease in the measured tar yield at maximum temperatures greater than 950 K is correctly predicted by the CPD model, and is a result of tar cracking to form light gas before it leaves the vicinity of the heated grid apparatus. This tar-cracking feature is unique to the CPD model.

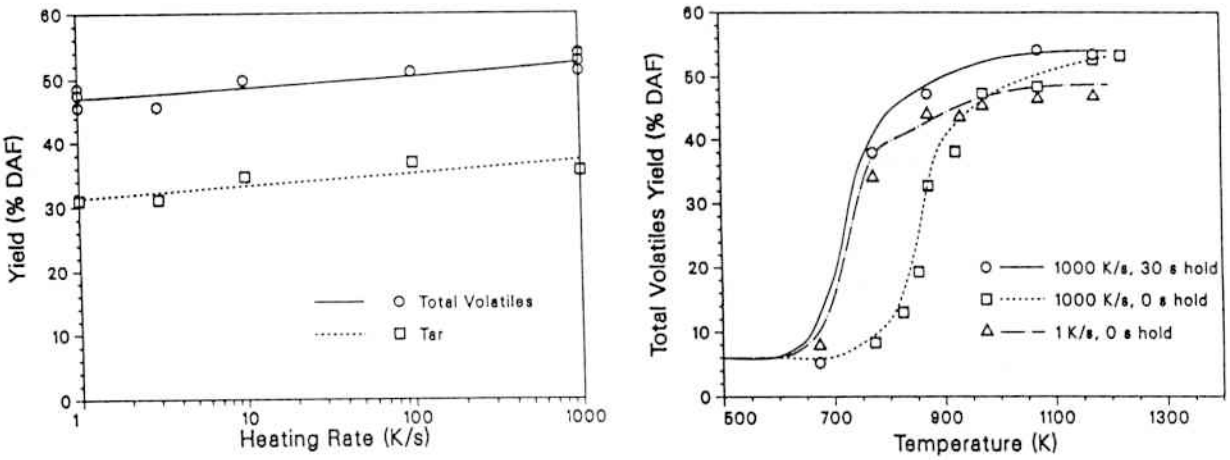


Figure 2. Comparison of best-fit CPD model calculations with the tar and total volatiles yield data (points) of Gibbins-Matham and Kandiyoti (1988) for the Argonne Premium Pittsburgh #8 coal. (a) Coal heated to 973 K at the designated rate and held for 30 s. (b) Coal heated to different temperatures.

The temperature dependence of the model can be explored further by comparison with devolatilization data obtained at high heating rates and long hold times at different temperatures. Freihaut also performed devolatilization experiments on Pittsburgh #8 hva bituminous coal at 1000 K/s, and varied the hold time from 0 to 100 s at different temperatures (Seery, et al., 1988). The tar yield measured at the 100 s hold time condition is much greater than the zero hold condition at moderate temperatures (700-900 K). He postulates that additional low-temperature pyrolysis and/or coking reactions are needed to model this phenomena. Using the chemical structure coefficients described above, and the values of E_ρ and A_ρ corresponding to the best fits to the Gibbins-Matham data, predictions of the Freihaut 100 s and 50 s hold data were performed using the CPD model. Quench times were estimated at 1000 K/s. As discussed earlier, the maximum tar yield is compared with the data for the long hold time and slow heating rate data, since pyrolysis products are swept from the vicinity of the hot screen at time scales faster than reaction time scales. The model also predicts the experimentally observed decrease in tar yield at 1000 K for the immediate quench (zero hold time) condition. The model successfully predicts the temperature dependence of tar evolution and the increase in yield at the 100 s hold time condition, as shown in Figure 3b. The comparison with the limited 50 s hold condition is within the accuracy of the tar yield data. The CPD model is able to

explain these experimental data without imposing any additional low temperature reactions.

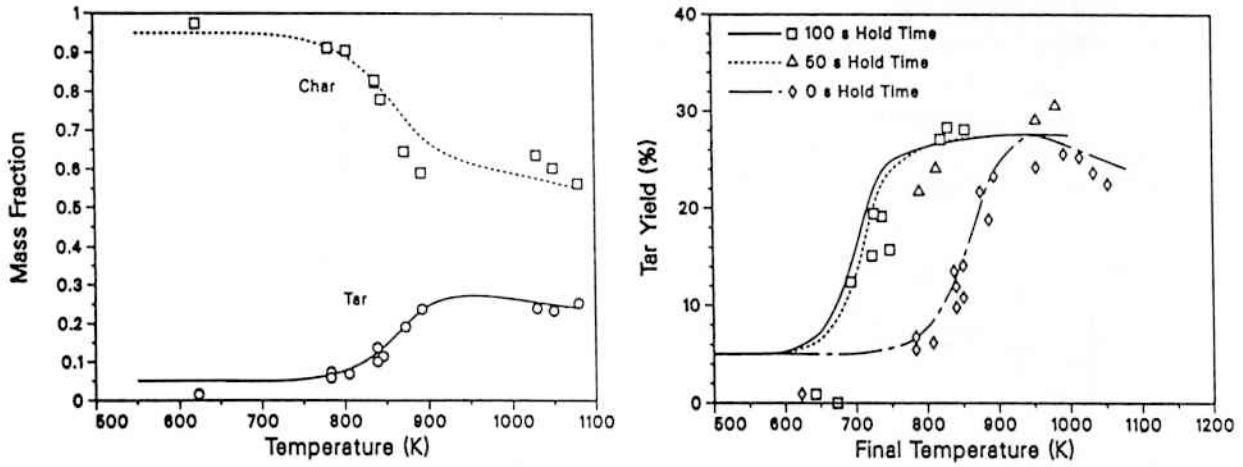


Figure 3. Comparison of CPD model calculations with Pittsburgh #8 tar yield data of Freihaut (1988). (a) Coal heated at 1000 K/s and immediately cooled at 1000 K/s. (b) Coal heated at 1000 K/s and held for different times before quenching.

Fletcher (1989b) performed devolatilization rate experiments that included simultaneous measurements of the temperatures, velocities, and sizes of individual coal particles in rapid heating experiments (approximately 10^4 K/s). The coal used in these experiments was PSOC-1451D, the same coal and size fraction studied by Freihaut (1988). Total volatiles yields were determined using four independent tracers (Ti, Si, Al, and total ash). The CPD model was used to predict the mass released during devolatilization for the experimental conditions studied by Fletcher, using coefficients for L_o, c_o, and f_∞ determined from the Freihaut data and the coal-independent rate coefficients discussed by Fletcher (1989c).. Model predictions are compared with the experimental data in Figure 4a. Considering the diversity in experimental conditions of the Freihaut and Fletcher work, the predictions of the time scales agree very well with the Fletcher data, especially the time at which devolatilization begins. The predicted and measured yields are also in good agreement, well within the experimental uncertainty in the data.

The CPD model can be used to predict the effects of heating rate over a broader range of temperatures and heating rates using the coefficients obtained from the least squares fits to the above-mentioned data sets. Figure 4b shows the heating rate dependence of the model for the devolatilization of Illinois #6 coal. In these calculations, the coal is heated to 1500 K at rates from 1 K/s to 10^5 K/s. The effect is two-fold: (a) the temperature at which the reactions occur increases as the heating rate increases, and (b) the tar and total volatiles yield increases as the heating rate increases. The competition between chemical reactions and heat transfer governs changes in the temperature regime where tar is released as a function of heating rate. The decrease in overall tar yield at higher temperatures, as evidenced in Fig. 7b, is due to gas phase thermal cracking, resulting in the production of light gas. At any given heating rate, the tar is released in a fairly narrow temperature window of approximately 100 K. The temperature regime of principal tar

release increases by approximately 50 K for each order of magnitude increase in heating rate.

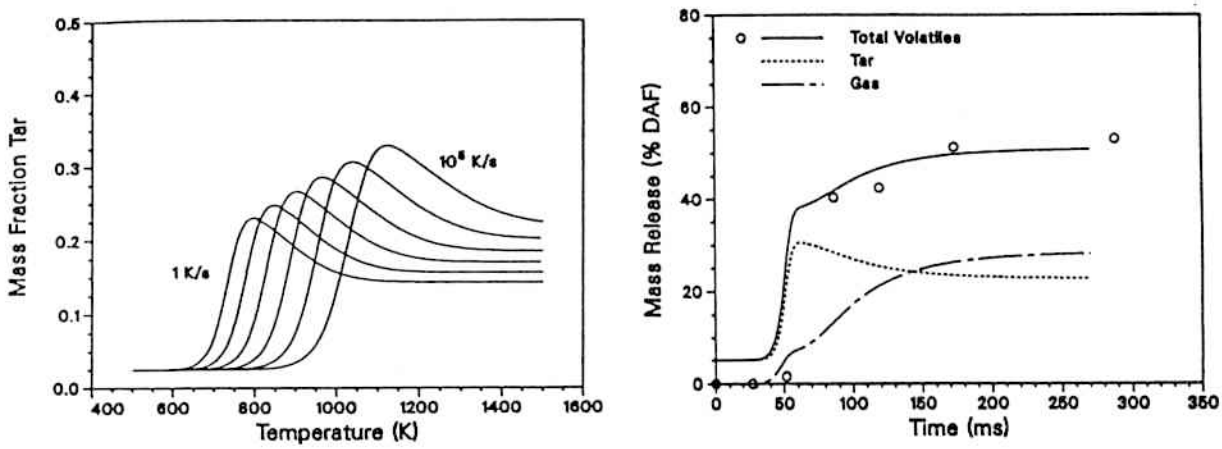


Figure 4. (a) Comparison of CPD model predictions with coal devolatilization data of Fletcher (1989b). (b) CPD model predictions of tar volatiles yield as a function of heating rate.

The total volatiles yield shows the two regimes of volatiles release: (1) a region dominated by the rapid tar release, followed by (2) a region of gas release at a rate slower than than that of tar release. As discussed earlier, this gas release is due to (a) release of side chains from char and tar clusters, and (b) cracking of heavy tar molecules to form lighter tar fragments with associated release of additional side chains. The two regimes of devolatilization can be seen upon close examination of the entrained flow reactor data of Fletcher (1989b), shown in Figure 4a. The temperature regime at which these pyrolysis reactions occur is 200-400 K lower than the temperature regimes reported in the literature. The reason for such discrepancies is thought to be inadequate determination of particle temperatures in many previous devolatilization experiments. Inefficient aerodynamic separation of tar from char particles during sampling of devolatilization products in early flow reactor experiments may also be a cause for some of the difference; the measurement of total mass release is inadequate if the tar redeposits on the char. The data used in determination of coefficients for the CPD model include measurement of individual particle temperatures during devolatilization and measurement of particle cloud temperatures by emission/transmission Fourier transform infrared (FTIR) spectroscopy. **We feel that this set of data finally answers questions concerning the range of reported devolatilization rates that are physically realistic.**

6. FUTURE WORK

The fact that the CPD model predicts non-zero initial tar yields is indicative of finite lattice clusters existing in the parent coal, which correspond to the amount of material extractable with a solvent such as tetrahydrofuran. This extractable material is thought to correspond to the mobile phase (bitumen) which is released from the coal in moderate heating experiments (100 K/s) at temperatures low enough (500-600 K) to indicate a vaporization mechanism of release rather than a bond scission mechanism. Future plans

include incorporation of a transport model into the CPD model to account for this early tar release in a more realistic manner. The characterization of chemical structure of char and tar as a function of reaction history will also continue for different coals. It is anticipated that the chemical structure information can help to guide model development. In addition, the coal devolatilization studies will be interact more with the char combustion studies in the coming year, since common coals are being studied.

7. REFERENCES

Fletcher, T. H. 1989a. Comb. Sci. Tech. 63:89-105.

Fletcher, T. H. 1989b. Time-Resolved Particle Temperature Measurements and Mass Loss Measurements of a Bituminous Coal During Devolatilization. Accepted by Comb. Flame. Also presented at the Spring Meeting of the Western States Section of the Combustion Institute, Salt Lake City, Utah (March 1988).

Fletcher, T. H., Kerstein, A. R., Pugmire, R. J., and Grant, D. M. 1989c. ACS Div. Fuel Chem. Prepr. 34:1272-1279.

Freihaut, J. D. 1988. Kinetics of Coal Pyrolysis and Devolatilization. Technical Progress Report for DOE Contract DE-AC22-84PC70768 by United Technologies Research Center, East Hartford, Connecticut (for the period Nov. 1, 1987 - Jan. 31, 1988).

Gibbins-Matham, J. and Kandiyoti, R. 1988. Energy and Fuels, 2:505.

Grant, D. M., Pugmire, R. J., Fletcher, T. H., and Kerstein, A. R. 1989. Energy and Fuels 3:175-186.

Ko, G. H., Sanchez, D. M., Peters, W. M., and Howard, J. B. 1988. Twenty-Second Symp. (Int.) on Comb., The Combustion Institute, Seattle, Washington.

Seery, D. J., Freihaut, J. D., Proscia, W. M., Jenkins, R. G., Essenhigh, R. H., Howard, J. B., Peters, W. A., and Sarofim, A. F. 1988. Kinetics of Coal Pyrolysis and Devolatilization. Proceedings of the DOE Advanced Research and Technical Development (AR&TD) Direct Utilization and Instrumentation & Diagnostics Contractors' Review Meeting, Pittsburgh, Pennsylvania (September 6-9, 1988)

Serio, M. A., Hamblen, D. G., Markham, J. R., and Solomon, P. R. 1987. Energy and Fuels 1:138.

Solomon, P. R., Serio, M. A., Carangelo, R. M., and Markham, J. R. 1986. Fuel 65:182-194.

Solum, M. S., Pugmire, R. J., and Grant, D. M. 1989. Energy and Fuels 3:187-193.

RATES AND MECHANISMS OF COMBUSTION OF PULVERIZED COAL CHARS

1. CONTRACT NUMBER: FTPA Number 0709

CONTRACTOR: Sandia National Laboratories
Livermore, California 94551-0969
(415) 294-2321

CONTRACTOR PROJECT MANAGER: Donald R. Hardesty

PRINCIPAL INVESTIGATOR: Reginald E. Mitchell
PETC PROJECT MANAGER: James D. Hickerson

CONTRACT PERIOD OF PERFORMANCE: October 1, 1988 - continuing

2. SCHEDULE/MILESTONES:

FY89 Program Schedule

	S O N D J F M A M J J A S
Subtask 1. Determination of Apparent Char Particle Burning Rates	———————
Subtask 2. Determination of Intrinsic Reactivities of Coal Chars	———————
Subtask 3. Determination of Nitrogen and Sulfur Release Rates	———
Subtask 4. Investigation of Char Fragmentation Phenomena	———
Subtaks 5. Development of Engineering Models of Coal Char Combustion	———————

3. OBJECTIVES:

The overall objective of this task is to characterize the physical and chemical processes that govern the combustion of pulverized coal chars with respect to coal type, particle size and temperature, and gas temperature and composition. Of particular concern are the apparent and intrinsic burning rates of coal chars and the release rates of nitrogen and sulfur during char burnoff. Efforts are directed toward correlating the intrinsic chemical reactivity of the char and the release rates of nitrogen and sulfur with properties of the parent coal. An effort is also directed toward determining the degree to which particle fragmentation influences local extinguishment or enhancement of burning during the final stages of burnoff. Specific research objectives are associated with the five subtasks indicated above in the FY89 Program Schedule.

The experimental endeavor will provide a data base on the reactivities of coal chars and on the release rates of N and S during char burnoff.

The endeavor will yield a more complete understanding of the mechanism of char oxidation and will elucidate the effects of fragmentation on particle mass loss rates. In addition, the endeavor will provide an accurate predictive model of the overall char combustion process.

4. BACKGROUND STATEMENT:

The overall burning rates of pulverized coal char particles depend upon the transport of oxygen to the outer surfaces of particles, the diffusion of oxygen through the pores of particles, and the intrinsic chemical reactivity of the carbonaceous particle material. The relative importance of these various effects depends upon the chemical and physical properties of the parent coal, the particle sizes and temperatures, and the temperature and composition of the gaseous environment. In environments characteristic of practical pulverized coal combustors, the overall particle burning rates are controlled primarily by the combined effects of pore diffusion and the intrinsic chemical reactivity of the particle material. As burnoff progresses, the internal surfaces of particles become more accessible to oxygen and the intrinsic reactivity becomes more rate controlling. Late in burnoff, the mineral matter content of particles influences the temperatures of particles and the times of burnout. Before complete burnoff, particles may fragment, which in turn, may lead to local extinguishment or enhancement of burning. The degree of fragmentation and extinction directly effects the amount of carbon in the ash of industrial coal combustors.

The oxidation rates of nitrogen- and sulfur-containing species depend upon the local temperature and gas composition. Hence, during pulverized coal combustion, the emissions of nitrogen oxides (NO_x) and sulfur oxides (SO_x) from pulverized coal combustors depend upon the release rates of nitrogen and sulfur from the char particles during burnoff.

Presently, the data base needed to describe coal char burning rates is incomplete and the information needed to characterize pollutant emissions from practical pulverized coal combustors is insufficient. It is our goal to provide the necessary information. In the experimental endeavor, data on char particle size, temperature, and extent of burnoff, as well as data on the chemical and physical properties of the char at various degrees of burnoff are used to answer fundamental questions concerning char oxidation rates and mechanisms, mode of particle burning, and effects of mineral matter on the overall combustion process.

5. PROJECT DESCRIPTION:

EXPERIMENTAL

The experimental approach involves monitoring coal char particles burning in a laminar flow reactor in which the gas temperature, composition, and velocity are well-characterized. A particle-sizing-pyrometer (Tichenor, et al., 1984) is used to make in situ measurements of the sizes, temperatures, and velocities of individual char particles at selected heights above the reactor inlet and hence, at different residence times and extents of burnoff. An iso-kinetic solids sampling probe is used to

extract char samples from the reactor at the same heights at which the in situ measurements are made.

Analyses of the char samples and of the feed coal provide values of the extents of burnoff (via ash tracer techniques), particle surface areas (via gas adsorption measurements), apparent densities (via bulk density and mercury porosimetry measurements), and elemental compositions (via organic elemental analysis and inorganic elemental analysis for metal oxides) at the various measurement heights. Of particular interest are the C, H, N, S, and O elemental contents and the ash content of the char samples. The aluminum, calcium, iron, potassium, magnesium, silicon, sodium, and titanium contents of the ash are determined as well. The Al, Si, Ti, and total ash contents serve as four independent means of determining the extent of burnoff, m/m_o, of each sample employing ash tracer techniques.

A high-speed framing camera is used to observe fragmentation events in the laminar flow reactor. Emphasis is on the initial heat-up and devolatilization periods, and on particles near burnout. Determination of the particle-size-distributions of collected char samples provides information on the extent of fragmentation in various gaseous environments.

THEORETICAL

The measurements are used in the mass, momentum, and energy balance equations that describe single particles burning in the laminar flow reactor in order to determine overall particle burning rates and kinetic rate parameters (Mitchell, 1987, 1988a). The char particle oxidation model used is based on the single-film model of a burning carbon sphere (Field, et al., 1967). It is assumed that oxygen is the sole oxidizer and that both CO and CO_2 are heterogeneous reaction products. The model makes allowances for Stefan flow in the boundary layer surrounding the particle and for decreases in both particle diameter and apparent density with burnoff. Account is made for the effects of ash on the effective heat capacity and emissivity of the particle.

The overall particle burning rate (q, gC/cm^2-s) is given by:

$$q = PM_c D_{ox} Sh/(dR'T_m \gamma \nu_o) \ln[(1 - \gamma P_s/P)/(1 - \gamma P_g/P)] \qquad (1)$$

where the total pressure is denoted by P, and P_g and P_s are the oxygen partial pressures in the ambient and at the particle surface, respectively. D_{ox} is the oxygen diffusion coefficient in the mixture of gases in the boundary layer; M_c, the molecular weight of carbon; and, T_m, the mean temperature between the particle (T_p) and the gas (T_g). R' is the gas constant and Sh is the Sherwood number which is taken to be 2. The change in volume during reaction, referred to unit volume of oxygen, is γ and ν_o is the stoichiometric number of moles of oxygen consumed per mole of carbon converted at the particle surface.

In terms of an apparent chemical reaction rate coefficient, k_s (which includes the combined effects of pore diffusion and the intrinsic chemical reactivity of the particle material), and an apparent reaction order with

respect to the oxygen partial pressure, n, q is expressed also by:

$$q = k_s P_s^n \qquad (2)$$

An implicit equation for the overall burning rate is obtained by combining Eqs. (1) and (2) in such a way that P_s is eliminated.

Data reduction yields Arrhenius parameters (A_a and E_a) for the apparent chemical reaction rate coefficients, the apparent order of reaction with respect to the oxygen partial pressure, and the CO to CO_2 product ratio at the particle surface, ψ. The measurements also permit the parameters for the intrinsic chemical reactivities to be calculated (Mitchell, 1988b) from expressions for the particle Thiele modulus and effectiveness factor (Satterfield, 1970). Data reduction also yields the release rates of C, H, O, N, and S relative to the overall particle burning rate.

6. RESULTS/ACCOMPLISHMENTS:

During the course of this project, data on the combustion characteristics of the chars of ten United States coals ranging in rank from lignite to hva-bituminous have been accumulated. The coals were obtained from the Penn State Coal Data Bank. In addition, data on the combustion characteristics of the chars of three bituminous coals from Australia and a bituminous coal from South America have been accumulated. For each of the coals, the sizes, temperatures, velocities, extents of burnoff, and apparent densities of their char particles burning in 6 and 12 mole-% oxygen in the temperature range 1550 to 1750 K have been measured. For the U. S. coals, the C, H, N, S, and O elemental contents, the ash content, and the Ti, Al, Si, Fe, K, Na, Mg, and Ca contents of the ash have been determined as a function of burnoff. Table 1 shows the coals investigated.

APPARENT REACTION RATE PARAMETERS

For the chars of two of the U. S. coals, the coals from Australia, and the coal from South America, kinetic parameters for the overall particle burning rates have been determined. For the Australian Bayswater coal, kinetic parameters for its clarain, fusain, and durain maceral concentrates have been determined as well. Table 2 shows the kinetic parameters determined for various values of ψ, the CO to CO_2 product ratio at the particle surface. Detailed analysis of the data obtained with the char particles of Pittsburgh #8 and Illinois #6 coals indicates that at particle temperatures exceeding 1800 K, CO is the sole heterogeneous reaction product, but as the temperature decreases, CO_2 formation increases. At temperatures in the range 1600 to 1700 K, about 15% of the carbonaceous particle material can be converted to CO_2 at the particle surface. The values determined for the activation energies are in the range expected for burning controlled by the combined effects of pore diffusion and the intrinsic chemical reactivity of the particle material.

For the Pittsburgh #8 and Illinois #6 coal chars, the kinetic parameters shown adequately fit the apparent chemical reaction rate coefficients obtained for data in both the 6 and 12 mole-% oxygen environments. For these coals, the average temperatures of particles that fell into the

Table 1. Coals Investigated.

Seam Name	PSOC #	State/Country	Reported Rank
Lower Wilcox	1443	TX/USA	Lignite
Blue #1	1445	NM/USA	Subbituminous
Pittsburgh #8	1451	PA/USA	HVA-Bituminous
Dietz	1488	MT/USA	Subbituminous
Illinois #6	1493	IL/USA	HVB-Bituminous
Hiawatha	1502	UT/USA	HVC-Bituminous
Smith Roland	1520	WY/USA	Subbituminous
Beaulah Zap	1507	ND/USA	Lignite
Pocahontas #3	1508	WV/USA	LV-Bituminous
Lower Kittanning	1516	PA/USA	LV-Bituminous
Bayswater	-	NSW/Aust.	HVB-Bituminous
Blair Athol	-	Queensland/Aust.	MV-Bituminous
Ulan	-	NSW/Aust.	Bituminous
Cerrejon	-	Colombia/SA	HVB-Bituminous

Table 2. Apparent Reaction Rate Parameters.

Coal	ψ	n	A_a ($gC/cm^2\text{-}s\text{-}atm^n$)	E_a (cal)
Pittsburgh #8	0.0	0.50	7.21	19310
	0.15	0.50	4.63	19090
	0.30	0.50	3.44	19010
Illinois #6	0.0	0.25	1.72	16790
	0.15	0.30	1.02	15630
	0.30	0.35	0.64	14380
Bayswater (12 mole-% oxygen)				
Clarain	0.0	0.50	522	34870
Fusain	0.0	0.50	226	32080
Durain	0.0	0.50	849	37200
Banded	0.0	0.50	1905	39840
Cerrejon				
(6 mole-% oxygen)	0.0	0.10	94	31640
(12 mole-% oxygen)	0.0	0.30	249	33400
Ulan				
(6 mole-% oxygen)	0.0	0.30	5.46E5	49980
(12 mole-% oxygen)	0.0	0.30	505	36230
Blair Athol				
(6 mole-% oxygen)	0.0	0.10	15	25590
(12 mole-% oxygen)	0.0	0.40	297	33090

ten-micron size bins in which the particle sizes were grouped were used in the data reduction scheme (see Mitchell, 1987). For the other coals, apparent chemical reaction rate coefficients were determined for individual particles. Although excellent fits to the rate coefficients were obtained when the data in the 6 and 12 mole-% oxygen environments were considered separately, no adequate fit was obtained when the two oxygen-level environments were considered together. This may suggest that the simple, empirically-based power-law rate expression is invalid for coal char oxidation.

Effect of Maceral Composition

Tests with the four maceral concentrates of the Bayswater coal indicate that the oxidation rates of the fastest burning (vitrinite) and slowest burning (inertinite) macerals differ by 15% to 30% over the temperature range 1500 to 2000 K. The vitrinite/inertinite content of the maceral concentrates tested were: clarain, 83.6/9.4; banded, 74.1/19.1; fusain, 24.2/63.4; and durain, 8.7/78.8. The banded lithotype is so-called because of its alternate bright and dark appearance, the development of which is ascribed to differential settling of various decayed plant entities and mineral matter during formation of the coal.

Figure 1 shows a comparison of the fits to the apparent chemical reaction rate coefficients determined for the maceral concentrates burning in the

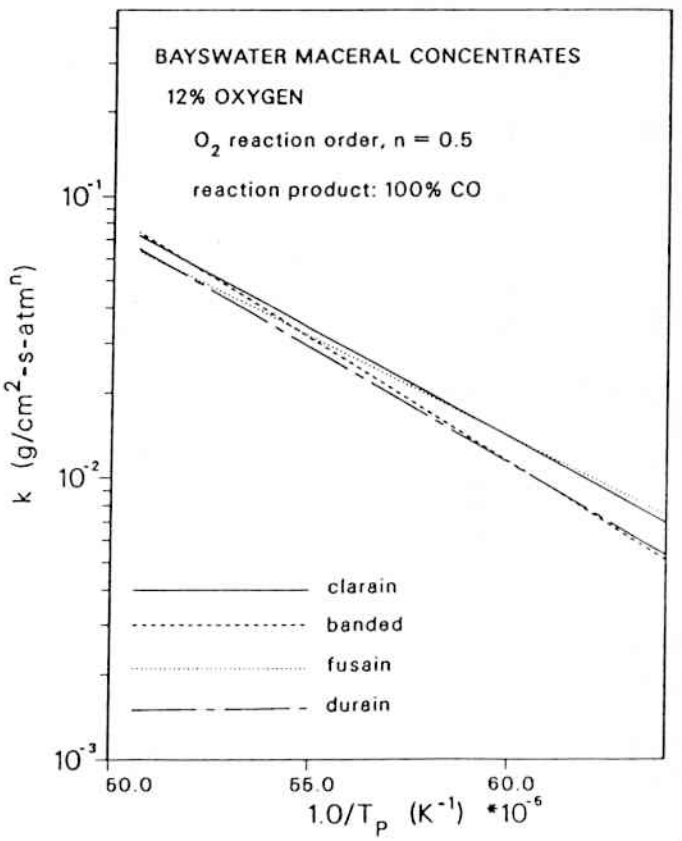


Figure 1. Comparison of Apparent Chemical Reaction Rate Coefficients Determined for the Maceral Concentrates of Bayswater Coal.

12 mole-% oxygen environment. Since the primary objective of tests with the Bayswater coal was to assess the differences in the high-temperature burning rates of the chars of coal macerals, data analysis was limited to the determination of apparent rate parameters when an apparent reaction order of 0.5 is assumed and when CO is assumed to be the sole heterogeneous reaction product. The figure indicates that in the particle temperature range 1500 to 2000 K, the vitrinite-rich clarain concentrate has the highest reactivity and the inertinite-rich durain concentrate has the lowest. These results are consistent with the lower temperature (1175 to 1500 K) drop-tube data reported by Bailey and Tate (1989). However at the higher temperatures, the differences in the reactivities of the macerals is not as great.

EFFECT OF ASH CONTENT ON PARTICLE TEMPERATURES

Data analysis indicates that the wide variations in the temperatures of particles of nominally the same size are a consequence of the particle-to-particle variations in ash content. Figure 2 shows the measured temperature distributions for the char particles of Lower Wilcox coal (which contains 15% ash, mf) and Blue #1 coal (which contains 4% ash, mf) burning in the 12 mole-% oxygen environment established in the laminar flow reactor. For each coal, particles in the 106 to 125 μm size range were used and the overall particle burning rates of their chars were within 85% of the diffusion-limited rates in the gaseous environment employed. Comparison of the distributions in the figure indicates that at the 12.7 and 19.1 cm measurement heights, the temperature distributions for the char particles of the Lower Wilcox coal are broader than those for the char particles of the Blue #1 coal. Only at the 25.4 cm measurement height (where burnoff exceeds 95%, daf, for each of the coals) are the distributions similar in breadth. At each measurement height, the Lower Wilcox coal produces more low-temperature particles than the Blue #1 coal. Theoretical calculations indicate that the low-temperature particles are high-ash particles that are either in their final stages of burning or had reached burnout before the measurement height was reached.

These results lead us to modify our data reduction scheme so as to determine overall burning rates and apparent rate coefficients for individual particles and not just for the average temperatures of particles that fall into the ten-micron size bins into which the particle sizes are grouped. Figure 3 shows apparent chemical reaction rate coefficients determined for the char particles of Lower Wilcox coal particles burning in the 12 mole-% oxygen environment at a height of 12.7 cm above the reactor inlet. The different symbols represent particles having calculated emissivities that fall into the ranges indicated in the figure. Particle emissivities are calculated using the measured particle intensities, sizes, and temperatures in Wien's equation modified for nonblack emitters (Mitchell, 1987). The calculations assume that the particles are spherical. Analysis of non-sphericity effects (Waters, et. al., 1988) indicates that the emissivities are correct to within 50%.

Two notable conclusions can be inferred from the linearity displayed in Fig. 3. First, the fact that particles of different ash content exhibit the same temperature dependence suggests that ash-catalysis effects are

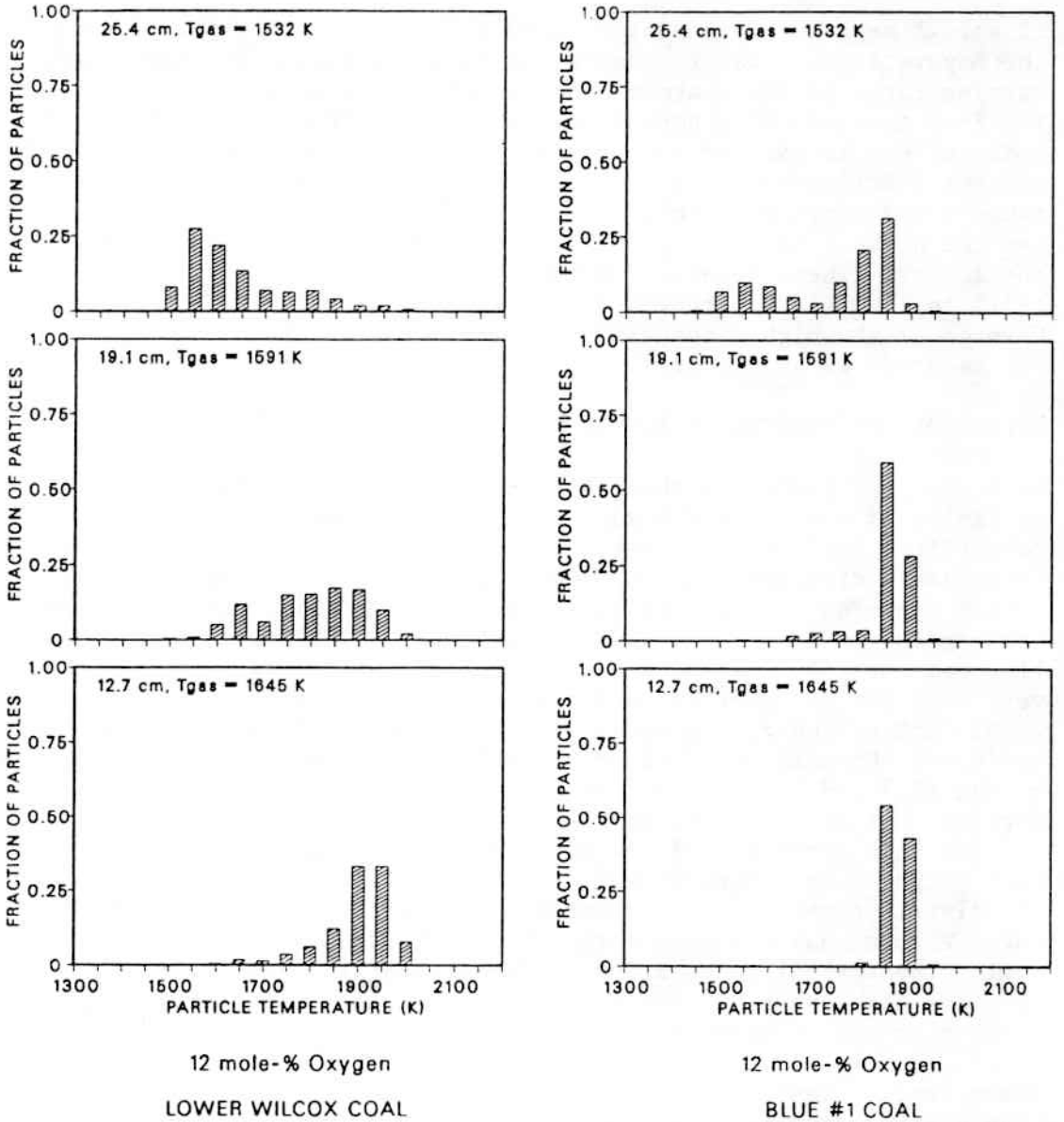


Figure 2. Temperature Distributions of Char Particles of Lower Wilcox and Blue #1 Coals Burning in 12 mole-% Oxygen. Initial Coal Particle Size Range: 106 to 125 μm.

negligible. If the reaction rate were influenced by the ash in the particle, one would expect for the temperature dependence to change with the ash content of the particle. Second, the fact that particles at different extents of burnoff exhibit the same temperature dependence suggests that the reaction mechanism does not change with burnoff. Since the linearity persist down to temperatures that indicate that the particles are barely burning (temperatures below the local gas temperature), the data suggests that the reaction mechanism remains unchanged throughout the lifetime of the particle. Despite the differences in reactivities of the coal macerals, the whole coal burns uniformly.

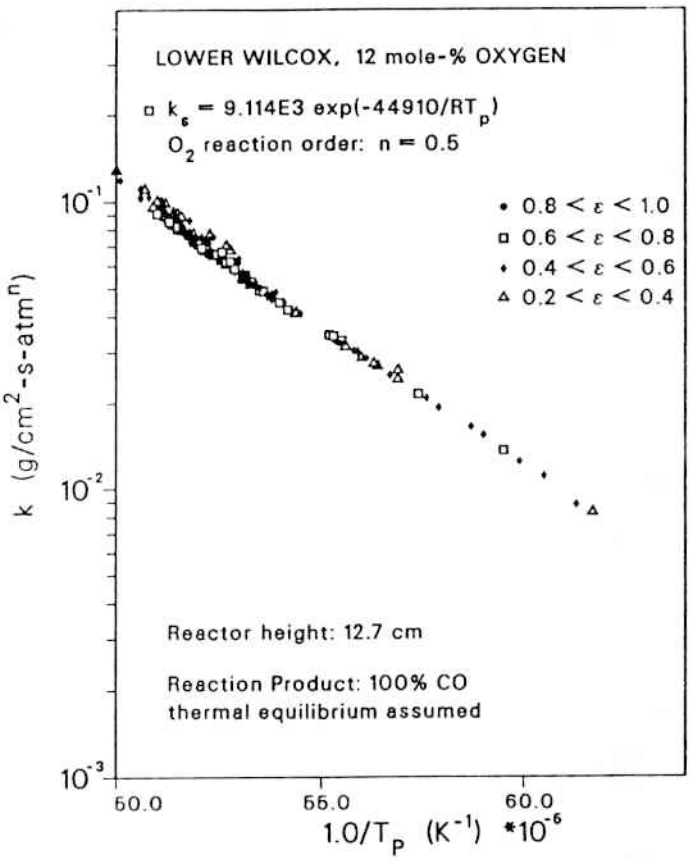


Figure 3. Apparent Chemical Reaction Rate Coefficients Determined for the Char Particles of Lower Wilcox Coal Burning in 12 mole-% Oxygen, 12.7 cm above the Reactor Inlet.

7. FUTURE WORK:

This mass of data obtained during FY89 needs to be analyzed in such a way that fundamental questions regarding the char combustion process can be answered. For the chars of each of the ten U.S. coals, we will determine the kinetic parameters that describe their apparent, overall particle burning rates and their intrinsic chemical reactivities. An important activity will be our attempt to correlate the intrinsic chemical reactivities of the chars with properties of their parent coal. In determining such rate parameters, we need to determine an appropriate reaction mechanism for the oxidation process. Analysis of the data obtained with several coals in different oxygen-level environments suggests that the simple, empirically-based, n-th order power-law expression may not be valid for coal chars. We plan to consider initially the more complex Langmuir-Hinshelwood mechanism as applied to the carbon/oxygen heterogeneous reaction. The effects of fragmentation on the rates determined will be assessed.

The total surface area available for reaction is needed in order to determine intrinsic rates. Efforts to determine the appropriate surface area (either the N_2-BET surface area, that determined via CO_2 adsorption

using the Polanyi-Dubinin equation, or the so-called active surface area determined via oxygen adsorption techniques) will be undertaken.

With the ten United States coals, we have obtained sufficient data to determine the nitrogen and sulfur elemental release rates from the chars during burnoff. We plan to answer questions concerning the effects of heating rate and coal type on the N and S release rates. We also plan to answer questions concerning how the sulfur release rates are dependent upon the forms of sulfur (inorganic, organic, sulfactic) in the coal.

We also plan to investigate the causes of the unburned carbon in the ash of industrial coal combustors. This effort will require combustion tests on chars in their final stages of burnoff (extents of burnoff greater than 98%, daf). We plan to determine if the low reactivity of certain coal constituents is a significant contributor to the unburned carbon and if it is possible that ash particles block pores or prevent oxygen from reaching internal particle surfaces (by for instance, char particles being embedded in mineral clusters) thereby retarding carbon oxidation.

8. REFERENCES:

Bailey, J. G. and Tate, A. G. (1989). Understanding and Modelling Coal Combustion, Advances in the Study of the Syndey Basin, Proceeding of the Twenty-third Symposium, March 31 - April 2, The University of Newcastle, NSW, Australia.

Field, M. A., Gill, D. W., Morgan, B. B., and Hawksley, P. G. W. (1967). Combustion of Pulverized Coal, BCURA, Leatherhead, p. 186.

Mitchell, R. E. (1987). Experimentally Determined Overall Burning Rates of Coal Chars, Comb. Sci. Tech. 53(2-3), 165.

Mitchell, R. E. (1988a). On the Products of the Heterogeneous Oxidation Reaction at the Surfaces of Burning Coal Char Particles, 22nd Symposium (Int.) on Combustion/The Combustion Institute, Pittsburgh, p. 69.

Mitchell, R. E. (1988b). Determination of the Intrinsic Reactivities of Pulverized Coal Chars at High Temperatures, 1988 Spring Meeting, Western States Section/Combustion Institute, Salt Lake City, March 21-22.

Satterfield, C. N. (1970). Mass Transfer in Heterogeneous Catalysis, MIT Press, Cambridge, 1970.

Tichenor, D. A., Mitchell, R. E., Hencken, K. R., and Niksa, S. (1984). Simultaneous In Situ Measurements of the Size, Temperature and Velocity of Particles in a Combustion Environment, 20th Symposium (Int) on Combustion/ The Combustion Institute, Pittsburgh, p. 1213.

Waters, B. J., Mitchell, R. E., Squires, R. G., and Laurendeau, N. M. (1988). Overall Kinetic Parameters for the Combustion of a Highly Non-Spherical Carbon Char, 22nd Symposium (Int.) on Combustion/The Combustion Institute, p. 17.

AN ENGINEERING MODEL FOR COAL DEVOLATILIZATION

1. CONTRACT NUMBER: DE-FG22-88PC88900

CONTRACTOR: High Temperature Gasdynamics Laboratory
Mechanical Engineering Department
Leland Stanford Junior University
Stanford, CA 94305
415/723-2234

CONTRACTOR PROJECT MANAGER: Asst. Prof. Stephen Niksa

PRINCIPAL INVESTIGATOR: Asst. Prof. Stephen Niksa

PETC PROJECT MANAGER: Mr. James Hickerson

PERIOD OF PERFORMANCE: March 4, 1988 to February 28, 1990

2. SCHEDULE/MILESTONES:

1989 Program Schedule

	J F M A M J J A S O N D
Flash Distillation	
Correlating UTRC Data Set	———
Depolymerization Model	——
Transport Analysis	———————
Entrained Flow Data	———
Coal Rank Effects	———

3. OBJECTIVES:

This research aims for an engineering model for the evolution of volatile matter from coal during p. f. firing, along with a detailed analysis of the chemistry and transport phenomena in the vicinity of entrained coal particles during combustion, to begin to understand ignition, heat release, and pollutant formation during the initial stages of p. f. firing. A separate task is developing bona fide depolymerization kinetics with reattachment into char, and flash distillation of small, volatile fragments as tar vapor, to explain the behavior of different coal types.

4. BACKGROUND STATEMENT

The first two tasks, the engineering model and devolatilization theory for different coals, are direct outgrowths of the earlier modeling of Niksa and Kerstein. Specifically, DISCHAIN and DISARAY introduced the impact of macromolecular configuration on

the evolution rates and yields during rapid coal pyrolysis. Closed form analytical expressions based on simplifying assumptions ensured computational requirements which are compatible with the constraints of large scale combustor codes. While suitable for vacuum pyrolysis, these models did not apply to pyrolysis under pressure, or attempt to predict tar characteristics.

FLASHTWO, the engineering model, extends the earlier models by explaining pressure effects with flash distillation, and predicts the molecular weight distributions (MWDs) of tar. FLASHCHAIN, the depolymerization model, predicts the complete distributions of all fragments, liquid or vapor, and is based, in part, on the structural parameters deduced from ^{13}C NMR analyses.

The third task, the transport analysis of entrained particles, is among the first detailed studies of the interplay among various transport mechanisms and chemical rates in the vicinity of entrained particles during the initial stages of combustion.

6. PROJECT DESCRIPTION:

There are three distinct modeling projects in this program: (1) A reaction model for coal devolatilization which is compatible with large scale combustor simulators yet predicts the yields of tar, gas, char, and unreacted coal throughout the technological operating domain, with heuristic adjustments for different coal types; (2) A theoretical framework based on bona fide depolymerization kinetics with recombination into char which accounts for the behavior of different coal types; and (3) An analysis of the chemistry, heat and mass transport in the vicinity of individual coal particles, to begin to describe the initial stages of the combustion of entrained coal particles.

7. RESULTS AND ACCOMPLISHMENTS:

THE ENGINEERING KINETICS MODEL

FLASHTWO (Niksa, 1988), the engineering model, was developed by analogy with a single-stage, equilibrium flash distillation, and has been validated against several wire-grid pyrolysis studies of HVA bituminous coals (Niksa, 1989). The model accurately depicts the influences of temperature, time, heating rate, pressure, and particle size. This theory yields the first mechanistic basis for the observed insensitivity of tar MWDs to temperature, and the tendency to form lighter tar at higher pressures is also explained. Hence, the influences of all of the important operating conditions on the devolatilization of high volatile bituminous coals can be understood in terms of only three mechanisms: (1) the disintegration of the coal macromolecule into primary fragments which are widely distributed in size; (2) the partitioning of the primary fragments into volatile and condensed species according to a phase equilibrium for continuous mixtures; and (3) competitive char formation in the condensed phase with the simultaneous evolution of non-condensible gases.

THE DEPOLYMERIZATION MODEL

Overview of the Theory

FLASHCHAIN, the depolymerization theory, is now fully developed (Niksa, 1989A). This model also rationalizes the influences of all operating conditions on the devolatilization of bituminous coals. Like DISCHAIN (Niksa & Kerstein, 1986) and DISARAY

(Niksa & Kerstein, 1986), it comprises simplified kinetic mechanisms and analytical expressions to account for configurational effects, and to describe their evolution in time. However, the complete size distributions of all fragments are now determined. And like FLASHTWO (Niksa, 1988), this theory invokes a phase equilibrium among intermediates in the condensed phase and tar components in the vapor to rationalize the pressure dependence. Whereas the fragment distribution in FLASHTWO is assumed a priori, it is now computed from the configurational model.

Coal is modeled a distribution of linear chains composed of refractory aromatic nuclei interconnected pairwise by two types of linkages, labile bridges and refractory char links. The initial coal constitution is specified by the proportions of labile and broken bridges and char links, and the probability that peripheral groups appear on the ends of fragments. Initially and throughout pyrolysis, the condensed phase species are subdivided into reactant, intermediate, and metaplast lumps, in order of decreasing size.

Labile bridges either dissociate during pyrolysis or spontaneously decompose into char links. These pathways are designated as bridge scission and spontaneous condensation, respectively. Both reaction rates are based on the same Gaussian distribution of activation energies, and a stoichiometric coefficient specifies the selectivity between these two pathways. Recombinations among the ends of metaplast fragments produce additional char links, and also additional gases if peripheral groups are present on the ends which participate.

Tar formation is also developed from the metaplast only, using the flash distillation analogy; i. e., a phase equilibrium relates the instantaneous mole fractions of like fragments in the tar vapor and metaplast. Tar quality is expressed in terms of its molecular weight distribution, and the proportions of peripheral groups, labile and refractory links, as a coarse scale for aromaticity.

All simulations in this study are based on the parameters in Table 1. The molecular weight of aromatic nuclei, and the MW ratios for bridges and peripheral groups were assigned from ^{13}C NMR analyses of HVA bituminous coals (Solum et al., 1989), to match the carbon aromaticities and measured average molecular weights of noncondensibles (25g/g-mole). At the tabulated initial probability for all links, there is 9.4 wt % of metaplast in the reactant, which is similar to the amounts of THF extracts from such coals. All other values and the rate parameters were assigned to match the transient product distributions and tar molecular weights for atmospheric pyrolysis at 10^3K/s. Once assigned, only the operating conditions of pressure, temperature, heating rate, and/or time were varied to match those in all other experiments. While the pressure is usually assigned as the ambient pressure, simulations of vacuum pyrolysis are based on a pressure of 0.025 MPa.

A simulation of each thermal history requires about 2 minutes on a 386 personal computer operating at 20 MHz, with an 8-Bit Fortran compiler.

Data Correlations

The predicted distribution of all reaction species for atmospheric pyrolysis is compared with measured weight loss and tar yields in Fig. 1. The thermal histories consist of uniform heating at 10^3K/s to the stated temperatures immediately followed by cooling at 10^2K/s. The correlations of both weight loss and tar yields are within the experimental uncertainty throughout. Note that the proportions of tar to gas decrease continuously, and that tar formation is completed by about 900K, but gas evolution persists through higher temperatures.

Table 1. Model Parameters.

Coal Characteristics

MW of Aromatic Nuclei	186 g/g-mole
MW Ratio, Bridges to Nuclei	0.785
MW Ratio, Char Links to Nuclei	0.300
MW Ratio, Peripheral Groups to Nuclei	0.134
Initial Fraction of Total Links	0.912
Initial Fraction of Labile Bridges	0.600

Rate Parameters

Reaction	A-Factor, s^{-1}	Ea, kJ/mole
Bridge Dissociation	3×10^{11}	176 ($\sigma = 25$)
Recombination	4×10^{14}	209
Per. Group Elim.	1×10^{15}	230

Selectivity Coefficient for Bridge Scission 0.35

$P^{SAT}_{metaplast}(T, MW) = 1.5 \times 10^3 \exp(-165\ MW^{0.6}/T)$, MPa

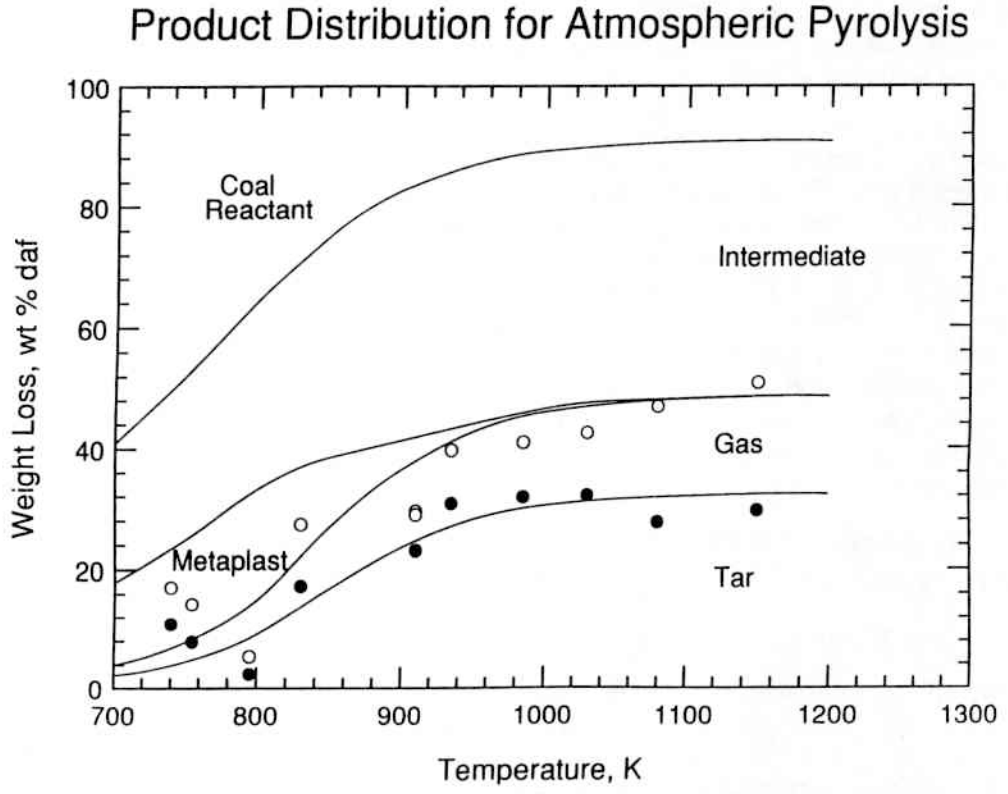


Fig. 1. The predicted distribution of reaction species for atmospheric pyrolysis for heating at 10^3K/s followed by immediate cooling at 100K/s, compared to Oh's measurements of weight loss and tar yields.

The largest fragments in the coal, the reactant lump, are rapidly converted into intermediates up to about 950K. Note that, due to spontaneous char formation, not all of the reactant fragments dissociate into either of the smaller lumps. The intermediate accumulates continuously, initially by fragmentation of the reactant and ultimately by bimolecular recombination of metaplast. The predicted amount of metaplast is maximized at 800K, then falls during the most rapid stage of tar evolution; its disappearance coincides with the end of tar formation.

The predicted number-average molecular weight of tar for vacuum and atmospheric pressure are compared with Oh's measurements in Fig. 2. At both pressures the predicted values are within the experimental uncertainty. The theory captures the observations that (1) the first tar fragments are somewhat lighter than the bulk of the tar fraction; and (2) increasing the pressure shifts the tar to substantially lower molecular weights. Both of these features are tied to the flash distillation mechanism. Although predicted distributions are omitted here, they all are of the form of Gamma-distributions.

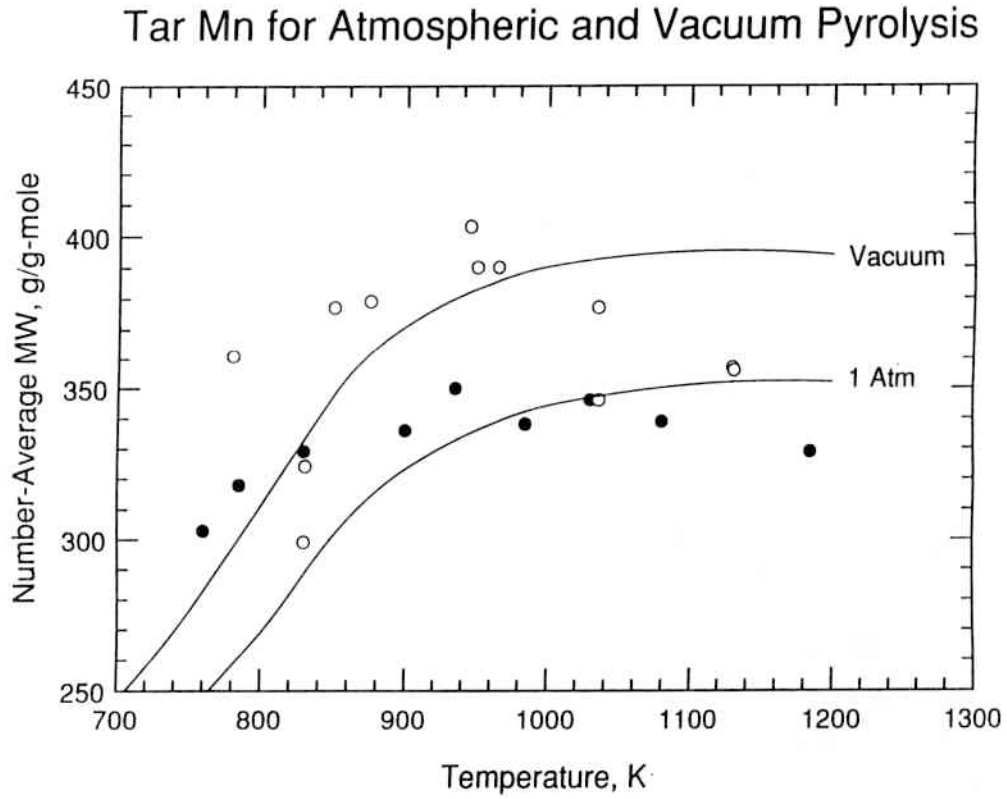


Fig. 2. An evaluation of the predicted number average molecular weights of tar for vacuum and atmospheric pyrolysis against Oh's GPC determinations. Thermal histories are the same as in Fig. 1.

Variations in the thermal history for nearly-atmospheric pyrolysis are examined in Fig. 3. These three cases depict the influence of extended reaction times at constant temperature following uniform heating, and variations in heating rate of three orders of magnitude. For the case of heating at 10^3K/s with immediate quenching, the predictions are within the experimental uncertainty, except at the highest temperatures. The predicted impact of a 30s reaction period at each temperature is quantitatively correct, in that most of the weight loss is observed at temperatures between 650 and 900K.

The predicted variation due to lowering the heating rate from 10^3K/s to 1K/s is qualitatively accurate, but the entire curve seems shifted from the data by about 30K. At higher temperatures the predicted weight loss is about 2–5% lower than the data.

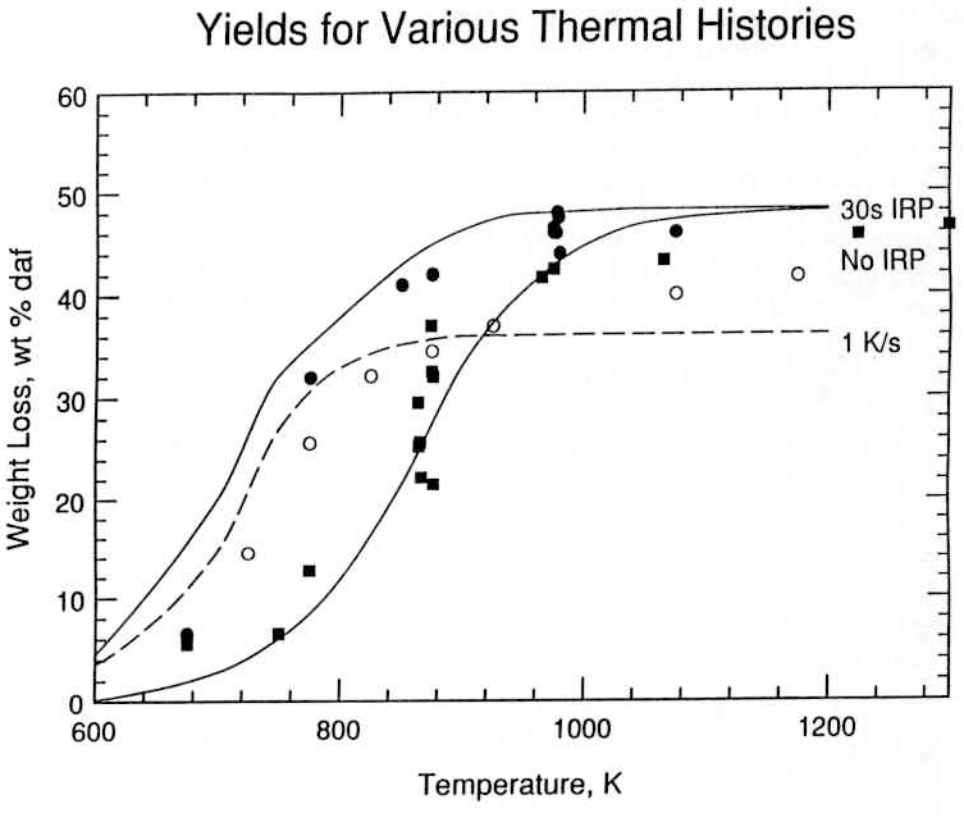


Fig. 3. An evaluation of the predicted weight loss for various thermal histories against the data recorded at 0, 12 MPa (Gibbons-Maltham, 1988). Both solid curves are for a heating rate of 10^3K/s, with different reaction times at constant temperature of 30s (upper curve and filled circles) and 0s (open circles). The dashed curve and open squares depict the behavior at 1K/s.

This theory omits both gas-phase tar deposition and mass transport limitations which have long been regarded as the mechanistic basis for the pressure effect; instead, it relies on the phase equilibrium between metaplast and tar to retain more light fragments in the condensed phases as the pressure increases. This mechanism strongly influences the tar yields, especially at pressures up to several atmospheres. In Fig. 4, predicted tar yields at three pressures are validated by the available data.

Qualitatively, this theory captures the influences of all of the important operating conditions on the devolatilization behavior of high volatile bituminous coals, and in most cases the quantitative agreement is within the experimental uncertainties. But its greatest potential lies in the formalism to rationalize the behavior of different coals. In this study, only the connection to the structural parameters from ^{13}C NMR analyses has been demonstrated, and the general reliability of the predictions is encouraging. Future reports will evaluate the predicted behavior for variations in the parameters which describe the initial constitution of the coal.

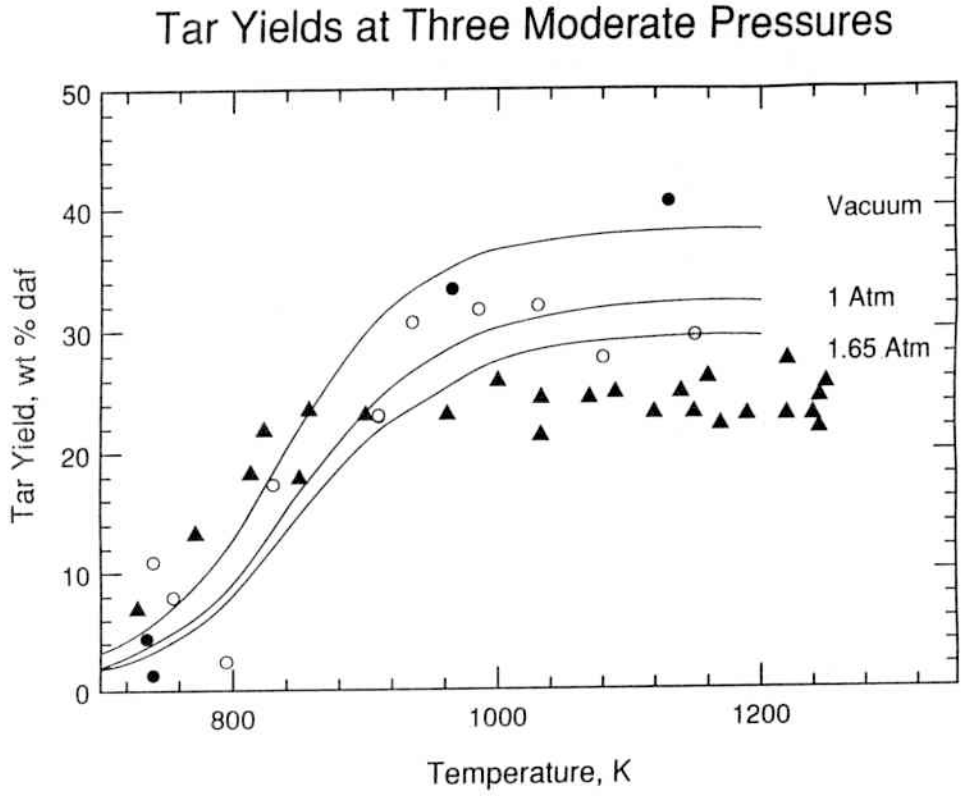


Fig. 4. An evaluation of the predicted tar yields for vacuum and atmospheric pyrolysis, with data from Oh, and for pyrolysis at 0.165MPa, with data from Suuberg et al., 1985. The thermal histories are the same as in Fig. 1.

TRANSPORT ANALYSIS OF AN ENTRAINED, DEVOLATILIZING PARTICLE

Physical Basis

For laminar flow fields and fuel particles in the pulverized size grade, thermal histories are often based on a convective heat flux evaluated in the Stokes limit, for which the extent of the thermal profile is nominally infinite and the Nusselt number for spheres is two. To account for the outward volatiles flux and the attendant reduction in the convective heat flux, many use the "blowing factor", which is an exact solution of the thermal profile with an outward flux, but again for the nominally infinite film.

Although widely implemented, applying these results to transient heating violates both mass and energy conservation. The inconsistency is seen most clearly in the idealized case where the particle is instantaneously injected into a hot stream, then heats up continuously at a non-uniform rate, as sketched in Fig. 5. The initial temperature gradient at the surface is nominally infinite for this case, as is the initial value of the Nusselt number. As the thermal profile develops the surface temperature gradient falls, causing the Nusselt number to relax continuously to two. Particle heating rates are thereby enhanced by the higher heat fluxes during the initial stages.

In contrast, applying a Nusselt number of two at the injection point implies that the evolution of the thermal profile is also instantaneous. This is impossible because the energy transfer associated with the formation of the fully-developed profile is nominally

infinite, since the film is unbounded. Where does this energy go? Certainly not into the particle, although the particle is in fact the only sink for energy in this system.

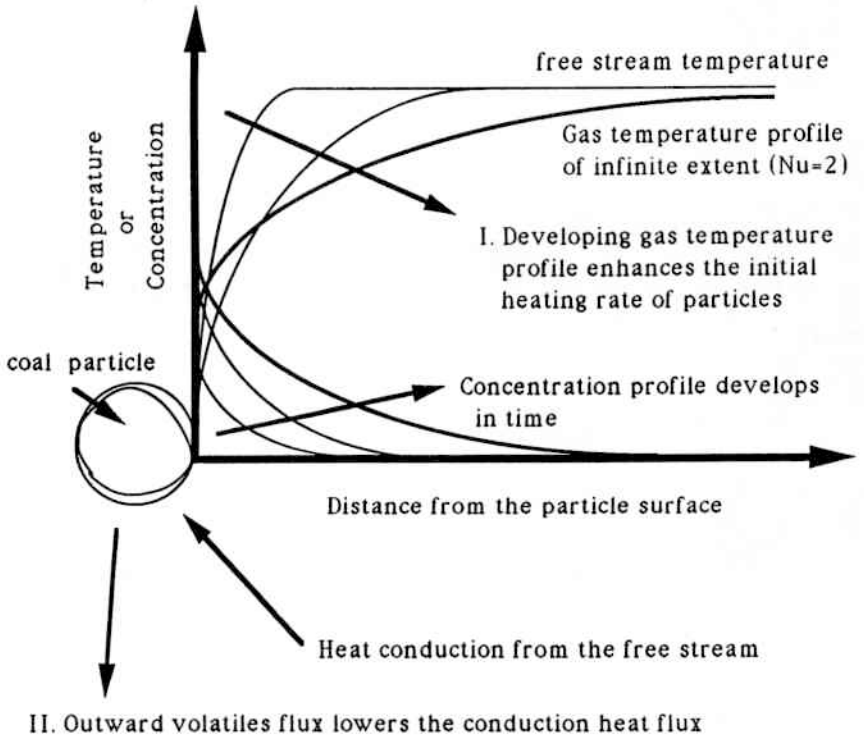


Fig. 5. Accumulation effects depicted for instantaneous injection of a fuel particle into a hot, isothermal stream.

Model Formulation

The analysis invokes the following assumptions: (1) There is no homogeneous chemistry since no oxidizer is present; (2) Internal heat conduction within the particle is relatively rapid; (3) Quasi-steady conditions prevail in the gas phase; i. e., the concentration and temperature profiles rapidly adapt to the changing conditions at the particle surface and in the far field, as a consequence of the disparate densities of the vapor and solid phases at atmospheric pressure; (4) Volatiles are coarsely lumped into a single component, and the devolatilization rate is based on the Distributed-Activated Energy Model (DAEM) (Anthony et al., 1975).

The transport equations are developed separately (Lau & Niksa, 1989). They are the conventional ones, except that global conservation relations in the system ensure that the total exchanges of mass and energy between the particle and film are conserved; these integral constraints define the time evolution of the thermal and concentration profiles.

Evaluation Against Measured Particle Temperatures and Yields

In all subsequent simulations, the DAEM parameters are: (i) Frequency factor (A_o) = 2.5 x 10^{10} s^{-1}, (ii) Mean activation energy (E_o) = 167 kJ/mole-K and (iii) Standard deviation in the activation energy distribution (σ) = 18.8 kJ/mole-K . These values were assigned from time-resolved weight loss measurements from HVA bituminous coals during heatup

at 0.5, 1, 100, 515 and 640 K/s in heated wire grids, as explained separately (Lau & Niksa, 1989A). The coal studied is a high volatile bituminous coal from the Pittsburgh Seam. All physical properties of the coal and volatiles are based on tabulations in the literature. For the coal studies, density and size changes are factored into the analysis by using a swelling correlation prepared by Fletcher, based on the measured sizes and yields of volatile matter.

It is important to realize that there are no parameters in the AEM which are adjusted to fit the data in this section. The DAEM parameters and thermophysical properties are assigned independently and remain the same for all operating conditions; furthermore, the free stream conditions, the swelling correlation, and the relation between time and distance are based on direct measurements.

The comparison between the AEM predictions and Fletcher's transient temperature measurements of coal particles appears in Fig. 6. Normalized devolatilization rates from the AEM appear as the dashed near-normal curves. The initial increase in particle heating rates predicted by the AEM is supported by the close agreement, and the predictions are within the experimental uncertainty throughout. For the two sets of ambient conditions in the coal studies, the initial heating rates are enhanced by a factor of two. The impact of convective blowing is also evident, although small because of the low reactor temperatures and correspondingly low devolatilization rates.

These data were also correlated with a conventional blowing factor (Fletcher, 1988), although large heuristic parameter adjustments were required for quantitative agreement. More importantly, the adjustments differ by more than a factor of two for these two reactor temperatures even though the reactor temperature varied by only 250K in these two cases.

The transient yields predicted by the AEM for the conditions in Fig. 6 appear with the measured values in Fig. 7. Since the DAEM does not predict the ultimate yield of volatiles, the data and model predictions are expressed as fractional conversions. While the quantitative discrepancies for the data at the lower reactor temperature are greater than the experimental uncertainty, the predictions are remarkably reliable considering that the rate parameters for the DAEM were assigned from data for heating rates from 0.5 to 640 K/s. Of course, the agreement could be improved by adjusting the input parameters in the DAEM, without degrading the comparison with the measured temperatures because blowing is weak.

The next case evaluates the predicted transient yields against data for faster heating rates and higher temperatures. With the same coal used in Fletcher's study, Haussmann recorded transient weight loss in a drop tube furnace at 1400K (Haussmann & Kruger, 1989). Due to the injector configuration and the small particle size, 52 microns, the nominal heating rate in this experiment approaches 10^5 K/s, which is about ten times higher than in Fletcher's study. Direct particle temperature measurements are unavailable, however, so this comparison involves only transient weight loss.

The predicted transient temperature and weight loss appear in Fig. 8. The agreement between the predicted and the measured weight loss data is within the experimental uncertainty throughout. The scaled devolatilization rate shows that, despite the faster heating rate, devolatilization is complete during heatup.

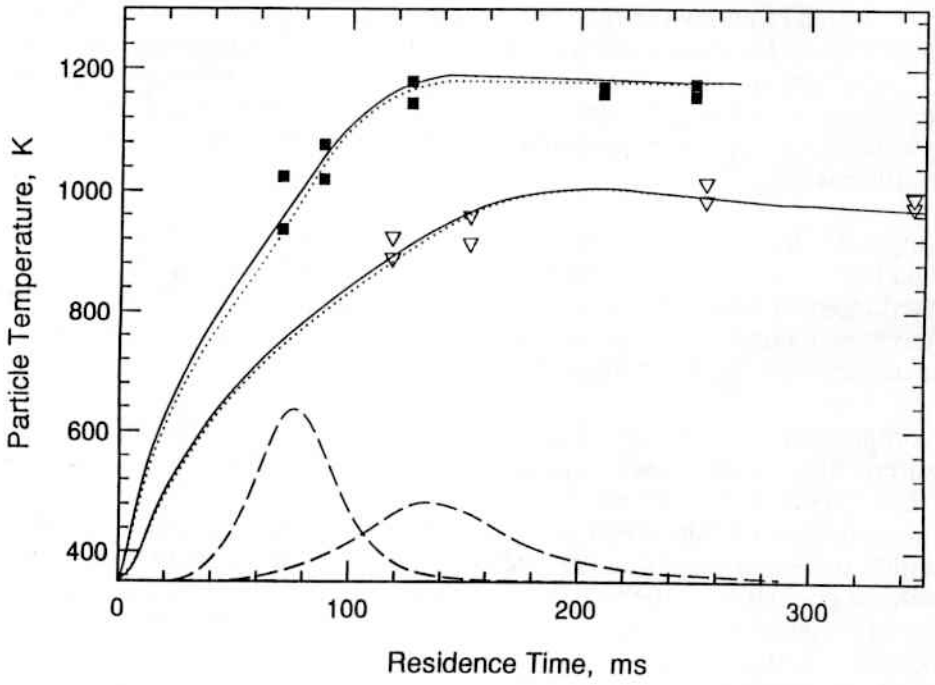


Fig. 6. Comparison of temperature histories based on the AEM with measured temperatures for 115 micron HVA bituminous (PSOC-1451) coal particles at nominal reactor temperatures of 1050K ( ) and 1250K, from Fletcher, 1988. The dotted curves which closely follow the AEM simulations are based on the Nu-correlation. The near-normal curves in the lower left are the nondimensional volatiles fluxes from the AEM simulations.

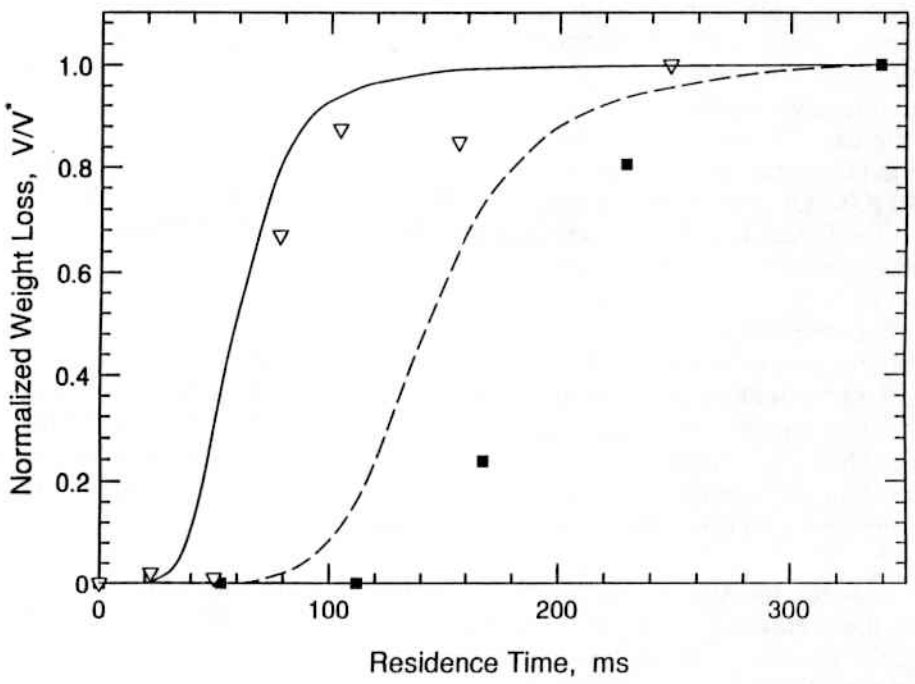


Fig. 7. Comparison of transient fractional weight loss from the AEM with measured values for 115 micron HVA bituminous (PSOC-1451) coal particles at nominal reactor temperatures of 1050K ( ) and 1250K, from Fletcher, 1988.

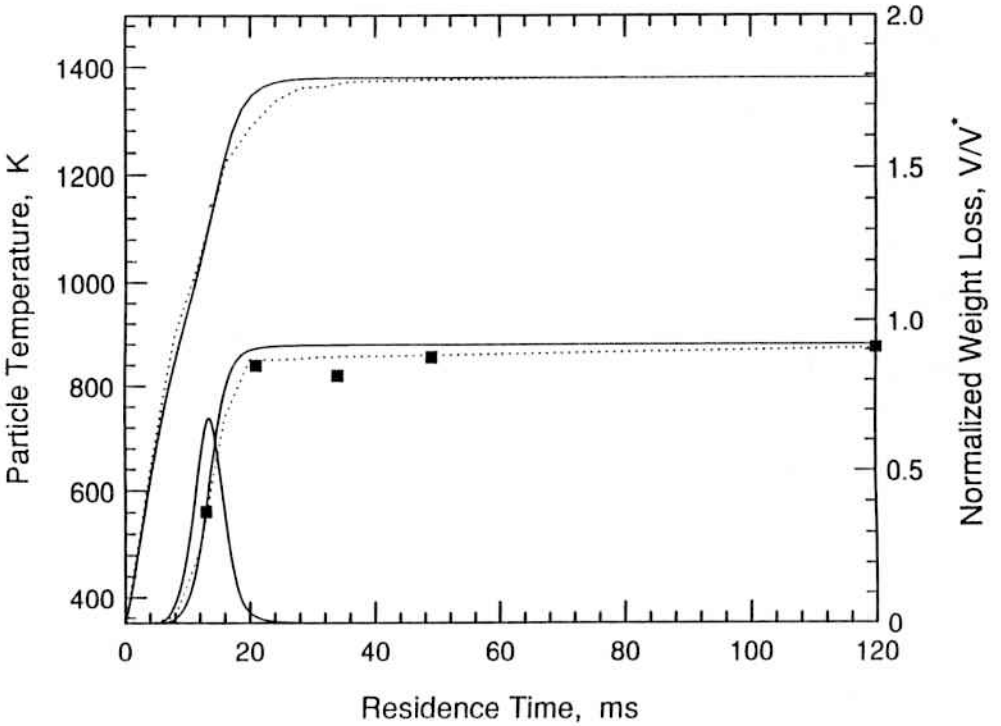


Fig. 8. Comparison of temperature histories (dashed curve) and weight loss (solid curve) from the AEM with weight loss for 52 micron HVA bituminous (PSOC-1451) coal particles at a nominal reactor temperature of 1400K (■), from Haussmann, 1989. The dotted curves which closely follow the AEM simulations are based on the Nu-correlation. The near-normal curve in the lower left is the nondimensional volatiles flux from the AEM.

NUSSELT NUMBER CORRELATIONS FOR TRANSIENT HEATING

While the evaluations against measurements support the accumulation effects predicted by the AEM, the model's utility would be restricted by its computational burden. We reanalyzed the transient heating of non-reacting particles to identify all relevant nondimensional parameters and then devised a correlation of the transient Nusselt number which represents the initial enhancements of particle heating rates. Once the blowing factor is incorporated, the correlation describes the transient heating of reacting particles as well. It is

$$Nu(\tau) = \left[\frac{35.1}{\tau^{0.75}\sqrt{\eta_t}} \left(\frac{t_{mix}}{t_c} \right)^{-0.4} + 2 \right] \left[\frac{\frac{P}{Le}}{\exp(\frac{P}{Le}) - 1} \right]$$

where P is a scaled devolatilization rate; τ is nondimensional time; Le is the Lewis number; η_t is a group of physical properties; and $\frac{t_{mix}}{t_c}$ is a ratio of time constraints.

Particle temperature histories based on the correlation appear as the dotted lines in Figs. 6 and 8; in all cases the deviations are less than 50K throughout all stages of transient heating.

7. FUTURE WORK

Both FLASHTWO and FLASHCHAIN will be fit to the data from different coals which was recently reported by Freihaut and coworkers at UTRC. The transport analysis has already been extended to use FLASHTWO as the devolatilization submodel. Flux expressions for oxygen transport and surface reactions are now being added, paving the way for finite-rate homogeneous chemistry throughout the film.

8. REFERENCES

Anthony, D. B., Howard, J. B., Hottel, H. C. and Meissner, H. P.: *Fifteenth Symposium (International) on Combustion*, p. 1303, The Combustion Institute, 1975.

Bautista, J. R., Russel, W. B., and Saville, D. A., Ind. Eng. Chem. Fundam. 25:536 (1986).

Fletcher, T. H., paper presented at the WSS/CI Fall Meeting, Dana Point, CA, Oct. 1988.

Gibbins-Maltham, J. and Kandiyoti, R., Energy Fuels 2:505 (1988).

Lau, C. W. and Niksa, S., Paper No. 89-9, WSS/CI Spring Meeting, Pullman, Wa, April 1989.

Lau, C. W. and Niksa, S., Combust. Flame, submitted, September, 1989.

Niksa, S. and Kerstein, A. R., Combust. Flame 66:95 (1986).

Niksa, S. and Kerstein, A. R., Fuel 66:1389 (1987).

Niksa, S., AIChE J. 34:790 (1988).

Niksa, S., Twenty-Second Int. Symp. on Combust., The Combustion Institute, Pittsburgh, PA, 1989, p. 105.

Niksa, S., ACS Div. Fuel Chem. Pre., 34(4), 1292 (1989A).

Oh, M. S., "Softening Coal Pyrolysis", Sc. D. thesis, Department of Chemical Engineering, MIT, 1985.

Solum, M. S., Pugmire, R. J., and Grant, D. M., Energy Fuels 3:187 (1989).

Suuberg, E. M., Unger, P. E., and Lilly, W. D., Fuel 64:966 (1985).

DETAILED MODEL FOR PRACTICAL PULVERIZED COAL FURNACES AND GASIFIERS

1. CONTRACT NUMBER: DE-FG22-85PC80752

CONTRACTOR: Brigham Young University
75 CTB
Provo, UT 84602
(801)378-4820

PROGRAM MANAGER: James D. Hickerson

PRINCIPAL INVESTIGATORS: Philip J. Smith and L. Douglas Smoot

SUBCONTRACTOR: Los Alamos National Laboratory

PERIOD OF PERFORMANCE: May 1, 1985 through August 30, 1989

2. SCHEDULE/MILESTONES:

1989 Program Schedule

	S	O	N	D	J	F	M	A	M	J	J	A
Task 1. Practical, full scale Model												
Demonstration of Numerical Methods	———	———	———	———	———							
Extend to Reacting Particle-Laden Flows							———	———	———	———	———	
Task 2. Model Evaluation												
Complete Sensitivity Analysis												———
Complete 3-D Computations	———	———	———	———	———	———	———	———	———	———	———	———
Compare Measured and Predicted Data								———	———	———	———	
Task 3. Subcomponent Models												
Prepare Research Publications	———	———	———	———	———	———	———	———	———	———	———	———
Task 4. Fouling and Slagging Submodel												
Complete Subcode Integration	———											

3. OBJECTIVES:

The general objective of this study is to improve and extend a generalized two-dimensional, pulverized coal combustion and gasification code for application to large-scale, practical configurations, and to evaluate and implement the resulting code on an industrial scale.

4. BACKGROUND STATEMENT:

On May 1, 1985, work was initiated on this contract which is supported by a consortium of industrial and governmental sponsors (see Table 1). This report presents progress made during the third year of this contract. Based on the demonstrated utility of the past axi-symmetric modeling work, the current contract is aimed at further improvement and extension of this technology to large-scale, three-dimensional pulverized coal furnaces and gasifiers.

Not all of the physical and chemical issues are resolved and therefore, the thrust of this study is not only to extend the code numerically to three-dimensions, but to conduct further work on subcomponents and review and incorporate on-going research by other investigators.

Table 1. Summary of Organizations and Technical Contacts for Consortium Study

1. Babcock & Wilcox
   Mr. William Oberjohn
2. Combustion Engineering Co.
   Mr. Gordon Robinson
3. Consolidation Coal Co.
   Dr. Stanley Harding
4. Electric Power Research Institute
   Dr. Arun Mehta
5. ESEERCO
   Mr. Rick Mancini
6. Foster Wheeler Development Corp.
   Dr. K.S. Ahluwalia
7. Tennessee Valley Authority
   Dr. Chao-Ming Huang
8. U.S. DOE/PETC
   Mr. James Hickerson
9. Utah Power & Light Co.
   Dr. Dee P. Rees

5. PROJECT DESCRIPTION:

The accomplishment of this objective has been planned over a four year period which term ended in August, 1989. The approach had been outlined as follows:

- Provide for a series of tasks for the four year study to be completed on an annual basis in order to evaluate progress toward the final goal.
- Organize and maintain a technical advisory committee, to include representatives from each of the organizations funding the project.
- Provide a cooperative program through a subcontract with Los Alamos National Laboratory, in order to obtain increased expertise in development of large scale codes and to provide for computational power to assist this research effort.
- Review and document available data on full-scale furnaces and gasifiers in order to provide a data base for evaluation of the extended code.
- Develop a single code to handle gasification, combustion, and fuels other than coal, including gaseous combustion.

During this four-year program, the following tasks were outlined for completion:

Task 1 - Practical, Full-Scale Model

Extend the two-dimensional code to apply to practical, three-dimensional, large-scale furnace and gasifier configurations.

Task 2 - Model Evaluation

a. Computational Evaluation: The 3-D model will be rigorously evaluated through a statistical sensitivity analysis to determine model parameters that most influence furnace and gasifier information.

b. Comparative Evaluation: Review, select and document a set of available data relating to practical, large-scale (often 3-D) furnaces and gasifiers and evaluate code predictions through comparisons with these data.

Task 3 - Subcomponent Models

Review, extend, correlate, incorporate and improve selected submodel equations and/or data into the comprehensive 3-D model.

Task 4 - Fouling and Slagging Submodel

Develop, evaluate and incorporate a submodel for furnace and gasifier fouling, slagging and corrosion into the 3-D model.

Task 5 - Reporting, Technology Transfer and Code Implementation
Provide for rapid implementation and application of results through reports and publications, technical advisory committee meetings and code workshops.

Three years were outlined to be used to extend the code to three dimensions, demonstrate numerical stability and improve submodel components. The final year was to focus on evaluation, documentation and implementation. Work accomplished during the first three years of this contract was summarized in three annual reports (Smith and Smoot, 1986, 1987, 1988), and reported in last year's AR & TD contractors review meeting (Smith and Smoot, 1988).

6. RESULTS/ACCOMPLISHMENTS:

Work during this last year of the contract has focused on code integration and evaluation, and 3-D computer graphics pre- and post-processors. This contract has been completed and preparation of the final report is in progress. A workshop on code usage is being organized. Technical papers further documenting the results of the work are being prepared. The accomplishments of this work are serving as the foundation for further extension and refinement of the 3-D combustion code under the National Science Foundation funded Advanced Combustion Engineering Research Center (ACERC).

This section reports briefly on work accomplished during this last year on model development, graphical pre- and post-processing, and overall model evaluation.

MODEL DEVELOPMENT

A three-dimensional reactive flow model for simulating complex, industrial furnaces has been developed, demonstrated, enhanced, and evaluated. Recent advances in computer hardware and in the modeling of partial differential equations have led to increased computational capabilities. This study is an effort to apply this new technology to the simulation of combustion in industrial coal-fired furnaces and gasifiers. A three-dimensional code has been developed specifically for furnaces. This model was used to study several turbulence submodels and numerical issues, including overall efficiency, robustness, pressure-velocity coupling, differencing errors, and grid resolution requirements.

Previous work at BYU laid the foundation for this study. Several comprehensive models (such as PCGC-2) and submodels have been previously developed and evaluated. An extensive literature review of existing 3-D combustion models revealed their common basis on the SIMPLE algorithm and their lack of demonstration with fine grid simulations. Iterative, decoupled numerical techniques were found to be the most applicable to this problem because of low computer-memory requirements and compatibility with turbulence submodels. PCGC-2 was extended to three dimensions for an evaluation of its numerical techniques, the comparison of SIMPLE algorithms variations, and a study of turbulence modeling in complex flows. The major accomplishments and observations of this study over the last year are listed below and are documented elsewhere (Gillis, 1989).

1. Turbulence modeling is an important contributor to the overall code and can dominate the solution of the Navier-Stokes equations. The disparity of scales encountered in industrial geometries requires highly-irregular grid structures and requires finite-difference formulation that can minimize false diffusion and non-uniform grid-differencing errors. Numerous

changes were required in the numerical techniques employed in PCGC-2. Table 2 summarizes some of the major changes.

Table 2. 3-D Code Enhancements over PCGC-2

Change	Significance
1. Boundary Condition Generality	All configurations possible
2. Weighted Central Differencing	Grid flexibility, highly-irregular grids
3. Nodal Upwind Formulation	Reduces false diffusion, Robust
4. Accelerated TDMA	Decreases code convergence times
5. SIMPLE-variation options	Improves speed and flexibility
6. Turbulence Submodels	Additional options, laminar flows
7. Vectorization	Increases speed on vector machines
8. Modular Structure	Increases code friendliness
9. Buoyancy Effects	Gravitational effects on flow field
10. Standard FORTRAN	Provides portability
11. Conservative Form Option	Greater numerical flexibility
12. Turbulence Initialization	Improves early convergence
13. Outlet Boundary Conditions	Improves code robustness

2. A weighted central-difference formulation has been incorporated to handle irregular meshes. This formulation moves control-volume faces to new locations, centering the node point in the cell. The new formulation dramatically reduces exact solution errors on non-uniform grids.

3. Numerical diffusion is, in part, caused by the incorrect evaluation of cell face velocities. A nodal differencing scheme was developed which significantly reduced equation error. This nodal scheme was not characterized by the poor convergence properties (stability) of higher order upwind differencing schemes.

4. A decrease in computation time was achieved through extensive vectorization of the code. The reduction was case dependent, but was approximately a factor of four over the history of the project. A major increase in efficiency resulted form changing the matrix solver from a line-by-line method to a plane-by-plane method. This change removed the recursion in the algorithm. Additional convergence acceleration was obtained by reformulating the matrix solver to be more implicit.

5. The k-ε turbulence model demonstrated superior predictive capabilities compared to a constant-eddy-diffusivity model and a mixing-length model. The k-ε model provided good agreement for simple and moderate flows but could not simulate all the features of some complex flow fields. The inability to simulate complex flows could be attributed to inadequate grid resolution or the assumption of isotropic eddy-diffusivity, and possibly to data accuracy.

6. A relaminarization model was incorporated into the turbulence submodel. This option allows the simulation of flows with regions of laminar, transitional, and fully turbulent flows. The relaminarization model compared favorably with simple turbulence and laminar pipe flows.

7. The turbulence submodel can dominated the overall convergence process in highly-turbulent flows. Studies of computational fluid dynamics numerical methods should be

conducted with a turbulence submodel if the final application involves turbulence. The importance of turbulence/velocity coupling tends to increase with increasing Reynolds numbers.

8. Domain decomposition has been incorporated and can greatly reduce computer storage requirements at the expense of computation time per iteration. The value of subdomaining depends on the memory-swapping ability of the specific computer being used.

9. Grid resolution requirements were established for three test cases. It was found that corner-fired furnaces require substantially fewer node points than wall-fired furnaces. Grid-independent simulations of a tangential-fired furnace were achieved for grid structures exceeding 15,000 nodes. Complex furnace flows can require up to 500,000 grid points.

10. Several variations of the SIMPLE algorithm were tested for robustness and speed. Convergence rates are strongly dependent on under-relaxation factors. Simulating highly-turbulent flows reduces the significance of algorithm selection on solution time. The determination of optimal algorithm and under-relaxation factors was found to be case dependent. Higher Reynolds number flows require lower under-relaxation factors. The SIMPLEC, SIMPLER, and SIMPLERC algorithms provided the best speed and robustness. This study recommends the use of SIMPLERC with an under-relaxation factor of 0.8.

PRE- AND POST-PROCESSING

Over the course of the last year a first generation graphical interface to the input and output of the 3-D code was completed. These pre- and post-processors are graphical software tools which aid in the construction of geometrical models for analysis and the subsequent visualization of the output data. Designed for engineering workstations, the programs utilize color graphics and simple user interfaces to allow maximum ease of use. The pre-processor allows the user to create a valid model graphically on the workstation using the mouse and keyboard. The user inserts and deletes planes into the model until the desired grid densities are achieved. Up to six separate windows can be used interactively to better visualize the geometry as it is constructed. The user may also assign cell types to any cell or group of cells with simple mouse pick commands. The geometry model is written automatically in standard format ready for use by the computational combustion code.

The post-processor takes the data from the converged analysis of the model and allows visualization using a variety of techniques. The user may choose one dimensional graphs, two-dimensional renderings such as contour or fringe plots, or may extract arbitrary surfaces from a three dimensional database for display. Positioning of the model for viewing is accomplished by simple graphical icons, and up to six independent windows can be active at once. The menu and mouse driven interface provides ease of use and cuts down training time. For more qualitative analysis of an entire three dimensional database, a separate rendering program produces translucent images visualizing the entire database in a single picture. This program combines the advantages of ray tracing with the power of hardware graphics output for truly useful images in seconds.

MODEL EVALUATION

Compilation of a 3-D Data Book

A three-dimensional combustion data book was created for this project to fulfill the objectives previously outlined and within the limits and quality of current three-dimensional combustion data. The data included in the data book are intended to be the most complete and highest quality of the three-dimensional data that could be located and obtained.

Although data exist that have not been compiled in this data book, unavailable resources were required to obtain them. For example, a set of relevant data was located at one facility that, technically, was available for distribution to the public domain. However, the company could not provide the necessary manpower to retrieve the data from files for distribution. The cost for data retrieval was estimated to be over five thousand dollars. Since the quality and suitability of the data were unknown, it was deemed infeasible to obtain the data.

The suitability of the data book for its intended purpose of providing a well documented source of data for model evaluation is marginal. A complete discussion and evaluation of all available data is documented in Phillips (1989). All classes of data are not represented in the data book. All sets that are included in the data book are incomplete in some way for modeling. Parametric test data are included, but more cases are needed. However, given the scarce nature of available 3-D data, the data book is a necessary first step towards providing an acceptable source of such data. The establishment of criteria for selecting data as well as specifying the most useful measurements for including in test programs will help guide future work in collecting combustion data. A summary of the compiled data is given in Phillips (1989).

Numerical Evaluation

During the last year several new numerical techniques were incorporated into the combustion code. The motivation for many of these changes was to improve the accuracy of model predictions. Their effort on convergence time was examined. Some slowing of overall convergence can be attributed to inaccuracies in the numerical approximations. The removal of these problems should improve convergence. Table 3 compares run times for several alternate formulations to determine the effect of numerical changes on code efficiency. Significant reduction in differencing error was obtained by using a weighted central and upwind nodal-differencing scheme (see Gillis 1989). Table 3 compares solution time for two upwind schemes (HUDS and NUDS). Convergence time changes resulting from the differencing scheme enhancements are shown. A study of the improvements in convergence rates resulting from the increased implicitness in the matrix solver follow in the

Table 3. Solution Time Reductions due to Numerical Changes

Numerical Option	Sudden-Expansion Flow [s]	Corner-Fired Furnace [s]
HUDS	30.70	467.01
NUDS	23.35	404.96
Convergence Checks	24.83	356.96
TDMA Change	22.48	326.42
Initialization	22.60	269.41
Total Reduction	26.4%	42.3 %

table. An enhanced initialization of velocities and turbulence variables was the last numerical change whose effect is quantified. This initialization not only reduces convergence time for many cases, but also increases robustness for large cases. The final row in Table 3 lists overall simulation-time reductions resulting from the numerical changes listed. The simulation time for the corner-fired furnace was nearly halved through these numerical modifications.

An examination of computed simulations and comparisons with experimental data are not adequate to assure accuracy of the numerical algorithm or to provide confidence that the computer code is free of programming errors. Comparisons of exact solutions with predictions from the computer model provide a richer evaluation of these plaguing numerical errors. Exact solutions can be obtained for the coupled set of partial differential equations for reacting flow by selecting a solution for each variable and analytically determining an extra source term on the right hand side of each equation to satisfy the equality. For example if the exact solution is selected such that:

$u = xyz$
$v = yz$
$w = z$
$k = y$
$p = xyz$
$\mu = \text{constant}$
$\rho = \text{constant}$

Then by letting

$$S_{pu} = \rho [\, 2xyz\,(yz + z + 1) + yz - 2y^2z^2 - x^2\,(z^2 + y^2)] \qquad (1)$$

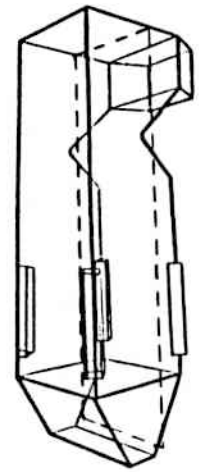
the x-momentum equation:

$$\frac{\partial(\bar{\rho}\tilde{u}\tilde{u})}{\partial x} + \frac{\partial(\bar{\rho}\tilde{v}\tilde{u})}{\partial y} + \frac{\partial(\bar{\rho}\tilde{w}\tilde{u})}{\partial z} - \frac{\partial}{\partial x}\left(\mu_e \frac{\partial \tilde{u}}{\partial x}\right) - \frac{\partial}{\partial y}\left(\mu_e \frac{\partial \tilde{u}}{\partial y}\right) - \frac{\partial}{\partial z}\left(\mu_e \frac{\partial \tilde{u}}{\partial z}\right) =$$
$$-\frac{\partial \bar{P}}{\partial x} + \frac{\partial}{\partial x}\left(\mu_e \frac{\partial \tilde{u}}{\partial x}\right) + \frac{\partial}{\partial y}\left(\mu_e \frac{\partial \tilde{v}}{\partial x}\right) + \frac{\partial}{\partial z}\left(\mu_e \frac{\partial \tilde{w}}{\partial x}\right) + \bar{\rho} g_x - \frac{2}{3}\bar{\rho}\tilde{k} + S_{pu}$$

will satisfy this solution exactly. Likewise, similar expressions can be derived for each of the differential equations in the equation set, and with appropriate boundary conditions the computed solution can be compared to the exact solution for numerical accuracy. Such an analysis has been conducted on the computer code developed for this project. Several errors in the original algorithm and coding were uncovered and corrected with the method (Gillis, 1989). The resulting code has reported each of the exact solutions tested to within computer truncation error. This analysis lends significantly more confidence to the accuracy of the numerical algorithm and the computer coding.

Data Comparison Evaluation

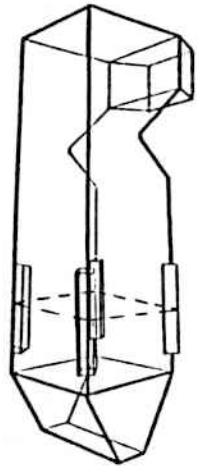
Several cases have been compared with what little experimental data are available. Representative of this type of evaluation is the study of the Large Scale Furnace Aerodynamics Test Facility (LSFATF) operated by Combustion Engineering in Windsor, Connecticut. The facility is a 0.46 scale model of the C.E. Boiler Simulation Facility used in combustion tests. The furnace is tangentially fired and contains a nose, as well as three rectangular flow obstructions hanging from the furnace ceiling, representing the superheater and reheater platens and panels. Ambient air was blown into the furnace at an equal velocity in both the fuel and air ports of all four corner burners. Some details of the geometry can be seen in Figures 1 through 4. Figure 1 shows a schematic of the furnace and identifies the planes which are expanded in figures 2-4. Figure 2 shows velocity vectors in a horizontal plane



A. Constant Depth Plane

Depth of 0.89 m

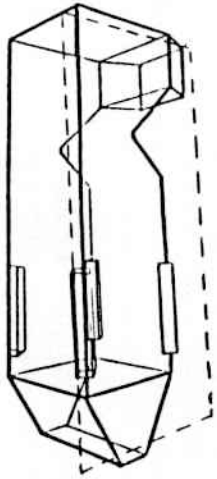
(Used in Figures 4.1, 4.2, 4.3, 4.6, and 5.7)



B. Constant Height Plane

Height of 1.5 m

(Used in Figure 5.6)



C. Constant Width Plane

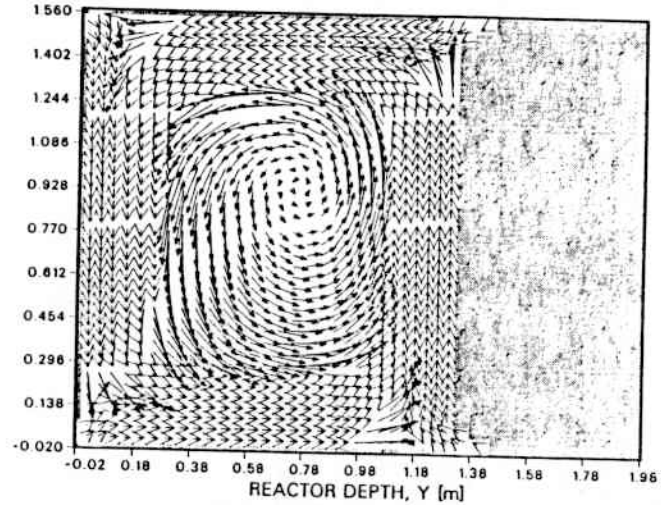
Width of 0.26 m

(Used in Figure 5.11 and 5.12)

Figure 1. Schematic of the furnace, showing Constant Depth Plane, Constant Height Plane, and Constant Width Plane.

V-W Velocity Vectors
Legend

Symbol	Scale
≡ wall, obstrustion	1.0 in = 0.475 m
≡ predicted velocity	1.0 in = 23.75 m/s
≡ predicted velocity	1.0 in = 237.5 m/s



Simulation date: 10-Aug-89
V Velocity Range: -22.6 to 19.0 [m/s]
W Velocity Range: -21.5 to 21.3 [m/s]

Figure 2. V-W Velocity Vectors.

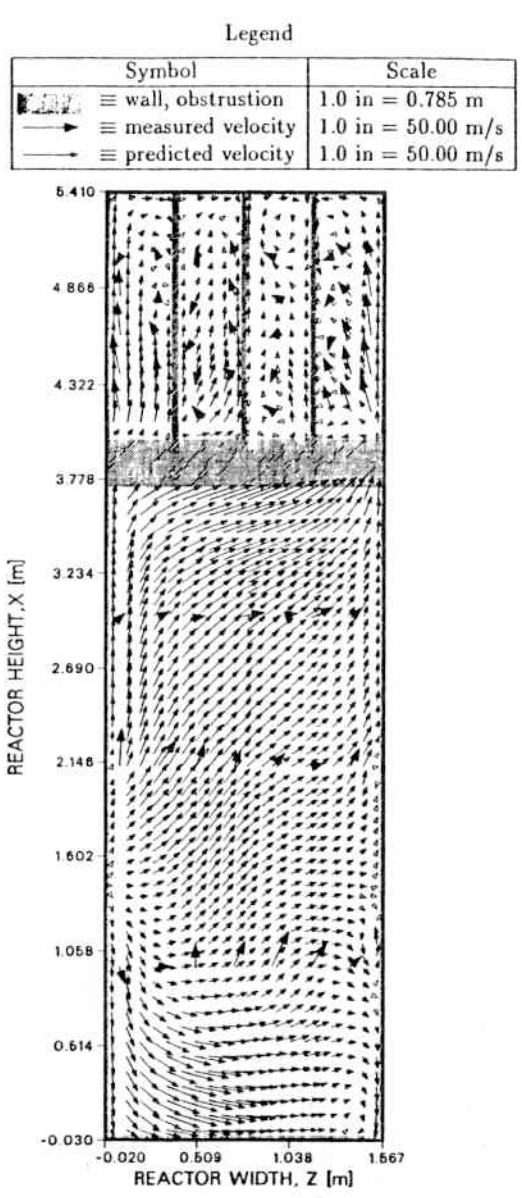


Figure 3. U-W Velocity Vectors.

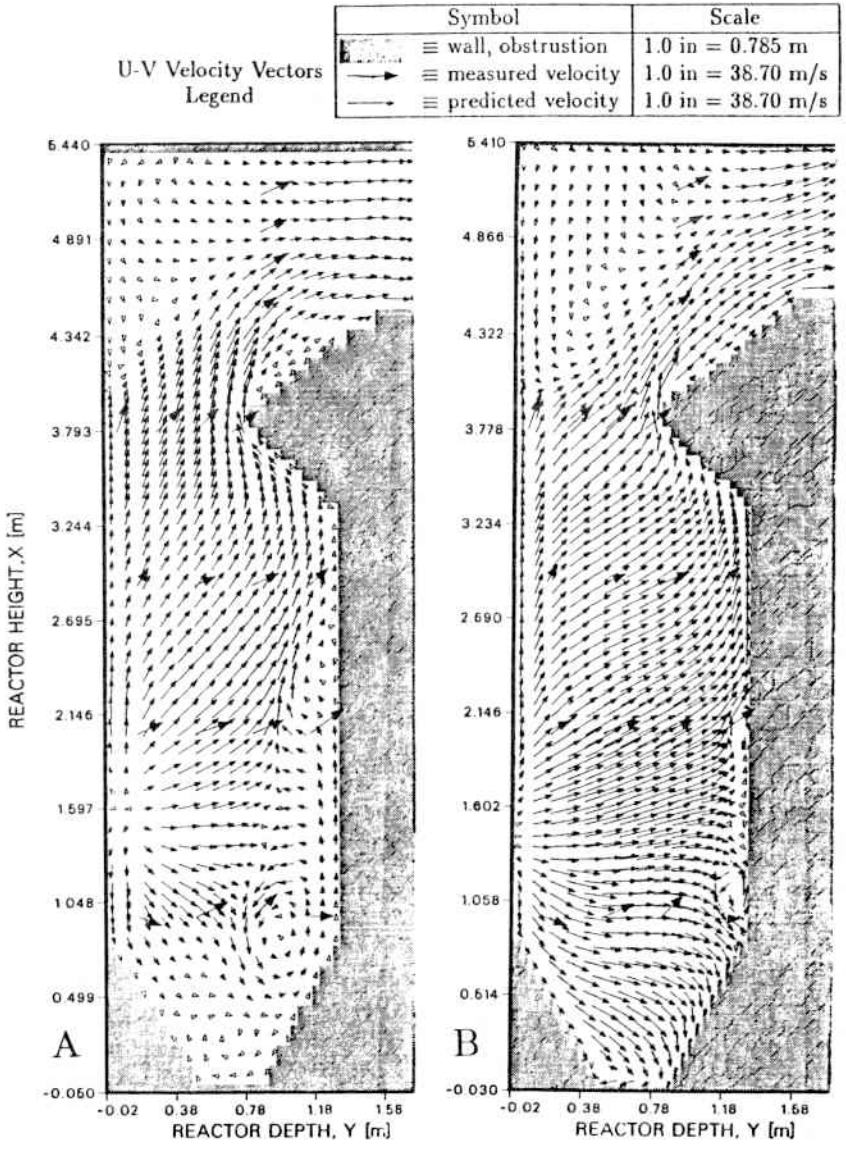


Figure 4. U-V Velocity Vectors.

passing through all four burners. A strong counter-clockwise swirling flow is predicted. Figure 3 represents a vertical plane which cuts through the furnace nose (at about 4 m) and the three panels attached to the furnace ceiling. Figure 4 gives additional geometric detail of the nose and ash pit. This figure also shows calculations performed at two different grid resolutions and quantifies the computational inaccuracies that are introduced when a calculation has not been demonstrated to be mesh-size independent. Simulations of the LSFATF case were performed on a Convex C-120 computer.

Experimental velocity data were obtained for the LSFATF facility via a calibrated five-hole pilot tube coupled to a computer controlled traversing data-acquisition system. Approximately 100 data points were obtained on each of seven different test planes. Additional information concerning the furnace, operating conditions and data acquisition can be found elsewhere (Koucky, et al., 1987; Phillips, 1989).

The filled arrowheads in Figures 3 and 4 signify experimental velocity vectors. These figures show reasonable agreement between predictions and data in the central area of the furnace. The predicted velocities at a height of about 1 meter compare favorably with overall trends, but magnitudes are predicted in excess of experimental values. Less favorable agreement is found in the platen region due to inadequate local grid resolution.

7. FUTURE WORK:

This contract has ended and reporting is currently underway. The final reporting and technology transfer tasks include a documented final report, technical journal publications, and a workshop for all sponsoring agencies to have hands on experience with code operation. Work on this computer model will continue under the NSF funded Advanced Combustion Engineering Research Center.

8. REFERENCES:

Gillis, P.A. 1989. "Three-Dimensional Computational Fluid Dynamics Modeling in Industrial Furnaces." Ph.D. Dissertation, Chemical Engineering Dept., Brigham Young University.

Koucky, R.W., Marion, J.L., and Anderson, D.K. 1987. "Development of Sorbent Injection Criteria for Sulfur Oxides Control from Tangentially Fired Coal Boilers." Report from Combustion Engineering, Windsor, CT.

Phillips, S.D. 1989. "Data Book for Evaluation of Three-Dimensional Combustion Models." Master's Thesis, Chemical Engineering Dept., Brigham Young University.

Smith, P.J. and Smoot, L.D. 1986. "Detailed Model for Practical Pulverized Coal Furnaces and Gasifiers." First Annual Progress Report.

Smith, P.J. and Smoot, L.D. 1987. "Detailed Model for Practical Pulverized Coal Furnaces and Gasifiers." Second Annual Progress Report.

Smith, P.J. and Smoot, L.D. 1988. "Detailed Model for Practical Pulverized Coal Furnaces and Gasifiers." Third Annual Progress Report.

Smith, P.J. and Smoot, L.D. 1988. "Detailed Model for Practical Pulverized Coal Furnaces and Gasifiers." AR & TD Contractor's Review Meeting, Morgantown, WV.

COMBUSTION RESEARCH FOR ADVANCED HEAT ENGINES

1. FTPA NUMBER: 0642.000

CONTRACTOR:

Sandia National Laboratories
7011 East Avenue
P.O. Box 969
Livermore, California 94551-0969
Phone: (415)294-2322

CONTRACT PROJECT MANAGER: Donald R. Hardesty

PRINCIPAL INVESTIGATOR: Larry L. Baxter

METC PROJECT MANAGER: Mike McMillian

CONTRACT PERIOD: October 1, 1988 – Continuing

2. SCHEDULE/MILESTONES:

1989 Program Schedule

Task	Month											
	O	N	D	J	F	M	A	M	J	J	A	S
Topical Report 1: The effect of surfactant on particle aggregation (experimental).		√										
Topical Report 2: The effect of disaggregation on combustor performance (modeling).			√									
Instruction in using code for heat engine applications								√				
Topical Report 3: The effect of the additive chemistry on surface layer formation (experimental).										√		

3. OBJECTIVES:

The objective of this year's activities for the experimental portion of this work is to identify the role of slurry additives, specifically surfactants, on the formation of aggregates during combustion. This has been investigated by in situ measurements of the particle size distribution of the atomized spray during the vaporization portion of slurry combustion. The experiments were conducted in a laminar flow reactor in which atomized droplets were entrained. Solid samples are also collected with rapid-quench sampling probes at various stages of combustion to augment the in situ measurements. The objective of this year's modeling activities is to modify an existing comprehensive model of coal-water slurry combustion to predict the effects of particle disaggregation on combustion behavior and to allow the future incorporation of mineral matter evolution submodels.

4. BACKGROUND STATEMENT:

The droplet and particle size of slurry droplets and particles has been recognized as one of the critical factors affecting the combustion characteristics of coal-water slurry flames [McHale, 1988]. Slurry atomizers generally produce droplets significantly larger than the average coal particle size. Therefore, a typical atomized coal-water slurry droplet contains several coal particles. The coal particles within a droplet generally aggregate to form a single large coal particle as the slurry dries. This large coal particle then combusts in the same manner as a coal particle of equivalent size and density [Sakai and Saito, 1983; Wei-Biao et al., 1985; Yao and Liu , 1983; Holve et al., 1987].

From a combustion viewpoint, it would be more advantageous for the coal particles to disaggregate during the drying stage than to form large aggregates. In earlier work under this contract, a significant effect of slurry surfactant on the morphology of the slurry particles subjected to relatively low gas temperatures ($\approx$ 500 K) was noted. This earlier work led to the formation of a hypothesis that the surfactant is partially responsible for the formation of the aggregates and that its elimination would promote disaggregation. The current experimental program is designed to test this hypothesis.

The modeling work performed under this contract is an extension of work done by the principal investigator while a graduate student. A recent review of comprehensive modeling is available elsewhere [Baxter, 1988]. The graduate work included developing a model to predict the characteristics of slurry flames in axisymmetric flow systems. The comprehensive computer code assumed that the droplets formed single large coal aggregates as they dried, consistent with experimental results reported in the literature. This contract involves relaxing that assumption in the comprehensive computer code and using the new version to predict the practical results of particle disaggregation during slurry drying.

5. PROJECT DESCRIPTION:

The experiments were conducted in a laminar flow reactor at atmospheric pressure. The reactor entrains a portion of the slurry spray in the vitiated flow of a methane flat flame (see Figure 1). An in situ diagnostic, developed at Sandia under METC sponsorship, is used to measure the particle size and velocity distributions and the particle number density as a function of residence time in this reactor. The instrument is called a particle-counter-sizer-velocimeter (PCSV) and is based on the measured intensity of light scattered from the focal volume of a laser beam [Holve and Self, 1979a - 1979b; Holve et al., 1987]. The measurements of interest to this study are confined to early residence times ($\leq$ 20 ms), during which droplets are vaporizing.

Slurries were supplied directly from slurry manufacturers and METC heat engine contractors. Slurry preparation techniques and solids loadings were the same for both those containing and those not containing surfactant.

The experimental results obtained from these experiments were included in the new version of the comprehensive computer code. This code was then used to predict the effect of particle disaggregation in high-pressure, turbulent heat engine combustors.

6. RESULTS/ACCOMPLISHMENTS:

Figure 2 illustrates the differences in droplet morphology noted in the low temperature environment. The aggregate generated from the slurry containing the surfactant has a smooth surface compared to that of the droplet from the slurry containing no surfactant. The results from the high temperature environment were qualitatively similar, although the fused surface layer was less extensive at high temperature.

A mechanistic interpretation of the results is postulated [Baxter et al., 1989] which qualitatively explains all of the observations to date. The role of the surfactant in the slurry is to coat the particles with similar ionic charge so they repel one another. This is the origin of the dispersing nature of the surfactant. As the droplet forms during the atomization process, the particles will tend to migrate to the droplet surface, where there are no repulsive forces from other particles. The smaller particles have higher charge to mass ratios and are more mobile, and will therefore preferentially migrate to the surface. Figure 3 illustrates these differences in droplets formed from slurries with and without surfactants. This mechanism indicates that the surface layer will be composed of both surfactant and very small particles and that it will be less likely to form if no surfactant is in the slurry. Both of these effects are supported by observations.

Results indicate that the average particle size of sprays formed from slurries containing no surfactant decreases during water vaporization. This decrease is interpreted as disaggregation, based on the results illustrated in the following two figures [Habib et al., 1989]. Figure 4 illustrates the mean particle size as a function of residence time for both slurries. Each point in the figure represents the average of 4–10 repeated measurements of the particle size distribution (psd) by the PCSV. Each psd is based on

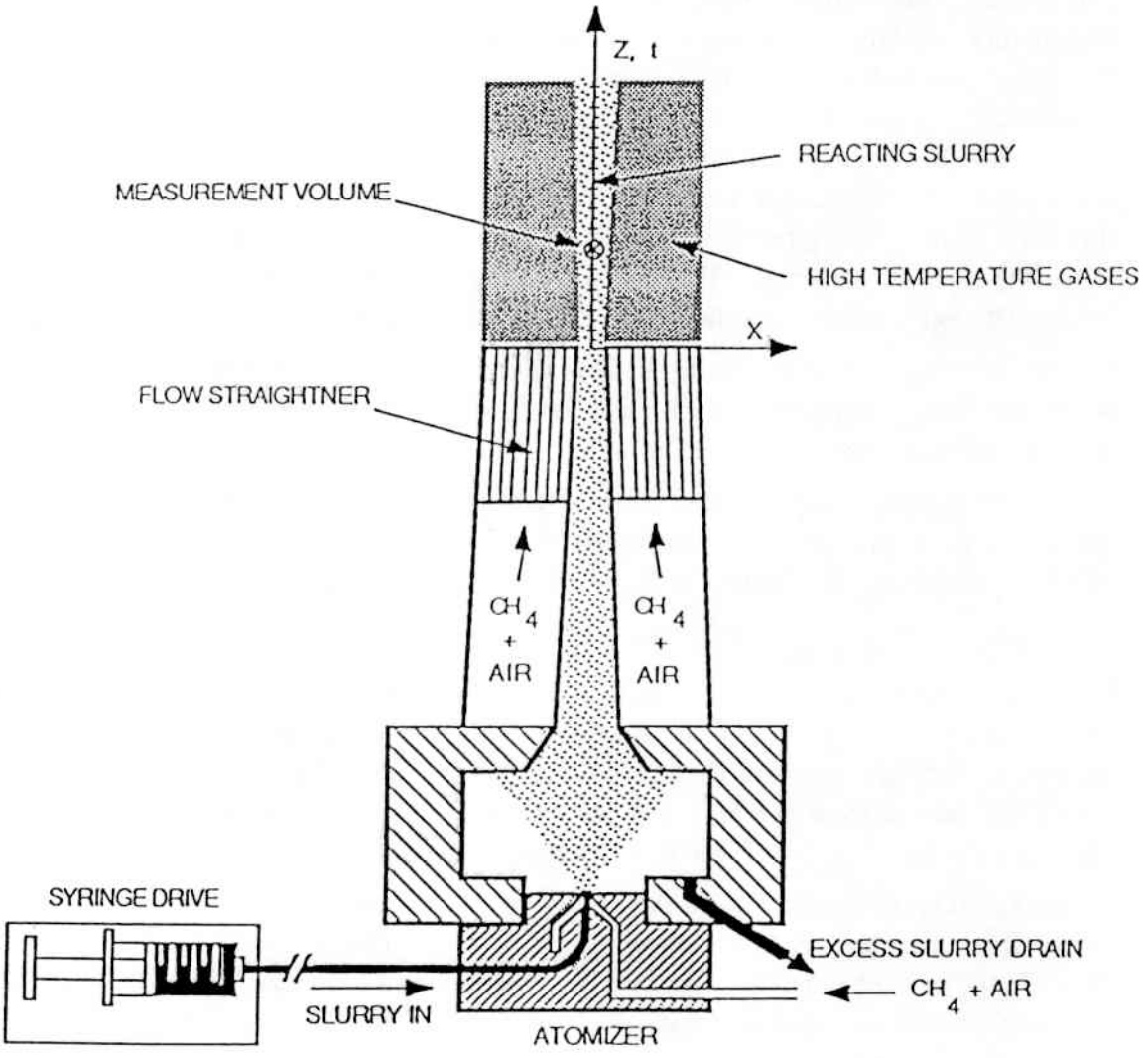


Figure 1: Schematic illustration of the laminar flow reactor used in this experiment.

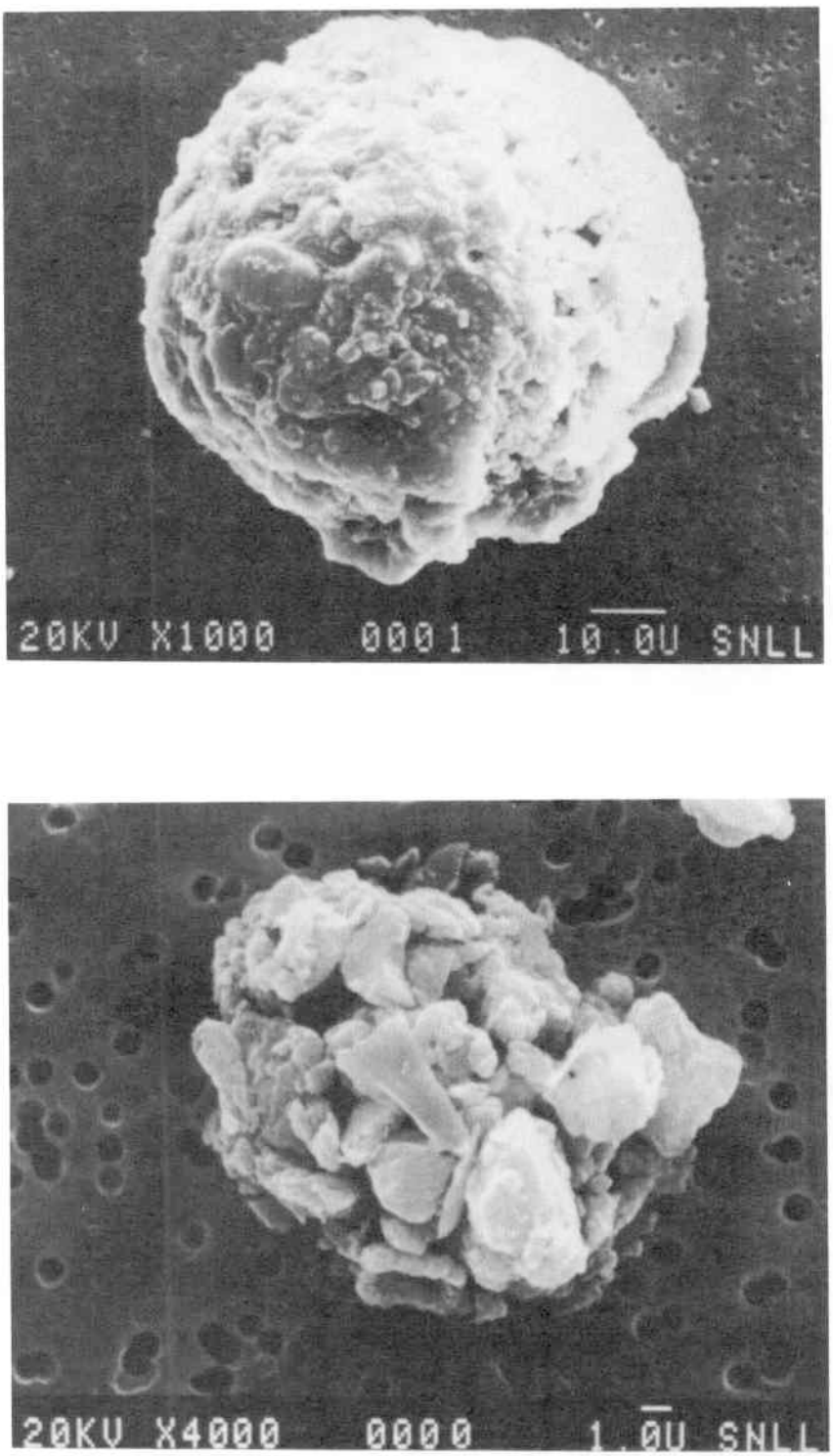


Figure 2: Micrographs showing typical aggregates formed from slurries with (top) and without (bottom) surfactant.

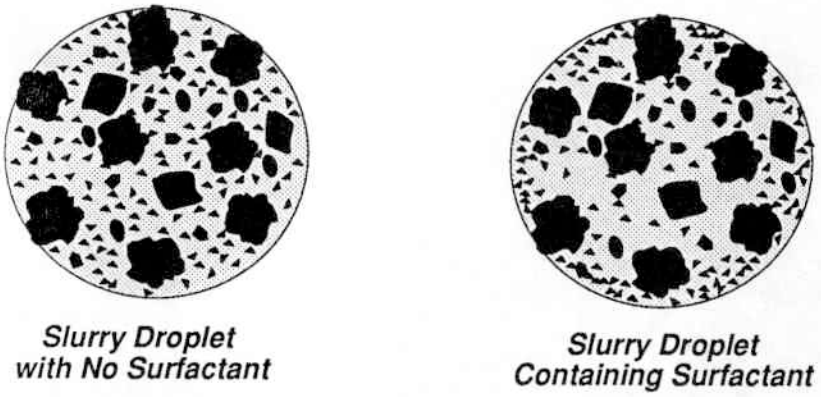


Figure 3: Schematic diagrams of droplet cross-sections illustrating the effect of surfactant on the radial concentration profiles of small particles.

information gathered from up to 60,000 individual particles. The figure also indicates 90 % confidence intervals for the mean particle size. There is no significant difference in the means of the atomized spray (0 ms residence time). At increased residence time, the mean size of the particles generated from the slurry containing no surfactant decreases relative to the slurry containing surfactant. The decrease is statistically significant and results in particles whose ultimate diameter is about 1.8 times smaller than the aggregates formed from the slurry with surfactant. The mean diameters shown are mass-equivalent diameters. Mass-weighted diameters are on the order of 40–50 μm for these data.

Results also indicate that particles generated from slurries containing surfactant disaggregate as they approach the end of their vaporization stage of combustion. Particle disaggregation increases the absolute number of small particles in the spray. Other particle conversion processes, such as combustion, decrease the average size of particles but do not increase the absolute number of small particles in the spray. Figure 5 illustrates the relative number of particles generated by disaggregation as a function of both particle size and residence time. Note that as residence time increases, increasingly large particles are formed. This trend supports the interpretation that disaggregation occurs near the end of water vaporization. Disaggregation will be inhibited by the surface tension of the water prior to significant vaporization and by softening of the coal as the particle temperature begins to rise. The most likely time for disaggregation to occur is near the end of vaporization and before the coal begins to soften.

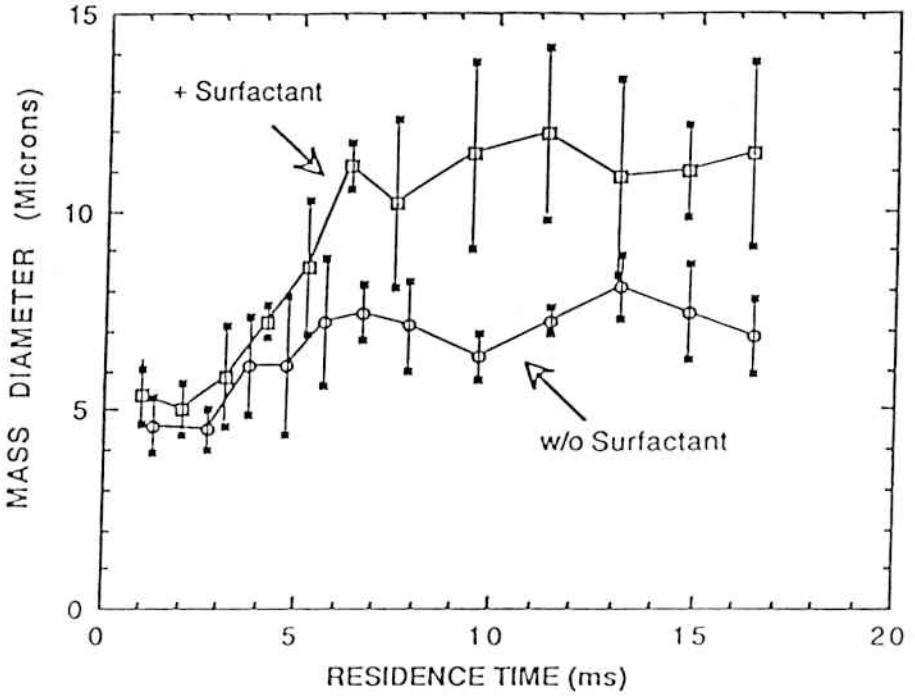


Figure 4: Mean particle size as a function of residence time for particles generated from slurries with and without surfactant.

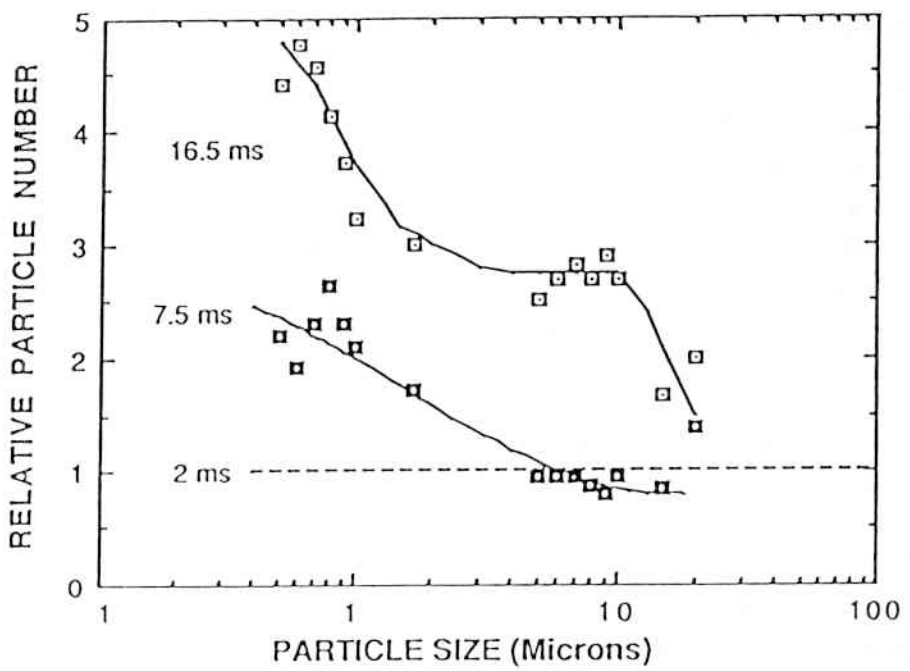


Figure 5: Relative number of particles generated by disaggregation as a function of particle size at two different residence times. All values are normalized to 2 ms residence time, the point at which the droplets pass through the flame.

The data from the preceding figures were used to predict the effect disaggregation may have on the combustion characteristics of interest to METC contractors developing slurry-fired turbines. Figure 6 illustrates some of the results. In this figure, gas temperature fields from three separate predictions are illustrated. The temperature is indicated by the height of the surface from the base. The axial and radial distances are indicated by the distances along the indicated edges of the surface. In all cases, the distances are relative to the slurry injector, which is on the centerline of the axisymmetric combustor.

In case (a), the flame is lifted from the burner, as indicated by the abrubt rise in temperature about one third of the distance from the slurry injector to the reactor exit. The effect of disaggregation is seen by comparing (a) with (b). In case (b), the flame has moved forward in the combustor and has attached to the burner. The flame shape, flowfield (not shown) and species concentrations (also not shown) have all changed substantially. Predicted carbon burnout and flame stability are both higher in case (b). Case (c) is similar to case (a) except that the assumed initial droplet size distribution is the same as the particle size distribution in case (b) after particle disaggregation. Case (c) illustrates the effect of better atomization but no disaggregation. As can be seen, the quality of atomization has a larger effect on the combustion behavior than disaggregation. The latter is significant, however. The predictions indicate that disaggregation can enhance most combustion characteristics if it can be achieved without compromising primary atomization.

We have initiated modifications to the comprehensive computer code which will allow incorporation of mineral matter release and transformation data into the code. Traditionally, coal off-gases are treated with a mixture fraction approach. The mixture fraction approach includes a basic assumption that the elemental composition of the off-gas does not change during coal combustion. This assumption is reasonable for the organic portion of the coal, with the possible exception of hydrogen. However, our work under separate contract has demonstrated that this assumption is inappropriate for the inorganic portion of the coal. Therefore, a more general approach is needed which allows the elemental and/or species composition of the off gas to change with time. Such an approach is being developed under this contract to allow modeling of mineral matter behavior.

7. FUTURE WORK:

The work on the effect of surfactants on slurry droplet disaggregation is now complete. Aside from cooperating with slurry manufacturers and heat engine contractors to test our results at larger scale, we have finished our planned efforts in this area.

The modifications to the comprehensive code are continuing with the ultimate aim of incorporating mineral matter evolution subroutines. The basic research needed to develop the subroutines is being done under separate contract. This work, if successful, will also allow the code to incorporate more detail in the coal combustion subroutines.

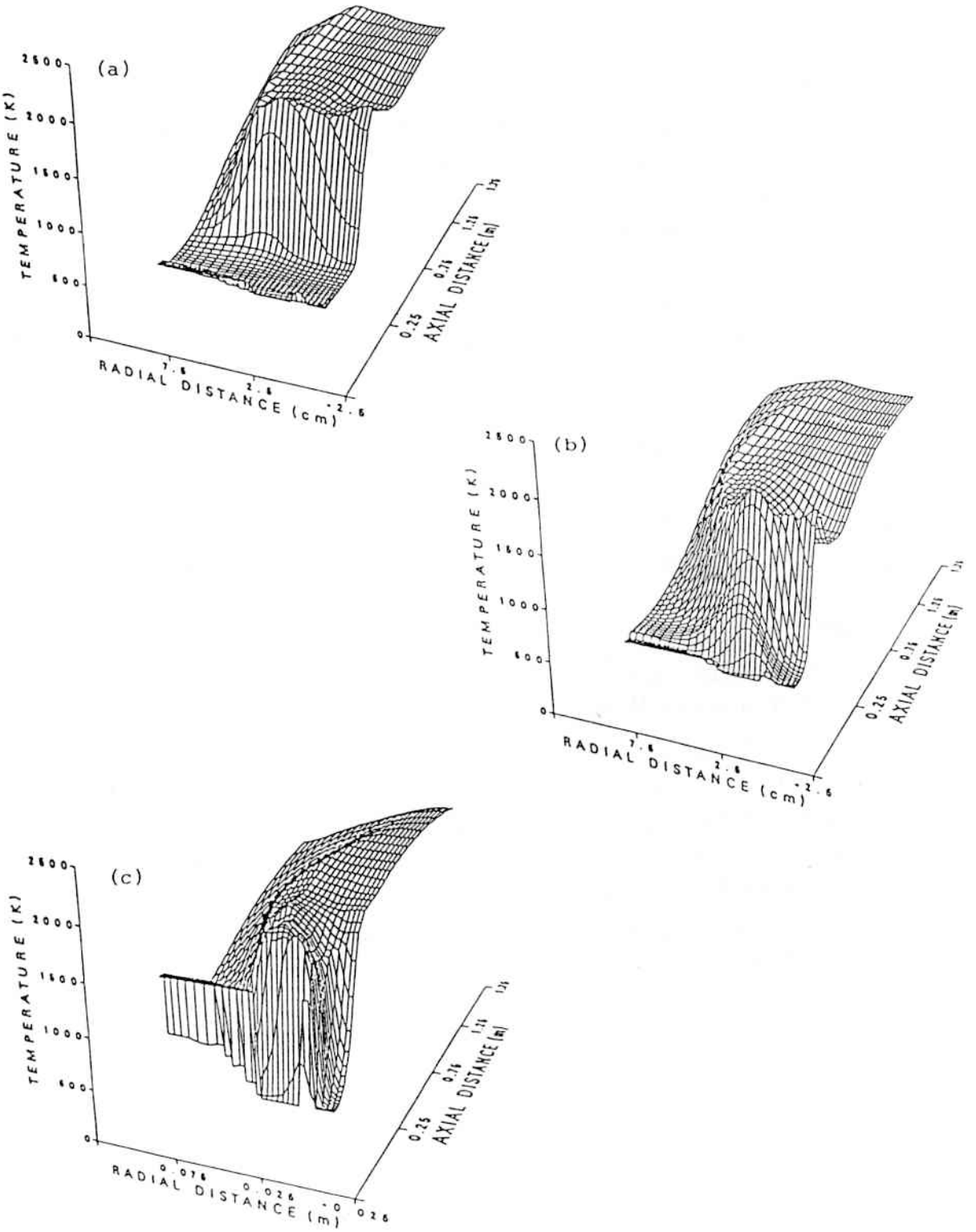


Figure 6: Temperature fields in axisymmetric combustors firing slurries which (a) do not disaggregate, (b) disaggregate and (c) do not disaggregate but are atomized to the same particle size distribution as the particles in (b) after disaggregation.

8. REFERENCES:

Baxter, L.L., Z.G. Habib and D.R. Dunn-Rankin, 1989. "The Influence of Slurry Surfactants on the Morphology of Aggregates," to be submitted to *Fuel.*

Habib, Z.G. and L.L. Baxter, 1989. "The Effect of Surfactants on the Disaggregation of Coal-Water Slurry Particles During Combustion," to be submitted to *Combustion and Flame*

Baxter L.L., 1988. "Overview of Pulverized-Coal Combustion and Gasification Modeling: Current Status and Needed Improvements," presented at the Fifth Annual International Pittsburgh Coal Conference, Pittsburgh, PA, September 12-16

Holve, D.J. and S.A. Self, "Optical Particle Sizing for *In Situ* Measurements Part 1," *Applied Optics* **18** (1979a)

Holve, D.J. and S.A. Self, "Optical Particle Sizing for *In Situ* Measurements Part 2," *Applied Optics* **18** (1979b)

Holve, D.J., T.H. Fletcher and K. Gomi, "Comparative Combustion Studies of Ultrafine Coal/Water Slurries and Pulverized Coal," *Combustion Science and Technology* **52**, (1987)

McHale. E.T., "Combustion of Coal-Water Mixtures," Proceedings of the Twenty-First Symposium (International) on Combustion, The Combustion Institute, (1988)

Sakai, T., and M. Saito, "Single-Droplet Combustion of Coal Slurry Fuels, " *Combustion and Flame* **51** (1983)

Wei-Biao, F., W. Jing-Bin, H. Hong-Qiao, and Z. Yan-Ping, "A Study of the Evaporation and Ignition of a Single Coal-Water Slurry (CWS) Droplet," *Combustion Science and Technology* **43**, (1985)

Yao, S., and L. Liu, "Behavior of Suspended Coal-Water Slurry Droplets in a Combustion Environment," *Combustion and Flame* **51** (1983)

ADVANCED COMBUSTION TECHNIQUES: PULSE ATOMIZATION

1. FTPA NUMBERS: AA3535 & AA5520 & AA5525

CONTRACTOR: U.S. DOE/METC
P.O. Box 880
Morgantown, WV 26505
(304)291-4629

METC BRANCH CHIEF: William F. Lawson

PRINCIPAL INVESTIGATORS: George A. Richards
David W. Shaw
Gary J. Morris
Michael J. Welter

METC PROJECT MANAGER: Michael M. McMillian

CONTRACT PERIOD OF PERFORMANCE: October 1988 to October 1989

2. SCHEDULE/MILESTONES

Evaluate pulse combustion atomization	10/88 to 10/89

3. OBJECTIVES

A novel utilization of pulse combustion is being tested as a candidate coal-water slurry (CWS) fuel injector. As described below, this approach to CWS atomization may offer a number of advantages over conventional airblast atomizers. The objective of the current work is to evaluate the potential use of a pulse combustor to atomize and burn coal-water slurry.

4. BACKGROUND

Atomization of coal-water slurry has received considerable research attention in recent years. Much of this work has been stimulated by ongoing efforts to develop coal-fueled gas turbines and diesels [1]. Recent investigations have shown that modified CWS airblast nozzles can achieve acceptable performance in gas turbine applications using air/liquid mass ratios as low as 0.5:1 at an atomizing air pressure ratio of 2:1 [2]. While this is performance is admirable, considerable benefit could be realized by reducing or eliminating the need to supply high-pressure airblast air. This is shown schematically in figure 1, where an idealized CWS turbine system is considered. The system operates at 10 atmospheres (atm), with a turbine inlet temperature of 2000 F. A conventional airblast atomizer operates at a pressure ratio of 2:1 and an air to liquid ratio (ALR) of 0.5:1. Airblast air is supplied to the nozzle by routing a portion of the combustor air through a second stage boost compressor to supply the needed 2:1 pressure ratio to drive the nozzle. Assuming the combustion air and products have a constant specific heat, C_p, of 1000 J/Kg-K, and considering isentropic compression (i.e.; ignoring compressor

inefficiency), it is seen that the work required to compress the needed airblast air reduces the system efficiency by 0.4 %. In an actual system, compressor inefficiencies or higher ALR's could be expected to raise this figure. Furthermore, in practical systems, the airblast air is cooled prior to the auxiliary compression, meaning that relatively cold air is introduced into the primary zone, which tends to lower primary zone carbon conversion [2]. It thus seems desirable to find a way to reduce or eliminate the need for high-pressure airblast air.

As an alternative to airblast atomization, it was hypothesized that a small pulse combustor could provide very effective slurry atomization. The "pulse atomization" concept is illustrated in figure 2. Coal-water slurry (CWS) is injected into the exhaust stream of a pulse combustor where the rapidly oscillating gases can atomize the viscous slurry. Because the pulse combustor oscillates near the ambient pressure, this approach could eliminate the need to supply high-pressure atomization air. While the success of this concept is speculative at this point, a number of earlier investigations have shown promising results in similar applications. A 1958 patent [3] discusses the use of a pulse combustor to atomize and disperse insecticide. Lockwood [4] has successfully used pulse combustors to atomize food slurries, producing a dry meal or powder. The high-temperature exhaust of a pulse combustor can both atomize and dry such slurries, such that pulse combustion spray drying systems have recently entered the commercial market [5]. In a related concept, Swamy et al. [6] have shown that an "acoustic" nozzle can improve the atomization and combustion of heavy fuel oils.

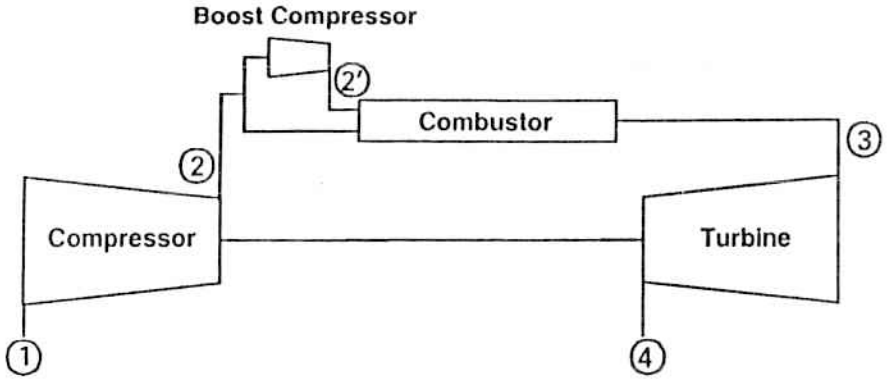
It is noted the pulse atomizer requires some auxiliary fuel aside from the CWS, but this auxiliary fuel will add to the CWS heat release and then be recovered in the turbine. Ideally, a successful atomizer will require a small input of auxiliary fuel per mass of CWS atomized, although no data are yet available to estimate what fuel input will be required.

5. PROJECT DESCRIPTION

Initial tests of pulse atomization were conducted using the Curtis Dyna-Jet pulse combustor shown in figure 3. This pulse combustor is sold commercially for model aircraft propulsion, and provided a rapid proof-of concept test. As shown, slurry was injected into the exhaust stream through a water cooled tube. Slurry flow rates up to 30 pounds per hour were atomized in this manner, producing a fine coal aerosol. This aerosol was sampled with a dilution probe and captured on fiberglass filters. Figure 4 shows a Scanning Electron Micrograph of the coal aerosol. The initial coal particle size was 16 microns. Noting the scale in the lower left corner of these figures, it is evident that the slurry has been essentially atomized back to the original coal grind.

While the Dyna-Jet provided a rapid test, the unit was very unreliable, with repeated reed valve failures, difficult starting, etc. To improve reliability, a pulse combustor based on the design of Kentfield [7] was constructed. This combustor is shown in figure 5, and operates without reed valves. The pulse combustor was fueled with propane. The unit was reliable, but the oscillation amplitude was insufficient to atomize CWS.

A slight modification of this combustor was found to substantially boost the oscillating pressure amplitude. As shown in figure 6, a blank flange capped the inlet and the fuel and air entry location were modified as shown. These changes resulted in very large amplitude pressure oscillations, often in excess of 35 pounds per square inch, with frequencies near 20 Hertz. These large amplitude pressure oscillations were thought to produce very high exhaust



$\frac{P_2}{P_1} = 10$

$\frac{P_2'}{P_2} = 2$

ALR = 0.5

AFR = 20.4

T_1 = 298 K

T_3 = 1370 K (2000°F)

Slurry LHV = 16.2 MJ/kg (7000 Btu/#)

$$\text{Compressor Work} = C_p(T_2 - T_1) = C_p T_1 \left[\left(\frac{P_2}{P_1}\right)^{\frac{\gamma-1}{\gamma}} - 1\right] = 277 \text{ kJ/kg air}$$

$$\text{Boost Compressor Work} = C_p(T_2' - T_2) \cdot \frac{ALR}{AFR} = C_p T_1 \left(\frac{P_2}{P_1}\right)^{\frac{\gamma-1}{\gamma}} \left[\left(\frac{P_2'}{P_2}\right)^{\frac{\gamma-1}{\gamma}} - 1\right] \frac{ALR}{AFR} = 3.1 \text{ kJ/kg air}$$

$$\text{Turbine Work} = C_p(T_3 - T_4) = C_p T_3 \left[1 - \left(\frac{P_4}{P_3}\right)^{\frac{\gamma-1}{\gamma}}\right] = 660 \text{ kJ/kg air}$$

$$\text{Heat Input} = C_p(T_3 - T_2) = C_p T_3 \left[1 - \frac{T_1}{T_3}\left(\frac{P_2}{P_1}\right)^{\frac{\gamma-1}{\gamma}}\right] = 794 \text{ kJ/kg air}$$

$$\text{With Boost} \quad \eta = \frac{660 - (277 + 3.1)}{794} = 47.8\%$$

$$\text{Without Boost} \quad \eta = \frac{660 - 277}{794} = 48.2\%$$

Figure 1. Idealized turbine cycle efficiency with and without boost compressor for atomization.

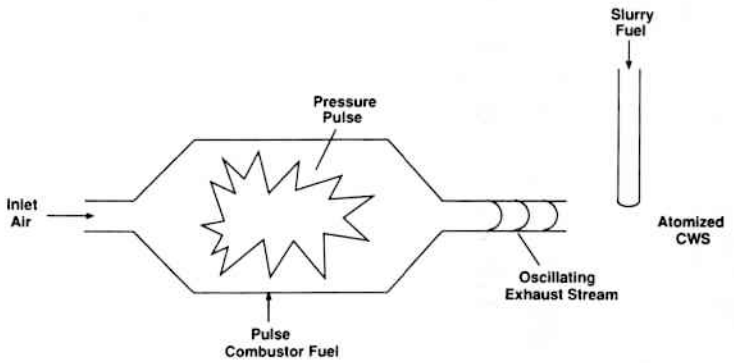


Figure 2. The Pulse-atomization concept.

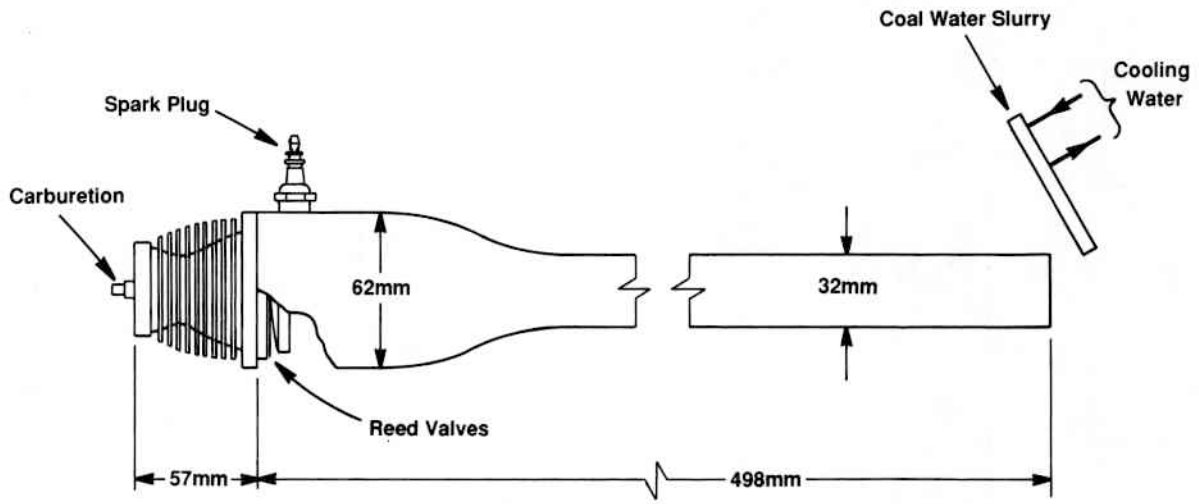


Figure 3. The Curtis Dyna-Jet pulse combustor.



Figure 4. Pulse-atomized slurry sample. Note scale in lower left corner. Fibers are the filter material. Figure at the right is a close-up (note change of scale) of an individual coal particle.

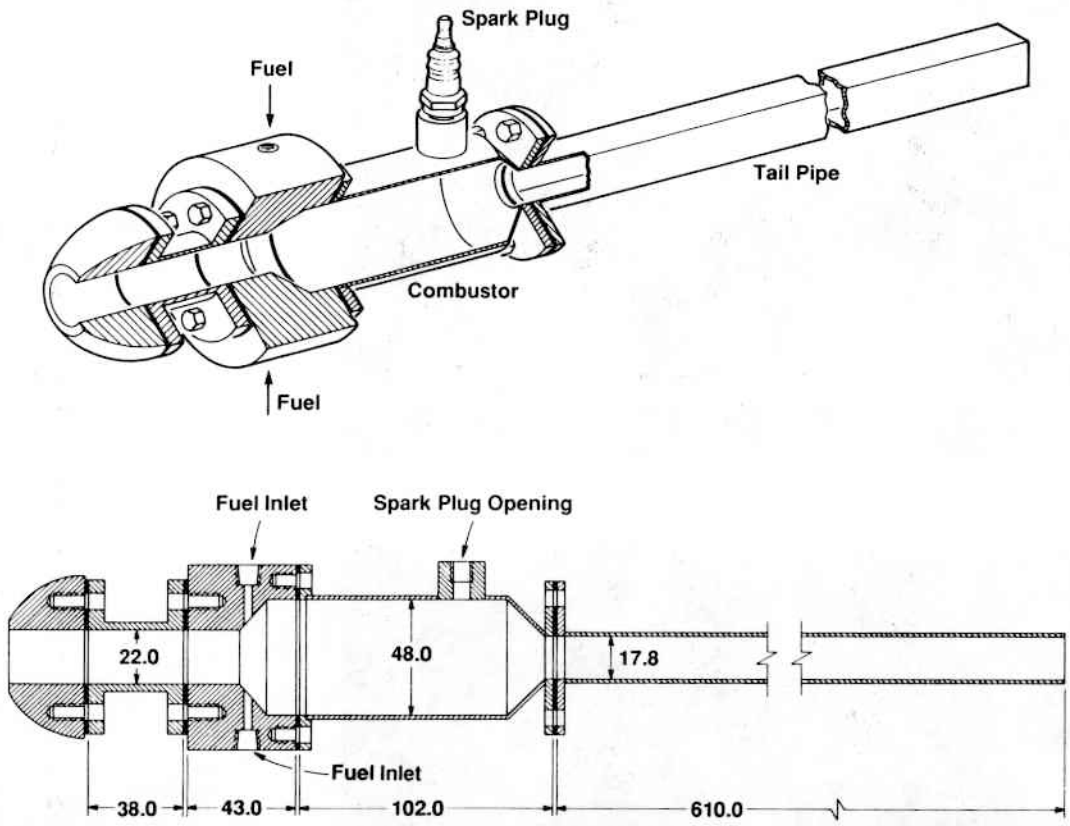


Figure 5. Combustor design of Kentfield [7]. Dimensions are in millimeters.

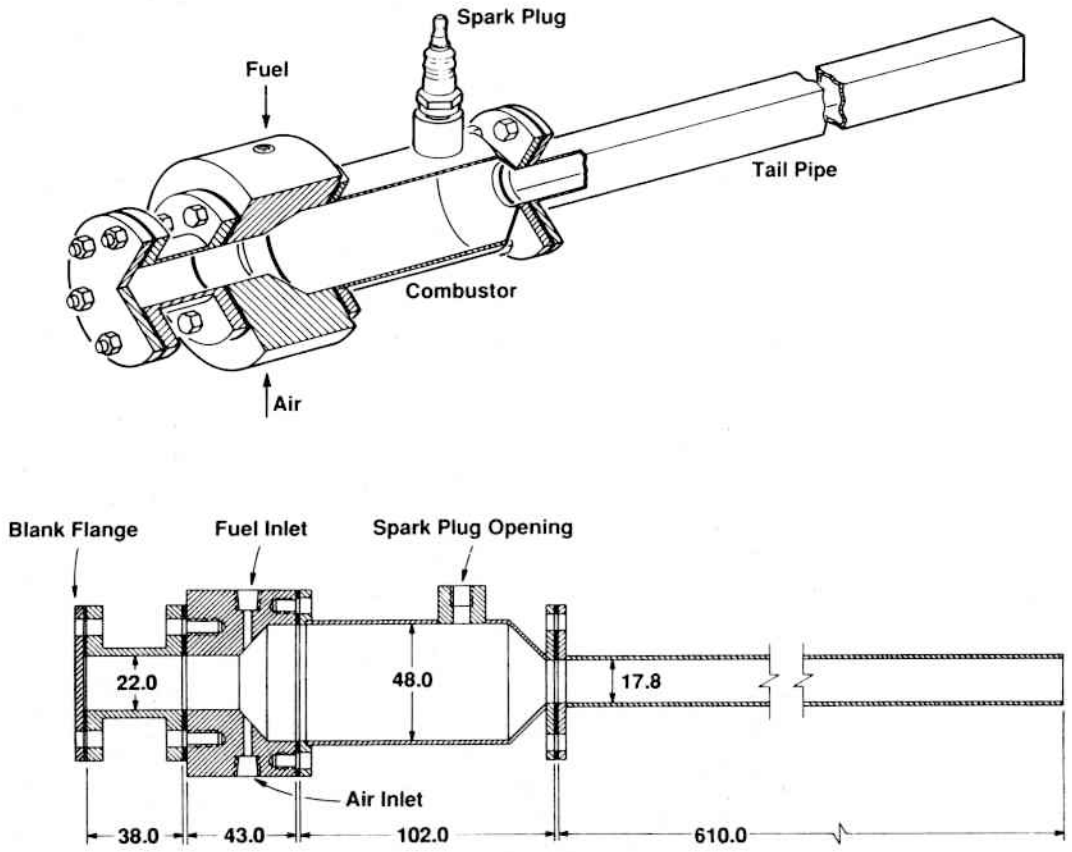


Figure 6. Modified combustor. Note blank flange and changes to air and fuel entry locations. Dimensions are in millimeters.

velocities and would therefore be desirable for atomization purposes. A complete study of this unique pulse combustion behavior has been documented elsewhere [8], and will not be discussed in detail here. Analysis of pressure and frequency data suggested that oscillations were controlled by the development of conditions needed for repetitive thermal explosions.

The large-amplitude pulse combustor (figure 6) has been incorporated into a pulse atomization/combustion test rig. Referring to figure 7, the test rig combines the pulse combustor and a refractory-lined, six inch (diameter) coal combustor. The coal combustor simulates the main combustor of a coal-fired gas turbine and supplies combustion air through a set of opposed ports to stabilize the CWS flame. As shown, CWS fuel is injected into the tailpipe of the pulse combustor for atomization and subsequent combustion.

6. RESULTS/ACCOMPLISHMENTS

Extended testing of high-amplitude pulse combustor (figure 6) has been completed. Results of these tests are fully documented elsewhere [8] and suggest that repetitive thermal explosions are responsible for observed oscillations. These tests have provided enough insight into the nature of the oscillation so that higher frequency oscillations can be achieved without sacrificing the large amplitude pressure oscillations. To date, frequencies as high as 50 Hz have been achieved while maintaining pressure oscillations in excess of 30 pounds per square inch.

Initial tests in the atomization/combustion rig (figure 7) have been completed. The first tests demonstrated successful combustion of the pulse atomized slurry at a heat release rate of 110,000 BTUH, with propane fueling the pulse combustor at a rate of 43,000 BTUH. These first tests were far from optimal but demonstrated proof-of-concept. The coal aerosol has not yet been sampled to quantify the extent of atomization because occasional sputtering of large drops was evident in the exhaust stream. Work in progress has identified the source of these large drops with potential improvements now under consideration.

7. FUTURE WORK

The observation of large, sputtered slurry drops was thought unacceptable. Two mechanisms were considered for their formation. First, the relatively low 20 Hz frequencies of the high-amplitude combustor could allow sufficient time between pulses for injected slurry to accumulate on the tailpipe wall <u>across</u> from the CWS entry tube. Higher frequencies would solve this problem, and work in progress has demonstrated frequencies as high as 50 Hz are possible at pressure amplitudes of more than 30 psi. In the current pulse combustor configuration, these higher frequencies require careful setting of flow rates and combustor wall temperatures, and have not yet been used for atomization. Instead, design and testing of a modified combustor is in progress to allow consistently higher frequencies with the large amplitude oscillations.

A second reason for the large, sputtered drops has been confirmed through high-speed photography. The relatively large size of the water-cooled slurry injection probe (0.5 inch diameter) has been shown to result in transient recirculation of injected slurry downstream of the probe. Photographs of water injected into the exhaust stream show that large drops of water can form and

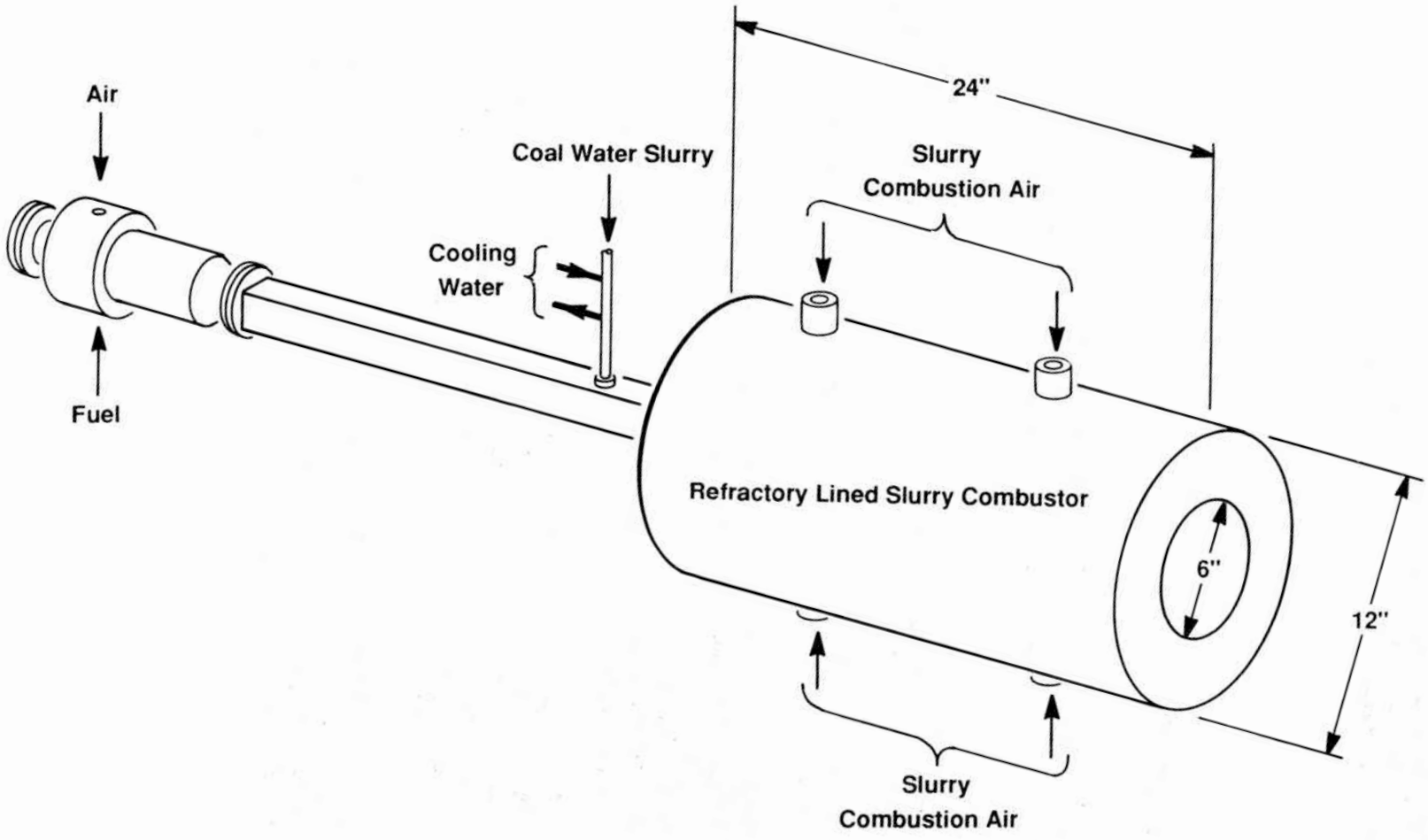


Figure 7. Pulse atomization/combustion test rig.

linger on the back side of the injection probe before being entrained into the flow. High-speed photography of this process continues with a number of different injection strategies being tried to eliminate the recirculation.

8. REFERENCES:

1. Dodge, F. T., Dodge, L. G., Johnson, J. E. "Nozzle Development," Final Report, Southwest Research Institute, METC Contract No. DE-AC21-86MC23005.

2. Roesler, T.C., and C. Wilkes, "The Optimization of a Coal-Water Slurry Atomizer", ASME paper 89 GT-111, presented at the ASME International Gas Turbine Conference, Toronto, Canada, June 1989.

3. Tenney, W. C., Frank, P. A., and Knox, S. E., 1958, "Machine for producing dispersions of liquids in air or other gases for the production of fog," U.S. Patent 2,857,332.

4. Lockwood, R. M., "Spray Drying Apparatus," U. S. Patent 3,618,655, November 9, 1971.

5. Chowdhury, J., "Pulse Combustion Lowers Drying Cost," Chemical Engineering, December 10, 1984, pp. 44-45.

6. Swamy, K. M., Narayana, K. L., and Murty, J. S., 1988, "Acoustic Burner Saves Liquid Fuel in an Industrial Burner," Energy Progress, Vol. 8, No. 2, pp. 118-120.

7. Kentfield, J. A. C., and Read, M. A., "A Pressure-Gain Combustor Utilizing Twin Valveless Pulsed-Combustors Operating in Anti-Phase," Proceedings of the Intersociety Energy Conversion Conference, 14th, Vol. 2., Boston, Mass., Aug. 5-9, 1979. Published by American Chemical Society. Also available IEEE cat. no. 79CH1477-9 ENERGY, Piscataway, NJ pp. 1774-1779.

8. Morris, G. J., Welter, M. J., Richards, G. A., "An Investigation of Pulse-Combustor Design for Slurry Atomization," in review for presentation at the ASME Energy-Sources Technology Conference, Fossil Fuel Combustion Symposium, New Orleans, LA, Jan. 14 - 18, 1990.

Session 2
Instrumentation and Diagnostics

Chairperson: Curtis V. Nakaishi

This session provides an overview of some of the instrumentation and diagnostics (I&D) projects. Adequate, accurate, and reliable I&D projects are necessary to effectively develop advanced fossil energy (FE) technologies. The I&D Program is primarily concerned with developing measurement techniques and process control schemes to support advanced coal-based conversion and utilization processes. It is not the discovery of I&D techniques or methods, but it is their application to the particular needs of the FE research programs that focuses this program through the use of the latest scientific and engineering advances. The primary emphasis will be crosscutting and should involve the theoretical, analytical, and experimental investigations that indicate the feasibility of I&D techniques, devices, or methods.

OPTICAL DETECTION OF CORROSIVE COMPOUNDS

1. **CONTRACT NUMBER:** A192

CONTRACT PERIOD: January 1, 1983 to September 30, 1989

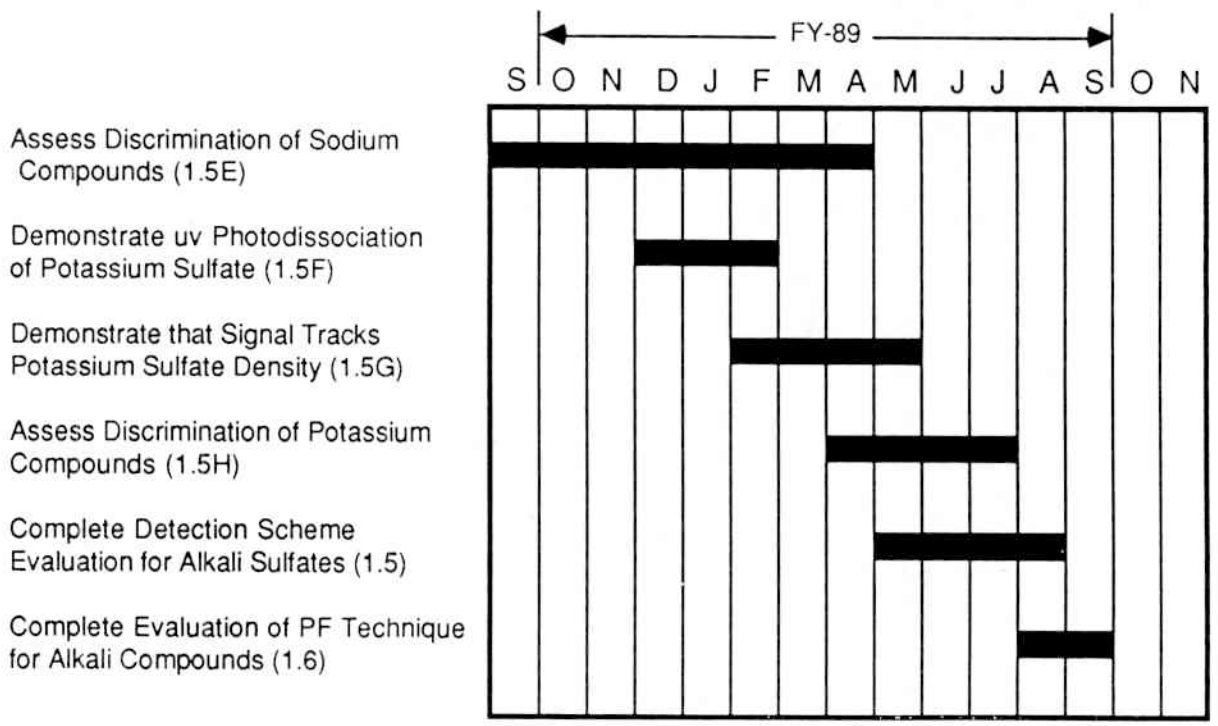
CONTRACTOR: Los Alamos National Laboratory
Los Alamos, New Mexico 87545
(505) 667-7121

PRINCIPAL INVESTIGATOR: Richard C. Oldenborg

METC PROGRAM MANAGER: Curt Nakaishi

2. **SCHEDULE/MILESTONES:**

FY1989 PROGRAM SCHEDULE



3. **OBJECTIVES:**

The overall objective of this program is to develop a laser-based optical diagnostic technique for the direct monitoring of trace levels of corrosive compounds, in particular, gas-phase alkali compounds, within the post-combustion coal gas stream. The diagnostic needs to be compound specific and sensitive to parts per billion (ppb) levels.

4. BACKGROUND:

An attractive option for the future generation of electrical power is to drive gas turbines with fuels derived from the economically priced and domestically prevalent resource coal. However, turbine components are susceptible to corrosion and deposition from even trace amounts of certain inorganic contaminants, particularly the alkali metals and their compounds (France 1984, Morgantown 1986). Alkali compounds can be destructive at even ppb levels, depending on their composition (halides, hydroxides, sulfates, or oxides) and form (molecular or particulate).

Commonly employed analytical methods include techniques based on atomic emission spectroscopy of samples extracted from gas streams (Haas 1985, Romanowski 1984). While having the required sensitivity, these methods, which measure the total alkali concentration, lack the desired specificity of composition and form and are inherently limited by sampling techniques. Clearly, new sensitive compound-specific techniques are needed for on-line in situ monitoring of post-combustion streams and to help elucidate the chemistry of these important compounds.

5. PROJECT DESCRIPTION:

The diagnostic currently under development is based on the photofragment fluorescence technique, in which atomic alkali emission is detected upon ultraviolet photodissociation of alkali-containing compounds. Figure 1 is a schematic representation of typical potential energy curves for an alkali compound. The internuclear separation plotted is the coordinate leading to the release of an alkali atom.

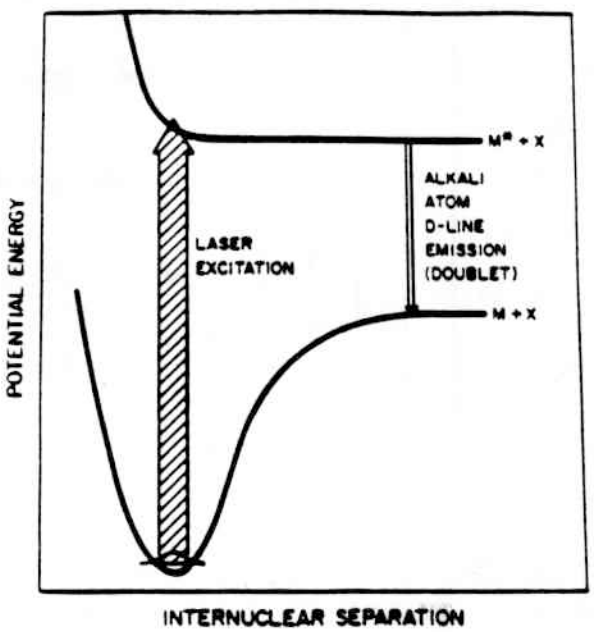


Fig. 1. Schematic illustration of photofragment fluorescence diagnostic concept.

This figure illustrates the concept behind this diagnostic technique. A uv laser excites the parent compound to a state that dissociates along a repulsive potential to yield an excited alkali atom. This atom then emits at its characteristic wavelength and the intensity of this emission is proportional to the original concentration of the parent compound. The sensitivity of this atomic photofragment fluorescence technique as an analytical method should be high since the atomic alkali emission is strong (~20 ns radiative lifetime) (Wiese 1969) and the absorption cross sections of the alkali compounds in the desired band are large ($\sigma > 10^{-17}$ cm^2) (Davidovits 1967). In addition, since practical applications involve measurements in high-temperature environments (600 to 950°C for gas turbine inlet temperatures), the limiting source of noise is due to statistical fluctuations in the blackbody emission background, and the inherently narrow bandwidth of the atomic emission allows for good wavelength discrimination from the blackbody background and correspondingly better sensitivity.

Compounds of the different alkalis (e.g., NaCl, KCl) can readily be distinguished by the emission wavelengths of the excited atoms (589 nm for Na*, 766 nm for K*). Discrimination between compounds of the same alkali but different anions (e.g., KCl, KOH) is more difficult, but can be achieved by examining the dependence of the alkali emission on the excitation laser wavelength. This can best be illustrated by comparison of threshold wavelengths, i.e., the wavelength needed to dissociate a vibrationally cold parent compound to yield the excited alkali atom. Threshold wavelengths vary among different compounds as the dissociation energies vary. The calculated energy required for the production of excited alkali atoms in the lowest $^2P^\circ$ state and the corresponding threshold wavelengths are listed in Table 1 (Oldenborg 1986). The compounds listed are some of the more important gas-phase molecules expected to be present in fossil fuel combustion environments. The calculation assumes that the photodissociation process shown in Table 1 is the predominant pathway leading to excited $^2P^\circ$ alkali atoms.

Absorption of the vibrationally excited compounds is important at the temperatures of interest and this "hot-band" absorption significantly broadens the bands in the photodissociation spectra to longer wavelengths. Considering a Boltzmann energy distribution and assuming comparable sensitivities, we estimate that if the threshold energies differ by at least 10 kcal/mole, then 100:1 discrimination can be achieved given some knowledge of the temperature. The variation in threshold energies shown in Table 1 is large enough that good discrimination between compounds containing the same alkali but different major anion groups (halides, hydroxides, monoxides, dioxides, and sulfates) should be feasible. However, interference between the different monoxides of the same alkali is likely.

In order for this optical diagnostic technique to be of practical importance in potential coal-gas fired turbine applications, it must meet three criteria. First, it must allow for discrimination among the various alkali compounds present. Second, it must be sensitive to part-per-billion levels. Finally, it must be quantitative, i.e., the signal must be a known function of the alkali compound concentration, preferably linear. We present here the results of our completed experiments on the photodissociation of sodium and potassium chlorides, hydroxides, and sulfates. These alkali compounds are of particular interest, since they are believed to be some of the predominant alkali-containing species in high temperature postcombustion coal gas streams. The dependence of the electronically excited alkali atom fluorescence ($^2P^\circ \rightarrow {}^2S$) on temperature, vapor pressure, and dissociation laser wavelength is discussed.

Table 1. Calculated Energetics and Threshold Wavelengths for Lowest $^2P^\circ$ State Production from Photodissociation of Selected Alkali Compounds

Photodissociation Process			ΔH(kcal/mole)	Threshold λ(nm)
NaCl	→	Na* + Cl	145.9 ± 2	195.9
NaOH	→	Na* + OH	130.0 ± 5	219.8
NaO	→	Na* + O	108.8 ± 4	262.7
Na_2O	→	Na* + NaO	108.0 ± 4	264.6
NaO_2	→	Na* + O_2	87.5 ± 5	326.6
Na_2SO_4	→	Na* + $NaSO_4$	160.1 ± 5[a]	178.5
KCl	→	K* + Cl	138.2 ± 2	206.8
KOH	→	K* + OH	122.6 ± 5	233.1
KO	→	K* + O	103.2 ± 3	276.9
K_2O	→	K* + KO	107.3 ± 3	266.4
KO_2	→	K* + O_2	78.7 ± 5	363.2
K_2SO_4	→	K* + KSO_4	151.8 ± 5[a]	188.3

[a] assumes equal bond strength for both alkali atoms.

The source of the gas-phase alkali compounds in these experiments is the equilibrium vapor pressure above the condensed-phase salt in the 450-1050°C temperature range. The alkali compound vapors are contained in quartz cells or formed into a molecular beam using effusive techniques. The uv laser wavelengths required for the photodissociation are obtained by stimulated Raman scattering of an ArF excimer laser output. This is a relatively simple technique for our laboratory experiments and should be readily adaptable for practical field applications. It provides from a single source the wide range of fixed wavelengths required to probe all the various alkali compounds. The emission from the atomic alkali doublet D-lines is observed through bandpass filters (589 nm for Na*, 766 nm for K*) with a photomultiplier tube.

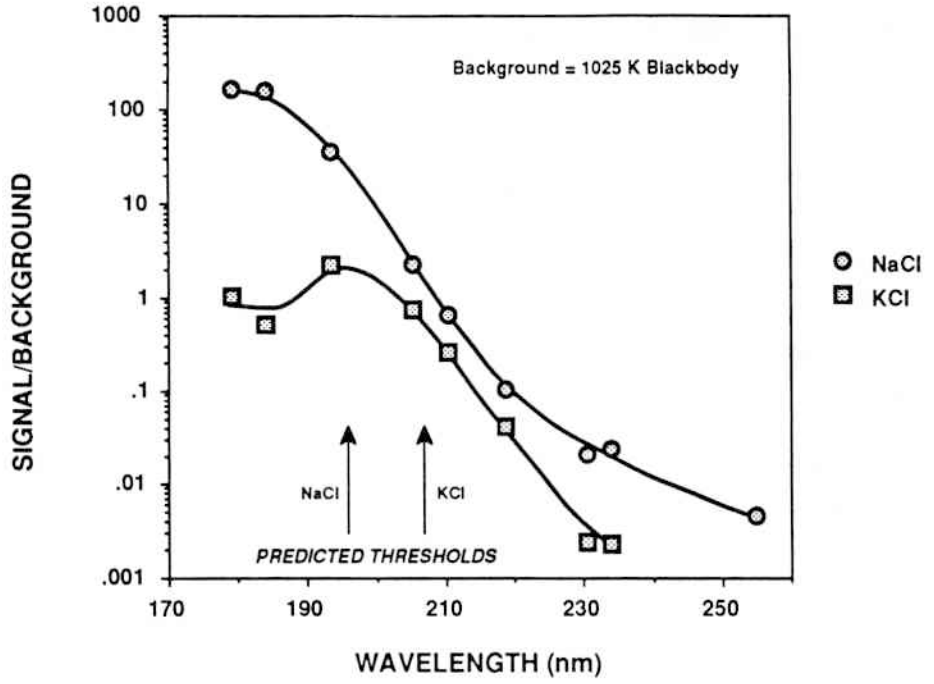


Fig. 2. Excited alkali atom production efficiency versus dissociation laser wavelength for NaCl and KCl at 800°C. Data for the two compounds are normalized to an equivalent density. The ordinate is the signal/background ratio that is expected for a concentration of 1 ppb.

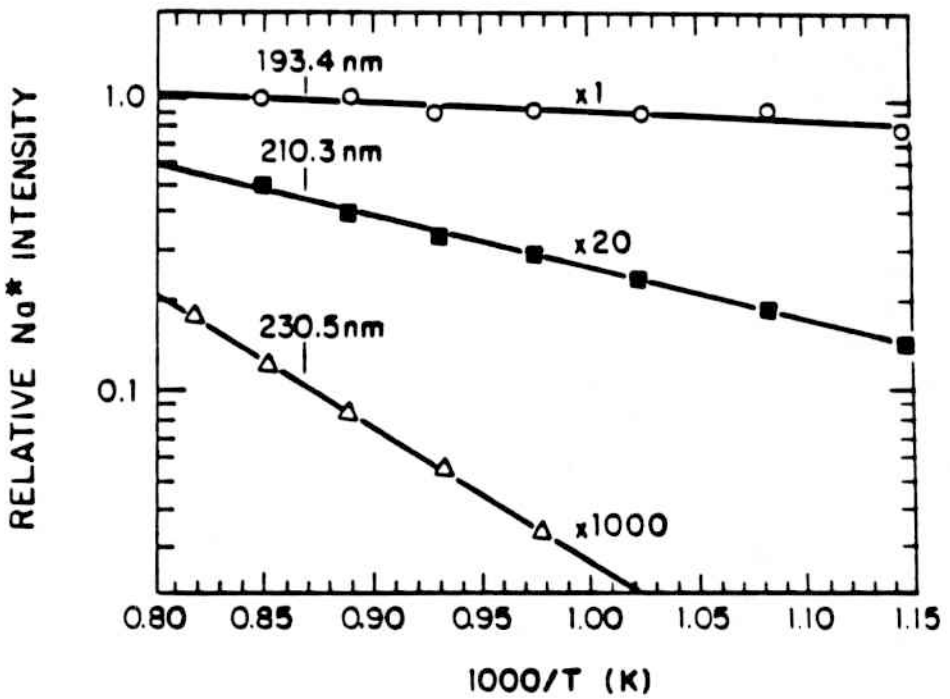


Fig. 3. Effect of cell temperature variation on the production of Na^* ($3\,^2P$) from NaCl. Data are normalized to unity for the 193.4-nm excitation wavelength and for a temperature of 850°C.

6. RESULTS/ACCOMPLISHMENTS:

ALKALI CHLORIDES

The relative production efficiency for the excited alkali emission, i.e., the emission intensity normalized for the laser energy, is shown in Fig. 2 for NaCl and KCl at a temperature of 800°C. The data for the two compounds are normalized to an equivalent density. The alkali compound density was low ($<1 \times 10^{15}$ molecules/cc) to minimize any contributions from dimers and radiation trapping of the atomic fluorescence. Note that this is a semilogarithmic plot, so that the production efficiency spans a wide dynamic range. The calculated threshold wavelengths of 196 nm (NaCl) and 207 nm (KCl) from Table 1 are indicated in the figure. The photofragment fluorescence signals from these compounds peak roughly 15 nm to the blue of the predicted thresholds, and drop dramatically at longer wavelengths. The fact that the signal is not zero at energies below the threshold can be qualitatively understood in terms of hot-band absorption and dissociation of vibrationally excited molecules. At these temperatures, a significant fraction of the alkali compound molecules are in excited vibrational states.

The application of this diagnostic technique in a quantitative fashion is much simpler if the signal intensity does not depend on the temperature of the compound being probed. This appears to be the case for the alkali chlorides at dissociation energies above the threshold. For example, the temperature dependence of the signal from a constant density of NaCl for three different dissociation wavelengths is shown in Fig. 3. The data are not corrected for the small changes in the alkali atom fluorescence quenching rate with temperature. At 193.4 nm and shorter wavelengths, little change in signal magnitude is seen over the temperature range 650 to 900°C, making these ideal diagnostic wavelengths for this compound. These wavelengths are shorter than the calculated threshold value of 195.9 nm. In contrast, data at the other wavelengths plotted in Fig. 3, i.e., 210.3 and 230.5 nm, show a marked temperature dependence. At these wavelengths an increase in signal with increasing temperature is clearly discernible. This behavior is consistent with the fact that wavelengths longer than the threshold value can only produce excited alkali atoms from the dissociation of vibrationally excited sodium chloride molecules. From this data we can conclude that for alkali compound diagnostic applications, the probe laser wavelength should be at or slightly shorter than the calculated threshold wavelengths so that the signal will not be dependent on the temperature of the compound being examined. The ArF laser wavelength 193.4 nm appears to be a reasonable and convenient choice for both sodium and potassium chlorides. While the shorter wavelengths of 179 and 184 nm have higher sensitivity for NaCl than does 193.4 nm, the use of these shorter wavelengths requires that all the oxygen be purged from the laser beam lines. This added difficulty, combined with the inherently lower laser energies at these wavelengths, offset any advantage these wavelengths might otherwise have and makes 193.4 nm the most practical choice for most anticipated applications. Figure 3 shows that the temperature dependence of the signal is well represented by an exponential in inverse temperature. For NaCl and KCl detection at 193.4 nm, the intensity of the photofragment fluorescence signal is proportional to $\exp(-726/T)$ and $\exp(-806/T)$, respectively, where the temperature, T, is in units of Kelvins.

The quantitative behavior of the photofragment fluorescence diagnostic is demonstrated by varying the temperature of the salt reservoir and consequently the vapor pressure of alkali chlorides in the cell. The typical result of such an experiment for NaCl at a fixed cell temperature of 750°C is shown in Fig. 4. The logarithm of the atomic alkali emission intensity from the 193.4-nm dissociation is plotted versus the inverse of the reservoir temperature. The sodium chloride in the reservoir is in the solid phase over the temperature range of the experiment. Therefore, the slope of this plot should be determined by the heat of sublimation of the the sodium chloride. Superimposed on the data in Fig. 4 is a curve calculated using the JANAF thermochemical tables showing the relative sodium chloride monomer pressure over the same temperature range. Since only relative intensities are measured in our experiment, the JANAF-derived curve is scaled to best match the data. Nevertheless, the excellent agreement between the calculated curve and the measured data demonstrates that our measured heat of sublimation agrees with the JANAF tabulation and that the diagnostic signal linearly tracks the monomer density over 5 orders of magnitude. Similar results have been obtained for the detection of KCl.

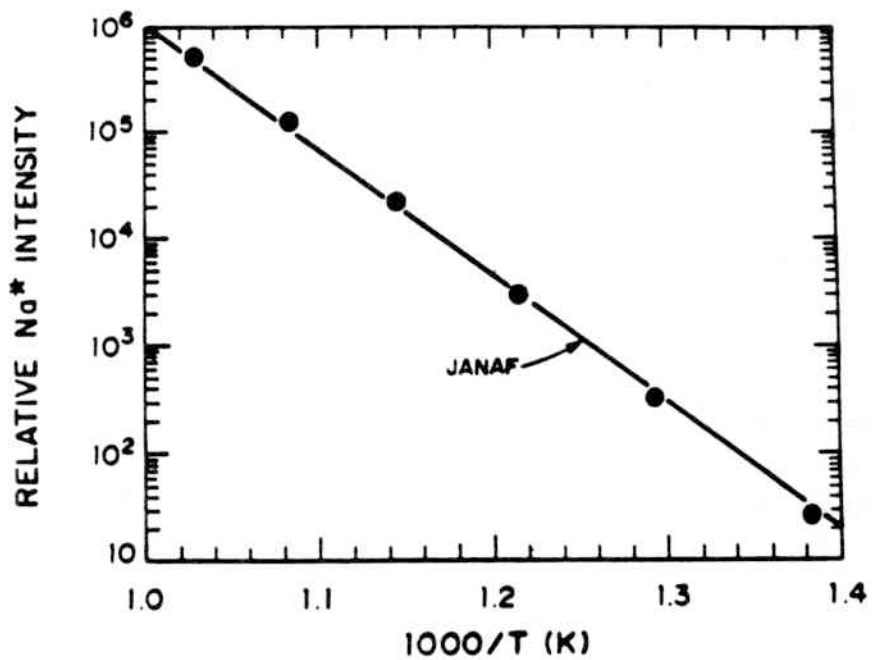


Fig. 4. Effect of reservoir temperature variation on the production of $Na^*(3\ ^2P)$ from NaCl at an excitation wavelength of 193.4 nm and for a fixed cell temperature of 750°C. The solid line shows the temperature dependence of the sodium chloride monomer pressure calculated from JANAF thermochemical tables, scaled to best match data.

The final issue to be addressed for the alkali chlorides is the detection sensitivity. Under our experimental conditions, as well as those of practical importance, the limiting source of noise is from statistical fluctuations in the blackbody emission background. Consequently, we define absolute detection sensitivity as the number density (or concentration) of molecules necessary to produce an integrated excited alkali atom fluorescence signal equal to the standard deviation in the background blackbody emission from our quartz cell integrated over the same time interval. This sensitivity is determined by measuring the fluctuations in the blackbody intensity and then extrapolating the signal versus vapor pressure data (e.g., Fig. 4) down to this value. This yields an absolute detection sensitivity for this photofragment fluorescence diagnostic technique of 4×10^6 molecules/cc for NaCl and 4×10^7 molecules/cc for KCl, for a single 193.4 nm laser pulse at a cell temperature of 750°C, a laser energy in the observation volume of 1.5 mJ/pulse (7.2 mJ/cm^2), and a 10-nm wide bandpass filter..

These sensitivity limits are for neat alkali chloride vapors in the absence of any gas that might quench the alkali atom fluorescence. Most practical applications, however, are at atmospheric pressure or greater. If we make the worst-case assumption that the atomic alkali emission is quenched with an approximately gas kinetic rate (4×10^{-10} cc/molecule-s), then these limits correspond to concentrations of 0.03 ppb for NaCl and 0.4 ppb for KCl. Using these detection limits, the ordinate in Fig. 2 was scaled so as to show the signal/background ratio that would be expected at a concentration of 1 ppb. These sensitivity limits are those expected for a single 193.4 nm laser pulse. At a laser repetition rate of 100 Hz, only two minutes of signal averaging could drop these values 2 orders of magnitude. In addition, replacing the present optical filters with narrower state-of-the-art filters could yield as much as an additional factor of 5 improvement, while increasing the laser energy in the present irradiation volume to the saturation limit could improve sensitivity a factor of 5.

ALKALI HYDROXIDES

The relative production efficiency for the excited alkali emission, i.e., the emission intensity normalized for the laser energy, is shown in Fig. 5 for NaOH and KOH at a temperature of 800°C. The data for the two compounds are normalized to an equivalent density. The calculated threshold wavelengths of 220 nm (NaOH) and 233 nm (KOH) from Table 1 are indicated in the figure. The photofragment fluorescence signals from NaOH and KOH peak at 224.4 and 240.6 nm, respectively, which, unlike the alkali chlorides, are slightly to the red of the predicted thresholds. However, both of these compounds could be probed most conveniently with the 2nd Stokes line in H_2 at 230.4 nm. While the data in Fig. 5 would indicate that this choice would result in a small decrease in sensitivity, higher fluences can typically be obtained at 230.4 nm compared to these other wavelengths and therefore no decrease in sensitivity will probably be realized in actual practice.

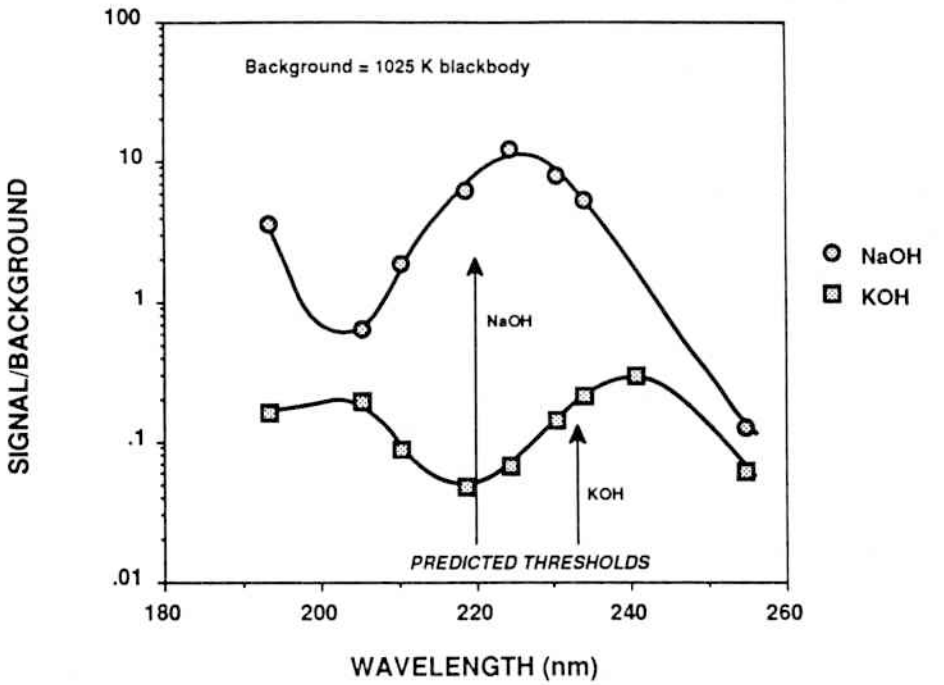


Fig. 5. Excited alkali atom production efficiency versus dissociation laser wavelength for NaOH and KOH at 800°C. Data for the two compounds are normalized to an equivalent density. The ordinate is the signal/background ratio that is expected for a concentration of 1 ppb.

The absolute detection sensitivity for these compounds was determined by comparing their measured photofragment fluorescence intensities with those of the corresponding alkali chlorides. The resultant sensitivity limits for this diagnostic technique are 2×10^7 molecules/cc for NaOH and 6×10^8 molecules/cc for KOH, for a single 230.4 nm laser pulse at a cell temperature of 750°C, a laser energy in the observation volume of 1.5 mJ/pulse (7.2 mJ/cm^2), and a 10-nm wide bandpass filter. If we make the worst-case assumption, as we did for the chlorides, that the atomic alkali emission is quenched with an approximately gas kinetic rate (4×10^{-10} cc/molecule-s), then these limits correspond to concentrations of 0.1 ppb for NaOH, and 7 ppb for KOH. Using these detection limits, the ordinate in Fig. 5 was scaled so as to show the signal/background ratio that would be expected at a concentration of 1 ppb.

The temperature dependence of the photofragment fluorescence signal for NaOH and KOH is expected to be small, as was the case for the chlorides, since the chosen probe wavelength, 230.4 nm, is near the calculated thresholds. This was indeed found to be the case. Again, the temperature dependence of the signal is well represented by an exponential in inverse temperature, and intensity of the photofragment fluorescence signal is proportional to exp(−424/T) and exp(−1936/T) for NaOH and KOH respectively, where the temperature, T, is in units of Kelvins.

ALKALI SULFATES

The photodissociation of alkali chlorides and hydroxides is relatively straightforward; the dissociation is linear in laser fluence, alkali atoms are the primary photoproduct, and the level of excitation in the alkali atom fragment increases as the excitation wavelength decreases. There was little doubt that the photofragment fluorescence technique would be applicable to these compounds. The objective of our studies of the alkali chlorides and hydroxides was, therefore, to quantify the technique and obtain the data base necessary for diagnostic applications. However, the alkali sulfate molecules are significantly more complex and the applicability of the technique to these compounds was never a foregone conclusion. For example, because of the complexity of the alkali sulfate molecule, a photofragment fluorescence signal could arise from either a single or multiple photon absorption process. A key experiment conducted early in our sulfate studies was to examine the dependence on laser fluence of the atomic sodium emission intensity from the photodissociation of the alkali sulfates. A linear behavior was observed that is clear evidence of a simple, single photon dissociation process, analogous to that of the alkali chlorides and hydroxides.

The relative production efficiency for the excited alkali emission, i.e., the emission intensity normalized for the laser energy, is shown in Fig. 6 for Na_2SO_4 and K_2SO_4 at temperatures of 800°C. The data for the two compounds are normalized to an equivalent density. The calculated threshold wavelengths of 179 nm (Na_2SO_4) and 188 nm (K_2SO_4) from Table 1 are indicated in the figure. The photofragment fluorescence signals from both Na_2SO_4 and K_2SO_4 maximize at the shortest wavelength that was studied, namely 179 nm. However, unlike the alkali chlorides and hydroxides, the photofragment fluorescence signals that are observed at wavelengths considerably longer than the predicted thresholds are still relatively strong. These signals are too strong to result solely from hot-band absorption and the dissociation of vibrationally-excited molecules. Rather, they are an indication that our threshold estimates for the alkali sulfates are probably incorrect. The threshold values for the alkali sulfates presented in Table 1 were calculated assuming that the bond strength for each of the alkali atoms was identical. The high signals at the long wavelengths shown in Fig. 6 suggest that removal of the first alkali atom from the sulfate compound is considerably easier than removal of the second and that the actual threshold is at longer wavelengths than our previous estimates. This results in photofragment fluorescence signals that are relatively flat over the entire wavelength range investigated. For both sodium and potassium sulfate, a probe wavelength of 193.4 nm appears to be a reasonable compromise between sensitivity and convenience.

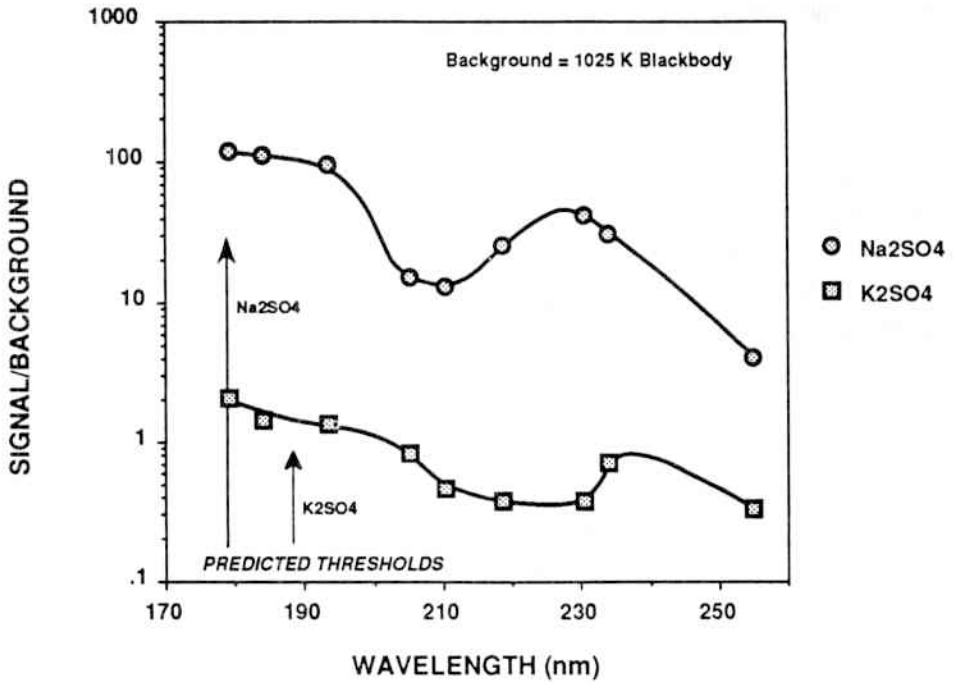


Fig. 6. Excited alkali atom production efficiency versus dissociation laser wavelength for Na_2SO_4 and K_2SO_4 at a temperature of 800°C. Data for the two compounds are normalized to an equivalent density. The ordinate is the signal/background ratio that is expected for a concentration of 1 ppb.

The absolute detection sensitivity for the alkali sulfates was determined by comparing their measured photofragment fluorescence intensities with those of the corresponding alkali chlorides. The resultant sensitivity limits for this diagnostic technique are 1 x 10^6 molecules/cc for Na_2SO_4 and 3 x 10^7 molecules/cc for K_2SO_4, for a single 193.4 nm laser pulse at a cell temperature of 750°C, a laser energy in the observation volume of 1.5 mJ/pulse (7.2 mJ/cm^2), and a 10-nm wide bandpass filter. If we make the worst-case assumption, as we did for the other compounds, that the atomic alkali emission is quenched with an approximately gas kinetic rate (4 x 10^{-10} cc/molecule-s), then these limits correspond to concentrations of 0.01 ppb for Na_2SO_4, and 0.3 ppb for K_2SO_4. Using these detection limits, the ordinate in Fig. 6 was scaled so as to show the signal/background ratio that would be expected at a concentration of 1 ppb.

Unlike the alkali chlorides and hydroxides, the temperature dependence of the photofragment fluorescence signal for Na_2SO_4 and K_2SO_4 is hard to predict, because the true threshold wavelengths are unknown. At an excitation wavelength of 193.4 nm, the signal was found to decrease with increasing temperature, contrary to the behavior observed for the alkali chlorides and hydroxides. The temperature dependence of the signal is still well represented by an exponential in inverse temperature, and intensity of the photofragment fluorescence signal is found to be proportional to exp(6280/T) and exp(7789/T) for Na_2SO_4 and K_2SO_4 respectively, where the temperature, T, is in units of Kelvins. Similar dependencies were observed at the other wavelengths investigated, i.e., the relative shape of the alkali sulfate photofragment fluorescence spectra changes little with temperature.

DISCRIMINATION BETWEEN DIFFERENT ANIONS

Figure 7 shows a superposition of the photofragment fluorescence spectra for sodium chloride, hydroxide, and sulfate. The signal to background ratio expected for a 1 ppb concentration of each compound is plotted vs laser wavelength. While the sodium chloride spectrum is notably different from either the hydroxide or the sulfate, the latter two spectra show considerable similarities. From this we conclude that in predominantly binary mixtures of sodium chloride and hydroxide, or sodium chloride and sulfate, the photofragment fluorescence technique will be able to determine the concentrations of both compounds. For example, near the optimum NaOH wavelength (230.4 nm), the signal from the NaCl dissociation is down more than 2 orders of magnitude. Likewise, near the optimum NaCl wavelength (193.4 nm), the signal from the NaOH dissociation is down more than a factor of 10. Consequently, the densities of both NaOH and NaCl should be measurable, provided they differ by less than a factor of approximately 100. However, in mixtures containing comparable amounts on sodium hydroxide and sulfate, it will be difficult to accurately determine the concentration of either compound using this technique because of the lack of contrast between their spectra. A comparison of the spectra for potassium chloride, hydroxide, and sulfate is quite similar to the sodium spectra show in Fig. 7, and the conclusions regarding discrimination between the three potassium compounds are identical to those of the sodium compounds.

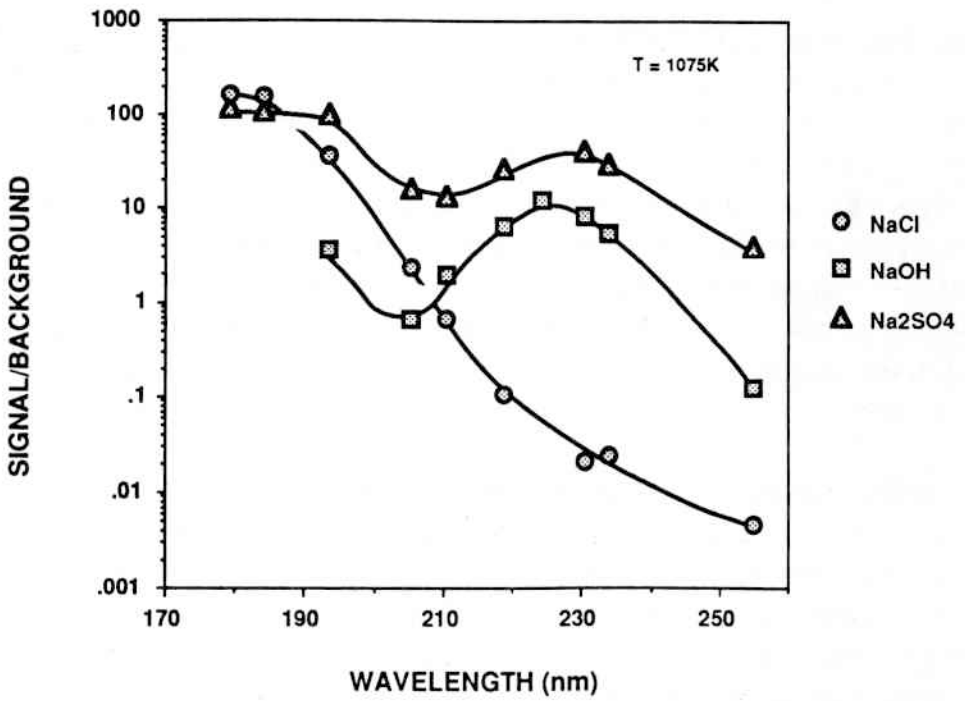


Fig. 7. Excited sodium atom production efficiency versus dissociation laser wavelength for NaCl, NaOH, and Na_2SO_4 at a temperature of 800°C. Data are normalized to an equivalent density. The ordinate is the signal/background ratio that is expected for a concentration of 1 ppb.

7. FUTURE WORK:

The research and development phase of the photofragment fluorescence work has now reached a reasonable and successful conclusion, and the work on this technique at Los Alamos has now ended. The next logical step for this program is to attempt to implement this diagnostic in actual post-flame combustion gases. As part of a separate project under the leadership of the PSI Technology Co., an attempt to do this implementation is underway. Recent reports of this work (PSI 1989) have noted success in establishing the feasibility of the photofragment fluorescence technique for detecting NaCl in these post-flame environments, and the extension of this work to the other alkali compounds is now in progress.

8. REFERENCES:

Davidovits, P.; Brodhead, D. C., ***J. Chem. Phys.***, 46, 2968 (1967).

France, J. E.; Grimm, U.; Anderson, R. J.; Kovach, J. J., Deposition and Corrosion of Gas turbines Utilizing Coal or Coal-Derived Fuel, DOE/METC/84-17, (1984).

Haas, W. J.; Eckels, D. E.; Wessels, T. E.; Kniseley, R. N., Real-Time Alkali Monitoring for Fluidized-Bed Combustor Flue Gas, in Proceedings of the Fourth Annual Contractors Meeting on Contaminant Control in Hot Coal-Derived Gas Streams, DOE/METC-85/3, (1985).

Morgantown Energy Technology Center, Hot Gas Cleanup for Electric Power Generating Systems, DOE/METC-86/6038, (1986).

Oldenborg, R. C.; Baughcum, S. L., ***Anal. Chem.***, 58, 1430 (1986).

PSI Technology Company, Quarterly Report No. 11 for Transformations of Inorganic Coal Constituents in Combustion Systems, PSI-1024/TR-950, section 6, (1989).

Romanowski, C.; Anderson, R. J., A Nonintrusive Technique for the Measurement of Vapor-Phase Alkali in Products of Combustion Gases, DOE/METC/84-30, (1984).

Weise, W. L.; Smith M. W.; Miles, B. M., ***Natl. Stand. Ref. Data Ser.*** (U.S. Natl. Bur. Stand.), NSRDS-NBS 22 (1969).

ON-LINE COMPOSITIONAL DETECTION TECHNIQUES

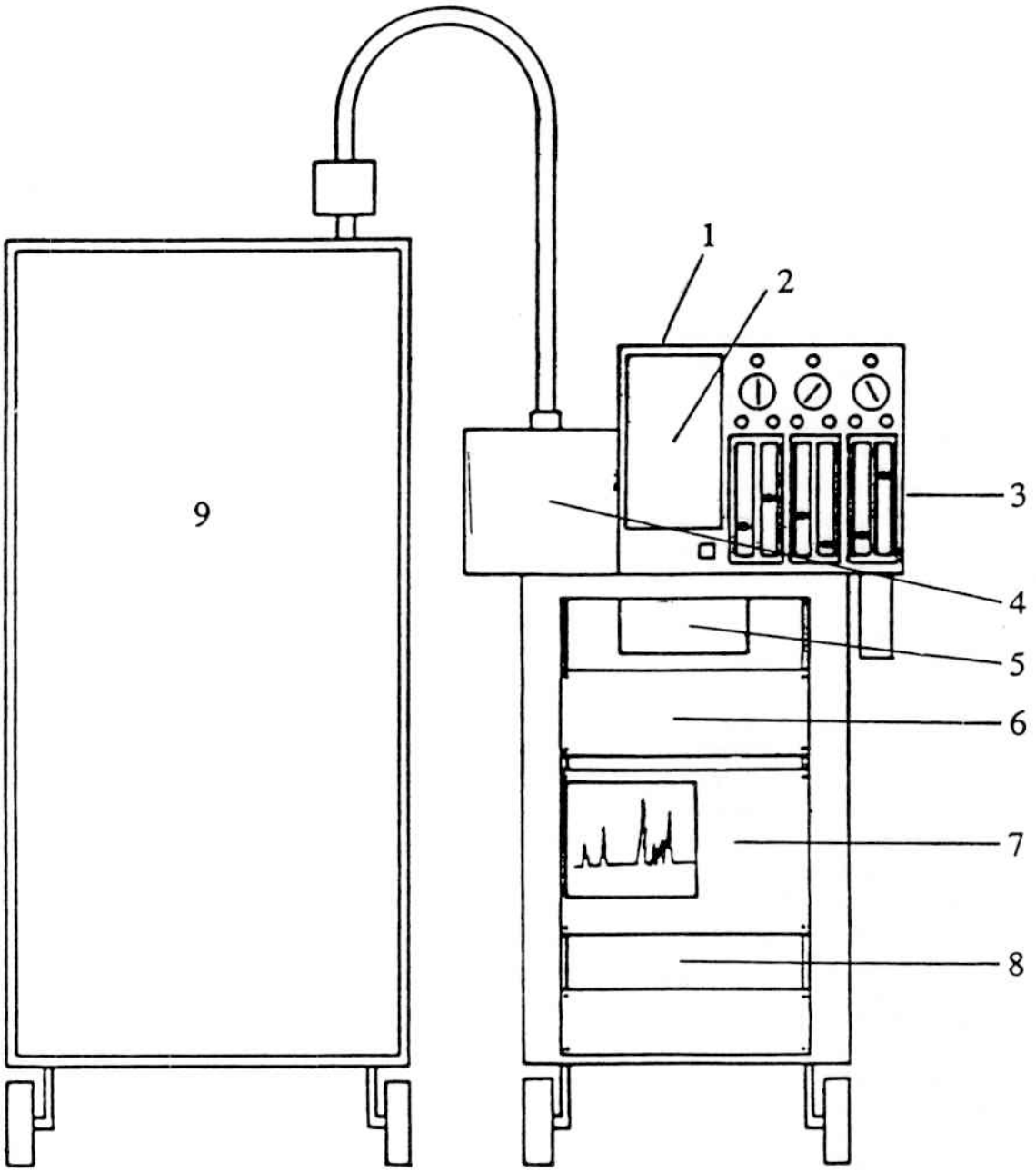
William P. Chisholm
Morgantown Energy Technology Center

Unique on-line compositional instrumentation is being developed at the Morgantown Energy Technology Center (METC) for the enhanced chemical analysis of high-temperature/high-pressure, fossil-energy-derived process streams. The instrumentation being developed is based on the application of spectroscopy for the analysis of process stream components. Overall, the advanced instrumentation being developed for on-line process stream analysis will have advantages over conventional off-line instrumentation in its abilities to deliver real-time data and to make measurements at or near process stream conditions. This tends to eliminate artifact and contaminant problems typically encountered during off-line chemical analysis. Also, *in situ* analysis is possible using some of the instrumentation being developed, which affords the scientist and engineer the opportunity to assess reaction mechanisms within the process pipe. The components which are currently being researched for their applicability for analysis using advanced instrumentation include major, minor and trace elements (in vapor, aerosol and solid phases) and certain nitrogen gas species (ammonia [NH_3] and nitrous oxide [N_2O]). Specific reasons for the development of instrumentation to be used in the analysis of process streams and their by-products include environmental assessment, protection of downstream components and determination of the performance of contaminant removal devices. A description of the instrumentation currently being developed follows.

- **Inductively Coupled Plasma Spectrometer (ICP):**

An ICP is being enhanced to extractively analyze a slipstream of coal-derived process gases for elemental (percentage, minor and trace) constituents. The unit was designed with the capability to analyze both gas phase and particles in a process stream. The primary application of this ICP is to investigate the performance of a variety of hot gas cleanup devices. By ascertaining the elemental concentrations at a variety of sampling locations, information can be obtained on cleanup device efficiency, mass balances, injected sorbent removal efficiencies, and trace elemental distributions. The principle of operation for this instrument is that a high-temperature, radio-frequency-induced plasma (utilizing argon and helium as plasma gases) thermally excites elements contained in the process slipstream. These elements subsequently release this excess energy at wavelength(s) characteristic of each particular element. The wavelengths are monitored using a monochromator. Theoretically, all elements can be analyzed using this ICP; however, the sensitivity/selectivity of the ICP for the analysis of many elements has yet to be determined. A process stream ICP has been designed, constructed and tested in the laboratory, as well as field tested on METC's bench-scale pressurized combustor. Figure 1 is a pictorial diagram outlining the major components of the ICP. Most of the development work has centered on selection of plasma gases and the redesign of the plasma torch to allow for ICP operation under high gas sample flow conditions (without plasma quenching). In order to ensure the integrity of the extracted sample, a high-temperature torch, capable of sustained operation at temperatures above 900 K, was designed and successfully tested. The mixed-gas operation combined with the high-temperature torch makes this a unique system. Recently, the size of the ICP

On-Line Inductively Coupled Plasma Spectrometer



1. HR320 Monochromator (Behind Torch Box)
2. Plasma Torch Access Door
3. Gas Flow Rotameters
4. Matching Network
5. MKS Mass Flow Controllers
6. RF Power Supply Control
7. EG&G Optical Multichannel Analyzer
8. Matching Network Power Supply
9. Henry Radio RF Generator

Figure 1

torch box/monochromator assembly has been reduced in size by 75 percent, and the entire system is now modular in order to facilitate on-line applications. Additionally, a lower flow torch is undergoing initial testing with promising results that could lower gas consumption by a factor of four.

Very recent/future ICP research will primarily be focussed in the following areas: (1) determining the effects of particle size versus emission intensity. This is important from the standpoint of determining the upper particle size that the plasma can totally decompose and excite; (2) providing real-time data acquisition. Several alternatives are being examined to build a low cost simple optical system that allows the user maximum flexibility in terms of choosing and changing the elements to be analyzed; (3) redesigning the torch to allow for low gas consumption. Alternative torch designs are being evaluated to lower the helium and argon gas flows for long-term economical operation; (4) providing on-line testing of the ICP. The ICP unit will be tested both on in-house units such as the fluid-bed gasifier and its hot gas cleanup system, and off-site at facilities such as the Texaco Gasifier, and (5) conducting calibration experiments. Calibration using laboratory combustors and spinning spouter reactors will be conducted to ascertain sensitivities and dynamic ranges for an array of elements.

• **Laser-Induced Breakdown Spectroscopy (LIBS):**
LIBS uses a very intense, short pulse of laser light focused through an optical access port into the process stream where a spark is formed. Thus, this technique analyzes a process stream *in situ*. Temperatures in the spark reach approximately 30,000 K, and all molecules in the spark are broken down into their constituent atoms. The light emitted from the spark is collected and analyzed to characterize the atomic composition. This LIBS system is unique in that only a single optical port is used. This single port provides both input for the laser beam and output for the emission data. METC has an operating LIBS system in the laboratory. Figure 2 shows a diagram of the LIBS apparatus and how it would be configured for measurements in a process stream. LIBS can be used to measure the atomic constituents of gases and particles, but recent laboratory work has indicated that its greatest utility may be in the *in situ* analysis of deposits on interior surfaces (e.g., turbine blades and filter surface). LIBS research work has concentrated on the development and evaluation of various calibration systems including acoustical wave generation and emission line ratioing. Current activities involve the application of LIBS for the analysis of elements in deposit samples formed by METC's Combustion Deposition Entrained Reactor (CDER). LIBS work will be concentrated on developing a calibration system, and on understanding the spark versus emission intensity. The calibration work will focus on using ion/ion ratios and atom/ion ratios or novel approaches such as absolute calibration. An effort will be made to improve, automate, and downsize the data collection system. Additionally, the LIBS will be evaluated to determine its potential use as a system capable of analyzing *in situ* materials deposited (especially sulfur) in high temperature reactor systems.

• **Infrared (IR) Gas Analyzers:**
Certain nitrogenous gas species in a gasification process stream, such as NH_3, are difficult to accurately measure using conventional methods of analysis (e.g., gas chromatography/mass spectrometry) due to the imprecision and artifact generation associated with these methods. NH_3 is an important species to analyze/control since it is both an environmental pollutant and a

In-Situ Laser Induced Breakdown Spectroscopy of Process Streams

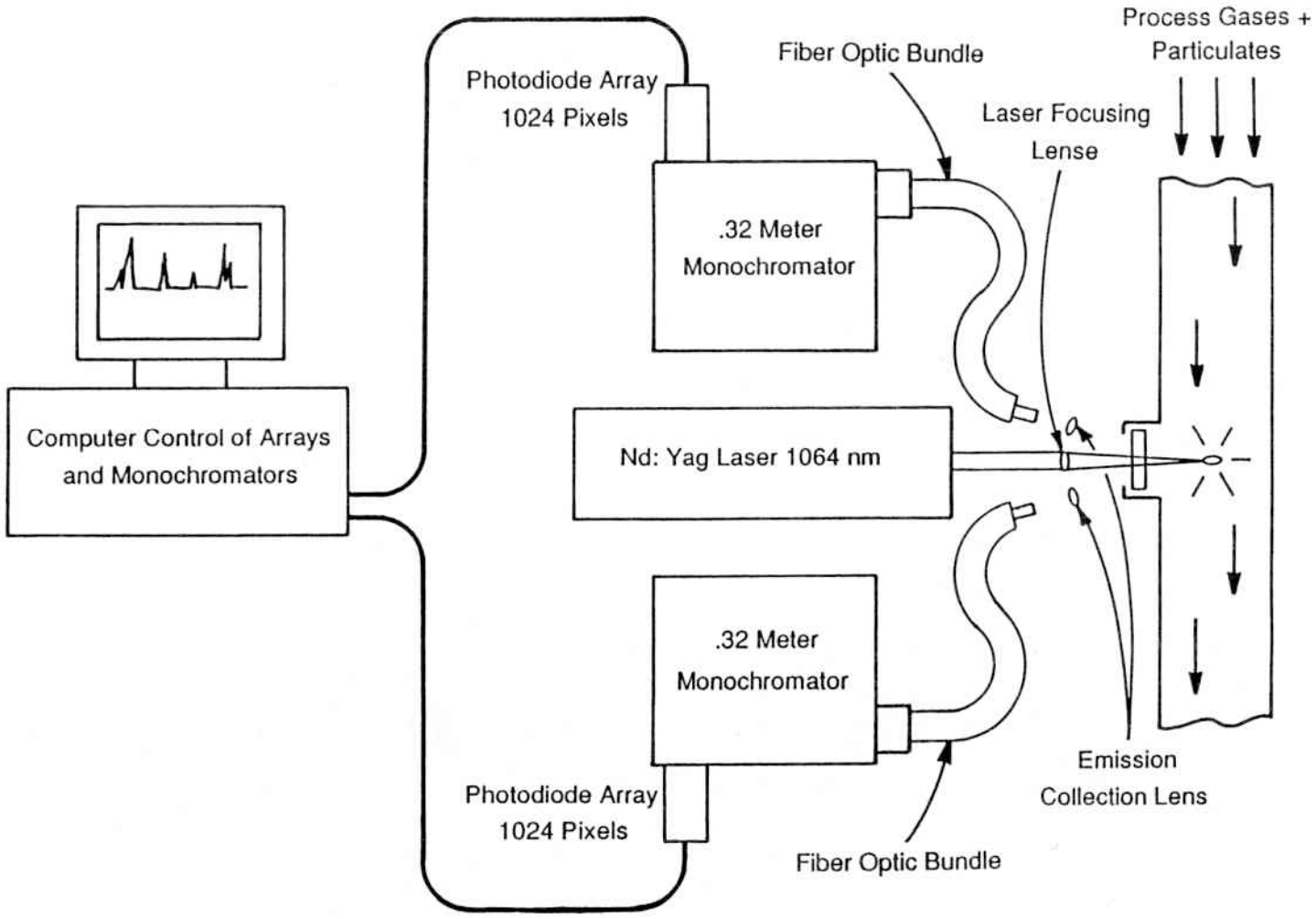


Figure 2

prominent precursor in formation of nitric oxides (NOx). Similarly, N_2O, an environmental pollutant more commonly found in low-temperature combustion processes, is also difficult to analyze due to artifact generation. METC is developing *in situ* methods for the analysis of these species by exploiting their infrared (IR)-active nature. The principle of operation is that an intense light source corresponding to specific IR wavelengths of maximal absorption for NH_3 and N_2O and low interferences from other gas species (such as water, carbon dioxide, carbon monoxide and sulfur dioxide) can be determined and that the degree of light absorption is proportional to concentration (See Figure 3). Recently, a sequence band tunable CO_2 laser was configured for absorption measurements. A detection scheme was developed using a gold-coated chopper to simultaneously modulate and split the continuous wave laser beam into reference and sample beams. These beams were in turn detected by pyroelectric detectors, which yielded the best response. Initial CO_2 laser absorption spectra on ambient pressure, room temperature NH_3 mixtures indicated that strong absorption could be detected on selected laser lines. However, operation at higher pressures brought on pressure broadening, resulting in absorption at many of the CO_2 laser emission lines. The CO_2 laser emission consists of a series of discrete emission lines, which were spaced 1-2 cm^{-1} apart. Such a noncontinuously tunable source of excitation made it difficult to evaluate the effects of pressure broadening, elevated temperatures, or spectral interference from added gases. Absorption work was subsequently carried out on an IR spectrometer. Currently, the appropriate IR wavelengths for analysis are being determined, and the effects of pressure broadening and temperature on laboratory measurements are being assessed. These scoping experiments are being conducted using a spectrometer in conjunction with a high-temperature/high-pressure absorption cell. In addition, a materials evaluation of the optical access windows has been performed. The windows must be "transparent" at the proper IR wavelengths, withstand high-temperature/high-pressure and be resistant to chemical reaction. Diamond is the window material of choice. The measurement of NH_3 at 570°F and 300 psig ahowed that NH_3 absorption bands reside in a "window" relatively free of strong absorption by interfering species. A weakly-absorbing peak also exists for N_2O. Completion of IR surveys should indicate the feasability of using IR absorption methods to monitor various gas species (NH_3, N_2O, NOx) at process stream conditions, either *in situ* or extractively. If a conventional Fourier Transform spectrometer cannot be effectively used to monitor these species, work will then focus on developing alternate schemes to detect those gases. Diode lasers, tunable over narrow ranges of wavelength which overlap absorption bands of individual gas species, are currently available and could potentially be used as an IR source for on-line applications. Initial focus will be placed on developing the technique for detection of N_2O, with other species to follow depending on the success of the technique. Such a device could then be applied to reactors on site to take measurements of concentrations of NOx species and precursors.

Preliminary studies indicate that NH_3 may be detectable at levels as low as 100 ppm at temperatures and pressures near 600°C and 18 atmospheres. These limitations are due to collisional broadening and spectral interferences. N_2O is spectrally available near 2550 wavenumbers, but the inherent weakness of this absorption dictates that it could only be exploited with a very intense source, i.e., a diode laser. Future work will include installing diamond windows in the sample cell to allow work at higher temperatures and pressures. A tunable diode laser will be acquired to exploit the weak N_2O absorption

On-Line Ammonia Monitor

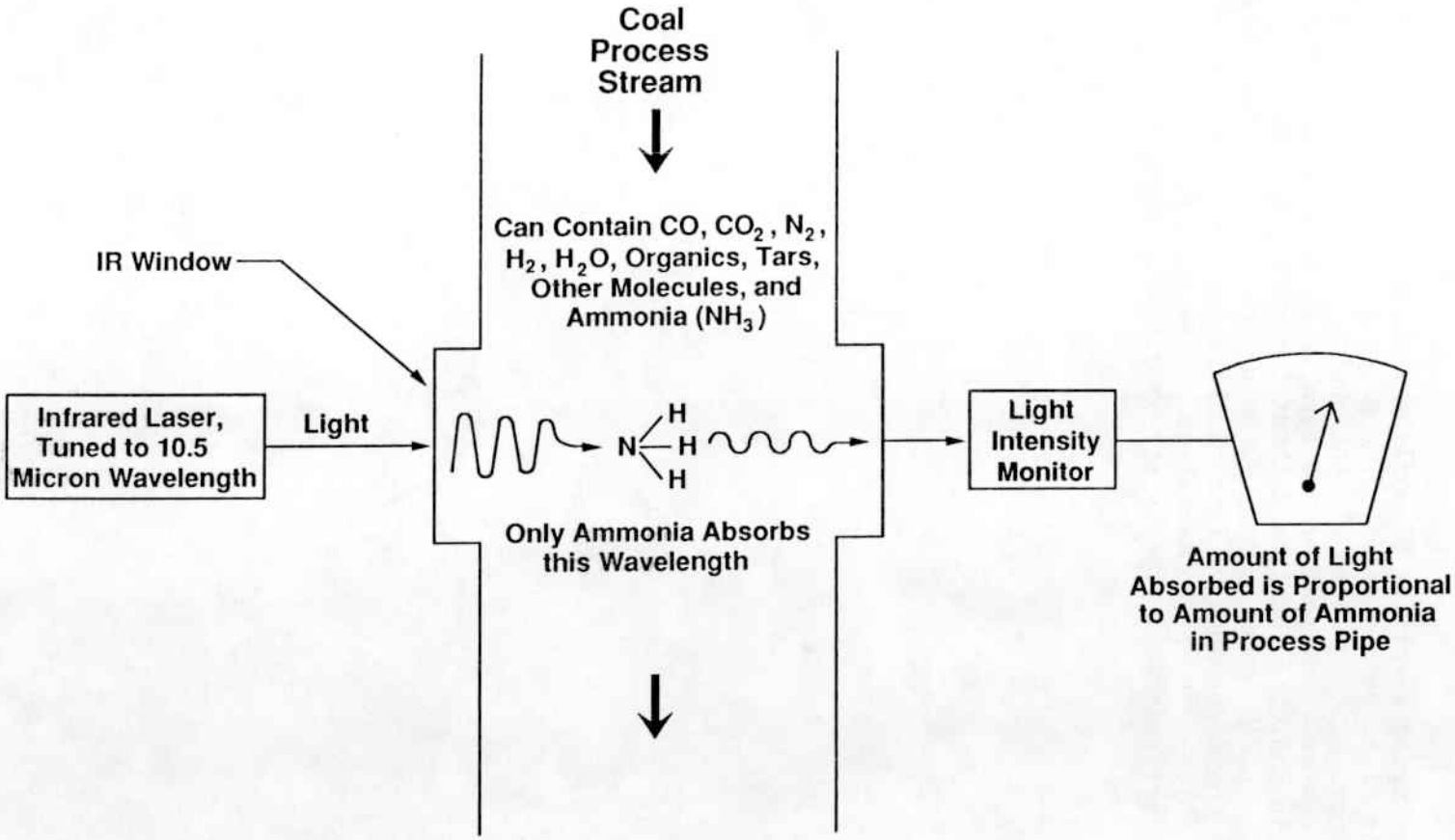


Figure 3

lines mention above. The spectrometer sample gas handling system will be enhanced to allow studies using more complex and realistic gas mixtures.

Summary:
METC is developing a variety of on-line instrumentation/monitors to be used in the analysis of process streams. The process stream components being measured include (major, minor, trace) elements which are entrained/contained in the process stream or slipstream or are associated with interior surfaces as deposits. In addition, on-line methods for analyzing nitrogen-containing gases (NH_3 in gasification streams; N_2O in combustion streams) are being developed. The major applications of these instruments are to measure components which have environmental or process operation significance and to assess the performance of process stream clean-up devices.

IN SITU REAL-TIME ANALYSIS OF PARTICULATES

1. FTPA NUMBER: 1260.000

CONTRACTOR: Sandia National Laboratories
Livermore, CA 94551-0969

PROGRAM MANAGER: Donald R. Hardesty (415) 294-2321

PRINCIPAL INVESTIGATOR: David K. Ottesen (415) 294-3687

DOE PROJECT MANAGER: Curtis Nakaishi

CONTRACT PERIOD OF PERFORMANCE: October 1, 1988 - Continuing

2. SCHEDULE/MILESTONES

1988 Program Schedule

	O	N	D	J	F	M	A	M	J	J	A	S
Laboratory Modifications	-------											
Spectral Window Identification	----------											
Particle Species Analysis	----------											
Theoretical Code Development	----------											

3. OBJECTIVES

The development of new optical methods for the in situ, real-time analysis of particulates and surfaces in combustion environments offers a major advance over current analytical techniques. Present hardware involves bulky, water-cooled quench probes inserted in the sample stream, and subsequent post-process analyses. In situ measurements will help resolve questions regarding the composition of fuel particles, soot, mineral matter fumes, and condensing particulates in the high temperature environment. The combined measurement of composition, size and velocity for individual particles will permit the calculation of compositional mass flux in particulate-laden flows. Such real-time measurements could also be extremely valuable for monitoring and process control.

4. BACKGROUND STATEMENT

Laser-based diagnostic techniques are being developed at Sandia for the study of particulates in combustion environments during real time. A technique using a high energy pulsed laser (laser spark spectroscopy) has been employed to measure the elemental composition of individual particles [Ottesen, et al., 1989] while a two-color light scattering measurement [Wang and Hencken, 1986] was developed to extract size and velocity information for single particles.

These techniques have been demonstrated at combustion temperatures, and in the collection of both light scattering data and subsequent laser-induced emission spectra from the same, individual particle. The laser spark method is particularly sensitive to the metallic elements, and promises to be useful in the determination of particle-to-particle variations of composition, and in the study of mineral matter transformations during combustion.

5. PROJECT DESCRIPTION

Our particle sizing and laser spark spectroscopy systems have been combined in order to determine the size, velocity and elemental composition of particulates in a combustion environment. The particle sizing system uses colinear beams from He-Ne and Ar ion lasers to generate scattered light signals from particles in a flow (described in detail in [Wang and Hencken, 1986]). Data reduction is based on calibrations using particles of known size and precision pinholes, and produces values of size and velocity for single particles.

Particle composition is determined in situ by using a high power Q-switched Nd:YAG laser to rapidly heat a particle producing a "laser spark" (see [Ottesen, et al., 1989] for experimental layout). The frequency doubled line at 532 nm wavelength is used to form a plasma on a coal particle with an incident energy of 100 mJ/pulse. Emission from this plasma is observed with a 0.5-m Spex monochromator with an intensified diode array detector.

Particles are entrained in a nitrogen flow along the center line of a laboratory flat-flame burner. A methane/oxygen/nitrogen flame is used to produce a hot combustion environment, and the assembly can be translated vertically allowing the optical systems to view individual particles at distances of 5 to 75 mm above the burner surface.

For times less than 1 μsec following the laser irradiation of the particle, the spectrum is very complex [Ottesen, et al., 1989]. This is due to the presence of strong continuum emission and highly ionized atomic species [Schmieder, 1983; Radziemski, et al., 1983]. At longer times the plasma cools so that the spectrum is dominated by emission from neutral and singly ionized species.

A dedicated minicomputer is used to control the timing of the several laser systems, to collect the scattering and spectral data and store it in memory, and to analyze the resulting data for particle size, velocity, and spectral emittance. This can be done on a particle-by-particle basis in near real-time, or on an ensemble of particle data in a post-processing mode.

6. TECHNICAL PROGRESS

Major technical progress during FY-1989 was made in the study of a several well-characterized reference coals representing a wide range of mineral matter content and composition, coal rank, and geographical origin. Our

primary goal this year was the calibration of the spark emission spectroscopic technique for quantitative analysis using reference materials. Additional improvements and refinements were also made to our analytical computer code.

The coals investigated were (1) New Mexico Blue #1, (2) Pittsburgh #8, (3) Illinois #6, and (4) Hiawatha. The samples were obtained from the Pennsylvania State University Coal Bank and were size-classified fractions of 106-125 μm mean diameter in order to minimize the effect of sample size on the resulting data. Particles were entrained in dry nitrogen using a motor driven syringe-type feeder, and several hundered laser spark emission spectra were obtained for each coal at room temperature.

An illustration of the number of species detected in laser spark spectroscopy of coal particles and their variability is given in Fig. 1. Both curves are for single particles of the Illinois #6 coal. The solid curve is a typical spark emission spectrum which is dominated by the neutral carbon transition near 248 nm, although detectable amounts of Mg, Ca, Al, Si, Fe and Ti are also observed.

The dashed curve in Fig. 1 is for another single particle of the Illinois #6 coal containing a large amount of iron. The bulk chemical analysis of this coal indicated a rather large average iron content (3.2 wt %), and this can be easily seen in the figure. A very large number of lines are observed for both neutral and singly ionized iron which can obscure a number of other important transitions (including the C I line near 248 nm!). This made it necessary to alter our analytical computer code in order to quantitatively treat these spectral interferences.

Quantitative elemental analysis of a plasma emission spectrum is straight forward only in those cases in which the condition of a local thermal equilibrium (LTE) holds. Previous workers [Radziemski, et al., 1983] using plasma excitation conditions very similar to ours have shown the LTE is obtained approximately one microsecond following plasma formation.

If this is the case, an effective temperature may be conveniently calculated for the plasma by comparing the relative intensities of two lines for a given species. Transitions of Mg II/Mg I and Fe II/Fe I at 280, 285, 260 and 302 nm wavelength

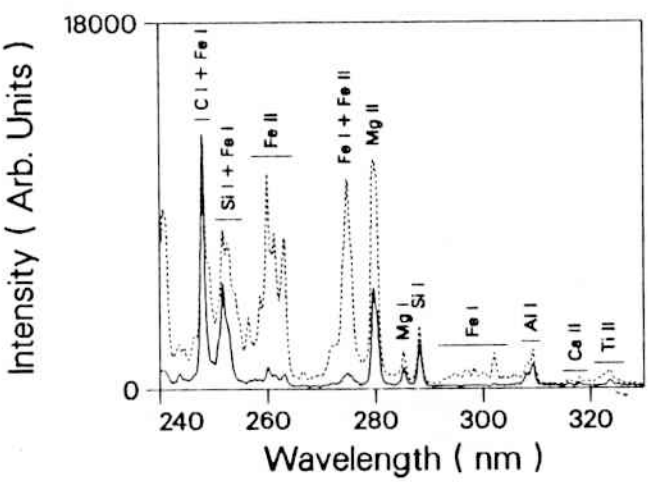


Figure 1. Laser spark spectra of two single Illinois #6 (PSOC-1493) coal particles illustrating variation in particle-to-particle composition (solid line - particle with low iron content; dashed line - particle with high iron content).

were used to calculate two plasma temperatures for each shot. Averages for over 500 particles for each coal are given in Table 1.

Table 1

Average Plasma Temperatures

PSOC #	Seam Name	T_{Fe} (K)	T_{Mg} (K)	(T_{Fe} / T_{Mg})
1445	New Mexico Blue #1	9,179 ± 683	9,842 ± 579	0.932 ± 0.051
1451	Pittsburgh #8	9,234 ± 776	10,055 ± 679	0.920 ± 0.068
1493	Illinois #6	9,129 ± 734	9,723 ± 595	0.940 ± 0.062
1502	Hiawatha	9,142 ± 758	9,956 ± 666	0.921 ± 0.075

Extremely reproducible plasma temperatures were obtained for the various coal types. Since our particles were of similar size, the temperature of the laser-induced plasma was expected to depend primarily on the incident laser energy, and this was very carefully adjusted to 100 mJ/pulse before each experimental run.

There is a noticeable difference between the two calculated temperatures. In all cases the Mg temperature is higher than the Fe temperature by about 7%. Although this is within the standard deviation of each temperature, its consistency suggests that the difference is real and systematic.

A possible explanation of the difference in calculated plasma temperatures is that the image of the laser spark on the monochromator entrance slit is not limited to an isothermal region of the plasma. Thus different regions of the plasma may dominate the emission spectrum for different elemental species.

After the corrected, integrated intensities for the several elemental emission lines were obtained along with an average plasma temperature, a fractional elemental composition was calculated for each particle, and an average value was calculated for each coal to compare with results from bulk chemical analyses. The fractional elemental concentrations were plotted against one another on a particle-by-particle basis. This would be expected to demonstrate the correlation (or lack thereof) of one element with another, and the amount of variation within such correlations for various coals.

As an example, consider the plot of Si vs. Al concentrations for the four coals in Figure 2. A linear correlation exists between these two species for the Pittsburgh #8 (plot a) and Illinois #6 coals (plot c). This might be expected due to the presence of both silicon and aluminum in clay-type minerals in these coals. The nearly identical slopes for the two plots indicates a similar Si/Al ratio for the two coals which agrees with the bulk analysis.

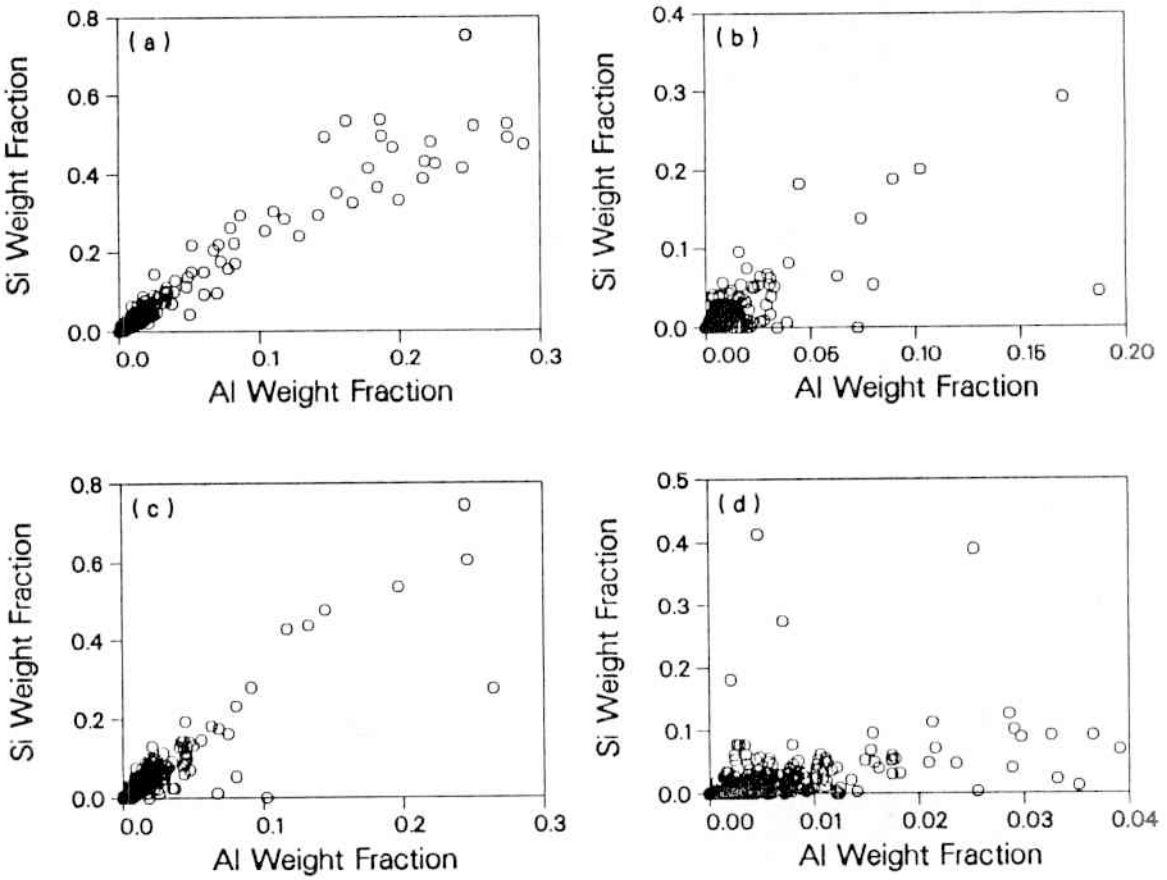


Figure 2. Si vs. Al concentrations in wt % for four coals on a particle-by-particle basis: (a) Pittsburgh #8, (b) Blue #1, (c) Illinois #6, (d) Hiawatha.

In considerable contrast, the points for the New Mexico Blue #1 (plot b) and Hiawatha (plot d) coals are quite scattered. This could arise from (1) differences in the Si/Al ratio for different clays which will vary from particle to particle, and (2) the presence of quartz-type minerals which will contribute to the observed silicon intensity in a fashion which is not correlated with the aluminum content.

Another variable which must be considered in interpreting our data is the way in which the various mineral constituents are distributed throughout a coal particle. Since the laser spark spectroscopy technique does not vaporize the entire particle during plasma formation, it is possible that inhomogeneities in elemental distribution might be reflected as increased scatter in our data.

For example, the Illinois #6 coal has been extensively studied at Sandia using SEM, and it has been determined that silicon is present in substantial amounts as both clay and quartz minerals. The fact that the plot of Si vs. Al content in Figure 2 for this coal is highly linear with relatively little scatter would seem to indicate that the two silicon-

containing minerals are evenly dispersed throughout the material which is vaporized during the laser pulse. This is in agreement with the SEM data which shows the quartz mineral grains to be particularly fine and evenly distributed throughout the organic matrix.

Magnesium is another element contained in clay minerals, often as a substituent for aluminum. Thus a plot of Si vs. Mg might also be expected to show correlations for the four coals similar to the Si vs. Al plots. These are shown in Figure 3. A good linear correlation does exist for the Pittsburgh #8 coal (plot a), although with some scatter in the points. This is less obvious for the Illinois #6 coal (plot c), although the points seem to be highly clustered about a straight line near the origin.

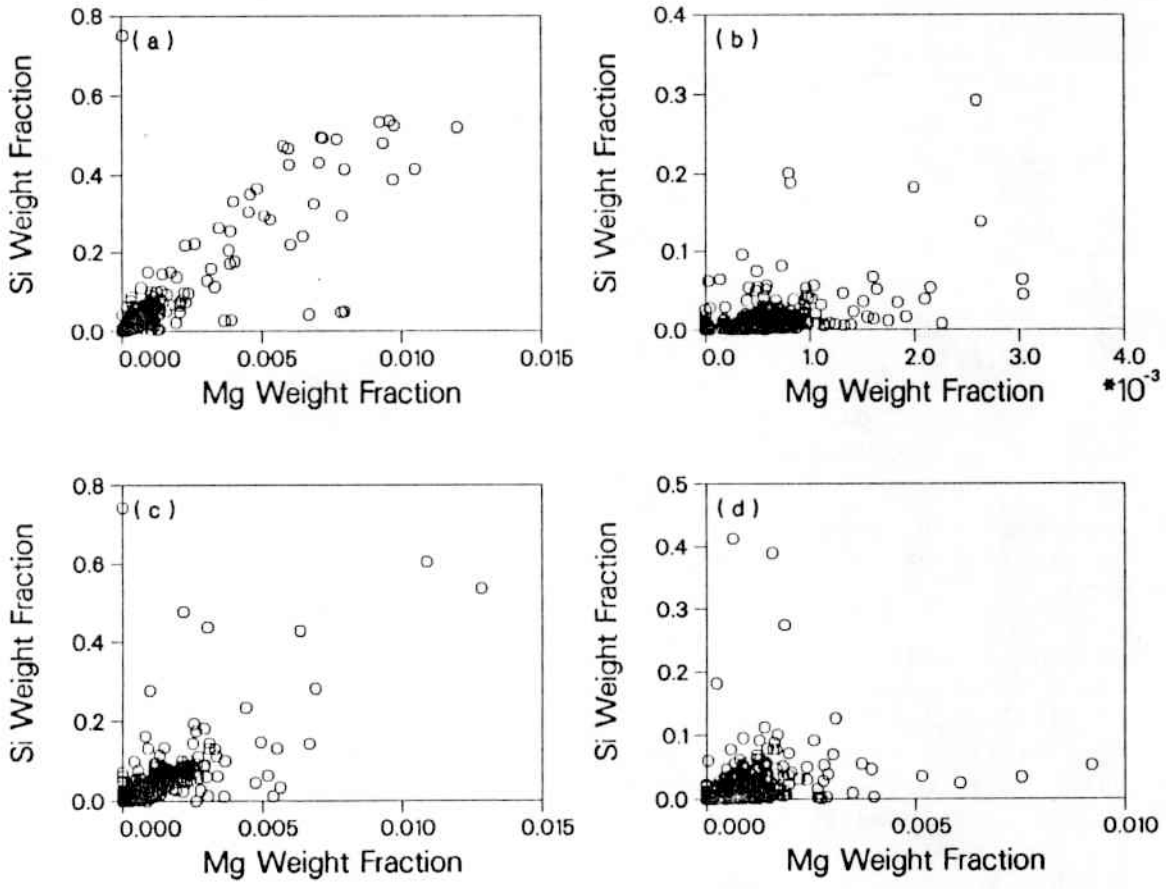


Figure 3. Si vs. Mg concentrations in wt % for four coals on a particle-by-particle basis: (a) Pittsburgh #8, (b) Blue #1, (c) Illinois #6, (d) Hiawatha.

Results for the two western coals are similar to the data for Si and Al. The considerable scatter of the points indicates a highly variable composition of the material vaporized. As a matter of fact, the data for the Hiawatha coal (plot d) suggest an anti-correlation in which particles containing a substantial amount of Mg are low in Si, and vice-versa.

This behavior is also seen in a plot of Fe vs. Si for the Illinois #6 coal as shown in Figure 4, plot c. The majority of the particles are seen to contain random small amounts of iron and silicon in the large cluster of points near the origin. In contrast, particles containing large amounts of these elements lie near their respective axis and suggest that the material vaporized from those particles was dominated by large inclusions of either Si- or Fe-containing minerals.

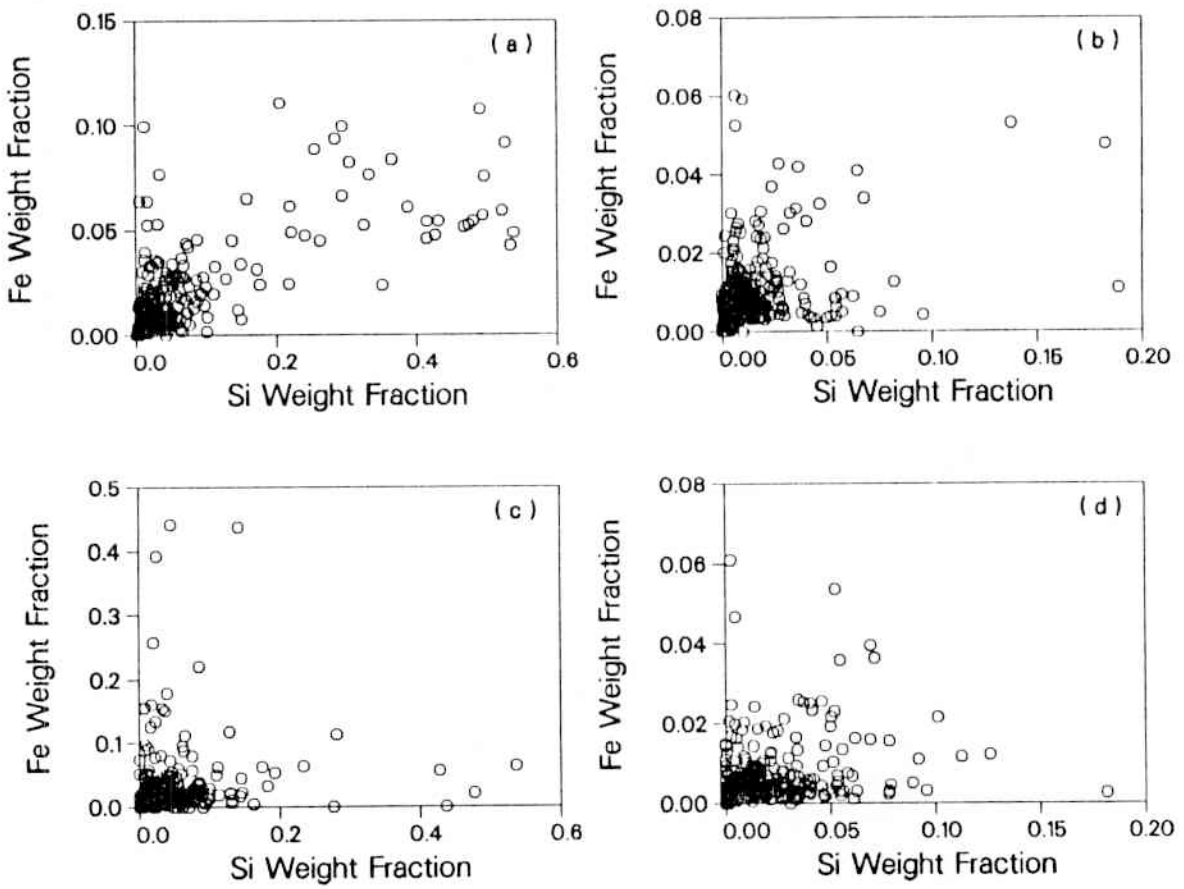


Figure 4. Fe vs. Si concentrations in wt % for four coals on a particle-by-particle basis: (a) Pittsburgh #8, (b) Blue #1, (c) Illinois #6, (d) Hiawatha.

Data for the Pittsburgh #8 coal (plot a) in Figure 4 are highly scattered and show a much more thorough mixing of Si and Fe species. Plots for the New Mexico Blue #1 and Hiawatha (plots b and d) also show a random distribution of these two elements.

Weighted averages of these particle-by-particle composition results have been computed and are compared to average bulk chemical analyses of these four coals in Table 2. It was necessary to divide the integrated intensity for each element by a sensitivity factor to account for matrix effects which caused the more volatile elements to be preferentially vaporized during plasma formation. These sensitivity factors were determined by

fitting our weighted average composition to values from bulk chemical analyses. In this sense, these coals have served as reference standards to calibrate the laser spark emission spectroscopy technique for quantitative analysis. The values of sensitivity factors giving the best fit of our experimental data are also given in Table 2 in the column "S Factor."

Table 2

Average Elemental Composition Analysis*

Element	N.M. Blue	Pittsburgh #8	Illinois #6	Hiawatha	S Factor
Si	1.20 / 1.07	5.80 / 4.18	3.60 / 3.70	1.66 / 2.44	0.98
Al	0.92 / 0.59	1.84 / 2.13	1.43 / 1.61	0.50 / 0.59	5.25
Fe	0.85 / 0.33	1.15 / 1.15	2.13 / 3.22	0.68 / 0.45	0.15
Mg	0.06 / 0.04	0.09 / 0.09	0.09 / 0.11	0.59 / 0.14	13.60
Ca	0.79 / 0.21	0.69 / 0.35	2.45 / 1.02	4.50 / 1.32	34.50
Ti	0.07 / 0.03	0.08 / 0.11	0.06 / 0.09	0.07 / 0.05	0.47

*Values given in the following format: Laser spark analysis / Bulk analysis, both given as weight %.

Several observations with regard to this analysis are in order. The bulk chemical analyses were performed on unsized lots of the raw coal, while our laser spark emission measurements were made on size-classified particles. The process of size classifciation is known to alter the average elemental composition of the coal, and this could be expected to cause some disagreement between the two results in the absence of other errors.

Some of our laser spark values tend to be too small for certain prominent elements in a given sample. The best example of this is in the iron analysis for the Illinois #6 coal which shows an underestimation of iron at high concentrations, and an overestimation of iron at low concentrations by the laser spark method. These results are probably caused by increasing amounts of self-absorption in the resonance emission lines for particles containing large iron-bearing mineral inclusions. Such saturation effects can be accounted for by the use of non-linear calibration curves.

A major difficulty in the analysis of a species by emission spectroscopy is seen in the case of calcium. The results in Table 2 are obviously in major disagreement with the bulk results and seem to stem from the fact that calcium is contained in coal particles in two forms. The first form is quite evenly distributed at a low concentration and is presumably associated with the organic matrix. The second form appears infrequently with very large emission intensities, and is probably due to limestone inclusions.

Treatment of the calcium emission lines from these two distinct cases in the same linear fashion leads to the total domination of the results by those few particles containing limestone. Obviously the observed integrated intensity for the Ca resonance transition used in our analyses is quite non-linear with concentration, and there are no cases with particles containing calcium at levels between these two extremes which could be used to calibrate the technique. Other weaker transitions are being investigated which may prove to have a more linear relation between integrated intensity and concentration.

Results for Si, Al, Mg, and Ti seem to be in relatively good agreement with the bulk analyses. Additional analyses of other well-characterized coals should serve to reveal any saturation trends, as in the case of iron. Some of the disagreement in results from the two methods may also be due to the use of bulk analyses for the whole coal as mentioned above. Results are currently being obtained for individual size fractions and will be compared to our laser spark data. Finally, there is no guarantee that concentrations from ICP analyses are totally accurate given the problems inherent in the process of chemical extraction preceding spectrochemical analysis.

7. FUTURE WORK

Future research directions are: (1) Extensive observation of laser spark emission spectra of particles in high temperature environments to study changes in composition as a function of combustion variables; (2) application of laser spark spectroscopy as a surface analytical technique for deposit formation: (a) study of model inorganic compounds at ambient temperature; (b) study of prepared surface deposits at ambient temperature; (c) depth profiling of surface deposit layers by repeated laser-induced plasma formation; and (d) study of model compounds and surface deposits at elevated temperatures.

8. REFERENCES

Ottesen, D. K., Wang, J. C. F., and Radziemski, L. J. 1989. "Real-Time Laser Spark Spectroscopy of Particulates in Combustion Environments," Appld. Spectrosc. **43**(6), 967.

Radziemski, L. J., Loree, T. R., Cremers, D. A., and Hoffman, N. M. 1983. "Time-Resolved Laser-Induced Breakdown Spectrometry of Aerosol," Anal. Chem. **55**, 1246.

Schmieder, R. W. 1983. "Techniques and Applications of Laser Spark Spectroscopy," Sandia Natl. Laboratories Report, SAND83-8618.

Wang, J. C. F. and Hencken, K. R. 1986. "In Situ Particle Size Measurements Using a Two-Color Laser Scattering Technique," Applied Opt. **25**, 653.

Session 3
Surface Science

Chairperson: Dennis H. Finseth

The lack of detailed understanding of the nature and reactivity of the coal surface is a significant limitation to rationally developing improved, surface sensitive beneficiation methods. In this session, improved methods for analyzing the physical and chemical nature of the coal surface are discussed. Investigation of the contact angle for fine coal powders and spectroscopic studies of surfaces are also included.

FUNDAMENTAL RESEARCH ON SURFACE SCIENCE IN SUPPORT OF PHYSICAL BENEFICIATION OF COAL

CONTRACT NUMBER	DE-AC22-87PC79905
CONTRACTOR	Research Foundation, State University of New York; Dept. of Chemical Engineering, State University of NY at Buffalo, Buffalo, NY 14260
CONTRACTOR PROJECT MANAGER	Prof. Robert J. Good
PRINCIPAL INVESTIGATORS	Prof. Robert J. Good Dr. Douglas V. Keller, Jr.
PETC PROJECT MANAGER	Dr. Dennis Finseth
CONTRACT PERIOD OF PERFORMANCE	Sept. 1, 1987 - Aug. 30, 1990

ABSTRACT

The objectives of this work are to obtain the basic surface chemical data, and to develop the relevant surface chemical theory, that will provide a foundation for the oil agglomeration and froth flotation processes of coal beneficiation.

Milestones of Project

1988-89 Program Schedule

	S	O	N	D	J	F	M	A	M	J	J	A
Acquire microscopes and other equipment	———											
Acquire coal samples	———	———	———	———	———	———	———	———	———	———	———	———
Measure contact angles of decane/water on coal	———	———	———	———	———	———	———	———	———	———	———	———
Measure contact angles of liquids in gas, on coal							———	———	———	———	———	———
Measure adsorption of octanol, etc., on coal	———	———	———	———	———	———	———	———	———	———	———	———
Laboratory scale oil-agglomeration studies	———	———	———	———	———	———	———	———	———	———	———	———
Develop liquid bridge theory	———	———	———	———	———	———	———	———	———	———	———	———
Develop theory of acidic and basic energy components of coal								———	———	———	———	———

3. OBJECTIVES

The objectives of this work are to obtain the basic surface chemical data, and to develop the relevant surface chemical theory, that will provide a foundation for the oil agglomeration and froth flotation processes of coal beneficiation.

4. BACKGROUND

Coal can be rendered nearly ash-free, and free from inorganic sulfur, by the oil agglomeration process and also by froth flotation. We are concentrating our efforts on the former. The basic surface chemical properties that control the two processes are, in a general way, the same.

In oil agglomeration (e.g., the Otisca T process) a coagulum is formed consisting of coal particles held together by liquid bridges of water droplets, in a continuum of oil. See Fig. 1. The water droplets between coal particles are stable; but those between particles of hydrophilic minerals are unstable, and the hydrophilic minerals are rejected from the coagulum. It is believed that iron pyrite, FeS_2, if cleaved, or released (by fracture) from coal, in wet, reducing conditions, is hydrophilic.

High-rank coal is hydrophobic; but with decreasing rank, and increasing oxygen content, coal becomes less hydrophobic; and low-rank coals such as lignite do not respond well to oil agglomeration, because they are hydrophilic. Bituminous coals with high oxygen content may respond poorly to oil agglomeration. But if a surface active additive such as n-octanol is employed, a surface modification occurs, and they apparently become sufficiently hydrophobic that they respond well. The mechanism by which low-rank coal is modified is, no doubt, adsorption; but measurements of the adsorption of higher alcohols on coal have not been made, in the past. The fundamental information about adsorption on coal, needed for selection of optimal additives, has not been available.

The surface-chemical theory of surfaces energy of coal macerals has not been developed. The trend of contact angles with coal rank is not understood. A recently developed theory (Good, 1989; van Oss, 1987; van Oss, 1988) of the hydrogen bonding surface parameters (as Lewis acids and Lewis bases) has not yet been applied to coal surfaces.

The mathematical theory of liquid bridges, as it applies to the oil agglomeration process, has not been worked out. A theory is needed, that would tell what oil-water-solid contact angles will lead to stable, mineral-free agglomerates.

5. PROJECT DESCRIPTION AND RESULTS

We have proceeded, in parallel studies, on several fronts in this investigation. We will report on the following:

- Oil-water-solid contact angles

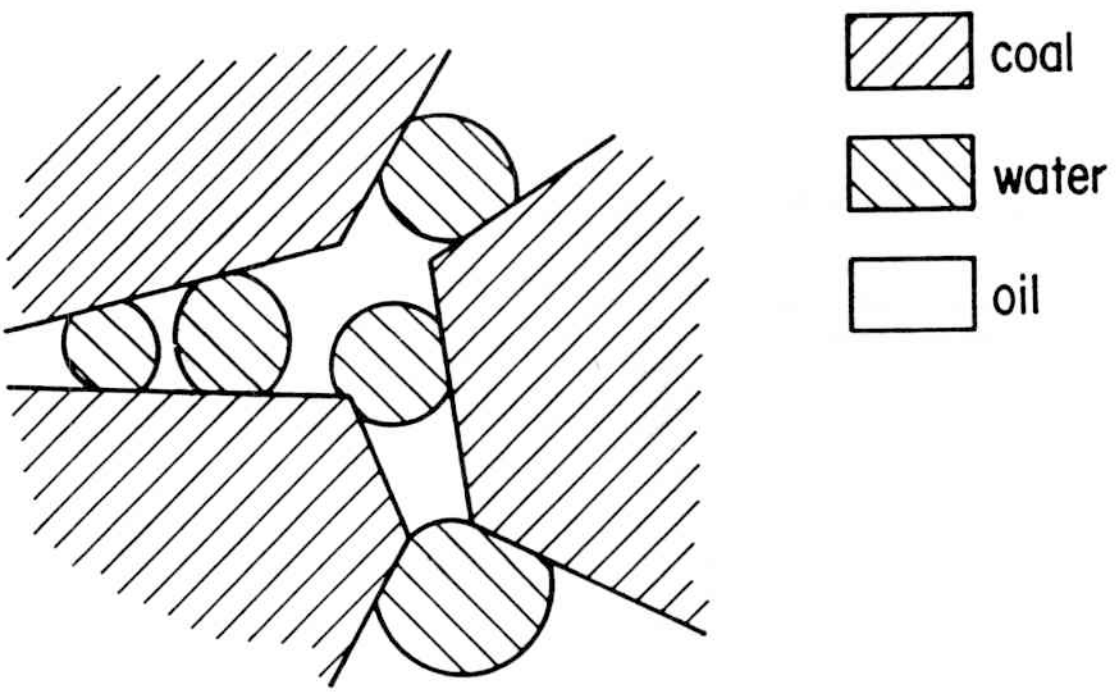


Fig. 1. A possible configuration for three coal particles, with bridges of water drops in oil. This figure is idealized; for example, a constant contact angle is shown, and the drops are all approximately the same size. The configuration of the drops corresponds to a contact angle, as measured through the oil phase, of approximately 50°.

- Contact angles of liquids in gas, on coal, and components of surface energy of coal due to acidic and basic behavior in hydrogen bonding
- Adsorption of alcohols on coal
- Early results in the liquid bridge theory of coal aggregate stability and pyrite rejection.

- Oil-water-solid (OWC) contact angles have been measured on particles of ground coal, using a microscope in an oxygen-free glove box. See Figure 2. The coal had been wet-ground, and stored in sealed containers, under water, until needed for measurement. It was dried, and a small amount was placed in the depression of a hollowed-out microscope slide. A small amount of decane was added, to wet out the coal, and then a droplet of water. Angles were measured either with rotatable crosshairs connected to an external degree scale, or by photographing (or using an advanced optical imaging system) and measuring at leisure.

Figure 3 shows a photograph of a particle of Kentucky #9, a bituminous coal, about 220 μm across, with a decane-water interface intersecting it. The illumination was from above as well as from beneath the stage. The bright areas had, in direct visual observation, the yellow color of iron pyrite. It is clear that two distinct contact angles were formed on the same particle. On the coal area, the angle was about 35°, and on the pyrite area, about 85°.

On various coal particles in the same sample of ground coal, we found contact angles grouped fairly closely (e.g., ± 2°) around three distinct mean values. For Panther Valley (anthracite) coal, these were 38°, 67° and 106°. (These results will be shown graphically, below.) Often, two of the three angles could be observed on the same particle, for grains as small as 50μm diameter. Figure 3 is one example; in another case, typically, angles of 39° at one side of a grain, and 63° on the other side, could be seen.

We interpret the observation of three discrete angles as being due to the presence of three distinct phases in the solid. The highest angle was due to regions of hydrophilic minerals, e.g. FeS_2 or shale or limestone, etc., or highly oxygenated carbon. The intermediate angle was due to regions of aromatic carbons on the surface. The lowest was due to regions of aliphatic or naphthenic carbons. It was not possible to identify the macerals that corresponded to the intermediate and lowest angles. For example, the specimens were not of the kind, or geometry, in which vitrinite reflectance could be determined.

Oil-water-solid contact angles were measured on macroscopic surfaces of coal (about 1 cm across) that had been polished in nitrogen, with a water slurry of fine alumina abrasive. The measurements were made under water, by pressing a drop of oil against the solid surface. This was done in the controlled atmosphere cell of a (modified) Rame-Hart contact angle instrument, which uses a horizontal telemicroscope with rotatable crosshairs to measure the angles. Advancing and retreating angles were measured (Neumann, 1979).

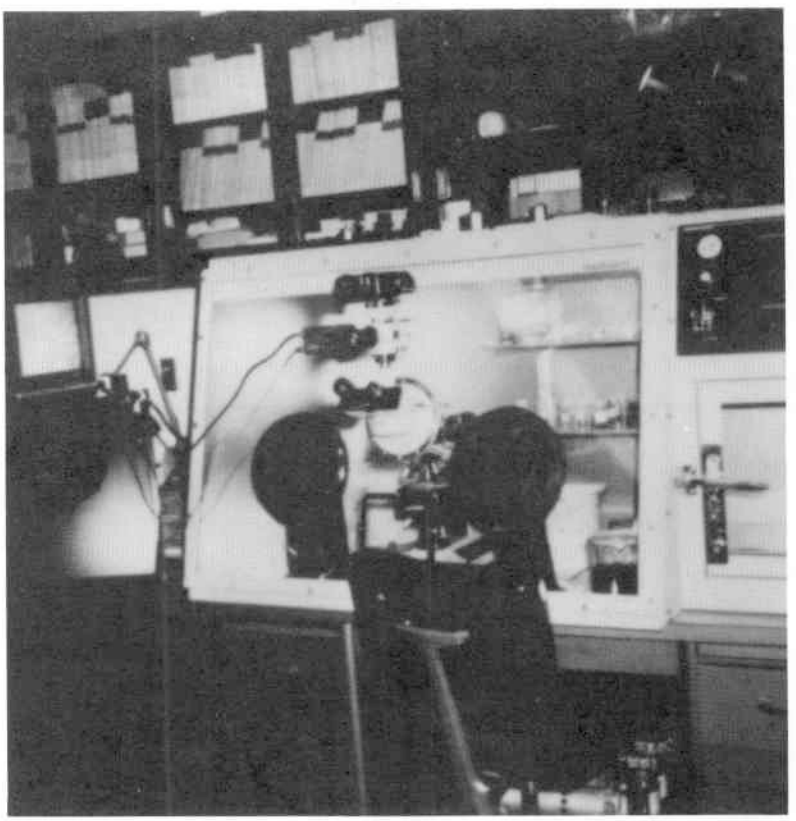


Fig. 2. Experimental system for measuring contact angles on microscopic particles. The experimental system consists of an Olympus BH2 microscope equipped with transmitted and reflected light attachments; Hoffman modulation system; an extended viewer mounted with simultaneous video and 35 mm capability and a goniometer eyepiece. The microscope is housed in a Forma Scientific glove box, so as to carry out measurements on the solids in an inert atmosphere. Contact angles are measured by using the goniometer eyepiece.

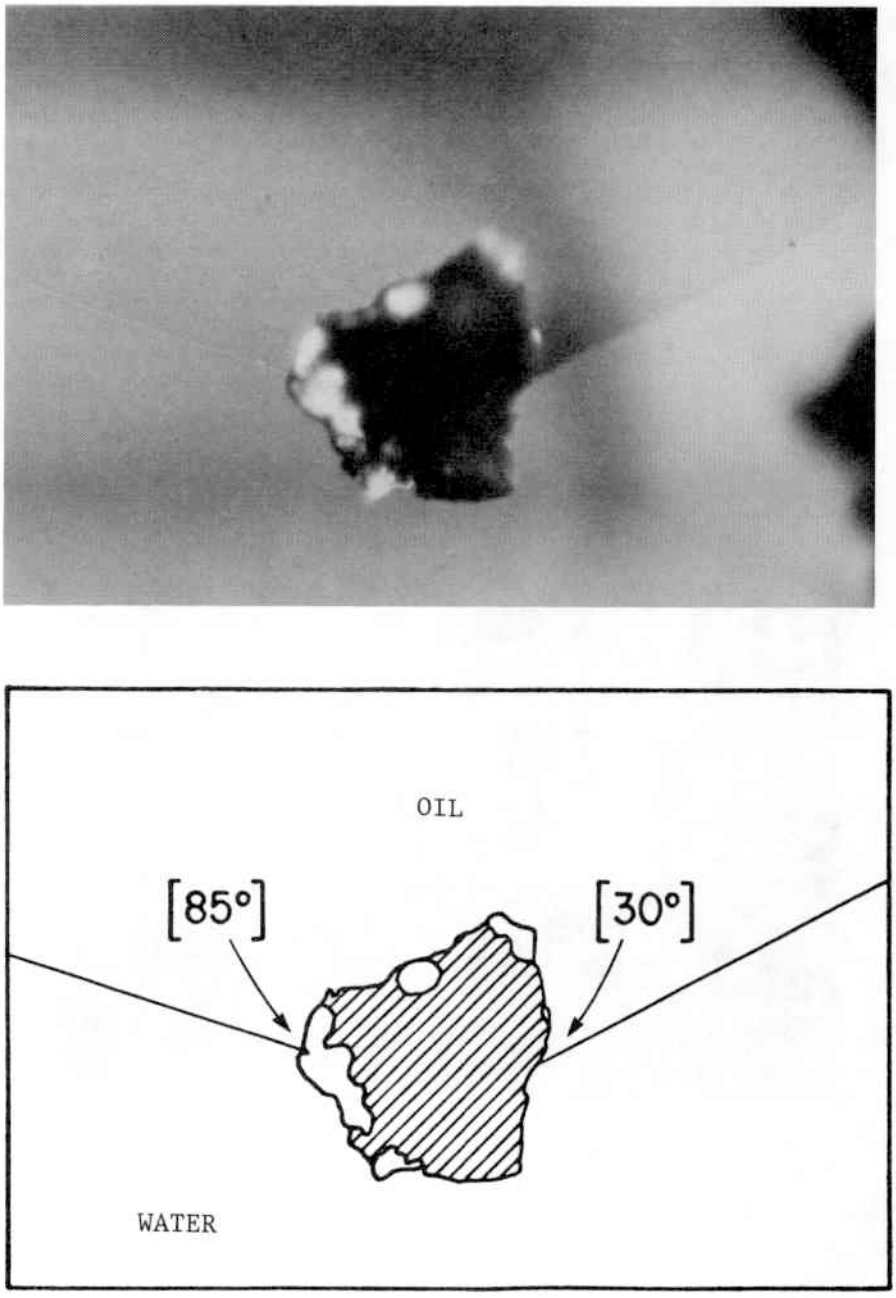


Fig. 3. A 220 μm particle of Kentucky #9 coal, containing iron pyrite (the bright areas) at a decane-water interface.

Hysteresis was large; for example, on an anthracite coal (Panther Valley mine) the advancing angle (measured through the oil phase) was 25° and the retreating angle, 84°. We interpret the oil-advancing angle as corresponding to the angle for the interface on higher-energy, or more hydrophilic, sites or patches on the coal. These may be mineral or aromatic maceral. The oil-retreating angle corresponds to areas of lower-energy, hydrophobic solid, most likely aliphatic or naphthenic carbon atoms or $-CH_2-$ groups.

No direct observation of a third, intermediate contact angle can be expected, in the case of macroscopic measurements on flat surfaces. Advancing and retreating angles on heterogeneous (or rough) surfaces can be observed reproducibly (Neumann, 1979). For a liquid in a gas, the advancing angle normally is a measure of the properties of the lower-energy patches or bands on the surface. The retreating angle is a measure of the properties of the higher-energy patches or bands. Angles between the advancing and retreating angles are not reproducible. This is because, in the process of advancing or retreating across a patchwork surface, the liquid front may come to rest in contact with (i.e., crossing) both higher-energy and lower-energy patches. Just where it comes to rest is a function of the volume of the drop, and the history of the system -- i.e., whether the drop edge has just crossed higher-energy or lower-energy patches. The observable angle will, then depend strongly on the distribution of higher-energy and lower-energy patches, along the line of contact. (If the liquid front has achieved a steady state advancing, or "recently advanced", angle, the contact line is, in effect, "hung up" on the lower-energy patches; and for a steady state retreating, or "recently retreated," angle, the contact line is, in effect, "hung up" on the higher-energy patches).

If patches that have an intermediate surface energy can exist, on a surface that has both higher- and lower-energy patches, then there will, in general, be no reliable way of detecting their presence. Only in rare cases would the contact line become "hung up" on the intermediate-energy patches; and this condition would be hard to distinguish from one in which no intermediate-energy patches existed, but only a distribution of areas of high energy and low-energy sites.

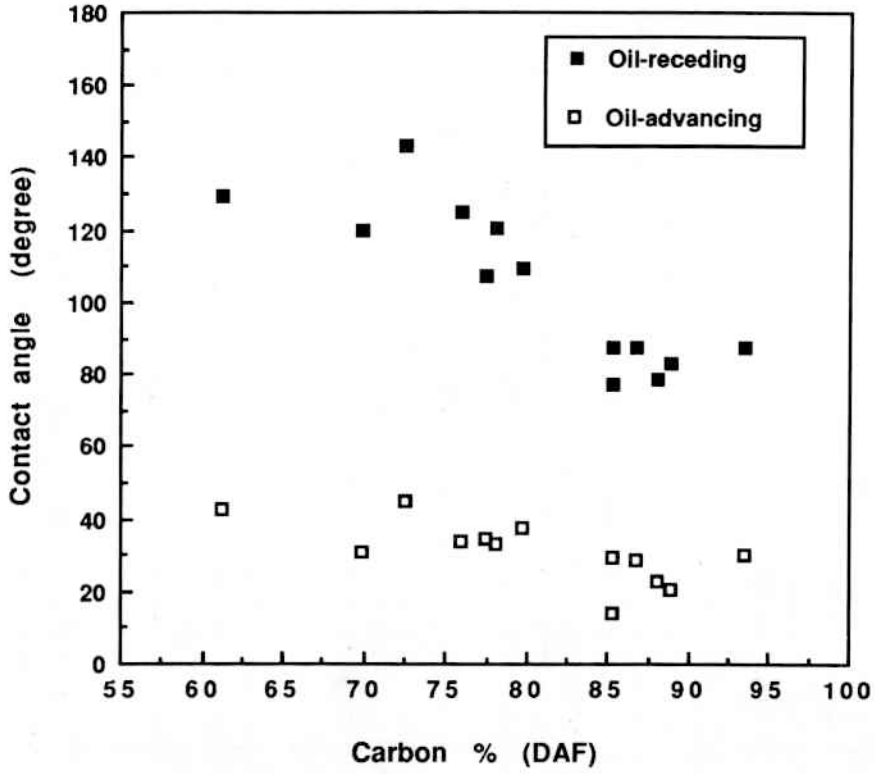
Figure 4 shows preliminary results of the two kinds of measurement of the oil-water-solid contact angles on different coals: samples from 13 different sources of coal, measured by the macroscopic method, and samples of particles from 7 different sources, by the microscopic method.

The comparison of Figures (4a) and (4b) is very suggestive. First, the oil-advancing angles on the particles of the 13 different macroscopic, polished samples clearly correspond to the angles that have been identified as due to paraffinic or naphthenic areas, on the particulate samples, measured microscopically.

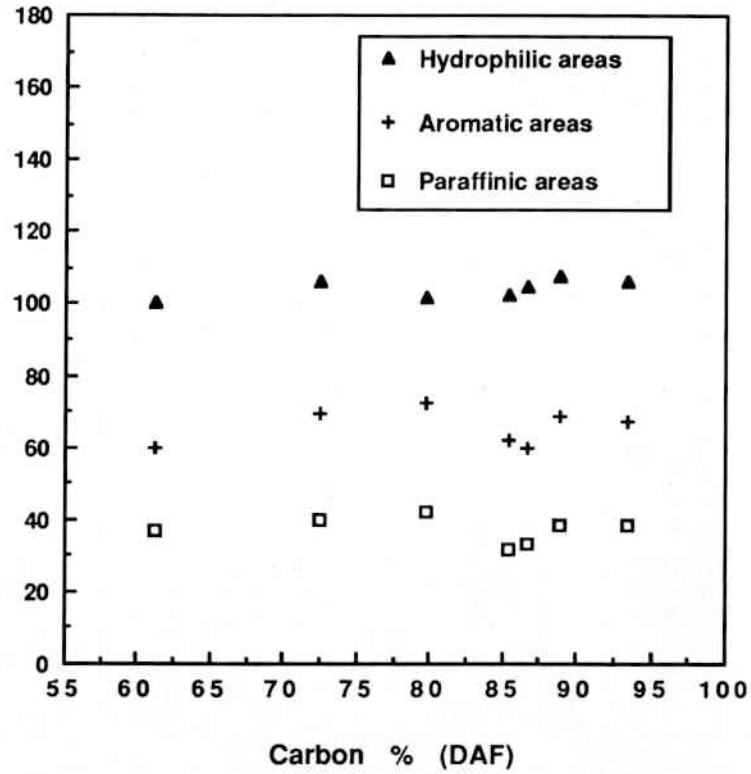
Second, the oil-retreating angles on the samples for polished, macroscopic samples, for the 7 with less than 81% carbon, (daf)

Figure 4 : Oil-Water-Coal Contact Angles, measured through oil

(a) On polished coals



(b) On ground coal particles



correspond fairly well to the angles on the ground particles that have been identified as mineral, or hydrophilic areas.

Third, the oil-advancing angles on the 6 macroscopic samples with greater than 81% carbon lie approximately halfway from the angles on the ground particles that correspond to mineral, hydrophilic areas, to the angles that we have identified with aromatic areas. The interpretation of the difference that we have just noted, in this first series of measurements, will be the subject of further investigation, which would include SEM and ESCA.

Figure 4 by itself does not reveal the full relation between the OWC contact angle and oil agglomeration. For example, particles of on lignite, the angle, 40° was observed, but with a low frequency, and 64° with a frequency that was only a little higher. 103° was the most common angle; and the number of the coal particles actually in the interface, relative to the number in the oil phase, was much smaller than in the case of higher-rank coals.

We are attempting to set up a "hydrophobicity index" (HI) that will quantify this kind of comparison between coals that have different responses to the Otisca T process. One formulation uses estimates of relative areas:

If A_i is the fractional area, among the particles, for which the observed value of θ_{OWC} is near θ_i.

$$HI = \frac{A_1+A_2}{A_1+A_2+A_3+A_4}$$

A_1 = area for $\theta_{OWC} \cong 35°$

A_2 = area for $\theta_{OWC} \cong 65°$

A_3 = area for $\theta_{OWC} > 100°$

A_4 = area that would correspond to 180°, e.g., water-filled pores in the surface.

The area, A_4 is the most difficult to estimate. It also may be the most important; for example, it is probably responsible for the difference between Illinois #6 (HI ≅ 0.15, agglomeration time > 60 minutes) and Upper Freeport (HI ≅ 0.64, agglomeration time less than 1 minute).

We have also measured microscopic oil-water-solid contact angles on coal particles which, after drying, were exposed to the laboratory atmosphere at room temperature for periods of up to 160 days. This was done in order to assess the effect of surface oxidation on the various

surface components of the coals, and to see whether the behavior of the contact angle was the same for all ranks of coal.

Figure 5 shows the results of these measurements on a bituminous coal, Upper Freeport. The behavior of Illinois #6 was very similar. Analysis of these data showed that the rate of change of contact angle with time was approximately twice as rapid for the aromatic sites as for the aliphatic or naphthenic sites.

Anthracite (Panther Valley mine) did not show this trend of contact angles with exposure to air. The study of this coal was incomplete at the time of writing; but the early result was that there was no increase in oil-water-coal contact angle, for any of the three angles were observed: nearly zero increase in in 30 days, and less than 5° increase after 100 days.

- Contact angles of liquids in gas, and the theory of the determination of surface energy components of coal.

We have measured the contact angles of a set of liquids on polished coal surfaces, for the purpose of determining the role of hydrogen bonding and acid-base interactions in oil agglomeration and flotation. The polishing and measurement were carried out (a) polishing in an oxygen-free atmosphere in a glove bag, and measuring in a pure nitrogen atmosphere; and (b) polishing in air and measuring in air. Both advancing and retreating angles were measured. Coal samples from a total of 14 different sources, having carbon content from 72 to 93%, were studied.

In the new approach to the acid-base interaction (Fowkes, 1979) of hydrogen bonding at interfaces, two new surface parameters are defined (Good, 1989; van Oss, 1988):

$\gamma^{\oplus}$ = Lewis (or Brönsted) acid component of surface free energy

$\gamma^{\ominus}$ = Lewis (or Brönsted) base component of surface free energy.

These, together, yield the acid/base component of surface free energy, γ^{AB}. Thus, for substance i,

$$\gamma_i^{AB} = 2\sqrt{\gamma_i^{\oplus}\gamma_i^{\ominus}}. \qquad (1)$$

For the i/j interface,

$$\gamma_{ij}^{AB} = 2(\sqrt{\gamma_i^{\oplus}} - \sqrt{\gamma_j^{\oplus}})(\sqrt{\gamma_i^{\ominus}} - \sqrt{\gamma_j^{\ominus}}). \qquad (2)$$

The surface free energy has an apolar component, γ^{LW}; and the total surface free energy, and interfacial free energy, are given by

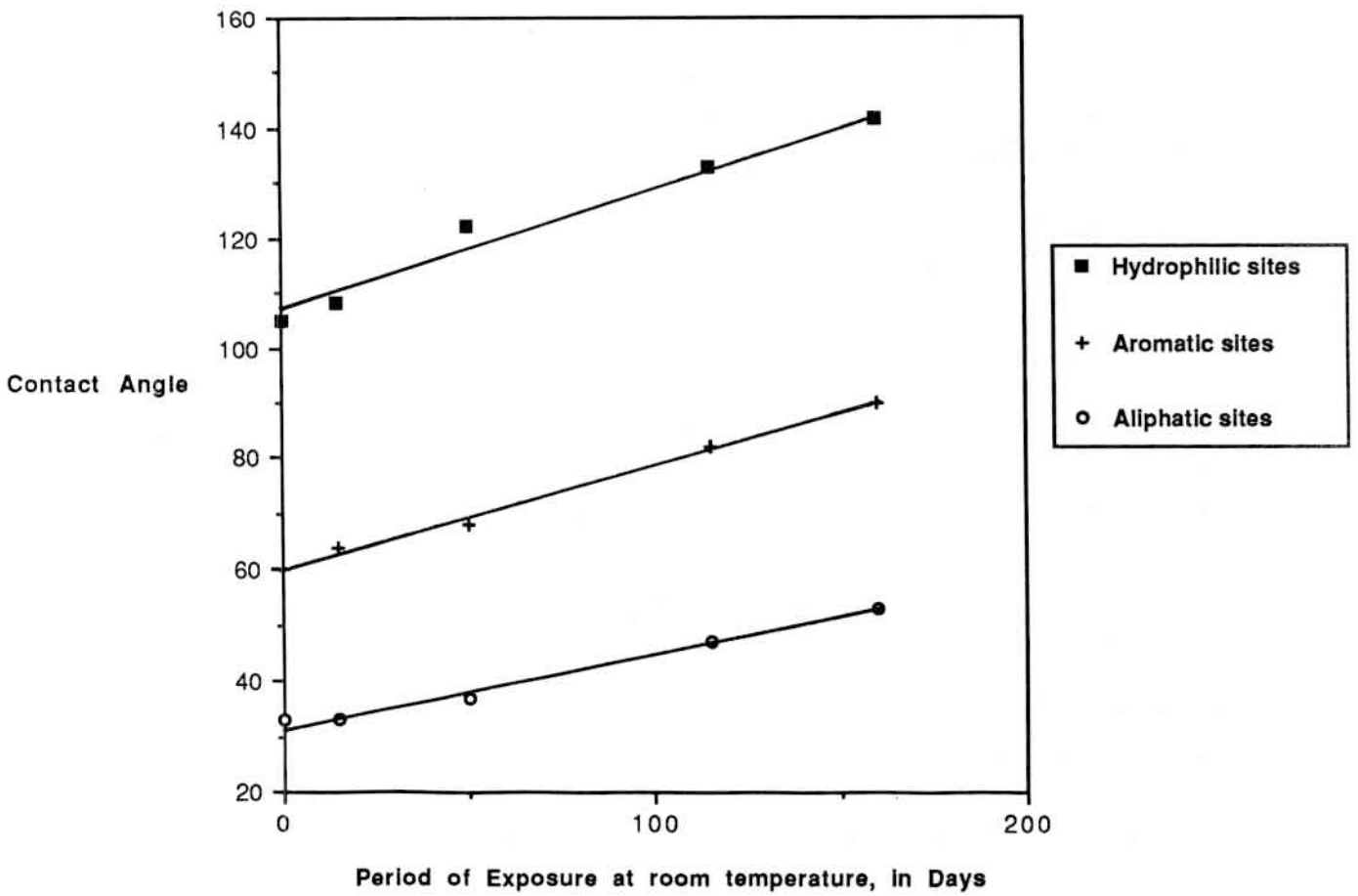


Fig. 5. Decane-Water Contact Angles on Oxidized Upper Freeport Coal As Measured Through the Oil Phase

$$\gamma_i = \gamma_i^{LW} + \gamma_i^{AB} \tag{3}$$

$$\gamma_{ij} = \gamma_{ij}^{LW} = \gamma_{ij}^{AB} \tag{4}$$

The apolar component of γ_{ij} is related to the apolar components for i and for j, by the equation

$$\gamma_{ij}^{LW} = (\sqrt{\gamma_i^{LW}} - \sqrt{\gamma_j^{LW}})^2 \tag{5}$$

Contact angles of liquids on solids are given by the well-known Young equation,

$$\gamma_{s\ell}\cos\theta = \gamma_s - \gamma_\ell \tag{6}$$

The so-called Good-Girifalco equation (Good, 1960) is, for the contact angle of an <u>apolar</u> liquid on a solid,

$$\gamma_s^{LW} = \frac{\gamma_\ell^{LW}(1 + \cos\theta)^2}{4} \tag{7a}$$

or, $$\gamma_\ell(1 + \cos\theta_{LW}) = 2\sqrt{\gamma_s^{LW}\gamma_\ell^{LW}} \tag{7b}$$

For a <u>polar</u> liquid, with surface tension γ_1, polar surface parameters $\gamma_1^{\oplus}$ and $\gamma_1^{\ominus}$, and apolar surface parameter γ_1^{LW}, the equation corresponding to (7b) is

$$\gamma_1(1 + \cos\theta_1) = 2(\sqrt{\gamma_1^{LW}\gamma_s^{LW}} + \sqrt{\gamma_1^{\oplus}\gamma_s^{\ominus}} + \sqrt{\gamma_1^{\ominus}\gamma_s^{\oplus}}) \tag{8a}$$

For a second polar liquid, with surface parameters γ_2^{LW}, $\gamma_2^{\oplus}$ and $\gamma_2^{\ominus}$, the equation can be written,

$$\gamma_2(1 + \cos\theta_2) = 2(\sqrt{\gamma_2^{LW}\gamma_s^{LW}} + \sqrt{\gamma_2^{\oplus}\gamma_s^{\ominus}} + \sqrt{\gamma_2^{\ominus}\gamma_s^{\oplus}}) \tag{8b}$$

Equations (7b), (8a) and (8b) constitute a set of three simultaneous equations, which can be solved for γ_s^{LW}, $\gamma_s^{\oplus}$ and $\gamma_s^{\ominus}$, in terms of the parameters of the two liquids γ_i^{LW}, $\gamma_i^{\oplus}$, $\gamma_i^{\ominus}$ (i = 1 or 2) and the three contact angles that are measured on the solid: θ_{LW}, θ_1 and θ_2. Three appropriate liquids for use on coal are diiodomethane (DIM), glycerol (GLY) and water (W). The parameters for these liquids have been determined -- (see Good, 1989) and (van Oss, 1987) for these liquids -- and are shown in Table 1.

Table 1

Surface Parameters for Test Liquids, in ergs/cm^2

	γ_ℓ	γ_ℓ^{LW}	γ_ℓ^{AB}	$\gamma_\ell^{\oplus}$	$\gamma_\ell^{\ominus}$
Water	72.8	21.8	51.0	25.5*	25.5*
Glycerol	64	34	30	3.92	54.7
Diiodomethane	50.8	50.8	0.0	0.0	0.0

*$\gamma^{\oplus}$ and $\gamma^{\ominus}$ for water are reference values, and all reported values of $\gamma^{\oplus}$ and $\gamma^{\ominus}$ are relative to these values, with the convention that $\gamma_W^+ = \gamma_W^-$.

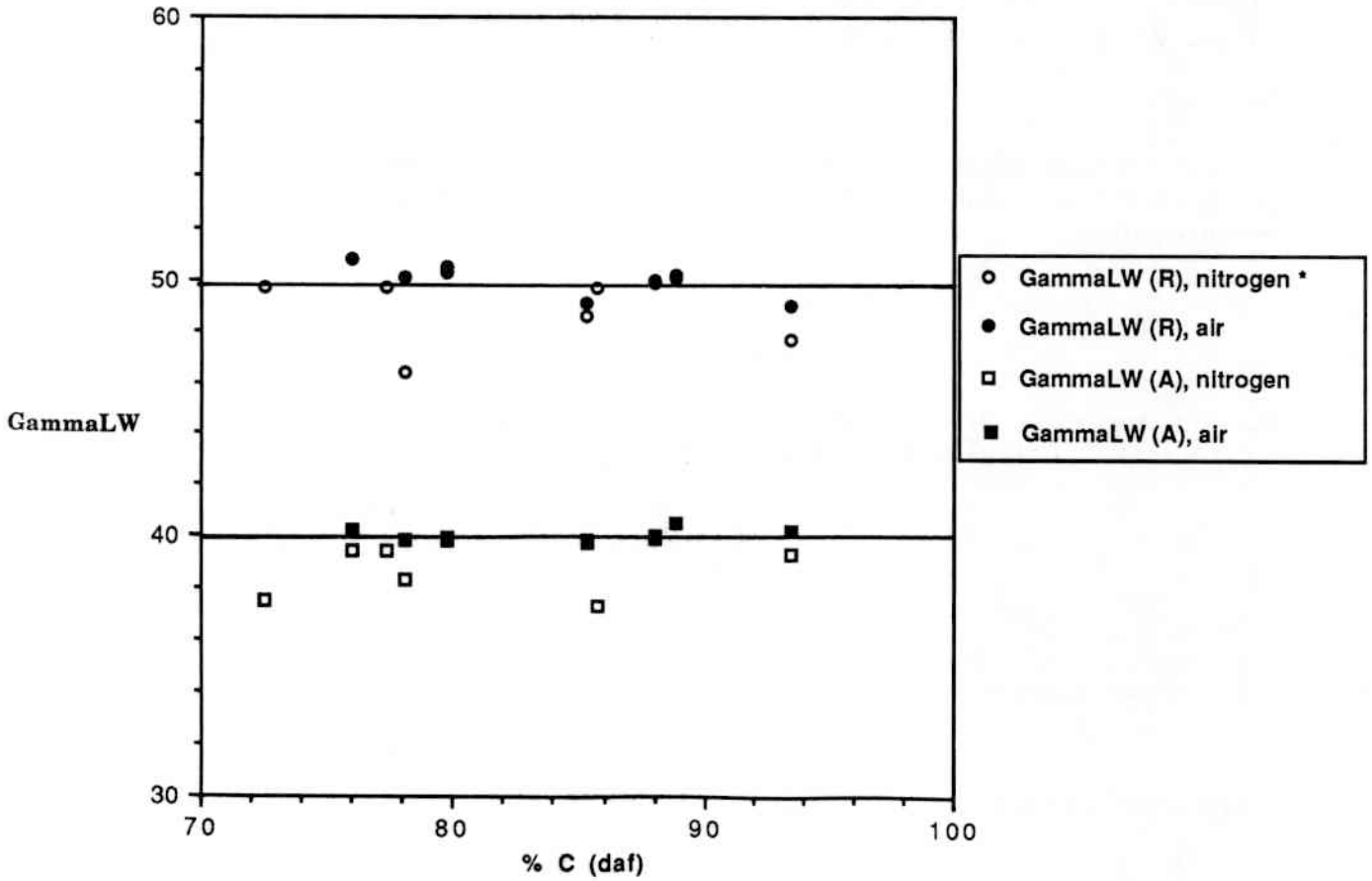
Typical contact angles data are given in Table 2, obtained with Upper Freeport (Mv bituminous) coal. The angles are the means of 30 to 32 measurements.

Table 2

Contact Angles in Nitrogen of Liquids on Upper Freeport Coal, and Calculated Surface Energy Components.

	Contact Angles in Nitrogen	
	θ_a, degrees	θ_r, degrees
Water	87.2	28.3
Glycerol	72.9	12.9
Diiodomethane	39.7	11.5
Computed surface energy, mJ/m^2		
γ^{LW}	39.8	49.8
$\gamma^{\oplus}$	0.0	2.0
$\gamma^{\ominus}$	2.5	31.7

Figure 6 shows the value of γ^{LW} for different coals, as a function of % carbon (daf), for coal polished in nitrogen and in air. The results of measurement of advancing angles, θ_a, and retreating angles, θ_r, are shown. It is clear that there is no significant trend with carbon content, for γ_a^{LW} (derived from θ_a data) or for γ_r^{LW} (derived from θ_r data.) The results for samples polished and measured in air lie below



* (A) : Based on advancing angles
(R) : Based on receding angles

Fig. 6. GammaLW on Various Rank Coals Polished in Nitrogen or in Air

data.) The results for samples polished and measured in air lie below those in nitrogen. However, the difference is barely significant, statistically, and may be considered, for the present, a second order effect. The two horizontal lines in Fig. 6 have been drawn to represent, respectively, all the data based on retreating angles, and all the data based on advancing angles. Our results are quite compatible with the earlier results of Aplan (1978), whose estimate of the critical surface tension for wetting of coal led to a γ^{LW} of 46.5 mJ/m^2, independent of coal rank. Aplan and Parekh did not make an explicit effort (as we did) to measure advancing and retreating angles.

We may interpret the value of γ_a^{LW}, of about 39.5 mJ/m^2, as probably representing the surface free energy of the hydrocarbon component of coal, independent of rank, and that this free energy is nearly the same for aromatic and for aliphatic or naphthenic surfaces.

The value of γ_r^{LW}, of about 49.5 mJ/m^2, corresponds to the surface free energy of a higher-energy component. We will postpone, until a later date, further speculation as to the physical meaning of this number.

Figure 7 shows the calculated values of $\gamma^{\oplus}$ as a function of % carbon (daf). We may first discuss the results as to $\gamma_a^{\oplus}$, the values from advancing angles. These all lie in the range, zero to 0.25 mJ/m^2; and there is no significant trend with % carbon. The mean is 0.1 mJ/m^2; and the difference between this mean and zero is barely significant.

The interpretation of this result is that the areas that correspond to the advancing contact angles contain no (or practically no) acidic groups or groups that can contribute a hydrogen atom or proton to a hydrogen bond. This is exactly what would be expected if these areas consist of aliphatic or naphthenic groups, or aromatic groups.

The $\gamma_r^{\oplus}$ values are appreciably different from zero. The mean for all the coal samples, both handled in nitrogen and handled in air, is close to 2.0 mJ/m^2. The scatter is considerable for both kinds of specimens, and the two means do not differ significantly.

The interpretation of this result is that the areas corresponding to the retreating angles contain acidic hydrogens, probably as hydroxyls; and that the oxidation that occurs during polishing (and measuring) in air does not lead to an important increase in the concentration or acidity of the hydroxyls. The data are too scattered for us to reach a conclusion as to the difference between aromatic areas and aliphatic or naphthenic areas, in regard to the acidity of the surface groups that take part in hydrogen bonding.

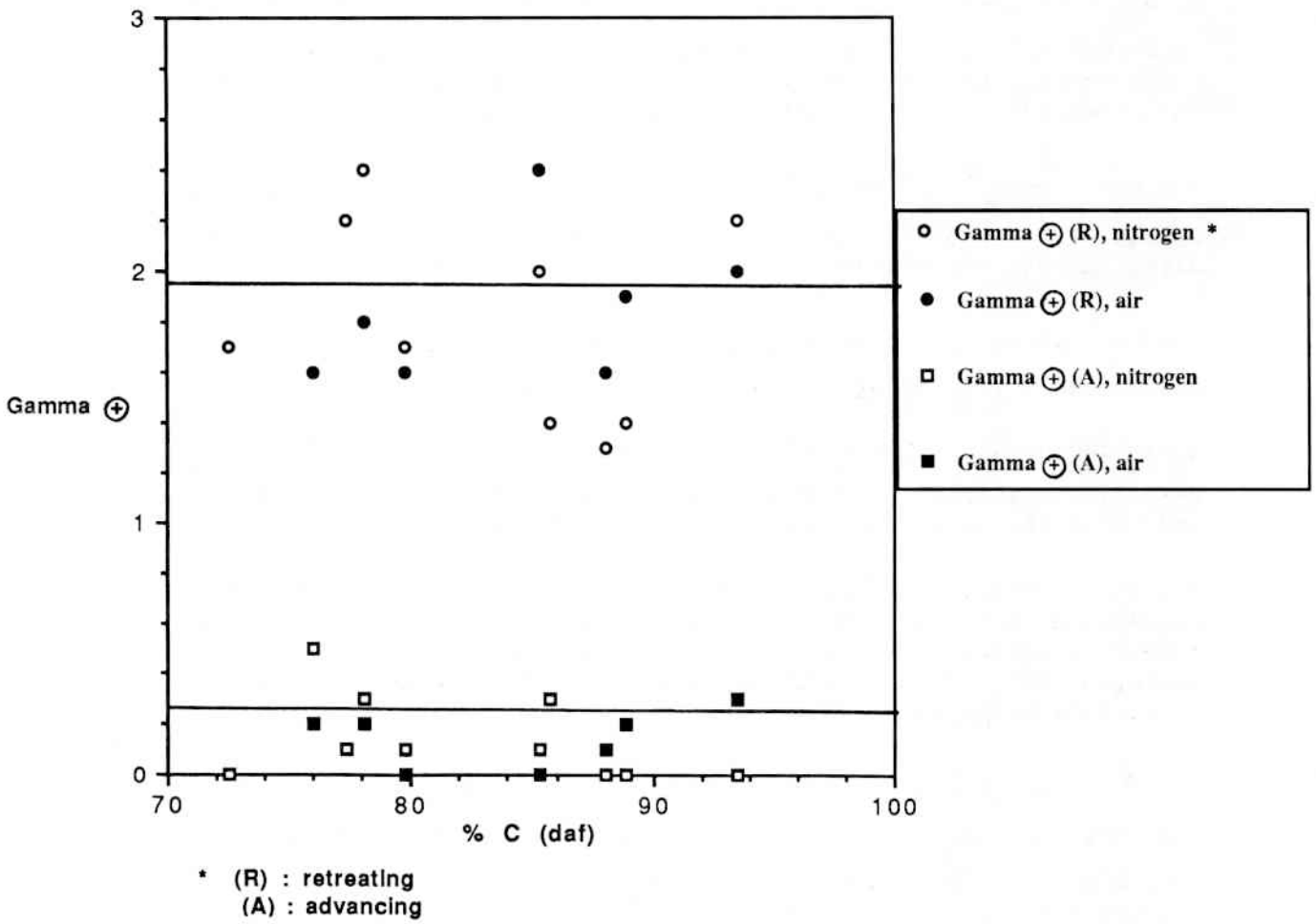


Fig. 7. Gamma ⊕ on Various Rank Coals Polished in Nitrogen or in Air

Figure 8 shows the calculated values of $\gamma^{\ominus}$ as a function of % carbon. It is clear that this basic parameter is strongly dependent on % carbon. Since % oxygen decreases as % carbon decreases, we can attribute the basic behavior to oxygen atoms in the surface. These are, probably, carbonyl groups, and also ether and possibly carboxyl groups. Hydroxyl groups may also contribute basic behavior, by way of the unshared pair electrons of the oxygens.

The trend, of a decrease of $\gamma^{\ominus}$ with decreasing % oxygen (increasing %C) is very evident, in the data in Figure 8. As we have just indicated, this could have been expected. At high % carbon, the curves appear to level off. This may correspond to a residual, zero-oxygen basic character, due to aromatic rings and ethylenic structures.

The same trend as that in Fig. 8, of $\gamma^{\ominus}$ with %C, was found with samples that had been polished in air and were measured in air. The values of $\gamma^{\ominus}$ based on retreating angles were about 5 mJ/m^2 higher than in Fig. 8, and the values of $\gamma^{\ominus}$ based on advancing angles were about 1 or 2 mJ/m^2 higher than those based on angles measured in nitrogen.

The fact that $\gamma_a^{\ominus}$, based on the advancing angle in Fig. 8, is considerably smaller than $\gamma_r^{\ominus}$, but is quite significantly larger than zero, indicates that the lower-energy areas contain significant concentrations of oxygen. This conclusion is supported by the comparison just noted, of the $\gamma_a^{\ominus}$ values from samples handled in air vs. those handled in nitrogen.

The relative magnitudes of $\gamma^{\ominus}$ and $\gamma^{\oplus}$, with the former being as much as an order of magnitude larger, is notable. The same order of difference has been observed on polymeric surfaces such as flame-treated polyethylene. [Good, 1989; Good and Shu, 1989; van Oss, 1987; van Oss, 1988].

- Adsorption measurements were made, from water and decane solution, of n-octanol and cyclohexanol, on two bituminous coals: Upper Freeport and Illinois no. 6. A brief report of the results is as follows:

The rate of adsorption was large, initially, in every case. In less than 100 minutes, the adsorption had achieved 96 to 98% of the value attained in 48 hours.

The two alcohols exhibited similar but not identical adsorption behavior; and the two bituminous coals were similar but not identical. Surface areas (as determined by the Langmuir method) were in the range, 30 to 150 m^2/gm, which may be taken to mean that most of the adsorption was on the internal surfaces of pores.

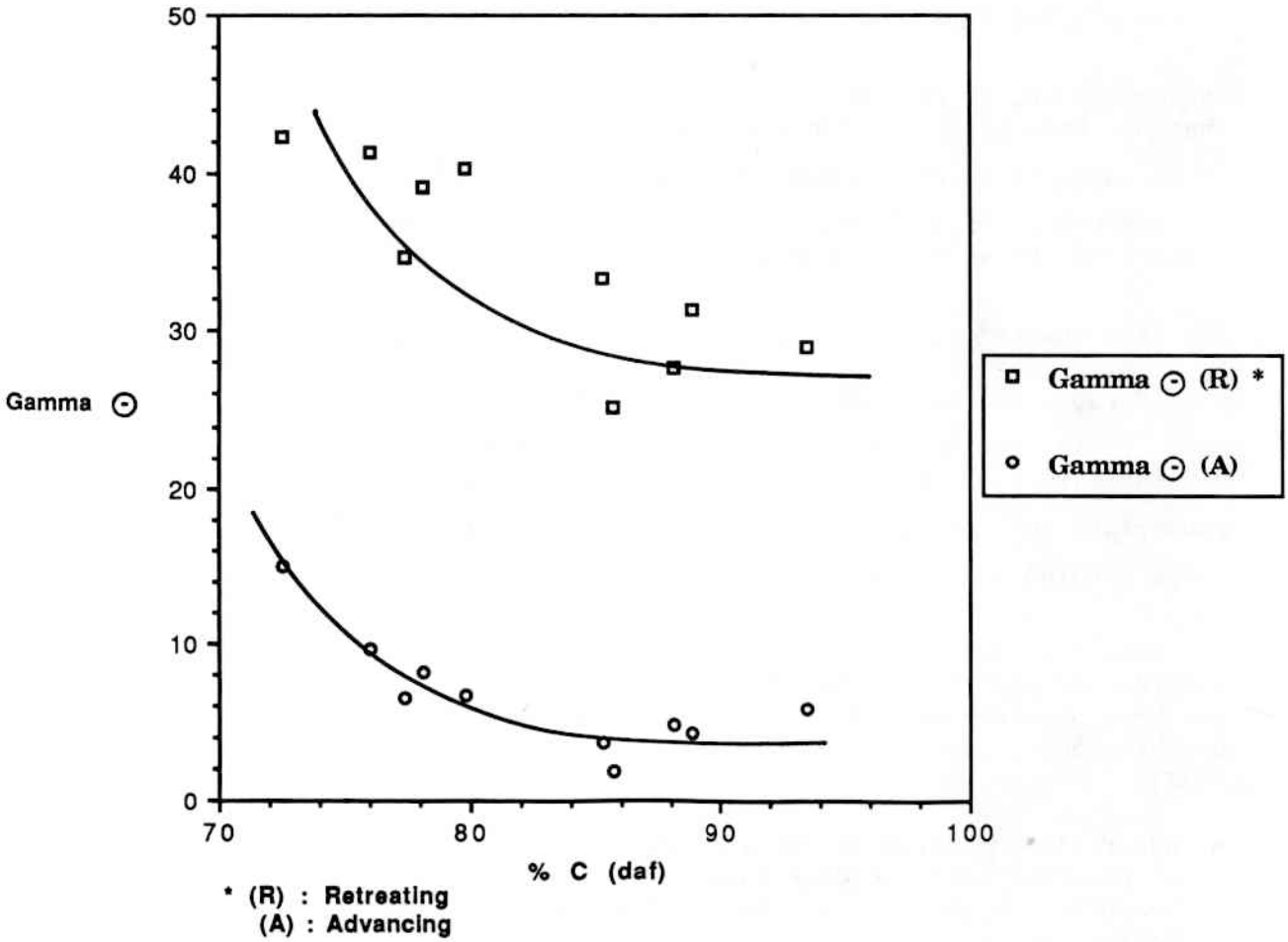


Fig. 8. Gamma ⊖ on Various Rank Coals Polished in Nitrogen

All the coal samples behaved as if two kinds of adsorption sites were present. The higher-energy sites had energies of adsorption, for a particular alcohol, that were about 20 to 30% larger than the energies for the lower-energy sites. The areas corresponding to the lower-energy sites were larger than the areas for the higher energy sites by about a factor of two.

- A liquid bridge model was employed for analysing the stability of agglomerates. Jaques, et al, (4), have discussed the role of liquid bridges in oil agglomeration. See also the report by Keller (5).

For the liquid bridges that are important in oil-agglomeration of coal, we can neglect gravitational effects. The common assumption, that the bridged particles are spherical, simplifies the mathematics of the problem, but leads to the omission of some important features. We have started with the assumption that the bridged structures have flat, parallel solid surfaces, and we will proceed in later contributions, to consider nonparallel surfaces that include edges and corners; and eventually we will investigate multiple bridges in aggregates of many particles which are both irregular and rough.

Figure (9) shows the resolution of the interfacial tension force due to the oil/water interface, in the direction perpendicular to the two solid surfaces. Clearly, this force will be zero if θ (as measured through the oil) is 180°, i.e., if the solid is "fully water-wet." It will also be zero if $\theta = 0$, i.e., if the solid is "fully-oil-wet." Between these extremes must lie the cases that are of interest to coal beneficiation processes. For instance, the question may be asked, Is the condition of a 180° angle on FeS_2, i.e. hydrophilicity to the extent of complete water wetting, necessary for rejection of iron pyrite particles from aggregates? A preliminary, qualitative, dynamic theory gives the answer, No.

Figure (10) shows the response of a system with a drop of water between two coal surfaces, to an increase in the distance between the particles. The location of the drop perimeter, on each of the coal surfaces, is assumed to be fixed; this is probably a good approximation to the actual behavior, since motion of a drop front along a surface commonly takes appreciable time (of the order of tens of seconds) for drops on solids in air.

It is clear from Figure (10b) that, when the contact angle lies between 0 and 90°, the net force will increase as the separation increases. If $\theta = 0$, there will be no force; and as θ approaches 90°, the increment in net force, with increasing displacement, will decrease to zero.

If θ increases to values greater than 90°, then, as may be seen from Figure (11), the net force will decrease, with increasing separation. This means that, under mechanical agitation, the aggregate will tend to be unstable. Not only will the net force decrease with increasing separation, but the narrowest region of the bridge -- see Fig. (11b) -- will tend to break, leaving two drops, one on each coal surface. When this happens, the net force drops to zero.

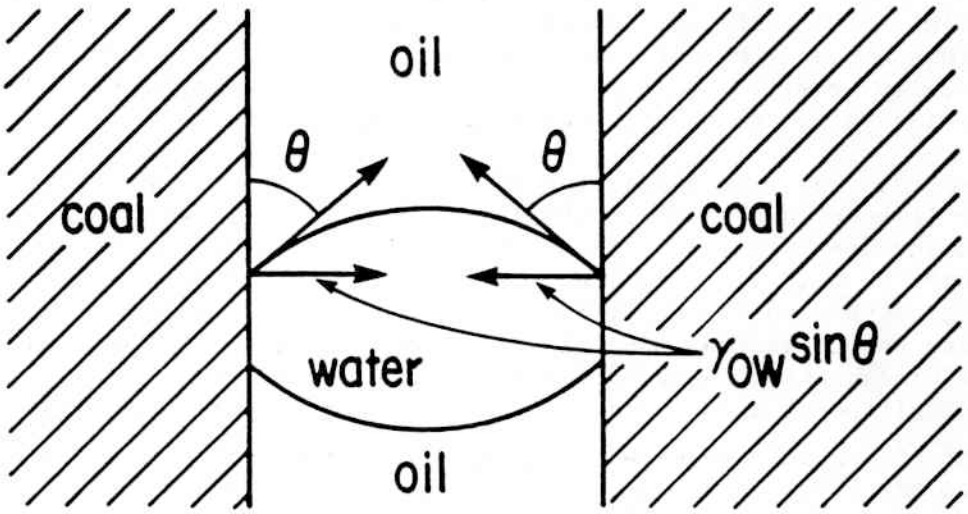


Fig. 9. A water drop "bridge". Two flat, parallel coal surfaces with oil and water between them. The net force drawing the two coal particles together, due to the oil-water interface, is $\gamma_{OWC}\sin\theta$, for unit length of the total contact line on the two solid surfaces.

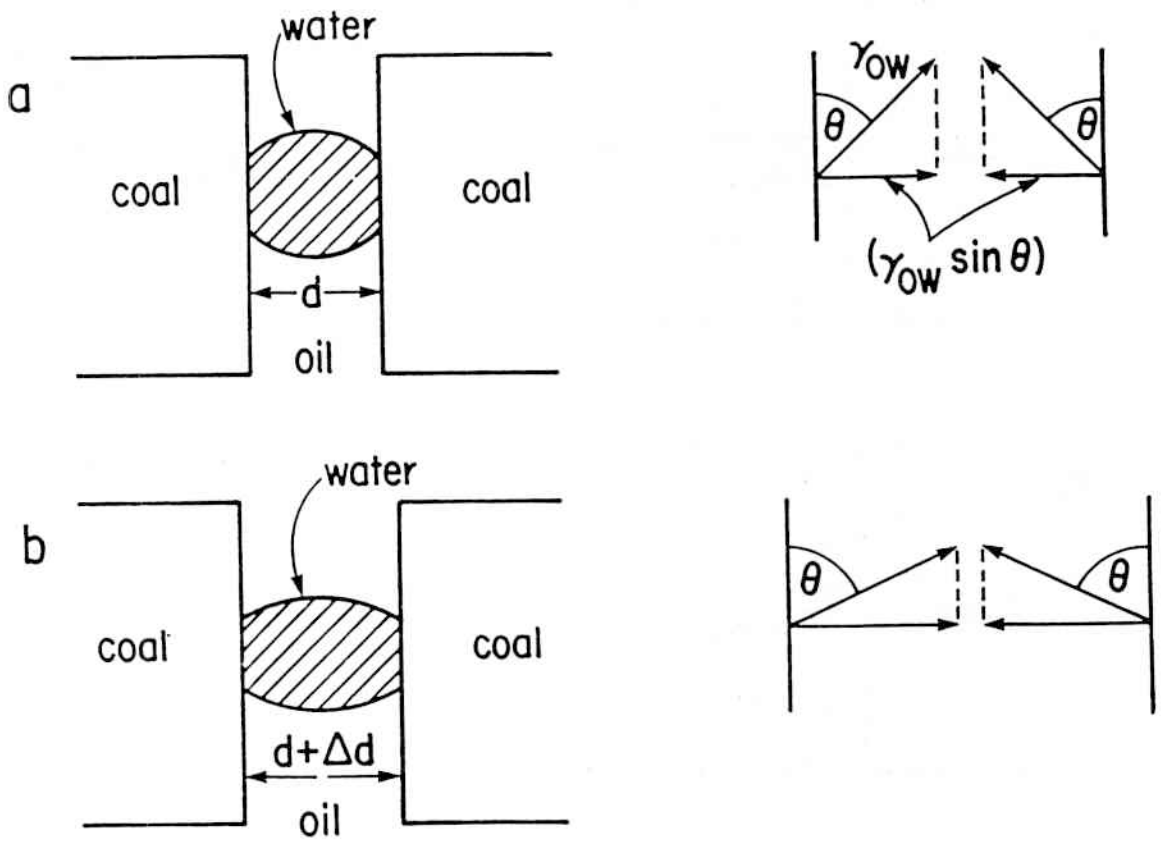


Fig. 10. When θ, as measured through the oil, is less than 90°, the surface tension force per unit of perimeter increases as d increases. So system resists an increase in the separation distance, d.

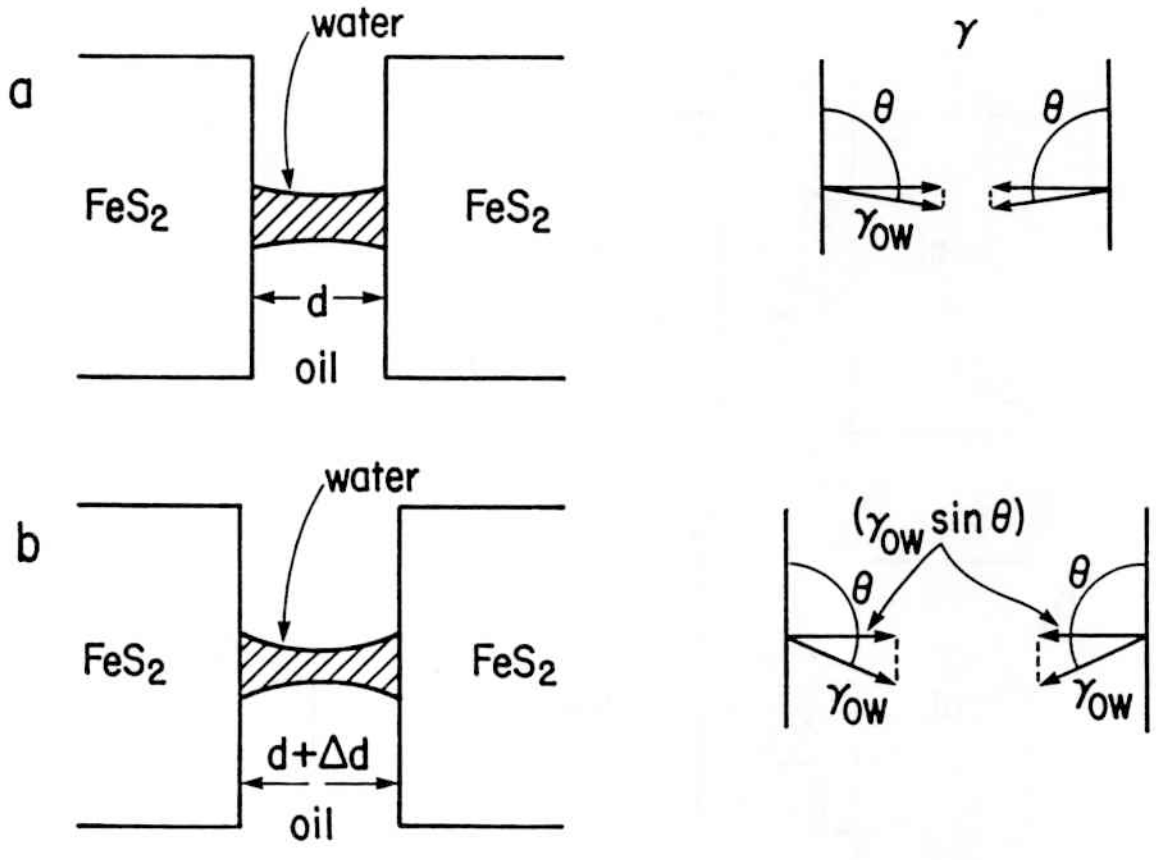


Fig. 11. If $\theta > 90°$, the force decreases as d increases. If there is a small but steady tensile stress pulling the 2 particles apart, then the resistance to separation may drop below that stress. The particles will separate.

The kind of unstability just described may set in when the value of θ is slightly less than 90°, because a small change of liquid bridge shape, with increasing displacement, can carry the system into the unstable region, as if θ were greater than 90°.

- Laboratory-scale oil agglomeration studies.

We have set up an Osterizer blender system for the direct study of oil agglomeration. We have made provision for control of the atmosphere over the sample, during agitation.

The hypothesis was suggested, that CO_2 could enhance the agglomeration process. Studies were made, of Illinois #6, with a CO_2 atmosphere.

In the standard Otisca T process, a water slurry of ground coal is diluted to the desired concentration (e.g., one part of coal by weight, to 20 parts of water) and placed in the blender. One part of oil is added, either before or after starting the blender. When a coagulum forms, it is separated from the water phase, by means of a screen. The reverse procedure can be used. After wet grinding, the coal can be dried, and the oil added to the dry powder, to wet it out. When water is added, and agitation in a blender is carried out, a coagulum forms after a short time (seconds to a few minutes) which contains water, oil and coal.

We have found, using Illinois #6 coal, that in the normal operation of the Otisca T process, the use of CO_2 does not lead to any appreciable shortening of the time to agglomeration. In a few cases, the time was lengthened. But when the reversed Otisca T process was used, i.e., with wetting out dry coal with oil, and using a CO_2 atmosphere, a reduction in agglomeration time by as much as a factor of 10% was observed with Illinois #6 coal. There was no change with use of CO_2 for Kentucky #9 coal.

This modification of the procedure may or may not be a practical measure. It has been found, in experiments at Syracuse, that though the oil-first technique leads to excellent agglomeration of the coal particles, there is a greater retention of pyrite or other ash-forming mineral than in the normal method.

The reason why this was so, was not clear. It may be that, once hydrophilic particles such as pyrite have been oil-wet, the displacement of oil by water is slow. It may also be, that in the step in which a water-free coal powder is formed (whether by dry grinding, or by wet grinding followed by drying) iron pyrite is oxidized enough that its surface becomes hydrophobic, and so the iron pyrite is not rejected from the agglomerate.

This experiment points to another consideration with respect to the oil agglomeration process. It may be that the controlling factor is the

kinetics of spreading and of the formation of the liquid bridges of water droplets. This possibility deserves study.

6. FUTURE WORK

- We plan to continue the study of the contact angle of the water-decane interface on coal, using samples from various, additional sources, and including the effects of oxidation. We will correlate the contact angle results with other properties of the coal samples, such as % oxygen. We will extend this study to iron pyrite, and possibly, to other inorganic minerals that are present in coal. Reducing additives will be studied.

We will study the frequency of appearance of angles in particular ranges, e.g., about 35°, about 65° and above 100°, within a particular coal sample.

- We will investigate further, the contact angles of selected liquids in nitrogen, on coal. We will try to elucidate the acidic and basic components of surface energy, by using other liquids besides those employed so far. We will also use SEM, ESCA, FTIR and other methods to study the surfaces.

- We will continue the study of adsorption of surface active additives, such as higher alcohols, on coal from various sources. We will investigate the differences between adsorption on the internal pore surfaces and on the external particle surface.

- We will extend the theory of liquid bridges to nonparallel solid surfaces.

- We will start a study of the kinetics of spreading, e.g., of oil under water, or vice versa, on coal and on inorganic solids.

7. REFERENCES

Good, R.J., Chaudhury, M.K., and van Oss, C.J., in "Fundamentals of Adhesion," L.H. Lee, ed., Plenum Press, N.Y., in press, 1989.

Good, R.J., and Shu., L.K., unpublished work.

Jaques, A.D., Hovarongkura, A.D., and Henry, J.D., AIChE Journal 25, 160 (1979).

Keller, D.V., Jr., and Bury, W., Colloids and Surfaces 22, 37 (1987).

Neumann, A.W., and Good, R.J., "Methods of Measuring Contact Angles," in Colloid and Surface Science 11, Good and Stromberg, Eds., Plenum Press, N.Y., 1979, pp. 31-91.

Parekh, B.K., and Aplan, F.F., in Recent Developments in Separation Science, Vol. IV, Li, Long, Stern and Somasundaran, eds., CRC Press, Cleveland, OH, (1978), pp. 107-113.

van Oss, C.J., Chaudhury, M.K., and Good, R.J., Advan. Colloid Interface Sci., 28, 35-64 (1987).

van Oss, C.J., Chaudhury, M.K., and Good, R.J., Chem. Rev., 88, 927-41 (1988).

ANALYTICAL CHARACTERIZATION OF COAL SURFACES AND INTERFACES

1. CONTRACT NUMBER: DE-AC05-84OR21400/FEAA290

CONTRACTOR: Oak Ridge National Laboratory
MS-6087, P.O. Box 2008
Oak Ridge, TN 37831
(615) 574-4959

PROGRAM MANAGER (CONTRACTOR): R. R. Judkins

PRINCIPAL INVESTIGATORS: E. L. Fuller, Jr., and V. J. Tennery

PETC PROJECT MANAGER: J. D. Hickerson/R. Lai

CONTRACT PERIOD: September 1, 1988 through September 30, 1989

2. SCHEDULE/MILESTONES:

1989 Program Schedule

	S	O	N	D	J	F	M	A	M	J	J	A	S
GRINDING EFFECTS ON BITUMINOUS COAL					X	X	X	X	X	X	X		
GRINDING EFFECTS ON SUBBITUMINOUS COAL											X	X	X
IMAGE ANALYSES OF ARGONNE POWDERED COALS									X	X	X	X	X
DRIFT ANALYSES OF ARGONNE POWDERED COALS								X	X	X	X	X	X
DEVELOP SAMPLE PREPARATION FOR TEM								X	X	X	X	X	X
MECHANICAL PROPERTIES MICROPROBE OF MACERALS								X	X	X	X	X	X
ESCA ANALYSES OF SURFACES AND REACTIONS								X	X	X	X	X	X

3. OBJECTIVES:

The objective of this project is to study the chemistry and structure of coals, including the properties of surfaces and interfaces. Particular emphases are given to the nature of the physical and chemical binding of sulfur and other detrimental components (nitrogen, mineral matter, etc.). The research in this project focuses on gaining a better understanding of these surfaces as related to the reduction of emissions from the various combustion techniques employed for advanced coal utilization projects.

4. BACKGROUND STATEMENT:

Environmental concerns require that combustion processes must be made more efficient and cleaner. The cleanup of the feedstocks for this direct utilization of coal is preferred over the stack gas cleanup to

avoid insult to health and environment. Separation of the residual amounts of noxious species from coal requires a more complete knowledge of the interaction of the various components across the surfaces and interfaces. Existing industrial processes are capable of removing some of the noxious components, but fall short of the desired goals that exist presently and/or will be mandated by legislation for cleaner exhausts. A more detailed understanding of the microstructure and surface chemistry is needed.

5. PROJECT DESCRIPTION:

The facilities at Oak Ridge National Laboratory are designed and developed to study the microstructure and the surface reactions of the type involved in the coal preparation processes. Most studies are on a laboratory scale but are strongly oriented to existing and proposed engineering programs. In this manner, the fundamental data are most quickly and economically applied to the industrial processing.

6. RESULTS/ACCOMPLISHMENTS:

This is a multifaceted program, involving several techniques for the characterization of the chemistry and structure of coal surfaces and interfaces. Much of the characterization involves extensive photographic and mathematical analyses which are too lengthy to include in this report. The reader is encouraged to peruse the cited references and/or contact the principal investigators for additional detailed information.

A. ELECTRON MICROSCOPY CHARACTERIZATION:

Scanning and transmission electron microscopy (SEM and TEM) and energy dispersive X-ray spectroscopy (EDS) were used to characterize coal powder specimens of both Illinois #6 and Pocahontas #3. Specimens were prepared by embedding the powders in epoxy using vacuum impregnation techniques, and metallographically polishing them to produce a cross section through the embedded coal particles. TEM specimens were prepared from the same embedded specimens using standard dimple-grinding and ion milling techniques.

Optical micrographs are used as the survey medium for identifying typical regions on polished specimens. Typical SEM secondary electron images of the two specimens are used for detailed comparison. We normally concentrate on two types of morphology-organic matrices and mineral-rich regions. The minerals appear lighter than the coal particles due to increased secondary electron emission associated with the minerals having higher average atomic number than the coal particles or the epoxy embedding medium. Although quantitative image analysis remains to be done, several morphological features are obvious. The grinding process has produced particles having a large range of sizes. The particles are generally angular with sharp corners which indicates that little deformation or reagglomeration occurred during grinding.

Considerable effort has been directed toward determining the location and distribution of organic and mineral sulfur and other mineral constituents. Initial TEM observations reveal that some mineral constituents can be quite small, such as mineral flakes which are on the order of 0.1 to 2.0 μm in the section normal to the bedding plane. EDS analyses of such particles in the TEM thin foils show them typically to be either clay minerals rich in aluminum, silicon, oxygen, and elements such as magnesium, calcium, iron, or sulfur-bearing minerals such as pyrite (FeS_2). The matrix material in comparison would typically show primarily carbon with minor traces of sulfur and perhaps silicon.

Numerous coal and mineral particles in the two polished specimens have been analyzed in the SEM by EDS techniques. EDS spectra were acquired at 20 kV to effectively excite both the light elements and any heavy elements present in mineral microconstituents within the organic matrix material. In general, particles were selected for analysis which showed no obvious large, bright inclusions (indicating the presence of heavy elements) in either secondary or backscattered electron images. The electron beam was rastered to generate X rays from particle areas of 200-300 μm^2. With this geometry, contribution to the spectra could be expected not only from the organic matrix material, but also from any minor mineral constituents within the analyzed volume, such as were observed by TEM.

Typical spectra from coal particles having no obvious larger mineral inclusions have been analyzed from each of the two specimens. Sulfur is present in both spectra. In fact, sulfur was detected in all spectra of coal particles from both specimens. Histogram analyses of the number of measurements of sulfur with a given concentration from individual particles versus concentration for the two specimens revealed considerably more sulfur in the Pocahontas #3 (as expected) and greater particle-to-particle variability in the sulfur content as compared to the Illinois #6 sample. Although there have been several articles published in recent years which present quantitative results from microanalyses by EDS or WDS methods, none that we have found give details of the methods and standards used for obtaining the quantitative results. We therefore have questions about suitable standards for quantitative analytical determination of low levels of sulfur in a primarily carbon matrix. In the present study the concentrations were determined using the Hall technique in which all spectra are normalized to each other by comparing the counts in a chosen background region devoid of characteristic peaks and determining the ratio to a pure sulfur standard. No absorption corrections were made; thus the absolute concentrations can be expected to be off by a small amount, but the relative concentrations should be directly comparable. Sulfur concentrations measured on individual particles agree well with the known bulk sulfur concentrations. A small quantity of chlorine is present in the Pocahontas #3 coal spectrum. Silicon was detected in the Illinois #6 coal spectrum and is present as a result of the small mineral constituents present in the coal particles as was discussed previously. Likewise, aluminum, potassium and calcium were occasionally detected in coal particles on both specimens.

B. SURFACE CHEMICAL ANALYSES USING ELECTRON SPECTROSCOPIC CHEMICAL ANALYSIS (ESCA):

Electron spectroscopic chemical analyses for this period were performed on two specimens of the Illinois #6 coal. Samples consisted of 100-mesh powders and a small polished block which contained bands of vitrinite and clarite (mixture of spores and vitrinite) which were greater than 2 mm in width. The presence of these maceral bands made this specimen amenable to small area ESCA experiments.

In these analyses we used a VG ESCALAB II. All ESCA data were produced with Al Kα (1428.5 eV) radiation with the anode operated at 20 kV and 15 mA (300 W) and the analyzer set in the constant analyzer energy mode at 20 eV. Photoelectron peak positions for all elements recorded were corrected for charging by referencing to the adventitious carbon C1s peak at a binding energy of 284.6 eV. Small area ESCA analyses were recorded with the slit setting that resulted in an analysis of 1000 μm diam areas.

A major consideration in our analysis of the polished surface was to determine whether we could differentiate between aliphatic carbon associated with exinitic type constituents and aromatic carbon found in vitrinite. Preliminary analyses failed to reveal any notable differences in the carbon C1s photoelectron peaks. However, small area multiplex data for carbon, nitrogen, and sulfur obtained from the aforementioned bands yielded some interesting results as shown:

Elements	At. %	
	Vitrinite	Mixed Band
C	97.704	97.110
S	0.697	0.997
N	1.598	1.890

The amounts of sulfur and nitrogen in the mixed band of microspores are significantly greater than in the vitrinite band. These observations are consistent with earlier published data by Harris et al. (1977) performed with an electron microprobe.

Electron spectroscopic chemical analysis spectra for all elements identified in the powdered coal sample were recorded in an overnight experiment in order to accumulate sufficient counts for some of the minor elements. Of particular interest was the presence of multiple photoelectron peaks for sulfur and nitrogen indicating their presence in more than a single compound. A computer-fitted spectrum was obtained for the sulfur 2p bands with the peak positions corrected by subtracting 3.5 eV. The sulfur peaks occur at 163.5 eV and 169.2 eV which are in good agreement with literature values for thiophene (organic sulfur) and sulfate (probably inorganic), respectively. The computer-fitted curves for nitrogen were more ambiguous than those for sulfur. A peak at 402 eV (398.5) appears to fit that of pyridine. However, the other nitrogen

peaks are not (at this writing) readily identified. We plan to do more detailed literature search to determine the roles of nitrogen.
A survey of the ESCA data for the powdered Illinois #6 coal suggests the presence of primarily aluminosilicate type minerals with almost no calcium carbonates. However, in the polished block we recorded much more calcium. These observations, though very preliminary, suggest removal of secondary minerals from this coal during crushing and sieving.

C. MICROMECHANICAL PROPERTIES OF COAL MACERAL SURFACES:

The mechanism of percussive grinding of coal is thought to be dependent on the mechanical properties of the individual macerals present in a coal (Kopp et al., 1989; Fuller et al., June 1989). Three macerel groups (exinite, vitrinite and inertinite, which includes fusinite and semi-fusinite) were selected for measurement. The locations of the macerals were mapped microscopically so that they could be relocated in the nanoindenter instrument. The spatial resolution of the indenter was ±1 μm and individual maceral fragments approximately 5 μm wide could be characterized. Each indentation was made under identical displacement-rate controlled conditions (5 nm/s) to a nominal displacement of 300 nm. The results were corrected for temperature drift. The physical property values are:

Maceral	(#)	H(GPa)	S(N/m)	E(GPA)
Exinite	33	0.50 (0.20)	9,110 (2,660)	6.42 (1.82)
Vitrinite	27	0.59 (0.09)	7,420 (860)	5.28 (1.20)
Fusinite	11	6.33 (0.41)	19,330 (2,780)	22.40 (2.15)
Semi- fusinite	5	12.72 (0.66)	37,410 (1,500)	45.38 (0.55)

(Values in parentheses represent one standard deviation)

The micromechanical properties for vitrinite and exinite in the Illinois #6 coal are nearly identical. However, as samples from other coals are studied, we anticipate that the properties of individual coal macerals will be influenced by the degree of coalification (rank) and perhaps other factors as well (e.g., the presence of mineral matter, pores, etc.). Plots of load (milliNewtons) vs displacement (nanometers) obtained in the nanoindenter reveal that approximately two-thirds of the maximum displacement for the exinite and vitrinite was plastic, while the deformation of fusinite and semi-fusinite was virtually all elastic.

There appear to be significant differences in the properties of exinite and vitrinite compared with fusinite and semi-fusinite. Hardness, stiffness and elastic modulus are an order of magnitude greater for

fusinite and semi-fusinite than for exinite and vitrinite. Whether the differences in the properties of fusinite and semi-fusinite are real is uncertain at this time since only five measurements were made on a single semi-fusinite fragment. Based on the limited data available, semi-fusinite appears to be approximately twice as stiff and hard as the fusinite in Illinois #6 coal. This relationship was unexpected, since fusinite is thought to have been heated to higher temperatures than semi-fusinite (perhaps as a result of ancient forest fires prior to the incorporation of the plant debris in the coal-forming swamp). If further study reveals that semi-fusinites are consistently harder and stiffer than fusinites, alternate explanations should be considered.

The mechanical properties of abundant maceral constituents are thought to be one of the primary factors that control the behavior of coal during the crushing and grinding which will precede most sulfur-removal processes. The mechanical behavior of coal is usually determined on large samples but the test results are often inconsistent. We hope that by measuring the mechanical properties of the individual components (macerals) present in a coal it will be possible to predict its behavior during percussive fragmentation of the coal.

D. DIFFUSE REFLECTANCE INFRARED SPECTROSCOPY (DRIS):

▪ Air Oxidation Studies: These studies were carried out over a temperature range of 75 to 400°C using equipment and techniques described previously (Fuller et al., 1985a; Fuller et al., 1985b). The very initial stage of air oxidation involves the consumption of aliphatic hydrogen from particle surfaces. Subbituminous coal (Wyodak) oxidation proceeds via oxygen insertion into the organic substrate sequentially forming aldo/keto groups, acid groups and acid anhydride groups. At lower temperatures the amount of anhydride formation is limited to the number of adjacent insertion sites on the surface of the coal particles. Above ca. 200°C the precursor acidic entities become mobile enough to allow them to come together and dehydrate. Above 400°C the anhydro groups predominate in the steady state production of carbon dioxide and water vapor. These studies show the merits of in situ real time DRIS for the extensive definition of the chemistry and structure of coal surfaces and interfaces (Fuller, 1988).

▪ Grinding of Bituminous Coals: Exposure of bituminous coal (Bruceton, PA) by grinding in neutral media (air or liquid water) does not alter the surface chemistry of the particles. In liquid water the fracture is more complete, producing a smaller particle size distribution. Grinding in alkaline media (i.e., 1 N NaOH) modifies the surface chemistry and structure of the coal particles. The process involves the incorporation of carbon dioxide by a Kolbe-Schmidt type of direct insertion into the phenolic components on the coal surfaces. The amount of hydrogen bonded hydroxyl is enhanced by grinding in alkaline media due to the additional hydrolysis of surface entities. In addition the clay mineral component of the bituminous coal is reduced below the detection limits by the alkaline media. More details are available (Fuller, September 1989).

▪ Argonne Premium Coal Sample Suite: The Argonne sample suite supplies the research community with a well documented set of samples that covers the wide range of maturation (lignite to low volatile bituminous) encountered in the U.S. coal reserves. The chemical compositions of the powdered samples have been measured nondestructively by DRIS without exposure to atmospheric vapors. The technique gives independent measures of relative amounts of (1) clay (illitic, kaolinitic, etc.), (2) aromatic C-H content, (3) aliphatic ($-CH_3$,$=CH_2$, and $=CH$), (4) aldehydic C-H, and (5) carbonyls (ketones, aldehydes, acids, anhydrides, carbonates, etc.). In addition, details of the complex hydrogen bonded ($-O-H\cdots O=$) structures are elucidated by DRIS to a degree not achieved by any other technique. Furthermore, DRIS data provide an excellent maturation (ranking) index of coals. Additional information is available (Fuller et al., September 1989; Fuller, September 1989; Fuller, December 1989).

▪ Grinding of Subbituminous Coal: Coal preparation techniques, used to provide feedstocks for direct utilization in combustion facilities, require extensive grinding. Separation of noxious elements (mineral matter, sulfur, nitrogen, etc.) is facilitated by grinding. Current and future needs for clean air require that more complete separation be carried out. Chemical cleaning processes can be combined and carried out simultaneously by incorporation of chemicals in the grinding media. The Powder River fields represent a significant portion of the reserves of coal. This is primarily subbituminous coal with a relatively low sulfur content. Most of this coal is near the surface in a rather flat terrain where mining is easy and restoration is not difficult. This work has shown that the argillic mineral matter hydrolyzes in aqueous grinding media and the hydrolyses are markedly enhanced in alkaline media. Direct incorporation of carbon dioxide is accomplished in the alkaline media to form ketone and acid salt groups on the surface of subbituminous coal particles. Diffuse reflectance infrared spectroscopy has been shown to be an excellent aid in defining the chemical and physical changes induced in the grinding processes (Fuller, June 1989).

E. SURFACE AREA AND POROSITY:

Gas adsorption methods provide detail relating to morphology of coal particles that is not obtainable by any other means. An equation is derived from statistical mechanical considerations to describe the physical adsorption process on solid surfaces. This derivation is predicated on the following assumptions: (1) The surface may be described as a large potential box either with or without localized areas of high bonding energy; (2) the molecules adsorbed on the surface are completely mobile and may either skate around, over or under each other (or elastically rebound); (3) the bonding energy between a molecule in a high energy localized site and molecule in the next layer is equal to the energy of liquefaction; (4) the bonding energy of the molecules where they are in the first pysically adsorbed layer is greater than the energy of liquefaction; (5) all other bond energies between adsorbed molecules is equivalent to the energy of liquefaction (including lateral interactions); and (6) the adsorbed molecules are indistinguishable from each other. This mathematical relationship is extremely useful in that it allows the direct calculation of surface area without any arbitrary

proportionality constant. The functionality of the treatment gives rise to the autoshielding relationship, $\theta = \ln\{-\ln[P(\theta=0)/P_o]\} - \ln\{\ln[P/P_o]\}$ where P is the equilibrium pressure of adsorbate of the solid sorbent at θ monolayer equivalent coverage. The term P_o is the reference pressure of the bulk liquid sorbate at the temperature of the isotherm. Additional considerations account for first layer adsorption on specific sites (i.e., chemisorption), microporosity, mesoporostiy, defects, etc. (Fuller and Condon, 1989).

7. FUTURE WORK:

During the next period, measurements will be continued using transmission electron microscopy and ESCA to characterize the crystalline and chemical binding properties of elements in selected coals from the Argonne coal suite. In addition, micromechanical characterization measurements will be extended to additional bituminous and non-bituminous coals. DRIS analyses will be extended to include coals that are directly utilized in combustion facilities. More details will be obtained for reactions encountered in weathering and processing of these coals. Emphasis will be placed on in situ simulation of the reactions of interest. Thermogravimetric analyses will be made of the reactions of various ranks of coals to enable more comprehensive understanding of the chemistry and structure of the coals as they exist in the mines and in their processed intermediates.

8. REFERENCES:

Fuller, E. L., Jr. and Smyrl, N. R. (1985a), Chemistry and Structure of Fuels: Reaction Monitoring with Diffuse Reflectance Infrared Spectroscopy, in Chemical, Biological, and Industrial Applications of Infrared Spectroscopy, edited by James R. Durig, Wiley-Interscience.

Fuller, E. L., Jr., and Smyrl, N. R. (1985b), Chemistry and Structure of Coals: Diffuse Reflectance Infrared Spectroscopy Equipment and Techniques, Fuel **64** 1143.

Fuller, E. L., Jr. (1988), Diffuse Reflectance Infrared Spectroscopy Studies of the Air Oxidation of Coal Surfaces, Proc. Symp. Coal Surfaces, Div. Fuel Chem. ACS **33** 691.

Fuller, E. L., Jr. (June 1989), Evaluation of Coal Chemistry and Structure by Diffuse Reflectance Infrared Spectroscopy, ACS Colloid and Surface Science Symposium, Seattle, WA, oral presentation.

Fuller, E. L., Jr., and Condon, J. B. (1989), Statistical Mechanical Evaluation of Surface Area from Physical Adsorption of Gases, Colloids and Surfaces **37** 171.

Fuller, E. L., Jr., Kopp, O. C., and Cathcart, J. V. (June 1989), Evaluation of the Colloid and Surface Properties of Coal Macerals: Microphysical Properties, ACS Colloid and Surface Science Symposium, Seattle, WA, oral presentation.

Fuller, E. L., Jr., et al. (September 1989), Chemical and Morphological Analyses of the Argonne National Laboratory Premium Coal Samples, ORNL report, in preparation.

Fuller, E. L., Jr. (September 1989), Chemistry and Structure of Coals: Effects of Grinding Media on a Subbituminous Coal, ORNL report, in preparation.

Fuller, E. L., Jr. (December 1989), Diffuse Reflectance Infrared Spectroscopic (DRIS) Analyses of the Argonne Premium Coal Sample Suite, oral presentation, Pacific Area Chemical Societies Meeting.

Harris, L. A., Yust, C. S., and Crouse, R. S. (1977), Direct Determination of Pyritic and Organic Sulfur by Combined Coal Petrography and Microprobe Analysis (CPMS) - a Feasibility Study, Fuel **56**, Letters to the Editor.

Kopp, O. C., Fuller, E. L., Jr., and Cathcart, J. V. (1989), Micromechanical Properties of Coal Maceral Surfaces, oral presentation, 38th Annual Meeting, Southeastern Section, The Geological Society of America, April 6-7.

Session 4
Components

Chairperson: Vijendra P. Kothari

The purpose of this program is to conduct fundamental research in component development, which is crosscutting in nature and would develop ideas to the proof-of-concept stage. The work will be directed so that it has an application to fossil energy line programs. The research most likely will cut across several scientific disciplines, exploring innovations in other areas that apply to fossil energy technology. Developing commercially viable technologies to allow the substitution of coal for petroleum and natural gas requires significant improvements in the current base engineering knowledge of components. Components for efficient and reliable systems that can operate without failure are lacking in many coal conversion and utilization applications. Difficulties in handling and transporting coal, coal-liquid mixtures, and liquids derived from coal are a specific challenge to the cost-effective operation of coal conversion and utilization systems. In this session, two areas of research are discussed:

- Fluid friction control devices to eliminate erosion in coal fuel environments and
- Ash letdown with Gravel Bucket device.

FLUID FLOW CONTROL DEVICE

1. CONTRACT NUMBER: DE-AC21-88MC24217

   CONTRACTOR: General Applied Science Laboratories, Inc.
   77 Raynor Avenue
   Ronkonkoma, New York 11779
   (516) 737-6100

   CONTRACTOR PROJECT MANAGER: Martin Novack

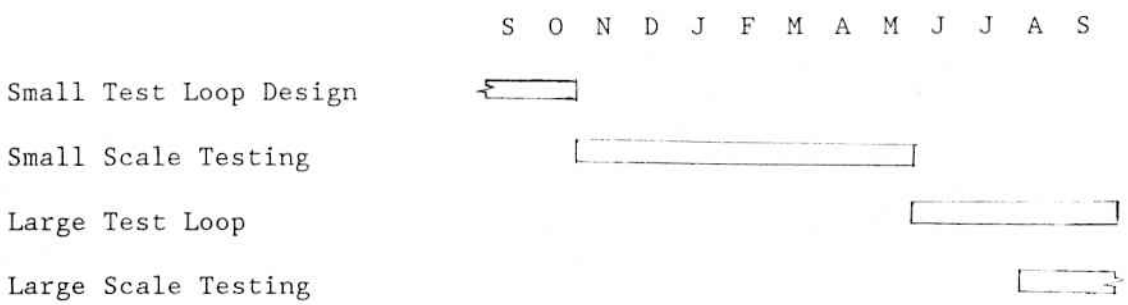
   PRINCIPAL INVESTIGATOR: Martin Novack

   METC PROJECT MANAGER: Thomas Dorchak

   PERIOD OF PERFORMANCE: March 1988 to March 1990

2. SCHEDULE/MILESTONES:

1989 FY Program Schedule



3. OBJECTIVES:

The objectives of this research program are to further develop a fluid friction control device (FFCD) for pressure reduction applications encountered in coal conversion and other processes at temperatures up to 1800°F and pressure up to 750 psig. The research is expected to improve the performance and reliability of the design and to further understand possible failure modes.

In order to increase the potential for the FFCD technology to be transferred to the private sector, an agreement shall be made with a valve manufacturer, with a strong marketing group, to obtain their perspective and input and to seek out markets for the FFCD and undertake production when market conditions are favorable.

4. BACKGROUND:

In a previous project sponsored by DOE/METC, an innovative laboratory-scale fluid friction control valve developed for pressure reduction service in coal conversion plants underwent development testing in a proof-of-concept test loop. The results of that project showed that the valve offered a potential solution to the problems of conventional control valves in these plants.

Conventional control valves normally used in coal conversion plant pressure letdown applications are subjected to high pressure - high temperature service in an environment leading to valve erosion and corrosion. In particular, erosion may be quite rapid since the valves must withstand the pressure reduction which usually takes place in a single-step throttling process in which energy within the fluid (gas) is rapidly released in the form of kinetic energy. The high velocity of fluid, with entrained solids that impinge upon valve surfaces, leads to the rapid erosive wear.

The FFCD is designed to dissipate friction induced energy losses uniformly over an extended surface flow path, and thus eliminate pressure reduction taking place in a single-step process. This feature of the FFCD, in which fluid velocity is reduced, has the potential of minimizing or eliminating the aforementioned problem associated with a conventional control valve when subjected to coal conversion plant pressure letdown conditions.

The principal of the FFCD is illustrated in Figure 1. Specifically, in this valve sketch shown for illustrative purposes, the solids/fluid mixture velocity is controlled in a flow path consisting of a helical groove machined into a traversing elongated valve stem. Other configurations employing the same principle, however, can also be used for these applications. Replaceable valve stems with both a constant, and subsequently an increasing (ramp) flow area in the direction of the flow have been used in prior tests. The stem is located within an outer tube shell (valve body) and can be positioned by a linear motor drive system, so as to be partially or fully engaged in, or retracted out of the fluid stream representative of a coal conversion process. While in the engaged position, the fluid is subject to a long tortuous flow path formed by the helical groove.

5. PROJECT DESCRIPTION:

The specific tasks required to accomplish the project goals are as follows:

- Small Test Loop - Modify existing test apparatus to enable testing of a small-scale FFCD.

- Small-Scale FFCD Fabrication and Testing - Valve to operate over a range of test parameters. Manufacturing and marketing considerations shall be included in a topical report.

- Large Test Loop - Design and construct a larger test loop for testing a scaled-up FFCD.

- Scaled-up Valve Fabrication and Testing - Fabricate and test a larger FFCD, incorporating the best design techniques developed from prior testing. Provide for technology transfer.

The primary technical effort is to design, build and test controllable FFCD's based on the aforementioned "tortuous path" friction method for pressure reduction of a particle laden test gas.

First, an analysis and computer program are used to calculate candidate FFCD flow passageway configurations, pressure drops and test gas flowrates under the varying conditions called for in the project test plan. A valve flow turn-down ratio of 4:1 is required while the upstream loop inlet pressure is maintained at a constant pressure. An existing test loop has been modified to enable testing of a small-scale FFCD subjected to particle laden test gas flow conditions of up to 1800°F and 800 psig.

The test loop can be described here by referring to Figure 2. Test gas, e.g., nitrogen, coming from a regulated pressurized supply source is heated in a hot air driven heat exchanger to 1200°F and then routed through an electric heater where it is further heated to 1800°F. To introduce abrasive particles into the test gas stream, a slurry mixture with 10 percent solids, by weight, is drawn from a mixing tank and pumped to pressures of up to 800 psig by means of a stroke-controlled diaphragm pump. The pumped slurry passes through a heat exchanger where it is heated and the water constituent vaporized. This mixture of abrasive particles and dry steam is then routed through a mixing chamber where it mixes with the test gas. The slurry represents only 5 to 10 percent of the total (test gas and slurry) flow rate so that the actual particle solids loading, by weight, in the gas is 0.5 to 1 percent. The abrasive solids/gas mixture is then routed through the fluid friction control device (FFCD). The FFCD is comprised of a control valve, combined with a pressure balance coil which provides the necessary pressure drop in the system to limit test gas flow when the friction control valve is wide open. After passing through the FFCD, the test gas, at a reduced pressure, is routed first through a cooler where the water in the mixture condenses, and then to a separator where the particles, in water are collected, and the test gas is vented.

The Test Program calls for parametric and endurance tests to be conducted which will simulate a wide range of flow control and pressure letdown conditions in various coal conversion processes. In particular, the FFCD will be subjected to a highly abrasive particle laden gas flow containing ash and char particulate at temperatures from 500°F to as high as 1800°F, at pressure drops up to 750 psi. Inconel alloy 625, a nickel-chromium-molybdenum alloy, has been selected for service in the valve locations subject to the high temperature gas flow.

Parametric testing is in progress in accordance with the test plan. To date, the FFCD has been subjected to test gas (air, steam and silica particles) temperatures and pressures of up to 1200°F and 500 psig, respectively, with flow turndown ratios of up to 3:1. The valve itself has operated satisfactorily without jamming or clogging for a total accumulated time of over 20 hours; however, because of intermittent operation of the high pressure particle injection system, the FFCD has

been subjected to flow with abrasive particles for approximately 10 hours. The abrasive particles used were Sil-Co-Sil 45, a ground silica which has a Moh's scale hardness of 7.

Examination of the internal surface of the valve body (tube shell) using an optical borescope indicates suspected polishing-type wear as evidenced by light reflections, in an area of active flow stream path - that is where a short section (~ 1/2 inch) of valve stem is engaged into the bore of the valve body when the valve is fully open. The valve body will be sectioned upon completion of testing to accurately measure any erosion.

Representative results of the parametric tests are presented in Figure 3 (a & b). Figure 3(a) shows the decrease in flowrate during FFCD turndown (stem engaged into valve body). Here the FFCD inlet pressure was maintained constant at 420 psig as the flow was decreased. Also shown on the same figure is a calculated theoretical curve. Corresponding test data for the FFCD inlet and outlet pressures are presented in Figure 3(b). These test results demonstrate the capability of the FFCD to provide flow control with flow turndown during pressure letdown operations. The difference in flowrate between the test data and theoretical curve is attributed primarily to bypass flow within the FFCD, and to a lesser extent, heat loss factors. Bypass flow within the FFCD results from a clearance that must be provided between the helically grooved valve stem outer diameter and the valve body internal diameter. Because of a fabrication methodology problem which occurred during construction of the valve, the "as-built" clearance was larger than designed. This resulted in a correspondingly greater flowrate during flow turndown than calculated, as the valve stem is engaged into the valve body. To a lesser extent, part of the higher than expected flowrate is attributed to heat loss factors which also arise during flow turndown. During this time there is progressively greater "overboard" heat loss from this insulated laboratory scale FFCD and test loop, which in turn leads to lower test gas temperatures with higher densities and corresponding higher flowrates as compared to the theoretical predictions.

Although the FFCD has operated without incident, both during steady state and flow turndown conditions, problems have been encountered in developing other sections of this test loop for high temperature, high pressure service. These problems included: stoppage of pumped slurry during flow turndown; poor slurry flow response to changes in the test gas flowrate; low test gas and slurry temperatures; electric heater element burnout; erosion of tubing; and other miscellaneous test loop development problems.

The stoppage of slurry during flow turndown is attributed to silica particles falling below their saltation velocities, necessary to prevent settling, in various parts of the test loop, and in particular, in the vicinity of the diaphragm pump ball check valves. Here, the particles appear to deposit on the valve seats, thereby preventing the valve balls

from seating properly. To alleviate this problem, the tube size (diameter) at the inlet and outlet of the pump and elsewhere in the slurry system was decreased to increase the slurry velocity.

The poor slurry flow response to changes in the test gas flowrate, especially during turndown is attributed to the damping action of an accumulator located in the pump discharge line which has been removed from the system. The pump discharge tubing and downstream heat exchanger coils now provide sufficient damping to the normal diaphragm pump pulsations.

As a result of poor heat transfer characteristics, the test gas preheater and slurry heating heat exchanges have been modified to increase their surface areas, and therefore their respective output temperatures.

Because of test loop tube erosion in a specific short radius bend location, an "el" fitting, with a relatively thicker wall, was installed to better withstand the erosive effects of the particle laden gas.

6. RESULTS/ACCOMPLISHMENTS:

- An existing small-flow test loop has been modified, and both parametric and endurance tests are in progress in accordance with the accepted test plan.

- The parametric tests have demonstrated the capability of the FFCD to maintain constant inlet pressure with flow turndown during pressure letdown operations with valve inlet conditions of up to 1200°F and 500 psig.

- The FFCD has thus far undergone over 20 hours of endurance testing, including approximately 10 hours with abrasive ground silica particles in the test gas.

7. FUTURE PLANS:

- Complete parametric and endurance testing on small-flow FFCD.

- Agreement shall be made with a valve manufacturer, to provide for manufacturer's input into valve design and for transfer of technology.

- Build a larger flow test loop and fabricate FFCD of appropriate scale for performance and endurance testing.

8. REFERENCES:

A Final Report of the preceding project prepared under Contract DE-AC21-88MC24217 is expected to be released shortly.

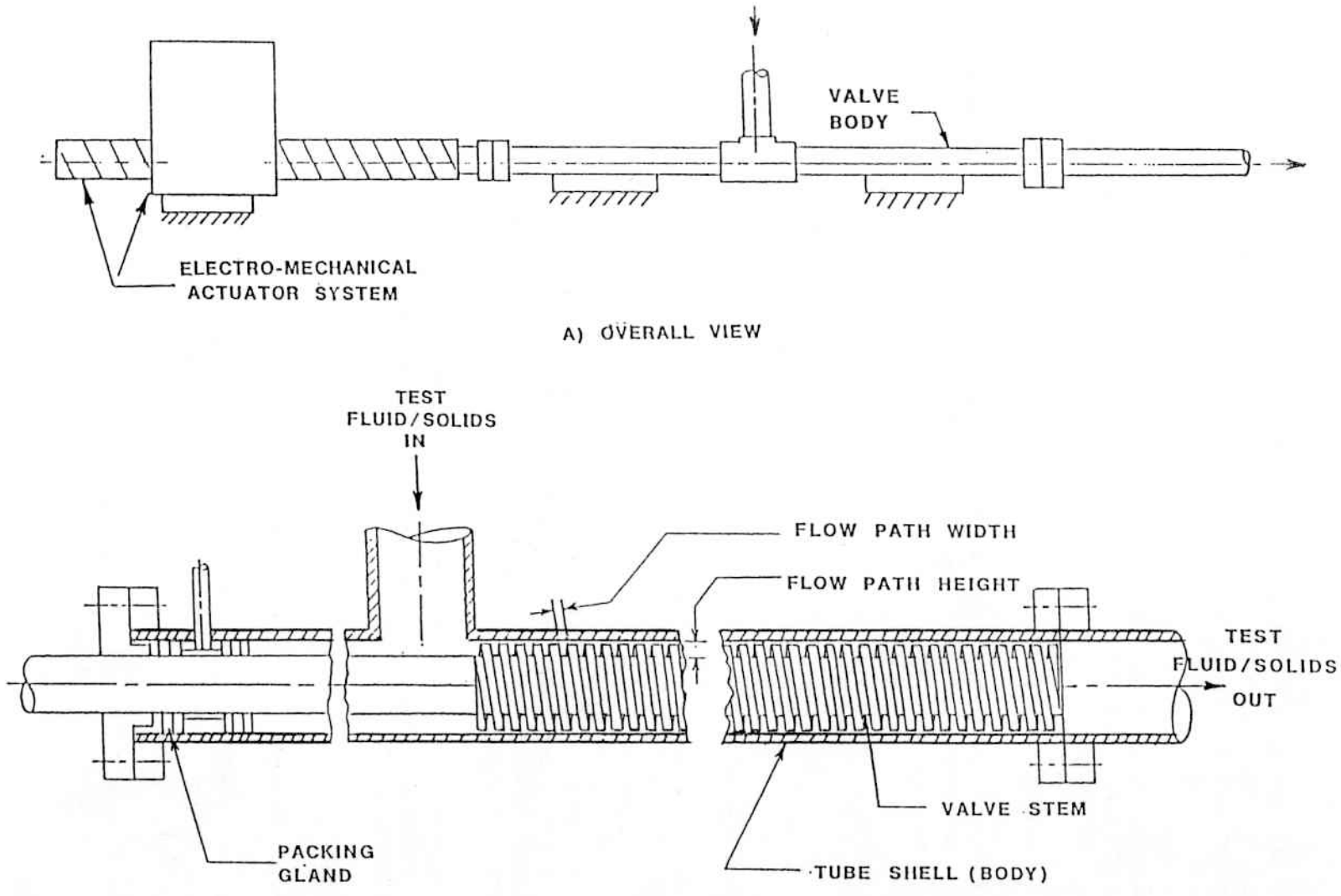


Figure 1. Conceptual Layout of Fluid Friction Control Valve Assembly

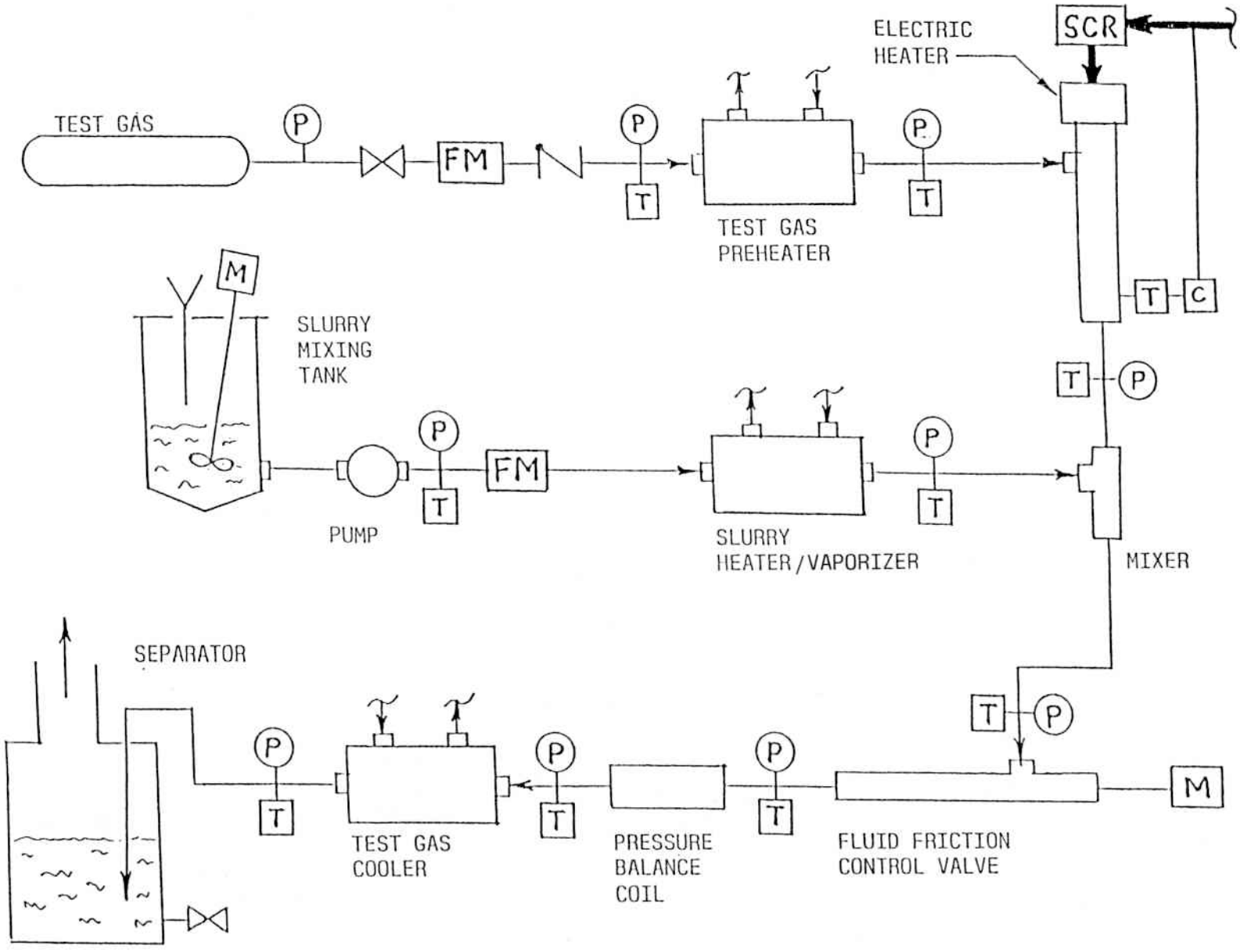
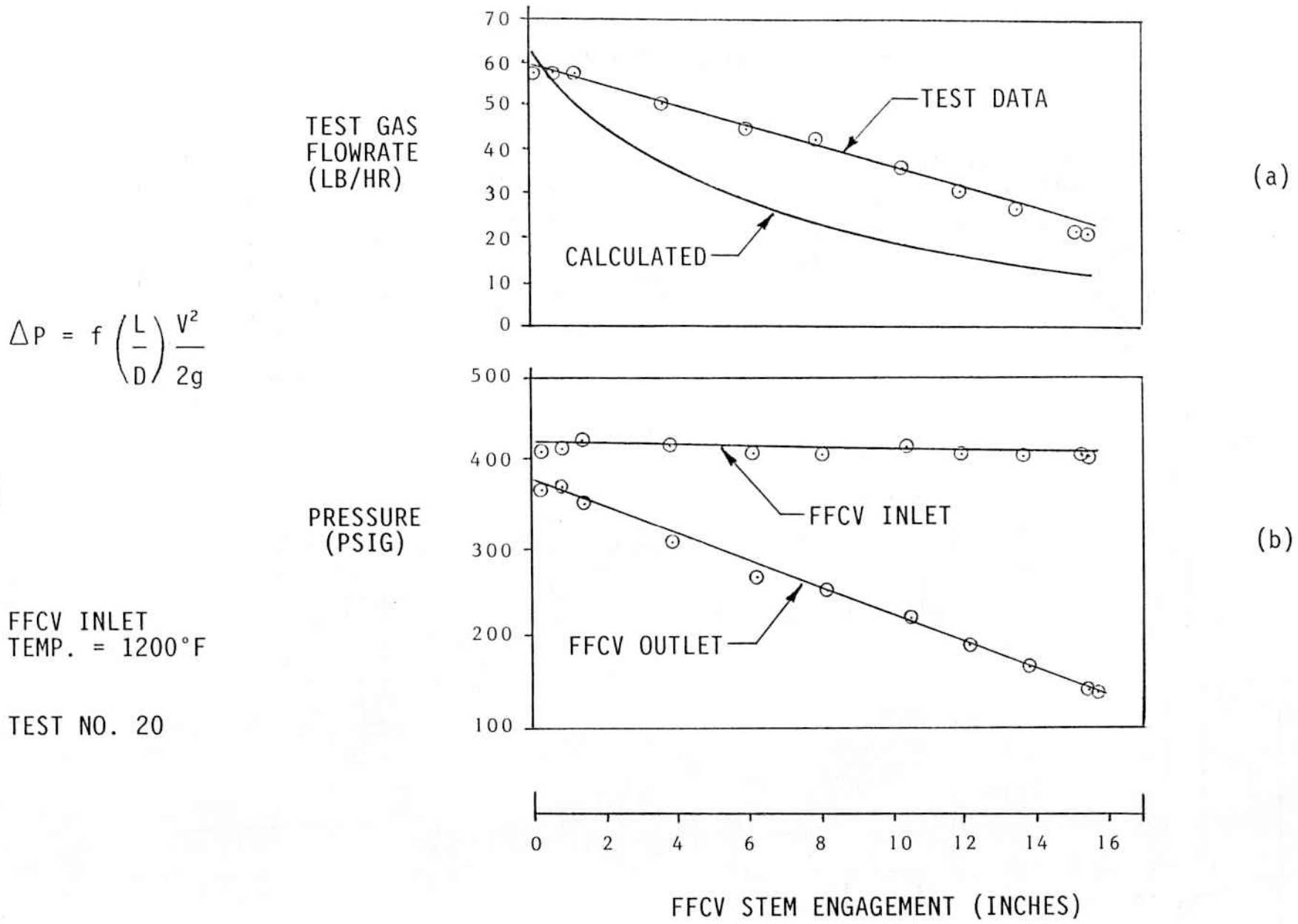


Figure 2. Test Flow Loop



$$\Delta P = f\left(\frac{L}{D}\right)\frac{V^2}{2g}$$

FFCV INLET
TEMP. = 1200°F

TEST NO. 20

Figure 3. Typical Flow Turndown Test Results

VALVELESS ASH REMOVAL FROM PRESSURIZED FLUID-BED COMBUSTION SYSTEMS

1. CONTRACT NUMBER: DE-AC21-89MC25151

CONTRACTOR: University of North Dakota
Energy and Mineral Research Center
Box 8213, University Station
Grand Forks, North Dakota 58202
(701) 777-5000

CONTRACTOR PROGRAM MANAGER: William B. Hauserman

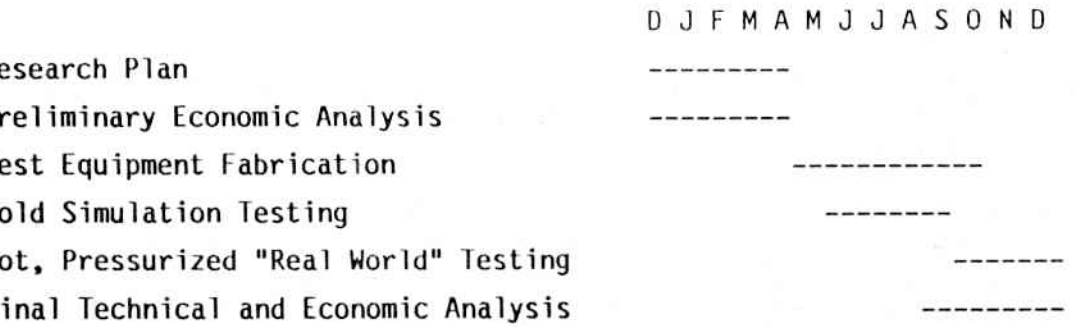
PRINCIPAL INVESTIGATOR: William B. Hauserman

METC PROJECT MANAGER: Thomas P. Dorchak

CONTRACT PERIOD OF PERFORMANCE: December 1, 1988 to December 1, 1989

2. SCHEDULE/MILESTONES:

1989 Program Schedule



3. OBJECTIVES:

The objective of this project is to demonstrate that hot ash can be removed from a pressurized fluidized-bed combustion (PFBC) system through a column of cheaply replaceable, coarsely crushed rock, in place of expensive, erosion-prone letdown valves. It is a further objective to predict the economic advantage of such a "gravel bucket" letdown device over a conventional lockhopper system, in which a major operating expense is the replacement of valve trim.

4. BACKGROUND STATEMENT:

This project will test an extension of the "gravel bucket" principle (Hauserman 1987, Johnson 1987) in which an erosive, high-pressure slurry passes through a bed of crushed rock with an adjustable flow path and cross-sectional area. The concept was inspired by the valve erosion problems of coal liquefaction plants. Valve erosion incurred in getting either a slurry or gas-borne solid out of any pressurized coal conversion or combustion system will be the major maintenance expense. This project extends the gravel bucket approach to removing solids from PFBC systems. If successful, a hot-gas gravel bucket could offer an economic alternative to a lockhopper plus a pair of expensive block valves.

Of several suggested options, research to date has identified the upward-flow, reverse fluidized-bed, as a preferred design concept. Ash-bearing gas flows upward through crushed rock, which is supported against a perforated plate when the pressure drop through the bed exceeds the bed's weight and the superficial gas velocity exceeds the terminal settling velocity of the largest particles. Thus the pressure drop through the packed bed can greatly exceed the bed weight, enabling the use of a much smaller volume of rock than would be needed to provide the same pressure drop by a packed or fluidized bed held down by gravity. If the bed becomes plugged, the flow decreases and aerodynamic forces supporting the bed decrease, allowing the bed to expand downward, releasing the impacted ash.

Figure 1 shows how increasing gas velocity through a packed bed leads first to fluidization as the pressure drop exceeds the bed's weight. Assuming free particle mobility, as flow increases, greater portions of material are packed against the perforated ceiling as the gas velocity passes the terminal settling velocity of successively larger packing particles.

The effective fluid density is that of the gas plus all entrained solids fine enough to pass freely through the packing. This includes the ash to be removed from the system as well as packing reduced in size by either erosion or tumbling action.

A theoretical model consists of either Leva's or Ergun's equations (Leva 1959) relating flow and pressure drop through a packed bed to design parameters, enabling computation of the point of incipient fluidization (a) and terminal settling velocities of the smallest (b) and largest (c) packing particles (see Figure 2, which shows a P(F) plot for a particular set of assumed conditions).

The higher the solids loading, the less gas will be needed to remove the required ash flow from a PFBC boiler. The smaller the required gas flow, the smaller the gravel bucket cross-section need be. Solids loadings of up to possibly 80% have been briefly observed.

A close approach to reverse fluidized-bed behavior has been observed in a slagging, fixed-bed gasifier (Hauserman 1983, Hauserman 1984) in which a massive bed of coarsely crushed coal, partially plugged with fine dust generated by thermal and mechanical attrition, bridged in the upper portion of the gasifier. This occurred at pressure drops of slightly below the weight of the bed, which was partly supported by wall friction. The bridged bed would periodically collapse, indicated by an abruptly decreased pressure drop.

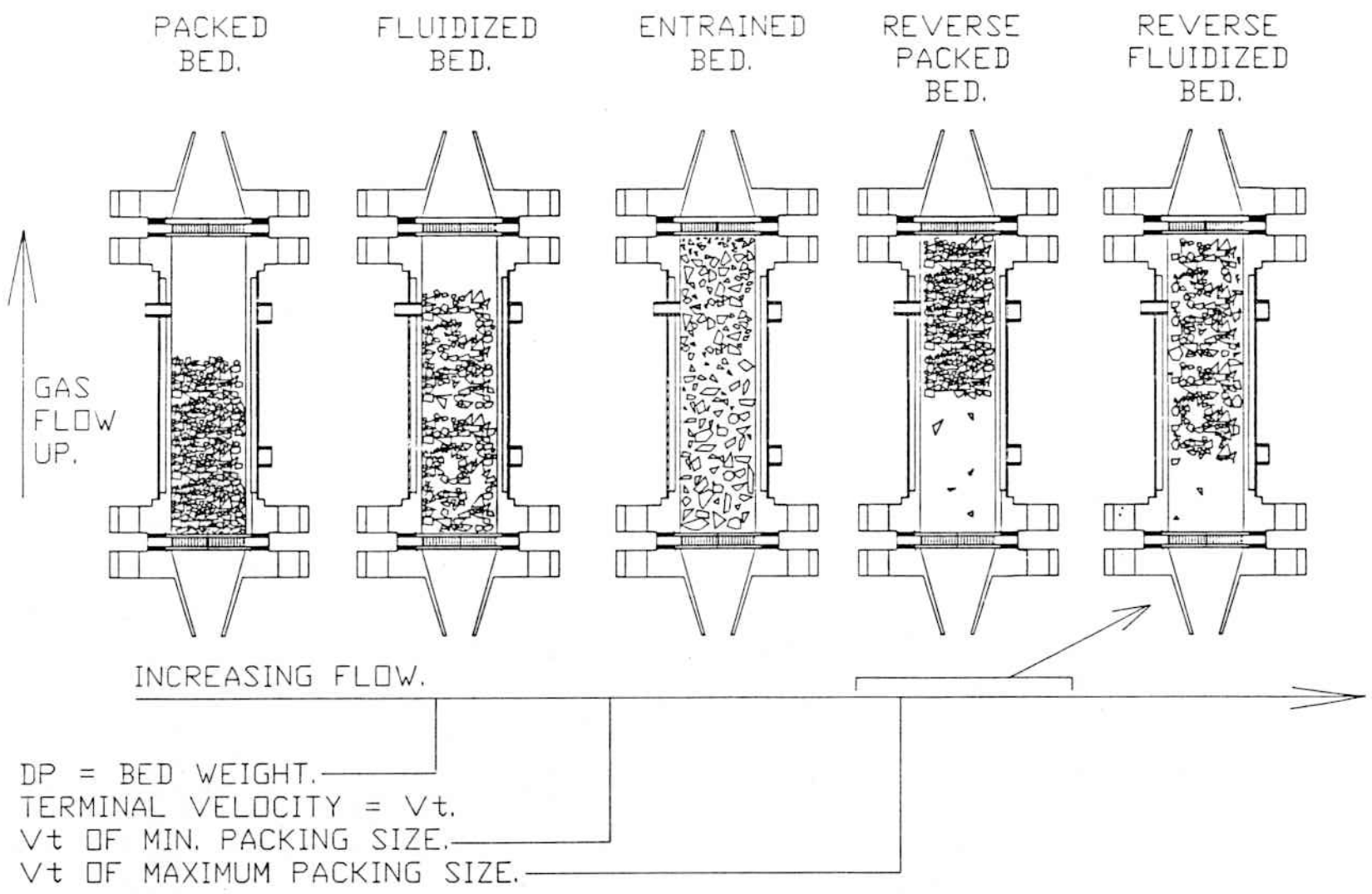


Figure 1. Packed Beds at High Flows.

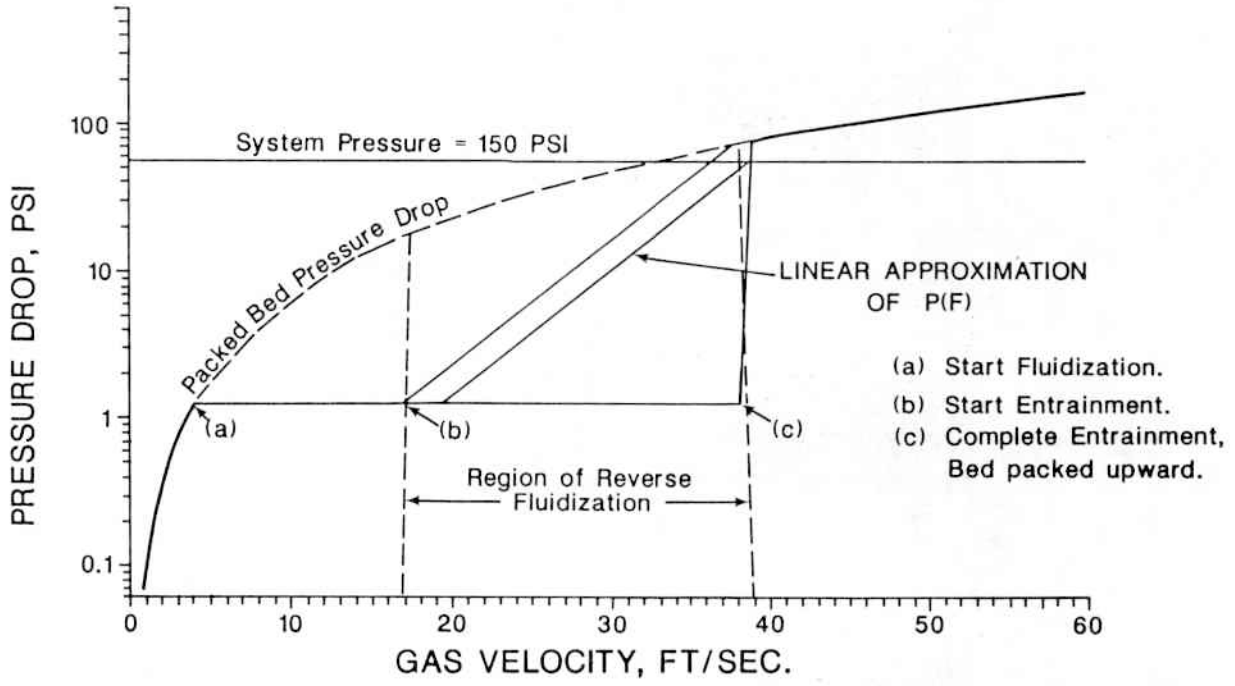


Figure 2. Reverse Fluidization.

A conceptual schematic of a gravel bucket ash letdown system is shown in Figure 3. While more complex than a lockhopper with two valves, its economic rationale is that the vessel will be smaller and the only valves in the system will not be subject to severe erosion, and thus amortized as long-term capital items. Based on operating data, lockhopper valves are replaced frequently, adding a major maintenance cost to the total annualized operating cost. The key factor in a final economic comparison will be the cost and useful life of acceptable, "conventional" valves.

5. PROJECT DESCRIPTION:

This project consists of two phases. The first, partially covered by this report, is a cold simulation study, using flows of air at ambient temperature and relatively low pressures carrying fine sand through packed beds in columns of clear plastic pipe, to qualitatively observe and confirm the phenomena described above. Flow and pressure drop data will be used to refine the mathematical model as a design basis for gravel devices at higher pressures and temperatures. The experimental apparatus is shown in Figure 4. It is a modified part of EMRC's circulating fluidized-bed simulation system.

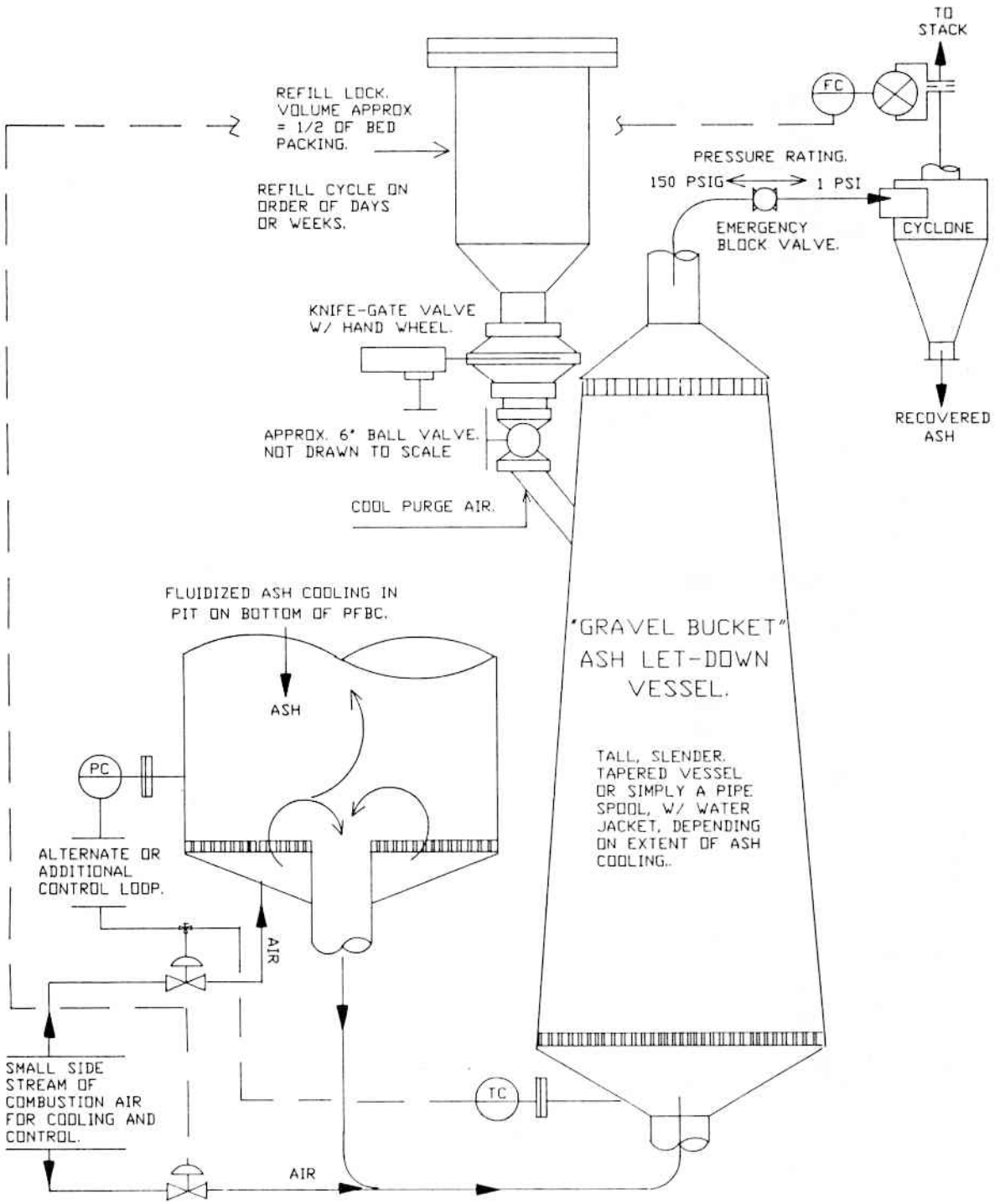


Figure 3. Valveless Ash Letdown System.

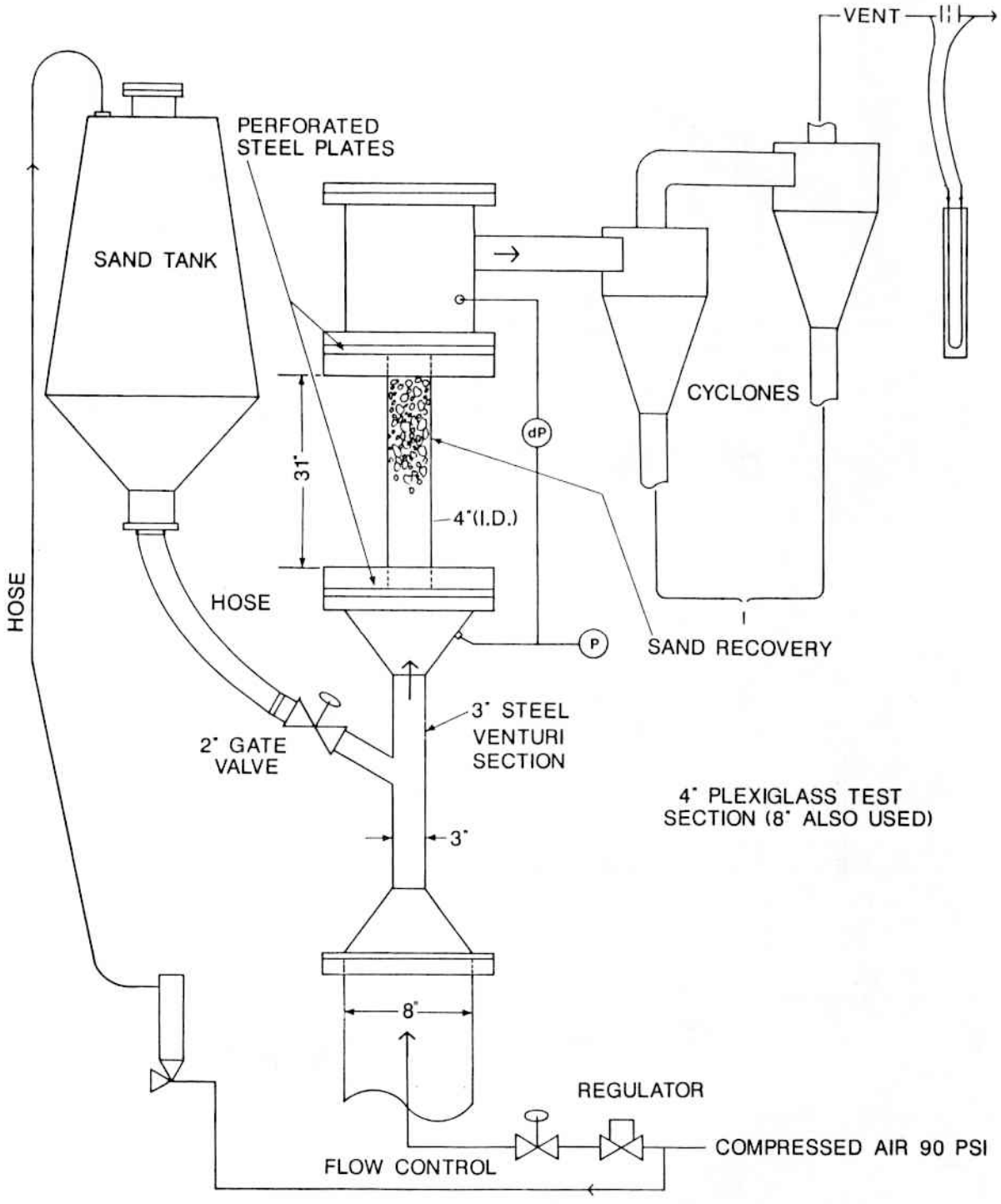


Figure 4. Gravel Bucket Simulator.

As the second phase, a test unit will be designed to accommodate actual PFBC ash letdown conditions of 150 psi and temperatures from 500°F to possibly 1500°F. It will be tested as an attachment to EMRC's pressurized combustion simulation system, designed primarily to characterize coal-derived and slurry fuels for gas turbine applications. To provide a stream of hot ash at PFBC pressures, a dense slurry of coal ash will be injected into the combustion zone, while burning natural gas or fuel oil to maintain the desired pressure and temperature. The reheated, entrained ash will be collected in a hot, high-pressure cyclone and discharged through the letdown device, essentially as shown in Figure 3.

Also included in this project is a study to quantify all letdown-related, annualized costs to define an economic window to allow the cost of a gravel bucket system or any other alternative ash letdown concept.

6. RESULTS/ACCOMPLISHMENTS:

Cold simulation tests have covered pressure drops of up to 10 psi and 240 cfm in a 4-inch-diameter test section for the following bed materials at depths of 11 to 30 inches.

	Size, inches	Specific Gravity	Sphericity	Void Fraction
Ceramic spheres:	1/4	2.36	1.0	0.393
	1/2	2.36	1.0	0.419
	3/4	2.36	1.0	0.442
Limestone:	1/2 to 1	2.36	0.7*	0.548
Porous lava:	1/4 to 1	1.50	0.5*	0.560

*Rough estimates.

A plot of pressure drop against air flow for 3/4" spheres in a bed depth of 11 inches with air alone is shown in Figure 5, compared with the calculated pressure drop for the same packed bed, from the mathematical model, using Ergun's equation. Note that, following a slight decrease in slope at initial fluidization, there is no major discontinuity, as predicted in Figure 2, but increasing portions of the bed merely shift to the upper end of the column, still in a packed condition. This indicates that the form of a predictive or design equation will be essentially the same as for packed-bed pressure drop. The observed pressure drop is substantially lower than predicted by theory, by an amount that increases with decreasing packing size. In addition to wall effects, this deviation is attributed to a higher void fraction in the uncompacted, air-supported beds than exists in firmly settled samples during liquid displacement tests.

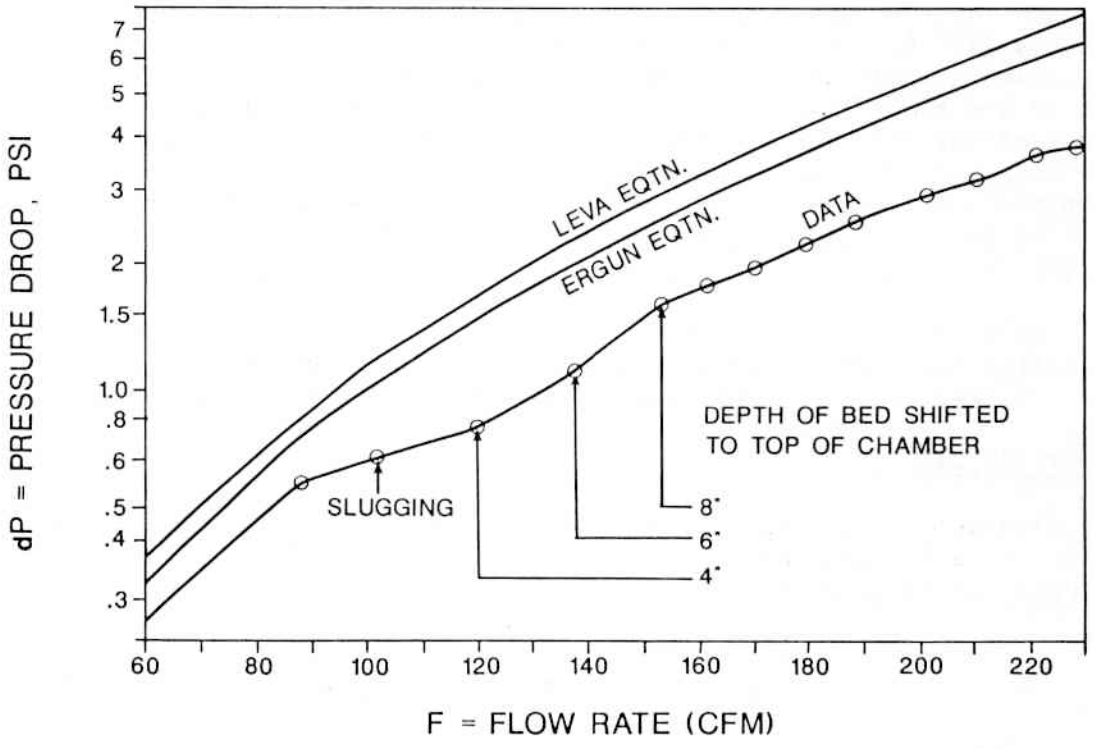


Figure 5. Example of dP(F) Data.

Ceramic spheres offer known sphericity and approximate void fraction to check theory against data. During sustained operation, it is expected that crushed rock in a gravel bucket letdown device will approach unity sphericity due to tumbling action. The lava rock was selected to observe the effects of a significantly different specific gravity. Sphericity for limestone and lava were estimated visually, while their void fraction was measured by liquid displacement. Pressure drop is extremely sensitive to both of these parameters, as well as to solids loading. As with the spheres, data for limestone and lava indicate a fair correlation of form with the simple packed-bed prediction, though with more random irregularities, as expected. Theoretical prediction shows excellent to very poor correlation with data, depending upon apparently minor variation in assumed values for sphericity and void fraction.

7. FUTURE WORK:

The cold simulation portion of the project, as defined above, is essentially complete, and design efforts are underway on a test unit to pass hot ash under actual PFBC conditions. Parallel to this project, though not a part of it, design efforts are underway on modification of the pressurized combustion system.

8. REFERENCES:

Hauserman, W.B. and M.D. Johnson. Use of Cheap, Sacrificial Materials for Valve Trim in Erosive Slurry Applications. Final Report, Project DE-AC21-85MC22109, April 1987.

Johnson, M.D. and W.B. Hauserman. Use of Cheap, Sacrificial Materials for Valve Trim in Erosive Slurry Applications - 2: The Gravel Bucket Valve. Second Interim Report, Project DE-AC21-85MC22109, April 1987.

Leva, Max. Fluidization, McGraw-Hill, 1959.

Hauserman, W.B. and W.G. Willson. Mechanical Problems in the Design of a Fixed-Bed, Slagging Gasifier. ASME Energy-Sources Technology Conference and Exhibition, Jan. 30-Feb. 2, 1983, Houston, Texas.

Hauserman, W.B. Structural Properties Affecting the Settling of Coarse Crushed Coal in Gasifiers. ASME Energy-Sources Technology Conference and Exhibition, Feb. 12-16, 1984, New Orleans, Louisiana.

Sessions 5A, 6A, 7A, AND 8A
Mineral Matter Behavior

Chairpersons: Philip M. Goldberg
Mahendra P. Mathur

Experimental and theoretical progress made during the past year in the areas of fragmentation and transformation is discussed, and mechanisms for mineral grain transformation are postulated. Overall goals of this effort are to develop a qualitative and quantitative understanding of the processes occurring during coal mineral matter transformations (to residual ash, aerosols, and vapors) in an environment typical of that found during pulverized coal combustion, and to develop a tractable mechanistic model capable of predicting the observed features of the overall mineral matter transformation process.

Information crucial to understanding the overall mineral matter transformation processes, such as the observed behavior and interactions of major minerals, the formation of residual ash and aerosols, and deposition tendencies, is presented.

TRANSFORMATION OF INORGANIC COAL CONSTITUENTS IN COMBUSTION SYSTEMS

1. CONTRACT NUMBER: DE-ACC22-86PC90751

CONTRACTOR: PSI Technology Company
A Division of Physical Sciences Inc.
20 New England Business Center
Andover, MA 01810
(508) 689-0003

CONTRACT PROJECT MANAGER: Dr. Arthur A. Boni
PSI Technology Company

PRINCIPAL INVESTIGATORS: California Institute of Technology
Prof. Richard C. Flagan

Foster-Wheeler Development Company
Mr. Richard W. Bryers

Massachusetts Institute of Technology
Prof. Adel F. Sarofim and Janos M. Beer

University of Arizona
Prof. Thomas W. Peterson and Jost. O.L. Wendt

University of Kentucky
Prof. Gerald P. Huffman and Frank E. Huggins

PSI Technology Company
Dr. Joseph J. Helble and Srivats Srinivasachar

PETC PROJECT MANAGER: Philip M. Goldberg

PERIOD OF PERFORMANCE: 30 September 1986 to 25 December 1989

2. SCHEDULE/MILESTONES:

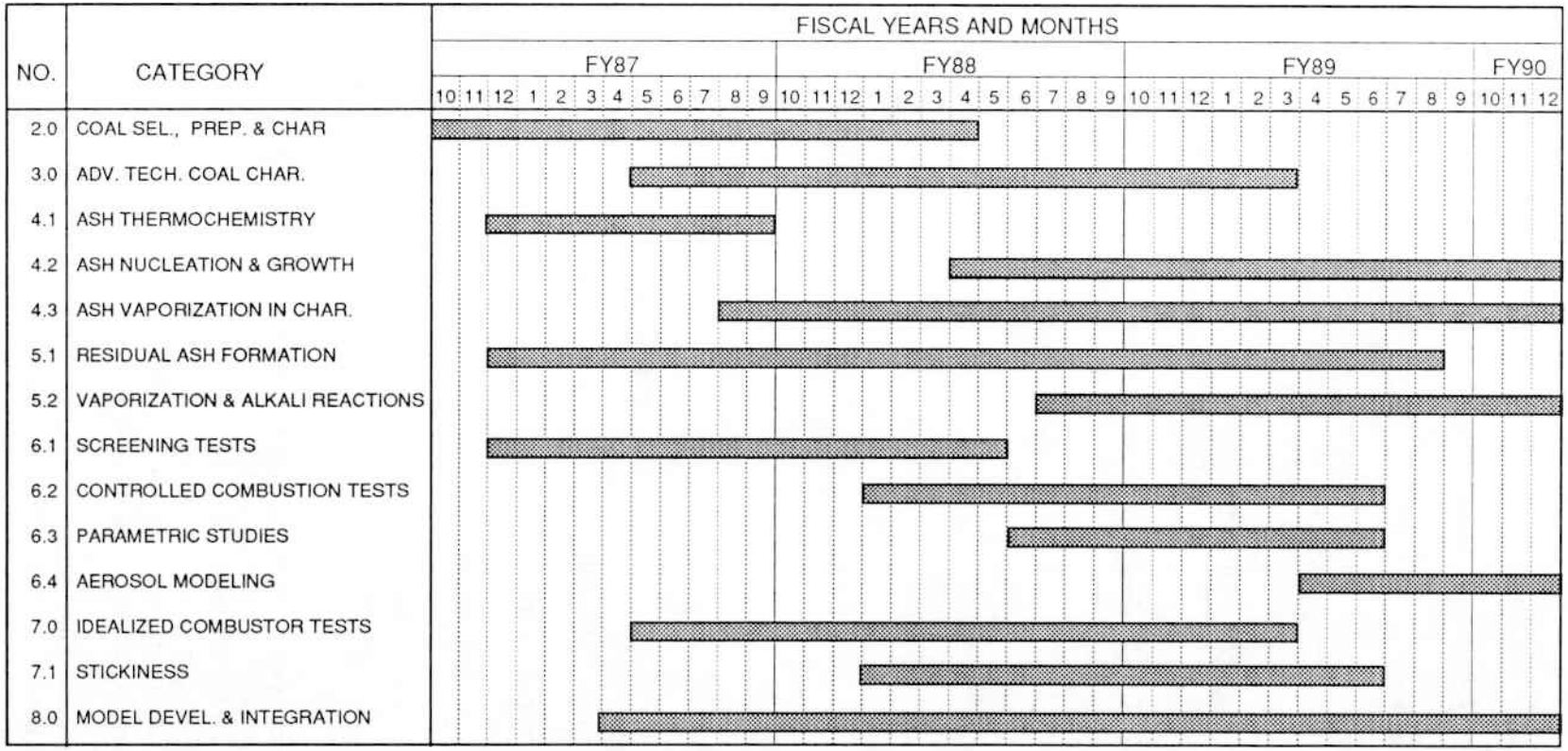
See schedule on next page.

3. OBJECTIVES:

The objectives of the project are as follows:

- elucidation and quantification of the physical and chemical processes that occur in an environment typical of pulverized coal combustion, and which control the partitioning of coal mineral constituents among products (residual ash, aerosols, and vapors).

- chemical and physical characterization of the coal, its intrinsic, included, and extraneous mineral forms, and the spectrum of ash-related products in detail.


NO.
CATEGORY
FISCAL YEARS AND MONTHS
FY87
FY88
FY89
FY90
10 11 12 1 2 3 4 5 6 7 8 9 10 11 12 1 2 3 4 5 6 7 8 9 10 11 12 1 2 3 4 5 6 7 8 9 10 11 12
2.0 COAL SEL., PREP. & CHAR
3.0 ADV. TECH. COAL CHAR.
4.1 ASH THERMOCHEMISTRY
4.2 ASH NUCLEATION & GROWTH
4.3 ASH VAPORIZATION IN CHAR.
5.1 RESIDUAL ASH FORMATION
5.2 VAPORIZATION & ALKALI REACTIONS
6.1 SCREENING TESTS
6.2 CONTROLLED COMBUSTION TESTS
6.3 PARAMETRIC STUDIES
6.4 AEROSOL MODELING
7.0 IDEALIZED COMBUSTOR TESTS
7.1 STICKINESS
8.0 MODEL DEVEL. & INTEGRATION

development of a tractable, mechanistic model capable of predicting the observed features of the mineral matter transformation process.

4. BACKGROUND:

The inorganic minerals found in all coals affect the performance of the combustion equipment in several significant ways. This inorganic material, transformed into ash during the combustion process, deposits on heat transfer surfaces and other surfaces of energy conversion equipment. These processes, referred to as slagging (if the deposit is in a molten state) or fouling (if the deposit is largely built up by condensing vapors) may lead to severe degradation of heat transfer (increased heat rate) and loss of equipment availability resulting from deposit removal. Additionally, the ash materials may cause erosion and corrosion of surfaces, also leading to increased system wear and decreased lifetime. It also has been found that a non-negligible amount of the ash is present as a fume/aerosol with particles less than a few microns in diameter and whose surfaces are enriched in trace elements. The emission of these "fine particulates" may present health concerns since they are difficult to remove with currently available particulate cleanup technology.

To better understand the transport, deposition, and emission characteristics of combustion-generated ash, it is first necessary to fully understand the factors governing the formation of ash during the combustion process. In this project, we are seeking to understand mineral transformations by testing the hypothesis that the transformation and partitioning of inorganic constituents into ash products are determined by two important features: 1) the individual mineral forms (size and association with adjacent minerals and carbon); and 2) temperature history of the gas phase environment encountered by the coal/ash particles. If this hypothesis is proved correct, then new methods for characterizing coals and their minerals, combustion testing methodologies, and slagging/fouling indices need to be developed to properly incorporate the heterogeneous nature of the coal/minerals and the combustion environment. Current methodologies, based on homogeneous/bulk properties which do not take into account the combustion characteristics, e.g., conventional ASTM ashing procedures, have been shown to be unreliable in predicting observed behavior in large-scale pulverized coal combustion systems.

4.1 ASH PARTICLE FORMATION

Two distinct ash particle size modes, one less than 1 μm and one typically centered at 10 to 20 μm, arise during combustion. As noted above, these distinct size modes may initiate different types of deposition in a boiler. In the following paragraphs, conditions giving rise to each size mode are briefly discussed within the context of this program.

4.1.1 Formation of Residual Ash (0.5 to 20^+ μm)

During the combustion of pulverized coal, the inorganic minerals associated with the fuel (e.g., quartz, illite, pyrite, kaolinite) undergo a complex series of transformations to form flyash particles. These minerals may either be included within the coal or excluded as free particles, uninfluenced by the carbonaceous matrix or by other minerals. The transformation processes experienced by these minerals include melting, water loss, outgassing of carbon dioxide (from encapsulated carbon), coalescence, fragmentation, vaporization, and chemical reaction. These processes determine the ultimate size and chemical composition of the resultant ash particles (Weingartner, 1974; Reid, 1984; Bryers, 1987; Austin et al., 1986). It is these transformed ash particles which, upon impacting heat transfer surfaces, may cause erosion if they are solid, or initiate deposition with subsequent reduction in heat transfer rates if they are molten.

For those minerals included within coal particles, the competition between fragmentation and coalescence is the most important factor in determining the final size of the residual ash particles. As the carbonaceous surface recedes during combustion, the embedded inorganic constituents are exposed. Most of the exposed matter remains attached to the carbon surface, as glassy spheres or high melting point irregular particles. The ash on the surface, as observed in microscopic studies of partially burned char particles, usually grows in size as the char surface recedes. Ash growth occurs by either the drawing together and coalescence of smaller mineral inclusions, or by the addition of the atomically dispersed elements (as they are released by the oxidation of the organic matter) to existing ash particles. The ash in a coal particle may therefore form an ash particle with a maximum mass that is governed by the total inorganic content of the coal particle, or it may form a number of smaller ash particles if char or mineral fragmentation occurs during combustion.

4.1.2 Submicron Fume Formation ($d_p < 0.5$ μm)

During pulverized coal combustion a fume of submicron particles is also formed from the inorganic species in the parent coal. Studies of the variation in chemical composition with particle size have revealed that much of the submicron fume is formed from volatilized coal ash (Flagan and Friedlander, 1978; Neville et al., 1981; Quann and Sarofim, 1982). At the high temperatures associated with the exothermic reaction of coal, volatile species (e.g., alkali metals) as well as refractory species (Si, Mg, Ca, Fe) may vaporize. Oxidation of the refractory species rapidly occurs, leading to supersaturation and a burst of homogeneous condensation. This high surface area fume grows by coagulation and by condensation of the more volatile species as gas temperatures decrease, with the net result being a fume that is submicron in scale. As these particles 1) are prone to deposit thermophoretically on tube surfaces, leading to tube fouling, and 2) may escape post-combustion cleanup equipment, it is essential that the factors governing

their formation, growth, and aerodynamic transport be understood in order to mitigate the effects of mineral matter during coal combustion.

The vaporization of the inorganic constituents in the coals depends strongly upon the composition and form of the inorganic inclusion. Detailed experimental studies to address vaporization in both synthetic and coal systems are being conducted at a variety of scales in an attempt to pinpoint the limiting factors in the process. The subsequent homogeneous nucleation of these vaporized inorganics can be described theoretically, using the classical Becker-Volmer-Doering model (Springer, 1978). Although absolute rates of new particle formation are often found to differ from theoretical predictions by many orders of magnitude, the major uncertainties in homogeneous nucleation theory are not particularly important in coal ash fumes since the volatilized species will nucleate extremely rapidly to form very large concentrations of ultra-fine particles. The nuclei then coagulate very rapidly. Hence, the absolute number of particles formed in the nucleation burst is not important in determining the dynamics of the fume some milliseconds later; no attempt at quantifying nucleation rates is therefore being made in this project. The mass of fume produced by nucleation and condensation is, however, critically important to describing the evolution of the fine particles and their ultimate fates. In many systems, this mass cannot be explained accurately from mineral thermodynamics arguments. Notably, pyrite produces a fume that has eluded mechanistic interpretation. Hence, experiments have been undertaken to unravel this puzzle.

The physical nature of the fume particles is also important. If the particles do not coalesce rapidly, the aerodynamic drag, diffusivity and collision cross sections will differ from the values assumed in the existing aerosol dynamic theory. Hence, an understanding of the coal ash fume requires the development of a generalized aerosol dynamic theory. Fundamental issues governing the structure of ash fume particles have been addressed through the use of model experimental systems.

4.2 ALKALI TRANSFORMATIONS

It is well known that the alkali species found in coals can lead to fouling of coal-fired boilers. These species, primarily sodium and potassium, are predominantly found as cation molecules bound to the organic coal matrix, or as chlorides in low-rank coals. In bituminous coals, alkali species are also bound in aluminosilicates such as illite. During combustion, the alkalis may be released into the vapor phase, where they eventually form sulfates, hydroxides and chlorides, depending on the amount of chlorine and sulfur in the system. While calculations show that the alkali appears to be primarily present in atomic form in the reducing atmosphere of the flame zone, conversion to the molecular form occurs very rapidly once an oxidizing environment is encountered. Kinetic calculations using available state-of-the-art kinetic rates performed at PSIT indicate that conversion from Na to NaCl and NaOH occurs on a time scale of tens of milliseconds; equilibrium calculations indicate that these molecular species are favored. These results

suggest that in the post-flame zone, where fouling occurs, the dominant alkali species are molecular, not atomic. Experiments to determine the levels of these molecular species arising from combustion of several coals are therefore being conducted.

The absolute amount of alkali species vaporized is also an important factor in understanding their effect on the deposition process. Neville and Sarofim (1985) found, in laboratory drop-tube studies of a Montana lignite, that the mass fraction of sodium found on ash collected via cascade impactor exhibited the size-dependence expected (D_p^{-2} in the continuum regime, D_p^{-1} in the free-molecular regime) from a condensation mechanism. They also found, however, that the extent of sodium vaporization decreased as the temperature increased, a result they attributed to the increased propensity of the Na to react with Si to form less-volatile sodium-silicates. Such behavior is consistent with the results of Wibberly and Wall (1982a, b), who used a surrogate "combustion gas" containing sodium vapor to show that, at the temperatures and the time-scales typical of pulverized coal combustors, Na could react with silica to form a sodium-silicate rich surface on existing silica particles. Later, Lindner et al. (1988) and Lindner and Wall (1988) capitalized on the sodium affinity of silicon by using clay mineral additives to "tie up" sodium in coals, thereby reducing the tenacity of the sodium-bearing deposits. Detailed experiments to unravel this mechanism during combustion of six of the program coals are currently underway.

5. PROJECT DESCRIPTION

In this integrated combustion study, eight common and uniform coals - Upper Freeport, Kentucky #9, Kentucky #11, Illinois #6 bituminous, Eagle Butte sub-bituminous, San Miguel and Beulah lignite, and Loy Yang brown - and synthetic chars are utilized to provide variations in mineral type and association. Variable temperature-time-stoichiometry histories as included in several combustion devices, scales, and laboratories (MIT, PSIT, and Arizona) are employed for testing hypotheses and obtaining data on ash partitioning. These include drop tube furnaces, idealized combustors and self-sustained combustion systems up to the 100,000 Btu/h level. Description of the process on a task by task basis is provided below.

Task 1 - Program Planning, Management, Reporting, and Peer Review

This task, performed by PSIT, consists of: 1) preparation and updating of a Program Plan; 2) overall coordination, management, and integration of the subcontractors and project results; 3) preparation of project reports; and 4) conduct of semiannual peer review/coordination meetings of the project Principal Investigators.

Task 2 - Coal Selection Preparation and Characterization

This task, performed by Foster-Wheeler Development Corp. (FWDC), consists of selecting, acquiring, preparing and distributing coals that

have desirable characteristics to permit an experimental determination of coal-related variables on mineral matter transformation and ash formation. These variables include coal type, coal and mineral size distribution, and mineral composition and its degree of association with the carbonaceous matrix. Mineral forms of importance include pyrites, illites, quartz, alkalis, and alkaline earths.

Task 3 - Advanced Techniques for Coal and Mineral Characterization

The University of Kentucky (UK) applies advanced analytical capabilities to determine the mineral forms, mineral size, and structure of coals and selected ash samples. The samples are analyzed by computer-controlled scanning electron microscopy (CCSEM), Mössbauer spectroscopy, X-ray diffraction, and X-ray Absorption Fine Structure (XAFS) spectroscopy.

Task 4 - Fundamental Studies of Selected Ash Vaporization, Nucleation, Condensation, and Coagulation Phenomena

Task 4, performed by CalTech, is a study of the vaporization, condensation, and growth of inorganic species. Studies of ash vaporization using model ash compounds to develop a quantitative data base on ash thermochemistry are conducted in various environments, in an electrodynamic balance and in a flow reactor. Experiments designed to measure the aggregate structure of coagulating particles are also conducted under this task. Modeling of these processes will include nucleation, coagulation, and condensational growth.

Task 5 - Fundamental Studies of Mineral Matter Vaporization and Residual Ash Formation

Complementary experimental and modeling studies are conducted at MIT in two areas. In the first, the MIT drop-tube furnace facility is employed to study the processes that control the size distribution of residual fly ash using both selected coals and model chars. A percolative fragmentation model is employed to describe the formation of residual ash. The second subtask has as its objective to determine the extent of vaporization of minerals contained in coals burned under simulated utility boiler conditions and to develop and test vaporization models.

Task 6 - Pulverized Coal Combustion Studies of Ash Enrichment by Volatiles and Fragmentation

The objectives of this task, performed using the University of Arizona 100,000 Btu/hr pulverized coal combustion test facility, are to develop mechanistic descriptions of the size and variation of fly ash aerosol formed from the combustion of pulverized coals under conditions of varying coal type and furnace environment. Mechanisms that determine the core and surface composition are to be elucidated. The idealized, but self-sustained, flame environment of this experiment permits an assessment of particle density and shear-field influences on ash formation. A model capable of describing the general particle distribution and composition characteristics is under development.

Task 7 - Idealized Combustion Determination of Ash Particle Formation and Surface Stickiness

In this task, PSIT employs an idealized combustion system to determine ash particle size and composition distributions for intercomparison with the dilute-phase combustion data of MIT and the self-sustained data of UA. A second phase of these experiments emphasizes the in-situ collection of ash particles and a determination of their stickiness as a function of coal variables and combustion environment, and employs pure minerals to determine stickiness ranges in idealized experiments. A final phase of this task implements a laser-based optical technique to determine the presence and concentration of gas-phase alkali molecular species in a drop-tube furnace combustion environment.

Task 8 - Model Development and Integration

By synthesizing the models developed under Tasks 4 through 6, a mineral matter transformation model capable of predicting ash particle size and composition distributions as a function of coal and combustion system variables will be produced. The information provided by this model and the experimental data base is then reduced as an engineering mineral matter transformation model that can be used to predict the distribution and nature of the ash products.

6. RESULTS AND ACCOMPLISHMENTS

6.1 COAL SELECTION AND PREPARATION

Eight coals were selected, each containing different mineral forms of the key inorganic elements responsible for slagging and fouling. The mineral-form matrix was selected to permit the determination of the transformation of various mineral forms during the process of combustion. Detailed chemical information was presented in last year's report (Boni et al, 1988); a brief summary of the selection rationale is repeated here.

Four Eastern bituminous coals were selected to evaluate the impact of pyrite form, size, and association with carbon on furnace and convective bank slagging. Although three Western coals (two lignites and one sub-bituminous) were selected for reasons other than the iron concentration, mineral forms, and carbon association, two of the lignites contained substantial concentrations of iron in mineral forms. The selection essentially extended the evaluation of differences in coal reactivity associated with differences in rank on the decomposition and transformation of pyrites. One of the coals is rich in calcium as calcite, which provides a direct comparison on the difference in thermal behavior of inorganically-bound calcium found in lignites with calcite most frequently found in bituminous coals. Three of the bituminous coals contain greater than 20 percent quartz, as determined by XRD. All four of the bituminous coals contained illite in significant concentrations.

Three Western coals were selected for varying forms and levels of concentrations of organically-bound calcium, sodium, and sulfur. It is the organically-bound mineral matter that is most responsible for fouling of convective surfaces. The Beulah, North Dakota coal from the Fort Union formation, was selected for its high sodium level, high sulfur level, and moderately high calcium level, and is also rich in pyrites by lignite standards. The Eagle Butte coal from the Powder River Basin, was selected for its high calcium, low sodium, and low sulfur levels. The increase in calcium-to-sodium and sulfur ratios should alter the type and temperature level of deposit formation. The Eagle Butte coal is rich in quartz (>40 percent), which may also alter the mechanism of deposit formation. The literature has clearly established a reduction in the decomposition temperature of $CaSO_4$ in the presence of free quartz and illite with the subsequent formation of fused calcium silicates. The third lignite was selected from the Texas lignite fields. This coal is very high in ash, and is low in calcium, present primarily as organically-bound matter. Zeolites are present in high concentrations. Loy Yang (Australian) brown coal is low in ash (2 percent) but high in Na, Cl, and Mg, and provides an ideal environment for studying the vaporization of inorganic species.

6.2 COAL AND ASH CHARACTERIZATION BY ADVANCED ANALYTICAL TECHNIQUES

Combustion products from the aforementioned coals are being investigated by computer-controlled scanning electron microscopy (CCSEM), X-ray Absorption fine structure (XAFS) spectroscopy, and Mössbauer spectroscopy at the University of Kentucky. Model compounds and coals have also been investigated after combustion treatment in drop-tube furnace tests. New CCSEM software programs have been developed for presentation of ash particle composition data in binary, ternary and quaternary phase diagrams, and extraction of particle size distributions for chosen composition ranges. XAFS spectroscopy was used to determine the structure of calcium and potassium containing phases in a variety of ash samples produced from the coals under investigation and in samples derived from drop tube furnace (DTF) experiments on pure illite and on calcium and silicon loaded sucrose chars. The melting and reaction pathways of the principal potassium and calcium phases were determined. Mössbauer spectroscopy was used primarily to determine the transformations of pyrite in DTF experiments.

In previous reports (Boni et al, 1987; Boni et al., 1988), detailed mineralogical analyses of all coals by CCSEM were presented. For these studies, the CCSEM hardware and software were similar to that used by the authors in previous work (Huffman and Huggins, 1984; Lee et al., 1978; Huggins et al., 1982). New modifications in the past year include improvements in software that allow relatively easy presentation of the composition data on a personal computer with an appropriate graphics monitor in the form of binary, ternary, and quaternary diagrams. Size distributions can also be generated for specific composition ranges. Preliminary discussions of this software have been given elsewhere (Huffman et al., 1989).

The Mössbauer spectroscopy measurements were carried out using a constant acceleration Mössbauer spectrometer and spectra analysis software (Huffman and Huggins, 1978, 1979). The XAFS measurements were conducted at both the Stanford Synchrotron Radiation Laboratory (SSRL) and the National Synchrotron Light Source (NSLS) at Brookhaven National Laboratory; experimental technique details are provided elsewhere (Huffman and Huggins, 1984). Briefly, a double crystal Si(111) monochromator was used in conjunction with a fluorescent Lytle detector. Helium pathways were constructed for the relatively soft X-rays.

The results of research utilizing these techniques have been summarized in a number of published and forthcoming papers (Huffman et al., 1989a, 1989b; Srinivasachar et al., 1989a-c; Helble et al., 1989a-c). The current discussion will briefly summarize the major results observed for each of the critical ash elements investigated.

6.2.1 Potassium

Samples of pure illite and mixtures of pure illite plus carbon were treated in DTF experiments at PSIT for various residence times. XAFS spectroscopy (near edge, XANES) clearly shows the progressive transformation of potassium from an ordered, crystalline state in illite to a disordered, amorphous glass derived from a molten aluminosilicate slag as a function of increasing residence time at a temperature of 1500 K. This is best seen from the progressive change in the potassium XANES shown in Figure 1. The spectra progress from that characteristic of illite to an XANES characteristic of K-containing aluminosilicate glass (Huffman et al., 1986). As discussed in more detail elsewhere (Srinivasachar et al., 1989b), the transformation is more rapid for illite mixed with carbon than for pure illite, presumably because the iron in illite is reduced to a ferrous state in the presence of carbon, but is ferric in the samples derived from DTF tests on pure illite. CCSEM results for both DTF ash samples and pilot scale ash samples show that there is little alteration in composition of the illite during the melting transformation.

6.2.2 Calcium

Calcium K-edge XAFS spectra of ash produced from Beulah lignite and Illinois No. 6 coal in both DTF tests and the pilot scale combustor at the Uiversity of Arizona showed that most of the calcium had been incorporated into the aluminosilicate glass phase. CCSEM measurements on the same samples showed a range of compositions for ash particles containing >80 percent of Ca + Si + Al (Figure 2), ranging from the CaO corner towards the kaolinite composition on the Al - Si boundary.

No $CaSO_4$ was observed in apparent contrast to earlier experiments (Huffman et al., 1989) in which $CaSO_4$ was found to be the dominant calcium phase in the initial layer of furnace deposits. Presumably, atmospheric and temperature conditions in the vicinity of furnace walls and tubes differ substantially from conditions existing during the

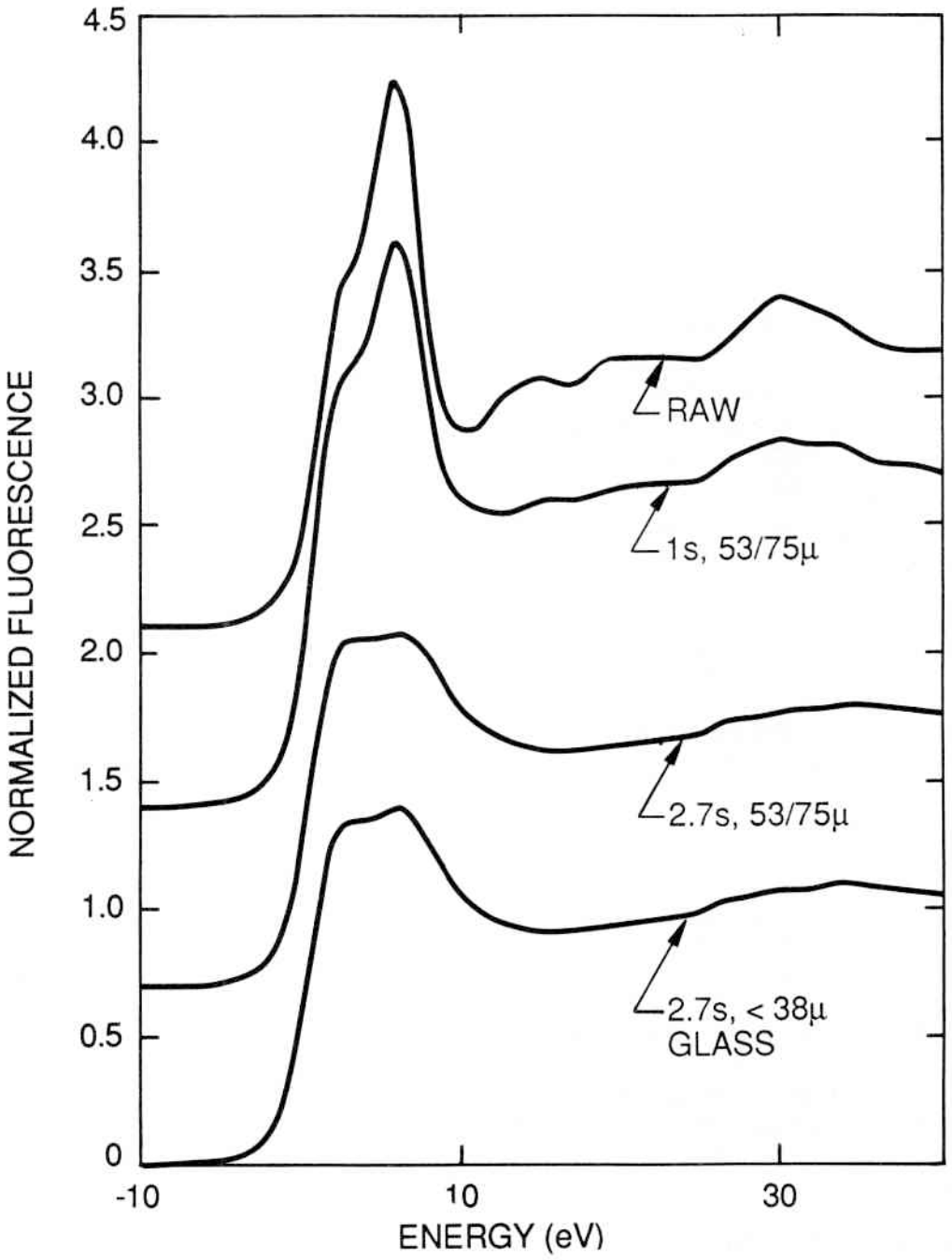


Figure 1. XANES Spectra Illustrating the Transformation of Illite to a Molten Slag with Increasing Residence Time in a DTF at 1500 K, 3 percent O_2.

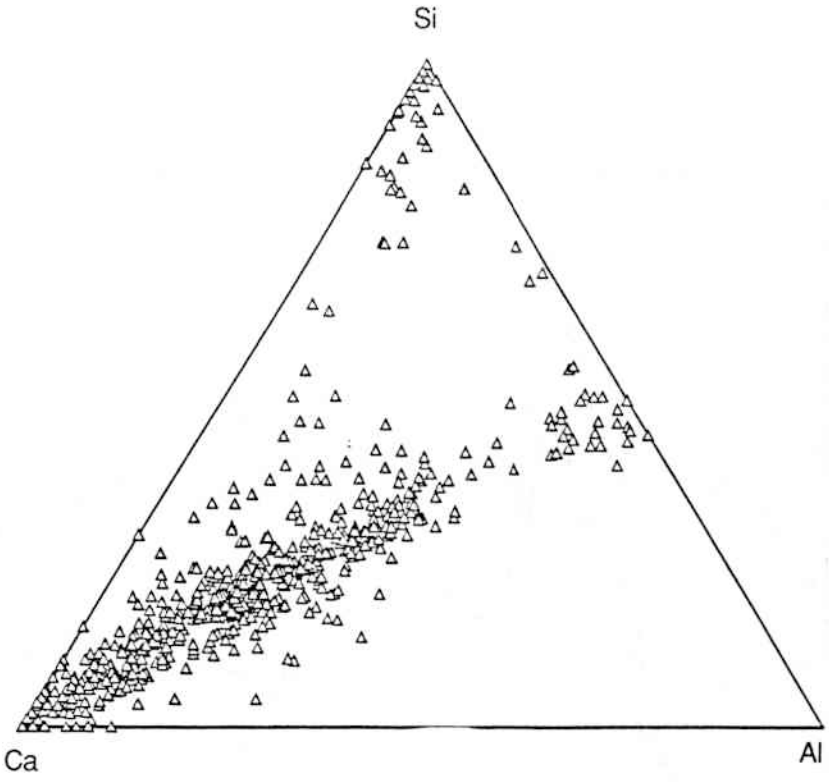


Figure 2. Ca - Si - Al Diagram Derived from CCSEM Data from a Drop Tube Furnace Combustion Experiment.

generation and collection of individual ash particles, leading to the formation of $CaSO_4$ from CaO transmitted to the walls and tubes.

6.2.3 Iron

In a previous paper (Huffman et al., 1989), the transformations of pyrite from coal subjected to DTF tests were examined by Mössbauer spectroscopy and CCSEM. Transformation to pyrrhotite followed by exothermic oxidation to magnetic yielding molten Fe-S-O particles was observed. These results were explained by a thermodynamic and kinetic theoretical treatment (Srinivasachar and Boni, 1989).

New DTF and Mössbauer experiments have been conducted to determine the transformations of pyrite in greater detail as a function of residence time and other parameters. Typical Mössbauer results are shown in Figure 3.

Mössbauer, CCSEM, and XAFS measurements are underway on the iron-bearing phases in ash samples produced from whole coals in the PSIT and UA combustors. Future studies will include the development of a combustion cell with which in-situ XAFS studies can be conducted. Further development of the phase diagram approach for analysis of CCSEM data is also planned.

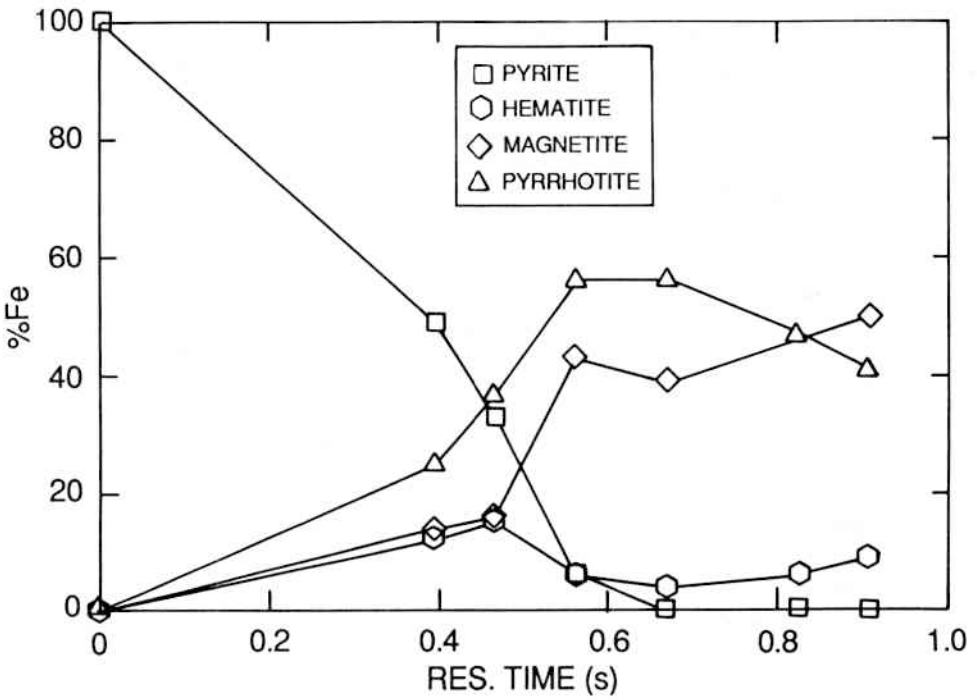


Figure 3. Iron Phase Percentages as a Function of Residence Time for Samples from DTF Tests on Pyrite (1500 K, 3 percent O_2, 75 to 90 μm).

6.3 FUNDAMENTAL STUDY OF ASH VAPORIZATION, CONDENSATION, AND COAGULATION

The experimental approach to the study of aggregate fume dynamics has been to perform controlled experiments using surrogate materials to study the evolution of refractory aerosols of known composition and properties. Aggregate particles have been characterized in terms of fractal structure through the processing of electron microscope images of the aggregate particles. The aerodynamic drag on particles has been measured directly to allow direct correlation of particle structure with particle drag. Additional experiments have been conducted using selected mineral systems relevant to ash particle formation to probe some of the processes that are responsible for the generation of fumes.

Three experimental systems have been used at Cal Tech for these studies:

- A rapid mixing isothermal reactor has been developed for use in the studies of the dynamics of ash aerosols. Volatile precursors are introduced into a hot gas flow in which they undergo rapid reaction leading to the formation of metal oxide vapors. A known mass of metal oxide fume is thus produced. Aerosol samples are extracted after different times for coagulation so that the evolution of the fume can be followed.

- An electrodynamic thermogravimetric analyzer has been used for direct observation of individual particles as they undergo reactions at temperatures ranging form 300° to 1000°C. This instrument is based upon the electrodynamic balance, a modern version of the Millikan oil-drop experiment in which a charged particle can be stably levitated. The particle is heated using a carbon dioxide laser and observed using a two-color pyrometer and a video camera.

- A drop tube furnace has been used to study fume formation during combustion or other thermal treatment of coal or coal minerals. This system is designed to react dilute suspensions of fuel or mineral at sufficient flow rates that direct observations of reaction products can be made, notably, measurements of the fume particles produced using state-of-the-art aerosol instrumentation.

6.3.1 Particle Structure Studies

Pyrogenous fumes, including soot, coal ash, and synthetic fumes (TiO_2, SiO_2, etc.) exhibit a common structure, namely agglomerates of approximately equiaxed particles (spherules) with sizes of a few tens of nanometers. The densities of pyrogenous fume agglomerates decrease with increasing size. Forrest and Witten (1979) observed that the aggregate mass varies as a power law of the size of that aggregate, i.e.,

$$m \sim r^D \qquad (1)$$

where D has been called the fractal dimension which generally has a value below the Euclidean dimension of 3.

While detailed description of the morphological structures of individual particles is impractical because of the multitude of possible shapes, the fractal scaling provides an approximate representation that can be used to correlate the essential features of these complex structures. Rogak and Flagan (1989) recently applied the method of reflections to calculate the drag on aggregate particles in the continuum fluid flow regime as a first step toward elucidating the drag on fume aggregates. Direct experimental measurements of the drag forces are needed to validate such models, particularly as one moves in to the transition regime wherein the particle size is comparable to the mean-free-path of the gas molecules and approximate solutions to the hydrodynamic equations become essential.

The dynamics of the fume aerosol have been studied experimentally using the rapid mixing isothermal reactor with a titanium dioxide aerosol generated by thermal decomposition of titanium tetraisopropoxide (TTIP) vapor. A constant vapor feed rate is provided using a syringe pump to discharge liquid TTIP into a warm carrier gas from a 20 µl syringe. Reaction is initiated by rapid mixing of the TTIP vapor with a larger flow of hot (550°C) nitrogen. At this temperature, the characteristic reaction time of the TTIP is approximately 100 µs, short enough to be considered to be instantaneous with respect to the aerosol dynamics

being studied. Titanium dioxide fume particles thus produced can be considered as rigid particles that do not coalesce significantly at the low temperatures of the experiments. Thus, the fume studies represent the limiting case of noncoalescing particles that has been examined theoretically by many investigators. Ultimate, experiments will be extended to probe particles that coalesce as they coagulate.

Aerosol samples are extracted from the reactor using a dilution quench sampling probe that has been designed to minimize coagulation between the probe inlet and the measurement point. A differential mobility analyzer (TSI Model 3071) was used to classify the fume particles in terms of their electrical mobility. In this instrument, the aerosol is passed through a bipolar charger, and then passes through a coaxial-cylinder electrostatic precipitator. For sufficiently small particles, only particles with a single charge are sampled. Particles that reach the inner cylinder at the right point are extracted in a small mono-mobility sample flow. A thermophoretic sampling probe was used to collect the classified particles on transmission electron microscope grid for subsequent structure analysis. The fume particles thus collected all have the same friction factor, so this experimental design allows examination of the particle structure/drag relationship. The mobility of the particle is characterized below in terms of the mobility equivalent diameter, i.e., the diameter of the single charged spherical particle that would pass through the mobility classifier at the same field strength.

Transmission electron microscope photographs of the particles were analyzed using a Macintosh II based image processing system. Fractal dimensionality was probed by three methods. The first, denoted D_{square}, is determined by measuring the fraction of the area occupied as the particle is covered by squares of different sizes. The second, D_{tile}, results from measuring the numbers of tiles of different sizes required to completely cover the aggregate. The third estimate, $D_{contour}$, is made by measuring the length of the perimeter of the aggregate as the contour defining the perimeter is dilated to increasing widths.

Figure 4 compares the fractal dimensions, the relative radius of gyration, and the aspect ratios estimated from particles of different mobility equivalent diameters, as estimated by averaging values determined from measurements of a number of particles in each mobility fraction. Particles of different mobility equivalent diameters show comparable relationships between the different measures of particle structure. The fractal dimensionality determined by the square and tiling methods are quite close, about $D \sim 1.8$, while the contour method gives a lower value, $D \sim 1.3$. This is not unexpected since the first two methods are designed to measure structure over length scales from 10 to 100 percent of the radius of gyration while $D_{contour}$ measures the structural features centered about 10 percent of the radius of gyration.

A comparison between the measured mobility radius and several characteristic radii that might be used to describe an aggregate particle reveals that, for mobility radii below about 100 nm, the projected area

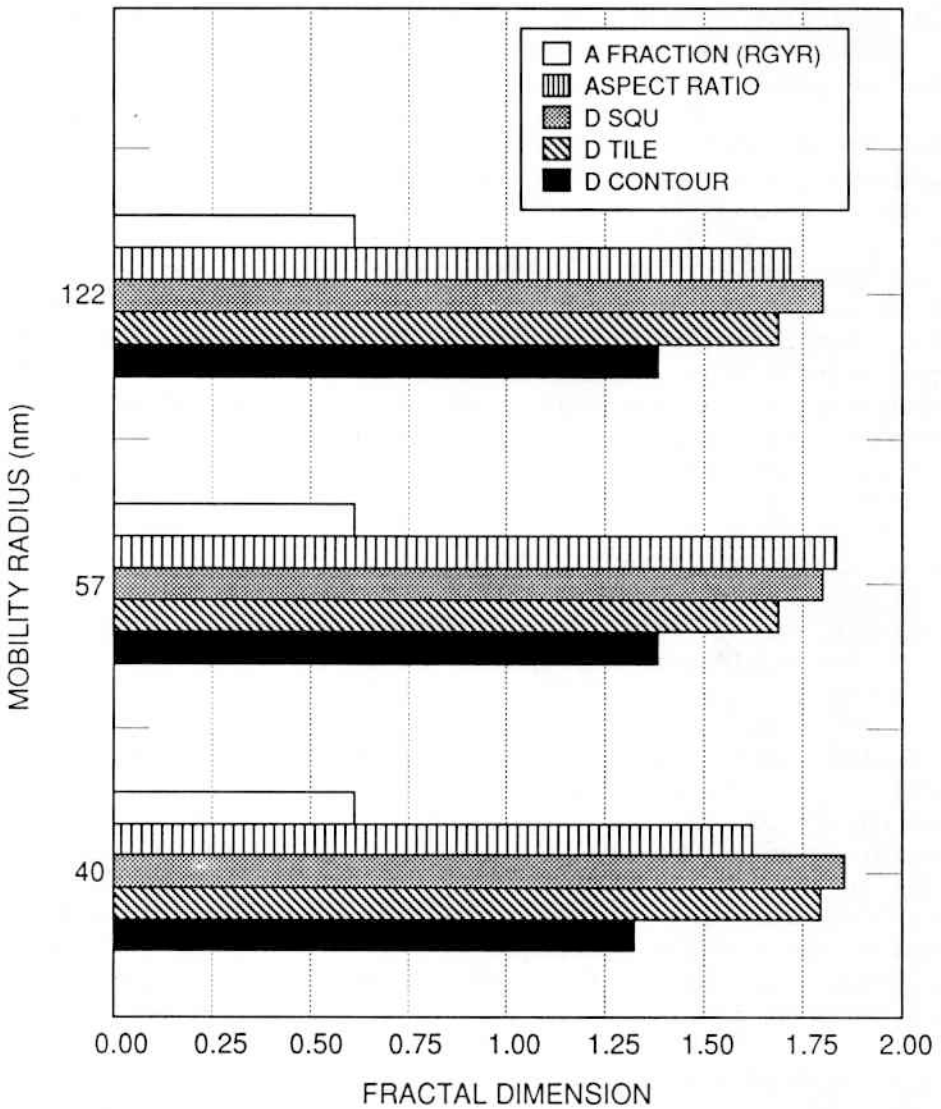


Figure 4. Comparison of Fractal Dimensions of TiO_2 Particles Determined by Analysis of Electron Microscope Images Using Different Algorithms.

equivalent radius agrees most closely with the mobility radius. This is not unexpected for low density aggregate particles that are comparable to or smaller than the mean free path of the gas molecules (about 65 nm at the conditions of measurement). In the free molecular limit, the drag is determined by the rate of impingement of gas molecules on the particle and is, therefore, proportional to the projected area of the particle. For larger particles, the mobility equivalent diameter is closer to the maximum extent of the aggregate, as one would expect for a particle in the continuum regime.

6.3.2 Dynamics of Aggregate Aerosols

Given models of the aerodynamic drag on aggregate particles, one can begin to assemble models that describe the evolution of a noncoalescing aerosol. The coagulation frequency function depends on the diffusivities of the particles and on the collision cross section. From the work on the drag on the aggregate particles, we may estimate the diffusivities with some confidence. Lacking a rigorous theory, one must estimate the effective collision radius for the aggregates, however.

With estimates of the collision frequency function, simulations of the dynamics of the fume aerosol can be undertaken to explore sensitivity of the aerosol dynamics to the particle structure. Calculations were performed using a modified version of the discrete-sectional solution to the aerosol general dynamic equation (Wu and Flagan, 1988) for particles with D = 1.8 in order to be consistent with the observed particle structure. Figure 5 shows the calculated number distribution as a function of the volume equivalent particle diameter. The aggregate particle size distributions are somewhat narrower than predicted for dense spheres, and the particles are found to grow faster as aggregates

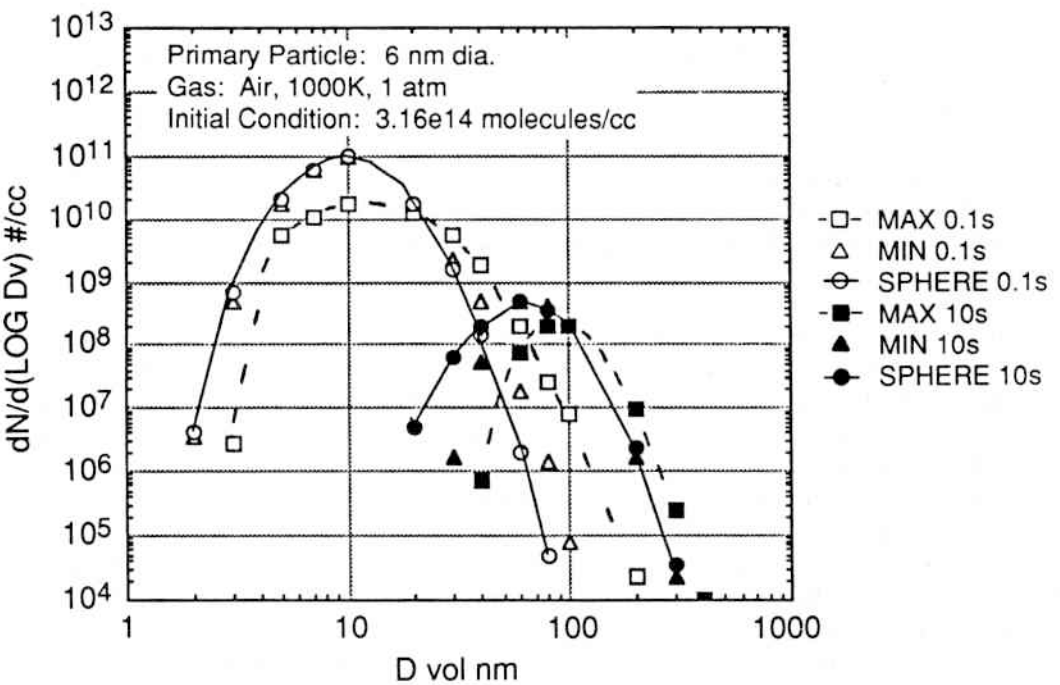


Figure 5. Particle Size Distributions for a TiO_2 fume calculated using the Sectional Solution to the General Dynamic Equation for Aerosols with Coagulation Frequency Functions Modified to Account for Noncoalescing Particles after Coagulation Times of 0.1s (small points) and 1.0s (large points). Results based on maximum aggregate coagulation rate (squares), minimum aggregate coagulation rate (triangles), and dense spheres (circles).

than as dense spheres. It should be noted that these results do not represent what would be measured. Mobility equivalent diameters of the aggregate particles would be even larger than the volume (or mass) equivalent diameters. Thus, it is apparent that any attempt to model the dynamics of aggregate fumes must take particle structure into account.

6.3.3 Fume Formation from Pyrite

Baxter and coworkers at the Sandia Combustion Research Facility have examined the mechanisms of iron fume formation in coal combustion and come to the conclusion that direct volatilization cannot explain the quantities of iron found in the submicron fume. Experiments were undertaken to probe the origin of that fume using two experimental systems. Initial experiments were undertaken using the electrodynamic thermogravimetric analyzer (EDTGA). This instrument allows direct observation of a single charged particle levitated electrostatically as it is heated using a CO_2 laser. Photophoretic forces acting on the particle as it is heated tend to drive the particle from a tightly focused laser beam. An Advanced Kinetics flowing gas laser was operated in TEM 01* mode to overcome this difficulty, simplifying the retention of the particle in the laser beam.

The particle temperature was estimated using a two color pyrometer, operating at wavelengths of 1.8 and 3.4 μm. Because the pyrite particles were irregularly shaped, and data on the optical properties of the pyrite are not available, temperatures determined in these preliminary experiments can only be considered to be estimates. Hence, the EDTGA observations of fume formation in pyrite pyrolysis and oxidation were followed by quantitative experiments using a drop tube reactor.

A single pyrite particle of approximately 50 μm size was suspended in air and subjected to several pulses of 10 ms duration from the CO_2 laser. The laser was operated at a steady state that maintained the particle at approximately 100°C and briefly pulsed to heat the particle. The particle was observed with the two color pyrometer and with a video camera using a Questar QM1 long range microscope. The initial pulse heated the particle to approximately 320°C, leading to the formation of a cloud approximate 4 particle radii in size. The charge-to-mass ratio did not change during this initial pulse (resolution on charge to mass ratio 1 part in 10^5). A slightly more intense pulse (T ~ 350°C) caused the particle to fragment. One of the fragments was selected for additional experiments. When pulsed to approximately 350°C, a cloud again formed around the particle with no apparent large fragments formed. During this pulse, the charge to mass ratio changed, corresponding to a 38 percent mass loss, assuming that the charge on the particle did not change. The residue ignited when pulsed one more time, and the particle was lost.

These experiments indicated the formation of a cloud at so low a temperature that direct evaporation of the mineral could not be

expected. Experiments were conducted using the drop tube reactor to examine the nature of this fume. Experiments were conducted in both nitrogen and air. Figure 6 shows the size distributions determined in air at furnace temperatures of 750 K and 1220 K. At the low temperature, the fume is found to consist of particles smaller than a few tens of nanometers in diameter. The minimum size resolution of the Differential Mobility Analyzer system used for these measurements is 15 nm, and indications are that the number concentration increased further at smaller sizes. The total volume of fume produced at this low temperature amounted to about 1 part per million of the original pyrite volume. Similar experiments performed in nitrogen resulted in a somewhat smaller number of smaller particles. Note that direct quantitative comparison between drop tube and EDTGA experiments cannot be made, as heating rates and mechanisms differ between the two approaches.

No direct observations of the particle composition have been made as yet. The possibility that these small particles are comprised of elemental sulfur cannot be rejected from these observations. When the particles were reacted at higher temperatures, the quantity of fume increased as indicated by the number distribution for the reaction of pyrite in air at 1220 K. The fume concentration increased further as the reactor temperature was increased to as high as 1673 K. Experiments were also performed in nitrogen at the higher temperatures. Again, the number and volume of the fine particles was larger for reaction in air than for the reaction in nitrogen. Complete determination of the fume volume generated under these higher temperature conditions was not possible, as the aerosol instrumentation did not extend to sufficiently large sizes. Additional measurements in this area are currently underway.

While the mechanisms of fume formation from pyrite remain unresolved, the very fine size of the fume particles generated by the pyrite reactions strongly suggests nucleation from the vapor phase. At the very high temperatures examined, the particles would be expected to undergo very rapid oxidation to sulfur dioxide if the primary particulate material were sulfur, so sulfur particles seem very unlikely. Direct observations of the particulate composition will be required to resolve the origin of the pyrite derived fume.

In summary, studies of the high temperature reactions of pyrite reveal the formation of large numbers of extremely fine fume particles at very low temperatures, suggesting kinetically controlled volatilization followed by homogeneous nucleation. The electrodynamic thermogravimetric analyzer graphically demonstrates the rapid production of the fume within a few radii from the surface of a hot pyrite particle. Subsequent quantitative experiments performed using a drop tube reactor verify the formation of this fume and reveal that the particles thus produced are only a few tens of nanometers in size. While the possibility that the fume observed at temperatures as low as 300°C is comprised of elemental sulfur cannot be ruled out, the persistence of ultrafine particles as the temperature is increased strongly suggests that more refractory species are at least partially responsible.

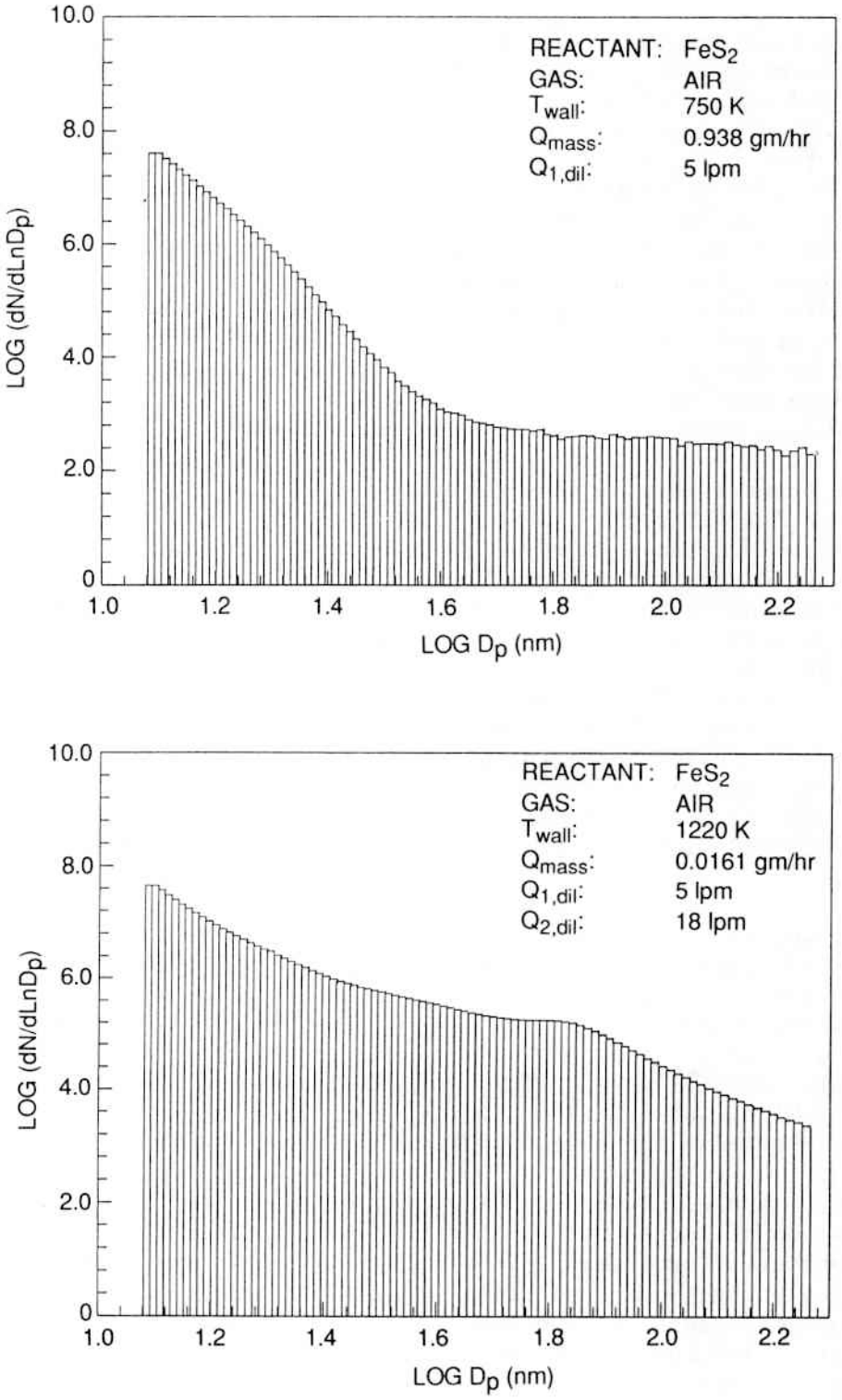


Figure 6. Particle Size Distributions from Pyrite Reactions in Air in a Drop Tube Furnace Measured using the Differential Mobility Analyzer. (A) Reactor temperature 750 K. (B) Reactor temperature 1220 K.

6.4 FUNDAMENTAL STUDIES OF THE RESIDUAL ASH FORMATION AND MINERAL MATTER VAPORIZATION DURING PULVERIZED COAL COMBUSTION

In the previous section, detailed experiments with synthetic samples to unravel the processes occurring during fume evolution were presented. Here, complementary experimental and modeling studies in coal systems are being used to develop a quantitative understanding of the processes governing mineral matter vaporization and residual ash formation. Experiments in the MIT laminar flow furnace facility are being used to determine the effect of coal type and char properties on the size distribution of residual flyash. A Monte Carlo simulation is used to obtain the distribution of mineral matter in the pulverized coal and this is combined with a percolative fragmentation model to obtain the residual flyash particle size. Complementary experiments on model chars are used to determine the rate of vaporization of mineral constituents which influence the formation of low melting point surface coatings on ash particles. In this section, highlights of each component of the study are presented.

6.4.1 Mineral Redistribution Model

The model was developed to investigate the variation of mineral composition and content from coal particle to coal particle. The investigation is possible by the redistribution of mineral inclusions to coal particles based upon the information on coal and mineral particle size distributions provided by CCSEM analysis by the University of Kentucky for as-received coal samples.

The simulated coal particles are represented as "boxes" in which the mineral inclusions will be randomly distributed. The model generates different sizes of "boxes" in such a way that the final box size distribution fits the real coal particle size distribution (psd), which is previously experimentally determined by a Malvern size analyzer. The coal psd ranging to 170 μm is equally divided into 17 size bins with the upper bound of each bin taken as the representative size.

In the model, mineral inclusions are considered as "balls," which will be randomly distributed to the "boxes." The mineral psd is again divided into six bins with the representing mineral inclusion sizes being 1, 4, 8, 16, 30, and 60 μm. The "balls" are generated to satisfy the experimentally determined psd.

As soon as the boxes (coal particle) and balls (mineral inclusions) of various sizes are generated, the model starts to randomly redistribute the balls to boxes. The probability of assigning an inclusion to a particle is proportional to the particle volume. When the randomly chosen box does not have any remaining free space to accommodate an additional ball, the ball is considered as extraneous mineral. Once all the balls are distributed, the remaining space in each box is considered as carbon. At the conclusion of the distribution of mineral inclusions, coal particles can be density and size classified to study the particle-to-particle variation of mineral content and composition distribution.

Examples of the validity of the model are provided by comparison of the model predictions with the distribution of coal between different density fractions measured by Bryers at Foster Wheeler. Figure 7 shows a comparison of model and experiment for the total mineral content of each of four density ranges. Excellent agreement is clearly obtained between model and measurement.

This model can also be used to predict the coal particle-to-coal particle variation in mineral content and composition. This is demonstrated for a utility grid (70 percent < 200 M) sample of Upper Freeport bituminous coal in Figure 8. If complete coalescence were to occur during combustion, the final composition of each ash particle could be calculated from the points in this figure.

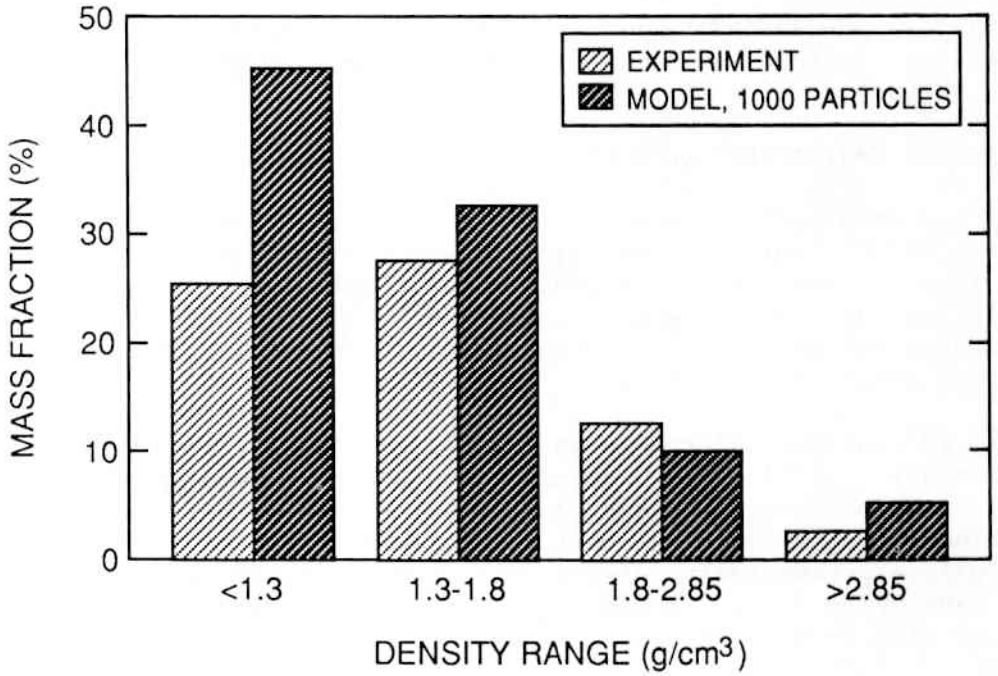


Figure 7. Total Mineral Content in Four Density Ranges of a 84 μm Upper Freeport Coal Sample.

6.4.2 Fragmentation Model

If char fragmentation were to occur, coalescence would not necessarily predict the composition of individual ash particles, given the information in Figure 8. To theoretically account for fragmentation effects, a model which represents a char particle as a cluster of connected occupied sites randomly distributed on a simple cubic lattice was developed. Two nearest-neighboring occupied sites are defined as being connected, with all occupied sites containing an equal fraction of the carbon mass of the initial char particle. The unoccupied sites are considered pores, and the surrounding environment is defined to be the

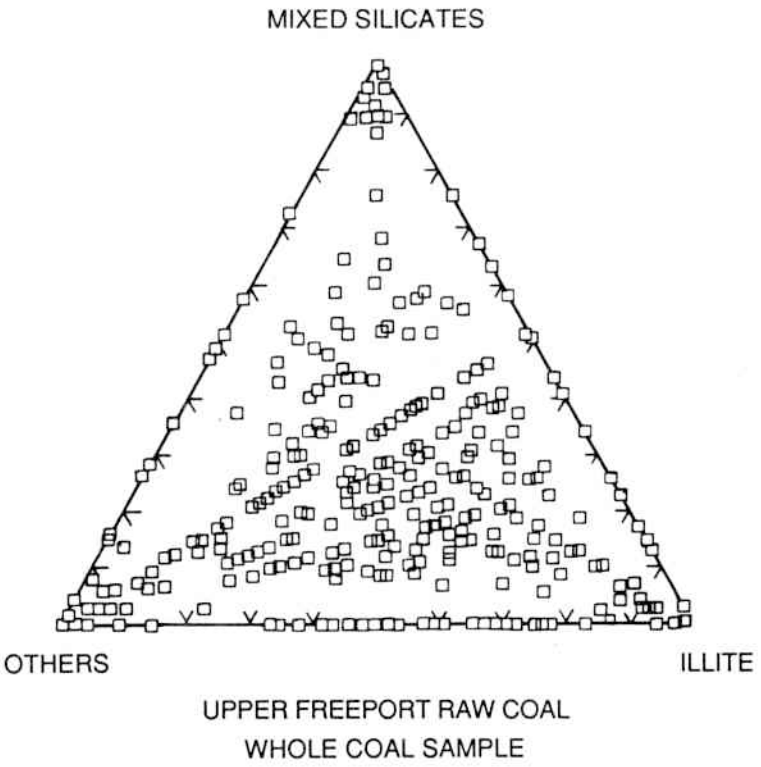


Figure 8. Variation of Mineral Composition Between Coal Particles.

reactant gas. Reaction is possible only when a given char site is directly in contact with the environment, thereby simulating reaction in the external diffusion controlled reaction regime. Mineral matter is distributed among the various char sites as an initial condition in the simulation.

Oxidation of the particle is represented by random removal of sites from the perimeter of the cluster, with the perimeter determined by checking the connectivity of pores to the surroundings. As a site is removed from the lattice, it is redefined as being unoccupied. No interior sites are removed until the outermost sites have been completely removed. Char fragments are generated when the removal of a site causes the separation of a cluster or clusters of sites from the parent cluster.

Every time a site is removed, the mineral matter that was associated with the reacted site is redistributed to one of the nearest-neighboring char sites, selected randomly. If the reacted site has no nearest neighbors, an ash particle is assumed to be separated from the parent char, and the separated particle is then stored in a bin. The coalescence of ash droplets on the receding char surface is taken into consideration by checking the distances and sizes of ash droplets and allowing combination when surface contact exists. The processes of reaction, ash redistribution, and coalescence continue until all of the char sites have been removed, signifying 100 percent char burnout.

Application of this model to a char with 10 percent macroporosity in the 2 μm size range is shown in Figure 9. These simulations, utilizing 1 μm mineral inclusions in a 50 μm coal particle, demonstrate that char fragmentation will produce an ash size distribution intermediate between the two extremes pictured below. Note that 1 ash/inclusion may not be a lower bound, as mineral fragmentation has been observed for certain species.

Char fragmentation results in particles being formed in the 1 to 4 μm size range. Experiments for monosized coal particle show that a minor fraction of ash in the fragmentation size range (Figure 10) is produced from combustion of Kentucky #9 size-graded coal. The extent of fragmentation has been found to increase with increases in the macroporosity of the coal and to decrease with increases in ash content, as the ash tends to act as a binder.

The importance of coal particle size and mineral matter distribution, has been determined using the model developed. In Figure 11, we show the ash size distribution for a typical pulverized coal calculated for the limiting cases of one ash particle per mineral inclusion and one ash particle per coal. This picture represents the cumulative experimental case for a true coal particle psd, whereas Figure 9 depicts model results from a single coal particle. The simulations show that much of the polydispersity of the ash sizes is contributed by the polydispersity of the parent coal. The experimental results in this case have a smaller particle size indicating the impact of fragmentation. The simulations for a polydisperse coal with fragments require extensive computations and have not been completed for this case.

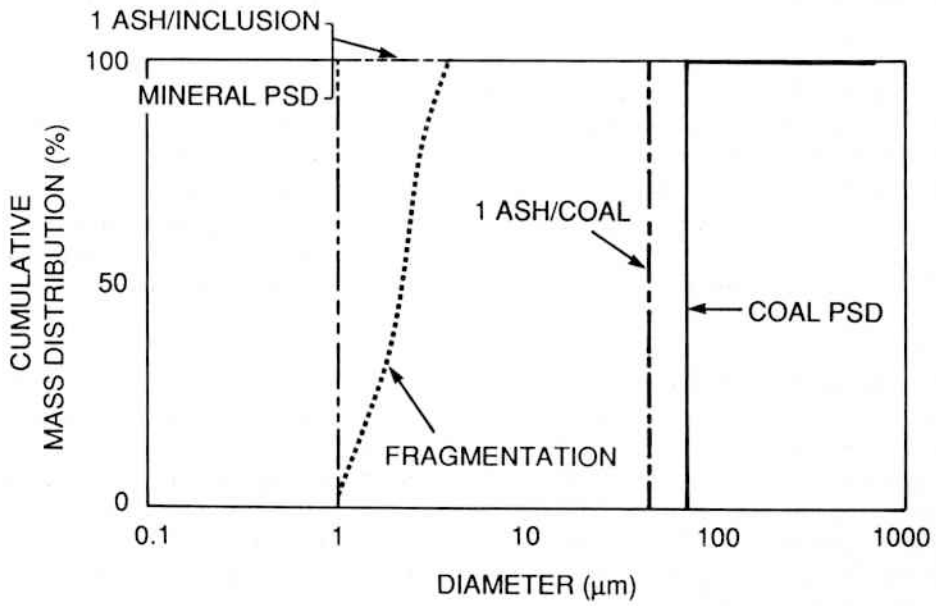


Figure 9. Particle Size Distributions of Coal, Mineral, and Ash (monodisperse coal and mineral psd's).

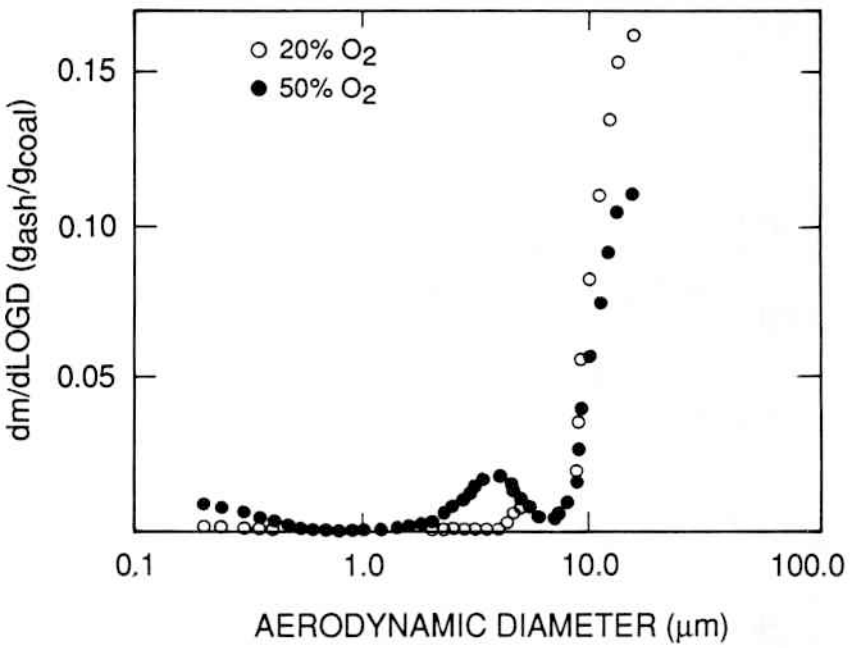


Figure 10. Ash Particle Size Distributions Obtained with Cascade Impactor from Laminar Flow Furnace Combustion of Kentucky #9, 63/75 μm, at 1750 K.

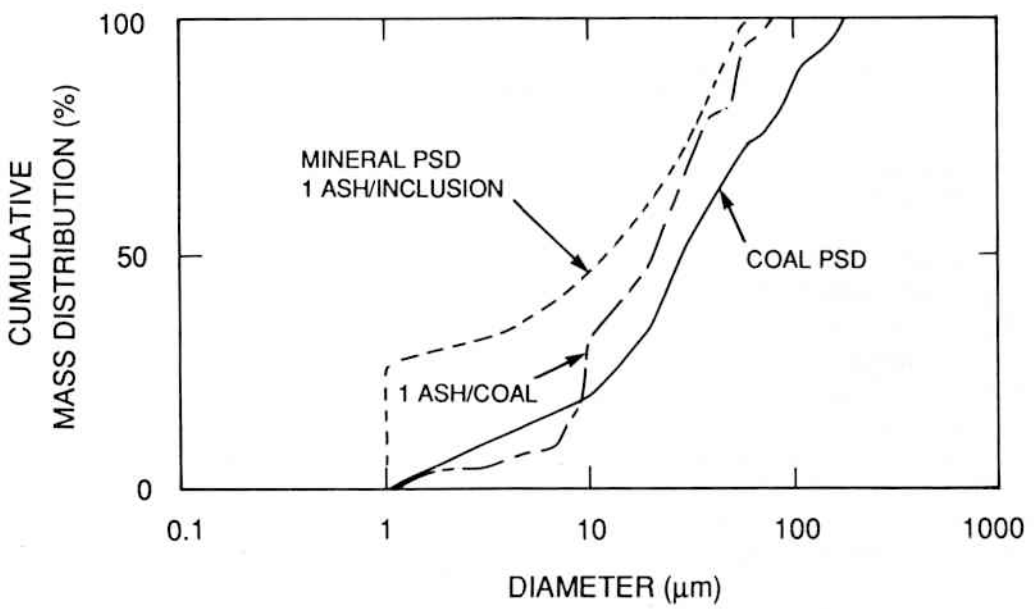


Figure 11. Particle Size Distributions of Coal, Mineral, and Ash for a Typical Pulverized Coal.

6.4.3 Mineral Matter Vaporization

A systematic study of the effect of mineral composition on vaporization has been conducted using both coals and model chars burned under identical conditions. Results such as those shown in Figure 12 demonstrating increases in sodium vaporization with temperature (O_2) for several fuels are being used to guide the refinement of vaporization models.

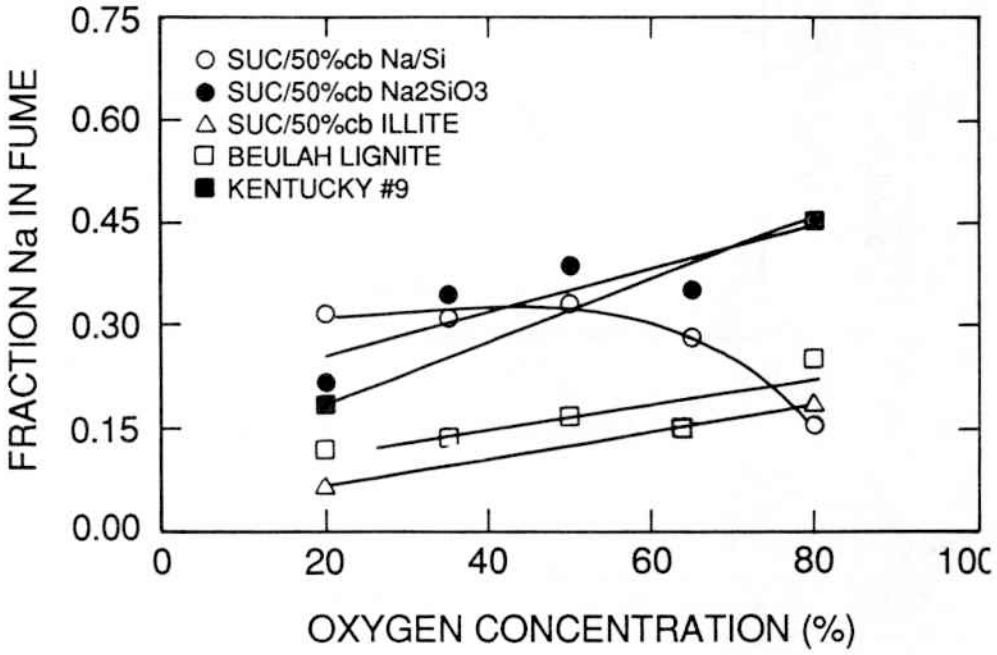


Figure 12. Fractions of Sodium in Submicron Fume for Various Feedstocks Oxidized at 1750 K.

6.5 RESIDUAL ASH FORMATION DURING COMBUSTION IN A LABORATORY SCALE FACILITY

The transformations of minerals to form ash particles (>0.5 μm) are studied by examining the products generated from combustion of both coals and synthetic chars at PSIT, and comparing these to the initial minerals present in the feedstock. Illinois #6 coal, for example, contains all of the major minerals embedded within the carbon matrix. Pyrite, silicates, calcite, and quartz are all present, with most being less than 20 μm in size. Given this, it can be anticipated that combustion transformations of these minerals will be coalescence-dominated. This becomes apparent from comparison of the mineral and combustion generated ash particle size distributions shown in Figure 13. For this coal, experiments were conducted in seven percent oxygen at 1750 K. Although the CCSEM-derived distributions are identical at particle diameters larger than 25 μm, a shift to larger diameters by coalescence of the smaller minerals is readily observed. The

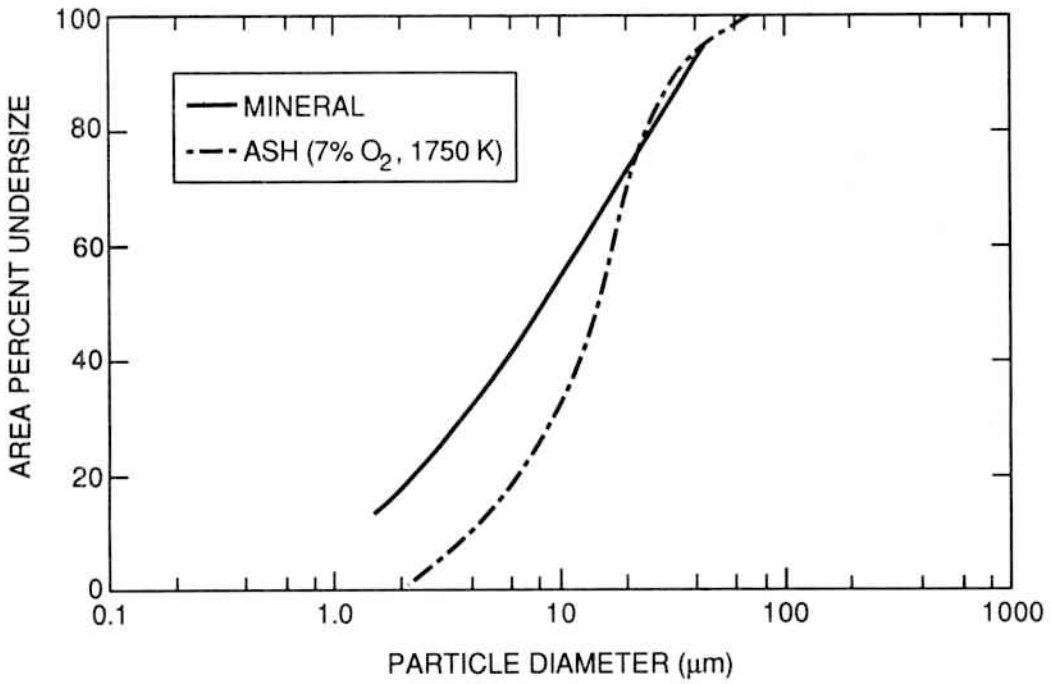
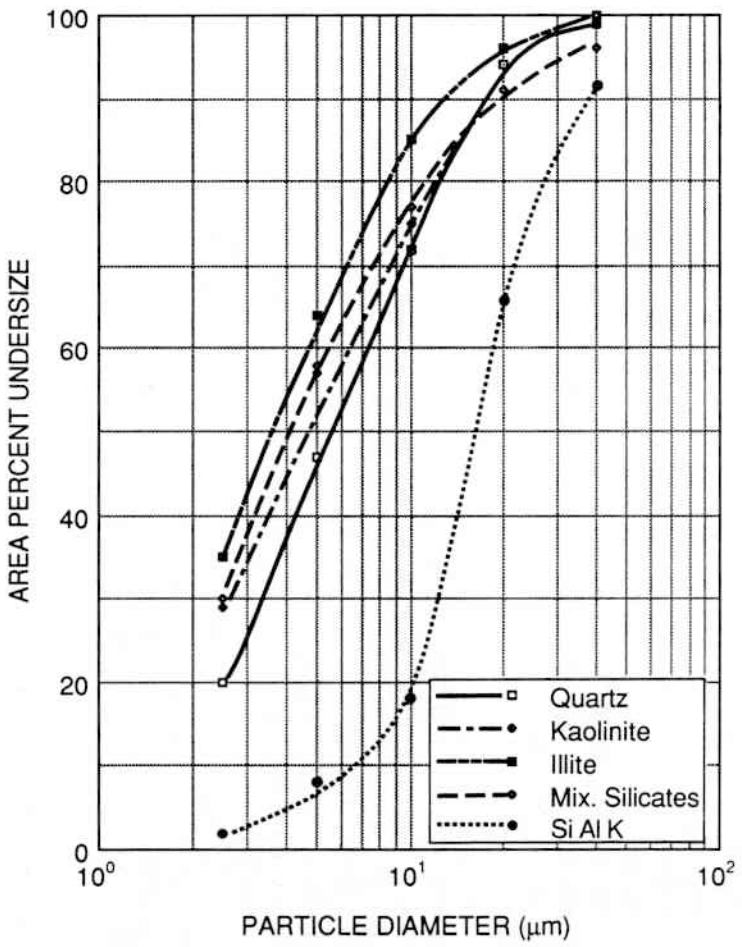


Figure 13. Mineral and Ash Size Distributions for Illinois #6, Obtained by CCSEM. Ash generated from laboratory combustion at 1750 K, 7 percent O_2.

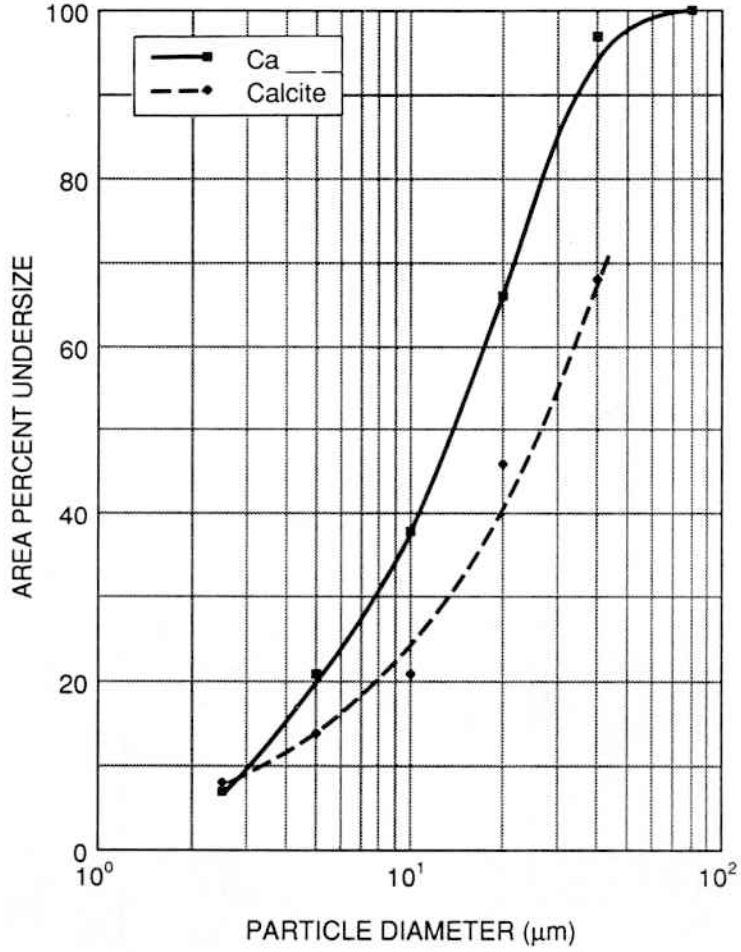
persistence of the same fraction of material in the 25 μm plus region is suggestive of either (1) excluded minerals, not associated with the carbonaceous matrix; or (2) the presence of char particles containing a few mineral particles, possible because of the low total ash content of this coal (8.6 percent). Analysis of individual mineral compositions identified quartz as the most likely candidate for either scenario, as quartz particles greater than 20 μm were found to be unchanged.

Examination of the size distribution of individual minerals and their corresponding ash products yields a similar result, as shown in Figure 14a. Plotted are the size distributions of the initial silica bearing minerals next to the size distribution of the Si-Al-K ash particles, representing 25 wt% of the total ash product. Again, comparison clearly demonstrates coalescence of the silicate ash particles, as seen in the shift of the curve to larger sizes corresponding to the mineral to ash transformation. Although only one silicate ash composition range is represented by this product curve, simple mass balances performed on the entire flyash distribution indicated other silicate-containing (i.e., glassy) ash particles behaved similarly.

Calcite transformations were also examined during the combustion of Illinois #6 coal. As seen in Figure 14b, comparison of calcium rich ash particles (most likely calcium oxide) representing seven area percent of



(a) Silica containing ash minerals and ash particles showing coalescence



(b) Calcite versus calcium oxide showing fragmentation

Figure 14. Mineral versus Ash Particle Size by CCSEM for Illinois #6.

the total ash, to calcite (calcium carbonate) minerals indicated a slight shift to smaller sizes, suggestive of calcite fragmentation. More than 85 percent of the calcium present in this coal was initially associated with calcite, while 65 percent of the calcium ultimately resided in CaO particles. Limited interaction between calcite-derived calcium and silicate ash particles is therefore indicated.

The importance of coalescence in the evolution of ash in Illinois #6 can be attributed in part to high (24 percent) levels of illite in the parent coal. To understand these transformations in more detail and in the context of the contribution of individual minerals, a detailed examination of the transformations undergone by both included and excluded illite under residence times typical of pulverized coal combustion was also undertaken. Illite is a predominantly potassium aluminosilicate mineral (ideal formula - $KAl_3(AlSi_5O_{10})(OH)_2$) typically present in American bituminous coals. In this study, samples of Silver Hill (Montana) illite in the size range of 53 to 75 μm exposed to high temperatures in the reactor for different residence times were examined by scanning electron microscopy. Illite particles in the feed were flaky with an aspect ratio of about 2.0 to 3.0 for most particles. Upon exposure to 1500 K for a residence time of approximately 0.5s, the color of the sample changed from a greenish gray to dark brown, reflecting the oxidation of iron to the ferric state. Particles lost their angular form partially at longer residence times and vitrification was evident, although the overall morphology still resembled that of the original particle. Examination of particles subjected to 1500 K for 2.5s, showed that a much larger fraction had become completely molten. Several large pores were present on the particle surface, suggesting gas evolution and even some bloating as a result of trapped vapor trying to escape through a molten matrix.

The evolution of the particle size distribution for both included and excluded illite was also followed to estimate the importance of processes such as swelling, coalescence, fragmentation and vaporization. In the first set of experiments, nominal 53 to 75 μm excluded illite particles were fed to the entrained flow reactor, held at 1500 K and 3 percent oxygen. Particle size was measured for both the initial raw sample and the transformed sample collected after 2s residence time. Examination of the size distributions indicated that no significant change in particle size occurred for the excluded illite during high temperature processing. The raw illite was concentrated in the anticipated size range, with a median diameter of 70 μm and a volume weighted (d_{43}) mean diameter of 69 μm. For the transformed illite, the median diameter was 71 μm and the volume weighted mean diameter was 72 μm.

The particle size evolution of illite included in char was examined in a second set of experiments. Synthetic char particles (75 to 106 μm diameter) containing 10 to 20 μm illite inclusions (a typical size range for bituminous coals) were burned at 1500 K under 7 percent oxygen, and the size of the resulting ash particles measured. In direct contrast to the excluded illite results just discussed, the included illite

demonstrated a significant increase in particle size indicating extensive coalescence (Figure 15). The inclusions began with a median diameter of 25.5 μm; subsequent to combustion, a median particle diameter of 51 μm was measured. This shift in particle size corresponds to the coalescence of eight to nine 25 μm inclusions per char particle, assuming that extensive thin-walled cenosphere formation does not occur.

In order to ascertain the conditions under which illite particles are sticky and can lead to deposition, capture efficiencies of the transformed illite particles were also determined as a function of gas temperature. The capture efficiency is the fraction of the particles that both impact and stick to a deposition target. Impaction efficiency is unity for the particle size (53 to 75 μm) and the velocity range used here. Figure 16 shows the capture efficiencies for different furnace temperatures and particle impaction velocities. When examined as a function of temperature, there is a dramatic increase in the rates of capture above 1400 K, except for the highest velocity. Microscopic observation of the deposit obtained at 1400 K showed that, even though the capture efficiencies were high, the deposit was powdery and very friable, while at higher temperatures the deposits were more bonded.

As the temperature is increased, the viscosity of the incoming illite particles decreases, and below a critical viscosity (approximately 10^7 poise) (Srinivasachar et al., 1988) the particles are sufficiently

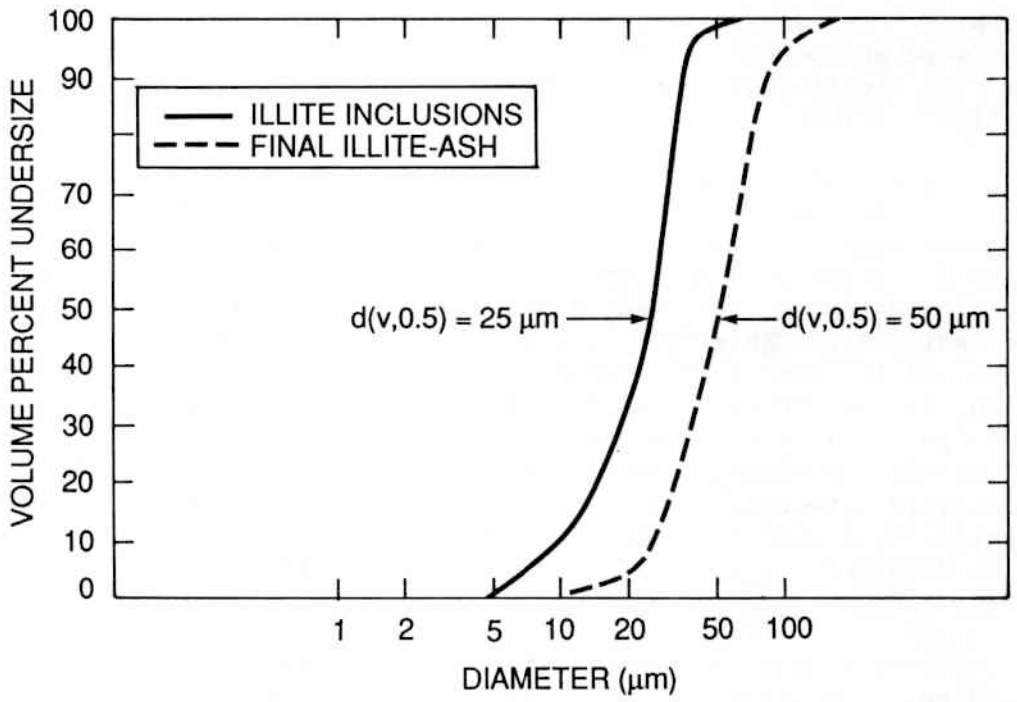


Figure 15. Comparison of Included Illite Size with Final "Ash" Size, Demonstrating Coalescence of Glassy Illite When Included in Carbon Matrix.

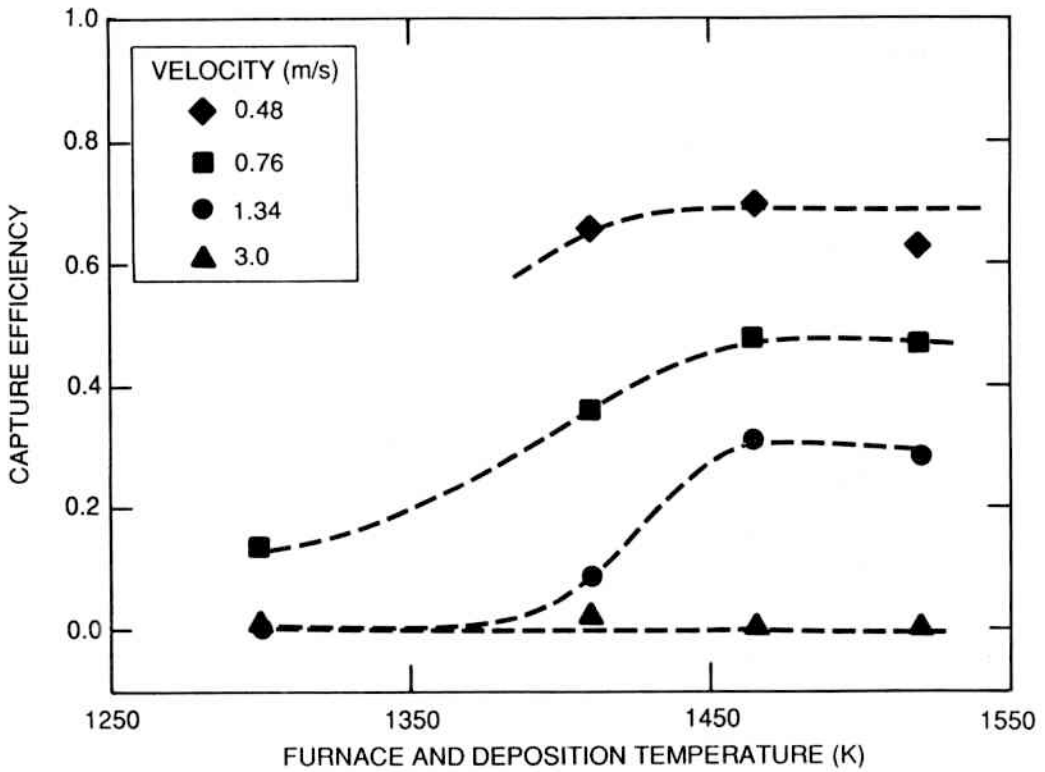


Figure 16. Deposition of Transformed Illite as a Function of Gas Temperature.

deformable that the energy of impact is dissipated, and the particles stick without rebounding. One would normally expect that the capture efficiency would increase as the particle velocity increases due to the increase in the impaction efficiency - however, in our case, the particles are large enough that all of them impact even at the lowest velocity. The observed reduction in the capture efficiency with increasing velocity must therefore be due to deposit erosion from the incoming particles. Analysis of these data will therefore require consideration of both deposition and erosion.

6.6 ALKALI TRANSFORMATION IN A SELF-SUSTAINED COMBUSTOR

Ash alkali species in pulverized coal can have a pronounced effect on the slagging and fouling characteristics during combustion as a result of fume formation and interactions with residual ash. The physical and chemical nature of alkali-containing species, the combustion characteristics and the complementary constituents in the parent ash all may influence the behavior of alkali species.

If a mechanism of alkali formation in the particle phase is to be proposed, it must account for these observations. A detailed understanding of the mineralogical analysis and organically bound alkali fraction must be included in the data analysis. Specifically, the six coals under discussion here were characterized by conventional

techniques. In addition, detailed mineralogical analysis was performed on size- and density-segregated samples of the pulverized coal, using computer controlled scanning electron microscopy (CCSEM).

6.6.1 Project Description

Research reported here utilizes a laboratory furnace designed for self-sustained combustion of pulverized coal at the Uiversity of Arizona. The issues to be examined in this work include:

- The influence of non-alkali species on the behavior of Na and K in ash.
- The influence of organically-bound mineral matter on the rates of vaporization of Na and K.
- The extent to which overall alkali content of the ash is an indication of the degree to which alkali vaporization occurs.
- The relationship between the size of potassium containing mineral inclusions and the vaporization of that metal.

Experiments were conducted using a laboratory downfired combustor described at previous Contractor's Review Meetings. The combustor was designed to have attributes of practical coal combustors, as far as temperatures and residence times are concerned, but still be sufficiently well defined to allow the extraction of rates and mechanisms.

The data to be reported here are concerned solely with the effects on fates of sodium and potassium in six different coals, all burned at a stoichiometric ratio of 1.2. Therefore, the temperature profile is not a controlled variable, but rather is that which occurs naturally for each specific coal, as it would in practice. Results should, therefore, be more easily extrapolated to field conditions.

6.6.2 Sampling and Analysis

Airborne ash particles were extracted from the furnace flue gas at the lowest sample port at the bottom of the furnace. The water cooled sampling probe allowed isokinetic sampling followed by rapid quenching (10^6 K/s) using dilution air (10/1 dilution ratio). The diluted sample was passed to a 30 lpm Anderson Impactor outfitted with a preseparator cup, eight plates, and an after-filter to collect the very small particles passing over the last plate. On each impactor plate a 0.2 μm pore-size Millipore filter was thinly coated with mineral-free grease to minimize bounce-off (Turner and Hering, 1987). The contents of the preseparator cup were added to those on the first plate, and each filter was acid (HF plus aqua regia) digested and analyzed for sodium, potassium, magnesium, silicon, calcium, aluminum, and iron using atomic absorption or emission as appropriate, hereafter denoted as AA.

Each run required analysis of samples from each of eight trays in the impactor plus the impactor after-filter. Two replicates are taken, making 18 samples in all. In addition, with all but the first and seventh impactor trays removed, the samples in the cup, on the first and seventh tray, and on the after-filter were combined to yield a "Total Filter" sample. Furthermore, the top tray is analyzed separately to ensure replication with the full impactor data. For each run, additional samples were retained from selected plates for subsequent Auger and XAFS analyses, which are not reported here. Two replicate runs were completed for each coal, and in the research reported here, data from each replicate run and each replicate sample have been averaged.

Specific emphasis in these experiments is on sodium and potassium, and the original form of these elements in the parent coal. Of the program coals, three possess levels of sodium and potassium worth noting. The first, Beulah Lignite, contains a fair amount of sodium, nearly all of which is acid soluble since the portion in the mineral matter is very small. Potassium levels are very low, but appear to be concentrated in minerals, including illite. However, additional CCSEM analysis on the mineral inclusion size distribution reveals that essentially all the minerals containing potassium lie in inclusions less than 2.5 μm in size, and from this, it can be inferred that potassium is evenly dispersed throughout the coal organic matrix.

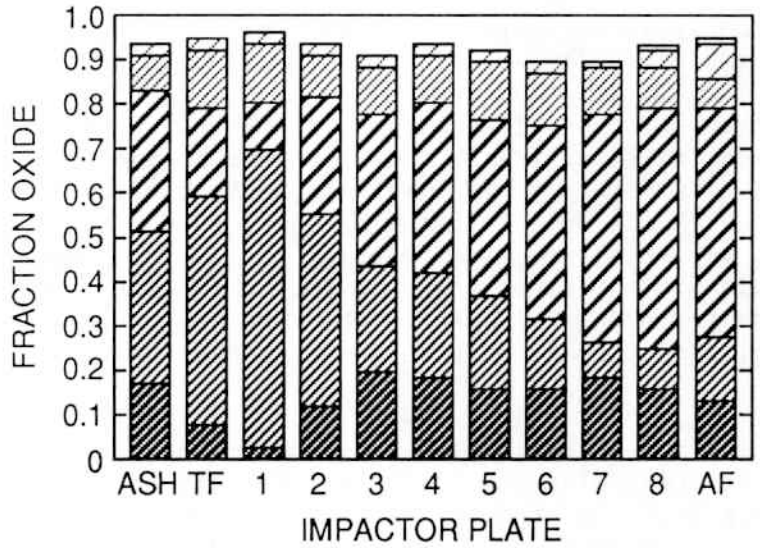
Eagle Butte is a sub-bituminous coal with high calcium levels. Only one fifth of the sodium lies originally in the mineral matter, the remainder is acid soluble. Potassium levels are very low, but predominately in the mineral form.

Loy Yang is an Australian coal with very low ash. However, the major constituent of the ash is sodium itself, which is accompanied by large amounts of chlorine. All the sodium is acid soluble. The particular samples of this coal used in the research reported here had been contaminated with fragments of glass, probably from bottles introduced into the fuel handling system at the power station source. Here it was possible to remove only the largest of these extraneous glass fragments.

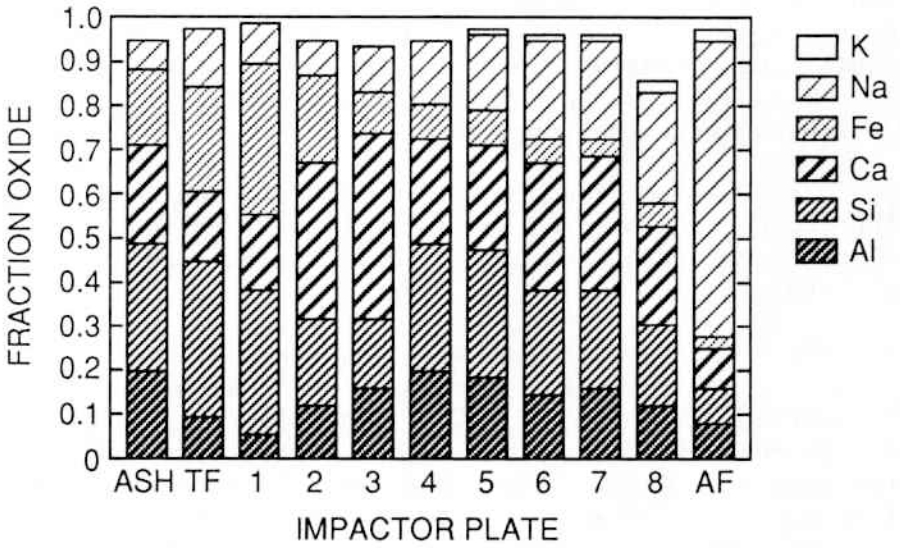
6.6.3 Results/Accomplishments

The bar charts in Figure 17 depict the size segregated (by stage) ash compositions for two selected coals. Also shown is the composition of the total filter sample, and that obtained from the ASTM ash analysis.

Beulah Lignite shows enrichment of both sodium (which was originally primarily acid soluble) and potassium (which occurs in small inclusions less than 2.5 μm throughout the coal) in the small particle ranges. Furthermore, the composition of the sample in the impactor after-filter suggests the presence of a sodium fume with particles sized less than 0.43 μm. There is a slight discrepancy between the composition of the total filter sample and that of the ASTM ash, with the total filter



(a) Eagle Butte



(b) Beulah Lignite

Figure 17. Ash Composition, as Fraction Oxide, versus Impactor Stage for Two Selected Coals. Also shown are ASTM ash (ash), total filter (TF), and impactor after-filter (AF) analyses. (a) Eagle Butte; (b) Beulah Lignite.

indicating an enrichment in silicon relative to the latter. The reason for this is not readily apparent.

Size segregated ash composition data from Eagle Butte also depicts enrichment of sodium in the small particle size range, although there is no suggestion of a fume. Calcium is concentrated in the smaller particle size ranges.

In general, sodium is enriched in the smaller particle size ranges. Potassium, on the other hand, may or may not be enriched on small particles even though in all cases it was predominantly present originally as a mineral. The data suggest that the size of the mineral inclusions may determine the propensity for potassium to vaporize and subsequently enrich the small particles via condensation.

Enrichment of certain metals in the small particle size range can occur through a number of mechanisms. The metal, possibly transformed into a volatile compound, can vaporize, and thereafter can either nucleate to form a fume or condense around existing particles to form an enriched surface layer around those particles. One can also argue that some enrichment can occur through preferential fragmentation of certain mineral inclusions.

The composition of the after-filter sample of the Beulah Lignite strongly suggests the presence of a sodium rich fume, which was less readily apparent in after-filter samples for the other coals.

If surface condensation (in the continuum regime) can account for enrichment of volatilized metals in certain size ranges, the concentration of that metal in the ash depends on particle sizes thus (Neville and Sarofim, 1982):

$$\text{Concentration} = a + \frac{b}{D_p^2} \quad . \tag{2}$$

Using the plate D_{50} cut-off diameter as a representative particle size for each plate one can plot the fraction of Na and K in the ash on each plate versus $1/D_p^2$, and this should yield a straight line when enrichment is dominated by surface condensation following previous vaporization.

Figure 18 shows such plots for sodium from three coals: Beulah Lignite, Kentucky #9, and Kentucky #11. Sodium enrichment on the four lower trays does appear to follow Equation (2), at least to a first approximation. This is not really surprising since sodium is originally present in the organic form for these three coals and therefore would be expected to volatilize and subsequently condense. It should also be noted that the Loy Yang sodium data did not correlate with Equation (2), indicating there here sodium constituted the bulk, and not just the surface layer, composition of the small particles.

Potassium enrichment, however, was found to follow Equation (2) for the Beulah Lignite and for the Kentucky #11, but not for the Kentucky #9. In all three coals, potassium was present originally as illite, and so the important point to make is that in some cases potassium from illite can vaporize and subsequently condense. The main difference between the two Kentucky coals lies in the size of the illite inclusions. The #11 originally contained more illite in small (< 2.5 μm) inclusions while the #9 contained more in large (> 10 μm) aggregates. The Beulah Lignite

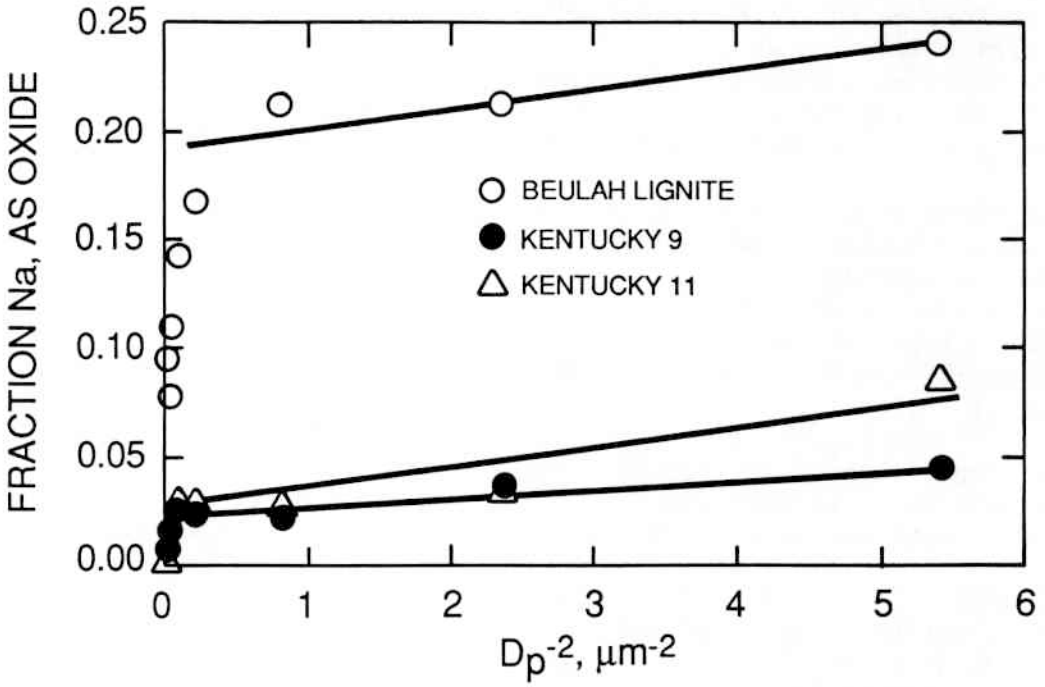


Figure 18. Na Concentration versus D_p^{-2}, Three Coals.

mineral inclusions containing potassium were also less than 2.5 µm, and so we may conclude that potassium in minerals can vaporize and subsequently condense, provided that the inclusions containing that mineral are sufficiently small to allow intimate contact with carbon during burnout. This suggests a reduction/vaporization/condensation mechanism for potassium minerals analogous to that proposed by Neville et al. (1981) for silicon and other refractory oxides. Large inclusions of illite show little or no evidence of vaporization and condensation.

Examination of the fraction of the total sodium distributed through all impactor stages and the after-filter demonstrates some interesting trends. Data for both the Loy Yang and the Beulah Lignite show more sodium in the after-filter than in the previous stages; the remaining coals do not, even though their submicron ash particles may be enriched in that element. These two coals were also the only ones showing evidence of a sodium fume, rather than mere surface enrichment, and so this suggests that it is the presence or absence of a coagulating sodium fume that really determines whether submicron particulate emissions are large or not.

The issue now is how to predict the fraction of sodium exhausted in the very small particle size range as a function of a measurable quantity characterizing coal composition. Figure 19 plots the fraction of total sodium ending up on a combination of the after-filter, stages 7 and 8, versus a measure of the fraction of the total sodium that can be considered to be organic. The latter is taken to be the ratio of acid

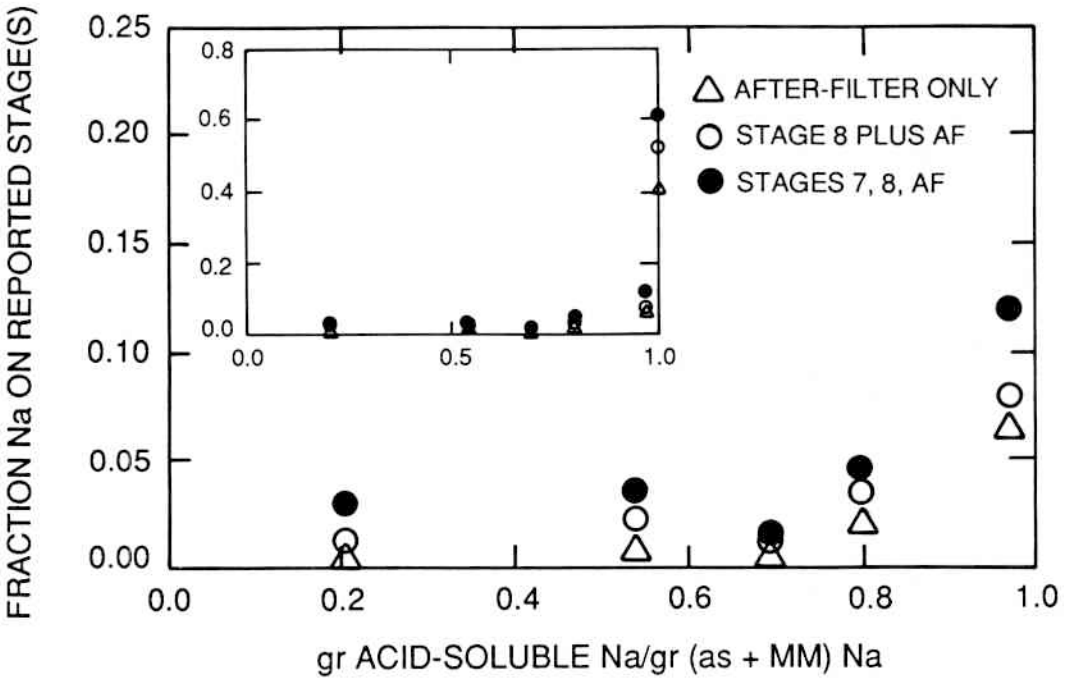


Figure 19. Fraction Na in Submicron Size Range versus Fraction Organic Na in Coal

soluble sodium to the total sodium, where the total is the sum of all the sodium identified in the mineral matter plus the acid soluble sodium. This total is usually greater than the ASTM sodium ash analysis, suggesting that some sodium may be lost during ashing. The inset shows data including the Loy Yang, while the main figure emphasizes the remaining coals (this being done, again, due to differing scales). Clearly the fraction of acid soluble sodium is a useful correlating variable. This may not be surprising since one might expect acid soluble sodium to vaporize during combustion. What may be surprising, however, is not how much, but how little of organic sodium actually ends up in the small particles.

The inset of Figure 19 shows an apparent discontinuity between the Beulah and the Loy Yang (the two coals with the highest organic sodium fractional content). The Loy Yang actually contains less sodium that the Beulah, because its ash content is low. Clearly, sodium vaporization is affected by the presence of other minerals, as has been previously suggested by Neville and Sarofim (1985). It is instructive to account for the presence of other species as in Figure 20 where the abscissa is the total organic sodium normalized by silicon as shown. Here the total organic sodium was taken to be the sodium on the total filter multiplied by the ratio denoting the fraction of that which is organic (see Figure 19) while the silicon was that on the total filter. Clearly, silicon has a strong inhibiting effect on the vaporization of sodium. Since, in our coals, total silicon was correlated with total

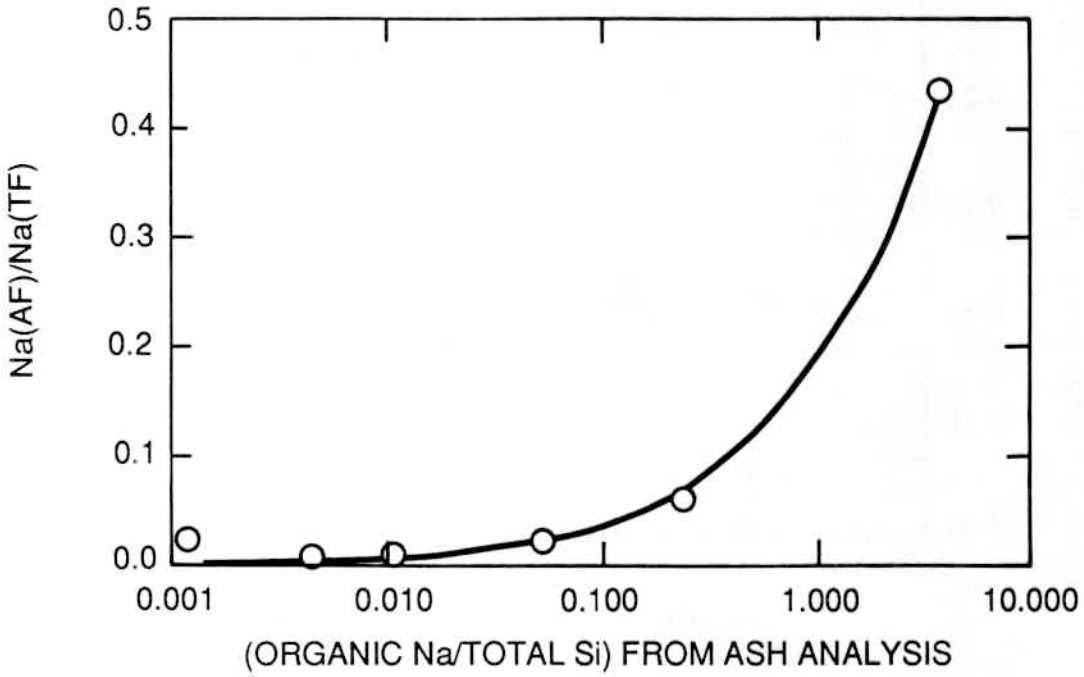


Figure 20. Fraction Na on AF versus Organic Na-to-Total Si Ratio.

aluminum and with other species (except calcium), one would obtain similar correlations using other species to normalize the organic sodium. Therefore, the data do not prove that silicon is the only inhibiting species. Calcium, however, can be shown definitely not to be the main inhibiting species and does not correlate as such, and silicon may on fundamental grounds be considered to be the most likely to scavenge sodium, whether or not it is combined with aluminum (see, for example, Wibberly and Wall (1982b) and Lindner et al. (1988)).

It should be noted that the fraction of potassium vaporized could not be correlated using simple relationships analogous to those depicted on Figures 19 and 20. This is not surprising, since it was noted above that potassium in the mineral form can also vaporize provided the mineral inclusions containing it are sufficiently small. The fraction of potassium vaporized, however, is always small.

In summary, alkali data suggest that the amount of sodium vaporized can be correlated with the fraction or organic sodium in the parent coal, and with the availability of a scavenging species, probably involving silicon, but not calcium. The fraction of organic sodium vaporized and finally ending up in the small particle size range can be quite low, especially in the presence of silicon in the ash.

6.7 ALKALI TRANSFORMATIONS DURING PULVERIZED COAL COMBUSTION: KINETIC MODELING AND EXPERIMENTAL MEASUREMENT

In order to fully understand the behavior of sodium in combustion environments, its form in the vapor phase must be known, as this will influence condensation patterns. Equilibrium calculations performed by Wibberley and Wall (1982a) demonstrate that under the reducing conditions present in a flame, atomic sodium will be the dominant sodium species in all but the most chlorine-rich coal systems. Under oxidizing conditions at temperatures greater than 1400 K, however, their calculations suggest that sodium chloride and sodium hydroxide will be the principal vapor phase species, although condensed phase silicates may dominate at temperatures below approximately 1700 K. The rates of these transformations in the complex reducing/oxidizing environment of a combustion environment, however, remain uncertain. Equilibrium indicates that condensed silicates and sulfates will be the principal sodium species at tube temperatures, but it does not indicate whether they will form rapidly and prior to condensation on tube and particle surfaces.

A kinetics scheme was developed to follow the transformations of atomic sodium in a combustion environment. The model, which employs the CHEMKIN code to solve the complex series of reactions, has been used to reproduce species profiles for $H_2/O_2/N_2/Na$ flames appearing in the literature (Hynes et al., 1984). Details of this model are presented elsewhere (Srinivasachar et al., 1989); a brief desccription of the highlights of the model follows.

6.7.1 Kinetic Model

Upon vaporization, atomic sodium quickly encounters the complex chemical environment surrounding the reacting char particles. Species such as H, OH, CO, O, and H_2O are present in this environment, and may affect the conversion of sodium to bound molecular states. Work in laboratory hydrogen flat flames has indicated this to be true, as experimental measurements of Na and OH coupled with kinetic modeling in lean hydrogen flames demonstrated that Na profiles roughly track the decay of H atoms (Hynes et al., 1984). In that study, the authors demonstrated that despite the existence of some 20 forward/ reverse reactions affecting sodium species in their hydrogen flame, the complex sodium chemistry was dominated by just seven reactions:

$$Na + H_2O = NaOH + H \quad (1)$$

$$Na + O_2 + M = NaO_2 + M \quad (2)$$

$$NaO_2 + H \rightarrow NaO + OH \quad (3)$$

$$NaOH + OH = NaO + H_2O \quad (4)$$

6.7.2 Sodium-Chlorine System

Understanding the transformations of sodium in a chlorine containing environment is an essential component in mitigating deposition and corrosion in the cooler convective region of many utility boilers. Although not present in large quantities in most U.S. coals, chlorine does appear in fairly high concentrations in selected British and Australian coals. Sodium levels in these fuels are typically high, allowing for the formation of sodium chloride in the flame and post-flame regions of a coal combustor.

Chlorine present as ionic linkages within the coal matrix is expected to volatilize rapidly prior to the release of sodium (Pearce and Hill, 1979). Residual chlorine present in the particle as NaCl will also volatilize rapidly, by dissociating in the reducing atmosphere of a pulverized coal particle to generate both atomic sodium and HCl. In either case, vapor phase Na and HCl quickly encounter the complex reducing-oxidizing chemistry of the flame and post-flame regions, where a variety of chemical reactions will occur in parallel as depicted schematically in Figure 21. Rate coefficients are from the literature (Jensen and Jones, 1978; Baulch et al., 1980; JANAF Thermochemical Tables, 1971). Note that several pathways exist for the formation of NaCl from Na, NaO, and NaOH reactions with HCl. NaO_2 may react with atomic chlorine to also form NaCl.

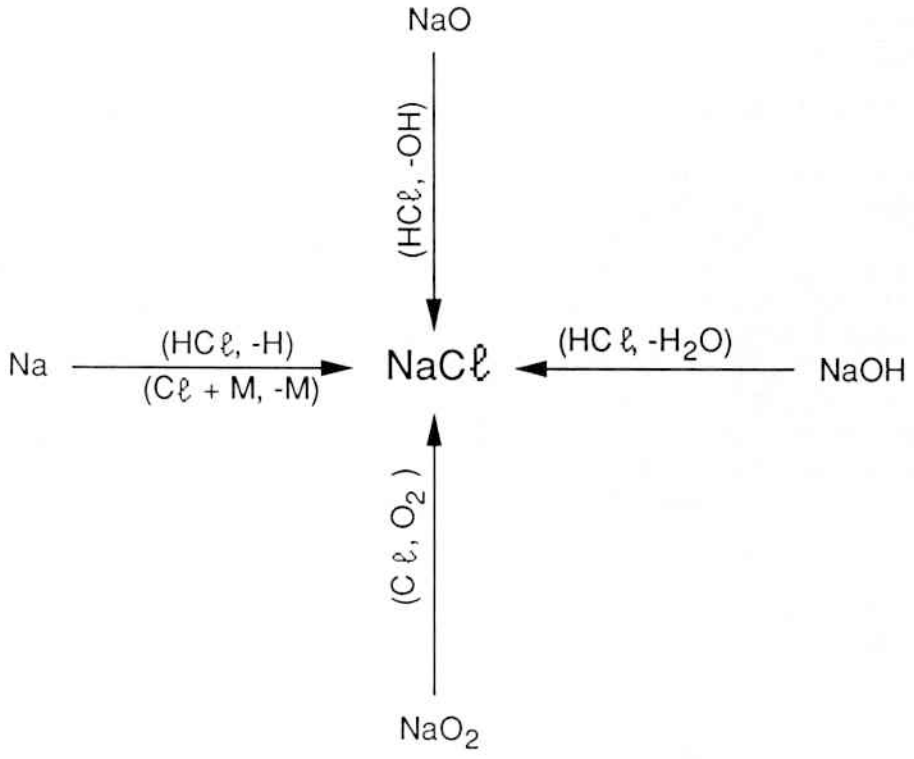


Figure 21. Schematic Depiction of Sodium - Chlorine System Interactions.

Utilizing these reactions and the appropriate rate coefficients, the model was extended to address the sodium-chlorine system. Calculations were performed with initial chlorine and sodium vapor loadings of 1 ppm each. Results from these calculations are presented in Figure 22, again demonstrating the two order of magnitude dominance of molecular sodium concentrations over atomic sodium. Atomic chlorine and atomic sodium levels decline by several orders of magnitude within 3 to 5 ms subsequent to the onset of oxidizing conditions at 1500 K, while sodium chloride and sodium hydroxide show a corresponding rapid increase in

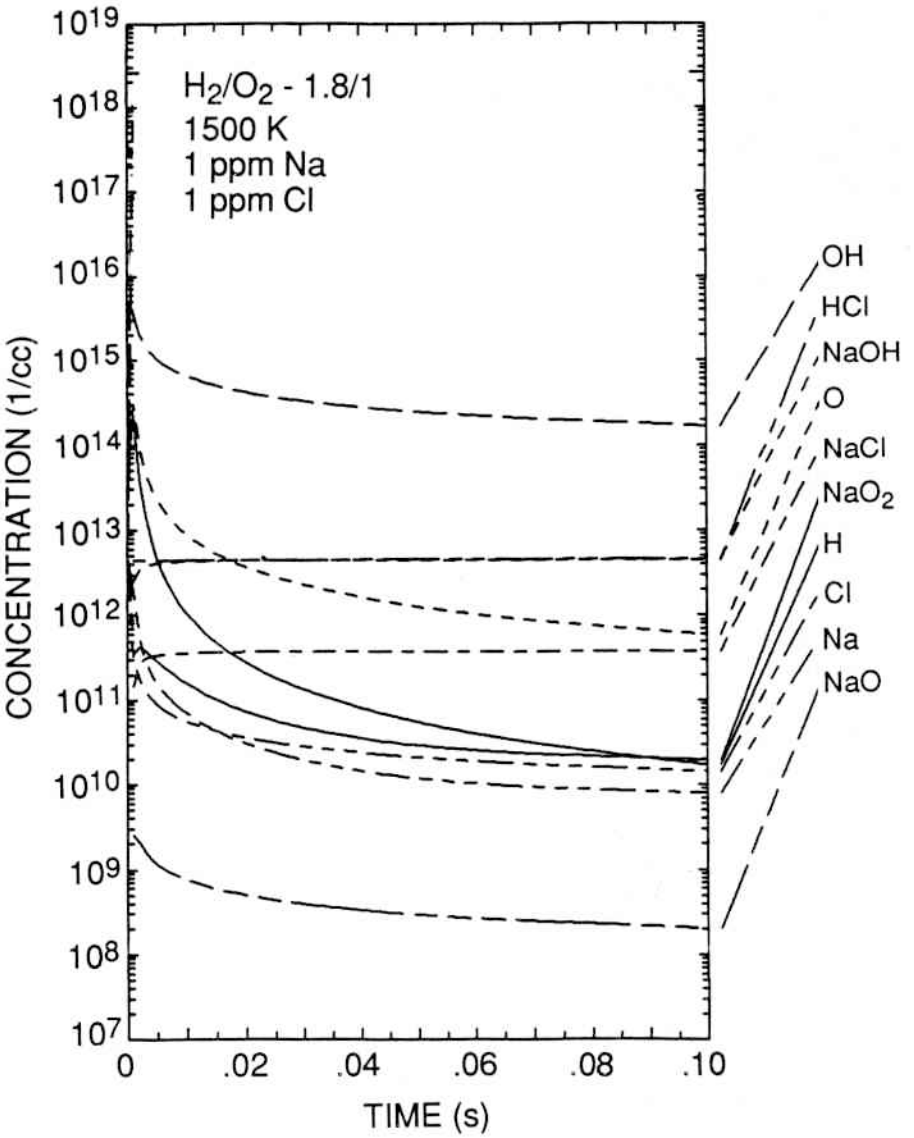


Figure 22. Sodium Transformations in the Presence of 1 ppm Cl at 1500 K.

concentration. At these low (1 ppm) starting values of chlorine, sodium hydroxide is seen to be the dominant sodium compound, present at 10 times the level of sodium chloride. Calculated equilibrium levels of the chloride and the hydroxide are in good agreement with the kinetically determined levels. When higher starting levels of chlorine (predominantly as HCl) are considered, fast kinetics cause equilibrium to be achieved rapidly, favoring sodium chloride over all other sodium species.

6.7.3 Alkali Molecular Measurements

Because of the importance of molecular species as identified in the literature and by these calculations, in-situ determination of alkali chloride and hydroxide species was conducted utilizing a laser-induced photodissociation and fluorescence technique developed at Los Alamos National Laboratory (LANL). Preliminary experiments were conducted with several samples to test the applicability of the LIPF technique to monitoring of NaCl concentrations in an atmospheric pressure environment. Experimental gas temperatures were maintained at 1200 K, with residence time (measurement location) fixed at 100 to 300 ms post-flame. Oxygen levels were varied between 10 and 30 percent oxygen in nitrogen. Coal particle feed rates ranged from 1 to 35 mg/min of (sieve and aerodynamically) classified 63/75 μm fractions.

In these experiments, Loy Yang Australian brown coal was burned at 20 percent O_2 and 1200 K at a variety of feed rates to test the response of the system to varying vapor phase NaCl concentration levels. Oxygen levels are constant through the course of these extremely fuel-lean experiments; i.e., each particle burns individually in 20 percent O_2 at all feed rates considered. As the results in Figure 23 demonstrate, a linear response was achieved as particle feed rates were varied from 1 to 5 mg/min. This linear response, which extrapolates through the origin, confirms the proportionality of signal strength to absolute vapor phase NaCl concentration levels. Error bars represent $\pm$ one standard deviation; 99 percent confidence limits are much smaller (typically $\pm$0.05V) due to the large number of data points (1000+) obtained per condition.

A comparison of normalized NaCl signal intensities for the various coals at the lowest feed rates and in 20 percent O_2 is presented in Figure 24. Sodium chloride levels are clearly greatest for the Loy Yang, consistent with the large quantity of Cl present in the parent coal. Illinois #6, noteworthy as one of the few U.S. coals which may contain chlorine in significant amounts, yielded the second highest concentrations of vapor phase NaCl. North Dakota Beulah, which contains large quantities of sodium but little or no chlorine, generated very low signal intensities confirming the selectivity of the LIPF technique for NaCl over NaOH at this excitation wavelength.

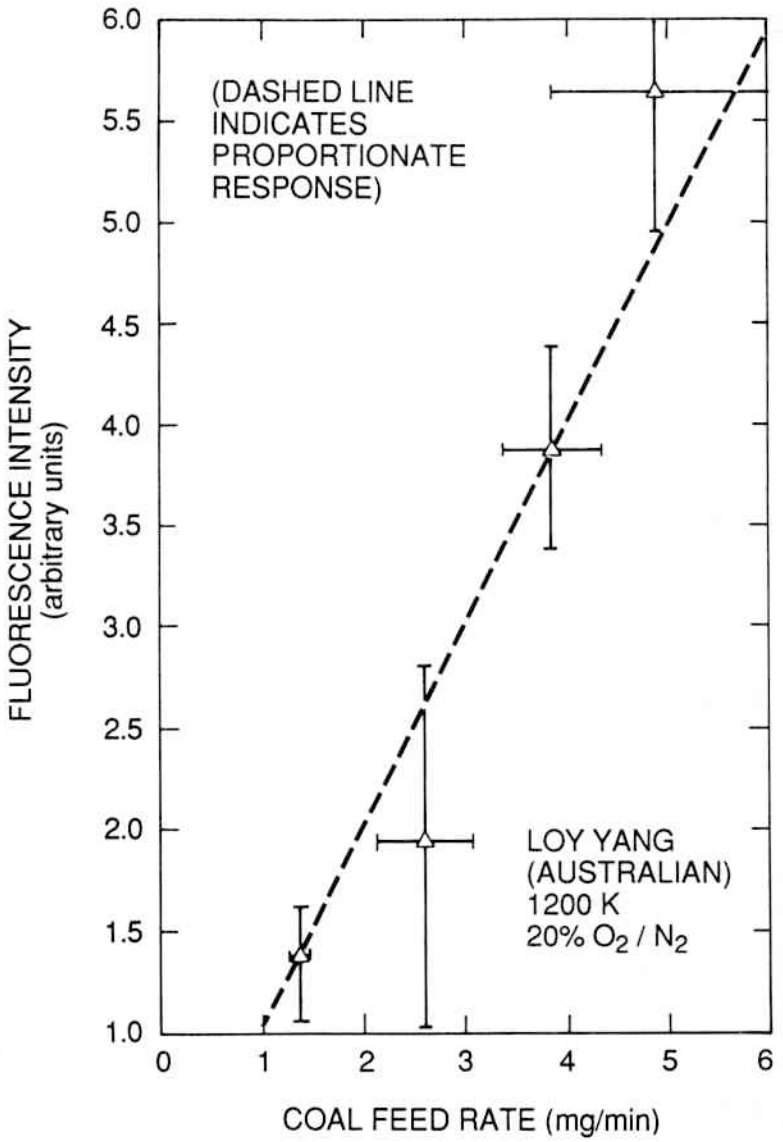


Figure 23. Effect of Feed Rate on Sodium Chloride Signal Strength.

6.8 ACCOMPLISHMENTS OF OVERALL PROJECT

In summary, the accomplishments of the project team are numerous, and some have been outlined above. However, we could provide the following list as the most significant:

- Established that the mineral form, size, and association principally determine the ash size and composition distribution. The combustion scale, from laboratory to pilot level, as measured in three independent laboratories using identical coal samples, yields nearly identical results for ash size/composition. For a range typical of pulverized coal furnaces, combustion conditions do not substantially affect the residual ash distribution. However,

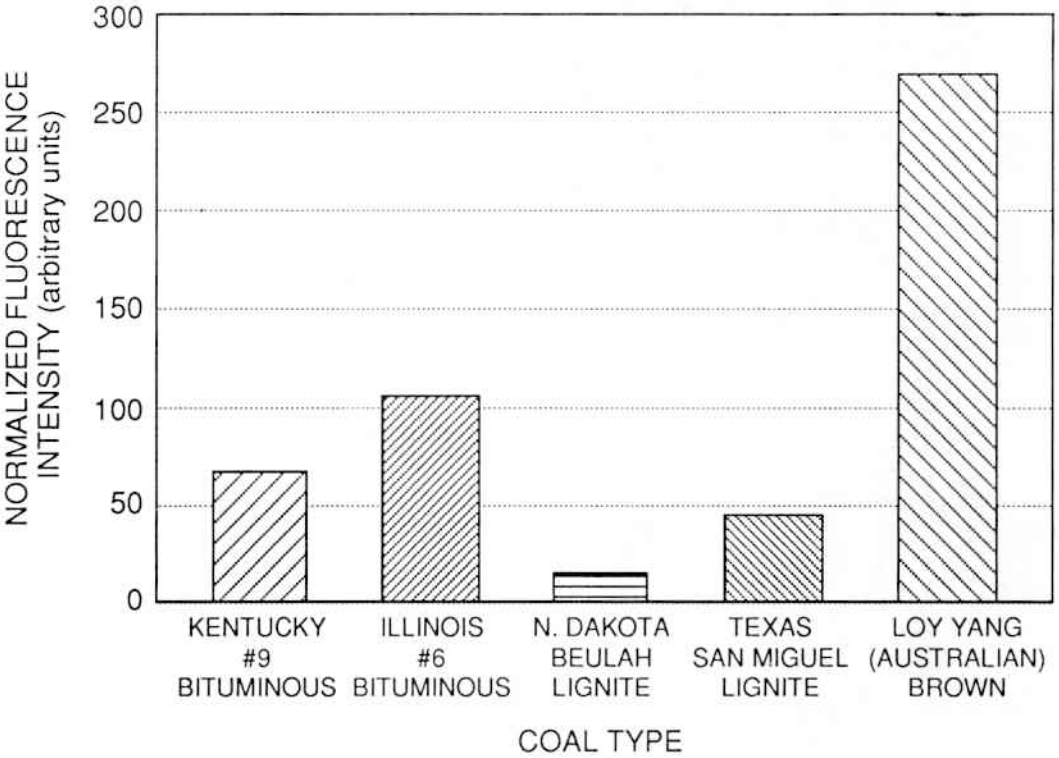


Figure 24. Effect of Coal Type on NaCl Level.

temperature of combustion and the quench rate are important factors in the fume formation and evolution process.

- Established that the minerals themselves can fragment substantially during combustion, thus yielding an ash size distribution that is less than the input mineral size distribution.

- Established that pyrite, illite, and silica are key minerals that contribute to slagging, and that the alkali (Na, K), calcium, and sulfur species, that occur principally as organically bound cations, dominate fouling.

- Developed and introduced CCSEM and software display capability to be used as new "routine" coal and ash characterization tools.

- Showed the feasibility of using LIPF as a new tool for studying alkali pathways in practical coal combustion systems. Our laboratory measurements and modeling have identified molecular alkali species as those that control the post-flame environment and contribute to boiler fouling.

- Initiated a cooperative project with an Australian group on initiation and control of fouling from brown coals. This group includes the State Electricity Commission of Victoria, the Electricity Trust of South Australia, CSIRO, and the University of Newcastle.

7. FUTURE PLANS:

At the present time, the project is in its final stages with respect to the present coal suite. We are synthesizing the data, and determining the parameters that control residual ash size/composition and fume composition for bituminous, subbituminous and lignitic coals. The key minerals, pyrite, illite, and silica determine the residual ash behavior, while the alkali and alkaline earth species control the fume. An engineering model is being developed to incorporate these key features. Beyond achieving the objectives of the project for this current suite of coals, we plan to extend this suite and additionally study the behavior of beneficiated coal fuels.

8. REFERENCES:

Austin, L.G., Abbott, F., and Kinneman, W.P., J. Inst. Energy, p. 196, December (1986).

Baulch, D.L., Cox, R.A., Hampson, Jr., R.F., Kerr, J.A., Troe, J., and Watson, R.T., J. Phys. Chem. Ref. Data 9, 295 (1980).

Boni, A.A., Bryers, R.W., Helble, J.J., Srinivasachar, S., Beér, J.M., Sarofim, A.F., Flagan, R.C., Huffman, G.P., Huggins, F.E., Peterson, T.W., and Wendt, J.O.L. (1988), "Transformation of Inorganic Coal Constituents in Combustion Systems," Proceedings of 1987 AR&TD Meeting, DOE/METC-88/684.

Boni, A.A., Helble, J.J., Srinivasachar, S., Flagan, R.C., Bryers, R.W., Sarofim, A.F., Beér, J.M., Peterson, T.W., Wendt, J.O.L., Huffman, G.P., and Huggins, F.E., in Proc. 1988 of the Advanced Research and Technology Development Direct Utilization and Instrumentation & Diagnostics Contractors' Review Meeting, NTIS Document No. DE89 0070296195 (1988).

Bryers, R.W., in Proc. EPRI Conf. on the Effects of Coal Quality in Power Plants, October (1987).

Charon, O., Kang, S.G., Graham, K., Sarofim, A.F., and Beér, J.M., "Variation in Coal Composition, a Computational Approach to Study the Mineral Composition," presented at 198th ACS National Meeting (April 1989). Submitted to Prog. Energy and Comb. Sci.

Flagan, R.C. and Friedlander, S.K. (1978), "Particle Formation in Pulverized Coal Combustion - A Review," in Recent Developments in Aerosol Science, D.T. Shaw, Ed. Wiley Interscience, New York, NY, pp. 25-59.

Forrest, S.R. and Witten, T.A. (1979), J. Phys. A. 12, L109.

Helble, J.J., Srinivasachar, S., and Boni, A.A. (1989a), "Factors Influencing the Transformation of Minerals During Pulverized Coal Combustion," presented at 198th ACS National Meeting (April). Submitted to Prog. Energy and Comb. Sci.

Helble, J.J., Srinivasachar, S., and Boni, A.A. (1989b), "Factors Influencing Mineral Transformations in Low Rank Coals," presented at the Fifteenth Biennial Low Rank Fuels Symposium, St. Paul Minnesota (May).

Helble, J.J., Srinivasachar, S., Boni, A.A., Kang, S.G., Sarofim, A.F., Beér, J.M., Shah, N., Huggins, F.E., Huffman, G.P., Peterson, T.W., and Wendt, J.O.L. (1989c), "Effects of Combustion Scale on Fundamental Mineral Transformations for Selected U.S. Coals," Pittsburgh Coal Conference (September).

Huffman, G.P. and Huggins, F.E. (1978), Fuel 57, 592.

Huffman, G.P. and Huggins, F.E. (1984), "Analysis of the Inorganic Constituents in Low-Rank Coals," ACS Symposium Series No. 264, pp. 159-174, Chemistry of Low-Rank Coals, edited by H.H. Schobert, Amer. Chem. Soc.

Huffman, G.P., Huggins, F.E., Levasseur, A.A., Durant, J., Lytle, F.W., Greeger, R.B., and Mehta, A. (1989a), "Investigation of Atomic Structures of Calcium in Ash and Deposits Produced During the Combustion of Lignite and Bituminous Coal," Fuel 68, 238-242.

Huffman, G.P., Huggins, F.E., and Shah, N. (1989b), "Behavior of Basic Elements During Coal Combustion," presented at 198th ACS National Meeting (April). Submitted to Prog. Energy and Comb. Sci.

Huffman, G.P., Huggins, F.E., Srinivasachar, S., Levasseur, A.A., Chow, O., and Mehta, A. (1989c), "Investigation of the Transformation of Pyrite in a Drop-Tube Furnace," Fuel 68, 485-490.

Huggins, F.E. and Huffman, G.P. (1979), "Mössbauer Analysis of the Iron-Bearing Phases in Coal, Coke, and Ash," Analytical Methods for Coal and Coal Products, Vol. III (Academic Press), Chapter 50, 371-423, edited by C. Karr, Jr.

Huggins, F.E., Huffman, G.P., and Lee, R.J. (1982), "Scanning Electron Microscopy-Based Automatic Image Analysis (SEM-AIA) and Mössbauer Spectroscopy: Quantitative Characterization of Coal Minerals," ACS Symposium Series No. 205, pp. 239-258, Coal and Coal Products: Analytical Characterization Techniques, edited by E.L. Fuller, Jr., American Chemical Society.

Huggins, F.E., Huffman, G.P., Srinivasachar, S., Levasseur, A.A., Chow, O., and Mehta, A. (1989), Fuel 68, 238-242.

Hynes, A.J., Steinberg, M., and Schofield, K. (1984), J. Chem. Phys. 80, 2585.

JANAF Thermochemical Tables (1971), Nat. Stand. Ref. Ser., Nat. Bur. Stand. 37.

Jensen, D.E. and Jones, G.A. (1978), Combust. and Flame 32, 1.

Kang, S-G., Helble, J.J., Sarofim, A.F., and Beér, J.M. (1988), Twenty-Second Symposium (International) on Combustion, The Combustion Institute, 231.

Lee, R.J., Huggins, F.E., and Huffman, G.P. (1978), Scanning Electron Microscopy, Vol. I, SEM Inc., AMF O'Hare, IL, 561-568.

Lindner, E.R. (1988), Ph.D. Thesis, Department of Chemical and Materials Engineering, University of Newcastle (NSW), February.

Lindner, E.R., Kosminski, A., Taylor, C., and Williams, R.G. (1988), "Effects of Additives on Fouling Behavior Characteristics of South Australian Brown Coals," Proc. Fourth Engineering Foundation Conf. on Mineral Matter and Ash Deposition from Coal, Santa Barbara, CA, February 21-26.

Lindner, E.R. and Wall, T.F. (1988), "An Experimental Study of Sodium-Ash Reaction During Combusation of Pulverized Coal," Proc. Fourth Engineering Foundation Conf. on Mineral Matter and Ash Deposition from Coal, Santa Barbara, CA, February 21-26.

Muller, C.H., Schofield, K., Steinberg, M., and Broida, H.P. (1979), Seventeenth Symposium (Int'l) on Combustion, The Combustion Institute, Pittsburgh, p. 867.

Neville, M., Quann, R.J., Haynes, B.S., and Sarofim, A.F. (1981), "Vaporization and Condensation of Mineral Matter During Pulverized Coal Combustion," 18th Symp. (Int'l) on Combustion, The Combustion Institute, Pittsburgh, PA, 1267-1274.

Neville, M. and Sarofim, A.F. (1985), "The Fate of Sodium During Pulverized Coal Combustion," Fuel 64, 384-390.

Oldenborg, R.C. and Baughcum, S.L. (1986), Anal. Chem. 58, 1430.

Pearce, W.C., and Hill, J.W.F. (1986), Prog. Energy Combust. Sci. 12, 117.

Quann, R.J. and Sarofim, A.F. (1982), Nineteenth Symposium (Intl.) on Combustion, The Combustion Institute, Pittsburgh, PA, pp. 1429-1439.

Raask, E. (1985), Mineral Impurities in Coal Combustion (Hemisphere Publishing Co., New York).

Reid, W.T. (1984), Prog. Energy Combust. Sci. 10, 159.

Rogak, S.N. and Flagan, R.C. (1989), "Stokes Drag on Self-Similar Clusters of Spheres," J. Colloid Interface Sci., in press.

Springer, G.S. (1978), Adv. Heat Transfer 14, 281-346.

Srinivasachar, S. and Boni, A.A. (1989), "A Kinetic Model for Pyrite Transformations in a Combustion Environment," Fuel 68, 829-836.

Srinivasachar, S., Helble, J.J., and Boni, A.A. (1989a), "Mineral Behavior During Coal Combustion -- 1. Pyrite Transformations," presented at 198th ACS National Meeting (April). Submitted to Prog. Energy and Comb. Sci.

Srinivasachar, S., Helble, J.J., Boni A.A., Huffman, G.P., Huggins, F.E., and Shah, N. (1989b), "Mineral Behavior During Coal Combustion: 2. Illite Transformations," to be published in Prog. in Energy and Comb. Sci.

Srinivasachar, S., Helble, J.J., Ham, D., and Domazetis, G. (1989c), "A Kinetic Description of Alkali Transformations in Combustion Systems," presented at 198th ACS National Meeting (April). Submitted to Prog. Energy and Comb. Sci.

Srinivasachar, S., Helble, J.J., Katz, C.B., and Boni, A.A. (1988), "Transformations and Adhesion of Minerals During Pulverized Coal Combustion," Proceedings from Engineering Foundation Conference on "Mineral Matter and Ash Deposits in Coal," Santa Barbara, CA (1988) (in press).

Turner, J.R. and Hering, S.V. (1987), "Greased and Oiled Substrates as Bounce-Free Impaction Surfaces," J. Aerosol Science 18(2), 215-224.

Weingartner, E.C. (1974), ASME Research Committee on Corrosion and Deposits from Combustion Gases Report.

Wibberley, L.J. and Wall, T.F. (1982a), Fuel 61, 87.

Wibberly, L.J. and Wall, T.F. (1982b), "Alkali-Ash Reactions and Deposit Formation in Pulverized-Coal-Fired Boilers: Experimental Aspects of Sodium Silicate Formation and the Formation of Deposits," Fuel 61, 93-99.

Wu, J.J. and Flagan, R.C. (1988), J. Colloid Interface Sci. 123, 339-352.

THE FATE OF MINERAL MATTER DURING PULVERIZED COAL COMBUSTION

1. FTPA NUMBER: 0709

CONTRACTOR:

Sandia National Laboratories
7011 East Avenue
P.O. Box 969
Livermore, California 94551-0969
Phone: (415)294-2322

CONTRACT PROJECT MANAGER: Donald R. Hardesty

PRINCIPAL INVESTIGATOR: Larry L. Baxter

PETC PROJECT MANAGER: James Hickerson

CONTRACT PERIOD: October 1, 1988 - Continuing

2. SCHEDULE/MILESTONES:

1989 Program Schedule

Task	Month											
	O	N	D	J	F	M	A	M	J	J	A	S
Sampling Probe and Low Mass Flowrate Coal Feeder							√				√	
PCSV and Spin Physics Camera Installation and Verification				√		√						
Fragmentation Studies												√
Fragmentation Model Development												√
CCL & CDL Data Analysis	√			√			√			√		

3. OBJECTIVES:

The long-term objective of this project is to gain quantitative understanding of the rates and mechanisms of selected aspects of mineral matter evolution, transport and deposition under conditions relevant to pulverized coal combustion. These selected aspects of mineral matter evolution include: (1) release of inorganic material from coal particles during reaction of the organic and inorganic portions of the particle and by vaporization; (2) changes in mineral matter composition during combustion; (3) size distributions of flyash formed during combustion; and (4) deposition of mineral matter on surfaces. These aspects of mineral matter evolution are studied as a function of coal and mineral type, total ash loading, rate of organic and inorganic reaction, local gas conditions, and time. The two major subtasks identified for FY89 are (1) Particle Fragmentation and (2) Mineral Matter Transformations During Coal Combustion.

4. BACKGROUND STATEMENT:

Mineral matter has been cited as "the nemesis of coal-burning industries" and as playing "the dominant role in fuel selection, in setting the design and size of the furnace, and in establishing how that boiler furnace will be operated" [Raask, 1985]. This project represents a fundamental investigation of mineral matter behavior during combustion that is focused on practically relevant aspects of the topic.

The first subtask addresses the topic of particle fragmentation and flyash formation. This subtask studies the relationship between flyash particle size distributions and char particle size distributions. The experimental portion of the project determines the extent of particle fragmentation during char oxidation. The theoretical portion deduces physical and mechanical mechanisms for fragmentation from these data. The modeling portion of the project involves incorporating the findings into a fragmentation submodel and then into a comprehensive computer code.

The second subtask addresses the topic of transformations of mineral matter during coal combustion. These are broadly categorized into areas of mineral matter release from coal particles, coalescence of residual mineral grains in the particle, and chemical/physical transformations of the mineral grains.

5. PROJECT DESCRIPTION:

Several facilities at the Sandia Combustion Research Facility are used in studying mineral matter behavior during coal combustion. These include the Coal Devolatilization Laboratory (CDL), the Char Combustion Laboratory (CCL) and the Multifuel Combustor (MFC). The former two laboratories are used principally to study the indicated aspects of the organic reactivity of coal. Both the CDL and CCL are laminar flow facilities operating at low particle loadings. They are referenced elsewhere [Fletcher, 1989; and Mitchell, 1989]. The MFC is schematically illustrated in Figure 1. It is a relatively new facility, first used this year in support of this project. The MFC is a long residence time ($\approx$ 3.0 s), turbulent flow combustor with adjustable gas concentration and temperature profiles. The combustor is operated at a firing rate and particle

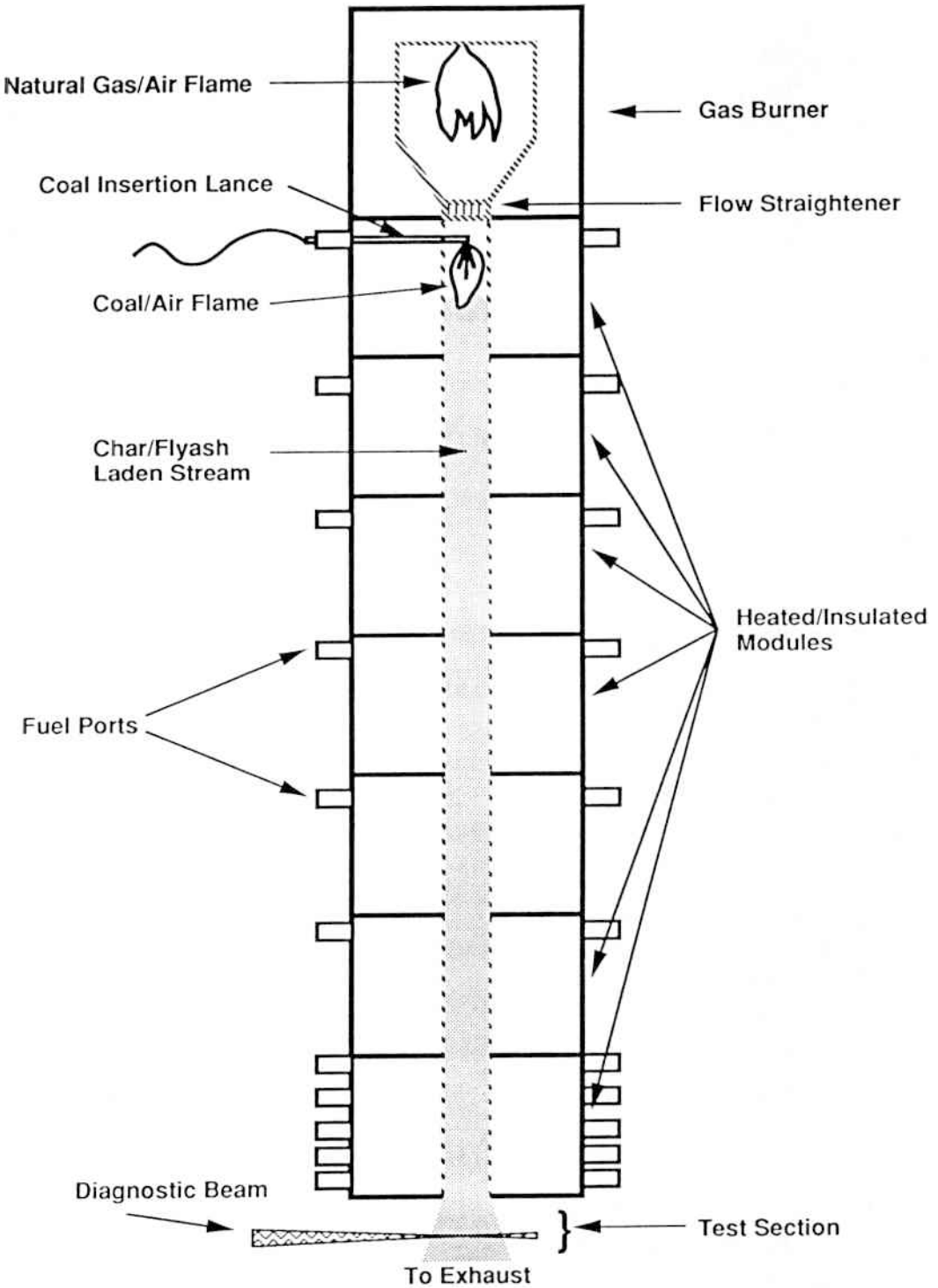


Figure 1: Schematic illustration of the multifuel combustor (MFC) used in this project.

loading typical of commercial-scale combustors. It allows both in situ and sampled analysis of the reacting, particle-laden flow at arbitrary residence times. It has been used primarily to study the extents and rates of particle fragmentation. Variations in particle residence time are achieved by moving the location of the fuel injection lance to the different ports in the reactor.

A host of in situ diagnostics and laboratory analyses are used in conjunction with this project. In situ diagnostics include particle sizing pyrometers, high-speed video imaging systems, and a Particle Counter Sizer Velocimeter (PCSV). Laboratory analyses include computer-controlled scanning electron microscopy (CCSEM), and a variety of elemental and other ASTM analyses of coal, char, flyash and deposits.

Fuels used during this project were selected either from the DOE-designated list of PSOC coals or from those coals being used in a separate investigation of mineral matter behavior under the direction of Physical Sciences Incorporated (PSI) [Boni, 1989].

6. RESULTS/ACCOMPLISHMENTS:

PARTICLE FRAGMENTATION

Fragmentation studies were completed for all coals shipped to Sandia by PSI. These included samples of Illinois #6 and Kentucky #9 coals and a Beulah lignite. Initial char size distributions and final flyash particle size distributions were measured using the PCSV. Quantitative estimates of the extent of char fragmentation and mechanistic descriptions of some aspects of the fragmentation process were deduced from these data.

Two types of char fragmentation have been defined in the analysis of these data. Type I fragmentation results in a fragment size distribution which includes a broad range of sizes. This is the most common type of fragmentation discussed in the literature and experimental evidence is available to describe the size distribution of the fragments [Quann and Sarofim, 1986, for example]. Type II fragmentation results in a fragment size distribution which is much more narrow. Ideally, all of the fragments could be considered to be the same size. Our data are most satisfactorily described by type II fragmentation, as discussed below.

Type II fragmentation can be characterized by a single, diameter-dependent parameter. This parameter, designated f, represents the ratio of the flyash particle size resulting from complete coalescence of char mineral to that actually observed. Alternatively, the cube of f represents the number of fragments produced from a given char particle. This parameter is determined uniquely as a function of size from a combination of mass and number balances. The particle mass balance is given by

$$\pi \frac{\rho_c d_c^3}{6} \omega_a = \pi \frac{\rho_a \left(f(d_a)\ d_a\right)^3}{6} \qquad (1)$$

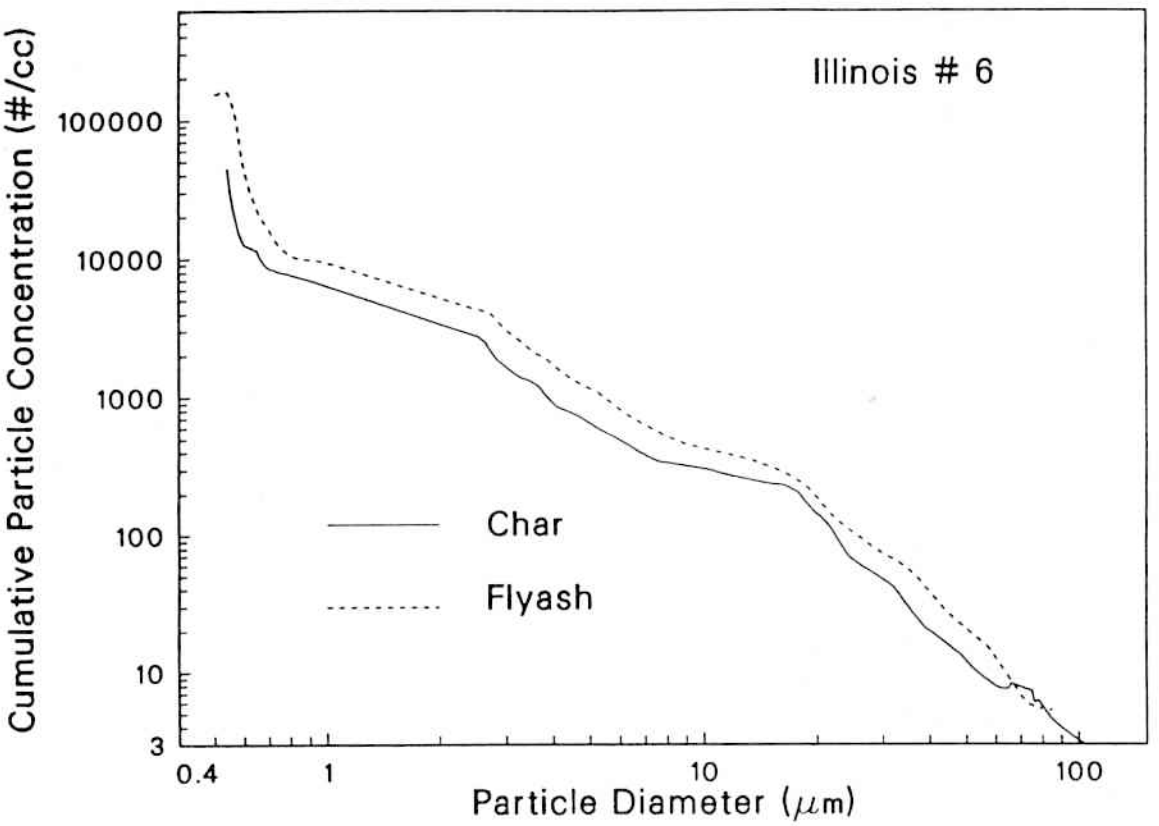


Figure 2: Concentration distributions of char and flyash as determined by the PCSV for the Illinois #6 coal.

where subscript c and a represent char and ash, respectively. Density, diameter, and mass fraction are represented by ρ, d and ω, respectively. This mass balance yields the relationship between char and flyash particle sizes.

$$d_c = \left(\frac{\rho_a}{\omega_a \rho_c}\right)^{1/3} f(d_a)\, d_a \tag{2}$$

For a given flyash particle size, the unknown quantities in this expression are the char particle size d_c and f. A particle number balance provides the second independent equation to allow f to be solved as a function of either d_c or d_a. This balance is written as

$$\int_{\infty}^{d_c} f^3(x) n'_c(x) dx = \int_{\infty}^{d_c} n'_a(x) dx \tag{3}$$

where n' represents the derivative of data such as those presented in Figure 2 with respect to particle size. (The data in Figure 2 are discussed later). That is, n' represents the particle concentration per unit particle size as a function of particle size. The variable x is used as a dummy variable of integration for particle size. Note that the relationship between d_c and d_a must be monotonic for this number balance to be valid.

An expression for the fragmentation factor f is obtained from this number balance by differentiating the equation:

$$f(d_c) = \left(\frac{n'_a(d_a)}{n'_c(d_c)} \right)^{1/3} \tag{4}$$

In a simple case, where f, ρ_a, ρ_c and ω_a are independent of diameter, the particle concentrations as a function of size (concentration distributions) for char and flyash take on a unique relationship on a log-log plot. The *shape* of each distribution is identical, with the flyash size distribution being shifted to smaller diameters by a constant factor (constant displacement on a logrithmic scale) logarithmic scale) as a consequence of both combustion and fragmentation (Eq. 2) and being shifted to higher concentrations as a consequence of fragmentation (Eq. 4).

Figure 2 illustrates the char and flyash cumulative concentration distributions typically measured for the high-rank coals during these experiments. These cumulative concentration distributions show the concentration of particles of a given size or larger at a point in the reactor. The illustrated data represent the average of 5-6 experiments for both the flyash and char of the Illinois #6 coal. These replicated experiments allow calculation of confidence intervals for the data. Similar data and confidence intervals were determined for each of the other coals studied.

Note that the two concentration distributions are quite similar in their functional shape on this log-log plot. Attempts to describe these data with type I fragmentation consistently lead to the conclusion that the size distribution of the flyash is limited to a very small range of particle diameters, i.e., type II fragmentation. The lignite concentration distributions were also reasonably represented by type II fragmentation, although they showed slightly more difference in shape than the data from the higher rank coals. The remainder of the data is analyzed in the context of type II fragmentation.

Figure 3 illustrates the variation of f with initial char diameter for the Kentucky #9 coal. Similar results were obtained for the Illinois #6 coal. The data suggest modest fragmentation of the high rank coals with the extent of fragmentation decreasing slightly, on average, with increasing mineral content. Typically, up to a few tens of flyash particles are generated per original coal particle. However, the largest char particles (70-150 μm) fragmented more extensively. These large particles form a small fraction of the overall particle flow stream on a number basis but are more significant on a mass basis.

Figure 4 shows similar data plotted as a function of *flyash particle diameter*, this time for the Illinois #6 coal. Note that the original flyash and char concentration distributions are similar (Fig. 2) despite reasonably large variations of f with particle size shown in Figure 4.

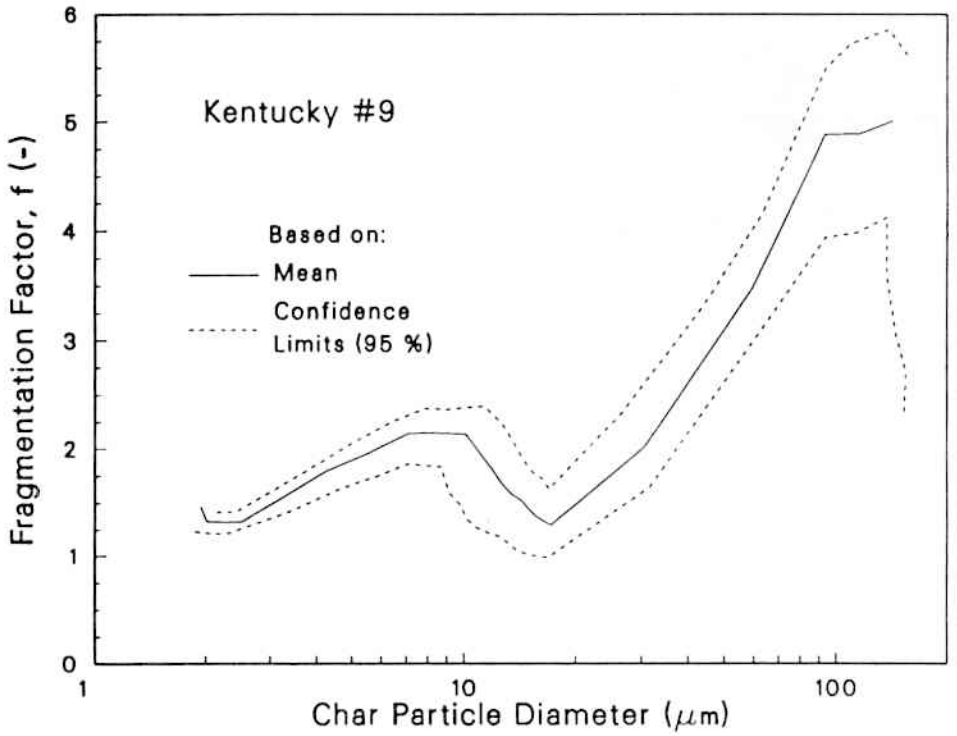


Figure 3: Variation of the fragmentation factor f with initial char diameter for the Kentucky #9 coal.

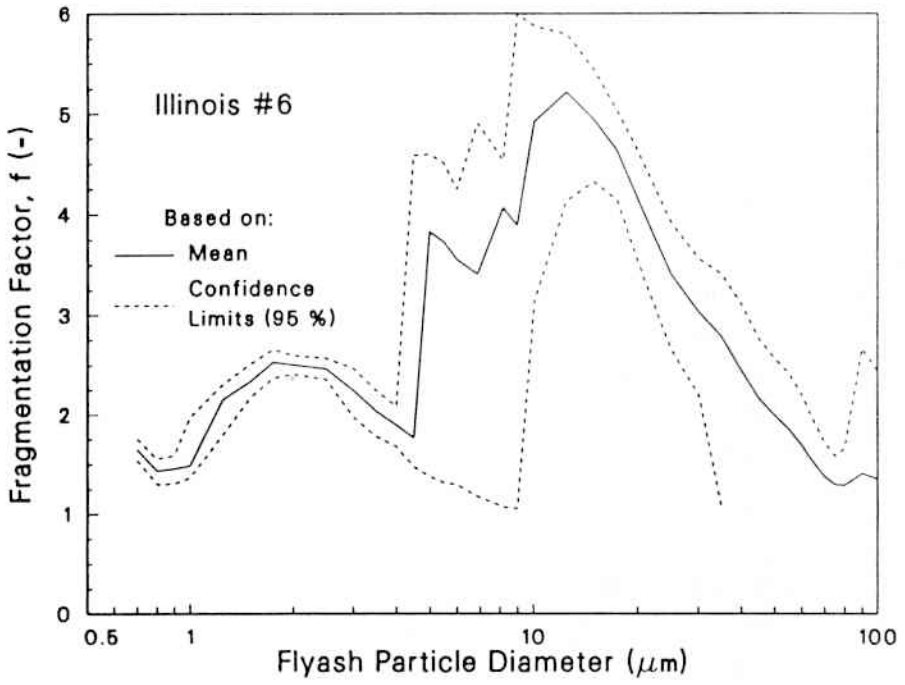


Figure 4: Variation of the fragmentation factor f with flyash particle diameter for the Illinois #6 coal.

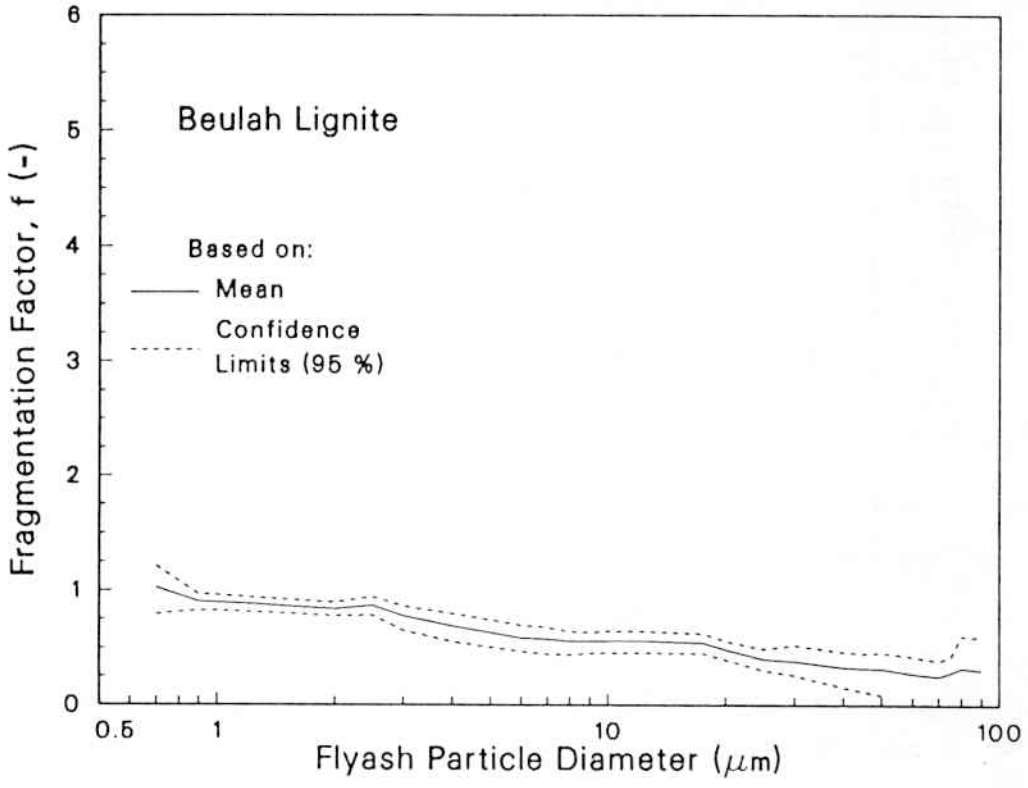


Figure 5: Variation of the fragmentation factor f with flyash particle diameter for the Beulah lignite.

Illinois #6 and the Kentucky #9 coals have similar organic and inorganic compositions. A Beulah lignite was investigated to determine sensitivity of the results to changes in coal rank and mineral composition. The fragmentation factor f for the lignite is shown in Figure 5 as a function of flyash particle diameter. Note that both the extent of fragmentation, indicated by the magnitude of f, and the mode of fragmentation, indicated by the diameter dependence of f are substantially different for the different rank coals. Essentially no char fragmentation is observed for the lignite.

The differences in the behavior of the different rank coals and the peaks in the fragmentation factor as a function of flyash particle size can be explained in terms of char morphology and the initial mineral size distribution in the coal. The chars formed from the high rank coals were cenospherical or mesocenospherical, i.e, contained large internal voids and relatively thin walls. This behavior appears to be more pronounced as the size of the char particle increases. The chars formed from the lignite appeared to be separated along boundaries of laminae and to have largely maintained their interior structural integrity. As the high rank cenospherical chars oxidize, the organic shell will begin to loose its structural integrity and would be expected to fall apart, forming

same number of flyash fragments. On the other hand, the lignite char appears not to disintegrate. Rather, the minerals coalesce along the surface to eventually form one mineral grain per original char particle.

The variation of the extent of fragmentation with size in the high rank coals has at least two possible explanations. The first is related to the fraction of mineral matter in the char. This fraction increases in these coals with decreasing particle size. As the fraction of mineral matter in a given char particle increases, the potential for mineral coalescence before char fragmentation also increases. Therefore, the number of fragments produced from the small, higher ash char particles would be expected to be smaller than the number produced from the large, lower ash particles.

The second explanation of the general trend deals with the details of char morphology. Cenosphere formation typically is attributed to the generation and coalescence of bubbles formed from volatiles released within the softened particle. Our preliminary observations suggest that the extent of cenosphere formation decreases with decreasing particle size. That is, the walls of small particles are thicker, relative to the particle size, than those for the large particles. If the small particles in fact have smaller internal voids relative to their size than the large particles, the small particles would present more opportunity for mineral grain coalescence and thus produce fewer fragments per particle than their larger counterparts. The details of the fragmentation experiments are discussed more completely by Baxter [1989b].

MINERAL TRANSFORMATIONS

Fundamental experimental and theoretical work completed curing FY89 illustrate several important aspects of mineral transformations during coal combustion. These include (1) mineral release associated with reactivity of the inorganic material [Baxter and Mitchell, 1989], (2) mineral release associated with organic reactivity [Baxter, 1989c], (3) mineral grain fragmentation during the early stages of combustion [Baxter, 1989a] and (4) the time dependence of particle capture efficiency on deposition surfaces [Baxter et al., 1989]. These issues are discussed more completely in the cited papers.

7. FUTURE WORK:

Future work includes testing of the several more detailed hypotheses generated as a consequence of FY89 progress. Specifically, we will test the hypothesis that organically bound minerals may be released by convective transport during coal devolatilization and the hypothesized mechanisms of char fragmentation discussed above. We also will continue analysis of ash deposition on simulated boiler surfaces in conjunction with industrial collaborators.

8. REFERENCES:

Baxter, L.L., R.E. Mitchell, 1989. "The Release of Iron During the Combustion of Illinois # 6 Coal," submitted to *Combustion and Flame*, and presented at the Sixth International Coal Conference, Pittsburgh Pennsylvania, September 25-29, 1989

Baxter, L.L., N.S. Harding and K.R. Hencken, 1989 "The Dynamic Variation of Particle Capture Efficiency During Mineral Matter Deposition in Coal-Fired Combustors," to be presented at the 1989 Joint Power Generation Conference , Dallas, TX, October 22-26

Baxter, L.L., 1989a "The Evolution of Mineral Particle Size Distribution During Early Stages of Coal Combustion," submitted to *Progress in Energy and Combustion Science*

Baxter, L.L., 1989b "Experimental Study of Char Fragmentation During Pulverized Coal Combustion," in preparation

Baxter, L.L., 1989c "Release of Inorganic Material During Coal Devolatilization ," in preparation.

Boni, A.A., J.J Helble and S. Srinivasachar "Transformation of Inorganic Coal Constituents in Combustion Systems," presented at the Advanced Research and Technology Development Direct Utilization, Instrumentation and Diagnostics Contractors Review Meeting, Morgantown, West Virginia, October 3-5

Fletcher, T.H., 1989 "Kinetics of Rapid Coal Devolatilization," presented at the Advanced Research and Technology Development Direct Utilization, Instrumentation and Diagnostics Contractors Review Meeting, Morgantown, West Virginia, October 3-5

Mitchell, R.E., 1989 "Rates and Mechanisms of Combustion of Pulverized Coal Chars" presented at the Advanced Research and Technology Development Direct Utilization, Instrumentation and Diagnostics Contractors Review Meeting, Morgantown, West Virginia, October 3-5

Quann, R.J. and A.F. Sarofim, 1986 "A Scanning Electron Microscopy Study of the Transformations of Organically Bound Metals during Lignite Combustion," *Fuel* 65:40

Raask, E. 1985 *Mineral Impurities in Coal Combustion*, Hemisphere Pub. , Washington

COMBUSTION INORGANIC TRANSFORMATIONS

1. CONTRACT NUMBER: DE-FC21-86MC10637

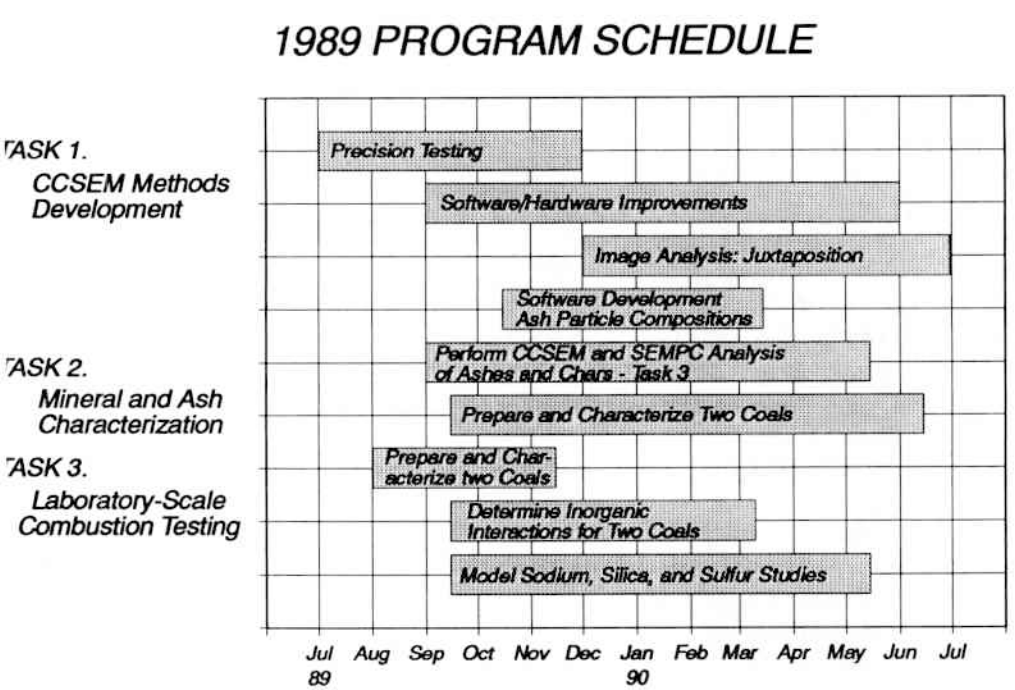
CONTRACTOR: Energy and Mineral Research Center
University of North Dakota
15 N. 23rd Street
Box 8213, University Station
Grand Forks, North Dakota 58202
(701)777-5177

PRINCIPAL INVESTIGATORS: Steven A. Benson
Chris J. Zygarlicke
Edward N. Steadman
Donald P. McCollor

PETC PROJECT MANAGER: Philip M. Goldberg

CONTRACT PERIOD OF PERFORMANCE: July 1, 1989 through June 30, 1992

2. SCHEDULE/MILESTONES:



3. OBJECTIVES:

The overall objective of this project is to develop a unified picture of the physical and chemical changes that occur in coal inorganic matter during combustion. The research is centered on three main tasks. The first task will involve developing the computer-controlled scanning electron microscope/microprobe methodology to determine the distribution

of mineral grains in pulverized coals. The second task will involve determining the inorganic components in coal and coal ash-derived components from coals and ashes. The third task will study the physical and chemical changes of inorganic components in coals and model mixtures using a drop-tube furnace.

4. BACKGROUND STATEMENT:

Many operational problems encountered during combustion of coal in utility boilers are related to the inorganic constituents of the coal. The problems include: deposition on heat transfer surfaces; formation of fine particulate that is difficult to collect; and erosion and corrosion of boiler parts. Because of the importance of these problems there is voluminous literature on the subject. However, a precise and quantitative knowledge of the chemical and physical transformations of the inorganic components in coal during combustion has not been obtained due to the complexity of the processes involved. At present, it is not possible to accurately predict the fate of the inorganic constituents during combustion as a function of coal composition and combustion conditions. The current methods use the composition of the coal ash produced under ASTM ashing conditions as a crude guide to predict the behavior of inorganic constituents of a specific coal during combustion. This technique can be used to predict average properties of the ash, since all the inorganic components are combined and allowed to interact during the ashing process. However, examination of fly ash shows that many different types of particles are present, each having its own composition and probably its own melting behavior. The wide variation of fly ash types is related to the wide variability in the abundance and distribution of inorganic constituents in a coal.

The extent of ash-related problems largely depends upon the abundance and mode of occurrence of inorganic constituents. The inorganic constituents in coals are distributed within the coal matrix as cations associated with organic acid groups and clays, organically coordinated species, and as discrete mineral grains. The minerals in pulverized coal are associated within coal particles, and as individual grains not associated with coal. In addition, minerals can be associated with other mineral grains. The juxtaposition of minerals in the pulverized coals must be determined in order to effectively predict their fate during combustion. The abundance of the inorganic constituents within the various modes of occurrence varies between coals and ranks of coal. For example, low-rank coals, unlike bituminous coals, contain high quantities of oxygen, of which a portion is associated in the coal as carboxyl groups. These organic acid groups can attract significant quantities of alkali and alkaline earth elements. In bituminous coals, most of the inorganic portion is present as discrete mineral phases. Due to these differences in association of inorganic components, these coals behave quite differently in utility boilers. For example, the higher-rank coals may contain significant quantities of iron, which can cause boiler wall slagging. The lower-rank coals may contain abundant organically associated sodium that upon combustion will vaporize and condense in the convective pass of a boiler, causing fouling problems.

In order to predict the effects of inorganic constituents during coal combustion on boiler performance, the distribution of intermediate materials (i.e., inorganic vapors, liquids and solids) must be known at any given point in a combustor as a function of coal composition and combustion conditions. The formation of intermediate inorganic materials consists of a complex combination of physical and chemical transformations. The transformations of inorganic constituents that occur during combustion of pulverized coal include: 1) coalescence of mineral grains, 2) evaporation and condensation, 3) formation of cenospheres, and 4) fragmentation of minerals. The interaction of the inorganic species during combustion and gas cooling can result in the formation of low-melting-point phases that stick to heat transfer surfaces and deposited materials.

5. PROJECT DESCRIPTION:

This project consists of three tasks focused on developing an understanding of the transformations of inorganic constituents during pulverized coal combustion. Task 1 focuses on improving the CCSEM methodology in order to determine the mineral constituents present in pulverized coal. Task 2 encompasses determining the composition and phase assemblages present in intermediate ash materials produced in Task 3 of this program and the PSI Technology Company (PSIT). Task 3 of the Combustion Inorganic Transformations Project will center on bench-scale drop-tube combustion and laser-induced atomic fluorescence experiments to delineate the sequence and overall physical and chemical changes that occur in coal inorganic matter to form fly ash during the combustion process.

Task 1 involves developing an automated CCSEM technique to determine mineral associations in pulverized coal. Specifically, the objectives are: to determine if the mineral grains are inherent or extraneous to coal particles and if they are associated with other minerals; to eliminate mineral-grain size biases that are associated with uncertainties caused by sample preparation and irregular shapes; to develop software to graphically represent the elemental correlations for ash particles; and to integrate chemical fractionation results and CCSEM analysis. This work will be coordinated with work currently being conducted at Massachusetts Institute of Technology (MIT), the University of Kentucky (UK), and Iowa State to enhance the determination of inorganic constituents in coals.

Task 2 involves the characterization of coals, chars and ashes using sophisticated analytical techniques. The specific objectives of this task are: to characterize coals using CCSEM and chemical fractionation of PSIT coals and EMRC sized fractions; to provide analytical characterization and interpretation of analytical results for ash samples provided by PSIT; to provide SEMPC, ESCA, SIMS, AA, ICP, and chemical fractionation analysis as needed for PSIT and Task 3 of this project; and to develop a classification scheme for fly ash particles based on physical and chemical characteristics.

Task 3 involves the use of laboratory-scale combustion equipment to combust carefully characterized and prepared coals and model mixtures.

Samples will be extracted at residence times representative of devolatilization, partial burn-out and complete burnout. The fly ash and chars produced are sized and characterized to determine the transformations of inorganic components that result during combustion. The results will provide a detailed profile of the inorganic transformations undergone by coals under combustion conditions. These results will provide "benchmark" values against which models of inorganic interactions may be compared, as well as allow comparison with data obtained from practical combustion systems. In addition, these results will aid in determining specific transformations on which to focus more in-depth studies.

6. RESULTS/ACCOMPLISHMENTS

To date, the inorganic components in four coals and their transformations during combustion have been examined in detail. The inorganic components have been determined by a combination of CCSEM (1) and chemical fractionation (2). The transformations of inorganic components have been examined during char combustion. These transformations have been examined by producing chars representing various degrees of burnout and determining the size and composition of the ash particles forming on the char. The final fly ash has also been examined in detail using a technique that quantitatively determines the distribution of phases and composition in the final fly ashes.

The results summarized in this report will include only those obtained in experiments with Upper Freeport bituminous coal from Pennsylvania. The size and composition of the mineral grains determined in polished sections of coal are summarized in Table 1 for the 53-74-micrometer-sized fraction of Upper Freeport. The mixed aluminosilicate category consists mostly of illite, as determined based on molar ratios of the elements analyzed by the microprobe. The mixed aluminosilicates dominated the mineral phases, followed by pyrite. The pyrite and mixed aluminosilicates account for 72% of the total mineral content. Calcite and quartz were also present. The total mineral content of the coal, as determined by CCSEM, was 16.8%. The ash content of this fraction, determined using ASTM techniques, was 19.6%.

Chars were produced at residence times of 0.05, 0.1, 0.2, 0.5 and 0.8 seconds at a temperature of approximately 1500°C. The chars were quenched and collected on a filter. The chars were analyzed using CCSEM to determine the size and composition of the ash particles forming on the surface of the chars. Some of the results obtained are summarized in Table 2. The types of particles analyzed are classified by mineral/phase reported on an area-percent basis.

The primary phases of interest in the Upper Freeport coals are the silicates and iron-rich phases. The distribution of silicates as a function of residence time is illustrated in Figure 1. The K-aluminosilicates (illite-derived species) increase rapidly and level off at high residence times. This is due to the incorporation of other quartz and clay minerals during combustion. Quartz content decreased with increasing residence time. The content of aluminosilicate components

Table 1. CCSEM Analysis of the 53-74-Micrometer-Sized Fraction of Upper Freeport.

Mineral/Coal (Area %)	Size cutpoints, μm based on multicyclone <1.2	1.2-2.1	2.1-4.4	4.4-8.0	8.0-11.0	>11.0	Area %[1] Min	Wt %[2] Coal
Quartz	0.04	0.16	1.64	1.55	2.19	1.16	6.7	1.13
Kaolinite	0.01	0.18	0.95	0.68	0.3	0	2.12	0.36
Mixed Aluminosilicate	0.1	0.64	3.48	6.5	3.15	42.13	42.13	7.11
Pyrite	0.07	0.4	1.38	1.6	0.65	30.28	37.60	5.11
Calcite	0.01	0.01	0.16	0.11	0.56	13.21	13.21	2.23
Gypsum	0	0.01	0.03	0	0	0.03	0.03	0.01
Coal								83.12
Total	0.23	1.51	7.87	10.84	8.18	71.37	100	100

[1] Area % of total mineral content
[2] Wt% of coal

Table 2. CCSEM Analysis of Upper Freeport Chars.

Mineral/Phase (Area %)	Residence time, seconds 0.05	0.1	0.2	0.5	0.8
Quartz	18	4.6	18.2	7.7	7.8
Aluminosilicate	17.7	17.7	15.4	18.8	26.7
Fe-Aluminosilicate	7.5	13.1	7.2	20.6	11.8
Potassium Aluminosilicate	28.5	38.3	44.0	49.2	40.6
Calcium Aluminosilicate	0.4	0.9	1.5	4.5	1.6
Iron Oxide	4.6	12.6	0.7	2.3	4.6
Pyrite/Pyrrhotite	19.5	4.3	0.5	0	0
CaO-rich	0	0	9.1	2.9	2.9
Rutile	0.1	3.3	0.1	0.1	0.1
Anhydrite	0	2.2	0	0	0
Aluminosilicate/Gypsum	0.1	0.1	0.8	0.2	0.2
Ankerite	0	0	0.1	0	0
Calcium Silicate	1.1	0.3	0.1	0.2	0.2
Unknown	2.3	2.6	2.3	3.3	3.3
Total	100	100	100	100	100

remained approximately constant with increasing residence time. The iron aluminosilicates showed a small increase in abundance with increasing residence time. The distribution of the iron-rich phases is illustrated in Figure 2. The pyrite/pyrrhotite species decrease in abundance with increasing residence time. The iron oxide species did not change dramatically, but show a gradual increase with increasing residence time. The iron-rich aluminosilicate species increased in abundance with increasing residence time. The iron from the pyrite interacted with the aluminosilicate species during the char combustion stage.

The fly ash (after complete combustion) was collected in a multicyclone in order to collect aerodynamically classified samples. Each of the size fractions was analyzed using the SEMPC technique. Details of the SEMPC technique can be found elsewhere (3). The results are summarized in Table 3. The first multicyclone stage (>11 micrometers) contained nearly 94% of the ash. The major phases identified by SEMPC include illite-derived, iron oxide, kaolinite-derived, anorthite, and an unclassified phase. Minor occurrences of quartz, albite, montmorillonite-derived, calcium oxide, spinel, and calcium titanate were also observed. Illite-derived phase is an amorphous K-aluminosilicate derived from the mineral, illite. The original Upper Freeport coal showed 37.6% illite on a mineral matter basis. The illite-derived had a steady decline in quantity with decreasing fly ash size. The distribution of kaolinite-derived was similar to that of illite-derived; Stage 1 showed the largest quantity with successively decreasing quantities in the smaller size fractions. Kaolinite was not very abundant in the coal; therefore, the kaolinite-derived is coming from some of the other aluminosilicate clays by volatilization of their loosely bound cations. Quartz and iron oxide have fairly even distribution in all of the stages except for Stage 5 and the final filter. The iron components were incorporated into the aluminosilicate melt phases.

The composition of the fly ash as a function of particle size is also reported in Table 3. The Si/Al ratios remain relatively uniform until the final filter, which had an extremely high ratio of 18.9. The K_2O and SO_3 contents increased dramatically in the final filter. In addition, a high level of SiO_2 and a small increase in calcium were also noted.

7. FUTURE WORK

The work that is being planned during this year includes the following:

Task 1. CCSEM METHOD DEVELOPMENT

1) A method to determine the included and excluded minerals in pulverized coal will be developed.

2) Software and hardware improvements will be made to increase data manipulation and graphics capabilities.

3) Coordinate CCSEM Analysis techniques with work being conducted at other organizations to enhance the determination of minerals in coal.

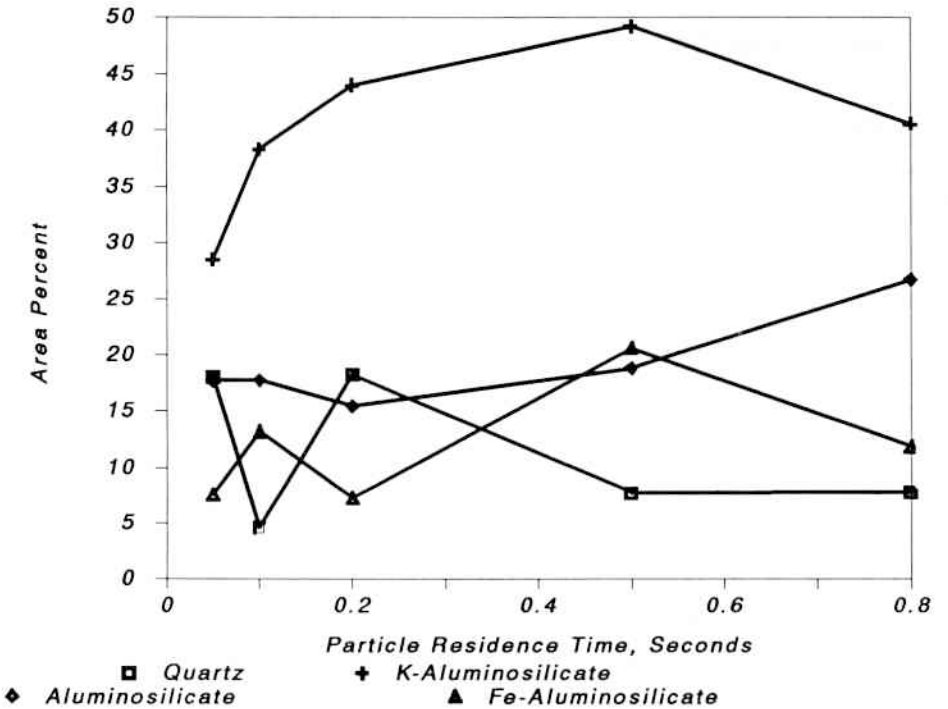


Figure 1. Distribution of Silicates for Upper Freeport Chars as a Function of Residence Time.

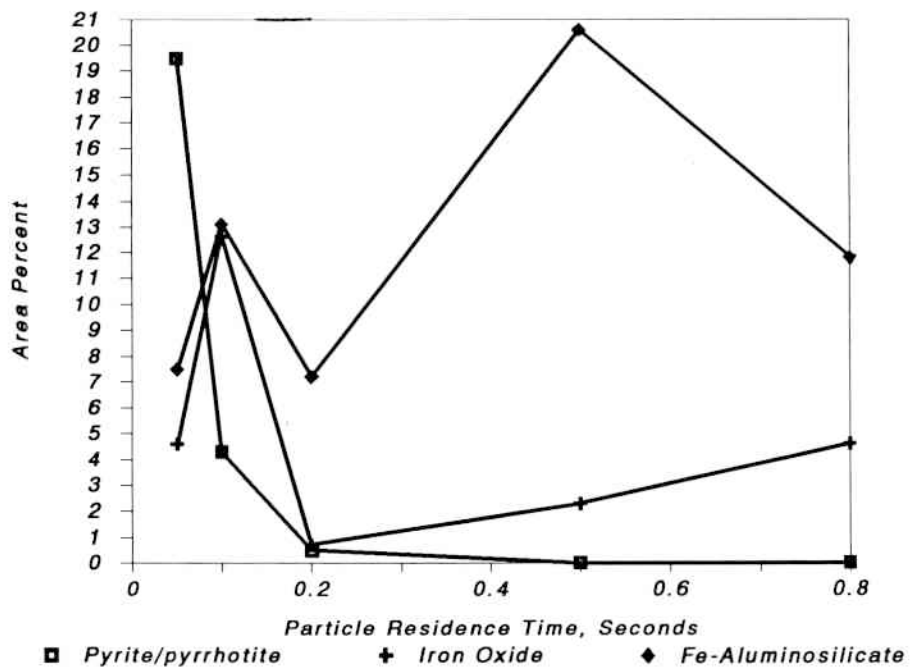


Figure 2. Distribution of Iron-Rich Phases in Upper Freeport Chars as a Function of Residence Time.

Table 3. Phases Detected by SEMPC for Upper Freeport Fly Ash (from 53-74-μm coal)

	Stage 1	Stage 2	Stage 3	Stage 4	Stage 5	Filter
Particle-Size Cutpoints (μm)	>11.0	6.0	4.4	2.1	1.2	<1.2
Percent Mass	93.9	1.0	1.9	0.7	1.3	1.2
Phase (Area %)						
Calcium Oxide	1.1	.4	0.0	0.0	0.0	0.0
Montmorillonite	0.0	.4	0.0	1.9	0.8	0.0
Illite-derived	63.1	46.5	35.5	29.9	27.6	0.0
Iron Oxide	2.5	2.3	2.5	1.2	0.4	0.0
Kaolinite-derived	18.1	9.5	3.7	1.2	0.0	0.0
Anhydrite	0.0	0.0	0.0	0.0	0.0	0.0
Anorthite	0.0	2.3	8.7	3.7	6.6	0.0
Albite	0.4	0.0	0.0	0.0	0.0	0.0
Quartz	1.1	1.5	1.2	1.2	0.8	0.0
Pyrrhotite	0.0	0.0	0.0	0.0	0.0	0.0
Pyrite	0.0	0.0	0.0	0.0	0.0	0.0
Spinel	0.0	0.4	0.0	1.2	0.0	0.0
Dolomite	0.0	0.0	0.0	0.0	0.0	0.0
Calcium Titanate	0.0	1.1	1.2	1.2	3.7	0.0
Melilite	0.0	0.0	0.0	0.0	0.0	1.6
Unclassified	14.5	36.2	47.3	58.5	60.5	98.4
Average Composition, wt%						
Na_2O	0.14	0.35	0.20	0.24	0.28	0.0
MgO	0.46	0.44	0.50	0.59	0.60	0.1
Al_2O_3	30.70	28.00	29.70	29.60	29.20	3.0
SiO_2	51.50	47.80	44.30	43.70	41.80	56.8
P_2O_5	0.00	0.19	0.28	0.19	0.28	0.1
SO_3	0.21	0.34	0.32	0.31	0.62	12.4
ClO	0.00	0.00	0.00	0.00	0.00	0.1
K_2O	5.96	4.69	4.08	4.07	3.97	8.2
CaO	1.81	3.29	4.36	3.67	4.83	5.8
TiO_2	1.25	1.87	2.35	3.26	3.96	3.1
Fe_2O_3	7.85	12.90	13.80	14.20	14.20	10.4
Average Si/Al Molar Ratio	1.7	1.7	1.5	1.5	1.4	18.9

Task 2. MINERAL AND ASH CHARACTERIZATION

1) Continue CCSEM Analysis of pulverized coals and ashes.

2) Perform CCSEM and SEMPC Analysis of chars and fly ash produced in Task 3.

3) Perform Auger, ESCA, and SIMS Analysis of chars and fly ashes from Task 3.

Task 3. LABORATORY-SCALE COMBUSTION TESTING

1) Produce chars and ashes from Kentucky #9 and San Miguel coals.

2) Determine the interactions of inorganic constituents while combustion synthetic coal/mineral mixtures.

8. REFERENCES

1. Huggins, F.E., Kosmack, D.A., Huffman, G.P., and Lee, R.J., "Coal Mineralogies by SEM Automatic Image Analysis," Scanning Electron Microscopy, I, AMF O'Hare (Chicago), IL 60666, p 531, 1980.

2. Benson, S.A., and Holm, P.L., "Comparison of the Inorganic Constituents in Low-Rank Coals," Ind. Eng. Chem. Prod. Res. Dev., 24, 145, (1985).

3. Kalmanovitch, D.P., Montgomery, G.G., and Steadman, E.N., "Computer Controlled Scanning Electron Microscopic Characterization of Coal Ash Deposits," ASME, 87-JPGC- FACT-4, (1987).

FLUID MECHANICS OF ASH DEPOSITION

CONTRACT NUMBER: PETC-89-RD21

CONTRACTOR:
Coal Combustion Division
Fundamental Combustion Branch
Pittsburgh Energy Technology Center
P.O. Box 10940
Pittsburgh, PA 15236

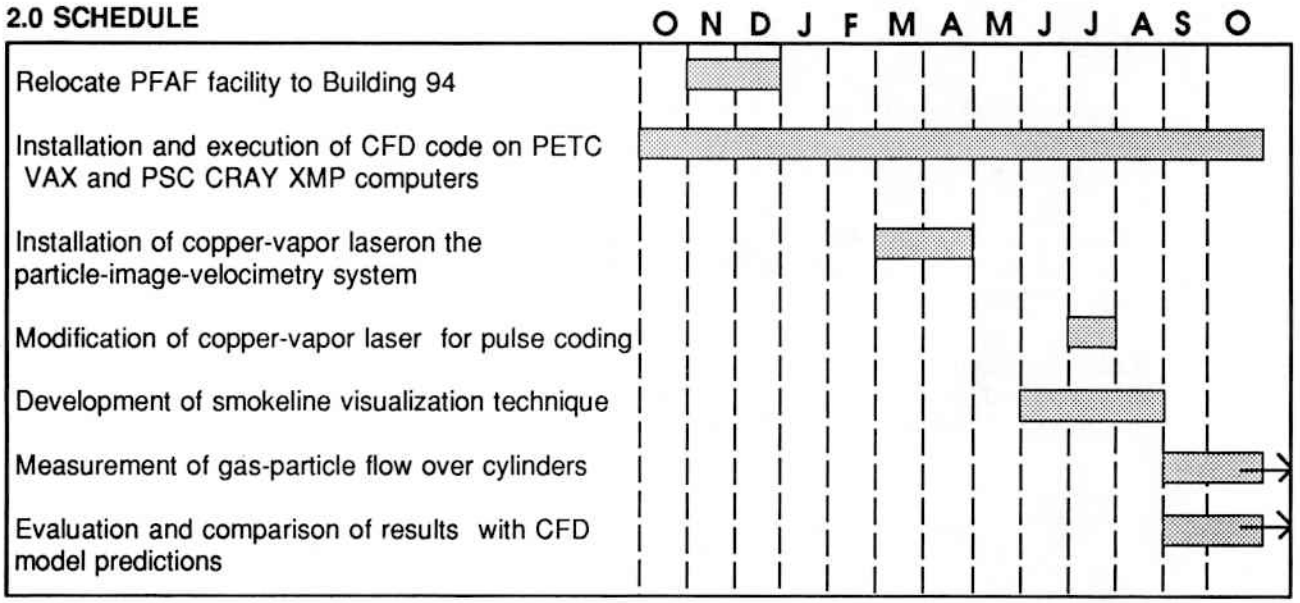
CONTRACTOR PROJECT MANAGER: F.D. Shaffer

PRINCIPAL INVESTIGATORS: F.D. Shaffer, E.R. Ramer, J.L.S. Chen, M.P. Mathur

PETC PROJECT MANAGER: J.D. Hickerson

PERIOD OF PERFORMANCE: October 1, 1988 to September 30, 1989

2.0 SCHEDULE



3.0 OBJECTIVE

The objective of this project is to develop a predictive capability for the delivery of ash particles to heat-exchanger tube surfaces. The approach taken to meet this goal is to make detailed measurements of the gas and particle flow fields through tube banks. Rather than making the measurements in an actual heat-exchanger tube bank, a laboratory simulation is performed. These measurements will be used to develop empirical correlations for the impact of particles on tube surfaces. The empirical information will also be used to evaluate and improve the predictions of computational fluid dynamics (CFD) models.

4.0 BACKGROUND STATEMENT

A major goal of the United States Department of Energy is to encourage the use of coal in combustion systems. The harsh effects of post-combustion gases (e.g., ash deposition) are a significant deterrent to this goal. The areas within a combustor most susceptible to these harsh effects are the heat-exchanger tube banks.

The economic impact of ash deposition in heat-exchange tube banks is tremendous. Losses may exceed $8 million/year in a 500 MW coal-fired steam generator [Honea, 1981]. Total losses due to ash deposition in heat-exchange tube banks of coal-fired combustors are estimated to exceed $5 billion/year in the U.S. alone [Watts and Levine, 1984].

Problems with ash deposition in heat-exchange tube banks have persisted for at least fifty years. One of the main reasons is that many phenomena contributing to the ash deposition process are not well understood. A recent report indicates that, given the economic impact of the problem, the amount of research reported on ash deposition is far too low [Watts and Levine, 1984].

Given this dearth of understanding and research, the design and maintenance of heat-exchange tube banks is largely based on experience and empiricism. At present, ash deposition is dealt with by frequent cleaning of tube surfaces by "soot blowing." The main design practice is to increase tube spacing and decrease gas velocity to reduce the severity of ash deposition problems [Barret, 1987]. Both of these design practices, however, may inhibit heat extraction rates.

Present design and maintenance practices are economically feasible for todays coal-fired boilers. However, it is likely that high-efficiency, low-pollution combustion systems will be needed in the next decade. If such systems are to be developed, a more comprehensive understanding of ash deposition in heat-exchange tube banks will be essential.

4.0 PROJECT DESCRIPTION

Overall ash deposition rates are determined by a balance between two interacting factors: the delivery of ash particles to tube surfaces and the ability of the tube surface (including a layer of ash deposits) to capture ash particles. This study is concerned only with the former. It does not encompass the formation of ash particles, nor the capture ability of a tube surface. Only the behavior of ash particles once they enter a tube bank is considered. The capture ability of the tube surface and the formation of ash particles are the subject of other DOE-funded studies.

To narrow the scope of this project further, only particles driven by a combination of gas drag, gravitational and inertial forces are considered. Such particles are often called inertially driven particles. Under typical heat-exchanger flow conditions, ash particles larger than about 5 μm can be considered as inertially driven. The majority of an ash deposit is made up of particles larger than 5 μm.

The approach taken in this project is to perform an experimental investigation of the gas and particle flow fields though tube banks. A simulation of the gas and particle flow fields in an actual combustor is achieved under laboratory, room-temperature conditions. This is possible by matching the appropriate dimensionless simlarity parameters. For this simulation, the main similarity parameters are the Reynolds and Stokes numbers. By conducting this study under laboratory conditions, the flow fields can be accurately controlled and are easily accessible for detailed flow measurements. Much of the FY89 effort was devoted to completing a laboratory facility to create and measure gas-particle flow fields. It is called the Particulate Flow Analysis Facility (PFAF).

Two unique flow-diagnostics systems have been developed as a part of the PFAF: a smokeline visualization system and a particle-image-velocimetry (PIV) system. With the smokeline visualization system, gas streamlines, gas pathlines and the transition from steady to unsteady flows (including laminar to turbulent flows) can be observed and measured. The PIV system measures lagrangian particle flow information (i.e., particle trajectories and velocities along a trajectory). It also measures particle-wall collision parameters such as impact locations, coefficients of restitution, and impact/rebound angles.

Development of the PFAF was completed in August of FY89. Measurements of the gas and particle flow fields over cylinders began in September of FY89. The tests are expected to last two to three months.

The first measurements made with the PFAF will provide a test case to verify that the PFAF is producing reliable data. Measurements of the flow of air and particles over a single cylinder will be made as the test case. The measurements will be compared with previously published predictions and measurments of gas flow over a single cylinder. The previously published data is considered to be accurate, at least for the region outside of the transient wake.

After the measurements of flow over a single cylinder are completed, the flow over two cylinders in tandem will be measured. The independent variables for these tests are the Reynolds number (based on the cylinder diameter), the particle Stokes number, and the cylinder separation distance. These will be varied over a wide range typical to coal-fired combustors.

A detailed description of the PFAF, including the smokeline visualization and the PIV systems, is given below. The measurements of gas and particle flow fields over cylinders are also described. Finally, initial results of the measurements and comparisons with CFD model predictions are presented.

4.1 WIND TUNNEL FACILITY

The PFAF creates accurately controllable gas and particulate flow fields in an environment conducive to detailed flow field measurements. A schematic of the PFAF components is shown in Figure 1. The main component of the PFAF is a wind tunnel. It is a once-through Eiffel type: room air is drawn through the test section with a fan and discharged back into the room. The wind tunnel has a venturi shape to minimize total pressure loss. The venturi shape also minimizes boundary-layer thickness in the test section. At the throat of the wind tunnel is an optically transparent test section. The transparent test section is 1 m long with a 0.33 x 0.33 m cross section. Air flow fields with velocities from 1 to 50 m/s can be generated in the test section. Turbulence intensities are less than 0.5% and the mean velocity varies less than 1% across the test section (outside the boundary layer). The flow facility components include an inlet section with turbulence damping grids and flow straightening vanes; a converging section; a transparent test section; a diverging diffuser section; a fan assembly; and a particle filter bank.

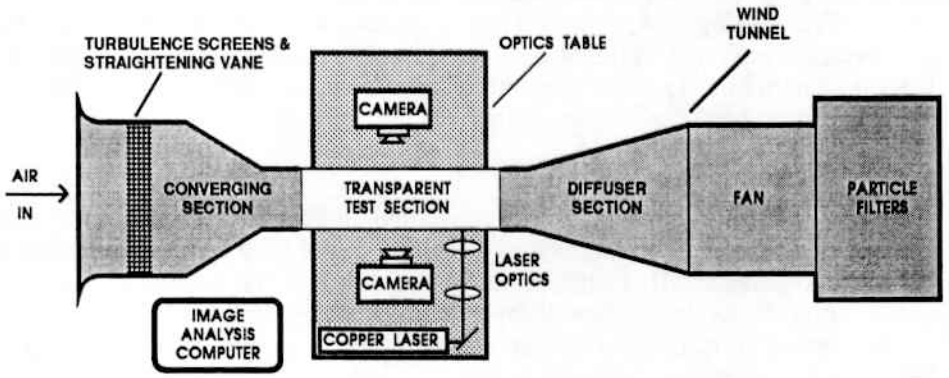


Figure 1. Components of Particulate Flow Analysis Facility

Inlet Section The inlet section conditions the room air before it is accelerated into the test section. It first provides a smooth-profiled acceleration of stagnant room air into the flow facility. The air then passes through a straightening vane consisting of a 0.1 m deep, aluminum honeycomb with 7 mm diameter, hexagonal cells. The straightening vane reduces the upper scale of turbulent eddies by a factor of 100, from the diameter of the inlet section (0.76 m) to the diameter of the straightening vane cells (7 mm). Next, the air flows through two high-porosity turbulence damping screens. These screens create small-scale isotropic turbulence which tends to dissipate or damp the overall turbulence levels of the air flow. A smoke-injection rake is also located in the inlet section just downstream of the turbulence damping grids. The smoke rake will be discussed later.

Converging section The air exits the inlet section into a profiled converging section which is designed to minimize boundary layer growth and pressure loss. The converging section reduces the cross-sectional area from 0.76 x 0.76 m to 0.33 x 0.33 m. Thus, the flow is accelerated by a factor of 6.25 in the converging section.

Test Section After the air is accelerated in the converging section, it immediately enters the test section. All measurements of the flow field are performed in the test section. It is 1 m long, but can be replaced with test sections of different lengths. Low-reflectance, 0.2 x 0.3 m, glass windows are centered on the sides and bottom of the test section. They provide maximum transmittance of laser light into the test section. They also enhance the quality of optical imaging measurements.

Diffuser Section A low-angle diverging diffuser section is located between the test section and the fan. It lowers pressure loss by providing a smooth transition between the square cross-section of the test section and the circular cross-section of the fan.

Fan Assembly A centaxial fan with a variable speed controller draws air through the flow facility. The fan is rated to deliver over 3500 scfm against a pressure of 0.11 m H_2O. However, with clean particulate filters, the total pressure loss through the wind tunnel is less than 0.05 m H_2O. The fan and controller assembly are capable of producing velocities from 1-50 m/s in the test section. The air velocity is controllable to approximately $\pm$0.03 m/s.

Filter Banks Fine particulates (1-100 μm) are often introduced into the wind tunnel. A bank of four high-efficiency particulate collection filters are placed at the flow facility exit. The filter bank removes all particles larger than 5 μm and over 40% of 1 μm particles.

4.2 PATHLINE FLOW VISUALIZATION

Visualization of gas flow patterns is an invaluable flow analysis tool. Smokeline visualization is one of the best tools to observe and measure streamlines and pathlines. With this visualization technique, a continuous stream of small particles (or droplets) is injected at a series of points in the gas flow field. If the particles injected at a point follow the same path, the particles are observed as continuous lines through the flow field.

For the smokeline technique to work properly all of the particles injected at a point must follow the same path through the flow field. Also, the particles must follow the gas flow. If the particles are small enough (i.e., have a negligible Stokes number) they will follow the gas flow. Particles with sizes less than a few microns will follow the gas flows for this application.

For the particles to follow the same path, the turbulence level (or unsteadiness) of the gas flow must be very low. If the turbulence or unsteadiness of the flow is too high, the particles will be dispersed and will not form visible lines through the gas flow. Turbulence intensities less than 1% may be required. This is well within the capabilities of most wind tunnels.

The problem with high turbulence or unsteadiness is found in the wake of the object used to inject the particles. Any object placed in a gas flow field will disturb the gas flow by forming a wake -- a wake which may contain unsteady, vortical structures and high turbulence levels. To minimize the wake created by an injector, its width normal to the flow must be made as small as possible. It also should be of a streamlined shape.

For design purposes, an estimate of the wake turbulence/unsteadiness can be achieved by considering the case of uniform crossflow over a smooth cylinder. For very low Reynolds numbers, less than 5, the flow is laminar on the downstream side of the cylinder. No recirculating wake develops. As the Reynolds number exceeds 5, a fixed, symmetrical pair of vortical rings forms on the downstream side of the cylinder. These symmetrical vortical rings extend about one diameter downstream. The flow outside the symmetrical vortices is essentially laminar. This condition exists for Reynolds numbers up to about 30 or 40. As the Reynolds number exceeds 40, a periodic formation of vortex rings is started: a single vortice is alternately formed on each side of the cylinder. This forms a long unsteady wake of vortices known as the Von Karman street. It can disturb the flow several hundred cylinder diameters downstream. As the Reynolds number is increased further, turbulent features are superimposed upon the vortex street.

The key to designing an injector is to keep the Reynolds number low enough that the Von Karman street is not created. For a cylinder, this requires Reynolds number less than 40. For streamlined shapes the Reynolds number may be slightly higher, possibly as high as 100.

This design criterion, that Reynolds number must be minimized, restricts the maximum velocity for which the smoke line technique can be employed. For example, for a flow velocity of just 1 m/s, the cylinder diameter must be less than 0.6 mm to keep the Reynolds number below 40. Fortunately, techniques have been developed which extend the upper velocity limit. Two injector designs have are predominant in wind tunnels: the electronic smoke wire and the pneumatic smoke rake. Bath are used with the PFAF.

The Electronic Smoke Wire With the electronic smoke wire technique, a thin wire is suspended across the gas flow field. The wire is coated with an oil substance that, when heated, vaporizes to form a dense smoke. Resistive heating of the wire is used to vaporize the oil substance. This technique can be used for relatively high velocities since the wire diameter can be as small as a few microns. Typical wire diameters are 50 - 100 μm, allowing velocities up to about 20 m/s while maintaining the Reynolds number below 40. Although this technique enables reasonably high velocities, it has one major drawback -- the oil on the wire is expended in a few seconds. Thus, the wire must be recoated with oil frequently. This is not always an easy task, considering the wire is enclosed in a wind tunnel. Automated methods have been developed to coat the wire. However, manual coating of the wire with an oil-saturated swab has been found to be the most advantageous [Battil and Meuller, 1980].

The electronic smoke wire developed at PETC uses a 0 - 50 V power supply to heat a 40 μm stainless steel wire. A removable door on the top of the test section allows access to coat the wire with oil. Interlock switches are placed on the access door which stop electrical flow to the wire when the door is opened. This avoids the possibility of electrical shock. As recommended by Battil and Meuller [1980], a colored oil originally developed for use in model trains is used.

The Pneumatic Smoke Rake The pneumatic smoke rake is an alternative to the electronic smoke wire. It is popular because it can produce smoke lines for hours without interruption. The upper velocity limit is lower than that of the electronic smoke wire, however. The smoke rake consists of a main carrier duct suspended across the wind tunnel. It has several smaller tubes connected to it at a right angle. These smaller tubes inject particles into the gas flow.

Smoke is formed outside the wind tunnel, then is pneumatically conveyed into the smoke rake. Several methods have been employed to produce smoke, from burning wood or cigarette tobacco to sophisticated systems employing chemical reaction. The most widely used is the formation of a droplet mist. This is the method used with the pneumatic smoke rake system developed at PETC.

It is difficult to make the width of smoke rakes (normal to the flow direction) smaller than about 1 mm. To maintain the Reynolds number below 40, the air velocities over a 1 mm diameter rake can't exceed 0.7 m/s. This velocity, of course, is too low for most wind tunnel testing. The upper limit of velocity in the test section can be significantly extended by placing the smoke rake in the inlet section of the wind tunnel. Electronic smoke wires usually are not placed in the inlet section because of its wide diameter (typically 1 to 5 m).

The pneumatic smoke rake system developed at PETC is illustrated in Figure 2. The main components include a smoke generator, a cooling chamber, a droplet impactor, and the smoke rake. A commercially available smoke generator by ROSCOE [1989] is used. Sub-micron sized droplets are produced by vaporizing a liquid under pressure then expanding the vapor through a nozzle. One of the main advantages of the ROSCOE generator is that the droplet mist poses no safety hazards.

The droplet mist is at a high temperature (up to 500° F) when emitted from the generator. This causes the mist to condensate on cooler surfaces. Condensation can cause problems with clogging the small injector tubes in the smoke rake. To avoid this problem, the mist is cooled to room temperature in a water-cooled, 0.33 x 0.33 x 1 m settling chamber. An air stream is introduced into the settling chamber to carry the mist to the smoke rake. After the cooling chamber, the mist is passed though an impactor consisting of a nozzle and a flat plate. The impactor is designed to collect droplets larger than 10 μm. The mist is then carried into the smoke and injected into the wind tunnel.

The pneumatic smoke rake developed at PETC is 0.76 m long and contains 40 injectors. An airfoil shaped tube with dimensions of 2 mm x 15 mm carries the mist to the injector tubes. The injector tubes are square with a 1.5 mm outer diameter and are 12.5 mm long. To reduce vibration of the smoke rake it is supported at its center by thin nylon lines. This design has been found to produce good smoke lines for velocities up to 5 m/s in the test section.

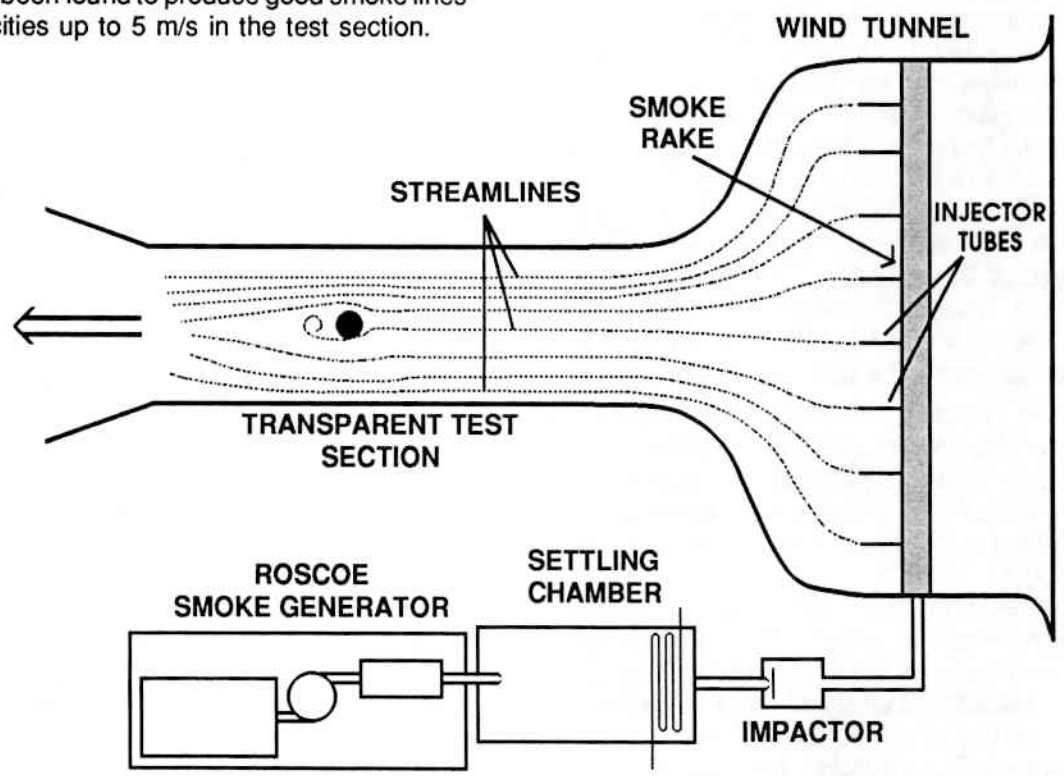


Figure 2. Pnuematic smoke rake system.

4.3 PARTICLE-IMAGE-VELOCIMETRY SYSTEM

A detailed discussion of particle-image-velocimetry (PIV) is given in the proceedings of last years ARTD Contract Review Meeting [Shaffer et al., 1988]. Therefore, only a brief description of the PETC PIV system is given here. For detailed information on PIV systems see Shaffer et al. [1988, 1989].

PIV is a technique to track the movement of particles through a flow field. The basic concept is to form a multiple-exposure picture of a particle moving through a flow field: a picture showing a series of images of a particle along its trajectory. The trajectory coordinates and the velocity along the trajectory are found by measuring the displacement between consecutive images, and knowing the time delay between images.

PIV is the optimum technique to measure particle-wall collisions. Impact locations, impact/rebound angles, and coefficients of restitution are measured for an individual particle. Accuracies (of velocity measurements) better than 1% have been achieved with PIV. This is comparable to the accuracy of a laser doppler anemometer (LDA). For this and many other applications, PIV has a definite advantage over LDA, since PIV obtains lagrangian-type information.

A schematic of the PIV system developed at PETC is shown in Figure 3. This PIV system uses a copper-vapor laser as the illumination source. It produces 30 nanosecond pulses at rates from 1 Hz to 40 KHz. The pulse energies are between 1 and 2 mJ. Multiple-exposure pictures are taken with a high-resolution (1280 x1024 pixel) camera. The pictures are digitized and displayed through a computer at a rate of 30 per second (ADC rates of 45 megabytes per second). Software has been developed at PETC for automated analysis of the multiple-exposure pictures.

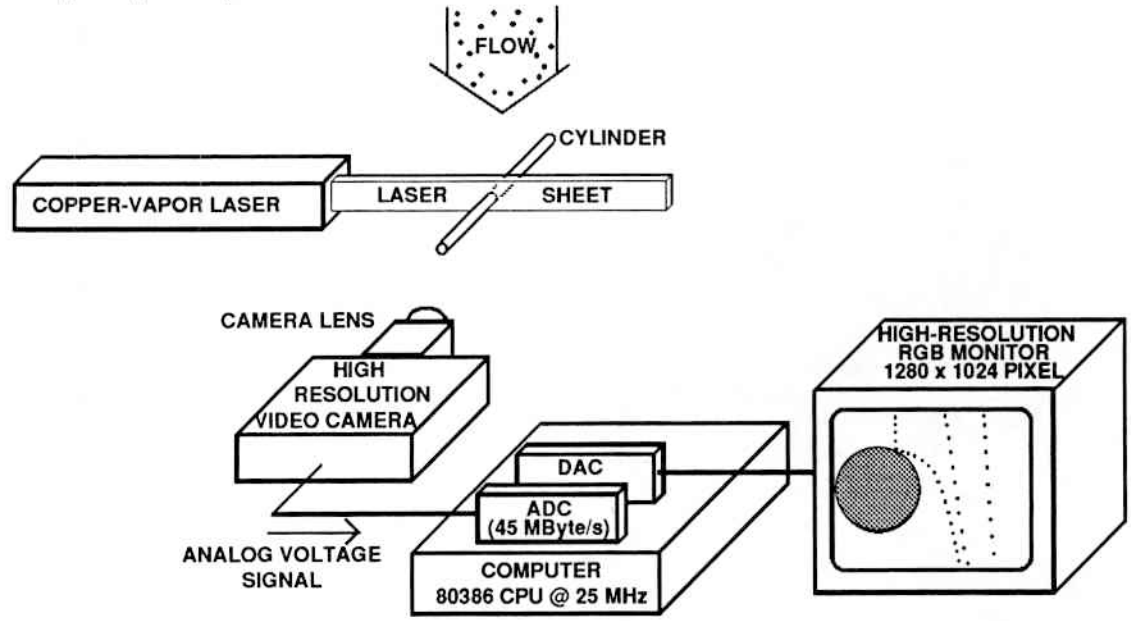


Figure 3. Components of the PIV system developed at PETC.

A reproduction of a PIV picture of a particle colliding with a flat plate is shown in Figure 4. This PIV picture was taken to test and calibrate the PIV system in the PFAF. The results of the analysis of this particle velocity are shown in Figure 5.

5.0 INITIAL RESULTS

The test plan for 1989 is to measure gas and particle flows over a single tube and two tubes in tandem. The measurements will be compared with the predictions of a recently-developed CFD model by Schuh et al. [1989]. The measured flow parameters include gas pathlines and velocities; particle trajectories and velocities along a trajectory; and particle-surface impact characteristics. The independent variables for the experiments and CFD model calculations are the tube Reynolds number, the particle Stokes number, and the tube spacing. They are varied over ranges typical to the convective heat-exchange tube banks of coal-fired combustors: the Reynolds number from 2000 to 10000, corresponding to gas velocities from 10 to 30 m/s in a combustor tube bank; the Stokes number from 0.05 to 5, corresponding to ash particle sizes from 10 to 100 μm; and the center-to-center tube spacing from 2 to 8 tube diameters.

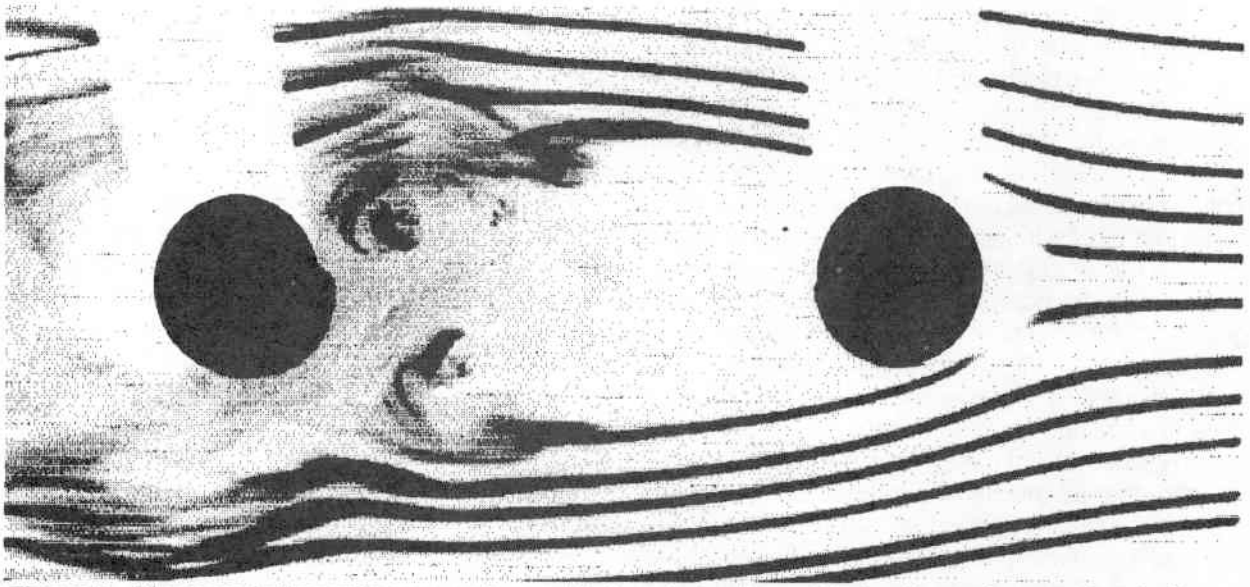


Figure 8. Measured streamlines over two cylinders in tandem. Center-to-center spacing is 4 diameters. The Reynolds number is 3160.

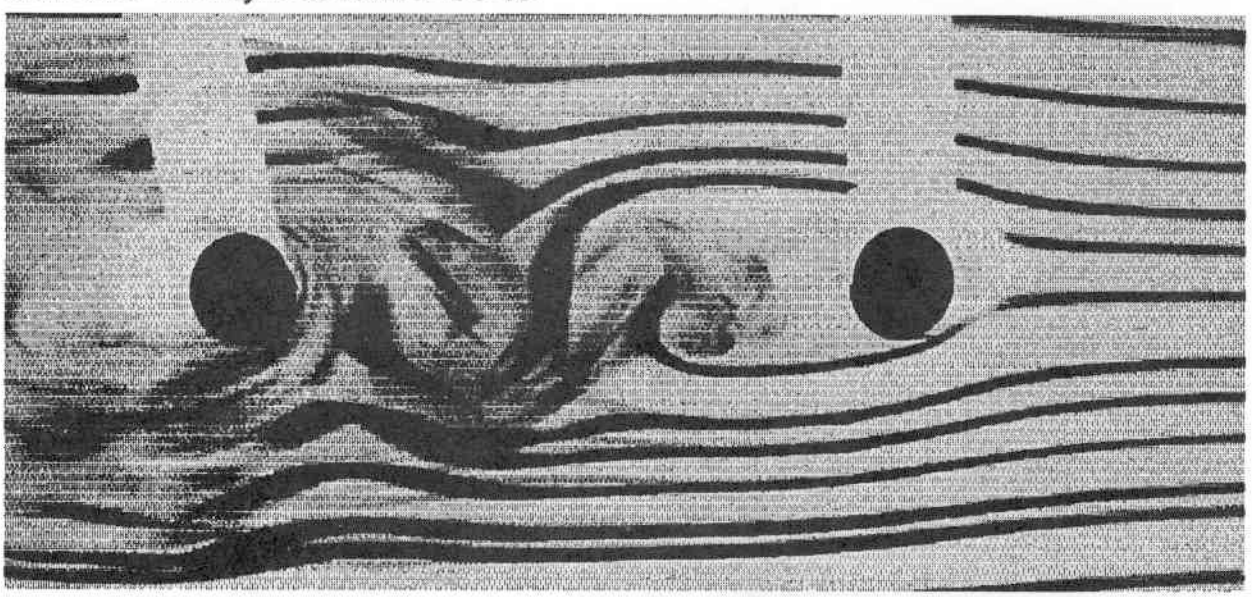


Figure 9. Measured streamlines over two cylinders in tandem. Center-to-center spacing is 6 diameters. The Reynolds number is 3160 .

ACKNOWLEDGEMENTS

The author would like to thank C. McCreary for excellent technical assistance with the development of the smoke-droplet generator system.

REFERENCES

Barrett, R.E., "Slagging and Fouling in Pulverized-Coal-Fired Utility Boilers: A Survey of Boiler Design Practices for Avoiding Slagging and Fouling," EPRI CS-5523, 1987.

Battil, S.M. and Meuller, T.J., "Visualization of Transition in the Flow over an Airfoil Using the Smoke-Wire Technique," *AIAA J.,* Vol. 19, No. 3, 1980.

Honea, F.I., "Survey of Ash-Related Losses at Low-Rank Coal-Fired Utility Boilers," Proc. Engr. Foundation Conf., 1981.

Ilias, S. and Douglas, P.L., "Inertial Impaction of Aerosol Particles on Cylinders at Intermediate and High Reynolds Numbers," *Chem. Engr. Sci.,* Vol. 44, No. 1,1989.

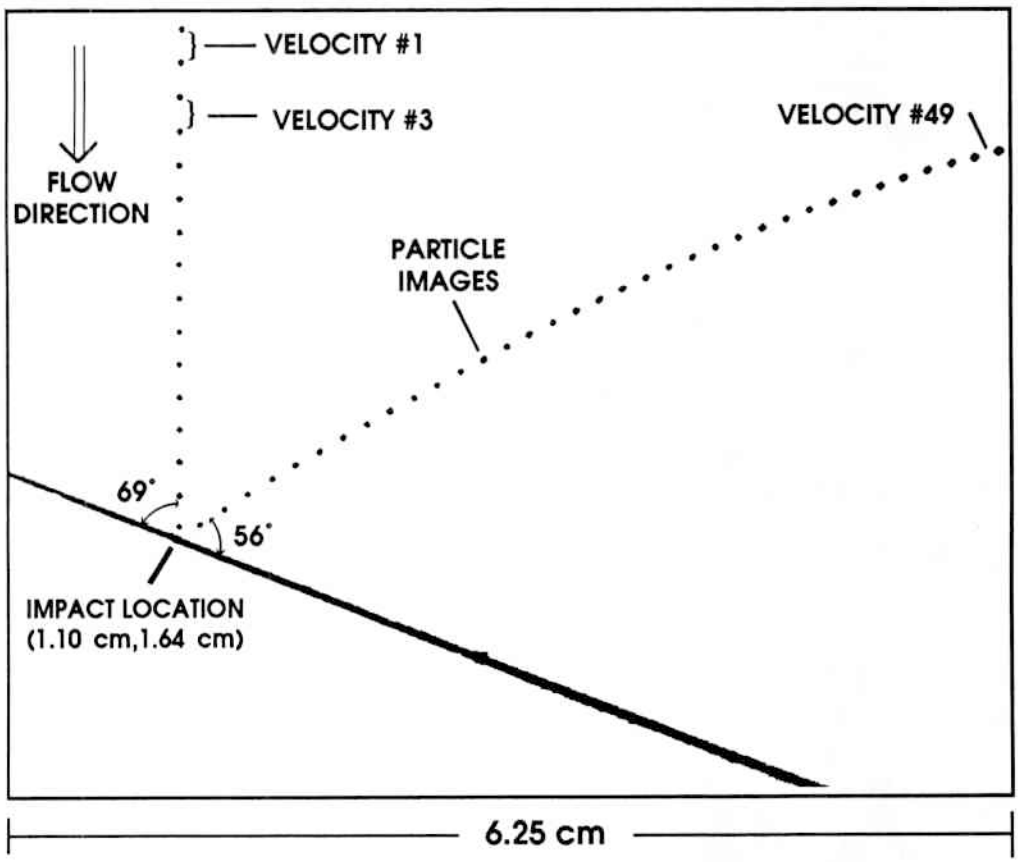


Figure 4. Reproduction of a PIV picture of a particle colliding with flate plate. The plate is oriented at an angle of 67.5° to the flow.

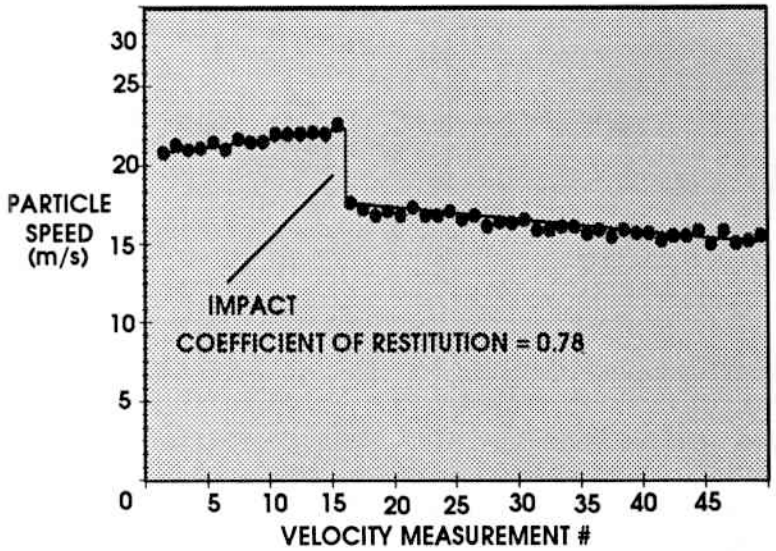


Figure 5. Measured speeds for particle trajectory shown in Figure 4.

Measurements of the gas flow over a single tube and two tubes in tandem have been completed and are being compared with the predictions of the model by Schuh et al. Figures 6-10 show examples of measured gas pathlines over a single and two cylinders at center-to-center spacings of 2, 4, 6 and 8 cylinder diameters. The Reynolds number is 3160. These pathlines were formed with the pneumatic smoke rake.

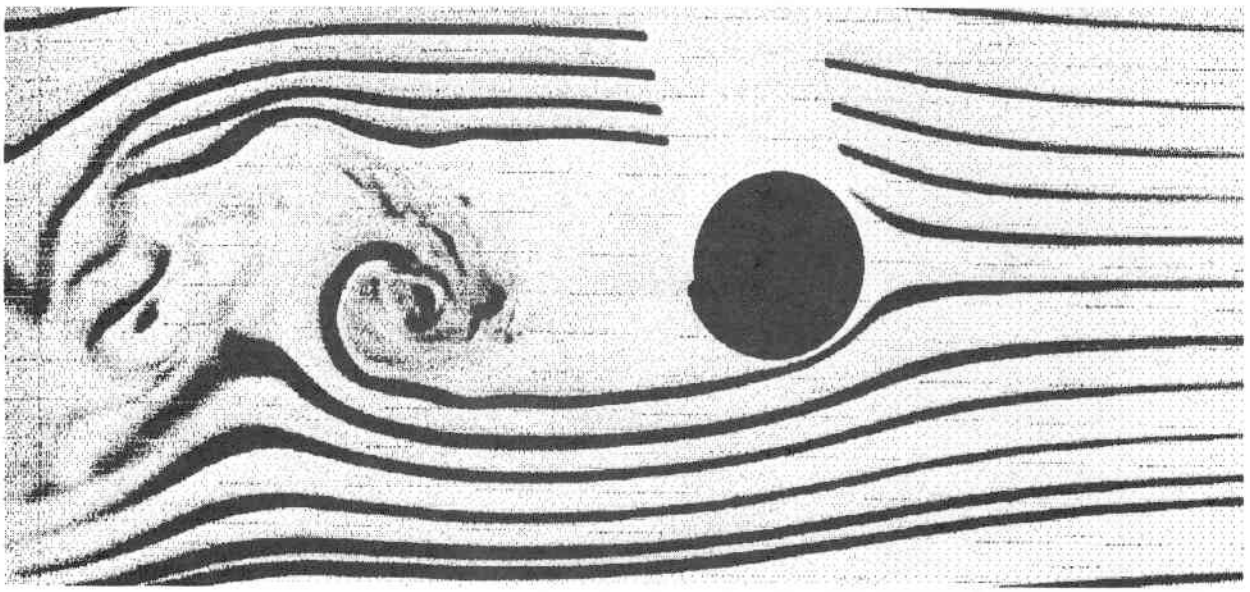


Figure 6. Measured streamlines over a single cylinder. The Reynolds number is 3160.

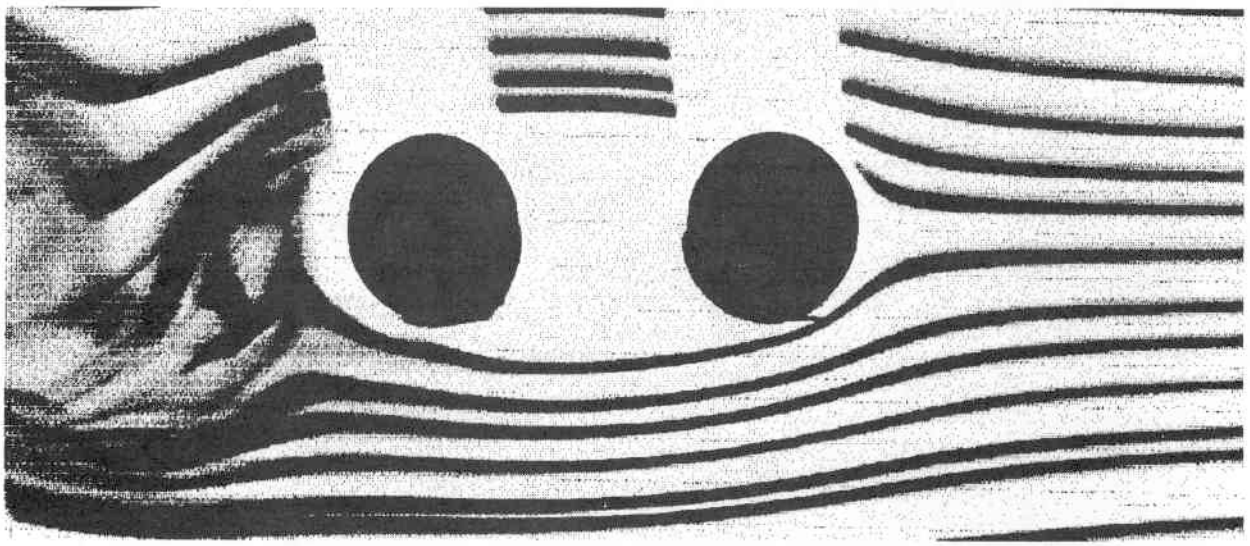


Figure 7. Measured streamlines over two cylinders in tandem. Center-to-center spacing is 2 diameters. The Reynolds number is 3160.

The measurements of the gas and particle flow fields are being used to evaluate the predictive capabilities of the CFD model developed by Schuh et al [1989]. This CFD model was developed to predict gas and particle flow over a single cylinder; two cylinders in tandem; and through an infinite cylinder array. It is based on a steady-state, k-ε turbulence model and includes a non-orthogonal, body-fitted grid generation scheme.

Figure 11 shows an overlay of the streamlines predicted by the Schuh model onto the measured pathlines for flow over a single cylinder. Initial results indicate that Schuh CFD model generates reasonable predictions of the gas flow upstream of the cylinder center. It does not, however, generate reliable predictions downstream of the cylinder center. This is expected for the application of a steady-state model to the wake region which is time dependent due to vortex shedding. A time-dependent model for gas and particle flow over cylinders was published recently by Ilias and Douglas [1989]. The predictions of this model will be compared with pathline measurements in 1990.

Measurements of particle motion are underway. Initial comparisons with the model predictions indicate that it provides reasonable predictions of particle motion -- again, only outside of the tube wake.

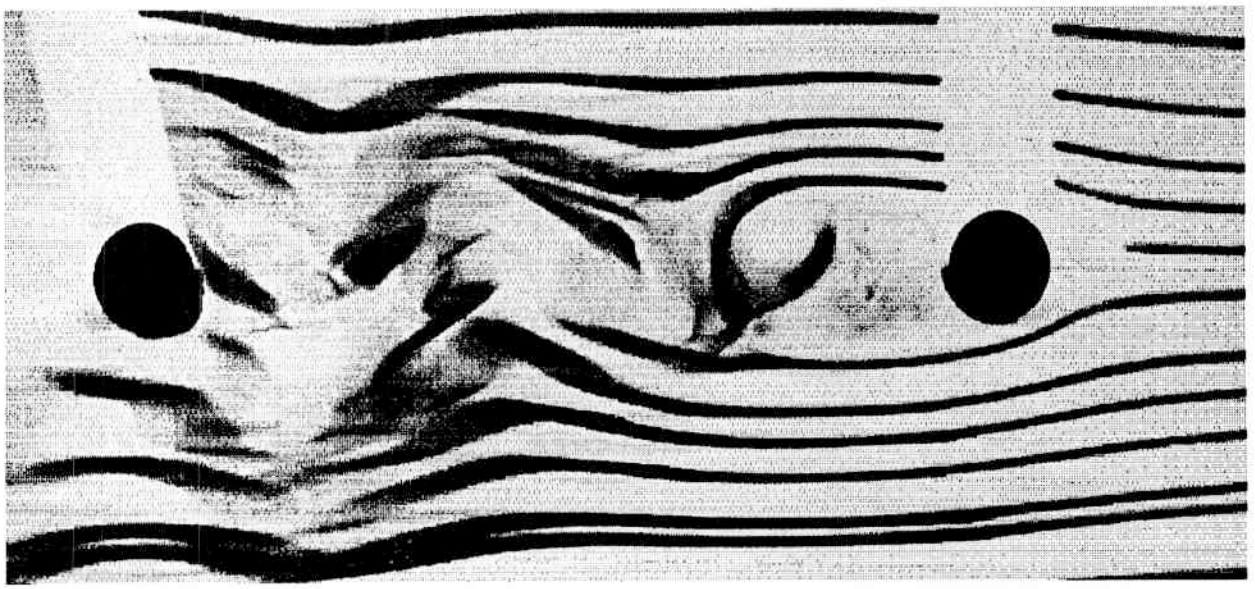


Figure 10. Measured streamlines over two cylinders in tandem. Center-to-center spacing is 8 diameters. The Reynolds number is 3160.

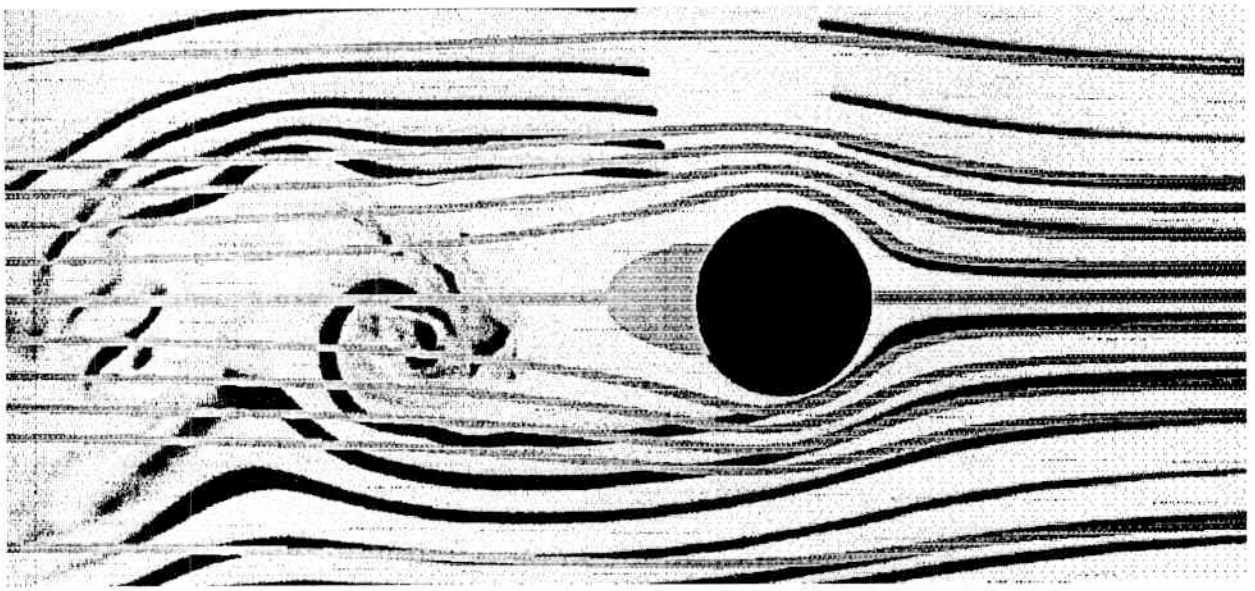


Figure 11. Overlay of streamlines predicted by Schuh CFD model (llight grey lines) onto measured streamlines shown in Figure 6 (dark lines).

Roscoe Laboratories, Inc., Port Chester, NY.
Shaffer, F.D., "Mechanics of Particulate Deposition," Proc. of the DOE Adv. Res. and Tech. Dev. Program Review Meeting, Pittsburgh PA, October 1988.
Schuh, M.J., Schuler, C.A., and Humphrey, J.A.C., "Numerical Calculation of Particle-Laden Gas Flows Past Tubes," *AIChE J.*, Vol. 35, No. 3, March 1989.
Shaffer, F.D., and Ramer, E.R., "Pulsed-Laser Imaging of Particle-Wall Collisions," Proceeding of the International Conference on the Mechanics of Two-Phase Flows, Taipei, Taiwan, June 1989.
Shaffer, F.D., Ekmann, J.M., and Ramer, E.R., "Development of Pulsed-Laser Velocimetry Systems Utilizing Photoelectric Image Sensors," Proceedings of the AIAA/ASME/SIAM/APS First National Fluid Dynamics Congress, Cincinnati, OH, July 1988.
Watts, R.L. and Levine, L.O., "Monitoring Technology Trends with Patent Data: Fouling of Heat Exchangers -- A Case Study," Proc. 22nd ASME Heat Transfer Conf., 1984.

Research on Thermophoretic and Inertial Aspects of Ash Particle Deposition on Heat Exchanger Surfaces in Coal-Fired Equipment

1. CONTRACT NUMBER: DE-FG22-86 PC 90756

CONTRACTOR:

Yale University
320 York Street
P.O. Box 1504A Yale Station
New Haven, CT 06520
(203) 432-4391

CONTRACTOR PROGRAM MANAGER:

Daniel E. Rosner,
Professor of Chemical Engineering;
Director, High Temperature Chemical
Reaction Engineering Laboratory

PRINCIPAL INVESTIGATOR: Daniel E. Rosner

DOE-PETC PROJECT MANAGER: James D. Hickerson

CONTRACT PERIOD OF PERFORMANCE: 9/1/86 - 12/31/89 (incl. 4 mo. no-cost extension)

PROJECT CATEGORY: Exploratory Study

2. PROJECT RATIONALE

Objectives: Our emphasis in the present DOE-PETC program is on developing and experimentally validating rational theoretical methods for predicting the role of *inertia* and ash particle *thermophoresis* in determining net deposition rates. We are also quantifying how simultaneous *vapor* deposition (*e.g.*, alkali sulfates) can influence the sticking and erosion associated with impacting particles, defining the role of *photophoresis* in contributing to the deposition of IR-absorbing particles of intermediate (ca 1-10μm) size, and we have initiated the quantitative study of deposit *microstructure*/deposition *mechanism* interactions.

Benefits: Engineers require rational design/optimization tools to economically predict the dynamics of net deposit growth and the thermal properties of the resulting deposits, for surfaces exposed to the products of coal combustion for a wide variety of combustor types, coal types, and operating conditions. These techniques should be based on an experimentally validated understanding of each of the mechanisms that deliver supermicron mineral matter to boiler tube surfaces and quantitative understanding of the fouling/erosion inevitably caused by such impaction in the presence of simultaneous inorganic vapor deposition.

3. PROJECT DESCRIPTION

Present Status: We are currently active in each of the following tasks:

a) Developing laboratory techniques to produce a high speed combustion gas jet laden with both inorganic particles of controlled size, and alkali sulfate vapor (Section 4.1); as well as techniques to experimentally determine particle thermophoretic diffusivities (Section 4.4).
b) Experimentally and theoretically studying the aerodynamic, and thermophysical factors governing impacting particle capture (and, ultimately, the ability of impacting particle to dislodge previously deposited particles).(cf. Rosner and Nagarajan,1987)
c) Extending our recent experiments and correlations of particle deposition to include the simultaneous effect of two (or more) deposition mechanisms (*e.g.* inertia + thermophoresis, Section 4.1) and recommend methods to predict deposition rates for geometries of engineering importance using available heat and momentum transfer data.
d) Evaluating the importance of *photophoresis* in the transport of small IR-absorbing particles in large fossil-fueled combustors and furnaces (Section 4.5).
e) Initiating the evaluation of Brownian and thermophoretic properties of unsymmetrical particle aggregates
f) Establishing quantitative relationships between particle deposition *mechanism* and the resulting particulate deposit *microstructure* (Section 4.2).

In progress(final 3 mos.): Bring research in areas a-f to point of publication of results in the archive engineering literature.(Section 5) Define fruitful follow-on investigations. for 1990-1993.

4. ACCOMPLISHMENTS

Our recent accomplishments can be conveniently divided into the following five sub-areas:

4.1 *Experimental Studies of Particle Deposition in the Simultaneous Presence of Inertial and Thermophoretic Effects*

We have developed numerical and asymptotic models to account for the simultaneous effects of inertia and thermophoresis on the transport of particles across LBLs with streamwise curvature. Our predictions are being compared with experimental data obtained using our seeded C_3H_8/air microjet burner set-up with curved platinum targets. In addition (and for comparison) we have also derived useful asymptotic ($Sc>>1$, $Re^{1/2}>>1$, $Stk<<1$) results for the effects of inertia on Brownian diffusion deposition rates on curved surfaces from isothermal LBL flows.

4.2 *Relation between Deposit Microstructure and Particle Deposition Mechanism*

As an extension of our earlier Monte-Carlo study of the subtle relations between particulate deposit *microstructure* and particle deposition *mechanism* (Tassopoulos, O'Brien and Rosner, 1989) we are now investigating alternative dynamical sticking laws, and performing associated 3-dimensional off-lattice simulations to assess their influence on the resulting deposit microstructure.An energy balance at the point of impact between the arriving and fixed particles (taking into account energy loss due to elastic/plastic deformation in the radial direction, and friction in the tangential direction) determines whether the arriving particle sticks or escapes. If the particle bounces, its new initial velocity is computed, and the particle is followed until its next contact with the deposit. We repeat this sequence until the particle "sticks" In this way we find that such models

result in much denser deposits than those obtained using our previous (relatively "unrestricted") active site criterion.

4.3 *Theory of Particle Deposition from 'Polydispersed' Aerosols*

We have developed theoretical methods which permit rapid prediction of total mass deposition rates from log-normally distributed aerosol populations of arbitrary spread (Rosner and Tassopoulos,1989),displaying results applicable to convective-diffusion of dense particles or agglomerates in the continuum or "free-molecule' regime Our results dramatically simplify the prediction of total mass deposition rates when one or several deposition mechanisms participate over important regions of the log-normal size spectrum. We have thus succeeded in generalizing a previous study (Rosner, 1989) which provided simple results for a 'single' mechanism (eg.,convective-diffusion) and 'coagulation-aged' (self-preserving') distributions.

4.4 *Application of Counterflow Diffusion Flames to the Determination of Inorganic Particle Thermophoretic Diffusivities*

We are obtaining experimental values of particle thermophoretic diffusivities in high temperature combustion gas environments using a recently developed counterflow laminar diffusion flame operated at low strain-rates.(Gomez, Smooke and Rosner,1988) In our preliminary experiments, the thermophoretic diffusivity of submicron TiO_2 particles in nitrogen-diluted counterflow gaseous diffusion flames was determined based on the existence of an easily observed ca. 1.5 mm thick thermophoretically-induced *particle-free ('dark') zone* and compared with the predictions of gas kinetic theory.Replacing N_2 by He(g) in these flames we experimentally determined a 'dark'-zone thickness of 2.8 mm, about 90% greater than in the nitrogen-diluted flame.Results from kinetic theory (Kn>>1) indicate a direct proportionality between the thermophoretic diffusivity, $\alpha_T D_p$, and the momentum diffusivity, ν, of the host gas. Replacing N_2 by He dramatically increases the momentum diffusivity of the host gas, which explains why the dark zone phenomenon is dramatized despite the larger strain rates needed to stabilize such flames

Determination of absolute $\alpha_T D_p$ -values requires accurate knowledge of the gaseous convective velocity at the particle stagnation plane (PSP) In our original approach we computed this velocity from a numerical code accounting for full molecular transport and nonequilibrium chemical kinetics. Unfortunately, discrepancies between the experimentally observed and calculated flame zone predictions (probably due to bouyancy effects neglected in the code) obliged us to develop an experimental technique to infer the axial velocity at the PSP from laser-velocimeter (LDV) measurements of the *radial* velocities at a fixed radial position as a function of axial coordinate, exploiting overall mass conservation.

4.5 *Role of Photophoresis in Combustors with High Radiative Heat Fluxes*

Particles can drift ('phoresis') as a result of nonuniform photon-particle heating in a 'host' gas. Our analysis (Mackowski, 1988) of the *photophoretic velocity* of aerosol particles (which includes both the 'free-molecular' and the more important 'slip-flow' regimes) shows that photophoresis can be a significant transport mechanism for micron-sized absorbing particles in high radiative transfer combustion environments (see, *e.g.*, Castillo, Mackowski and Rosner, 1988).We have determined dimensionless transport coefficients (proportional to the ordinary Stanton number for mass transport; see e.g. Rosner 1986,1988) as a function of radiative/convective energy flux ratio and carbonaceous particle size for laminar boundary layer flow past a cooled wall. Large effects on the deposition rate of intermediate size particles (eg, between 1 and 10 micrometers) are found if the radiative flux is comparable to or exceeds the ordinary (Fourier) energy flux. We will be extending this work to include the effects of inevitable particle *asymmetries,* including agglomerate (shape) effects, and the role that energy transfer might play in the coagulation dynamics (Rosner et.al. 1989) and deposition dynamics of such aerosol populations

5. PUBLICATIONS

Castillo, J.L., Mackowski, D., and Rosner, D.E., "Photophoretic Contribution to the Transport of Absorbing Particles Across Combustion Gas Boundary Layers", ACS-Div. Fuel Chemistry ; Presented at the Symposium on Ash Deposition, 197th Annual ACS Mtg., Dallas TX, April 9-14, 1989 *Progress in Energy and Combustion Science* (in press).

Gomez, A., Smooke, M.D. and Rosner, D.E., "Application of Counterflow Diffusion Flames to the Determination of Particle Thermophoretic Diffusivities", Presented at the 22nd Int. Combustion Symp. (Poster session) August 15-19, 1988, Seattle, WA.

Konstandopoulos, A.G., Goldman, Y. and Rosner, D.E., "Experimental Studies of Inorganic Particle-Laden High Temperature/Velocity Jet Impingement at Collecting Surfaces; Sticking and Deposit Erosion in the Simultaneous Presence of Condensing Alkali Sulfate Vapors"; Presented at the 18th Annual Meeting of the Fine Particle Society, Symposium on Multiphase Flow, Boston, MA 8/3-7/1987 (Ms. in preparation, 1989)

Konstandopoulos, A.G., Goldman, Y. and Rosner, D.E., "Experimental and Theoretical Studies of the Combined Effects of Particle Inertia and Thermophoresis on Deposition Rates across Laminar Combustion Gas Boundary Layers" (Ms.in preparation, 1989)

Mackowski, D., "Photophoresis of Aerosol Particles in the Free Molecular and Slip-Flow Regimes", *I.J.H.M.T.* ,**32,**(5) 843-854 (1989)

Park,H.M. and Rosner, D.E..,"Combined Inertial and Thermophoretic Effects on Particle Deposition Rates in Highly Loaded Dusty-Gas Systems, *Chemical Engineering Science*,**44** (in press,(1989))

Park,H.M., and Rosner, D.E., "Boundary Layer Coagulation Effects on the Size Distribution of Thermophoretically Deposited Particles", *Chemical Engineering Science*,**44,**(in press (1989))

Rosner, D.E., "Mass Transfer across Combustion Gas Thermal Boundary Layers — Power Production and Materials Processing Implications", in **Heat Transfer in Fire and Combustion Systems**, HTD **45**, ASME, NY-NY, 3-8 (1985)

Rosner, D.E., **Transport Processes in Chemically Reacting Flow Systems**, Butterworths, Stoneham, MA (1986); Second Printing, August 1988

Rosner, D.E., "Total Mass Deposition Rates from 'Polydispersed' Aerosols"; *AIChE J.* **35,**(1) 164-167,(1989)

Rosner, D.E., "Experimental and Theoretical Studies of Inorganic Matter Deposition from Combustion Gases", Final Technical Report on DOE-METC Grant DE-AC21-85MC22075 (1988); see also, Invited paper for the Benjamin G. Levich Memorial Volume of *Physicochemical Hydrodynamics* , **10**, Nos. 5,6,663-674(1988)

Rosner, D.E., and Nagarajan, R., "Toward a Mechanistic Theory of Deposit Growth from Ash-Laden Flowing Combustion Gases: Self-Regulated Sticking of Impacting Particles and Deposit Erosion in the Presence of Vapor 'Glue'", in *AIChE Symposium Series* **83,** No.257, *Heat Transfer-Pittsburgh 1987* (R.W. Lyczkowski, ed.) 289-296 (1987)

Rosner,D.E. and Tassopoulos,M, "Deposition Rates From Polydispersed Particle Populations of Arbitrary Spread",*AIChE J.* **35,**(9),(1989)

Tassopoulos, M., O'Brien, J.A., and Rosner, D.E., Simulation of Microstructure/Mechanism Relationships in Particle Deposition,"*AIChE J.* **35**,(6),967-980,(1989)

Tassopoulos,M. O'Brien, J.A., and Rosner, D.E. "Simulation of Deposits Generated by the Capture of Particles that Follow Deterministic Trajectories"; to be presented at the 1989 AIChE Annual Meeting, 6-10 November 1989, San Francisco, CA.

RADIATIVE PROPERTIES OF ASH AND SLAG

1. **CONTRACT NUMBER:** DE-AC22-87PC79901

   CONTRACTOR: Advanced Fuel Research, Inc.
   87 Church Street
   East Hartford, CT 06108
   (203) 528-9806

   CONTRACTOR PROGRAM MANAGER: Dr. Peter R. Solomon

   PRINCIPAL INVESTIGATOR: Dr. Peter R. Solomon

   PETC PROJECT MANAGER: Dr. James Hickerson

   CONTRACT PERIOD OF PERFORMANCE: July 29, 1987 to March 29, 1990

2. **SCHEDULE/MILESTONES:**

	1987		1988				1989				1990
Quarter:	0	1	2	3	4	5	6	7	8	9	10
Project Planning	---										
Measurement Technique Validation				---	---	---	---				
Deposit Sample Acquisition				---	---						
Sample Characterization					---	---	---				
Measurement of Radiative Properties of Deposit Samples				---	---	---	---	---	---	---	---

3. **OBJECTIVES:**

   The objective of this project is to make laboratory measurements of the radiative properties of ash and slag deposit samples that have been extracted from combustion devices. The results from this project will lead to an improved understanding of combustion system operation.

4. **BACKGROUND STATEMENT:**

   Thermal radiation plays a key role in the operation and efficiency of combustion systems, accounting for over 90% of the heat transfer. The radiative heat transfer in coal-fired boilers is dominated by the properties of inorganic deposits and bounding surfaces, and of particulates, which are present in the system. The properties governing the emission, absorption, and attenuation of the radiative energy by deposits and entrained particulates are a key element in accurately predicting the radiative heat transfer. They are also necessary for in-situ determination of current deposit condition (composition, temperature) from optical measurements. The radiative properties of particles are characterized by the extinction efficiency, absorption efficiency (or emissivity) and scattering efficiency. That of deposits by the reflectance, transmittance, and absorptivity. These characteristics depend on the complex refractive index, the particle size or layer thickness and the material's

morphology (porosity, inhomogeneities, grain boundaries, etc.).

This paper describes the determination of the radiative properties of deposits from combustion devices. Measurements of radiative properties of materials at high temperatures are made by a technique employing a sample heating device that is coupled to a Fourier Transform Infrared (FT-IR) spectrometer to measure emission, hemispherical-directional transmission, and hemispherical-directional reflection of a sample. By this technique, the temperature at the measurement point and the spectral emittance (emissivity) of the surface can both be obtained. The complex index of refraction that is required to calculate emissivities is determined by a transmission spectroscopic technique that employs fine sample particulates suspended in KBr and CsI matrices.

5. PROJECT DESCRIPTION:

APPARATUS

A schematic of an FT-IR spectrometer, coupled with our apparatus that provides the transfer and collection optics for measuring directional reflectance (specular and diffuse), transmittance, and radiance from a surface is shown in Fig. 1.

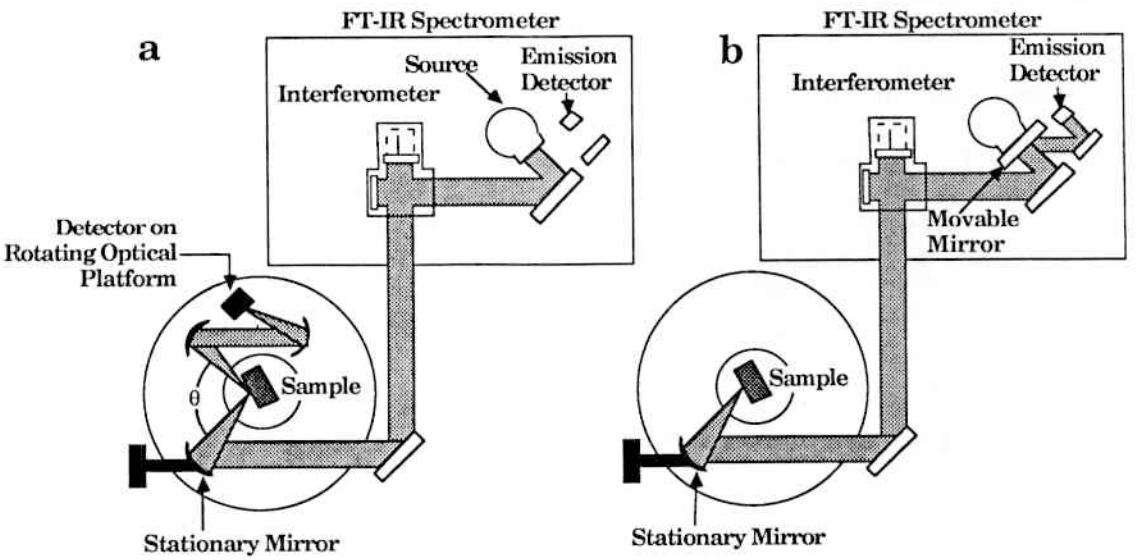


Figure 1. Schematics of Optical Paths for a) Reflectance and Transmittance Measurements, and b) Radiance Measurements.

For the reflectance measurement (Fig. 1a), the FT-IR spectrometer's source radiation is directed through the interferometer where it is modulated, then directed to a stationary mirror located near the outer edge of the rotating optical table. This stationary mirror is an off-axis parabolic mirror having an acceptance angle of 26 1/2° and a 12" effective focal length. The modulated IR radiation is focused onto the surface of interest and is then collected by a matching mirror that is secured to the rotating table. From here the radiation is focused onto a detector that is sensitive to the modulated radiation.

Defining the center of the incident IR beam to be 0°, the center of the collected beam can be positioned at any angle from θ = 15° to θ = 195°. Since the width of the

mirror is 5°, the radiation transmitted or reflected around the circle can be determined by taking data every 5°. θ = 15° corresponds to the specular reflection angle for all samples studied.

To make quantitative measurements, the FT-IR reflection and transmission experiments require normalizing the sample spectrum with a reference (or background) spectrum. For reflectance measurements, a first surface gold mirror (totally reflecting) was placed at the sample position but mounted to rotate so that the specularly reflected beam can be focused onto the detector for all detector angles. This allows for a reference spectrum to be taken at each collection angle θ. Typically the deviation around the optical table is less than ± 2%. A reference spectrum at θ = 180° can be taken in the absence of the gold mirror. Each angular measurement of reflected or transmitted radiation can then be normalized by a reference spectrum to indicate the percentage of the available incident radiation which was detected in each angular direction.

For radiance measurements, the radiation emitted from a hot sample surface is collected by the stationary mirror and directed backwards through the FT-IR spectrometer's interferometer to an emission detector (Fig. 1b). The optical path and emission detector were calibrated for energy losses and responsivity by placing a black-body cavity emitter at the sample location. Room temperature background radiation was also accounted for in the radiance measurements.

Samples were mounted by holding them at the edges with spring steel slats. This arrangement allowed for both fine resolution positioning at the IR focus, and for the elimination of extraneous radiation from the collection optics. Sample heating was accomplished with either a propane or oxy/acetylene torch. Contributions from the combustion products, CO_2 and H_2O, in the beam path were confined to narrow spectral regions, allowing for easy extrapolation to a continuum spectrum when either back heating or front heating techniques were applied. Surface temperature uniformity for a slab of Al_2O_3 at 2000 K was determined to be ±5 K over an area slightly larger than the focal measurement spot (3-4 mm diameter) and uniform to ±25 K across a 12 mm diameter.

MEASUREMENT TECHNIQUE: RADIATION CLOSURE

Radiation incident on a slab of material is either reflected, absorbed or transmitted:

$$\rho_\nu + \alpha_\nu + \tau_\nu = 1 \qquad (1)$$

where α_ν is the absorptivity, ρ_ν is the hemispherical-directional reflectance and τ_ν is the hemispherical-directional transmittance, and where the subscript ν indicates a spectral quantity. By a Kirchhoff analysis it can be shown that the emissivity, ϵ, is equal to the absorptivity, α (Bohren and Huffman, 1983).

$$\epsilon_\nu = \alpha_\nu \qquad (2)$$

The direction-hemispherical spectral reflectivity is defined by Siegel and Howell (1981). For this measurement a collimated beam is incident on the sample, and the radiation reflected into the complete reflection hemisphere defines the direction-hemispherical spectral reflectivity. Likewise, the transmittivity is the direction-hemispherical spectral transmittivity, and the emissivity is the directional spectral emissivity (Myers

et al., 1983). Measurement of the directional emissivity would be made for outgoing radiation at only one angle. The direction of this outgoing radiation will be nearly normal to the sample, as shown in Fig. 1. The above expression, a statement of energy conservation, is true for samples with either optically smooth or rough surfaces, and is the basis for the method that we present for the measurement of emittance and temperature of a surface.

The disposition of the sample, optics, and heating techniques are such that direct measurements of hemispherical properties with this apparatus are not possible. For radiation incident normally on the sample, measurement of the bi-directional reflectivity in the θ plane is sufficient to characterize the reflectivity over the complete reflection hemisphere if the sample is an isotropic scatterer. In our experiments the radiation will be incident at a direction very close to the surface normal. In that case, "integration" of the measured bi-directional reflectivity and transmittivity over all angles of the hemisphere will yield the required directional-hemispherical properties for isotropic scatterers (Siegel and Howell, 1981). In doing this we make use of well known reciprocity relationships (Siegel and Howell, 1981).

In applying this technique, the precise temperature at the measuring point is determined from the measured radiance at one, two or several frequencies using the emissivity, ϵ_ν, obtained from

$$\epsilon_\nu = 1 - \rho_\nu - \tau_\nu \qquad (3)$$

Once the temperature is known, the full spectral emittance can be obtained from the radiance and compared to that obtained from the reflection and transmission.

MEASUREMENT TECHNIQUE: COMPLEX INDEX OF REFRACTION

To measure the optical constants n_ν and k_ν for ash and slag deposits, AFR has developed a technique using a transmission measurement for particles embedded in a matrix of alkali halide. This method eliminates the inaccuracies inherent in reflection techniques when applied to inhomogeneous materials such as ash or coal. The objective of the procedure as originally developed was to determine values of n_ν and k_ν which were consistent with extinction measurements using KBr and CsI pellets (an extension of the method of Brewster and Kunitomo (1984)) and also consistent with the emissivity measurements. The technique has previously been described (Solomon et al., 1987).

6. RESULTS:

SPECTRAL EMITTANCE BY REFLECTANCE/TRANSMITTANCE CLOSURE

The technique of determining the spectral emittance as calculated from the measured directional-hemispherical reflectance and transmittance (closure), and the use of this emittance to determine the sample temperature from the radiance was validated by performing the technique on calibration samples. Metal and dielectric samples (specular and diffuse reflecting) were tested at temperatures up to 2226 K. Comparison to the literature for emittance and to surface bonded thermocouples for temperature measurements validated the technique. The closure technique is summarized below and is illustrated in Fig. 2 for a surface of a non-transmitting sample.

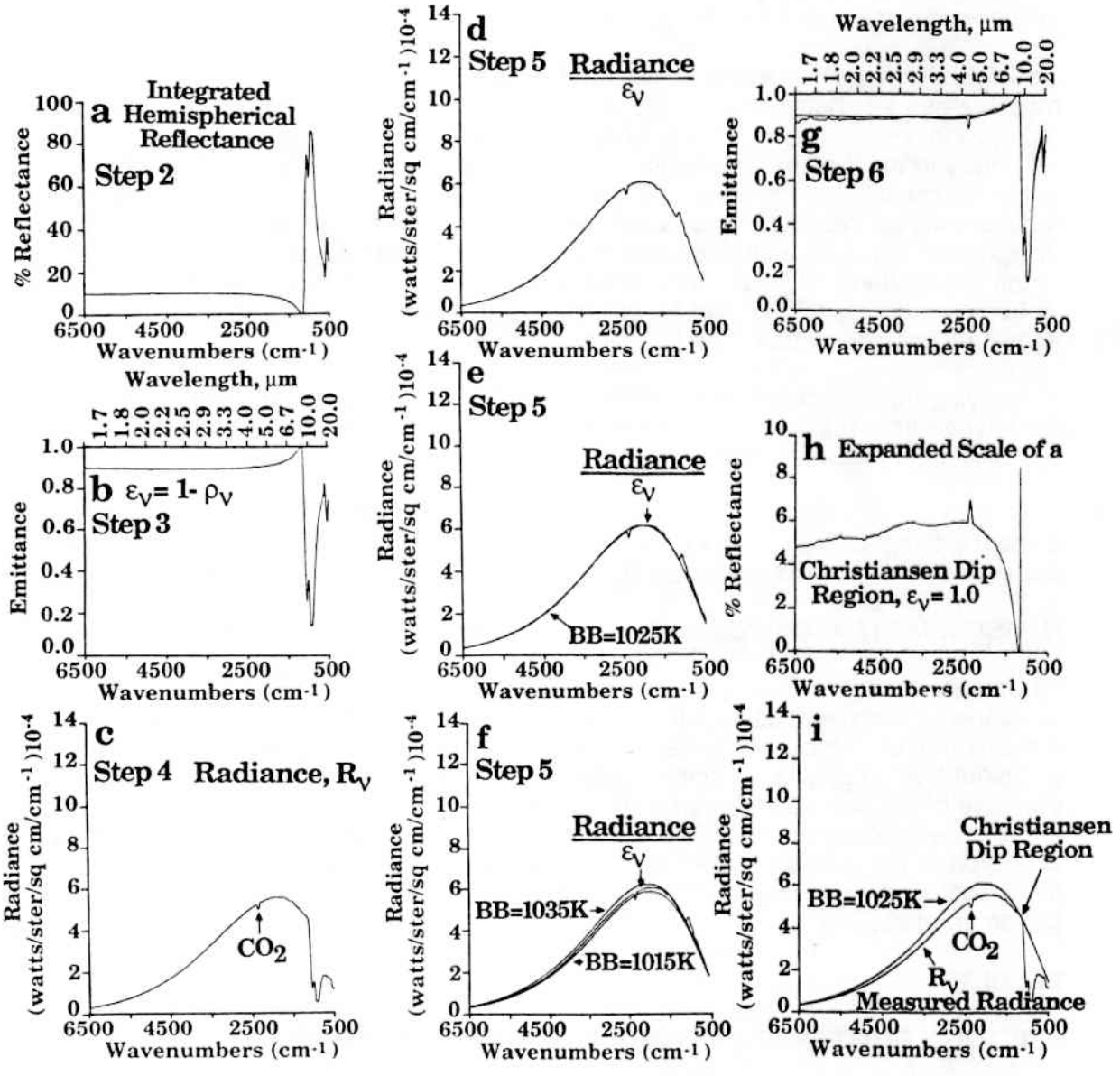


Figure 2. a-g) Sequence for Spectral Emittance and Surface Temperature Measurement from Reflectance Closure and Radiance Measurement for a Non-transmitting Slab of Polished Si_3N_4. $T_{surface}$ = 1025 K ±5 K. h-i) Reflectance and Radiance Measurements Indicating Christiansen Dip Region where ϵ_ν = 1.0.

Step **1.** Measure the reflected and transmitted IR radiation as a function of angle around a hot sample.

2. Calculate the hemispherical reflectance/transmittance by integrating and summing over all angles (Fig. 2a).

3. Apply **closure** ($\epsilon_\nu = 1 - \rho_\nu - \tau_\nu$) (Fig. 2b).

4. Measure the radiance, R_ν, at one angle from the hot surface (Fig. 2c).

5. Using the radiance measurement and the spectral emittance (in the regions of greatest certainty) determine the surface temperature by matching R_ν/ϵ_ν (Fig. 2d) with theoretical curves for $BB(T)_\nu$ as shown in Fig. 2e-f.

6. Recalculate the spectral emittance over the complete spectral range with the radiance measurement and the surface temperature determined in Step 5 $\epsilon'_\nu = R_\nu/BB(T)_\nu$. ϵ_ν' is compared to ϵ_ν determined in Step 3 in Fig. 2g.

For many of the calibration samples, the reflectance/transmittance measurements indicated a spectral region where there was less than 0.1% reflected or transmitted energy. Figure 2h shows this point for the opaque slab ($\tau_\nu = 0$) of silicon nitride to be at 1206 cm^{-1}. This spectral region is attributed to the Christiansen effect (Bohren and Huffman, 1983), which is when the real part of the refractive index of the material is one and so, it matches that of air. Under these conditions almost no reflection will be observe if the imaginary part is low. This Christiansen dip defines a spectral region where $\epsilon_\nu \approx 1.0$, thus allowing a fast and accurate method of determining the surface temperature and spectral emittance since the temperature of the material can be determined by direct comparison to theoretical curves for $BB(T)_\nu$, as shown in Fig. 2i. The complete spectral emittance is then calculated as described in Step 6. For materials that exhibit a Christiansen dip, the method thus serves as verification of the spectral emittance determined by reflectance closure.

SPECTRAL EMITTANCE OF ASH AND SLAG

Table 1 list the ash and slag deposits acquired for this program. Spectral emittance determinations have been measured as a function of temperature, and physical state (i.e., fused, molten, sintered, or particulates). Powdery deposits were pressed into 2 mm thick wafers. All of the samples were thick enough to be optically opaque ($\tau_\nu = 0$) to the incident IR radiation. Surface bonded thermocouples, when present, agreed within ± 50 K of the temperature determined spectroscopically.

Figure 3a compares several samples of fused slag deposits that originated from the firing of Illinois No. 6 coal, but collected at different locations in B&W's and BYU's combustion devices. All of the fused samples exhibit a high spectral emittance (> 0.9) over a wide temperature range. Variations below 1500 cm^{-1}, which is the characteristic region of infrared band absorption for mineral species found in ash and slag, possibly indicate discrete differences in chemical composition. Shaded in the figure are the interference regions of the combustion products of the flame used to heat the samples.

Surface morphology is shown to greatly effect spectral emittance in Fig. 3b, where a sintered deposit consisting of individual particles that are weakly held together is compared to the same material after grinding into smaller particles and pressing into a wafer, and after melting the material. Fusing the sintered deposit results in a

TABLE 1
SLAG AND ASH SAMPLES

SAMPLE NO.	SLAG OR ASH DESCRIPTOR	ACQUIRED FROM	COAL	FIRED AT	PHYSICAL DESCRIPTION
1	Slag from refractory back wall of BCTU*	Babcock & Wilcox (B&W)	Illinois No. 6 (bituminous)	B & W	Sintered Deposit
2	Slag from top of slagging panel in BCTU	B & W	Illinois No. 6 (Bituminous)	B & W	Fused Deposit
3	Slag from Tube No. 2 of slagging panel in BCTU	B & W	Illinois No. 6 (Bituminous)	B & W	Dusty Deposits
4	Slag from Tube No. 4 of slagging panel in BCTU	B & W	Illinois No. 6 (Bituminous)	B & W	Dusty Deposits
5	One-time molten pool of slag from inside BCTU	B & W	Illinois No. 6 (Bituminous)	B & W	Fused Deposit
6	Eagle Butte Ash	Stanford University	Eagle Butte (Subbituminous)	Paynee Station Brush, Colorado	Powdery Ash
7	San Miguel Ash	Stanford University	San Miguel (Texas Lignite)	San Miguel Station San Miguel, TX	Powdery Ash
8	Illinois No. 6 Ash	Stanford University	Illinois No. 6 (Bituminous)	Labadie Station	Powdery Ash
9	BYU Furnace Wall Refractory	Brigham Young University (BYU)	----------	BYU	Hard Alumina & Chromium Based Material
10	BYU Slag	BYU	Illinois No. 6 (Bituminous)	BYU	Fused Deposit

* BCTU: Basic CombustionTest Unit at B & W

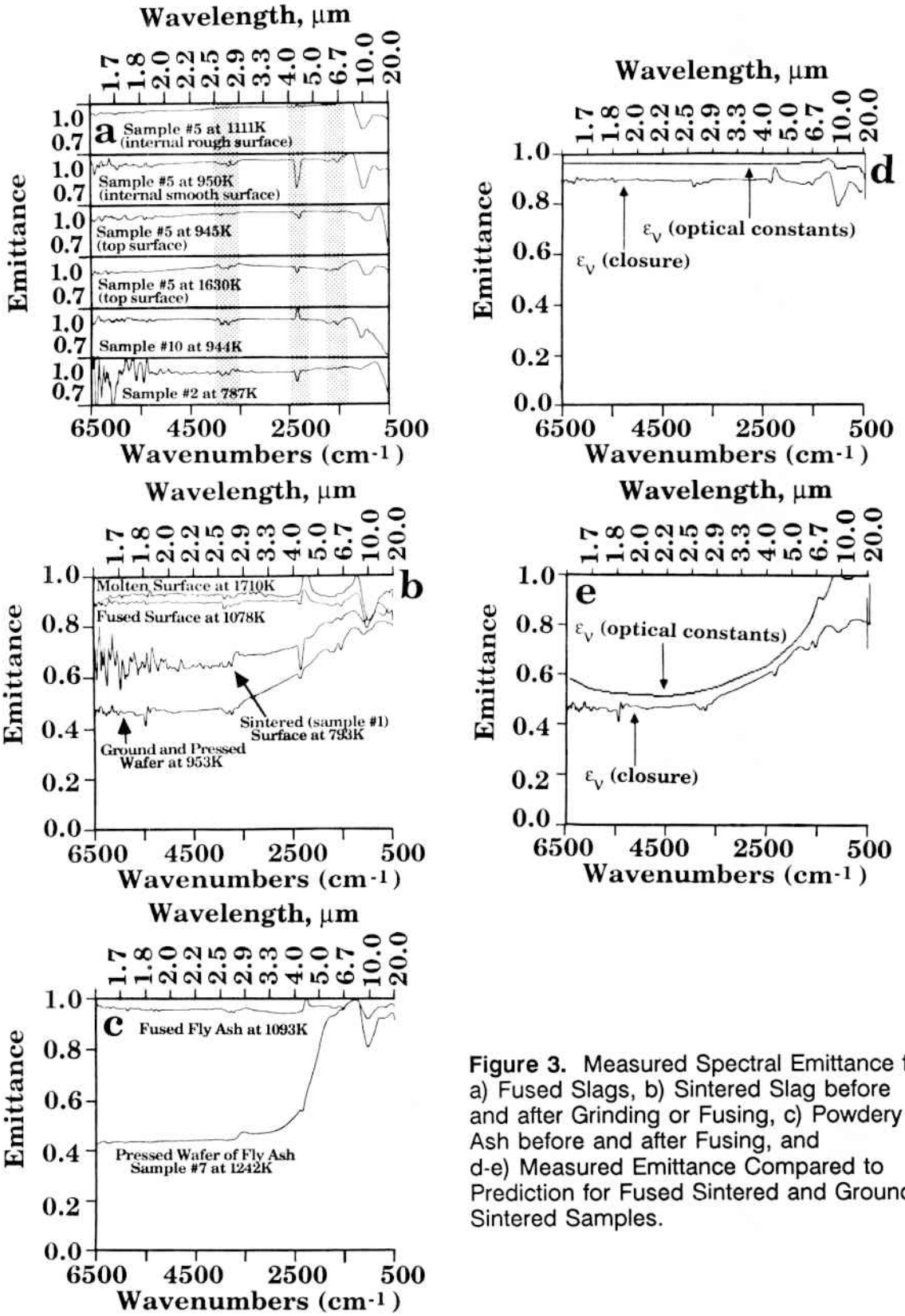


Figure 3. Measured Spectral Emittance for a) Fused Slags, b) Sintered Slag before and after Grinding or Fusing, c) Powdery Ash before and after Fusing, and d-e) Measured Emittance Compared to Prediction for Fused Sintered and Ground Sintered Samples.

spectral emittance similar to those shown in Fig. 3a. In the molten or liquid state, the spectral emittance is apparently only slightly higher than the fused state, but does exhibit a Christiansen dip were ϵ_ν = 1.0. The hot CO_2 band at ~4.5 μm is produced by the torch that is directly heating the measured spot. The melting point of the material was determined to be ~ 1400 K. The individual particles of the surface of the original sintered deposit increase the scattering efficiency of the material, which will cause a wavelength dependent drop in emittance. By grinding the material to smaller particulates, the scattering efficiency is further increased and hence, results in a lower emittance. Figure 3c also demonstrates the change in spectral emittance for fine particulates of powdery ash (sample no. 7) after fusing the material.

To predict the spectral emittance from n_ν and k_ν, the surface condition of the sample must be considered to choose an applicable model. For opaque slabs, which can be used to describe the fused deposits, the emittance can be calculated from (Bohren and Huffman, 1983).

$$\epsilon_\nu = 1 - \frac{(n_\nu - 1)^2 + k^2_\nu}{(n + 1)^2 + k^2_\nu} \qquad (4)$$

Figure 3d compares the predicted and measured spectral emittance for the fused surface of the sintered deposit. The prediction is in reasonable agreement with the measured emittance for this and the other fused surfaces. Discrepancies may be attributed to the model assuming a smooth homogeneous surface, which seems to be a good approximation, but not necessarily absolute for the fused surfaces.

For the pressed wafer of ground material, the surface and sub-surface is comprised of tightly packed particles. This suggests that an inhomogeneous model should be used that recognizes both the discreetness of each scattering particle and multiple scattering effects. We report here the results of calculations based on a two component model derived by Bohren (1987). In this model,

$$\epsilon_\nu = 1 - \frac{(\sqrt{1-\bar{w}_o g} - \sqrt{1-\bar{w}_o})}{(\sqrt{1-\bar{w}_o g} + \sqrt{1-\bar{w}_o})} \qquad (5)$$

where the single scattering albedo $\bar{w}_o$ is defined by the efficiency ratio $Q_{scattering}/(Q_{scattering}+Q_{absorbance})$, and g is the asymmetry parameter which lies between 1 (strict forward scattering) and -1 (strict backward scattering).

Figure 3e compares the measured spectral emittance for a pressed wafer of ground sintered deposit with that calculated from Eq. 5. For the ground material, a particle size distribution centered around 1.0 μm was used with n_ν and k_ν to determine $\bar{w}_o$, and g = 0.6 for this case. The agreement is reasonably good. Better agreement should be achieved when the actual particle size distribution is better defined and when g is input as a function of wavelength.

7. FUTURE WORK:

Work will continue on spectral emittance measurements of ash and slag by the techniques described. The physical characteristics of the material are attributed to causing the largest changes in spectral emittance, and work will concentrate on

identifying the parameters necessary as input for model predictions. Changes in emittance as a function of chemical composition will also be investigated.

8. REFERENCES:

Bohren, C.F., Am. J. Phys., **55**, 524, (1987).

Bohren, C.F. and Huffman, D.R., Absorption and Scattering of Light by Small Particles, Wiley & Sons, Inc., NY, (1983).

Brewster, M.W. and Kunitomo, T., Trans. ASME, **106**, 678, (1984).

Myers, V.H., Ono, A., and DeWitt, D.P., "A New Method for Measuring Optical Properties of Semitransparent Materials at High Temperatures", AIAA 18th Thermophysics Conference, June 1-3, Montreal, Canada, (1983).

Siegel, R. and Howell, J.R., Thermal Radiation Heat Transfer, 2nd Edition, Hemisphere, Washington, (1981).

Solomon, P.R., Carangelo, R.M., Best, P.E., Markham, J.R., and Hamblen, D.G., Fuel, **66**, 897, (1987).

OPTICAL PROPERTIES OF FLY ASH

1. CONTRACT NUMBER: DE-AC22-87PC 79903

CONTRACTOR: Stanford University
Stanford, CA 94305
(415) 723-1745

CONTRACTOR PROJECT MANAGER: Sidney A. Self

PRINCIPAL INVESTIGATOR: Sidney A. Self

PETC PROJECT MANAGER: Mr. James D. Hickerson

PERIOD OF PERFORMANCE: September 15, 1987 through December 14, 1990

2. SCHEDULE/MILESTONES:

Task I. Characterization of Fly Ash	9-15-87 to 12-14-90
Task II. Measurement of Optical Constants of Slags	9-15-87 to 12-14-90
Task III. Calculation of Radiant Properties of Fly Ash Dispersions	9-15-88 to 12-14-90
Task IV. Measurement of Radiant Properties of Fly Ash Dispersions	9-15-88 to 12-14-90

3. OBJECTIVES:

The aim of this project is to provide a fundamental scientific basis for understanding and calculating radiative heat transfer in coal combustion systems, particularly as influenced by the presence of inorganic constituents deriving from the mineral matter in coal.

4. BACKGROUND STATEMENT

The calculation of radiative heat transfer requires specification of the spectral absorption and scattering coefficients (a_λ and σ_λ) and the scattering phase function (Φ_λ) of the medium. While the contributions to these properties by the infrared-active gases (CO_2 and H_2O) are well-documented, the contributions by the dispersed particulate phase (fly ash) may be large and are poorly understood. In general, the particulates produce two opposing tendencies on radiation transfer. Scattering impedes the transfer of gas radiation, while the particle emission enhances the overall radiation transfer.

Calculation of the optical properties of a particulate dispersion rests on the Mie theory for a single particle. This theory is available only for a homogeneous, isotropic sphere and requires specification of the size parameter $x \equiv (\pi d/\lambda)$ and the complex refractive index $m \equiv (n - ik)$ of the particle material, a function of composition, wavelength and temperature. The optical properties of the dispersion is then obtained by convolving the Mie theory for a single sphere with the size and refractive index distributions of the polydispersion.

In practice, it is not possible to invert measurements of the optical properties of a particulate dispersion to infer the size and refractive index distributions of the particulates. Even if one knows the size distribution from independent measurements, one can infer, at best, only some effective average refractive index. Because of the impracticality of obtaining fundamental data on the complex refractive index of particulates from measurements on a polydispersion, and in view of the heterogeneity of composition of fly ash, an alternative strategy has been adopted.

5. PROJECT DESCRIPTION:

The basic approach is to measure the optical constants (i.e. the components n, k of the complex refractive index) on bulk samples of synthetic slags, for which reliable techniques are available. Such measurements are being made over relevant ranges of wavelength, composition and temperature, and will constitute the fundamental data base for computing radiation transfer in fly ash laden combustion gases. To utilize such data on the optical constants of slag in calculations of radiation transfer in dispersions, it is also necessary that the ash be characterized with respect to its size and composition distributions. Characterization of a range of ashes constitutes a second component of the work. It should be recognized that this basic approach rests on the fortunate fact that the vast majority of fly ash particles are spherical, optically isotropic (because they are vitreous) and homogeneous, although the composition varies significantly from particle to particle.

The planned research program consists of four tasks, as outlined below.

TASK I – CHARACTERIZATION OF FLY ASH

Representative samples of fly ashes are being characterized with respect to their size and composition distributions, including correlation of composition with size over ranges of interest for radiation transfer. Ashes from six coals selected for study under the concurrent PETC program on "Transformation of Inorganic Coal Constituents in Combustion Systems" have been obtained from electric power plants or from samples produced earlier in the 10^6BTU/hr combustor at Foster-Wheeler.

Size distributions are determined by Coulter counter, while size-composition distributions are being obtained from automated SEM-EDX microprobe analyses.

In addition, techniques have been developed for ash separation by both size and density by combined wet sieving and centrifuging in liquids of various specific gravity, as well as separation of the magnetic component (magnetite from the combustion of pyrite). Analysis of the separated fractions will yield further information on the size-composition distributions.

TASK II – MEASUREMENTS OF THE OPTICAL CONSTANTS OF SLAGS

Coal slags and fly ash are basically impure calcium-aluminosilicate glasses. The host glass is essentially transparent ($k \leq 10^{-4}$) in the visible and near infrared, with a very strong absorption band ($k \sim 1$) in the range 8–12 μm due to vibration of the Si-O bond. The principal infrared-active impurity is iron (as the ferrous ion) which produces significant absorption ($k \sim 10^{-4}$-10^{-3}) in the range 0.5–5 μm, important for radiation transfer at combustion temperatures.

Synthetic slags of controlled composition are produced by melting appropriate mineral

oxides in a furnace at ~1560°C and cooled slowly to produce homogeneous bulk samples. For measurements at low temperatures (to ~800°C) thin wafers (50–500 μm) are cut and optically polished. The optical constants over the wavelength range 0.5–5 μm are determined by measuring the absorption and surface reflectance and use of the Fresnel relations. For the range 5–13 μm where the absorption is too strong ($k > 10^{-2}$) to allow direct measurements of absorption on thin wafers, k is obtained from surface reflectance measurements at normal incidence using the Kramers-Kronig relations.

At high temperatures (≥1600°C) where the slag is liquid, an alternative technique has been devised for measuring the absorption of thin liquid layers, by a double pass using reflection from a submerged platinum mirror. The absorption coefficient (and hence k) is determined from the change in signal when the liquid film depth is changed by a known amount by raising or lowering the mirror by a micrometer-controlled increment.

For the longer wavelengths ($\lambda \geq 5$ μm), where the absorption is too strong ($k \geq 10^{-2}$) to allow direct absorption measurements on a thin film, n and k is determined solely from surface reflectance measurements on the liquid slag using the Kramers-Kronig technique.

The final outcome of Task II will be a set of correlation formulae for the complex refractive index of synthetic slags as a function of composition, wavelength and temperature. These formulae will constitute a fundamental data base for the calculation of radiation transfer in ash-laden combustion gases.

TASK III – CALCULATION OF THE RADIANT PROPERTIES OF FLY ASH DISPERSIONS

Sample calculations are being made for typical ash loadings, size distributions and compositions for simple geometries, with two main purposes: first, to provide insight and physical understanding of the role of fly ash in radiative heat transfer in combustion systems; second, to indicate the sensitivity of the results to the characteristics of the input data. Such calculations will also be used to determine appropriate conditions and to predict the expected measured radiative properties for the experiment of Task IV.

TASK IV – MEASUREMENTS OF THE RADIANT PROPERTIES OF FLY ASH DISPERSIONS

This experiment is designed to critically test our ability to predict the measured spectral absorption and scattering coefficient of fly ash dispersions under well-controlled laboratory conditions utilizing the optical property data developed in Task II. Particular attention will be paid to assessing the contribution of the char component in typical ashes. Any discrepancies between calculated and measured quantities revealed by these tests will be resolved by appropriate further studies.

6. RESULTS AND ACCOMPLISHMENTS:

TASK I. CHARACTERIZATION OF FLY ASH

Ash from the following six representative U.S. coals are being studied

- Upper Freeport, PA (Bituminous)
- Kentucky #9 (Bituminous)
- Illinois #6 (Bituminous)
- Eagle Butte, WY (Sub-Bituminous)
- San Miguel, TX (Lignite)
- Beulah, ND (Lignite)

The first four come from the pilot combustor at Foster-Wheeler, and include samples from both a baghouse and an upstream cyclone. The lignite ashes are from power plants.

The ash size distribution is determined using a Coulter multisizer. This instrument is superior to alternative sizing techniques because the ash can be effectively deagglomerated in the electrolyte solution. Moreover, it has high resolution (256 channels), wide dynamic range (~15:1 in diameter for a single orifice) and excellent statistics (typically $>10^5$ particles). The manufacturer suggests that particles with diameters between 2% and 65% of the orifice diameter are accurately sized, but we find a lower limit of 3.5%.

Because fly ash typically has a very broad distribution, we have developed a technique to extend the sizing range from 1.2 μm to 180 μm by combining data obtained using two or three orifices of appropriate diameters. A log-normal distribution, truncated outside this range, is found to fit the data very well. This distribution function is:

$$f(D) = \frac{\frac{1}{\sqrt{2\pi}\, D \ln\sigma}\ \exp\left[-\frac{1}{2}\left(\frac{\ln D/D_n}{\ln\sigma}\right)^2\right]}{\int_a^b \frac{1}{\sqrt{2\pi}\, x \ln\sigma}\ \exp\left[-\frac{1}{2}\left(\frac{\ln x/D_n}{\ln\sigma}\right)^2\right]} \qquad a \le D \le b \tag{1}$$

$$f(D) = 0 \qquad D < a \text{ and } D > b$$

Here D is the diameter, D_n is the median diameter, σ is the geometric standard deviation and a and b are the limits of measurements. The reason for using a truncated log-normal distribution is that we cannot measure particles outside the limits a and b. Hence the distribution is normalized by the finite integral, which would have the value unity if all the particles were measured ($a \to 0$, $b \to \infty$).

Equation (1) is the distribution by diameter. The same equation represents the distribution by surface area or volume if D_n is replaced by D_s and D_v respectively, where $D_s = D_n \exp(2ln^2\sigma)$ and $D_v = D_n \exp(3ln^2\sigma)$. These relations between the median sizes by diameter, surface area and volume are basic properties of the log-normal distribution (Aitchison and Brown, 1957).

The parameters D, σ, for the best fit distribution are found by minimizing the sum of the mean square differences between the function and the data. Figure 1 shows the data and best fit log-normal distribution by volume for the Kentucky #9 ash, using orifices of 30 μm and 100 μm. The scatter at large sizes is statistical because there are few particles of large size. Data and the best fit truncated log-normal distributions by diameter, area and volume are shown for the same ash in cumulative undersize plots on log-probability scales in Figure 2. In this format the log-normal distributions plot as parallel straight lines. The median diameters based on diameter, area and volume are respectively 1.46, 5.49 and 10.64 μm, while the standard deviation is 2.26. By diameter, 40% of the particles are less than 1.2 μm, but by area and volume the percentages are only 3% and 0.4% respectively. For radiative transfer, it is the distribution by area that is most relevant and, for infrared wavelengths, the contribution of the submicron fraction to Mie scattering is negligible because the size parameter ($\pi D/\lambda$) is small.

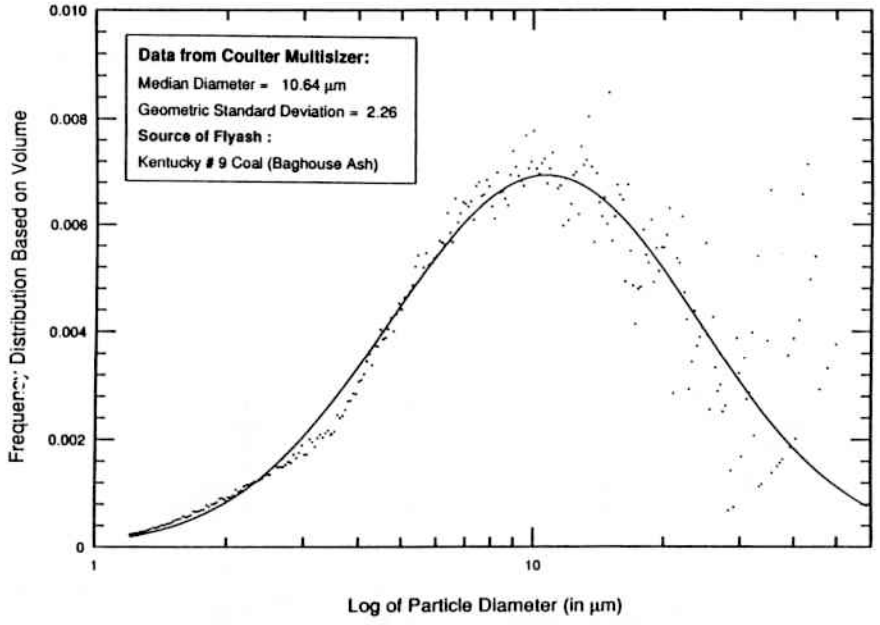


Figure 1. Size Data from Two Orifices Fitted to Log-Normal Distribution.

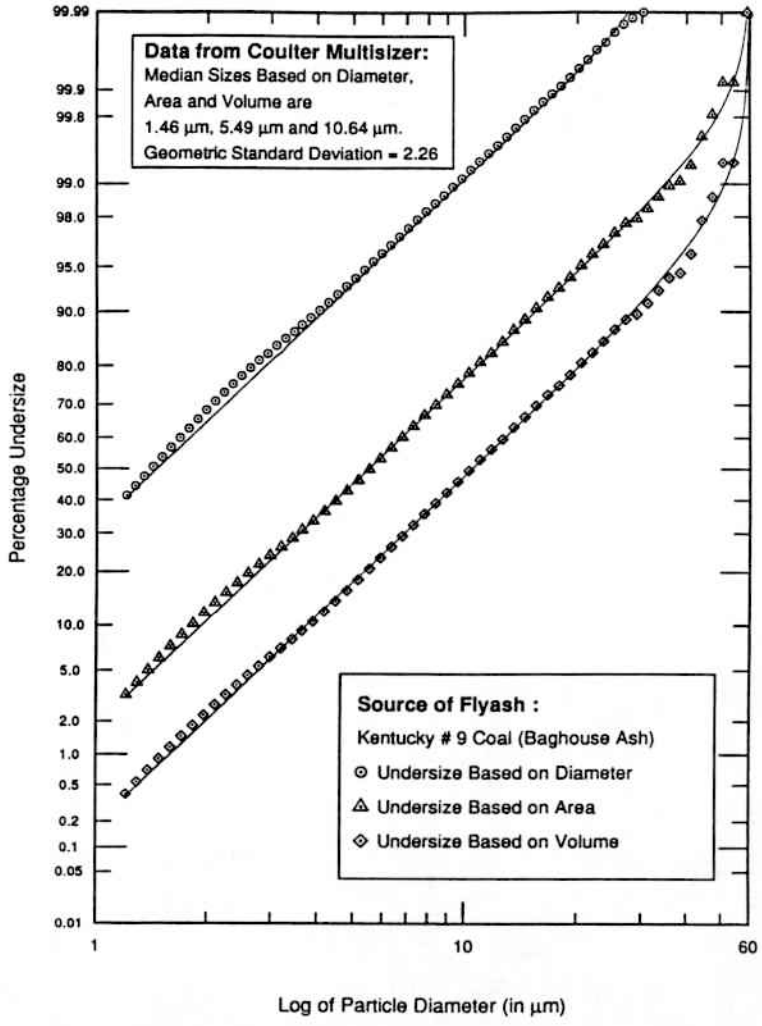


Figure 2. Size Data Fitted to Cumulative Log-Normal Distribution.

The size distribution parameters for the six ashes are tabulated below:

Table 1. Size Distribution Parameters of Fly Ashes.

Source of Ash	Median Diameter by Volume	Standard Deviation
Kentucky #9 (Baghouse)	10.64 (μm)	2.26
Kentucky #9 (Cyclone)	15.67	2.02
Upper Freeport (Baghouse)	9.25	2.80
Illinois #6 (Baghouse)	9.70	3.02
Illinois #6 (Cyclone)	14.72	2.14
Beulah (Baghouse)	12.80	2.95
Beulah (Cyclone)	11.63	2.34
San Miguel	32.23	2.89
Eagle Butte	14.15	2.36

The chemical composition and size of individual ash particles is being determined by computer controlled scanning electron microanalysis (CCSEM) at University of North Dakota Energy Research Center (UNDERC). Micrographs of the sampled fields in the first set of analyses revealed that the ash was inadequately deagglomerated. We have now developed a technique for producing satisfactory samples on SEM stubs by freeze-drying ultrasonically dispersed ash suspensions in acetone. Future samples will be prepared at Stanford for CCSEM analysis at UNDERC.

Codes have been developed for statistical analysis of the CCSEM data. Size distributions will be checked against results from the Coulter multisizer. Compositional classes, appropriate for generating refractive index classes, will be created from the data, as well as composition-size correlations. Additionally, the CCSEM data will be correlated with results from other analytical techniques described below.

A technique for accurate density classification of ash by centrifugal separation of small samples (~1.5 gm per patch) has been developed. Five liquids of density 1.6 to 3.2 g/cm^3 are prepared by mixing carbon tetrachloride, di-bromo methane and di-iodomethane. The lighter fractions include primarily char and cenospheres while the denser fractions contain particles high in iron. Information from analysis of the separated fractions will be compared with CCSEM data.

It is observed that most ashes contain magnetic particles containing magnetite (Fe_3O_4). Since iron in the ash plays an important role in its optical properties, it is important to establish the proportion of iron occurring as magnetite relative to that incorporated in the glassy particles. A technique of magnetic separation of ash ultrasonically dispersed in distilled water has been developed. This shows that 12% by mass of Illinois #6 ash is magnetic. The magnetically separated fractions will be subjected to further microanalytical techniques. The char content is being determined by low temperature ashing.

TASK II. MEASUREMENT OF THE OPTICAL CONSTANTS OF COAL SLAGS

The vast majority of fly ash particles consist of impure aluminosilicate glass. The objective of this task is to measure the optical constants, i.e. the components (n, k) of the

complex refractive index, of bulk samples of such glassy slags over appropriate ranges of composition, wavelength and temperature. Given such data, along with information on the size and composition distributions of a given ash, Mie theory can be used to compute the radiative properties of fly ash dispersions.

The host glass, usually composed of silica, alumina, calcia and magnesia in that order, is essentially transparent ($k < 10^{-4}$) through the visible and near infrared (to $\lambda \sim 5$ μm), but is dominated by a very strong absorption band ($k \sim 0.1-1$), due to vibration of the Si-O bond, in the range $\lambda \sim 8-12$ μm. Absorption in the visible and near infrared is controlled by minor, transition metal constituents, notably iron, of the host glass. In earlier work at Stanford (Goodwin, 1986), extensive measurements of (n, k) were made for a range of compositions (up to 16% iron, as Fe_2O_3) over the wavelength range 0.5 – 12 μm for optically polished wafers at temperatures to 800°C. The main objective of the current work is to extend these data to high temperatures (1600°C) when the slag is liquid. No discontinuous changes in (n, k) are expected because the liquid and vitreous solid states are essentially continuous.

As established in the work of Goodwin on solid slag samples, two separate techniques are required to determine n and k over the whole wavelength range from the visible to $\lambda \sim 12$ μm. For $\lambda \leq 5$ μm, where k is small enough ($< 10^{-2}$) that the transmission T of a thin layer of slag (thickness h) is not too small to allow accurate measurement, the absorption index, k, can be found from the formula $T = \exp(-4\pi kh/\lambda)$. The real index, n, can be found from measurements of the near normal reflectance, R_n, using the Fresnel formula $R_n \approx [(n-1)^2 + k^2]/[(n+1)^2 + k^2]$.

For $\lambda \geq 5$ μm, where k is too large to allow transmittance measurements, values of n and k may both be inferred solely from reflectance measurements (provided they are made over a large enough wavelength range) by use of the Kramers-Kronig relations which are analytic formulas relating n and k in integral form.

For high temperatures, where the slag is molten, the same two basic methods may be used, but the experimental techniques must be modified. Also, since the measurements must be made inside a high temperature furnace, considerable technical difficulties must be overcome.

Transmittance Measurements

An iron-bearing synthetic slag (SA05) was produced by mixing powdered oxides which were heated at 10°C/min in a furnace, held at 1600°C for approximately 12 hours, and cooled at the same rate. Electron microprobe analysis and backscatter electron images showed that the resulting slag was homogeneous with proportions 55.1 wt% SiO_2, 27.6 wt% Al_2O_3, 12.4 wt% CaO, and 4.9 wt% Fe_2O_3.

To measure the absorption index, a "submerged reflector" technique is used whereby a platinum mirror is suspended just below the liquid surface and the absorption index is measured by double pass through the thin, overlying slag layer. By measuring the change in absorption when the mirror is displaced by a small increment Δh, the absorption index can be found from the change in transmission from the formula

$$T_{h+\Delta h}/T_h = \exp(-4\pi k(2\Delta h)/\lambda) \qquad (2)$$

without having to know the reflectivity of the platinum mirror.

A schematic of the apparatus used for both the transmittance measurements (via a submerged reflector) and the near normal reflectance measurements is shown in Figure 3. The gold reference mirror is not used for the transmittance measurements. The ceramic filament of the Nernst Glower broadband source is imaged through a chopper (670 Hz) onto a platinum mirror inside the furnace. The platinum mirror is suspended just below the liquid slag surface and the vertical position of the crucible of molten slag is adjusted independently of the platinum mirror. A dial indicator (readability ~ 2 μm) is used to accurately determine the change in depth (typically $\Delta h \sim 100-500$ μm). The platinum mirror is tilted slightly from the plane of the liquid surface, allowing the optics to collect only that portion of the incident beam which is reflected once from the mirror. This transmitted beam is then imaged onto the entrance slit of a grating monochromator through a longpass filter (to eliminate higher order wavelengths) and the resulting spectrally selected radiation is detected using a HgCdTe detector. The signal is measured synchronously using a lock-in amplifier.

Near-Normal Reflectance Measurements

Measurements of the near-normal reflectance of molten synthetic slag were made by realigning the optics to collect the first surface reflection from the sample in the furnace. A gold reference mirror was placed outside the furnace and mirror M4 was moved in and out of the optical path to allow reflectance measurements relative to the gold reference mirror (for which the reflectance is known).

The Kramers-Kronig relations were utilized to reduce the near normal reflectance data to n and k. The form of the Kramers-Kronig relations used here are in terms of the reflection coefficient r and phase shift on reflection θ_R. The reflection coefficient r is related to the reflectance by $R_n = |r|^2$ and the phase shift is defined via $r = |r|\exp(i\theta_R)$. In this form we have

$$\theta_R(\omega) - \pi = -\frac{\omega}{\pi} P \int_0^\infty \frac{\ln R_n(\omega')}{\omega'^2 - \omega^2}\, d\omega' \tag{3}$$

where P denotes the principal value of the integral.

Once $\theta_R(w)$ is computed using a sufficiently wide wavelength range of reflectance data, n and k are computed using the relations

$$n = \frac{1 - R_n}{1 + R_n + 2\sqrt{R_n}\cos\theta_R}\ ; \qquad k = \frac{-2\sqrt{R_n}\sin\theta_R}{1 + R_n + 2\sqrt{R_n}\cos\theta_R} \tag{4}$$

A computer program was written to compute n and k from the reflectance data using the Kramers-Kronig relations. The integral shown in equation (3) can be evaluated analytically outside the wavelength range for which we have data by assuming the reflectivity is constant outside the range of available data. That is, assuming

$$R_n(\omega) = R_n(\omega_a),\ (\omega \le \omega_a); \quad R_n(\omega) = R_n(\omega_b),\ (\omega \ge \omega_b) \tag{5}$$

where $\omega_a \le \omega_b$ is the frequency range of the available reflectance data. By subtracting $\ln R_n(\omega)/(\omega'^2 - \omega^2)$ from integrand of Eq(3), which is allowed since $\int_0^\infty 1/(\omega'^2 - \omega^2) = 0$,

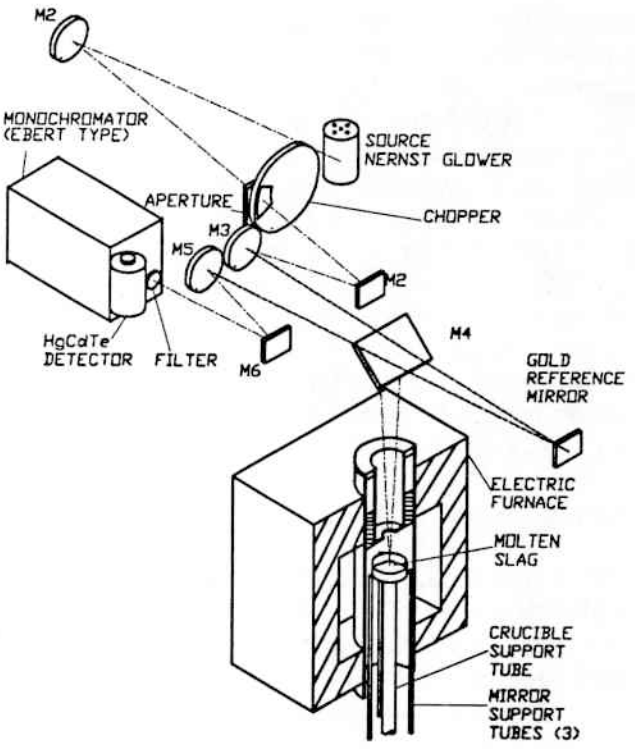


Figure 3. Schematic of the Optical System for Measuring Transmittance and Reflectance of Molten Slag.

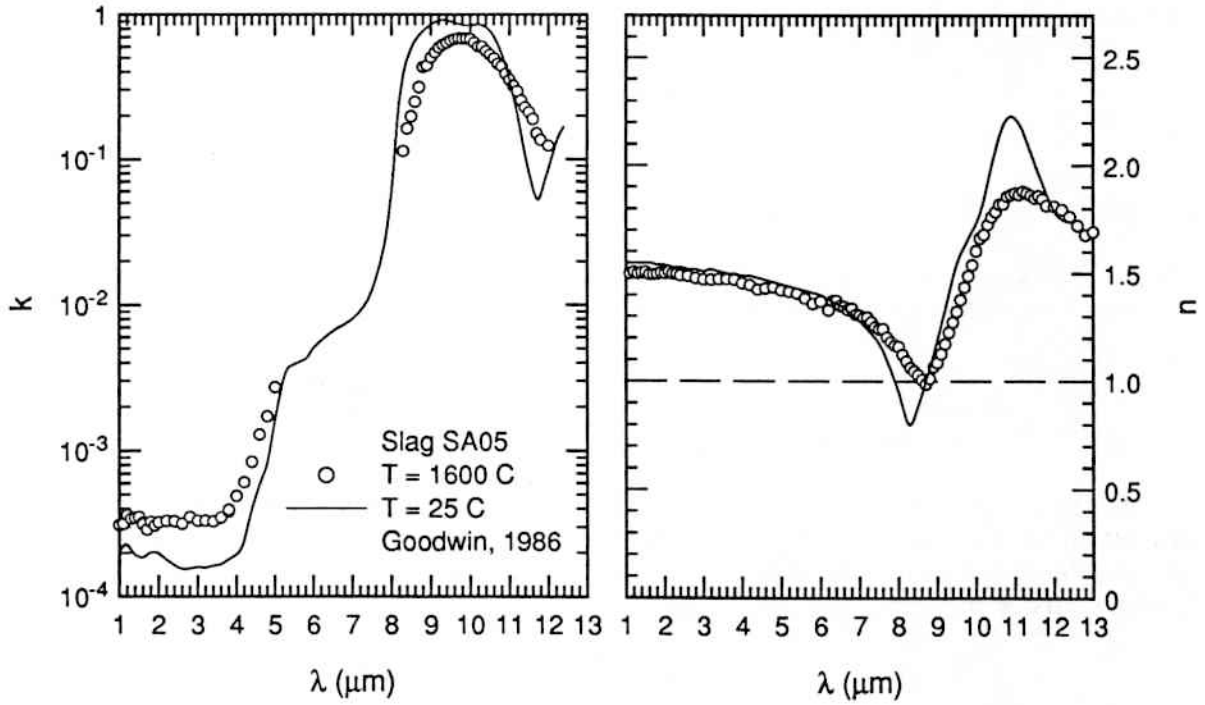


Figure 4. The Complex Refractive Index of Molten Slag SA05 Compared to Room Temperature Data for the Same Slag.

the integrand becomes finite and can be computed easily. This procedure is only viable for $k \geq 0.1$ or so, since below that value the influence of k on the reflectance is too small.

Other changes to the apparatus were required before accurate reflectance measurements could be made. Since the optical path from mirror M4 to the reference mirror is cold and the path from M4 to the slag surface is hot, the infrared active gases (H_2O and CO_2) cause different transmittances for the two paths. Therefore, a hood was constructed which allowed the entire optical system to be purged with nitrogen.

Results

In both the transmission and reflectance measurements a 50 ml crucible was filled with approximately 30–40 ml of slag SAO5 and heated at 10°C per minute to a steady maximum temperature of 1600°C. The resulting measured values of n and k are shown in Figure 4. All of the values of n were obtained from the reflectance measurements as were the k values for $\lambda \geq 8$ μm. The k values for $\lambda \leq 5$ μm were obtained from transmittance (submerged reflector) measurements. The absorption index could not be determined in the range $5 < \lambda < 8$ μm since k is too large to allow transmission measurements and too small ($k < 0.1$) for Kramers-Kronig analysis.

Also shown in Figure 4 are the room temperature results of Goodwin for a synthetic slag of similar composition. The figure shows that temperature has little effect on n in the wavelength range $1 \leq \lambda \leq 7$ μm. The small decrease in n can be explained by the slight decrease in density as the slag temperature is increased. In the wavelength range beyond 7 μm the O-Si-O stretching vibrational absorption band is evident, but is broadened by the increase in temperature. The peak value of k (near 9.5 μm) is significantly decreased by the increase in temperature. This broadening of the absorption band also shows up as a decrease in the variation of n through the same wavelength range. The wavelength at which n passes through unity is shifted to longer values at the elevated temperature.

The increased temperature increases the absorption index k in the wavelength range 1 – 5 μm for this particular slag. This slag was produced in air so we expect, based on results of Mossbauer spectroscopy from Goodwin, that the ferrous (Fe^{2+}) valence state accounts for approximately 60 to 70 percent of the total iron while the ferric (Fe^{3+}) valence state accounts for the remaining 30 to 40 percent. If a slag with similar composition is produced in a reducing environment, all of the iron can be ferrous iron and the absorption index k will be reduced by increasing temperature for wavelengths less than approximately 2.5 μm. Therefore, one must consider not only the total iron content, but also the valence state of the iron before making conclusions about the influence of temperature on k in this limited wavelength range.

These measurements appear to be the first such comprehensive measurements on liquid slag and were reported in a recent publication (Ebert and Self, 1989).

TASK III. SAMPLE CALCULATIONS OF THE RADIANT PROPERTIES OF FLY ASH DISPERSIONS

This task provides computational capabilities to support the other tasks. It includes the following components.

(i) A Mie scattering code to calculate the absorption and scattering efficiencies and phase function of a single sphere of specified size parameter and complex refractive index. A modified Mie code allows such computations for hollow spheres.

(ii) A code to convolve the results from (i) over a specified size distribution and loading to compute the absorption and scattering coefficients and phase function of a homogeneous polydispersion.

(iii) A code to sum the results of (ii) for a number of classes of particles of varying refractive indices and size distributions, i.e. for a heterogeneous polydispersion.

(iv) A radiation transfer code to calculate the absorption, scattering and emission characteristics of a homogeneous, isothermal slab of dispersed ash on a spectral basis.

(v) A code to integrate the spectral results from (iv) over wavelength to yield the total radiative properties of the slab.

Calculations using these codes are being used to provide sensitivity analyses to guide the characterization work of Task I and to design and evaluate the results of Task IV. Illustrative results from these codes were reported in an earlier publication (Ebert and self, 1988).

TASK IV. MEASUREMENT OF THE RADIANT PROPERTIES OF FLY ASH DISPERSIONS

The purpose of this task is to validate the whole approach adopted in this program. Specifically, this bench-scale experiment is intended to compare the measured optical/radiative properties of a dispersion of well characterized ash with those calculated on the basis of the known size/composition distribution using the correlation formulae relating the composition and complex refractive index resulting from measurements on bulk samples of synthetic slag (Task II).

Considerable thought has been given to the various possible approaches to satisfying the objectives of this task. Several experiments have been done to guide our design of an apparatus for measuring the scattering and absorption properties of dispersions of fly ash. As a result of these experiments, and from extensive prior experience of fly ash in connection with research on electrostatic precipitation, it has been determined that there is no satisfactory way to satisfy the aims of this task using a gaseous dispersion of fly ash because it is not possible to adequately disperse and deagglomerate the ash into a gas stream. Unless the ash is adequately dispersed, as it exists in the radiant boiler of a pulverized coal-fired combustion system, one cannot expect calculations, based on Mie theory for a dispersion of spheres to properly agree with laboratory measurements.

For these reasons, our design efforts for Task IV are based on making measurements on a dispersion of fly ash in liquid, for which our experience shows we can obtain stable, well-deagglomerated dispersions of ash. Because there is no single liquid which is adequately transparent over the wavelength range 1–12 μm, we plan to use a combination of three liquids, CCl_4, CS_2 and bromoform to cover the full range. Windows of BaF_2 will be used to contain the liquid suspension in an absorption/scattering cell. A small flow loop, incorporating the measurement cell, an ultrasonic bath and a peristaltic pump is being assembled for this work which will employ the same infrared optical equipment used for measurements on slag samples under Task II.

Calculations have been made to determine the ash loading required in the liquid suspension to yield extinction values, E, in the range 3–30%. The lower limit is set by the

accuracy of measuring the transmission T = (1–E) by ratioing the transmitted infrared signals with and without particles present in the cell. The upper limit is set by the need to restrict measurements to the single-scatter regime, so as to avoid the complication of allowing for multiple scatter i.e. radiation transfer calculations. Because the extinction varies widely over the full wavelength range, it will probably be necessary to adjust the ash loading in the liquid in different wavelength ranges.

7. FUTURE WORK

Under Task I, the size distributions of the selected ashes have now been adequately determined, using the Coulter instrument for diameters > 1 μm. The techniques developed to size broad distributions using multiple orifices will be the subject of a future publication. Future efforts will concentrate on characterization of the chemical composition distribution, particularly by CCSEM, now that a satisfactory technique for producing well dispersed samples has been established.

Under Task II, we have now resolved all the technical problems associated with making measurements of the optical constants of liquid slags at high temperature and have successfully made the first comprehensive measurements on one synthetic slag containing 5% iron (as Fe_2O_3). It remains to duplicate such measurements on slags of varied compositions, and to correlate the results of the high temperature measurements with the earlier results for low temperatures. The final outcome of this task will be a set of correlation formulae giving the dependence of the optical constants of fly ash components on composition, wavelength and temperature.

The computer codes developed under Task III will be used to predict the radiative properties of well-characterized ash dispersions to be measured in Task IV. They will also be used to make representative calculations of the radiative properties of hot fly ash dispersions for the generic problem of an isothermal slab, and used for sensitivity studies of the contributions to radiation transfer from particles of various size and composition classes.

Now that a promising approach for realizing the objectives of the experiment of Task IV has been identified, apparatus is being assembled and preliminary tests planned to establish the techniques to be employed. Initial measurements will probably focus on measuring a reasonably monodisperse, homogeneous dispersion of spheres (e.g. glass beads) since this will provide a critical test of our ability to relate measurements and calculations under well controlled conditions. Subsequently, measurements on well-characterized fly ash samples will be made.

8. REFERENCES

Aichison, J., and Brown, J. A. C. (1957), *The Log-Normal Distribution*, Cambridge University Press.

Ebert, J. L., and Self, S. A. (1989), The Optical Properties of Molten Slag, 1989 National Heat Transfer Conference, HTD-Vol. 106, Heat Transfer Phenomena in Radiation, Combustion and Fires, 123-126.

Ebert, J. L., and Self, S. A. (1988), Radiation Heat Transfer in a Dispersion of Fly Ash, Proceedings of Engineering Foundation Conference on "Mineral Matter and Ash in Coal," Santa Barbara, Feb. 1988.

Goodwin, D. G., and Mitchner, M. (1986), Measurements of the Near-Infrared Optical Properties of Coal Slags, Chemical Engineering Communications **44**, 241-255. Also: Goodwin, D. G., Infrared Optical Constants of Coal Slags, Topical Report T-255, High Temperature Gasdynamics Laboratory, Stanford University, July 1986.

Session 5B
Diesels

Chairperson: William C. Smith

One of the barrier technical issues for coal-fueled diesel engines is component durability and associated wear due to coal and its products of combustion. In this session, three approaches to address this issue are discussed:

- Wear reduction systems utilizing powder lubrication for piston rings and liners to minimize the deposition, erosion, and wear;
- Wear reduction systems utilizing liquid piston rings to minimize deposition, erosion, and wear; and
- Wear reduction systems utilizing a novel fluidic fuel injection system to minimize the deposition, erosion, and wear.

WEAR REDUCTION SYSTEMS:
POWDER-LUBRICATED PISTON RINGS FOR COAL-FIRED DIESEL ENGINES

1. CONTRACT NUMBER: DE-AC21-88MC25252

CONTRACTOR: Mechanical Technology Incorporated
968 Albany-Shaker Road
Latham, New York 12110

CONTRACTOR PROGRAM MANAGER: Dr. Hooshang Heshmat

PRINCIPAL INVESTIGATORS: Dr. Hooshang Heshmat

METC PROJECT MANAGER: Mr. William Cary Smith

CONTRACT PERIOD OF PERFORMANCE: October 1988 to October 1990

2. SCHEDULE/MILESTONES:

Task		Months after Receipt of Contract																						
No.	Description	1	2	3	4	5	6	7	8	9	10	11	12	13	14	15	16	17	18	19	20	21	22	23	24
1	Particulate-Lubricated Ring Conceptual Design																								
2	Experimental Ring Evaluation																								
3	Particulate-Lubricated Ring Engine System Design																								
4	Reporting and Program Management																								
	Final Report																								

3. OBJECTIVES

The overall objective of this program is to deal with the problem of severe wear occurring on the piston rings and liners of coal-water-slurry (CWS) fueled engines. A secondary concern is the contamination of the crankcase oil by the coal combustion products. The new approach for the resolution of this difficulty consists of replacing the present oil-lubricated system with a powder-lubricated system that would utilize coal ash, either alone or in combination with another powder.

The feasibility of this particular lubrication concept for reducing ring/liner wear is to be demonstrated in a series of experiments utilizing redesigned and properly selected components. Wear performance of suitable ring/liner materials lubricated with a powder that incorporates the abrasive ash particles is to be evaluated in terms of load capacity, friction, and rate of wear. New concepts of quasi-hydrodynamic lubrication and appropriate experimental techniques are employed to arrive at

the best combination of ring design, ring and liner materials, and powder constituents. This new technology relying on the quasi-hydrodynamic formation of a film by a powder lubricant offers a possibility of significantly reducing wear in CWS-fueled engines. In addition, the use of a powder-lubricated system in the upper portion of the cylinder can be made to isolate the particulates from the lower portions of the engine, thus further reducing engine wear.

With these tasks accomplished, semiempirical relationships and experimentally proven design data should become available for the design of a powder-lubricated system for operational piston rings. The final product of this project will be the development of a conceptual design for the installation of powder-lubricated piston rings in a full-scale CWS-fueled diesel engine.

4. BACKGROUND

Diesel technology has achieved good engine performance with CWS fuels. These efforts, however, have not yet resolved the serious wear problem caused by the abrasive nature of the ash content of this fuel. Even with the cleanest coal, the CWS ash content is 10 to 20 times that of a heavy residual fuel oil. The wear on the piston rings and liners is due not only to the ash, but often to the coal particulates as well. With CWS as a fuel, wear is 20 to 150 times that found with conventional engines — all due to the abrasive coal ash. Using higher viscosity oils or harder materials like ceramics will be of little help when such high multiples of wear are involved. In addition, the penetration of the abrasive ash, as blowby and transfer by the piston rings, into the crankcase oil also causes wear in the lower parts of the engine. Continuation of such high rates of wear degrades engine performance and limits the life of the engine.

Due to extreme speed variations in reciprocating motion, piston rings are called upon to operate in all possible regimes of lubrication — boundary, mixed, starved, and full hydrodynamic. This situation is particularly critical at top dead center (TDC) where the velocity is zero and the temperatures and loads are high. Consequently, as shown in Figure 1, wear is highest at that point. The presence of abrasive particles in this situation will drastically accelerate the wear process. To overcome this basic problem, an approach beyond conventional palliatives is needed. A new tribosystem, powder lubrication, will be used to generate a lubricating film persisting at all speeds.

This mode of lubrication is based on the work of previous investigators and on experiments conducted by the author and documented in the references. The basic postulate of this theory is that powder flow exhibits some of the basic features of hydrodynamic lubrication. Such a quasi-hydrodynamic behavior holds only for a certain range of particle size with respect to particular tribomaterials combinations. If one were to plot a generic curve for wear versus particle diameter for a given set of tribomaterials combinations, one would obtain a relationship on the nature of Figure 2. Given the proper size and appropriate surface geometry, the particles exhibit a layer-like shearing reminiscent of genuine fluids. This is deemed responsible for the experimentally observed drop of wear when debris is present between two contacting surfaces.

In practical terms, the above considerations call for a system approach to match the requirements of this quasi-hydrodynamic mode of lubrication with several important subelements: the geometry and material of the piston rings, the surface properties of the liner, the size and mechanical and chemical characteristics of the powder,

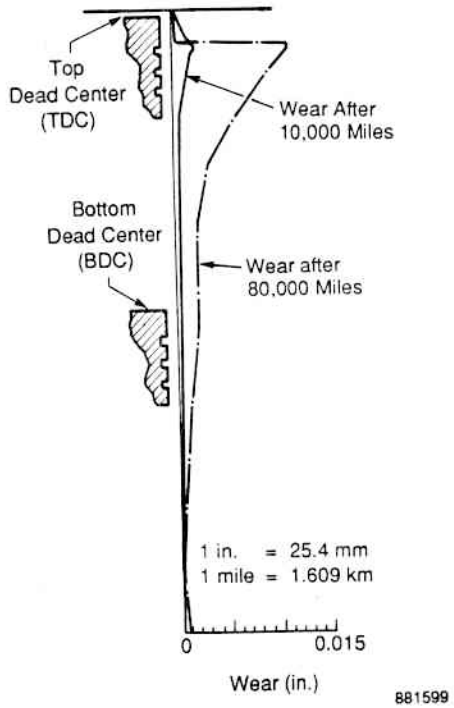


Figure 1. Wear Intensity over an 11-in.Long Cylinder Bore.

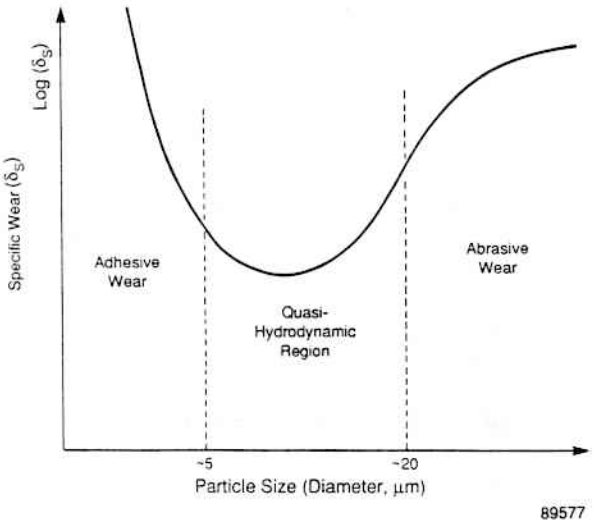


Figure 2. Generic Wear Curve Using Abrasive Powder Materials for a Set of Tribomaterial Combinations.

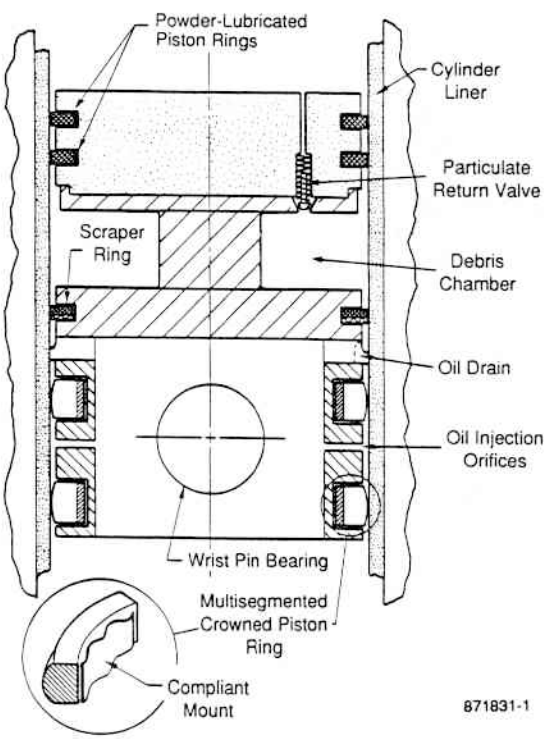


Figure 3. Hybrid Powder-Lubricated Piston Ring with Hydrodynamic, Compliant-Mount Piston Ring.

and the lubricant delivery and scavenging system. These factors are to be evaluated in a series of experiments to establish the specific parameters required for this radically new mode of piston ring lubrication.

5. PROJECT DESCRIPTION

The project, although based on a new concept in lubrication theory, is yet practical and experimental. The program is aimed at ascertaining the feasibility of lubricating piston rings either with coal ash alone or in conjunction with an externally supplied lubricant powder. By absorbing the abrasive ash into the structure of a lubricating film, wear is expected to be significantly reduced. At the same time, improved liner sealing will reduce blowby and contamination of the rest of the engine system. Figure 3 shows the basic concept of such a particulate lubrication system in an engine.

The 24-month effort has been structured to experimentally evaluate the friction and wear characteristics of powder-lubricated piston rings and to lay out the required design parameters for a CWS-fueled engine application. From its inception, the project has been visualized as consisting of three stages:

- Component Analysis. Conceptual design studies have concentrated on ring configuration, taking account of their compliance. Existing MTI analytical capabilities dealing with compliant structures and finite element techniques were utilized in these studies. Five designs were analyzed, and three were selected for testing. Simultaneously, a search went on for the proper materials for the piston rings and liner, as well as for a suitable particulate lubricant. As a start, present-day conventional rings were used, followed by new configurations and new materials.

- Experimental Program. Because the concept of particulate lubrication is new, there is no analytical base for estimating wear performance. Consequently, heavy reliance must be placed on experimentation. In the present context, the tests had two basic goals: first, to test the feasibility of introducing particulate lubrication in the piston rings of diesel engines; and second, to quantify the behavior of the quasi-hydrodynamic film, so as to have empirical correlations for calculating load capacity, friction, rate of wear, etc.

  In order to accomplish the above task, a rig developed by MTI for studying oscillatory friction and wear was modified to serve the needs of the program. Its general construction is shown in Figure 4. The specimens were installed so as to simulate their actual mounting in the engine. The tests were planned to assess the effects of ring geometry, ring loads and surface speed, ring/liner materials and powder lubricants on film formation, friction coefficient, and wear rate. Tests were conducted with oil-lubricated, totally unlubricated, and powder-lubricated surfaces to assess the impact of particulate lubrication. Details of the test program are given in Section 6.

- Application to Actual Engine. Using the optimum ring design determined from the experimental data, an overall powder-lubricated piston ring assembly will be developed. This will consider both the upper and lower parts of the cylinder. The final lubrication system will be designed to control friction and wear in the piston rings exposed to a CWS fuel, properly exhaust the excess ash from the cylinder, and prevent ash and coal particles from reaching the crankcase.

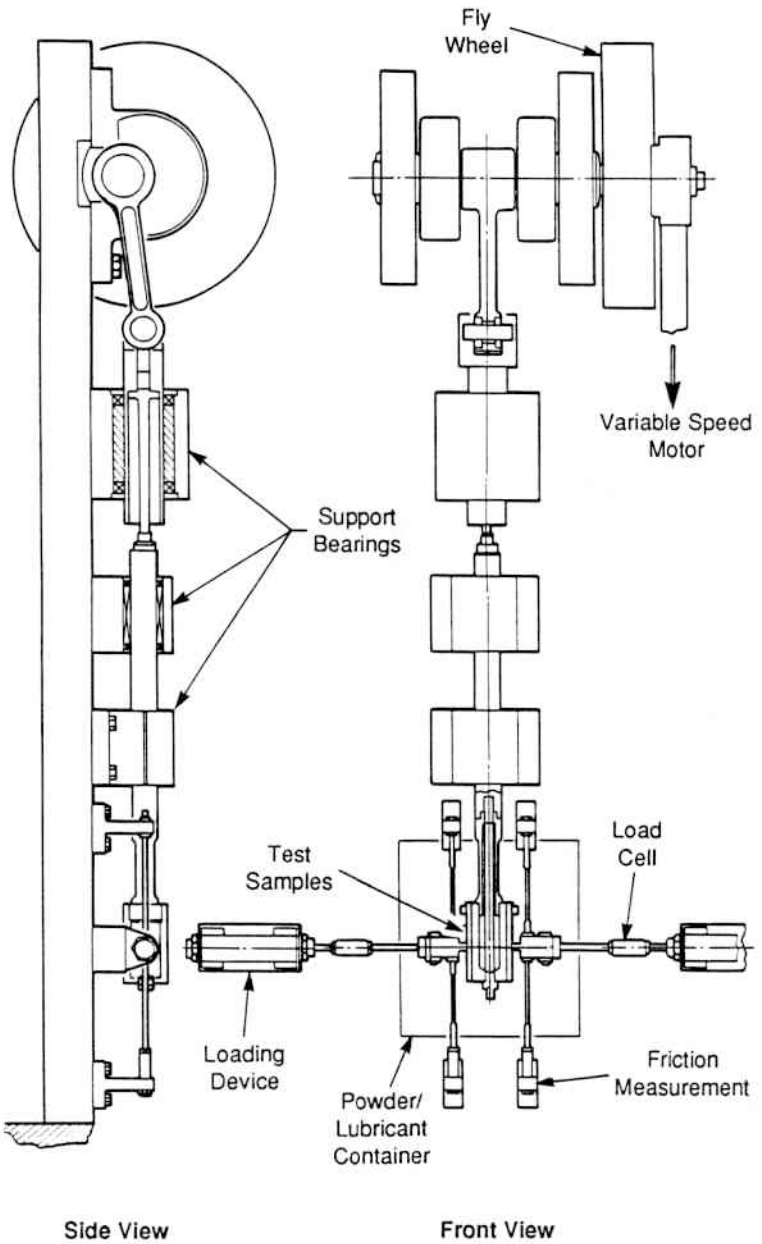


Figure 4. Rig for Evaluating Ring/Liner Interaction with Particulate Lubrication.

6. RESULTS AND ACCOMPLISHMENTS

The work accomplished on this program will be discussed under four headings: the preliminary analysis, selection of ring materials and powder lubricants, the experimental rig setup, and the test results.

NOMENCLATURE

A	Area	$\underline{h}_o$	Minimum film thickness
F_f	Frictional force	$\bar{h}$	(h/h_o)
L	Distance traveled	$\bar{h}_i$	(h_1/h_o)
V	Surface velocity	h_1	Inlet film thickness
W	Applied load	p	Pressure
b	Fraction of tapered portion	u	Velocity
f	Friction coefficient	δ	Wear volume
h	Film thickness	ϕ	(δ/WL)

ANALYSIS

In order to successfully apply particulates to piston ring lubrication, new ring designs must be developed. Two such ring geometries are shown in Figure 5. Based on an analysis using a fifth order rheological model, the formation of a quasi-hydrodynamic film depends critically on the presence of an inlet contour in the ring. Geometries forming a converging wedge are required to promote the inflow of powder into the clearance space. The designs of Figure 5 provide converging wedges in both the upstroke and downstroke directions. The optimum converging angle $\bar{h}_i = h_1/h_o$ is dependent on the usual hydrodynamic quantities as well as on the characteristics of the powder lubricant and mating materials. In addition, a number of constants of the rheological model enter the picture. The parametric study conducted to evaluate performance of the piston ring designs of Figure 5 were done under constant speed and various film ratios $\bar{h}_i$. The study did not, at this stage, vary the physical and chemical properties of the triboparticulates. These, as well as the constants of the rheological model, were taken from experimental data available at MTI from previous research (Heshmat 1989). Thus, in the use of the computer code, the following parameters were kept constant:

Geometry		Rheology	
$\bar{h}_i$	= 3 and 4	$\partial u/\partial y$	$= (1/\eta)\,\tau + \alpha\tau^3 + \gamma\tau^5$
b	= 0.878	α	$= 7.34 \times 10^{-5}$
A	= 1-in.^{2}	γ	$= 9.96 \times 10^{-5}$
U_{av}	= 181 in./sec	η	$= 2 \times 10^{-6}$

In the diverging portions of the rings, the pressure was assumed to be atmospheric.

Sample solutions for $\bar{h}_i = 3$ for both the crown and trapezoidal rings are shown in Figure 6. The effect of varying $\bar{h}_i$ for the trapezoidal ring yielded the following results:

$\bar{h}_i = 4$.....W = 40.8 lb, F_f = 2.53 lb, f = 0.062
$\bar{h}_i = 3$.....W = 40.3 lb, F_f = 2.54 lb, f = 0.062

It appears from these and other runs that the trapezoidal configuration performs 4 to 12% better in terms of load capacity; and 5 to 11% better in terms of the

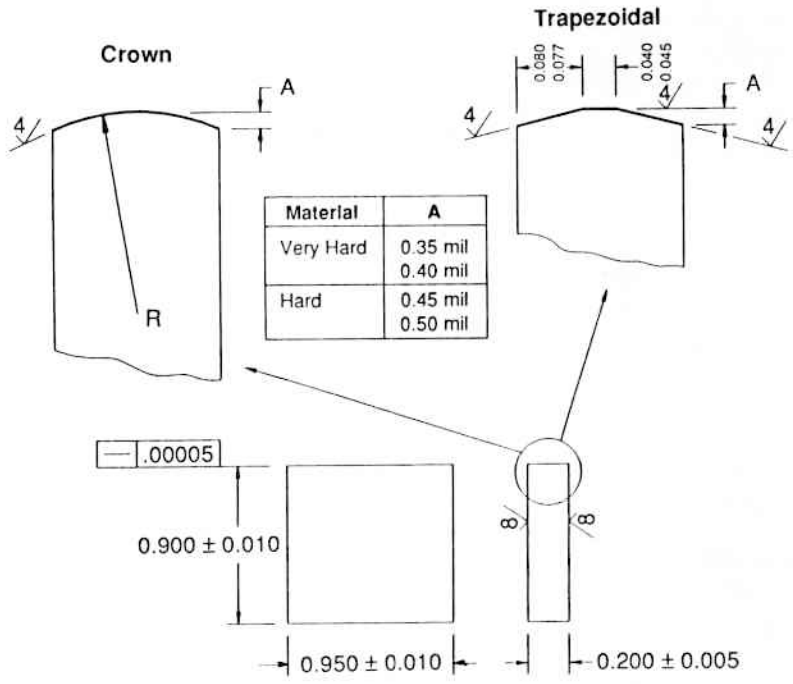


Figure 5. Two Piston Ring Designs for Powder Lubrication.

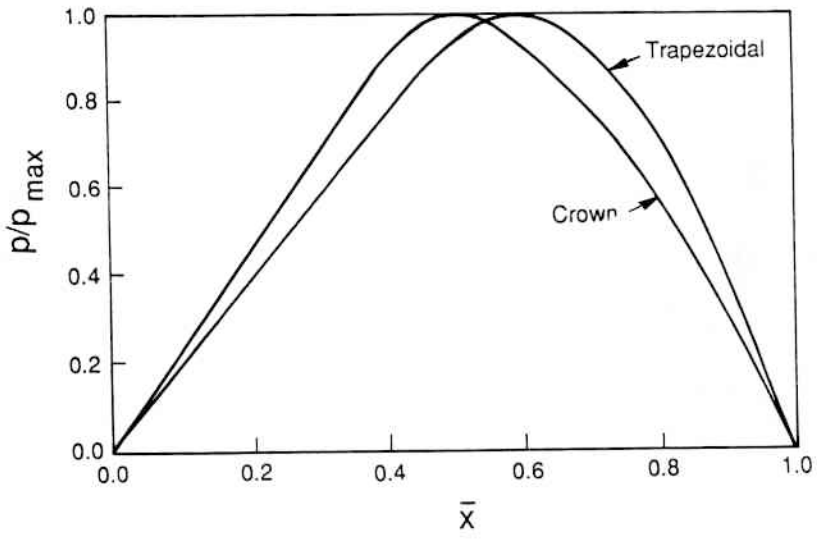


Figure 6. Performance of Rings with $\bar{h}_1 = 3$.

coefficient of friction. As seen above, the variation of film thickness ratio, $\bar{h}_i$, had an insignificant effect on the trapezoidal ring, while a decrease of $\bar{h}_i$ from 4 to 3 in the crown ring caused a drop in load capacity of 8.6%. Thus, while the optimum $\bar{h}_i$ for liquid lubricants is around 2.5, with powders the optimum is quite different.

SELECTION OF RING MATERIALS AND POWDER LUBRICANTS

Materials had to be chosen for three of the basic elements of the system: the ring, liner, and particulate lubricant. For each of these, two alternatives were included. To obtain a comparative evaluation of the new designs and materials, the test matrix commenced with present day practices. Thus, in addition to the two new ring designs given in Figure 5, the conventional flat surface ring was also used. Likewise, one of the ring materials tested was the present day ductile iron ring. Since it was difficult to obtain a sizable quantity of ash from an actual CWS-fueled diesel engine, a substitute from a coal-operated electric power plant had to be used. The fly ash was from a bituminous coal with a 55 Hardgrave index and containing 1.7% sulfur. Its size distribution after refinement, given in Figure 7, corresponds closely to the ash of a CWS-operated diesel engine. Figure 8 gives its appearance, as obtained from the power plant; this was refined by ball rolling before being used in the tests.

The other powder chosen was a carbon graphite, which is a relatively good solid lubricant. This was a 99.9% pure graphite C of -325 mesh, with an average size of 2 μm. The material for the liner was a 134 nitralloy, and as an alternative ring material, tungsten carbide was chosen. The specifications of the materials and the combinations in which they were used are given in Table 1.

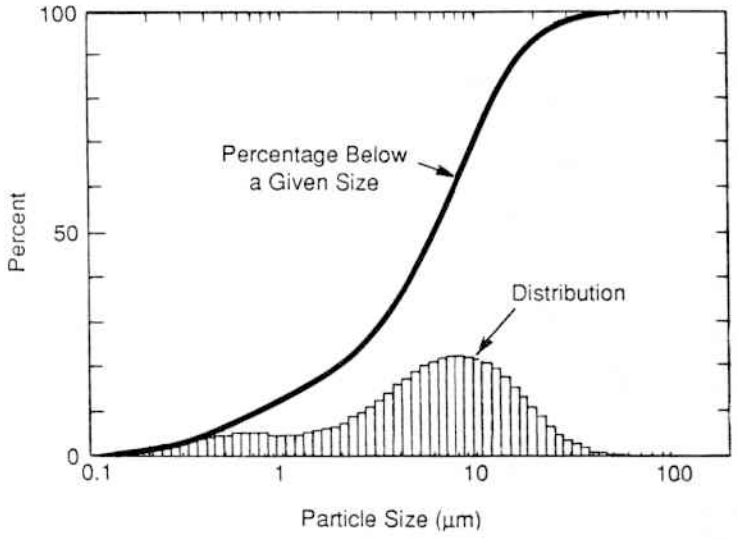


Figure 7. Size Distribution of Fly Ash Used.

Table 1. Materials Combinations Used.

Test No.	Rings	Liner	Powder
1	Type 100-70-03 Ductile Iron	135 Nitralloy	Bituminous Coal Fly Ash 1.7% Sulphur
2, 3			
4, etc.	GE Carboloy 44-A Tungsten Carbide		Graphite C 99.9% Pure Average Size: 2 μm

THE EXPERIMENTAL RIG SETUP

MTI's reciprocating wear tester was converted into a suitable vehicle for the present program. A schematic of the test setup is shown in Figure 9. A vertical block, reciprocating at frequencies to 900 cpm and a half stroke of ±1.5 in., was lined on opposite sides with nitralloy plates against which the two piston rings were positioned. These rings were compliantly mounted in brackets that were capable of recording both the applied normal loads and the frictional forces acting on each ring. The lower end of the reciprocating block was equipped with a perforated stirrer, or paddle, for the purpose of agitating the powder lubricant and making it accessible to the test rings. The entire assembly was enclosed by a transparent chamber made of plexiglass. The test rig and the chamber enclosing the test section are shown in Figures 10 and 11. The ring arrangement and the specimen dimensions are given in Figure 12.

Measurements included the cycle variables: speed; the applied load, W, on each ring; and the frictional force on each ring. Figure 13 shows a sample of these data recorded simultaneously on the oscilloscope printout. Several features of these readings should be noted as follows:

- The values of 30 to 60 lb normal load corresponded to the 150 to 300 psi pressures acting on the ring in actual application.
- Although W as an input was meant to be constant, its value, as shown in the bottom two waves of Figure 13, oscillated around their mean value by as much as ±5 lb. This could amount to 10 to 15% of the main load. The variation was due to the dynamic forces generated by the reciprocating motion of the liner block.
- Since both W and F_T varied during the cycle, the position and value of the maximum coefficient of friction was not always clearly discernible. It was usually taken to be the point where friction was at its maximum, namely at TDC.

The rate of wear after a test duration of Δt was determined in two ways. One was to measure the differences in ring height before and after the test; the other was to weigh the specimen. In some cases, particularly with regard to the liner sample,

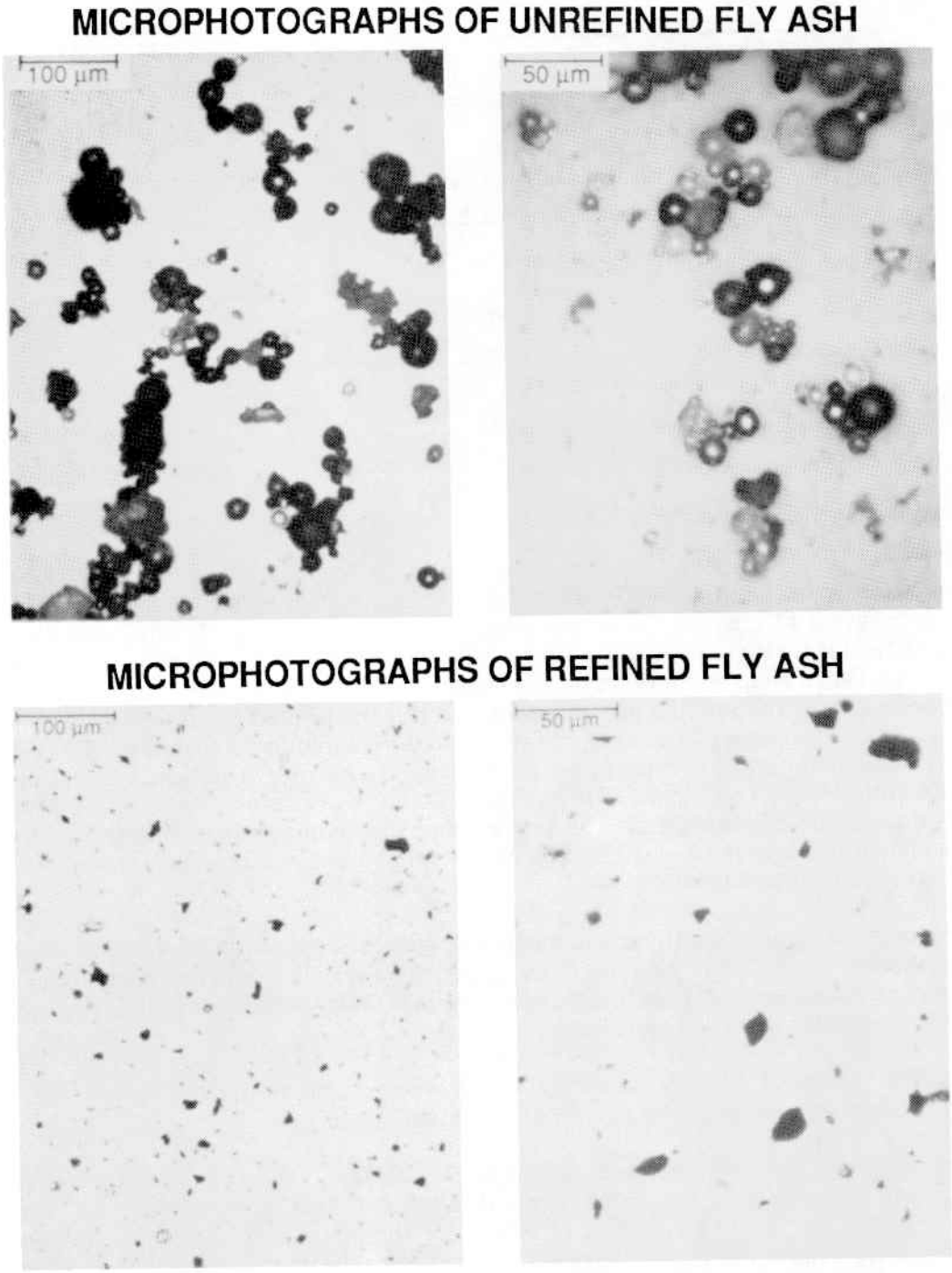


Figure 8. Fly Ash of Coal.

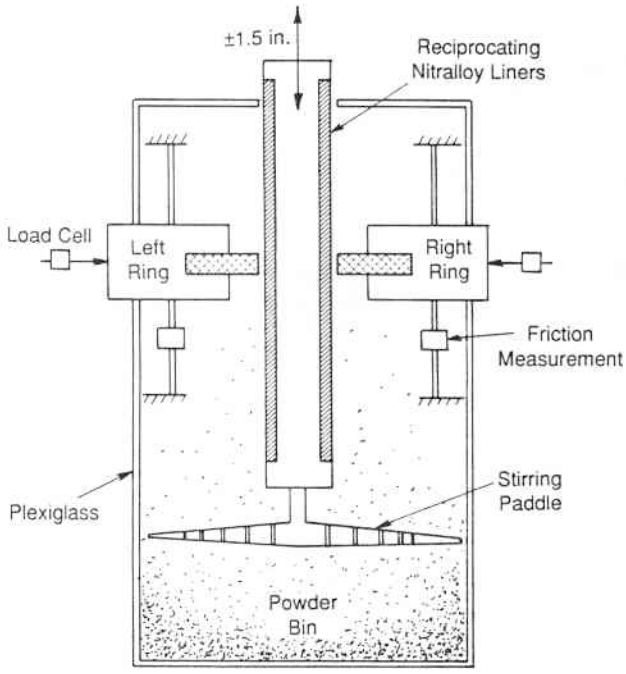


Figure 9. Schematic of Experimental Setup.

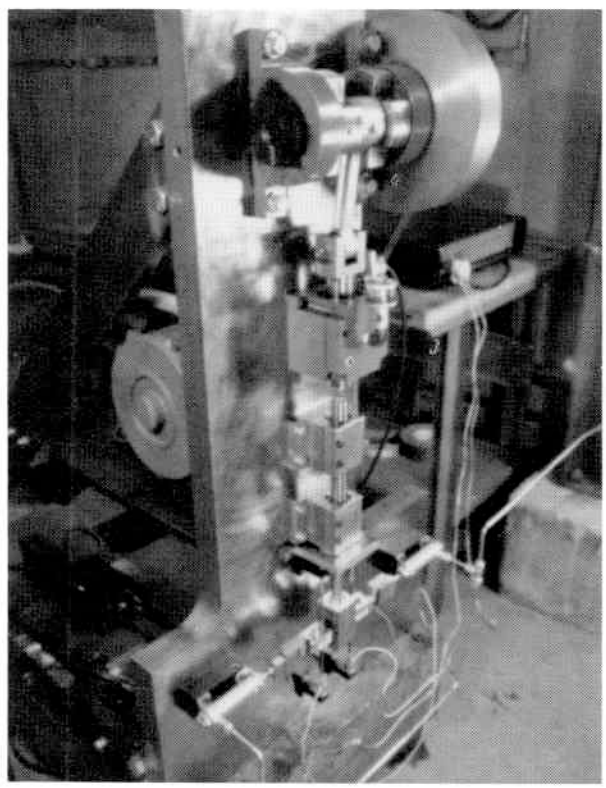


Figure 10. Test Rig.

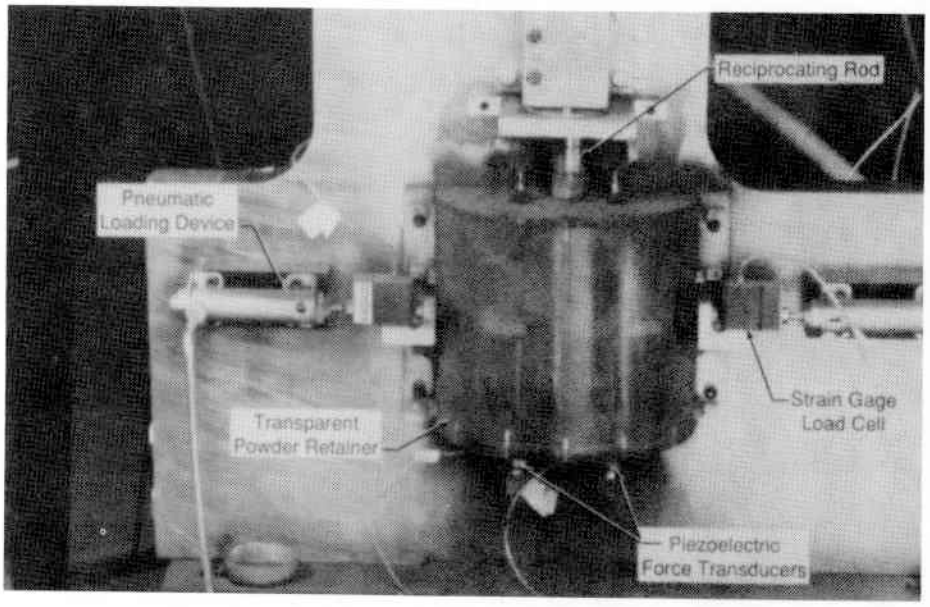


Figure 11. Test Section.

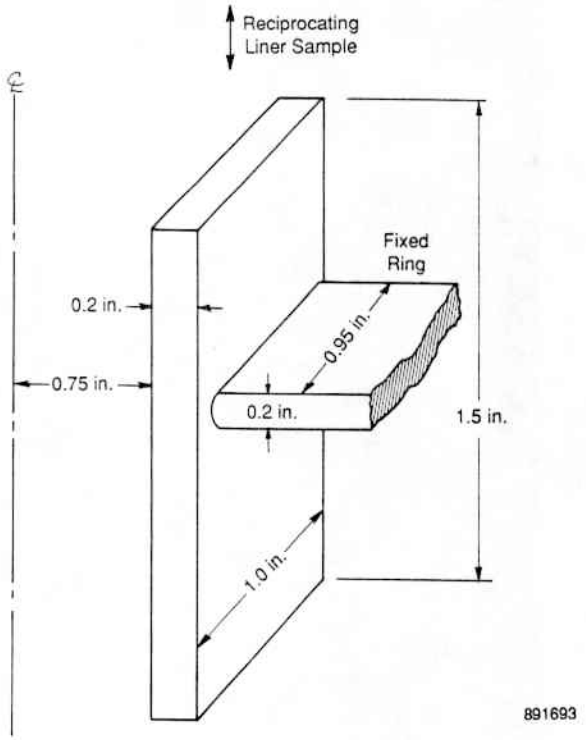


Figure 12. Dimensions of Ring and Liner Sample.

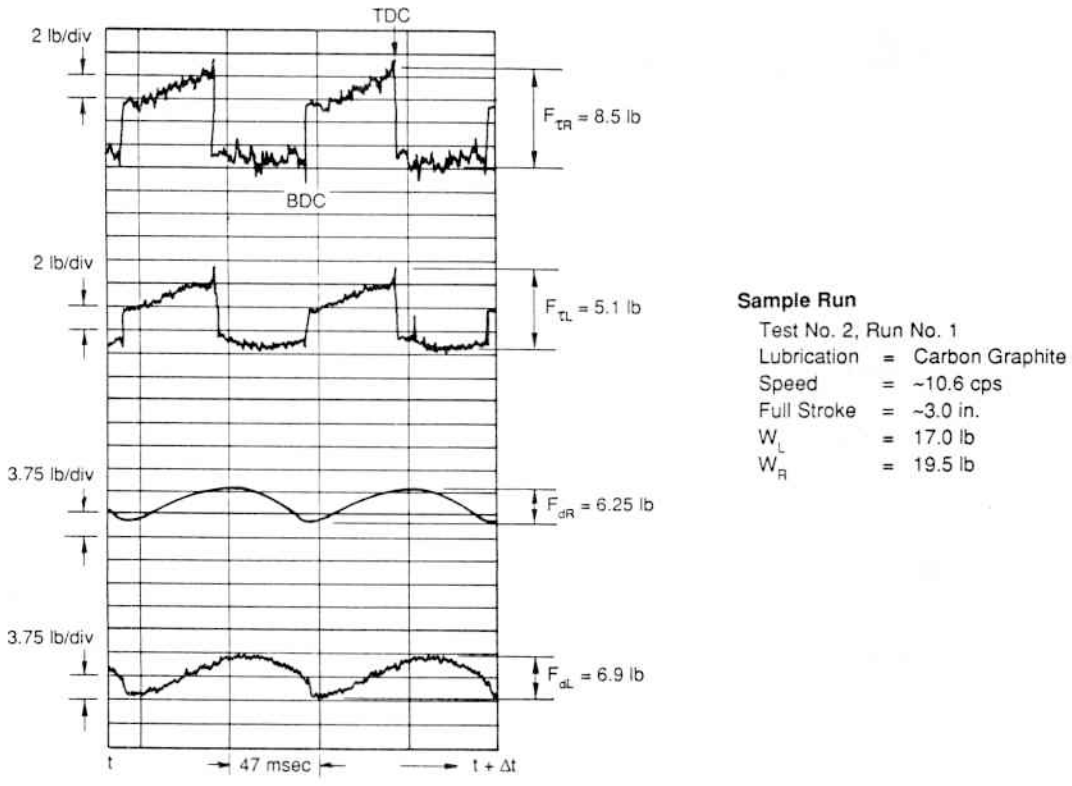


Figure 13. Normal and Tangential Forces on the Rings.

Table 2. Test Matrix for CWS Powder Lubrication.

Ring and Liner / Lubricant	Conventional	New Ring Designs			
	Ductile Iron[1] Ring vs. Nitralloy[2] Liner			Tungsten Carbide[3] for Both	
	Flat	Trapezoidal	Crown	Tapezoidal	Crown
Oil	Completed	--	--	--	--
Grease	Completed	--	--	--	--
Graphite	--	Completed Test No. 2	Completed Test No. 3	Completed Test No. 4	Completed Test No. 5
50% Graphite + 50% Ash	--	Planned	Planned	Planned	Planned
Ash	Completed Test No. 1	Planned	Planned	Planned	Planned

[1]Type 100-70-03

[2]135

[3]GE Carboloy 44-A

there was negative wear; that is, material was deposited on, instead of worn off, the surface.

TEST RESULTS

The scheduled matrix of runs for the project is given in Table 2. Of this the following four series of tests have been completed.

- Preliminary Runs — Conventional (flat) Ring and Oil Lubricant. These tests with oil served essentially to check out the system and the proper functioning of the instrumentation.

- Test No. 1 — Conventional Ring with Ash. These tests were run for a total of 126 min at speeds to 600 cpm and loads to 30 lb.

- Test No. 2 — Trapezoidal Profile with Graphite. These runs lasted for a total of 215 min at linear speeds to 225 ft/min and loads to 60 lb

- Test No. 3 — Crown Ring with Graphite. These tests were plagued by test rig malfunction due to side motions of the reciprocating plate. The problem was rectified, however, and the the tests concluded as planned.

Each of the runs extended over a time interval, Δt_n. During this period, frequency, load, and friction were recorded. At the end of Δt_n, the amount of wear was measured. These data were plotted in the form shown in Figure 14, where the abscissa represents a cumulative energy term given by the sum of all the incremental energy terms $\sum \Delta WL$. The ordinate is made up of points representing the average wear function, ϕ, given by

$$\sum \delta_n / \sum WL = \text{Total Amount of Wear} / \sum_{n=1}^{k} \Delta(WL)_n$$

The results of the individual tests can be summarized as follows:

- Test No. 1. Using the conventional flat ring with ash confirmed previous field reports. At a loading of 30 lb, severe damage occurred on the rings and severe-to-moderate damage was noted on the liner samples. Calculated friction coefficients were equal to 2 and higher.

- Test No. 2. In this series of tests, the trapezoidal piston rings were tested with carbon graphite. The runs covered the whole range of loads from 15 to 60 lb and speeds to 900 cpm. Run 1 lasted 47 min with no wear. After two more runs, one lasting 107 min and the other 61 min, piston ring wear of the order of 1 mg was measured. There was practically no change in the liner surface. During these tests, the piston ring maximum contact pressure was calculated to be some 7000 psi and maximum surface speed to be 225 ft/min. The maximum dynamic friction coefficient was measured to be 0.12 at TDC. Overall test results with the powder lubricant were excellent. A plot of the amount of wear as a function of time or energy input is given in Figure 15.

  In the same series of tests, a set of two rings (trapezoidal) was simultaneously tested: one in an unlubricated condition and the other with a carbon graphite powder. This was achieved by incorporating thin foils as scrapers on either side

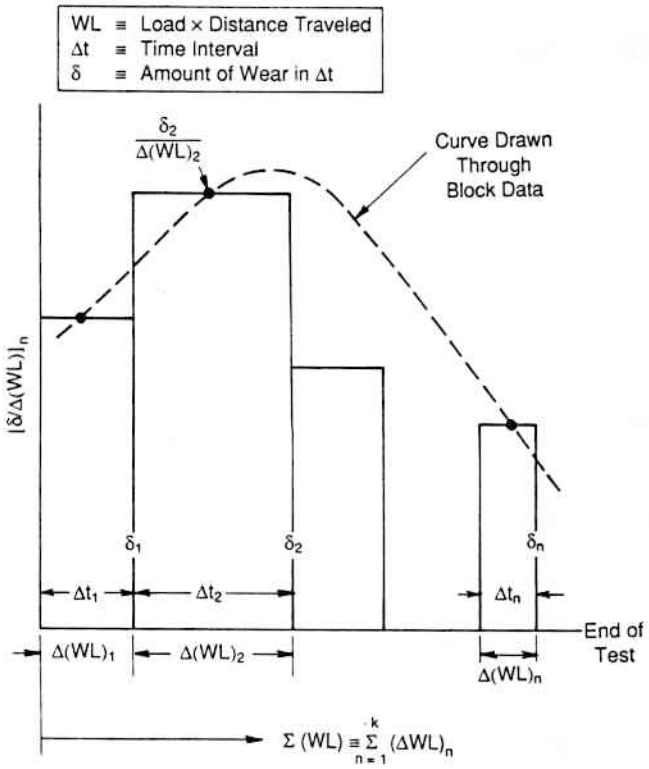


Figure 14. Method of Compilation of Wear Data.

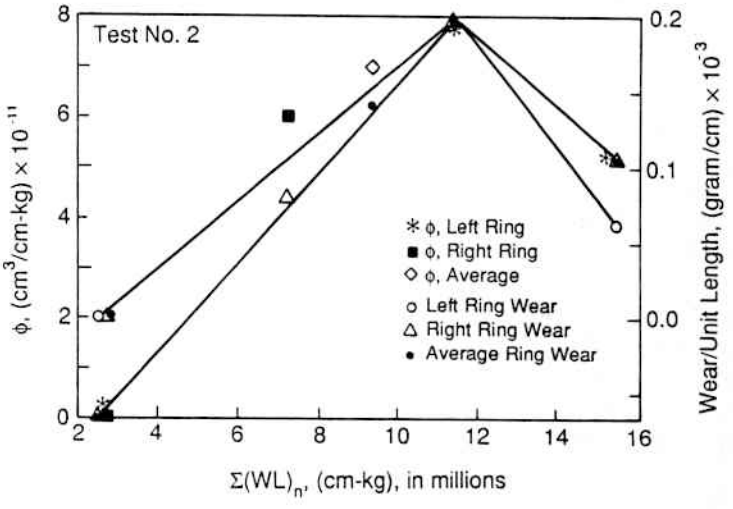


Figure 15. Combined Average Wear for Ring-Liner Assembly.

of the piston ring specimen. The scrapers prevented the entrance of lubricant into the contact zone, as shown in Figure 16. The test duration was 107 min, under loads to 60 lb and speeds of 300 and 600 cpm. The dry piston ring showed a weight loss of 1.544 g (0.08-in.-thick material was worn off), and the liner sample showed a weight gain of about 0.0103 g. The wear tracks and wear marks appeared to be adhesive type wear.

The lubricated piston ring/liner specimens tested along with the aforementioned dry ring showed no sign of wear. After test, a small amount of weight gain could be measured: for the ring, the gain was 0.6 mg, and for the liner sample 7.7 mg. This is related to carbon graphite film formation.

- Test No. 3. This series of tests used the crown ring profile with graphite as a lubricant. The duration of run 1 was 49.5 min with a maximum load to 45 lb. No wear had occurred in any of the test samples. The piston ring samples showed 0.2-mil-thick graphite-type film buildup.

  Run 2 was terminated after 25 min due to the test loads showing substantial deviations of ±5 lb from the nominal load. The results showed an uneven and misaligned wear pattern on the right test ring with a weight loss of 251 mg; the left ring showed a slight surface wear of about 1.4 mg. The cause of the uneven load distribution was found to be in the reciprocating block assembly, which had become loose, causing the right piston ring to become misaligned and overloaded.

  The rings were replaced and run 3 was run for 49.5 min. During this run, a high-pitched noise often developed when the load was raised over 30 lb. Visual examination revealed abrasive wear marks on the right piston ring with a wear depth of 0.65 mil. No wear could be detected on the left ring.

  In order to check the responsibility of the test ring dynamics for wear results, the right and left rings were interchanged. The test was run for 167 min with speeds to 606 cpm and loads to 45 lb. During this run, too, whenever the load exceeded 40 lb, a high-pitched noise developed. Generally, however, the friction coefficient stayed below 0.2, mostly around a low 0.08. After the tests, the left ring showed a wear depth of 4 mil — a weight loss of 101.5 mg — indicative of a severe misaligned condition along the entire ring width.

  The total accumulated test time with the crown ring was 266 min with a maximum load of 45 lb. Aside from the rig malfunction, overall test results with the crown ring were satisfactory.

The results of all three test series are summarized in Table 3 and Figure 17. The table gives detailed data for the various combinations of ring design and powders in terms of friction and wear data for each individual ring tested. It is clear from the foregoing discussions that powder lubrication has proven itself to be a viable scheme and that the trapezoidal design seems to hold an advantage over the other designs.

7. FUTURE PLANS

Two parts of the project remain to be completed. One is to run the tests mapped out in Table 2. This essentially entails the testing of the various rings with a mixture of ash-graphite as the lubricant, and if successful, with the ash alone. The other part pertains to the development of a powder-lubricated ring concept to be

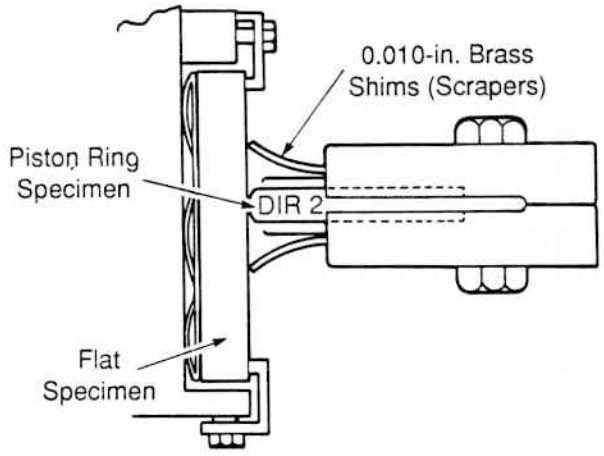


Figure 16. Schematic Showing Piston Ring Assembly with Scrapers for Conducting Unlubricated Dry Test.

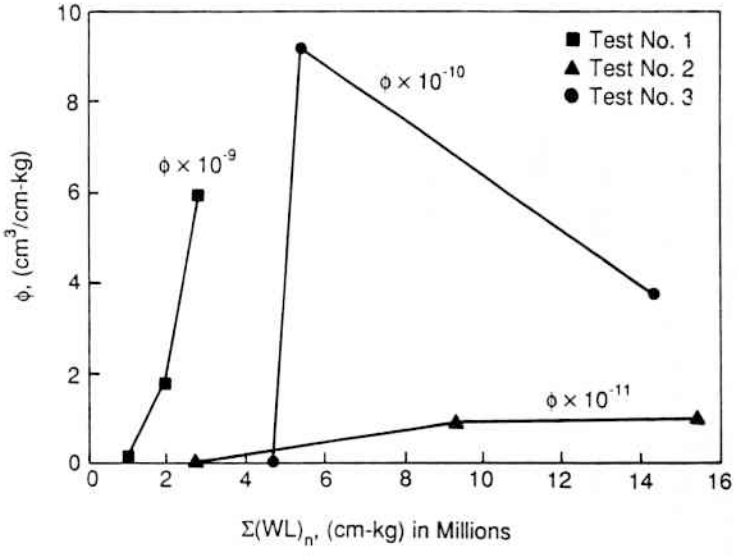


Figure 17. Combined Average Wear for Ring-Liner Assembly.

Table 3. Summary of Test Results.

ϕ, cm^3/kg-cm ($\times 10^{-9}$)				Energy, cm-kg ($\times 10^{+5}$)				$\left(\frac{\text{Weight Change}}{\text{Unit Length, g/cm}}\right)(\times 10^{-3})$				ϕ, cm^3/kg-cm ($\times 10^{-12}$)				
Rings		Liners		$\Delta (W \cdot L)$		$\Sigma (\Delta W)$		Rings		Liners		Both Rings	Both Liners	Ring and Liner		Total Rings and Liners
Left	Right	Left	Right	Left	Right	Left	Right	Left	Right	Left	Right			Left	Right	
Test No. 1																
1.90	61.40	0.90	0.41	9.4	11.3	9.4	11.3	0.53	20.00	0.27	0.15	31,660	651	1397	30,910	16,150
1.50	1.40	2.50	1.78	8.4	9.7	17.8	21.0	0.37	0.39	0.68	0.56	1,430	2147	2016	1,561	1,789
0.20	22.50	0.85	0.25	8.0	9.1	25.8	30.2	0.04	6.00	0.22	0.08	11,310	549	502	11,360	5,930
Test No. 2																
0.00	0.00	0.00	00.0	25.0	27.0	25.0	27.3	0	0	0	0	0.1	0.1	0.1	0.1	0.1
0.08	0.06	-0.11	0.01	88.5	44.6	113.6	72.0	0.20	0.08	-0.32	0.01	70	-51	-16	34	9
0.05	--	-0.03	--	40.9	0.0	154.4	--	0.06	--	-0.04	--	--	--	10	--	--
Test No. 3																
0.05	-0.04	-0.01	0.00	44.6	48.3	44.6	48.3	0.06	-0.06	-0.02	0.00	2	-7	17	-22	-3
-0.13	3.18	0.08	0.53	6.5	7.7	51.1	55.9	-0.03	0.72	0.02	0.14	1,523	306	-26	1,854	914

Note:
+ = Loss
- = Gain

integrated into a CWS-operated diesel engine. This system will be designed to control friction and wear in the upper portion of the cylinder, properly exhaust excess ash, and prevent particulates from infiltrating the lower portions of the engine.

8. REFERENCES:

Anson, D. et al. Development Plan for a Coal-Water-Slurry-Fired Diesel Engine for Cogeneration Applications. U.S. DOE Report No. DOE/CE/40741-T1 (DE87012003), July 1987.

Baskey, R. H. An Investigation of Seal Materials for High-Temperature Applications. ASLE Trans. 3 (1960): 116-23.

Battelle Memorial Institute. A Study of Refractory Materials for Seal and Bearing Applications in Aircraft Accessory Units and Motors. WADC-TR-58-299 (ASTIA 203787), 1958.

Berthier, Y., M. Brendle, and M. Godet. Boundry Conditions: Adhesions in Friction. Leeds-Lyon Symposium, Interface Dynamics (1987): 19-25.

Berthier, Y., M. Godet, and M. Brendle. Velocity Accommodation in Friction. STLE Paper 88-TC-3A-2.

Campbell, C., and C. E. Brennan. Computer Simulation of Granular Shear Flows. J. Fluid Mech. 151 (1985): 167-88.

Cowin, S. C. A Theory for the Flow of Granular Materials. Powder Techn. 9 (1974): 61-9.

Elrod, H. G. Granular Flow as a Tribological Mechanism. Paper IV(i), Tribology Series 12; Interface Dynamics, Proceedings of the 14th Leeds-Lyon Symposium of Tribology (1987).

Godet, M., and Y. Berthier. Continuity and Dry Friction: Osborne Reynolds Approach. 13th Leeds-Lyon Tribology Symposium, September 1986.

Gray, S. Friction and Wear of Ceramic Pairs Under High Temperature Conditions Representative of Advanced Engine Components. Ceramic Engineering and Science Proceedings 6, no. 7-8 (1985): 965-75.

Heshmat, H. Quasi-Hydrodynamic Lubrications with Dry Triboparticulate Matter Experiment and Theory. Mechanical Technology Incorporated Technical Report No. 89TR29, 1989.

Heshmat, H. The Effect of Dynamic Loads in Tribometers - Analysis and Experiments. Symposium Proceedings, 16th Leeds-Lyon Symposium on Tribology 14 (1989).

Heshmat, H. Application of Powder Lubrication Technology to the Critical Components of Coal-Fueled Diesel Engines at High Temperatures. Prepared for DOE, METC, Morgantown, West Virginia, March 1988.

Heshmat, H. Powder-Lubricated Piston Ring Development Program. Prepared for U.S. Army Aviation Systems Command, Propulsion Directorate, Lewis Research Center, June 1987.

Heshmat, H. Centrifugal Separation of Particulate Matter in Cyclocentrifuge. Mechanical Technology Incorporated, Internal Technical Report 80TR17, 1980.

Heshmat, H., and O. Pinkus. The Interaction of a Gas with Solid and Liquid Particles. MTI Paper P266, Presented at EPRI/EPA Symposium, Transfer and Utilization of Particles Control Technology, February 1986.

Heshmat, H., O. Pinkus, and M. Godet. On a Common Tribological Mechanism Between Interacting Surfaces. STLE Preprint No. 88-AM-5E-2, Presented at the 43rd Annual Meeting, Cleveland, 1988.

Hsu, Bertrand D. Progress on the Investigation of Coal-Water Slurry Fuel Combustion in a Medium-Speed Diesel Engine; Part II: Preliminiary Full Load Test. Presented at Energy-Sources Technology Conference and Exhibition, January 1988.

Likos, William E., and Thomas W. Ryan III. Experiments with Coal Fuels in a High-Temperature Diesel Engine. Presented at Energy-Sources Technology Conference and Exhibition, January 1988.

Mechanical Technology Incorporated. Solid Lubrication Roller Bearing Development. Work being conducted under Air Force Contract No. F33615-87-R-2707; J. Walton, Program Manager; H. Heshmat, Principal Investigator.

Nikolakakis, I., and N. Pilpel. Effects of Particle Shape and Size on the Tensile Strengths of Powder. Journal of Powder Technology 56, no. 2 (1988): 95-103.

Oike, M., N. Emori, and T. Sasada. Mild-Severe Wear Transition in Metal Rubbing with SiC Abrasive Grains Interposed between Mating Surfaces. Journal of JSLE, International Edition, Tokyo.

Oike, M., N. Emori, and T. Sasada. Effect of Fine Ceramic Particles Interposed Between Sliding Surfaces on Wear of Metals. JSLE Int. Trib. Conf., 1985.

Rao, A. K. et al. Operating Results of the Cooper-Bessemer JS-1 Engine on Coal Water Slurry. Presented at Energy-Sources Technology Conference and Exhibition, January 1988.

Timoney, S., and G. Flynn. A Low-Friction, Unlubricated SiC Diesel Engine. The Adiabatic Engine: Past, Present & Future Developments.

Wallerstein, S. Application of a Powder Lubrication System to a Gas Turbine Engine - Part II. AFAPL-TR-65-43, Part II.

Wallerstein, S. Application of a Powder Lubrication System to a Gas Turbine Engine - Part III. AFAPL-TR-65-43, Part III, December 1966.

WEAR REDUCTION SYSTEM - LIQUID PISTON RING

1. CONTRACT NUMBER: DE-AC21-88MC25035

CONTRACTOR: Tecogen Inc.
P.O. Box 9046
45 First Avenue
Waltham, MA 02254-9046
(617) 622-1400

CONTRACTOR PROJECT MANAGER: Robert J. Raymond

PRINCIPAL INVESTIGATORS: Robert J. Raymond
Tze-Ning Chen
Luco DiNanno

METC PROJECT MANAGER: Nelson F. Rekos, Jr.

PERIOD OF PERFORMANCE: September 27, 1988 to September 26, 1990

2. SCHEDULE/MILESTONES:

Task	FY '89 O N D J F M A M J J A S O N D	FY '90 Q2 Q3 Q4
1. Analytical Modeling	———————————	
2. Cylinder Scrubbing Simulation Rig		
2.1 Design and Build	———	
2.2 Test	————	
3. Single Cylinder Liquid Piston Ring Rig		
3.1 Design and Build	—————	
3.2 Test	————	
4. Reports	———————————	

3. OBJECTIVES:

The primary objective of this project is to gain a fundamental understanding of the physics of the "liquid piston ring" concept and to establish its technical feasibility for solving the problem of cylinder liner and piston ring wear in coal-fueled reciprocating engines. This concept involves maintaining a "liquid piston ring" above the top metallic piston ring to prevent ash from coming into contact with piston rings and cylinder liners which are in relative motion, thereby allowing the use of conventional materials.

To establish the technical feasibility of this concept, the following technical issues are to be investigated.

- Particle scrubbing from the cylinder surface.
- Leakage of liquid into the combustion chamber.
- Leakage of liquid past the piston ring.
- Heat transfer and evaporation of the liquid.
- Circulation and cleaning of the liquid.
- Lubrication of the piston ring.

4. BACKGROUND STATEMENT:

The problem of high component wear in reciprocating coal-fueled engines has been identified as one of the main obstacles in the development of diesel engines operating on coal/water slurry. Early work carried out in Germany and reported by Soehngen (Soehngen 1976), Thermo Electron/Sulzer Bros. tests on a low speed diesel engine (Nydick 1987), and the wear studies carried out on a locomotive diesel engine by General Electric Co. (Flynn and Hsu 1988) all confirmed the high wear rate of the piston ring and cylinder liner with coal fuel when conventional materials were used. Coal ash particles were also found in the engine sump, which can cause wear of the bearings and cams.

There are two approaches to dealing with the ash present in the engine cylinder after combustion. In the first approach, the engine is constructed with component materials that operate with ash present at rubbing surfaces and retain acceptable wear rates. Some encouraging results have been reported based on a short-duration test of coated piston rings and liners (Flynn, Leonard, and Mehan 1989). The second approach is to prevent the ash from coming into contact with surfaces that are in relative motion, thereby allowing the use of conventional materials. The "liquid piston ring" concept is based on the latter approach.

Figure 1 illustrates the liquid piston ring concept that is the subject of this study. A liquid ring is located above the top

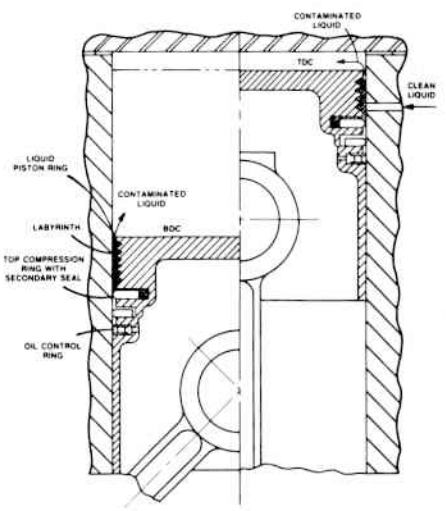


Figure 1. Liquid Piston Ring Concept Schematic (Once-Through System).

metallic piston ring which would scrub ash particles from the path of the moving piston rings and piston skirt through relative motion of the labyrinth containing the liquid ring and cylinder liner. The clean liquid (possibly water or a water/oil emulsion) is supplied to a labyrinth seal area formed in the top of the piston. The clean liquid could be supplied above the top metal compression ring through the liner or the piston, and the contaminated liquid could be removed through the stationary liner or the moving piston. The liquid is circulated through a particle removal system and reinjected into the liquid ring. In the case where a small amount of liquid through-flow is required, the contaminated liquid in the ring can discharge directly into the cylinder where the ash and liquid would then be discharged with the rest of the exhaust products. Another major advantage of this concept is that the liquid ring also prevents wear inducing particles from reaching the engine sump and causing wear of bearings and cams.

This project addresses the various technical issues just listed in order to establish the technical feasibility of the liquid piston ring concept.

5. PROJECT DESCRIPTION:

The two-year research program includes analysis of the system and proof-of-concept bench tests to determine the technical feasibility of the concept of the "liquid piston ring" in achieving an acceptable wear rate for the cylinder liner and piston ring in a coal/water-slurry-fueled engine. A decision will be made based on the result of this study as to whether or not the concept is worthy of a single-cylinder-firing engine test.

5.1 ANALYSIS

The two major technical issues to be addressed in the concept analysis are the following:

- Dynamic behavior of the liquid ring, which determines the leakage of the liquid into the cylinder and the effect of the labyrinth geometry on that leakage.

- Heat transfer from the cylinder liner and the piston to the liquid ring, which affects the evaporation and loss of liquid in the ring.

An analytical model has been developed to describe the dynamics of the liquid ring in order to examine the effects of the inertia force, viscous drag on the liquid by the cylinder wall, and pressure drop due to flow across the labyrinth. The analysis will provide criteria on the liquid ring design for minimal leakage of the liquid into the combustion space and on the maximum allowable temperature of the liquid to avoid flashing.

A simplified analysis of the heat transfer to the liquid piston ring through the piston and the cylinder liner will determine whether or not the liquid ring can be maintained without boiling.

5.2 BENCH SCRUBBING SIMULATION TEST

A bench simulation model was designed and built to study the fluid motion in the liquid ring annulus as the piston moves up and down. Since the effectiveness of scrubbing the particles off the wall is related to the fluid velocity and shear rate adjacent to the wall surface, it is the object of this study to develop the optimum labyrinth geometry for maximum shear rate and turbulence.

Figure 2 shows the test section of the bench simulator, which consists of a piston inside a transparent cylinder. The labyrinth in the piston is scaled up in size for ease of visual observation, and the piston speed is adjusted to duplicate the Reynolds number in a real engine. A bench study will also be carried out on the adhesion of particles on oil covered surfaces and the effect of adding surface active agents on particle removal.

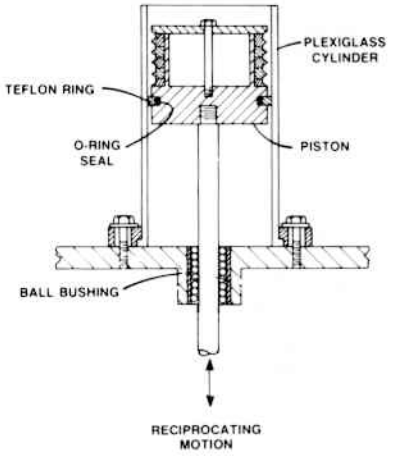


Figure 2. Cylinder Scrubbing Simulator.

5.3 SINGLE-CYLINDER LIQUID PISTON RING TEST

A single-cylinder liquid piston ring test rig will be designed and built up from a commercially available single-cylinder engine which will provide the basic reciprocating mechanism. The engine will be motored by a variable-speed motor drive system. The test rig will be designed with sufficient flexibility to allow testing both the recirculating and once-through version of this concept and to investigate all of the important design variables as determined in the analysis.

The rig will be used to verify the effectiveness of the labyrinth configuration selected from the bench simulator study. Particles will be fed to the cylinder wall, and liquid fluid will be continuously supplied and removed from the annulus ring while the piston is reciprocated at the simulated speed. The cylinder liner and piston rings will be examined periodically to determine the effectiveness of the design. Wear on the piston rings will be compared for the different cases; namely, conventional design with and without particle contamination, and liquid piston ring design with particle contamination.

In addition to the particle scrubbing and wear of the rings and liner, the leakage of the liquid into the cylinder space and the piston ring design to seal effectively against the leakage of contaminated liquid into the crankcase will also be investigated.

Although this model does not provide the temperature conditions of a real engine, it provides the information required to establish the feasibility of the liquid piston ring concept with respect to the reduction of wear of the piston rings and cylinder liner for a coal-fired diesel engine.

6. RESULTS/ACCOMPLISHMENTS:

During this period of performance, the major effort has been directed at the development of an analytical model to describe the dynamics of the liquid ring and the design and building of the bench simulator for testing different labyrinth geometries for maximum scrubbing action.

6.1 DYNAMICS OF LIQUID RING

An analytical model to describe the dynamic behavior of the fluid ring has been developed. The model includes the inertial force generated from the reciprocating motion as the liquid ring moves up and down with the piston, the viscous drag on the liquid due to its motion relative to the cylinder wall, and the pressure drop resulting from flow across the labyrinth. Although simplifying assumptions are made regarding the flow pattern and the viscous drag, the model will help to identify the important design parameters for the liquid ring.

For a simple annular ring model, as shown in Figure 3, the static pressure in the liquid at a depth l from the top free surface can be expressed as a function of the liquid ring configuration and the instantaneous engine operating parameters:

$$p - p_o = \frac{\mu C_v l V}{g h^2} + \frac{n l k}{(\pi D C h)^2} \frac{\dot{m}^2}{2 g \rho} + \frac{\rho l}{g} (a + g) \qquad (1)$$

where:

n	=	number of labyrinth per inch
l	=	depth of liquid ring from top free surface
h	=	liquid ring thickness
V	=	piston velocity
a	=	piston acceleration
D	=	piston diameter
$\dot{m}$	=	mass through flow rate
ρ	=	liquid density
μ	=	viscosity of liquid
C_v, C, k	=	correction constants for assumed velocity profiles

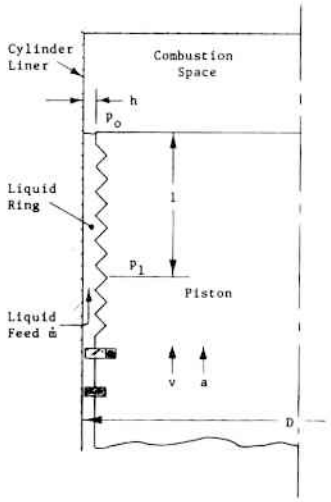


Figure 3. Model of Liquid Piston Ring.

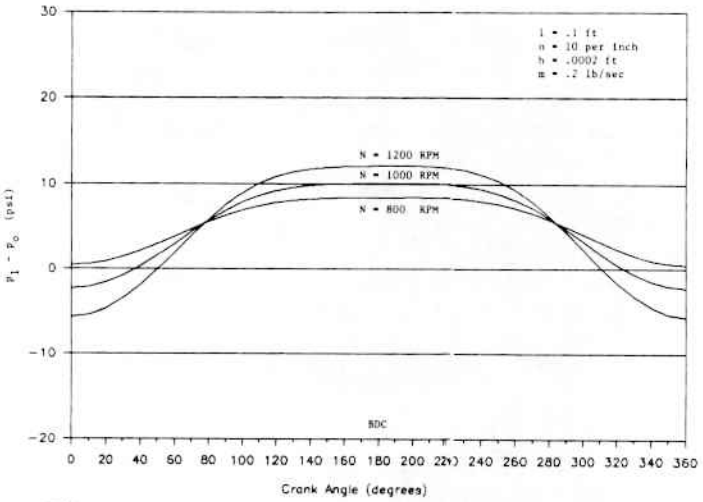


Figure 4. $(p_1 - p_o)$ vs. Crank Angle at Variable Engine Speed.

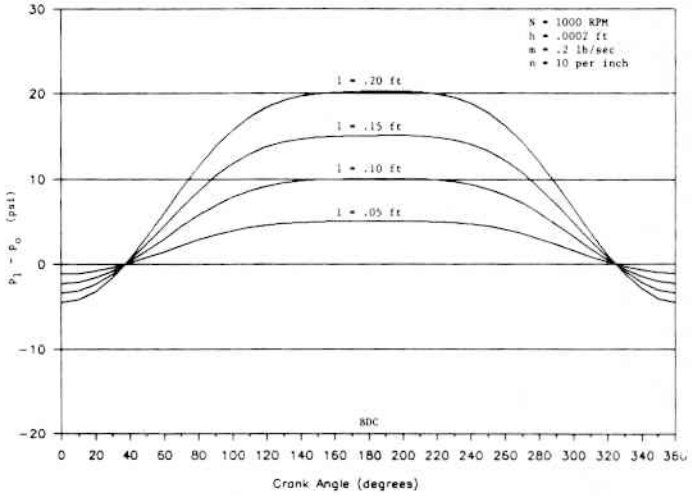


Figure 5. $(p_1 - p_o)$ vs. Crank Angle at Variable Liquid Ring Depth.

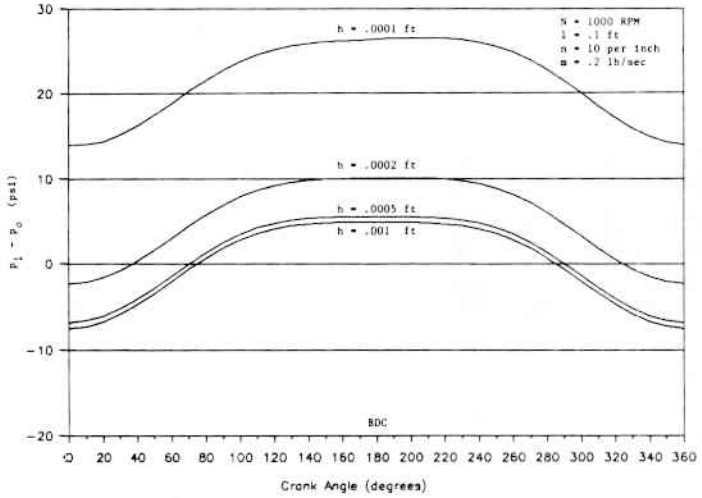


Figure 6. $(p_1 - p_o)$ vs. Crank Angle at Variable Liquid Ring Thickness.

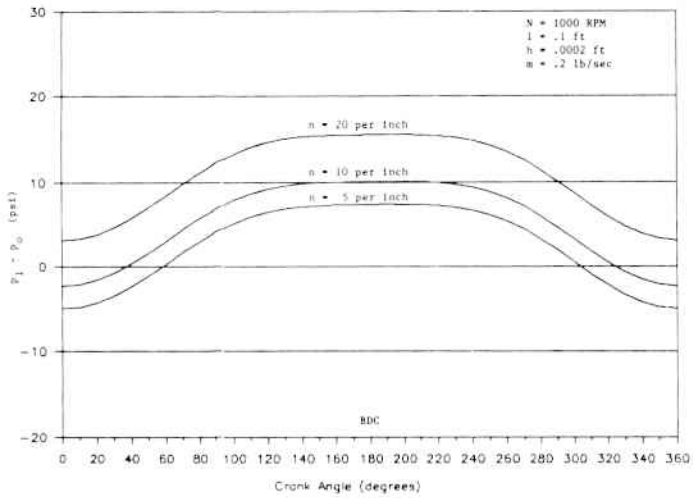


Figure 7. $(p_1 - p_o)$ vs. Crank Angle at h = 0.0002 ft and Variable Number of Labyrinth Per Inch.

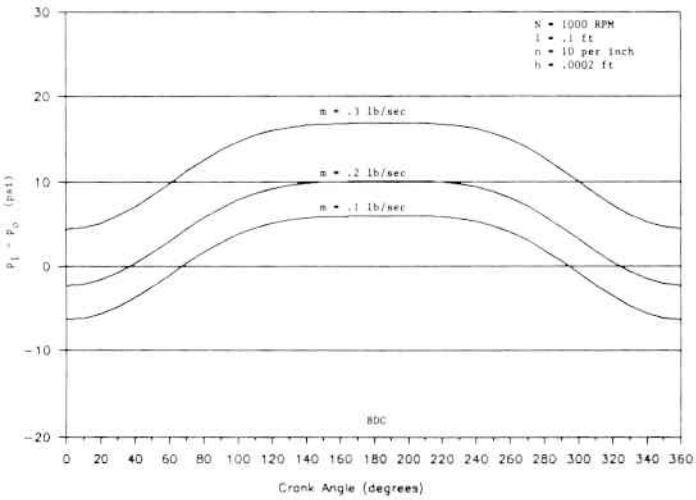


Figure 8. $(p_1 - p_o)$ vs. Crank Angle at h = 0.0002 ft and Variable Liquid Through Flow Rate.

Figures 4 through 8 show for a 9" bore x 10.5" stroke engine the variation of pressure differential between the top and bottom of the liquid ring in one revolution of the engine and the effect of the various design and operating parameters. For a certain geometry and engine speed the pressure at the bottom of the ring drops below the cylinder pressure when the piston is near TDC. This suggests that, at the end of exhaust and beginning of intake stroke, such a condition may result in boiling of the liquid if its temperature is high enough to exceed the equilibrium condition. Therefore, for a given engine, the liquid flow rate, the heat transfer to the liquid ring through the piston and the cylinder liner, and the liquid ring geometry determine the integrity of the liquid ring. Boiling the liquid near the end of the exhaust stroke could be desirable since the vapor generation helps to discharge the liquid and the suspended particles into the cylinder space and exhaust through the exhaust valves. Engine testing will be needed to determine whether or not boiling will help to scrub the wall and discharge the contaminated

liquid. If so, the liquid ring can be designed to enhance the boiling condition.

When the ring thickness is larger than 0.0005 ft in the typical medium-speed engine, the ring height and engine speed are the only two major controlling parameters on the pressure in the liquid. When the ring thickness is reduced to 0.0002 ft, as shown in Figures 6, 7, and 8, the labyrinth pitch and the mass through flow rate also become effective in controlling the liquid pressure.

6.2 HEAT TRANSFER

The amount of heat transfer to the liquid ring determines the temperature rise of the liquid supplied to the ring and therefore imposes a minimum flow rate required to maintain the liquid ring. Preliminary analysis based on experimental data on heat flux into the piston and the cylinder liner of diesel engines (Morel and Keribar 1985, French and Hartles 1965) indicated that the heat transfer to the liquid ring is too high for the once-through system with reasonable flow rates. To reduce the heat transfer to the liquid, certain modifications will be required in the piston design and the cooling system for the cylinder liner. Specific recommendations in these areas will be established later.

6.3 BENCH SCRUBBING SIMULATION

A bench scrubbing simulator (Figure 2) was built up from a single-cylinder engine. The simulator piston is attached to the engine piston and is driven by a variable speed drive through a gear reducer. The test setup is shown in Figure 9. The speed of the simulator can be varied from 10 rpm to 200 rpm. The labyrinth on the piston is scaled up to permit visualization of the fluid motion in the labyrinth region as the piston reciprocates up and down. Polystyrene beads illuminated from the side through a slit act as the tracer for the fluid motion. A video camera is used for recording.

Figures 10 and 11 show the vortex motion of the liquid induced by the relative motion between the piston and the cylinder wall. The vortex reverses when the piston reverses its direction. The geometry of the labyrinth affects the vortex formation and its size and location. The simulator will be used to identify the optimum labyrinth geometry according to the following criteria:

- To produce maximum flow velocity and shear rate adjacent to the wall to scrub the particles off the surface.
- To provide sufficient agitation of the particles in the labyrinth so that no accumulation of particles will occur.

7. FUTURE WORK:

Analysis of the liquid piston ring system will be continued. The analytical model for the liquid ring dynamics will be applied to a number of typical locomotive and stationary diesel engines. Heat transfer analysis will be extended to provide recommendations on the

piston design as well as modifications on the engine cooling system to reduce the heat transfer to the liquid ring.

A number of labyrinth geometries will be tested on the bench simulator. Two or three geometries will be selected for testing in the single cylinder test rig.

The single-cylinder engine used for the simulator drive (Figure 9) will be modified to drive a single-cylinder liquid piston ring test rig. The labyrinth geometries identified from the simulator test will be tested to verify the effectiveness in scrubbing the particles from the wall and reducing the piston ring and liner wear.

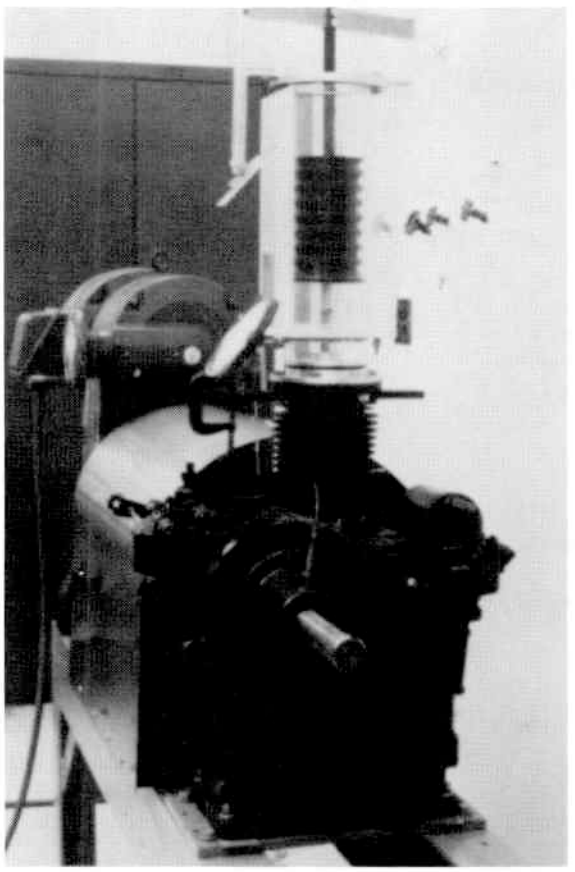


Figure 9. Bench Scrubbing Simulator.

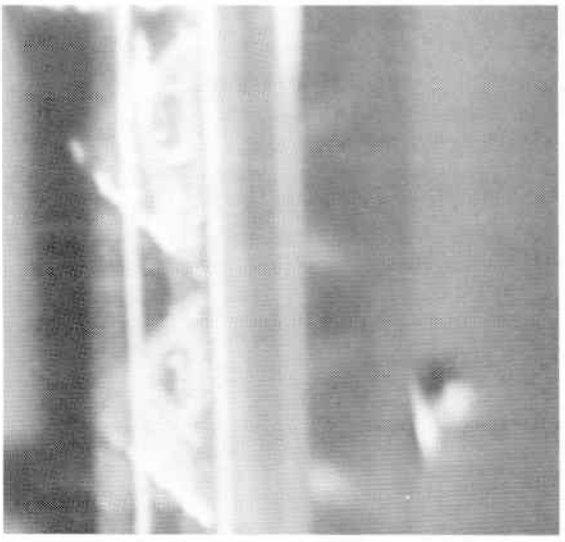


Figure 10. Particle Trace Photograph of Fluid Motion in Labyrinth.

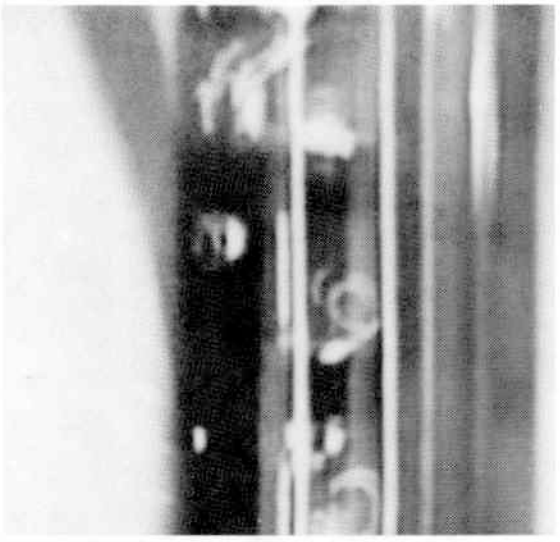


Figure 11. Particle Trace Photograph of Fluid Motion in Labyrinth.

8. REFERENCES:

Flynn, Paul L. and Hsu, Bertrand D. (GE Transportation Systems), Coal Fueled Diesel Developments, SAE Paper 881159, 1988.

Flynn, Paul L., Leonard, Gary L., and Mehan, Richard L., Component Wear in Coal Fueled Diesel Engine, ASME Paper 89-ICE 15, January 1989.

French, C.C.J. and Hartles, E.R., Engine Temperature and Heat Flows Under High Load Conditions, Paper 8, Thermal Loading of Diesel Engines, I. Mech. E., London, Proceedings 1964-1965, Vol. 179, Part 3C.

Morel, T and Keribar, R., A Model for Predicting Spatially and Time Resolved Convective Heat Transfer in Bowl-in-Piston Combustion Chambers, SAE Paper 850204, 1985.

Nydick, Dr. S.E., Development of a Coal/Water Slurry-fueled Diesel Engine for Industrial Cogeneration, Final and Summary Report, Report No. DE-AC02-82CE40539-06, NTIS, February 1987.

Soehngen, E.E., Development of Coal-Burning Diesel Engines in Germany - A State-of-the-Art Review, NTIS Report No. FE/WAPO/338701, August 1976.

FLUIDIC COAL FEED SYSTEM

1. CONTRACT NUMBER: DE-AC-86MC23006

CONTRACTOR:
Adiabatics, Inc.
630 South Mapleton
Columbus, IN 47201
(812) 372-5052

PROGRAM MANAGER (CONTRACTOR): Patrick Badgley

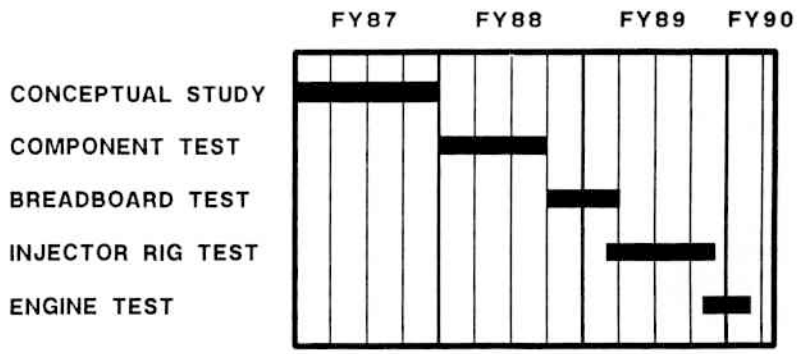
PRINCIPAL INVESTIGATORS:
Roy Kamo (Contractor)
Allen Holmes (Subcontractor)
Sam Kumar (Subcontractor)

METC PROJECT MANAGER: William C. Smith

CONTRACT PERIOD OF PERFORMANCE: September 29, 1986 to January 31, 1990

2. SCHEDULE/MILESTONES:

FLUIDIC FUEL FEED SYSTEM



3. OBJECTIVES:

The objective of this program is to improve the operating life of coal slurry fuel controls and injector components through the use of fluidic technology. No-moving-parts fluidic fuel control and injection systems are to be analyzed, designed, bench tested and engine tested to confirm that the problems of wear and clogging can be significantly reduced or eliminated in a coal slurry fuelled diesel engine. Specific technical objectives include:

- Identification of fluidic flow control and atomization techniques that are applicable to the design of coal slurry fuel injector functions.
- Design, fabrication and bench testing fluid control conponents which can be used to implement control or injection circuits.

- Design, fabrication and bench testing of a breadboard fuel injection system which combines the individual fluidic components into a complete system.

- Design, fabrication and bench and engine testing of a fluidic fuel injector in a coal fuelled diesel engine.

4. BACKGROUND:

The two major problems which limit the usefulness of coal as an alternate fuel in diesel engines are: the inability to efficiently atomize coal slurry fuels, and material wear due to particulate matter in the fuel. Coal slurry fuels are more difficult to atomize than diesel fuel because they are more viscous and exhibit non-Newtonian characteristics. The wear problems encountered by DOE's coal diesel contractors are so severe that they have resorted to schemes to lower injection pressures and to using exotic, hard materials for the nozzle spray holes such as diamond compact.

5. PROJECT DESCRIPTION:

This project addresses the application of fluidic devices to solve the problems of efficient atomization of coal slurry fuel and of injector component wear. The investigation of injector nozzle orifice design emphasizes reducing the pressure required for efficient atomization. The effort to minimize injector wear includes the novel design of components allowing the isolation of the coal slurry from close-fitting injector components.

A team was put together to draw on expertise in the areas of analysis and design of fluidic controls, fluidic component fabrication, and coal fuelled diesel engine testing. Adiabatics, Inc. as the prime contractor, is responsible for the overall program management and coordination, and engine testing. Defense Research Technologies, Inc. is responsible for the conceptualization, analysis, and design of fluidic controls. Teknocraft, Inc. is responsible for component fabrication and laboratory scale testing.

Fluidic technology (or fluidics) employs various fluid dynamic effects, such as boundary layer wall attachment (Coanda effect), fluid stream interactions, and vortex throttling to do functions normally accomplished with moving-parts fluid power components such as valves, pressure amplifiers, and fluid logic components. Fluidic technology was first introduced by the Diamond Ordnance Fuze Laboratories (now Harry Diamond Laboratories) in 1959. The technology is employed in many aerospace, medical, military, and industrial applications where corrosive, erosive fluids are controlled and where reliability is required in particularly harsh operating environments.

6. RESULTS/ACCOMPLISHMENTS:

The program has identified several types of fluidic devices which are

particularly applicable for use with coal slurry fuel. Previous reports at both the Heat Engines Contractors Conferences and the AR&TD Contractors Review Meetings have discussed various fluidic concepts and how they could be applied to an injection system. A single approach has been selected to proceed from concept to engine testing. This concept is known as the Vortex Throttling Nozzle (VTN). The VTN combines is a single component the functions of a vortex type throttling valve and a vortex swirl nozzle. A review of the applicable technology and nomenclature for these three components are as follows:

VORTEX SWIRL NOZZLE

The vortex swirl nozzle consists of a swirl chamber, spin chamber, outlet port, and inlet port arranged as shown in Figure 1. Slurry fuel enters the nozzle in a direction tangent to the edge of the swirl chamber. Due to its direction of entry, the fluid attains a tangential velocity and forms a free vortex in the chamber. In a free vortex, angular momentum is conserved and angular velocity increases as the fluid swirls towards the center of the chamber. This produces a low static pressure in a region along the central axis of the nozzle chamber. Above a certain injection rate (determined by the properties of the fluid and the geometry of the nozzle) the static pressure near the center of the vortex falls below the static pressure on the outlet side of the nozzle. When this occurs hydrodynamic forces act to produce an air core that extends from the back surface of the spin chamber along the central axis of the nozzle through the outlet. Here the pressure in the air core region is equal to the pressure on the outlet side of the nozzle.

Fluid leaves a swirl nozzle through the annular space that is formed between the air core and walls of the outlet. The diameter of the air core determines the width of the gap that is formed between the walls of the nozzle and the inner core boundary. The size of the air core has been reported by Som (ref. 1) to be related directly to inlet Reynolds number, chamber length, diameter, convergence angle and the outlet diameter of the nozzle.

The jet flow leaves the nozzle in the form of a hollow conical sheet (film) which breaks up into droplets downstream of the nozzle. The relative size of the air core and size of the nozzle determine the initial film thickness and nozzle discharge coefficient. The properties of the fluid, and tangential velocity components of the emerging jet determine the angle of divergence, and ultimately the size of the droplets that are formed by the fuel charge.

VORTEX THROTTLING VALVE

A vortex throttling valve is fundamentally a variable flow restrictor without moving parts which has the capability of approximating the flow characteristics of a mechanical valve. The flow geometry of a vortex valve is shown in Figure 2. The valve is comprised of a cylindrical vortex chamber, two inlets referred to as the supply port and the control port, and an outlet port.

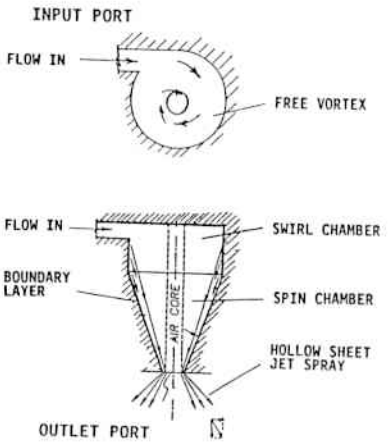


FIGURE 1. VORTEX SWIRL NOZZLE

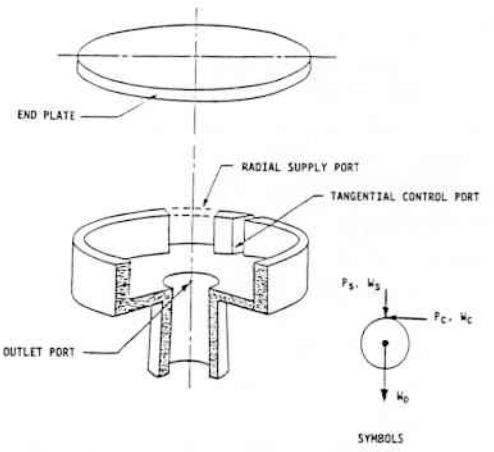


FIGURE 2. FLUIDIC VORTEX THROTTLING VALVE

In the absence of a control flow, the supply fluid passes directly through the vortex chamber at maximum flow. When the pressure in the control port is raised above the supply pressure, control flow enters the vortex chamber and imparts a rotational component to the supply flow. This interaction creates a free vortex in the chamber. Increasing the control pressure increases the throttling action of the vortex and reduces the total flow passing through the chamber until the supply flow is reduced to zero and only the control flow is present.

The ratio between the maximum supply flow rate when the control flow is zero to the control flow rate at which it reduces the supply flow to zero is called the turndown ratio. The turndown ratio is used as a measure of the valve's throttling effectiveness. Turndown can be bistable (on-off) or proportional to the control flow depending upon the vortex chamber geometry. The amount of flow needed to produce full turndown of the supply flow is usually 5-15 times less than the maximum supply flow before turndown. The relative amount of fluid required to produce turndown depends primarily upon the geometry of the vortex chamber and viscosity of the fluid. The time to produce turndown is a function of the empty-fill time of the vortex chamber which is equal to the chamber volume divided by the volumetric flowrate.

VORTEX THROTTLING NOZZLES

A vortex throttling nozzle is a combination vortex valve and swirl nozzle. Figure 3 describes the principal features of a vortex throttling nozzle. In a vortex throttling nozzle the functions of each component have been combined in order to reduce circuit volume and, therefore, reduce response time. A vortex throttling nozzle is similar to a vortex valve in that it consists of a vortex chamber, control port, outlet port, and a supply port. However, as in the swirl nozzle, the supply port is offset to one side of the vortex chamber to produce a vortex flow. Due to its tangential entry, the fuel forms a free vortex in the chamber and emerges from the nozzle in the form of a hollow conical sheet. The relative location of the entry port with respect to the radial centerline

and the entrance velocity and Reynolds number determine the droplet size, cone angle and overall characteristics of the jet spray pattern.

SLURRY FUEL CONTROL CIRCUITS

Previous studies conducted during the course of this contract have focused on establishing various approaches to slurry fuel control circuit design (Holmes, ref. 4). As a result of these studies, two slurry fuel control circuits were selected for evaluation. The first circuit employs a solenoid-actuated vortex throttling nozzle in a rail type fuel distribution system. The second employs a biased vortex throttling nozzle in a jerk pump type system. The rail type system with solenoid valve control of the injection was selected for engine test.

In the rail system shown in Figure 4, the fuel slurry is supplied to the throttling nozzle from a pressurized accumulator. Compressed air is

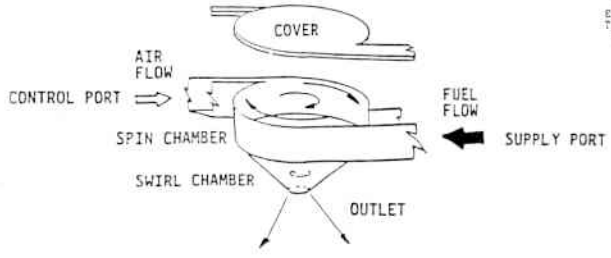


FIGURE 3. VORTEX THROTTLING NOZZLE

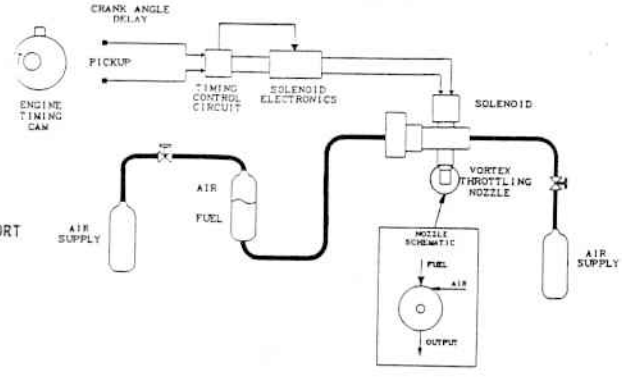


FIGURE 4. COMMON RAIL TYPE CWS FUEL INJECTION SYSTEM

supplied from an engine-driven compressor through a solenoid valve to the control port of the throttling nozzle to control the on-off time of the fuel flow. The solenoid valve is actuated by timing signals generated in the electronic control module, which in turn receives its signals from a sensor on the engine timing cam. The injection process is initiated when the solenoid valve is closed which stops the compressed air flow which turns off the vortex. The fuel flow rate is controlled by a regulator which delivers air pressure to the accumulator. The injection period ends when the solenoid valve is opened and a vortex is produced by the control air.

TEST FACILITY DESCRIPTION

During the last year the testing has transitioned from Teknocraft's facility in Palm Bay, Florida to Adiabatics in Columbus, Indiana. During this transition it was necessary to maintain a minimal test capability at Teknocraft so that they could test completed injector assemblies before shipment to Adiabatics for engine test. The new facility at Adiabatics consists of a coal slurry handling and pumping system which can provide CWS at pressures up to 5000 psi. A high pressure air supply system. An electronics control package which can drive and control the injector is

synchronization with the engine, and an instrumentation system to measure pressures, flows and temperatures.

COAL SLURRY SYSTEM - Figure 5 is a schematic of the coal water slurry handling and pumping system. This newest slurry handling system is designed to eliminate known problems and provide us with a dependable source of coal slurry with minimal maintenance. The system has worked quite well and has been troublefree. The slurry is stored in a conical bottom fiberglass tank with a discharge fitting at the bottom of the cone. From here the slurry flows into a triplex type positive displacement pump with a variable speed motor control and normally back to the tank to provide recirculation and mixing. The actual high pressure pumping system uses a bladder type accumulator as a batch type pump. To fill the accumulator a series of valves are opened which connect the outlet of the triplex pump to the accumulator. The valve allowing the CWS to recirculate back to the tank is then throttled to provide the pressure to completely fill the accumulator (200 to 300 psi). A city water connection and a series of valves are provided to enable the triplex and accumulator pump systems to be flushed without disturbing the CWS in the tank.

AIR SUPPLY SYSTEM - The selected injector concept requires a source of air at a pressure twice as high as the slurry pressure. To provide this pressure an existing natural gas compression system was modified to provide air at pressures up to 5000 psi as shown in Figure 6. In addition to providing control air, this system also provides the pressure to drive the accumulator pump for the CWS.

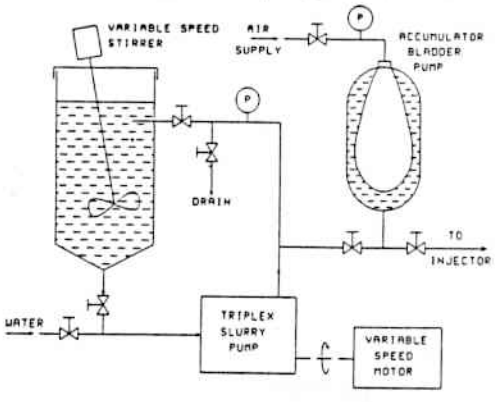


FIGURE 5. CWS HANDLING SYSTEM

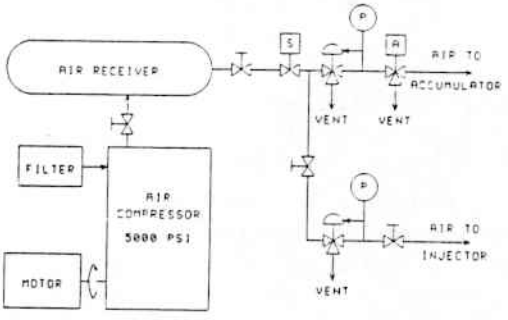


FIGURE 6. AIR SUPPLY SYSTEM

INJECTOR DRIVE ELECTRONICS - Figure 7 is a schematic of the driving circuitry for the injector solenoid. This system is triggered by a crankshaft position sensor on the engine and consists of a delay circuit which is used to control injection timing, a pull in circuit that rapidly opens the solenoid, and a duration control circuit that times the length of the injection pulse.

TEST ENGINE - The CWS test engine is a single cylinder Caterpillar model 1Y73 which is modified to run without cooling and with a hotter than normal precombustion chamber. Figure 8 is a sketch which shows the details of these modifications.

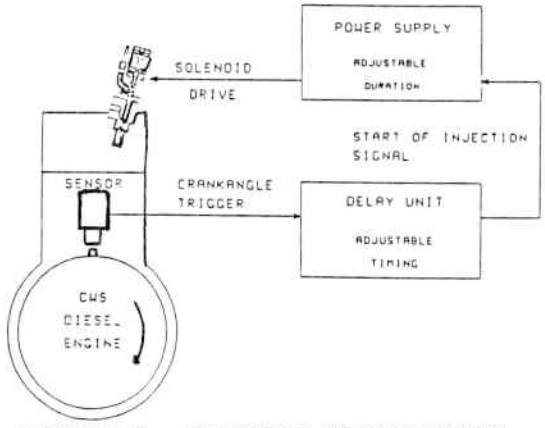


FIGURE 7. INJECTOR ELECTRONICS

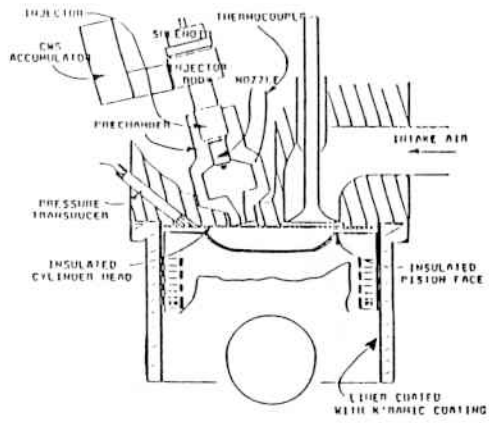


FIGURE 8. TEST ENGINE MODIFICATIONS

INSTRUMENTATION - The fluidic injector and auxiliary test equipment are equipped with instrumentation which allows us to record the flow rates and dynamic pressures of both the control air signal and the CWS. The engine is instrumented with a crankangle encoder for accurate crank position determination and a fast response cylinder pressure transducer. These signals are fed to a high speed data acquisition system which records the synchronized crank position and cylinder pressure data and executes data reduction programs to generate instantaneous rate of pressure rise and heat release curves. The engine is also instrumented with standard temperature and pressure instrumentation which is recorded on a computer based data logging system.

FLUIDIC INJECTOR HARDWARE

The basic fluidic injector consists of a vortex throttling nozzle (VTN) and a high speed valve which shuts off the control air to allow the CWS to inject into the engine. There is only one moving part in the control air valve and there are no moving parts in the VTN. Figure 9 is a simplified schematic diagram of the injector showing the solenoid operated air valve and the VTN.

Obtaining an adequate high performance solenoid operated control air valve has been the key pacing component in testing a complete injector assembly. The air valve is normally open and must be closed to start the injection and opened to end the injection. The valve must be able to close and open again in times as short as one millisecond. Several normally closed solenoid operated valves have been developed which have the capability of opening quickly and then closing but they were not adaptable to being made into normally open valves. Because of the critical requirements for this component and since it is not available commercially, we selected to have a primary design with a solenoid valve especially designed for this application and backup designs using available components.

The first backup design was a bit of a Rube-Goldburg approach which used a normally closed solenoid pilot-operated valve and an additional valve assembly to invert the signal (Figure 10).

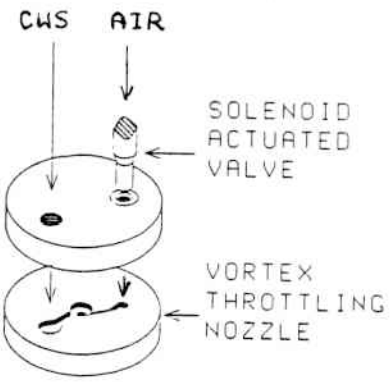


FIGURE 9. VTN INJECTOR OPERATION

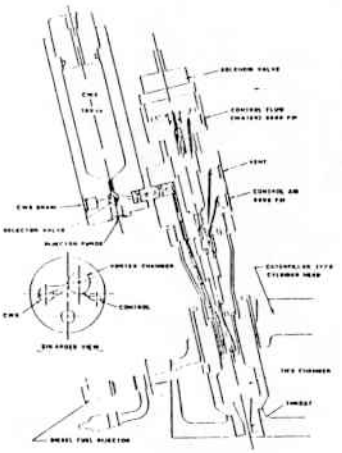


FIGURE 10. BACKUP INJECTOR # 1

The second backup injector used an available high speed solenoid coupled to a standard diesel type fuel injector to make a normally open valve assembly (Figure 11). With this approach there is a small amount of air that leaks past the seal portion of the injector needle which is vented to prevent the solenoid assembly from being pressurized.

The Primary injector design (Figure 12) uses a sealed, pressurized solenoid valve assembly. This approach eliminates the need for a seal between the high pressure control air and the solenoid. This approach eliminates the expensive, close fitting guide portion of the valve which makes it possible to design the injector with no rubbing parts by using a flexure support for the valve.

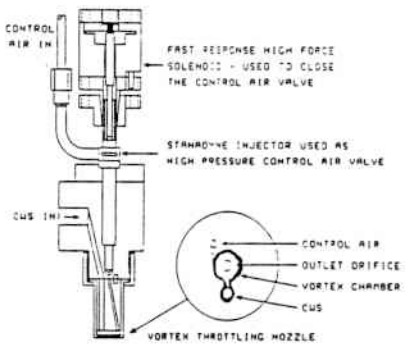


FIGURE 11. BACKUP INJECTOR # 2

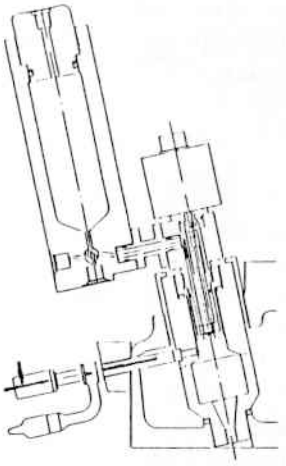


FIGURE 12. PRIMARY INJECTOR DESIGN

BENCH TEST RESULTS

All three of the fluidic injectors were tested using both water and CWS as the injected fluid. The first injector tested was the servo actuated backup injector. Figure 13 is recording of the servo pressure acting on the top of the control air valve and the pressure in the CWS accumulator.

The curve shows that the servo system is working well and that the pressure builds up and decays quickly. There is a corresponding drop in CWS pressure during the injection period which is very regular. The injections from this injector were very consistent and the injector operated well over large pressure and flow ranges; however the duration of the injection was too long to use it for engine testing.

The second backup injector was designed to eliminate the servo actuation system. The solenoid valve part of this injector works extremely well and provides very rapid shutoff of the control air with durations as short as one millisecond but the system was plagued with new problems in the fluidic element which was the same physical part which had performed well with the first injector. The problem was that the control air would back up into the fuel supply and stop injecting. Attempts to raise the fuel pressure to prevent this behavior caused the injector to spray fuel continuously. Occasionally the injector would operate properly, but it would soon revert to flowing either all air or all fuel. Four additional fluidic vortex throttling nozzle geometries were tested to determine if this problem could be eliminated. Figure 14 shows the geometries of the

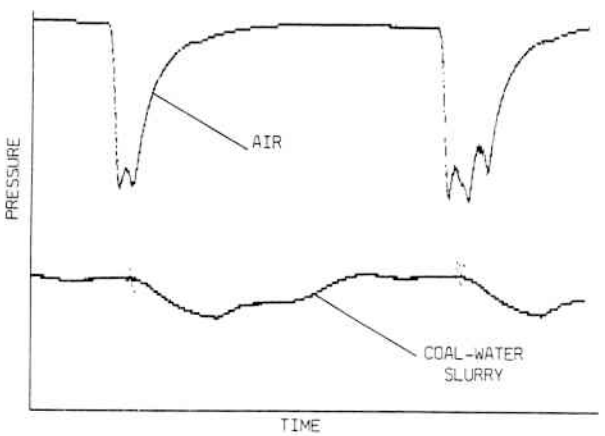


FIGURE 13. BACKUP #1 PERFORMANCE

VERSION	OUTLET DIAM.	CHAMBER HEIGHT	CONTROL WIDTH	CHAMBER DIAM.	SUPPLY WIDTH
A	0.030 (0.76)	0.030 (0.76)	0.010 (0.25)	0.210 (5.33)	0.050 (1.27)
B	0.030 (0.76)	0.020 (0.51)	0.010 (0.25)	0.210 (5.33)	0.050 (1.27)
C	0.040 (1.02)	0.020 (0.51)	0.010 (0.25)	0.210 (5.33)	0.050 (1.27)
D	0.030 (0.76)	0.025 (0.64)	0.006 (0.15)	0.240 (6.10)	0.240 (1.02)
E	0.030 (0.76)	0.025 (0.64)	0.006 (0.15)	0.240 (6.10)	0.240 (1.02)
F	0.030 (0.76)	0.030 (0.76)	0.010 (0.25)	0.420 (10.7)	0.050 (1.27)

FIGURE 14. VTN GEOMETRIES

different designs. Figure 15 is an empirically derived plot which is used to determine whether a vortex valve will be proportional or operate in a bistable regime with hysteresis. The original nozzle was designed to fall on the boundary between these two regimes which was believed to be ideal for a low hysteresis on-off valve. However, the test results indicated that the valve was strongly bistable with large hysteresis. The first modification was to reduce the height of the channels by simply reducing the height of the existing disk shaped element. As shown from the curve this change should have made the valve more proportional and less likely to have problems. Upon testing it proved to be only slightly better but still suffered from the problem of having air back up into the fuel line. A second modification opened up the nozzle exit diameter. which forced us back towards the bistable regime but reduced the ratio of control flow to supply flow (turn-down ratio) which also makes control easier. Testing of this design was also better but still far from acceptable. The last two designs were new fluidic components with identical dimensions but with different relative locations between the control and supply ports. These

designs further improved the turn-down ratio and also made the valve more proportional. Tests results with these designs showed better behavior (Figures 16 & 17). Additional testing with this injector is currently being conducted.

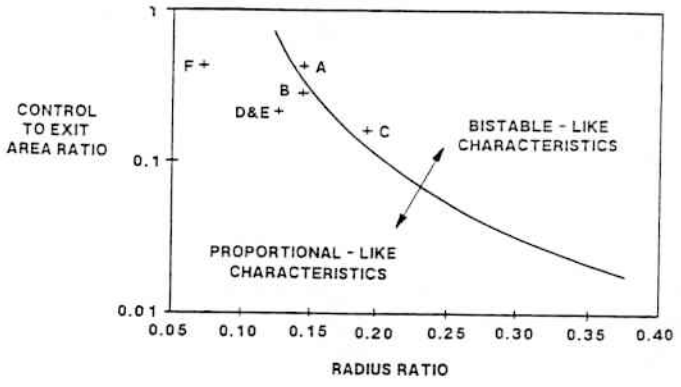


FIGURE 15. VORTEX VALVE OPERATION

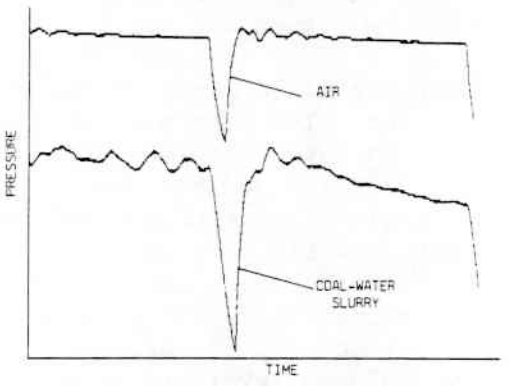


FIGURE 16. BACKUP # 2 PERFORMANCE

The last injector to be available for test was the primary design with a pressurized solenoid with no gas leakage. This injector went through several design iterations to solve problems of solenoid leakage, valve stem breakage, valve seat sealing and adequate solenoid force to close against high gas pressure. The first tests with this injector with water instead of CWS demonstrated that good injection behavior is attainable. Additional testing with CWS is underway.

7. FUTURE WORK:

The remaining work on this program consists of additional bench testing followed by engine testing to demonstrate injector performance and durability.

This program can demonstrate the technical feasibility of a fluidic injector with air as the control fluid. However, is is not practical to use air as the control fluid because the parasitic loss involved in compressing the air is too high (Figure 18). A much better fluid to use

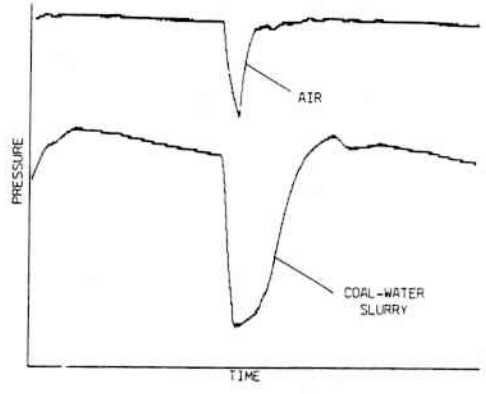


FIGURE 17. BACKUP #2 PERFORMANCE

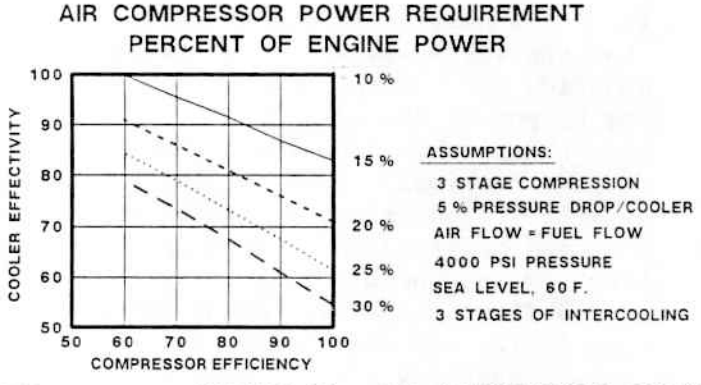


FIGURE 18. AIR COMPRESSORE POWER

is high pressure steam which is pressurized as water and heated by waste exhaust energy to make steam.

8. REFERENCES

1. Som, S.K., and Mukherjee, "Theoretical and Experimental Investigations on the Formation of Air Core in a Swirl Spray Atomizing Nozzle," Applied Scientific Research 36: (1980) pp.173-196, Martinus Nijhoff Publishers bv, The Hague, (Printed in the Netherlands).

2. Holmes, A.B. "Fluidic Fuel Feed System," Proceedings of the Annual Heat Engines and Gas Stream Cleanup Systems Contractors Review Meeting, DOE/METC (DE87001072), April, 1987.

Session 6B
Turbines

Chairperson: Donald W. Geiling

The barrier technical issues for coal-fueled gas turbines are those associated with deposition, erosion, and corrosion (DEC) due to the products of coal combustion. In this session, three approaches to addressing these issues are discussed:

- Developing models to better understand and predict DEC phenomena,
- Developing an indirect-fired gas turbine cycle to transfer DEC problems from the turbine hot gas path to a ceramic heat exchanger, and
- Developing airfoil designs that minimize erosion without sacrificing aerodynamic efficiency.

ASSESSMENT OF FOULING, EROSION, AND CORROSION OF COAL-FIRED GAS TURBINES

1. FTPA NUMBER: AA-15-05/ANL 49777

CONTRACTOR: Argonne National Laboratory
9700 South Cass Avenue
Argonne, Illinois 60439
(312) 972-5979

PROGRAM MANAGER: D. K. Schmalzer

PRINCIPAL INVESTIGATORS: R. K. Ahluwalia and K. H. Im

METC PROJECT MANAGER: E. L. Parsons

CONTRACT PERIOD OF PERFORMANCE: October 1, 1988 through April 30, 1989

2. SCHEDULE/MILESTONES:

	O	N	D	J	F	M	A
Update Particle and Vapor Deposition Models	———						
Topical Report on Fouling of Gas Turbine Passages		———					
Topical Report on Sodium-Sulfate Hot Corrosion of Turbine Superalloys						———	

3. OBJECTIVES:

To update particle and vapor deposition models and to issue final reports on fouling of gas turbine passages and on sodium-sulfate hot corrosion of turbine superalloys.

4. BACKGROUND STATEMENT:

The development of coal-fired gas turbines requires deposition, erosion, and corrosion (DEC) protection of turbines from ash contaminants in the products of combustion. The severity of turbine degradation depends upon a number of variables including coal ash thermochemistry, ash content, combustion particulate size distribution, gas temperature, surface temperature, and blade aerodynamics. The present task has been concerned with the development of semi-phenomenological models for predicting DEC modes of interaction between and contaminants and the blade surface as a function of turbine operating conditions and fuel chemistry.

5. PROJECT DESCRIPTION:

The contaminants entering a coal-fired gas turbine will consist of particulate matter (flyash, nucleated ash and unburnt char) and vapor species (primarily alkali sulfates). Previous work entailed analytical models that describe the following:

- Condensation of alkali sulfate and refractory oxide vapors in a gas turbine environment (Ahluwalia et al. 1984).
- Deposition of particles/vapor on pressure/suction surfaces of turbine blades (Ahluwalia et al. 1986).

- Effect of boundary layer nucleation on mass transfer of alkali sulfates to cooled turbine blades (Ahluwalia and Im 1985; Cha, Ahluwalia and Im 1989).
- Corrosion correlations for turbine alloys (Ahluwalia and Im 1988).
- Flyash adhesion on pressure surface (Ahluwalia, Im and Wenglarz 1989).

6. RESULTS/ACCOMPLISHMENTS:

FOULING OF GAS TURBINE PASSAGES

Fouling of coal-fueled gas turbine passages is perceived as being a highly complex problem. A number of factors must be considered because they affect either the rate and mechanism of contaminant delivery to the blade surface, or physical interaction (adhesion) between the contaminants and blade/deposit surface, or spallation of deposit. Although a complete quantitative understanding of the fouling factors has not yet been attained, the following qualitative discussion can be offered on the basis of theoretical and experimental work performed to date (ANL/FE-89/2).

Particle Delivery

The rate and mechanism of ash delivery to blade surface depends on particle size, blade aerodynamics, boundary layer characteristics, and free-stream turbulence field. On the pressure side, with progressively larger particle size, the delivery mechanism changes from thermophoresis (requires temperature difference between gas and blade), to eddy impaction (requires turbulent boundary layer), to inertial impaction. For a given temperature difference, the thermophoretic deposition velocity declines with particle size whereas that by inertial impaction varies as the square of the particle size. Turbulent eddy deposition velocity generally displays an internal maxima with respect to the particle size. The transition from thermophoresis to eddy deposition mechanism is determined by blade cooling, surface velocity, and boundary layer turbulence. The crossover from eddy impaction to inertial impingement depends on the blade aerodynamics and the somewhat dissimilar influence of boundary layer on viscous damping. Since the inertial deposition velocity is directly proportional to the blade curvature, the crossover occurs at a smaller particle size for a smaller gas turbine.

On the suction side, particles deposit by diffusive transport mechanisms, namely thermophoresis and eddy impaction. These display the same dependence on particle size as observed for pressure surface. A significant difference arises from the centrifugal drift velocity segregating particles near the pressure surface and from particle redistribution due to the dispersive action of the turbulent fluctuations. Small particles remain uniformly dispersed in the flow field because of low drift velocity and high turbulent diffusivity. For the large particles that can sustain a finite drift velocity and have a sluggish turbulent diffusivity, a significant depletion occurs in particle concentration at the suction surface. For these particles, effective deposition velocity decreases rapidly with particle size and flow distance. Since the drift velocity scales directly with blade curvature, the larger the gas turbine the smaller the depletion in suction surface concentration.

Particle Size Distribution

For particles larger than about 1 μm, inertial deposition velocity to the pressure surface of a commercial gas turbine is two-to-three orders of magnitude larger than the deposition velocities associated with diffusive transport mechanisms. Since the inertial deposition velocity scales up as the square of the particle radius, there is an incentive to seeking means by which the flyash size distribution can be restricted to as small size as possible.

Coals suitable for gas turbine applications are likely to undergo a physical cleaning step resulting in removal of much of extraneous ash. In that case, the flyash size distribution that evolves after combustion will reflect the size spectrum of the mineral inclusions in coal. During char combustion, the surface recedes and exposes the inclusions which may be in molten state. If the inclusions intercept one another, they may fuse to form a single large droplet. Over the combustion period, a single inclusion may participate in multiple fusion events. Once char is consumed, further fusion of slag droplets is unlikely because of decreased interception/collision frequency (Spiro et al. 1987). In general, the finer the coal grind, the smaller the mineral dispersions and hence the product of combustion particles. Furthermore, the char burnout time decreases with coal grind (inversely proportional to particle size if combustion is diffusion limited) favoring the formation of finer droplets (smaller available interception time).

For dry coal feed, the foregoing arguments suggest that fouling problem will ease with coal micronization. For coal-water slurries, however, combustion tests in gas turbine and non-turbine combustors reveal little benefit from smaller coal particles in the slurry. Apparently the combustion efficiency is determined by atomization droplet size distribution and not coal particle sizes if maximum coal diameters are smaller than maximum droplet diameters. This is generally attributed to coal particles contained within an individual atomized droplet forming an agglomerate consequent to vaporization of the water content. The subsequent combustion behavior is characteristic of the agglomerate rather than the parent coal particle. There is some experimental evidence to suggest that the same conclusion holds for the resultant flyash size distribution.

Particle adhesion can be envisioned as a two-step process. In the first step, a fraction of the particles arriving at a surface are retained to form a deposit. Concurrently, ash particles impacting the surface at a high velocity erode some of the deposit. The net ash accumulation rate then represents the dynamic equilibrium between particle retention and deposit spallation. For the suction surface, the contribution of the spallation term to the sticking coefficient may be negligible since the particles transported by diffusional mechanisms have a limited capacity for deposit erosion. For the pressure surface, deposit spallation rate should scale up directly with particle size. Thus, in principle it may be advantageous to have a small fraction of large size particles in the total ash burden. In the absence of a protective ash deposit, these would pose an erosion threat to the blade surface. In the deposition regime of operation, these would provide a control on net ash accumulation by spalling-off some of the deposit.

Slurry Atomization

Factors that impact slurry atomization also affect flyash size distribution and delivery to blade surfaces. As remarked earlier, combustion behavior of slurries prepared from micronized coal is rather insensitive to the coal grind. Highly loaded micronized CWF slurries are generally prepared by mixing with a larger size cut fraction. Slurry atomization characteristics are known to depend upon nozzle design, air fuel ratio, additives used, high shear ($>10,000\ s^{-1}$) slurry viscosity, coal loading, coal grind, and ash content. Generally, slurries prepared from finer coal particles are more difficult to atomize. Also the lower the coal loading, the better the atomization. This is probably related to the relationship between particle loading and fuel viscosity. Wenglarz et al. (1987) noted a five-fold reduction in slurry viscosity upon reducing coal loading from 52% to 48%. The coal had 0.69% ash and maximum particle diameter of 15 μm.

Coal Combustion

Time-temperature history experienced by ash during coal combustion is likely to impact its adhesion behavior. Anderson and Romanowski (1985) observed the sticking coefficient to increase with reactor/combustor temperature in a laminar entrained furnace operated with dry coal feed. Kimura et al. (1987) observed that combustion of beneficiated coal-water mixtures under gas turbine conditions (10-13 ms residence time) proceeds through formation and burnout of porous and buoyant cenospheres, 1-20 μm in diameter. The cenosphere diameter was considerably larger than the coal diameter, indicating a significant degree of agglomeration of coal particles within atomized droplets. Based on their study of potassium-oxygen bonding in ash from low-temperature ashing and in the products of combustion, they propose that alkali metals are not volatilized in short residence time turbine combustors.

For highly cleaned coals, char can constitute a significant fraction of particulate burden if complete burnout is not achieved. As an example, at 99% burnout efficiency, particulates from 1% ash coal combustion contain 50% carbon. Besides increasing particulate concentration, residual char serves to modify the size distribution function and hence the delivery rate to the blade surfaces. The density of porous char is much smaller than that of ash and this too affects the delivery rate. Because of the extremely short residence time and low temperatures, residual char is unlikely to complete burnout in transit through the gas turbine. The portion deposited on the blade surface, however, has ample exposure time for gasification. Thus, to a first approximation, residual char accelerates the ash delivery rate to blade surfaces without physically contributing to blocking of the blade passages.

The presence of residual char may also affect ash adhesion characteristics. It influences ash chemistry by creating slightly reducing conditions on the blade surface (a deleterious effect). The heat liberated from char combustion raises the deposit temperature (small effect) and its sintering rate. The weight loss associated with surface combustion may help to dislodge some of the deposit. Residual char which impacts the surface without retention probably contributes to deposit erosion. From the corrosion standpoint, unburnt char may alter the mode of blade material wastage from one of oxidation to sulfidation.

Coal Beneficiation

Physical or chemical cleaning of coal impacts nearly all aspects of the fouling problem. It may affect ash chemistry by selective addition or deletion of certain active constituents. For example, chemical beneficiation of a high volatile bituminous coal using aqueous pressurized caustic left residues of soluble alkali metals from the chemical leaching step and chloride ion from the acid neutralization step (Spiro et al. 1987). The milling step resulting in increased iron content from the products of comminution. The acid leach also removed a major portion of the calcium carbonate/hydroxide.

As discussed earlier, for very finely ground coal, flyash size distribution is controlled by the size of spray droplets generated from atomization. At this stage, there is little benefit to further reduction in coal size. Similarly, although the particulate delivery rate decreases in direct proportion to the ash content, the fouling rate may become insensitive to coal cleaning if the sticking coefficient was to increase or if the surface buildup is controlled by deposit spallation which suffers with decrease in concentration of the eroding particles.

Blade Cooling

In some modern gas turbines, increases in turbine inlet temperatures have been made possible by the ability to control metal temperatures by means of blade cooling. With conventional fuels, blade cooling provides control on material corrosion rates and mechanical properties such as creep strength, ultimate strength, and low cycle fatigue strength. When coal is used as a fuel, it also serves as a method for controlling deposition.

Results to date indicate that blade temperature is one of the most important parameters affecting deposition of coal ash on blade surface. Table 1 represents a compilation of surface temperature effect on sticking coefficient for various coals combusted under different conditions of pressure, temperature, residence time and flow field, and for different deposition targets. Particle adherence invariably decreases with lowering of surface temperature. The deposit on pressure surface is bombarded by inertially impacting particles. The resulting spallation is a function of particle kinetic energy, impact frequency and the deposit strength that develops from interparticle sintering. The rate of sintering is often an exponential function of temperature. At low metal temperatures, the sintering time is finite and comparable to deposit erosion time. The deposit remains poorly bonded and is easily spalled. An uneven deposit structure develops from random shedding of the deposit. In contrast, the deposits at high metal temperatures are tightly bonded and exhibit a more uniform structure.

Since the thermophoretic delivery rate is proportional to the temperature gradient, it is enhanced by blade cooling. Similarly, vapor deposition rate increases as the blade surface is cooled below the dew point. In some past tests using oils doped with MgO to combat vanadium-induced hot corrosion, maximum fouling rate was observed at an intermediate temperature (Rose 1982). This is generally explained on the basis of the balance between enhanced thermophoretic/vapor deposition rate and increased deposit erosion rate with blade cooling. For a coal combustion system, a similar trend could conceivably occur (although there is no experimental evidence) if

Table 1. Particle Adhesion Data

Fuel	Ash Content, %	Combustion	Target	Gas Velocity, m/s	Reactor Temp., K	Gas Temp., K	Surface Temp., K	Sticking Coefficient	Remarks
Arkwright		LER[a]	PFP[b]	136-150	1478-1700	1090-1216	1090-1216	0.02-0.24	Non-protoypical gas turbine combustion
AMAX-II		LER	PFP	133-148	1478-1700	1069-1200	1069-1200	0.06-0.18	
Spring Creek		LER	PFP	139-153	1478-1700	1036-1168	1036-1168	0.27-0.38	
Lignite		LER	PFP	134-141	1478-1700	986-1168	986-1168	0.19-0.88	
Acid-washed Lignite		LER	PFP	135-146	1478-1700	998-1104	998-1104	0.21-0.55	
CWM 1	1.25 Physical Cleaning	RQL[c]	Wedge[d]	155		1325	1156-1325	0.05-0.10	Large amount of residual carbon in products of combustion
		RQL	Wedge	155		1256	1050-1170	$3x10^{-4}$-$7x10^{-4}$	
CWM 3	0.69 Physical Cleaning	RQL	Wedge	155		1325	1156-1329	0.05-0.10	
		RQL	Wedge	155		1256	1256	0.02	
Arkwright		LER	PFP	250	1373	1100	1100	0.08-0.13	Ca/S = 0
		LER	PFP	250	1373	1100	1100	0.05-0.10	Ca/S = 1
		LER	PFP	250	1373	1100	1100	0.01-0.02	Ca/S = 2
		LER	PFP	250	1373	1100	1100	0.01-0.025	Ca/S = 5
		LER	PFP	250	1573	1300	1300	0.07-0.14	Ca/S = 1
		LER	PFP	250	1573	1300	1300	0.14-0.18	Ca/S = 2
Blue Gem		LER	PFP	250	1373	1100	1100	0.005	Ca/S = 0
Upper Freeport		LER	PFP	3-4	1743	1573	773	0.15-1.0	Boiler application
Beulah-Zap		LER	PFP	3-4	1743	1573	773	0.30-0.50	Boiler application
OTISCA CWM	0.76-0.87 Physical Cleaning	TCC[e]	Cascade	Choked flow at throat		1366[f]	Film cooled	0.03-0.04 in 23 hrs[g]	Deposit Thickness pressure side = 100-1000 μm suction side = 100 μm

[a]Laminar Entrained Reactor
[b]Perpendicular Flat Plate
[c]Rich-Quench-Lean Turbine Combustor
[d]Internally Cooled Wedge
[e]Turbine Can Combustor
[f]Turbine Inlet Temperature
[g]Fractional Throat Area Closure Rate

sodium sulfate in vapor or fine particulate form assumes the role of a glue agent.

Turbine Inlet Temperature

The rate of ash accumulation increases drastically with turbine inlet temperature. The effect manifests itself in two ways. For a fixed ash impurity concentration, the overall sticking coefficient increases with gas temperature. Secondly, higher fuel-air ratio is required to raise the turbine inlet temperature and this translates into greater ash throughput.

The deleterious effect of high gas temperature on fouling can be compensated by blade cooling. At a low gas temperature, ash accumulation becomes almost independent of the substrate temperature. When this condition is reached, the passage closure rate reduces to being a function of the turbine inlet temperature alone.

Because of the poor thermal conductivity of the deposit, the apparent surface temperature is closer and hence more sensitive to the gas rather than substrate temperature. This is especially true for poorly sintered deposits having low thermal conductivity. As the deposit builds up or if the gas temperature is high, sintering occurs, the deposit thermal conductivity improves, and the blade temperature begins to influence the temperature of the surface exposed to flow. Observations on deposition on a cylindrical pin exposed to CWM combustion products in a gas turbine environment suggest the existence of an activation barrier to crystallization (Spiro et al. 1987). At 1367 K gas temperature, the deposit was crystallized while an amorphous structure evolved at 1200 K. This would imply that the ash deposit formed at a lower turbine inlet temperature would be more susceptible to spallation and the accumulation rate would be correspondingly slower.

Just as for blade cooling, the rate of thermophoretic delivery of fine particles accelerates with gas temperature. The rate of sodium sulfate mass transfer by vapor condensation follows a similar trend. Thus, if one accepts the sodium sulfate glue limited deposition hypothesis, ash accumulation rate would be predicted to increase with turbine inlet temperature.

Sorbent Injection

Limestone is being considered as a potential additive for upfront capture of sulfur during coal combustion. Depending upon the combustor arrangement (in-line or off-line), flow configuration (plug flow or swirl flow), Ca/S ratio and degree of sulfur capture, some or all of reacted ($CaSO_4$) and unreacted limestone will pass through the gas turbine and participate in the passage fouling process.

Early data from G.E. turbine simulator test rig indicated that better than 60% sulfur capture was possible at a Ca/S ratio close to unity. However, the cascades exhibited catastrophic fouling, forcing unscheduled test abandonment.

Data from a laboratory-scale deposition facility at Morgantown Energy Technology Center (METC) show a highly temperature-dependent fouling behavior of the sorbent additives. For Arkwright coal containing 6.93% ash and 2.2-2.8% sulfur, the sticking coefficient increased with sorbent injection when the reactor was operated at 1573 K and the equilibrated target temperature was

1300 K. On the other hand, the sticking coefficient decreased with limestone addition at 1373 K reactor and 1100K target temperatures. At the lower operating temperature, the higher the Ca/S ratio, the lower the sticking coefficient (see Table 1).

With sorbent injection, the sticking coefficient by itself is not a true measure of fouling severity because of the associated increase in the entrained particulate loading. Table 2 reinterprets the METC deposition data to show that much of the benefit of reduced sticking coefficient at high Ca/S ratio does not translate into reduced deposition rate. The conclusion is even more striking for a clean coal with a higher sulfur-to-ash ratio.

According to METC data, the sticking coefficient appears to approach the value appropriate for limestone as Ca/S ratio is increased. For untreated Arkwright coal, the deposit appears to behave like limestone at Ca/S ratio of 5 (limestone/ash = 5.64) and 1100 K target temperature. At a low target temperature, limestone is less sticky than Arkwright coal ash and vice-versa at 1300 K target temperature.

Table 2. Effect of Sorbent Injection on Fouling

				Arkwright Coal, S/Ash = 0.36		Clean Arkwright Coal, S/Ash = 2	
Reactor Temperature	Target Temperature	Ca/S	Sticking Coefficient	Relative Particulate Loading	Relative Fouling Rate	Relative Particulate Loading	Relative Fouling Rate
1373	1100	0	0.11	1	1	1	1
		1	0.05	2.13	0.97	7.25	3.30
		2	0.015	3.25	0.44	13.40	1.84
		5	0.01	6.25	0.60	32.25	2.93
1573	1300	0	0.25	1	2.27	1	2.27
		1	0.10	2.13	1.94	7.25	6.59
		2	0.18	3.26	5.33	13.50	22.09

Deposit Cleanability

As the deposit builds up and deteriorates turbine performance to an unacceptable level, a cleaning operation must be performed, Deposit cleaning can be done with turbine on-line or off-line. On-line cleaning is preferred since it restores turbine performance without shutdown. Generally, the restoration of performance is less than complete and the efficiency degrades with successive on-line cleaning operations. After several cycles, the turbine must be taken off-line for a thorough cleaning.

Ash deposits from liquid fuel combustion have been cleaned on-line by injecting ground nutshells through the combustor dilution holes (Rose, 1982). Fine (1000 μm) and coarse (4000 μm) grinds of nutshells have been used in a cascade system fired with residual oil doped with MgO under full operating conditions: 1394-1533 K firing temperature, 628-1172 K surface temperature. The fractional throat area recovery was found to depend upon

the size of nutshells, firing temperature, and blade surface temperatures. Large nutshells yielded better cleaning than small nutshells. The deposit tenacity largely determined its susceptibility to nutshelling. The lower the blade/gas temperature, the greater the area recovery. With water-cooled blades, almost 100% area recovery could be obtained with large nutshells. Ash cleanability was found to be more sensitive to blade rather than gas temperature.

The technique of injecting crushed nutshells with dilution air while maintaining 1366 K combustor exist temperature has also been tested for CWM ash deposits (Kimura et al., 1987). A large fraction of the leading edge and pressure-side deposits were removed by direct inertial impaction. The technique was ineffective against the suction-side deposits, apparently because of insignificant secondary impaction of particles rebounding from pressure surface. In this particular series of tests, no recovery of nozzle throat area was obtained because the throat closure was primarily due to deposit buildup on the suction side.

A thorough off-line cleaning procedure involves turbine shutdown, water washing of blade deposits, and refiring. After shutdown, water is generally sprayed through the combustor fuel nozzle with turbine rotor on crank speed. The low air flow entrains injected water droplets and carries them to the blade surface. The deposit is soaked and saturated with water and the water-soluble portion dissolves. The deposit is weakened and on refiring of combustor blown off. Experience with residual-oil firing indicates that for water-cooled blades (672-944 K metal temperature), 100% area recovery can be obtained after a water washing/refiring sequence (Rose 1982). For air-cooled blades (1172-1233 K), up to 90% of throat area lost to deposits could be restored with water washing. The adherent deposit consisted mostly of water-insoluble MgO.

In one series of tests, blade deposits (mostly insoluble) from CWM combustion were subjected to water washing for 30 minutes, followed by refiring of combustor on oil for three minutes (Kimura, 1987). Only a minimum removal of pressure-side deposit was observed, although water washing loosened much of the leading edge and pressure side deposits. Subsequent abrasive cleaning with nutshells removed much of the leading edge and pressure-side deposits. The suction-side deposits were almost completely removed by the water-washing procedure.

SODIUM SULFATE INDUCED HOT CORROSION

A topical report ANL/FE-89/3 was prepared describing a rational methodology for predicting N_2SO_4 induced hot corrosion of turbine alloys. The methodology is based on coupling of a fundamental sodium sulfate mass transfer model with static, accelerated corrosion laboratory tests at intermediate temperatures. The following conclusions have been drawn concerning Type II hot corrosion of cobalt-base alloys.

- Corrosion rate increases with turbine inlet temperature because of its influence on sodium sulfate mass transfer.
- Within 873-1173 K blade temperatures, there is a range where the corrosion rate is maximum and must be avoided. This conclusion may interfere with the desire to employ blade cooling as a means of limiting turbine fouling.

- It appears that selective cleaning of sulfur from fuel is a valid technique for improving corrosion resistance.
- Corrosion rate is quite sensitive to sodium impurity concentration. Sample calculations show that a blade (Co-30Cr) life exceeding 20,000 h/mm of tip wastage is possible for blade temperatures held between 1000 K and 1173 K if sodium concentration in the gas entering the turbine (T_{ip}=1550 K) is restricted to 40 ppb. Under the same conditions, the blade life decreases to 5000 h/mm of tip wastage if the sodium concentration is relaxed to 200 ppb.
- The higher the chromium content, the faster the rate of growth of the chromium scale, making the oxide film more protective. At chromium levels higher than about 37.5-40 wt %, the cobalt dissolution rate decreases significantly because of the absence of a liquid phase required for accelerated corrosion (Luthra 1985).
- In the Type II hot corrosion regime, addition of aluminum (up to 5 wt %) to Co-40Cr alloy almost always increases the corrosion rate by retarding the growth of the protective oxide scale. This effect is most promiment at high chromium levels where the liquid phase normally does not form. At higher temperatures, aluminum addition may be beneficial to suppress the vaporization of chromium oxide scale.
- The resistance of CoCrAlY coatings to low temperature hot corrosion is inferior to Co-Cr-X coatings containing greater than about 37.5% Cr and a small amount of an active element X. Even at high temperatures, the resistance of the high chrome cobalt coatings is comparable to the conventional CoCrAlY coatings (Luthra and Wood 1984).

The correlation methodology is generally applicable to Na_2SO_4 hot corrosion in a coal-fired gas turbine environment. Coal ash, however, may have a significant potassium content in addition to sodium. It is well known that combined sodium and potassium sulfates are more aggressive than either alone. In principle, our sodium sulfate mass transfer model with use of appropriate thermodynamic and transport data should be equally valid for potassium sulfate. The corrosion correlation will be more complicated since an extra variable, namely potassium sulfate mass fraction in the mixed salt deposit, must be included.

The presence of ash deposits on the blade surface may alter the Na_2SO_4 corrosion chemistry. The presence of unburnt carbon in the deposits may change the mode of corrosion attack from one of oxidation to sulfidation or even carburization. In some recent tests, corrosion of a CoCrAlY coating was observed after only a few hours of exposure to coal combustion particulates rich in unburnt carbon.

In a coal-fired gas turbine system, possible synergism between erosion and corrosion is also of concern. For example, depending on the oxidation kinetics, impacting flyash particles may erode the oxide scale exposing the bare metal underneath to catastrophic hot corrosion attack. In general, the corrosion behavior of a material is governed by the mechanical and chemical properties of the surface oxide scales and these are affected by the reactivity of the erodents. The phenomena of ash deposition and material erosion are somewhat mutually exclusive. Thus, one is likely to encounter either deposition-corrosion or erosion-corrosion regimes.

7. REFERENCES:

Ahluwalia, R. K., et al. 1984. Behavior of Coal Ash and Alkali Matter in a Coal-fired Gas Turbine System. 84-GT-217, 29th Int'l Gas Turbine Conference, Amsterdam, The Netherlands.

Ahluwalia, R. K., and Im, K. H. 1985. Mass Transfer of Trace Species from a Superheated Stream to a Subcooled Surface. Int'l J. Heat & Mass Transfer 28(11):2061-2070.

Ahluwalia, R. K., Im, K. H., Chuang, C. F., and Hajduk, J-C. 1986. Particle and Vapor Deposition in Coal-fired Gas Turbines. 86-GT-239, 31st Int'l Gas Turbine Conference, Dusseldorf, West Germany.

Ahluwalia, R. K., and Im, K. H. 1988. Correlation between Sodium Sulfate Mass Transfer and Low-temperature Hot Corrosion. 88-GT-133, Gas Turbine and Aeroengine Congress, Amsterdam, The Netherlands.

Ahluwalia, R. K., Im, K. H., and Wenglarz, R. A. 1989. Flyash Adhesion in Simulated Coal-fired Gas Turbine Environment. ASME J. Engng. for Gas Turbines & Power 111(4).

Ahluwalia, R. K., and Im, K. H. 1989. Fouling of Gas Turbine Passages. ANL/FE-89/2.

Anderson, R. J., and Romanowski, C. J. 1985. Deposition Tendencies for Selected Coals Combusted at Atmospheric Pressure, Second Annual Pittsburgh Coal Conference, Pittsburgh, PA.

Cha, S. S., Ahluwalia, R. K., and Im, K. H. 1989. Boundary Layer Nucleation. Int'l J. Heat & Mass Transfer 32(5):825-835.

Im, K. H., and Ahluwalia, R. K. 1989. Sodium Sulfate Induced Hot Corrosion in Gas Turbines. ANL/FE-89/3.

Kimura, S. G., Spiro, C. L., and Chen, C. C.. 1987. Combustion and Deposition in Coal-fired Turbines, ASME J. Engng. for Gas Turbines & Power 109:319-324.

Luthra, K. L., and Wood, J. H. 1984. High Chromium Cobalt-base Coatings for Low Temperature Hot Corrosion, Thin Solid Films 119:271-280.

Luthra, K. L. 1985. Kinetics of Low Temperature Hot Corrosion of Co-Cr-Al Alloys, J. Electrochem. Soc. 132(6):1293-1298.

Rose, R. S. 1982. Advanced Cooling Full-Scale Engine Demonstration Program, EPRI-AP-2605

Spiro, C. L., Kimura, S. G., and Chen, C. C. 1987. Ash Behavior During Combustion and Deposition in Coal-fueled Gas Turbines, ASME J. Engng. for Gas Turbines and Power 109:325-330.

Spiro, C. L., Chen, C. C., Kimura, S. G., Wong, S., and Greegor, R. B. 1987. Characterization of Products from a Direct Coal-Water-Mixture Fired Gas Turbine, Fuel 66:563-567.

Wenglarz, R. A., Ames, F. E., Williams, J. R., and Wilkes, C. 1987. Combustion of Coal Water Fuels under Gas Turbine Conditions, Proc. 12th Int'l Conf. on Slurry Technology, New Orleans, LA.

LOW-PRESSURE-RATIO REGENERATIVE EXHAUST-HEATED GAS TURBINE

1. CONTRACT NUMBER: DE-AC21-89MC26051

CONTRACTOR: Massachusetts Institute of Technology
Energy Laboratory and
Department of Mechanical Engineering
Cambridge, MA 02139

CONTRACTOR PROJECT MANAGER: William J. Duggan

PRINCIPAL INVESTIGATOR: David Gordon Wilson

GRADUATE RESEARCH ASSISTANT: Luis A. Tampe

METC PROJECT MANAGER: Michael H. McMillian

PERIOD OF PERFORMANCE: January 13, 1989 - July 31, 1990

2. SCHEDULE/MILESTONES:

1989/90 Program Schedule

	J	F	M	A	M	J	J	A	S	O	N	D	J	F	M	A	M	J
Task 1 - LPR Cycle Study	XXXXXXXXXXXXXXXXXX																	
Task 2 - Engine Design								XXXXXXXXXXXXX										
Task 3 - Performance Analysis														XXXXXXXXXX				
Task 4 - Economic Assessment														XXXXXXXXXX				
Task 5 - Heat-Exchanger Fouling	XXXXXXXXXXXXXXXXXXXXXXXXXXXXXXXXXX																	
Task 6 Report																XXXXXXXXXXXXX		

3. OBJECTIVES.

The objectives are to study the exhaust-heated regenerative gas-turbine cycle in the form incorporating a high-effectiveness periodic-flow regenerator to decide on its feasibility, attractiveness and promise as a coal-fired power unit. Preliminary designs will be made of four alternative versions of the cycle. Two alternatives are the basic cycle with and without an intercooler in the compressor. For each of these alternatives, the type, size and configuration of the resulting engine are to be found if it is designed optimally from a clean sheet (the "blue-sky" design), and if the engine is designed using the maximum degree of commonality with one or more existing engines.

The size and configuration of a ceramix-matrix rotary regenerator will also be found. Because the feasibility of the cycle depends critically on the performance of the regenerator when operating between the clean compressed air delivered from the compressor and the products of coal combustion in the turbine exhaust gases (using the best available technology for the combustion and gas-cleanup system), an objective of the first part of the program is to examine the behavior of coal-ash particles as they impact actual rotating ceramic-matrix regenerators and are carried under the seal regions, and as they respond to various alternative methods of particle removal.

4. BACKGROUND STATEMENT.

THE EXHAUST-HEATED CYCLE.

In this cycle the heat addition between the compressor outlet and the turbine inlet takes place in a heat exchanger. The hot gas is formed by combustion of a fuel in part or all of the turbine-outlet stream. The combustion products then leave the heat exchanger and the engine without passing through the turbine (figure 1).

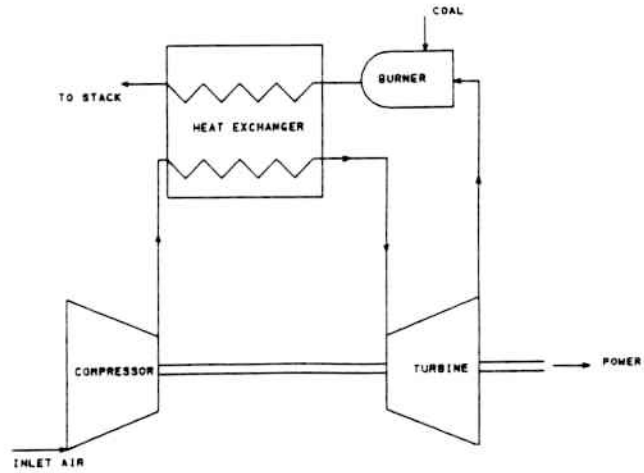


Figure 1. EXHAUST-HEATED CBEX CYCLE.

The exhaust-heated cycle was studied extensively by the late Prof. D.L. Mordell of McGill University from 1949 until about 1957 (Mordell, 1955). His preliminary analysis indicated that a heat-exchanger effectiveness of at least 75 percent is necessary to make the cycle attractive. Compared with a conventional open-cycle gas turbine with the same temperature ratio (turbine-inlet temperature divided by the compressor-inlet temperature), pressure ratio (compressor-outlet pressure divided by the compressor-inlet pressure), and component efficiencies, the exhaust-heated cycle will yield the same specific power. The thermal efficiencies of both cycles would be equivalent for the above case only if the heat-exchanger effectiveness of the exhaust-heated cycle were 100 percent.

Donald Mordell constructed an exhaust-heated gas turbine using a Dart gas turbine, a slagging cyclone combustor, and a specially designed shell-and-tube heat exchanger (figure 2). Mordell's rig showed that dry-ash fouling of the heat-exchanger surface was not nearly as critical as he at first had thought. The slagging cyclone furnace proved to be extremely well suited for combustion

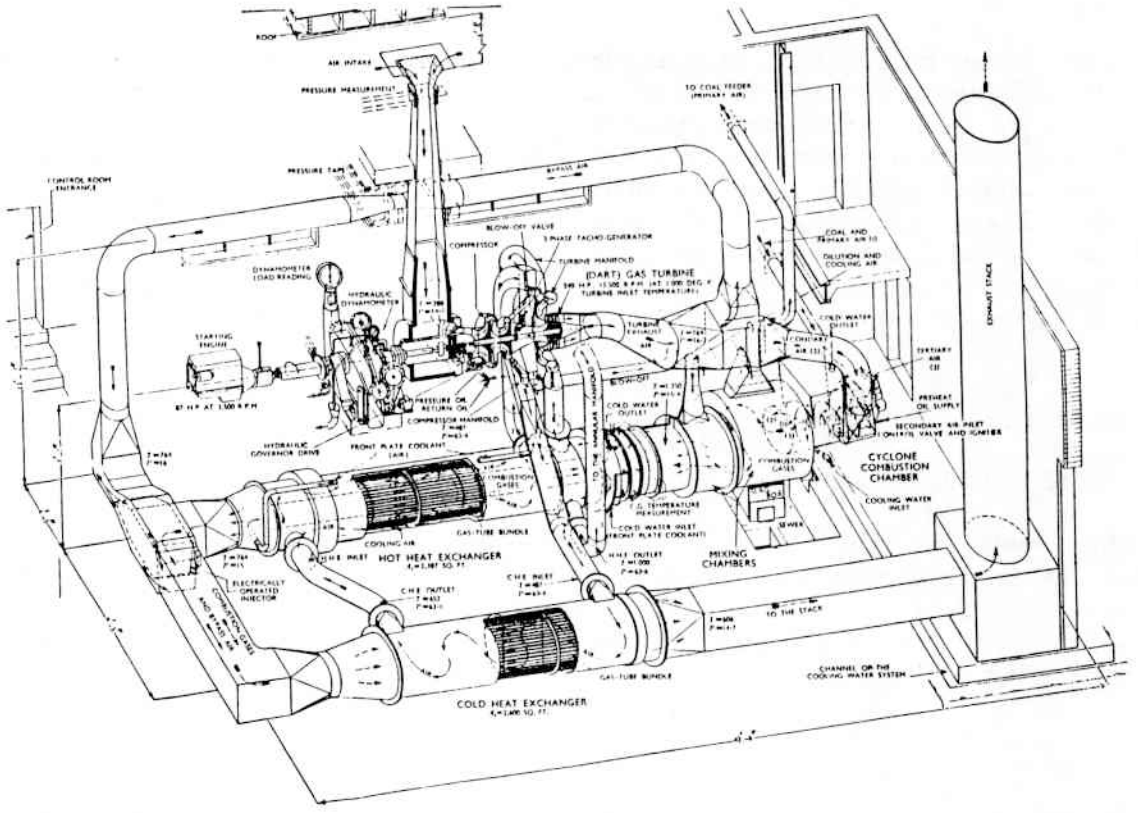


Figure 2. MORDELL'S EXHAUST-HEATED GAS TURBINE (from Mordell, 1955).

of coal at atmospheric pressure and the high turbine-exit air temperatures. The heat-exchanger tubes showed some corrosion due to sulphur condensation. Despite the very low effectiveness of his heat exchanger, Mordell's unit demonstrated that the exhaust-heated cycle is a practical way of burning coal in the gas turbine.

Although Mordell achieved successful long-duration running, the cycle attracted few later imitators. The principal reason was the use of a metallic tubular heat exchanger of 60 percent effectiveness. Thus a large proportion of the fuel heat was lost at the start and the engine efficiency decreased accordingly. The turbine-inlet temperature was reduced from its design value of 1100K, 1520F, to 1000K, 1340F, because of the limitations of the metallic heat exchanger with its highly stressed tubes. The thermal efficiency and specific power were thereby further reduced, and the actual power was 400 kW (540 hp) instead of the design value of 625 kW (840 hp).

The program proved the concept, however: erosive and corrosive damage to the turbine in a coal-burning gas-turbine engine could be eliminated by employing the exhaust-heated cycle.

LOW-PRESSURE-RATIO (LPR) CYCLE.

There are two principal choices of thermodynamic gas-turbine cycle: the "simple" or CBE (compressor-burner-expander, or turbine) cycle, and the heat-exchanger or CBEX cycle (the "X" signifying the addition of a heat exchanger) (Wilson, 1984). An exhaust-heated cycle inherently works on the CBEX cycle because the fuel merely increases the temperature of the turbine exhaust before as much heat as possible is recovered in the heat exchanger and trans-

ferred to the air leaving the compressor. For each thermodynamic cycle there is an optimum pressure ratio for each combination of temperature ratio and component losses. For the simple CBE cycle the pressure ratio for maximum thermal efficiency is high, forty-to-one or higher for today's high-temperature turbines. For the heat-exchanger (CBEX) cycle the pressure ratio for maximum cycle efficiency reduces as component losses are reduced. The loss having the greatest effect is the thermal loss in the heat exchanger.

THE USE OF A CERAMIC REGENERATOR.

The advantages of an exhaust-heated cycle could be realized only if a higher-temperature heat exchanger is used. Hague International is incorporating its ceramic recuperator (LaHaye and Zabdotny, 1989). An alternative device is the rotary ceramic regenerator.

In this device the ceramic is unstressed by pressure or centrifugal forces and enables the heat exchanger to handle very high temperatures. At present the limit (for gas- or liquid-fueled turbine engines) is a gas temperature at heat-exchanger inlet of 1100 - 1200C (2000 - 2150F), but experts within the industry forecast no difficulty in reaching, with development, the same temperature as is used for uncooled ceramic rotor blades, 2500F, 1375C. In a coal-burning application, so high a temperature would probably not be used. It would be desirable to limit the temperature to that at which a dry ash could be reasonably assured for some coals, about 1100C or 2000F. This has the pronounced advantage that any of several ceramic materials could be used, allowing the choice of one resistant to the products of coal combustion. The question of ash stickiness is discussed briefly below.

The disadvantages of the rotary ceramic-matrix regenerator are:

1. high leakage under the high-pressure seals;

2. a present limitation in the size of heat exchanger that can be produced, meaning that with current size limits, engines of sizes over one megawatt will have at least two disks; and

3. a damaged reputation following disastrous material failures in an ambitious Ford truck-engine program in the early 1970s. An improved material was quickly substituted, but industry confidence was lost, and the program shut down.

The leakage is partly a function of size: the level found in the DOE-NASA CATE (Ceramic applications in turbine engines) program (Helms 1984) in a standard 400-hp (300-kW) twin-regenerator turbine was about four percent. There is little doubt that greatly improved seals could be developed. A level of leakage of two percent has been assumed to be possible for our analysis (Hagler 1988).

COMBUSTION AND SULFUR REMOVAL.

The engine and cycle as described can use the best available technology for both combustion and sulfur removal. The sulfur treatment can be incorporated into the combustion system, or can be located between the combustor and the heat-exchanger inlet, or in the cooler stream leaving the heat exchanger.

This cool stream could then be passed to a waste-heat boiler, but the temperature will be low enough, about 180C or 360F, that there will be comparatively small potential for a "bottoming-cycle" engine.

All of these aspects - combustion, sulfur removal and waste-heat recovery - are considered to be outside the scope of the present work.

ASH STICKINESS.

The principal uncertainty in any coal-burning plant concerns corrosion, deposition and erosion resulting from the products of combustion. Only deposition presents a serious problem for the exhaust-heated cycle.

Deposition depends crucially on the stickiness of the ash and on the temperature of the gases and of the surfaces. The ash stickiness will be highly variable for different coals and different degrees of beneficiation. Using a relatively low firing temperature will ensure that the main constituents of the ash are solid, but the presence of alkalis in the coal could bring about stickiness in the high-temperature region of the heat exchanger. (A program is proposed below to study this question and to produce solutions if, in fact, there is a problem.)

5. PROJECT DESCRIPTION.

CYCLE STUDIES.

Cycle-performance-prediction programs are to be used to analyze two principal alternative forms of the exhaust-heated gas-turbine cycle: one without intercooling (CBEX cycle, figure 1) and one with an intercooled compressor (CICBEX cycle, figure 3). Various turbine-inlet temperatures, pressure drops,

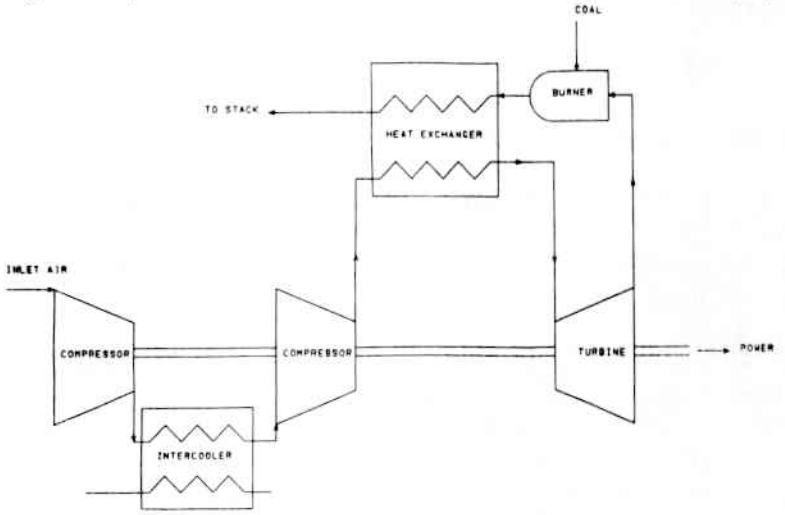


Figure 3. EXHAUST-HEATED CICBEX CYCLE.

heat-exchanger effectivenesses, and component efficiencies are to be examined as appropriate for various levels of technology. Data for the best-available technology for the combustion and sulfur-removal processes are specified.

Two cycles have been selected for preliminary design. One is a so-called "blue-sky" design: one in which the designer assumes an optimized design for

a commercial production run of a certain number of units (to be decided upon). Another choice of cycle is for a unit the turbomachinery components of which could be constructed largely from available gas-turbine engines.

ENGINE PRELIMINARY DESIGN.

A mean-diameter design (as is normally carried out for preliminary design) will be made of the compressor and turbine of the "blue-sky" engine. Blade rows having low aerodynamic loading will be used, to favor a long life and high efficiency rather than the extreme of lightness and compactness.

The axial-flow turbine will also be lightly loaded. We will specify a minimum of three stages, even though it would be possible to accomplish the required work in a single stage. The use of three stages removes the serious efficiency penalty from the leaving losses of a single stage (figure 4). The blade speed is reduced from that required for a single-stage design, greatly reducing the steady-state stresses and the potential of damage from foreign objects (there should, of course, be no particulates from combustion of coal in an exhaust-heated cycle). The low stresses give the designer the freedom to choose from a wider range of materials than would otherwise be available.

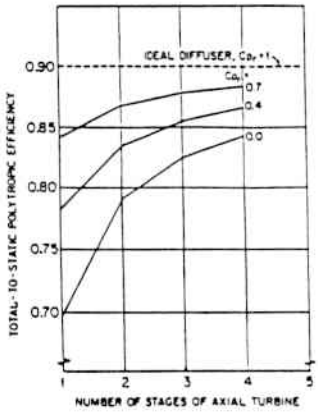


Figure 4. AXIAL-TURBINE EFFICIENCY AS FUNCTION OF NUMBER OF STAGES AND DIFFUSER EFFECTIVENESS (from Wilson, 1984).

We have tentatively chosen a design power level at a fairly low figure, between 1 and 2 MW. The reasons are that, for gas turbines, this size range is large enough for compressor and turbine efficiencies to be within a point or two of their final asymptotic large-size values; it is a range that allows a choice of heat-exchanger type; and it is a popular power level that would enable a manufacturer to plan for a long production run and thus to achieve significant cost savings.

Heat-Exchanger Design.

The turbine-inlet temperature will have been chosen in the cycle studies with reference to post-cleanup combustion-gas-deposition characteristics, and to present and likely future capabilities of suitable heat-exchanger materials. Preliminary-design studies of alternative heat-exchanger configurations will be made on a lumped-parameter basis (ie using mean-temperature fluid properties on each side).

PERFORMANCE ANALYSIS.

The plant performance at reduced load and speed (and at various combinations) and at high-ambient-temperature conditions is to be predicted using cycle-analysis codes.

ASSESSMENT OF SYSTEM ECONOMICS.

The manufacturing cost of the proposed engine(s) is to be based on the preliminary-design drawings. We shall estimate the weight of the principal components and estimate the manufacturing cost based on the known cost of producing items of similar materials, similar complexity and similar production rates. The running cost can be calculated directly from the performance prediction and from a duty cycle that will be proposed to the program manager.

EXPERIMENTAL STUDIES OF HEAT-EXCHANGER FOULING.

Some simple preliminary experiments on the behavior of dry particles entering a regenerative heat exchanger will be carried out on an actual ceramic-matrix rotary-regenerator core. A fan in a loop circuit will be used to induce flow at one part of the core and to force flow out through a second part. We will use velocities similar to those at design-point conditions, but the gas densities will be between those of the hot and cold flows. The core will be rotated, and measurements of the change in the pressure drops through the core will be recorded (over a test duration of some hours) with increasing loading of dry and, if used, sticky particles.

High-magnification high-speed video records will be made of particles striking the face of the matrix and of their adherence or removal under various conditions. Pressure-drop-flow data will again be taken.

If complete cleaning is not obtained in conditions equivalent to running conditions, seal modifications will be tried to test the possibility of removing deposits off the face of the matrix.

6. RESULTS/ACCOMPLISHMENTS.

EXPERIMENTS ON REGENERATOR FOULING.

The apparatus is now (September 1989) being built and debugged, and no data are yet available.

THERMODYNAMIC CYCLES.

To avoid ash stickiness the maximum cycle temperature in both the CBEX and the CICBEX cycles was selected at 1373 K (2000 F). (For some coals, this temperature requires a degree of gas cleanup.) The maximum cycle temperature will of course occur at the combustor exit. (See figures 1 and 3.) The remaining variables in the cycle studies were thus the pressure ratio, the heat-exchanger effectiveness, and the component efficiencies. A computer program was developed to calculate the thermal efficiency of both the CBEX and the CICBEX cycles for varying pressure ratios. In addition, the computer

program sized the required ceramic regenerator(s) and calculated the mass-flow-rate leakage across the heat-exchanger seals.

The highest effectiveness apparently so far achieved in a heat exchanger of this type is slightly over 0.95 in the Allison GT 404. An effectiveness of 0.975 could be obtained on that unit by approximately doubling the current matrix thickness (Wilson and Korakianitis, 1985).

Hagler (Hagler 1987) developed an equation for calculating the mass-flow-rate leakage across the seals of the regenerator. The leakage is directly proportional to the pressure ratio of the gas turbine, r, and to the size of the regenerator. This equation was incorporated into the computer program we developed to calculate the cycle efficiency. Obviously, the larger the percentage or proportional leakage, the more the thermal efficiency and specific power will be penalized since less flow is available to pass through the expander. We feel that Hagler's equations are pessimistic (leakages of 3 percent and more across the seals) because they do not account for the labyrinth effect of the matrix-seal combination, and because actual test results showing lower leakages have been reported. We have accordingly reduced the leakage by a constant factor to determine the effect this would have on the overall thermal efficiency. (Wilson and Tampe, 1989).

We present the data as graphs showing thermal efficiency versus specific power for various pressure ratios. Here specific power has been defined as:

$$W' \equiv \text{specific power} \equiv \frac{W_{net}}{CpM_i T} \qquad (1)$$

Where Wnet ≡ net cycle work
Cp ≡ specific heat of air
m^i ≡ inlet mass flow rate to the compressor
T ≡ inlet air temperature to the compressor

The expander and compressor polytropic efficiencies were specified to vary with pressure ratio. The details of the modelling equations are given in reference 8 (Wilson and Tampe, 1989).

The cycle thermal efficiency is defined as usual:

$$\text{thermal efficiency} \equiv \frac{W_{net}}{\text{Heat Added}} \qquad (2)$$

Here the net work, Wnet, includes mechanical losses in the shaft, the power required to supply the coal (assumed to be 1/3 hp), the power needed for the turbine oil pump (assumed to be about 3 hp), and the power needed to rotate the regenerator.

The cycle pressure losses used in the program were assigned as follows. For the CBEX cycle with a heat-exchanger effectiveness of 0.975 the pressure losses were 9 percent plus whatever pressure drop was calculated for the regenerator (usually of the order of 4 percent). For the CICBEX cycle with an effectiveness of 0.975 the losses were 11 percent plus the calculated regenerator pressure drop (as before these were of the order of 4 percent).

EXHAUST-HEATED CBEX CYCLE

Once the mass-flow rate, the component efficiencies, and the regenerator effectiveness were selected we needed to choose only an appropriate pressure ratio. Figure 5 shows the performance of the gas-turbine engine for pressure ratios ranging from 2 to 12. The maximum thermal efficiency, equal to 0.495, occurs at a pressure ratio of 2.6 and has a specific power also of 0.495. The cycle having maximum specific power, equal to 0.784, occurs at a pressure ratio of 7 and has a thermal efficiency of 0.418. As the pressure ratio increases mass-flow losses in the regenerator seals also increase; for the two cases above the leakage increases from 2.1 percent to 5.8 percent, using a simple model of the regenerator seals.

The pressure drop across the compressed-air side of the regenerator decreases with increasing pressure ratio. If the pressure drop is allowed to become too small the flow entering the regenerator from that side will not distribute evenly over the entire face area, thus leading to a decrease in the heat transferred. For the two extreme cases being discussed the compressed-air pressure drop across the regenerator falls from 1 percent to only 0.1 percent.

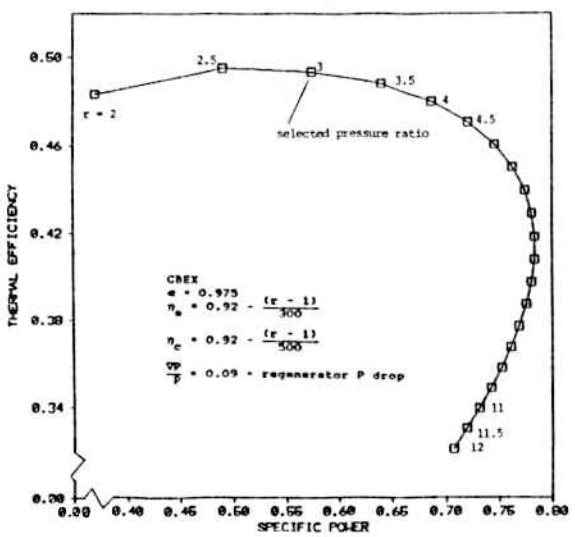


Figure 5. CBEX EFFICIENCY CURVE.

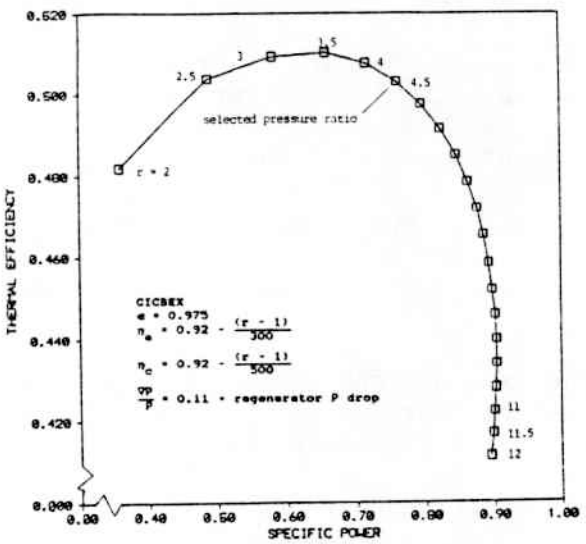


Figure 6. CICBEX EFFICIENCY CURVE.

The pressure ratio of the CBEX cycle was chosen at a value higher than that giving maximum thermal efficiency, it being our judgment that an economic optimum would be reached with a somewhat higher specific power (a lower plant first cost). The economically justifiable optimum pressure ratio would be chosen at a later phase in the design. The resulting CBEX cycle is:

air mass-flow rate	=	11.51 kg/s
pressure ratio	=	3.0
thermal efficiency	=	0.49
mass-flow leakages	=	2.25 percent
specific power	=	0.58
net work	=	2.0 MW
pressure losses	=	12.9 percent
coal consumption	=	0.12 kg/s

EXHAUST-HEATED CICBEX CYCLE

A few simple runs with the CICBEX modified program showed that a mass flow rate of only 8.7 kg/s (19 lbm/s) would be needed to produce 2 MW with this cycle.

Figure 6 contains the result of varying the overall pressure ratio from 3 to 12. The maximum thermal efficiency of 0.51 occurs at an overall pressure ratio of 3.4, with a specific power of 0.65. The predicted mass-flow leakage at this pressure ratio is 2.9 percent and the cold-side regenerator pressure drop is 0.7 percent. The maximum specific power of 0.904 occurs at a pressure ratio of 10. The mass leakage and cold-side pressure drop for the latter are predicted to be 8.3 percent and 0.12 percent respectively.

As in the CBEX cycle, the final pressure ratio was selected between that giving maximum specific power and that giving maximum thermal efficiency. The obtained CICBEX cycle is summarized below:

air mass-flow rate	=	8.74 kg/s
pressure ratio	=	4.5 (ie, about 2.2 in each compressor)
thermal efficiency	=	0.50
mass-flow leakages	=	4.1 percent
specific power	=	0.76
net work	=	2.0 MW
pressure losses	=	14.6 percent
coal consumption	=	0.12 kg/s

CONCLUSIONS

We have selected the optimum pressure ratio for both the CBEX exhaust-heated cycle and the CICBEX exhaust-heated cycle. The choices made in both cases concerning component efficiencies and regenerator effectiveness are reasonable and should be possible within our present state of technology. The small improvements in thermal efficiency and specific power of the intercooled cycle do not appear to justify the additional first cost and the cooling-water requirement.

RECOMMENDATIONS

When this work was proposed it was stated that "the engine and cycle as described can use the best available technology for both combustion and sulfur removal", and these aspects were considered to be outside the scope of the work proposed. However, the performance of the heat exchanger is critically dependent on, in particular, fouling of the passages, so that it is vital that alternative strategies be considered should fouling be found to be a serious problem. The principal constituent of concern is alkali, which could contribute to ash stickiness and to deposition from the vapor phase inside the very small passages of the ceramic-matrix regenerator.

The following appear to be the principal alternative strategies.

1. Allow vapor-phase deposition to occur until the heat-exchanger performance has deteriorated to a critical level. At this point use supplemental, eg, natural-gas, firing and reduce the speed of rotation

of the ceramic matrix so that it increases in temperature throughout and causes the deposits to be "boiled off" the passages. Condensing capture surfaces could be provided downstream of the heat-exchanger exhaust to reduce alkali emissions and depositions on boiler surfaces.

2. Use two heat exchangers in series: a high-temperature exchanger in which the alkali would remain in the vapor phase, and a low-temperature exchanger before which the alkali would have already been deposited. In between would be a small switched unit in which the gases would be cooled to just below the alkali-solidification temperature, perhaps by water spray, so that the solid alkali could be removed, perhaps by centrifugal separator.

3. Use a combustor-outlet temperature below that at which any coal will have any ash stickiness present. This may require that the temperature be restricted to below 1600 F, 1145 K, at which the thermodynamic efficiency and power output of the cycle would be considerably reduced.

4. Remove the alkali vapor through the system under development by Argonne National Laboratories and funded by DOE/METC. This is essentially a fixed-bed granular sorber using activated bauxite.

5. Employ the system being developed by GE under DOE/METC funding to "render the ash nonadherent", principally through kaolin addition.

6. Use the Allison/Westinghouse or Solar slagging-combustor plus hot-gas-cleanup systems, also funded by DOE/METC. These promise to produce an outlet stream substantially free of particulates and with greatly reduced alkali content.

7. Substitute a pebble heater, as developed by Babcock and Wilcox, (Norton 1946) for the rotary ceramic-matrix regenerator. Such a device should have a reduced susceptibility to the effects of alkali deposition.

8. Substitute a flexible-band regenerator, as originally proposed for study. This type of regenerator, besides being less susceptible to the effects of alkali condensation, should have a negligible rate of mass-flow leakage, giving substantial improvements in cycle thermal efficiency and in specific power. (This is a novel type of heat exchanger for which a preliminary patent filing has been made by MIT.)

Any one of these approaches could provide a complete solution to any ceramic-matrix deposition problem involving alkali or particulate constituents.

8. REFERENCES

Hagler, Carla D., The Design of a Ceramic Rotary Regenerator for a Regenerated Low-Pressure-Ratio Gas-Turbine Engine, M.S. Mechanical Engineering Thesis, MIT, April 1987.

Hagler, Carla D., and David Gordon Wilson, Considerations for the Design of High-Effectiveness Ceramic Rotary Regenerators for Regenerated, Low-Pressure-Ratio Gas-Turbine Engines, presented at Joint Propulsion

Conference, Boston, MA, July 1988.

Helms, Harold E., Peter W. Heitman, Leonard C. Lindgren and Samuel R. Thrasher, Ceramic Applications in Turbine Engines, final report, General Motors Corp., Allison Gas Turbine Div., report NASA CR-17415, October 1984.

LaHaye, P.G. and Ernie Zabdotny (1989) Externally Fired Combined Cycle (EFCC), (proceedings of a DOE METC conference, to be published).

Mordell, D.L., An Experimental Coal-burning Gas Turbine, Proc. of Institution of Mechanical Engineers, 1955, Vol. 169, No. 7.

Norton, C.L., Jr., The Pebble Heater - A New Heat-Transfer Apparatus, Jl. Amer. Ceramic Soc., Vol. 29, No. 7, pp. 187-193, NY, 1946.

Wilson, David Gordon, The Design of High-Efficiency Turbomachinery and Gas Turbines, MIT press, Cambridge, MA, 1984.

Wilson, David Gordon, and T.P. Korakianitis, High Efficiency Brayton-Cycle Engines for Marine Propulsion, MIT Sea Grant Program, MIT, 1985.

Wilson, David Gordon and Luis A. Tampe, Proposed Cycles for the Coal-Fired Exhaust-Heated Gas Turbine, Report prepared on August 11, 1989 for DOE Contract DE-AC21-89MC26051, MIT.

ADVANCED TURBINE DESIGN FOR COAL-FUELED ENGINES

1. CONTRACT NUMBER: DE-AC21-89MC26052

CONTRACTOR: United Technologies Research Center
Silver Lane
East Hartford, CT 06108
Phone (203) 727-7000

PROJECT MANAGER (CONTRACTOR): Bruce V. Johnson

PRINCIPAL INVESTIGATOR: Joel H. Wagner

METC PROJECT MANAGER: Donald W. Geiling

CONTRACT PERIOD OF PERFORMANCE: December 19, 1988 - June 19, 1991

2. SCHEDULE/MILESTONES:

PROGRAM SCHEDULE

Tasks:	FY1989 O N D J F M A M J J A S	FY1990 O N D J F M A M J J A S
o Turbine Airfoil Design Study	******----	
o Erosion and Deposition Models	******	
o Effects of Airfoil Designs on Erosion and Deposition	****----------	
o Three Dimensional and Rotor-Stator Interaction Effects	*----------	
o Report		****

3. OBJECTIVES:

The primary objective of this project is to identify and test turbine airfoil shapes and aerodynamic characteristics which may result in improved turbine and vane life for coal-fueled heat engines. The effects of particles on turbine airfoil erosion will be determined analytically with the airfoil aerodynamic flowfield and a particle trajectory analysis. Although most of the analytical work with the 2-D trajectory analysis will be focused on the aerodynamics at the midspan location, a literature survey and an exploratory analysis of the 3-D flow effects on the erosion characteristics will be conducted. The anticipated result of this program will be a better understanding of the effects of the turbine stage design parameters on erosion which, ultimately, may lead to improved turbine life through the effective management of particles from the combustion process.

4. BACKGROUND STATEMENT:

Current stationary gas turbines have been developed to burn relatively clean fuels, i.e. oil and natural gas. Much of the stationary gas turbine technology has been derived from aircraft gas turbines where the emphasis has been placed on high temperatures, light-weight components and high thrust. The aircraft engines burn clean petroleum fuels which produce relatively small amounts of particulates and condensable solids during normal combustion. Coal-fueled gas turbines will operate in a significantly different and hostile environment, with particulates and condensible material in the combustion products, where durability is more important than weight. Three significant problems, that were identified early in the development of coal-fueled engines, are the rapid wear of the turbine airfoils due to particulate erosion, the accumulation of deposits on portions of the airfoil surfaces due to slag deposition and the rapid corrosion of airfoils after the breakdown of surface coatings. The technology development study contained in this program is focused on improving the durability of the turbine through the development of erosion resistant airfoils and turbine operating conditions.

5. PROJECT DESCRIPTION:

This program compliments current coal-fueled gas turbine efforts under the Heat Engines program at METC. The total program is divided into two phases. Phase I - Turbine Airfoil Selection is an analytical effort which consists of the design and evaluation of turbine stage designs for comparison with a baseline turbine stage. The P&W Turbine Design System is used to design airfoils with aerodynamic characteristics which are expected to decrease particle erosion. The United Technologies Large Scale Rotating Rig will be used as a model for the first stage of the baseline design. A particle trajectory computer code and a surface erosion model are used to assess the relative merits of the turbine stage designs. Phase II - Optional Turbine Airfoil Testing and Verification is a combined analytical and experimental study with particle trajectory and aerodynamic experiments in a stationary cascade. Phase II will determine whether the particle traces in an advanced gas turbine airfoil blade row are accurately predicted by the UTRC particle trajectory code.

A mathematical model is employed to assess the erosion on the surfaces of the airfoils. A surface erosion model was chosen from the literature and modified as required. This model is based on previously published studies and ongoing coal-fired combustion and turbine research.

The effects of the airfoil design on erosion will be determined from the aerodynamic and particle trajectory/surface interaction calculations. The analysis used to determine the aerodynamic response of coal and ash particles in the turbine stage is described by Dring et al. (1975). His analysis of the equations of motion for particles shows that two parameters, the Stokes number, St, and a particle density Reynolds number, σ_p, govern the trajectories of particles (Equations 1 and 2).

For a given flow flowfield, only two parameters are varied to do a parametric particle trajectory analysis for a given set of particle initial conditions (i.e. initial location, speed and direction).

$$St = (\rho_p U_i D_p^2)/(18\mu_i b_x) \qquad (1)$$

$$\sigma_p = (Re_{b_x})/(\rho_p/\rho_i) \qquad (2)$$

The initial speed and direction of particles for the stationary vane are coincident with the flow. However, the initial speed and direction of particles for the rotating blade row are determined from a statistical analysis of the particles which exit the stationary blade row. In this manner, the particle parameters are transferred from the stationary reference frame to the relative reference frame of the rotating blades.

The particle trajectory analysis is performed for many particle initial locations for ranges of Stokes and particle density Reynolds numbers to obtain a statistical distribution of particle impact parameters on the airfoil surfaces. These surface interaction parameters are input to a surface interaction analysis code. The code yields surface distributions of erosion rate based on the particle loading at the turbine inlet.

ANALYSIS OF RESULTS

Erosion results for the airfoils of each turbine stage will be compared to the results of the baseline stage. Criteria for the comparison of the results will include local peak values of erosion as well as integrated surface averages. In this manner each turbine stage design will be rated for erosion resistance.

6. RESULTS/ACCOMPLISHMENTS:

Typical baseload operating conditions for the turbine simulation have been specified from discussions with the DOE COTR. Gas products of combustion of CWS (Coal Water Slurry) fuel have been determined for meanline, flow path and trajectory calculations. The meanline design for the baseline turbine has been completed. Particle rebound parameters have been developed from the literature and are used in the trajectory calculation code. A literature survey of erosion results has been completed. A basic erosion model has been chosen and incorporated in a post processing trajectory analysis code (PPTAC). The ranges of particle parameters for analysis have been established from review of the open literature and notes received from the DOE COTR. Particle trajectory calculations for the baseline turbine first stage have been completed. Each of the technical items mentioned is discussed in detail below.

BASELOAD OPERATING CONDITIONS

The turbine baseload operating conditions have been specified and are listed below.

METC Specified Parameters:

- Rotation Rate = 3600 rpm
- Turbine Pressure Ratio(basis: inlet/atm.) = 12.2
- Turbine Inlet Pressure = 180 psia
- Turbine Inlet Temperature = 2100 F
- Maximum Turbine Blade Surface Temperature = 1400 F

With the wide range in unit power ratings of the demonstration programs (2 to 200+ MW systems), the 75 to 100 MW power rating range was chosen for the gas turbine simulation. Turbine engines of this size typically have 3 to 4 turbine stages. A three stage turbine was chosen with the idea that at least one of the new turbine designs would decreased stage loading, thereby, requiring an additional stage to maintain a fixed power rating.

GAS PRODUCTS OF COMBUSTION

Gas products of combustion of CWS fuel have been determined for the meanline, flow path and trajectory calculations. The products of combustion were determined using the coal properties of the UCC-1 coal of Rosfjord (1986) mixed to a 50 percent solids loading instead of 60 percent, as indicated in TABLE II of that report. This coal water slurry (CWS) fuel was subsequently treated as a hydrocarbon fuel with the following molecular structure.

$$C_{0.2375}H_{0.5581}O_{0.2004}N_{0.0039}$$

A combustion analysis to determine the proper mixture ratio to obtain the specified turbine inlet temperature resulted in a fuel-lean fuel/air ratio of 0.065 lbCWS/lbmAIR (equivalence ratio of 0.37). A fuel/air ratio for DF2 fuel (#2 heating fuel), used in lieu of CWS in the meanline code, was determined for use in the turbine simulation analyses. This was completed by determining the fuel/air ratio for DF2 (simulated by the molecular structure CH_2) to obtain similar ratios of gas products from the combustion of CWS. This analysis resulted in a fuel/air ratio of 0.032 lbmCH_2/lbmAIR (equivalence ratio of 0.47). The DF2 fuel specification prompts the meanline code to evaluate the properties of the combustion products mixture rather than requiring user input properties.

MEANLINE DESIGNS

The goal of the baseline meanline design was to design the baseline turbine which would include a first stage with velocity triangles similar to that of the UTRC Large Scale Rotating Rig (LSRR) and would produce a net power in the range of 75 to 100 MW. Additional design parameters were chosen for the first stage of the meanline design.

These parameters were selected based on the operating characteristics of the UTRC LSRR (i.e. C_x/U) and typical gas turbine power plant values (i.e. Velocity Ratio, V_m^x).

A cross section of the first stage airfoils for the baseline turbine is provided in Figure 1. The meanline design for the baseline turbine

is shown below in Table 1. The second and third stages are shown to substantiate the validity of the first stage baseline design. A thorough description of the mechanics of gas turbine meanline analysis is described by Oates (1978).

Table 1. Baseline Turbine Meanline Design.

Net Power Unit Rating, MW	79
Turbine Power, Btu/sec	201730
Turbine Flowrate, lbm/sec	670
Pressure Ratio	11.3 P_{tin}/P_{tout}
Turbine Inlet Temp., F	2100

	First Stage	Second Stage	Third Stage
Pressure Reaction (%)	50.0	50.0	50.0
Temperature Reaction (%)	54.7	61.9	63.5
Percent Work Split	26.9	36.6	36.5
Inlet Radius Tip, in.	37.89	38.08	43.37
Inlet radius Root, in.	32.51	32.17	28.98
P_t/P_s	1.73	---	---
Efficiency	87.8	---	---
C_x/U	0.58	---	---

PARTICLE TRAJECTORY CODE

The UTRC Particle Trajectory Code is used to calculate particle trajectories within the airfoil cascade. The particle equations of motion are solved as described by Dring et al. (1979). Flowfield information is obtained from a Cascade Flow Analysis Code (CASPOF). Trajectory results and surface interaction data are stored in a database for analysis by the Post Processing Trajectory Analysis Code.

Particle Aerodynamic Drag Model

Particle trajectories are calculated based on the relative velocity between the particle and the fluid. The difference in fluid and particle speed and direction imparts an accelerating force on the particle due to aerodynamic drag. All other forces on the particle are appropriately neglected as described by Hussein and Tabakoff (1973). The aerodynamic drag coefficients used by Dring and the present program are shown algebraically and graphically in Figure 2. Those of Hussein and Tabakoff are also shown graphically for comparison.

Particle Rebound Model

Restitution coefficients for fly-ash have been developed from the results of Tabakoff and his coworkers for coal ash particles and a variety of potential airfoil materials. This generic rebound model reflects the general response of several different particles and surface materials. The tangential and normal velocity rebound parameters developed for this program are presented below and in Figure 3.

Tangential Velocity Restitution Coefficients:

$$V_{t2}/V_{t1} = 1.0127 - 1.3458*B_r + 0.9569*B_r^2 - 0.2263*B_r^3 \quad (3)$$

Normal Velocity Restitution Coefficients:

$$V_{n2}/V_{n1} = 0.9813 + 0.0907*B_r - 2.7278*B_r^2 + 3.5867*B_r^3 - 1.1964*B_r^4 \quad (4)$$

where B_r is expressed in radians relative to the surface.

	Vane	Blade
R_{mean}, in.	35.2	35.2
b_x, in.	5.317	5.685
T/b_x	1.300	0.956

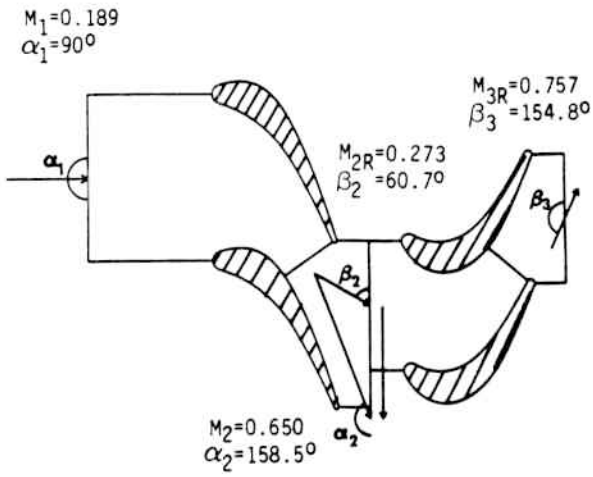


Figure 1. First Stage of Baseline Turbine.

$Re \le 1.0 \qquad C_d = 4.5 + 24/Re$

$1.0 \le Re \le 60$

$$C_d = 10^{1.455 - 0.842 \log Re + 0.067 \log Re^2}$$

$60 \le Re \le 3000$

$$C_d = 10^{2.007 - 1.383 \log Re + 0.199 \log Re^2}$$

$3000 \le Re \qquad C_d = 0.4$

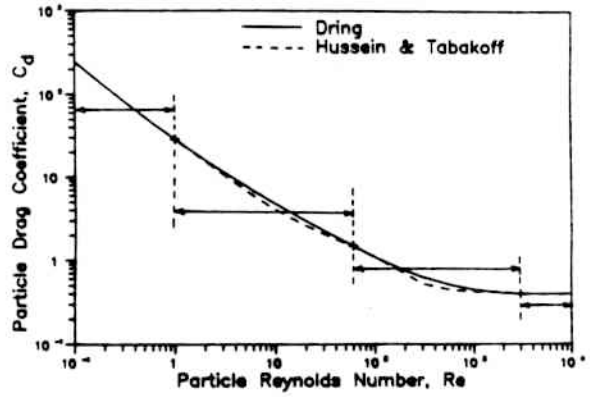


Figure 2. Aerodynamic Drag Coefficients.

POST PROCESSING TRAJECTORY ANALYSIS CODE (PPTAC)

The UTRC PPTAC is used to analyze trajectory results from the "First Pass" and "Second Pass" particle trajectory calculations. Results from the "First Pass" are used to concentrate the initial starting locations of the particles which will hit the airfoil for the "Second Pass" and also to provide initial conditions for particles for the downstream airfoil row which do not impact the airfoil. The statistics from the PPTAC analysis of the "Second Pass" are used to determine surface interaction statistics for erosion prediction and to provide initial conditions for subsequent airfoil rows for the particles which impact the airfoil before passing through the airfoil row.

The erosion results are obtained by dividing the pressure and suction sides of the airfoil into an equal number of segments. Surface impact statistics for each surface segment are generated from the "Second Pass" trajectory results. Erosion is determined from the sum of the

erosion values predicted for each impacting particle on each surface element. The predicted erosion rates are normalized with respect to the turbine inlet particle loading.

EROSION MODEL

The erosion model (equations 3 and 4) developed by Menguturk and Sverdrup (1977) is used to predict the erosion of the turbine airfoils. Menguturk's erosion model has the desirable features that (1) it has a single erosion maxima within the range of 0 to 90 degrees, (2) allows for finite erosion at 90 degrees and (3) requires relatively simple coding to reproduce the characteristic shapes of erosion vs. impact angle.

$$E = K_1*((V*\cos(B))^m)*\sin(n*B) + K_2*(V*\sin(B))^m \quad (5)$$
for $B < B_o$

$$E = K_1*(V*\cos(B))^m + K_2*(V*\sin(B))^m \quad (6)$$
for $B > B_o$

where:
- E = Erosion in cm^3/gram of erodent
- K_1 = Erosion constant = 2.1E-9
- K_2 = Erosion constant = 1.8E-10
- B = Impact angle relative to the surface in degrees
- m = Exponent for effect of velocity on erosion = 2.25
- n = $90.0/B_o$
- B_o = Constant to set B_{max}, B_o = 45 degrees
- B_{max} = Impact angle for maximum erosion = 30 degrees
- V = Velocity in m/sec

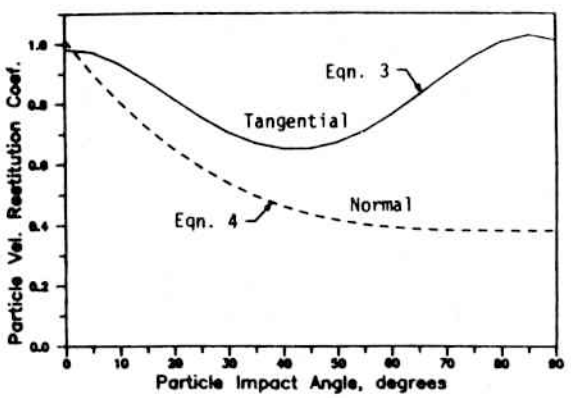


Figure 3. Generic Rebound Model.

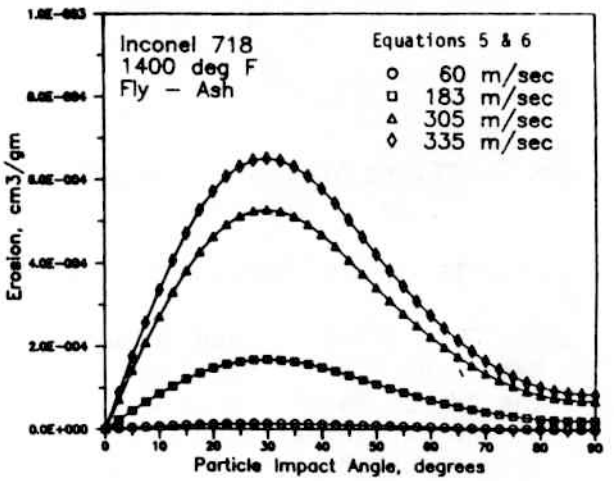


Figure 4. Adjusted Menguturk Erosion Model Sample Predictions.

The model has been adjusted to reflect the erosive characteristics of ash on nickel-based superalloys, typical of high performance, cooled turbine airfoils. The constants used are based on previously published studies and ongoing coal-fired combustion and turbine research. The erosion results used to adjust the model for this program were drawn

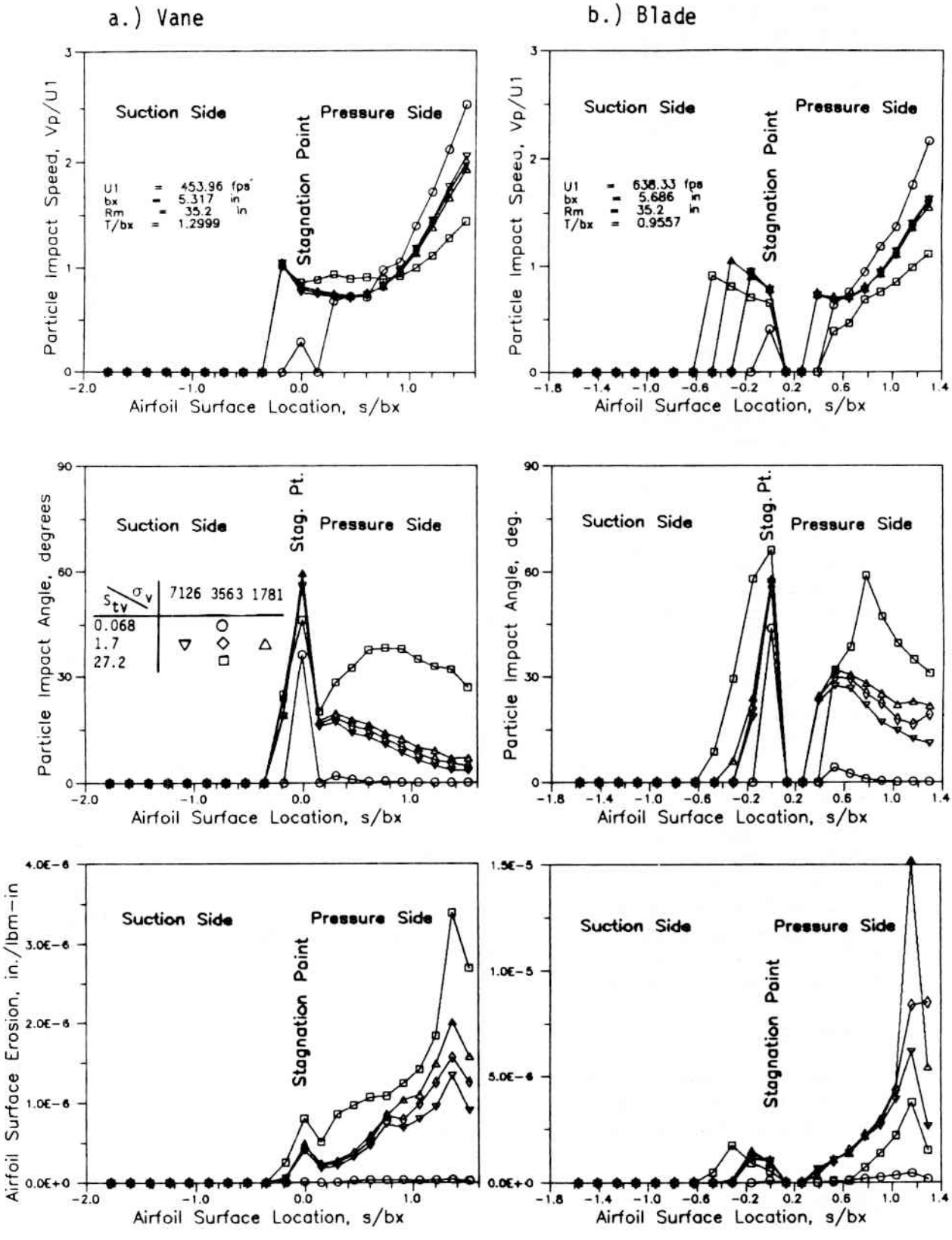


Figure 5. Average Impact Statistics and Predicted Erosion for Baseline Turbine.

primarily from the works by Levy, Tabakoff and coworkers and Beacher and Mansour (1986) because of their direct application to the utilization of coal combustion in energy producing systems. Predictions of erosion for a range of impact velocities and a range of impact angles using this model are shown in Figure 4. The shapes of the curves are typical of those for a ductile metal.

RANGES OF PARTICLE PARAMETERS

It is generally accepted that particles with diameters less than 5 μm pose little threat to turbine durability. However, particles leaving the combustor before any hot gas clean up can be as large as 100μm. Therefore, particle diameters of 5, 10, 25, 50 and 100 μm have been chosen for the turbine erosion analysis. Three particle densities of 1.25, 2.5 and 5 gm/cc will be used in the analysis to simulate the possible range of fly-ash density for a wide range of turbine scales. The corresponding Stokes, St, and particle density Reynolds numbers, σ_p, are 0.068, 0.272, 1.7, 6.8, 27.2 and 7126, 3563, 1781, respectively.

SURFACE STATISTICS AND EROSION

A total of 18,000 particle trajectories were calculated for the five Stokes numbers and three particle density Reynolds numbers. The post processing trajectory analysis code (PPTAC) was used to determine average surface statistics (average impact speed and angle), as well as, surface erosion rates adjusted for turbine inlet particle loading. Preliminary results of average impact statistics and predicted erosion rates for the vane and blade airfoil surfaces for the baseline turbine are shown in Figure 5. The interpretation of the results regarding estimated turbine life is currently in progress.

7. FUTURE WORK:

Midspan airfoils for three additional stages will be designed using the Pratt and Whitney Turbine Design System. Each stage includes one stationary vane row followed by one rotating blade row. The midspan airfoils will be designed using correlations for profile loss, secondary loss, blade tip leakage and incidence loss. Completed airfoil designs will be evaluated for characteristics of erosion using the UTRC Particle Trajectory and PPTAC analysis routines.

8. REFERENCES:

Beacher, B.F. and Mansour, M.L.: Erosion of a Coal-Burning Gas Turbine by Ash Particles. Turbomachinery Performance Deterioration. Edited by W. Tabakoff. ASME FED-Vol. 37, pp. 81-93, May 1986.

Dring, R.P., Caspar, J.R. and Suo, M.: Particle Trajectories in Turbine Cascades. AIAA Journal of Energy, Vol. 3, No. 3, pp. 161, May 1979.

Erosion Study in Turbomachinery Affected by Coal Ash Particles. Report FE-2465-13, Contract DE82-007059 (DOE/ET/10620-13), October 1981.

Levy, A. V.: The Erosion of Metal Alloys and Their Scales. Proceedings -Corrosion-Erosion-Wear of Materials in Energy Fossil-Energy Systems. Edited by A.V. Levy, DE83-009716 CONF-820144--, pp. 298-376, January 1982.

Levy, A.V.: Studies of Material Erosion in Coal Conversion. Fossil Energy Materials Program Conference Proceedings. US DOE/METC ORNL/FMP-87/4, pp. 467-491, August 1987.

Levy, A.V., Yan, J. and Patterson J.: Elevated Temperature Erosion of Steels. Wear, Vol. 108, pp. 43-60, 1986.

Menguturk, M. and Sverdrup, E.F.: Calculated Tolerance of a Large Electric Utility Gas Turbine to Erosion Damage by Coal Ash Particles. Erosion: Prevention and Useful Applications. Edited by W.F. Adler, ASTM STP664, pp. 193-224, October 1977.

Oates, G. C. (editor): The Aerothermodynamics of Aircraft Gas Turbine Engines. AFAPL-TR-78-52 Air Force Report, p. 18-4, July 1978.

Rosfjord, T. J.: Coal-Water Mixture Combustion Technology Development. Final Technical Report, DE-AC21-83MC-20404, May 1986.

Tabakoff, W.: Study of Particle Rebound Characteristics and Material Erosion at High Temperatures. Fossil Energy Materials Program Conference Proceedings. US DOE/METC ORNL/FMP-87/4, pp. 492-516, August 1987.

Tabakoff, W.: Erosion Behavior of Materials in Multiphase Flows. Proceedings - Corrosion-Erosion-Wear of Materials in Energy Fossil-Energy Systems. Edited by A.V. Levy, DE83-009716 CONF-820144--, pp. 642-676, January 1982.

Tabakoff, W., Hamed, A. and Ramachandran, J.: Study of Metals Erosion in High Temperature Coal Gas Streams. Transactions of ASME, Vol. 102, pp. 148-152, January 1980.

Tabakoff, W., Kotwal, R. and Hamed, A.: Erosion Study of Different Materials Affected by Coal Ash Particles. Wear, pp. 161-173, 1979.

Tabakoff, W. and Vittal, B.V.R.: High Temperature Erosion of Inco 600 Metal. Wear, Vol. 86, pp. 89-99, 1983.

Tabakoff, W., Hamed, A. and Eroglu, H.: Study of Particle Rebound Characteristics and Material Erosion at High Temperature. Final Report ORNL/Sub/84-89628/01, December 1987.

Tabakoff, W. and Malak, M.F.: Laser Measurements of Fly Ash Rebound Parameters for Use in Trajectory Calculations. Journal of Turbomachinery, Vol. 109, pp. 535-540, October 1987.

Wakeman, T. and Tabakoff, W.: Measured Particle Rebound Characteristics Useful for Erosion Prediction. ASME Paper 82-GT-170.

Wakeman, T. and Tabakoff, W.: Effect of Particle Rebound Characteristics on Erosion of Turbomachinery Components. ASME Paper 83-GT-169.

* U.S. GOVERNMENT PRINTING OFFICE: 1990--749-784/H5783